Lakehead University

The petrology, mineralization and regional context of the Thunder mafic to ultramafic intrusion, Midcontinent Rift, Thunder Bay, Ontario

Brent E. Trevisan

A thesis submitted to the Department of Geology in partial fulfillment of the requirements for the Degree Masters of Science

December 2014

ABSTRACT

The 1108 Ma Thunder mafic to ultramafic intrusion is a small, 800 x 100 x 500 m, Cu-PGE (platinum group element) mineralized body, located on the outskirts of Thunder Bay, Ontario, and associated with the early magmatic stages of the Midcontinent Rift (MCR) based on geochemical similarities to mafic and ultramafic rocks of the Nipigon Embayment and an unpublished $^{207}Pb/^{206}Pb$ zircon age of 1108.0 ± 1.0 Ma. The Thunder intrusion is similar to the other known mineralized early-rift MCR intrusions; however, it is the only known occurrence hosted by the metavolcanic and metasedimentary assemblages of the Archean Shebandowan greenstone belt. Major textural and geochemical differences can be used to subdivide the intrusion into a lower mafic to ultramafic basal unit and an upper gabbroic unit; the similar trace and rare earth element ratios of the two units suggest a single magmatic pulse that has undergone subsequent fractional crystallization and related cumulate phase layering. The estimated parental composition of the Thunder intrusion has a mg# ($MgO/(MgO + 0.9*FeO^T)$) of 57 which represents a more evolved magma than other early-rift mafic to ultramafic intrusions. This may indicate the involvement of multiple staging chambers during the accent of the parent magma.

Trace and rare earth element patterns are consistent with an ocean island basalt source but with indications of contamination such as high Th concentrations and the presence of a negative Nb anomaly. The εNd_T values from the intrusion range between - 0.7 and + 1.0, with no trends indicative of wall rock participation, whereas the $^{87}Sr/^{86}Sr_i$ ratios range from 0.70288 to 0.70611 and trend towards wall rock values of 0.70712 and 0.70873. The weak correlation between εNd_T and $^{87}Sr/^{86}Sr_i$ is also a feature of the Nipigon Sills where it has been interpreted to be due to shallow-level crustal contamination whereas plots of MgO and SiO_2 versus εNd_T indicate contamination at depth by an older crustal source.

Ni-Cu-PGE sulphide mineralization (20 m of 0.22 wt. % Cu, 0.06 wt. % Ni, 0.25 ppm Pt and 0.29 ppm Pd) is hosted by feldspathic peridotite in the lower mafic to ultramafic unit adjacent to the footwall of the Thunder intrusion. Sulphides typically occur from 1 - 5 modal %, rarely up to 30 modal %, with textures ranging from medium- to fine-grained disseminated, globular and rarely net-textured. Pyrrhotite, chalcopyrite and rare pentlandite with common secondary marcasite-pyrite replacement occur along with trace michenerite, kotulskite, merenskyite, sperrylite, hessite, electrum and argentian pentlandite. Whole rock geochemical data displays fractionated Ni-Cu-PGE patterns with depletion of iridium-platinum group elements (IPGE) relative to platinum-platinum group elements (PPGE).

Sulphide $\delta^{34}S$ values from the Thunder intrusion range from -2.0 to +3.8 ‰ and are similar to values for the metavolcanic host rock that range from -3.1 to +2.3 ‰. Two samples from the basal mineralization zone sulphides yield $\Delta^{33}S$ values of 0.066 and 0.122 ‰ and one sample from the metavolcanic wall rock yields 0.149 ‰. The $\delta^{34}S$ and $\Delta^{33}S$ values for the Thunder intrusion fall within range of typical upper mantle. The sulphur source appears to be of mantle origin, however, the assimilation of crustal sulphur is a possibility but hard to distinguish as the wall rock S isotope and S/Se^{T} signature is similar to that of upper mantle.

ACKNOWLEDGEMENTS

This study is a collaborative project between Lakehead University, the Geological Survey of Canada and the Ontario Geological Survey as part of the Ni-Cu-PGE-Cr project, Targeted Geoscience Initiative-4 (TGI-4) with funding provided by the Natural Resources Canada's Research Affiliate Program (RAP). In-kind whole rock geochemistry analyses were provided by the Ontario Geological Survey Geoscience Laboratories in Sudbury.

I want to first and foremost thank my Lakehead University supervisor Dr. Pete Hollings for all his assistance and guidance during my MSc studies. When applying to Lakehead University's MSc program, I approached Dr. Pete Hollings and said word for word: "I am interested in a project encompassing igneous petrology and associated ore deposits, and Thunder Bay regional geology". As luck would have it, he was able to find me a project that suited my interest. The Thunder intrusion was a perfect candidate satisfying all that I asked for.

I want to thank my TGI-4 supervisor Dr. Doreen E. Ames from the Geological Survey of Canada for all her assistance and guidance during my MSc project. Having a 'third-party' supervisor really helped in sense of sticking to the TGI-4's research objectives and seeing the MSc project to its fullest potential.

Next I would like to thank Dean Rossell from Rio Tinto. Apart from his involvement with facilitating access to the mineral claims, Dean provided valuable input throughout my MSc study by an exploration standpoint.

Big thanks to Dr. Jim Miller from the University of Minnesota Duluth who presented me with the opportunity to run a field trip out to the Thunder intrusion in contribution to the UMD's Precambrian Research Center workshop series on Cu-Ni-PGE deposits of the Lake Superior Region in fall 2013. This workshop helped out significantly with advancing my research and understanding of Ni-Cu-PGE magmatic sulphide exploration.

Special thanks to the following individuals for their volunteered and in-kind assistance throughout my MSc study: Jason Freeburn from Lakehead University's Geography Department, Rob Cundari, Mark Puumala, Dorothy Campbell, and Stuart Dunlop from the Resident Geologist Program, Ontario Geological Survey, Geoff Heggie from Panoramic Resources Ltd., and Anne Hammond and Kristi Tavener from Lakehead University's Geological Laboratories.

A shout out to the "Gabbros" of CB 3032: Ben Kuzmich, Wes Lueck, and Ayat Baig for being such great colleagues and friends. We all started our MSc's around the same time and encouraged each other to finish.

Last but not least, the rest of my colleagues for making LU a friendly working environment; and, Julie Vilcek, Mom and Dad, friends and family for all their support.

TABLE OF CONTENTS

ABSTRACT ii
ACKNOWLEDGEMENTS iv
TABLE OF CONTENTS v
LIST OF FIGURES ix
LIST OF TABLES xii
LIST OF ABBREVIATIONS xiii
1. INTRODUCTION 1
1.1 Background 1
1.2 Objectives 4
2. REGIONAL GEOLOGY 5
2.1 The Superior Province 5
2.2 The Shebandowan greenstone belt 7
2.3 The Quetico Subprovince 9
2.4 Paleoproterozoic sedimentary rocks 10
2.5 Mesoprotereozoic sedimentary rocks 10
2.6 The Mesoproterozoic Midcontinent Rift 12
2.6.1 Overview, geologic setting and structure 12
2.6.2 The Keweenawan Super Group 16
2.6.3 The Midcontinent Rift Intrusive Supersuite 19
2.6.3.1 Subvolcanic intrusive complexes 19
2.6.3.2 Alkaline and carbonatite intrusions 20
2.6.3.3 Mafic dike and sill swarms 20
2.6.3.4 Mafic to ultramafic intrusions 21
2.6.4 The current tectono-magmatic model of the Midcontinent Rift 23
2.7 Exploration history of the Gorham Township and vicinity 27
2.8 The discovery of Ni-Cu-PGE mineralization 29
2.9 The Thunder intrusion and vicinity 31
3. METHODOLOGY 34
3.1 Location and access 34
3.2 Field work 35

3.2.1 Introduction 35
3.2.2 Geological mapping of the Thunder intrusion and vicinity 35
3.2.3 Re-logging of the available diamond drill core 36
3.2.4 Sampling procedure and locations 36
3.3 Analytical methods 37
3.3.1 Introduction 37
3.3.2 Whole-rock geochemistry 37
3.3.3 Rb-Sr and Sm-Nd isotope analysis 38
3.3.4 S isotope analysis 39
3.3.5 As, Bi, Sb, Se, Te analysis 41
3.3.6 SEM-EDS analysis 41
3.3.7 Electron microprobe 41
4. RESULTS 44
4.1 Introduction 44
4.2 The Thunder intrusion geological map 44
4.2.1 The Thunder mafic to ultramafic intrusion 44
4.2.2 Contact relationships 49
4.2.3 The marginal country rock 51
4.2.5 North-trending gabbroic dikes 54
4.3 Core logging 57
4.3.1 Diamond drill hole 05TH001 57
4.3.2 The northern margin diamond drill holes 60
4.3.3 Diamond drill holes within the core of the Thunder intrusion 64
4.3.3.1 Diamond drill hole 07TH006 67
4.3.3.2 Other intrusive units 68
4.3.4 Geological cross-section 69
4.4 Petrography 70
4.4.1 Lower mafic to ultramafic unit 71
4.4.2 Upper gabbroic unit 73
4.4.3 Pegmatitic gabbro 75
4.5 Alteration 77

4.5.1 Alteration veins within the Thunder intrusion 77
4.5.2 Contact metamorphism 81
4.6 Mineralization 82
4.6.1 The basal mineralization zone 84
4.6.2 Pyrrhotite-rich massive sulphide veinlet 87
4.6.3 Sulphide stringers 89
4.6.4 The upper mineralized zone 91
4.6.5 Chalcopyrite-rich massive sulphide veinlets 93
4.6.6 Sulphide-bearing wall rock 95
4.6.7 Platinum-group minerals and Au- Ag-minerals 95
4.7 Olivine chemistry 101
4.8 Whole Rock Geochemistry 104
4.8.1 Down-hole variations in major element geochemistry of the Thunder intrusion 105
4.8.2 Harker variation diagrams of the Thunder intrusion 111
4.8.3 Trace and rare earth element geochemistry of the intrusive rocks 111
4.8.4 Metal patterns and correlations of the Thunder intrusion 120
4.9 Sulphur isotopes and Se/S ratios 124
4.10 Radiogenic isotopes 129
5. DISCUSSION 131
5.1 Introduction 131
5.2 Petrology of the Thunder intrusion 132
5.2.1 Correlation of the intrusive units comprising the Thunder intrusion 132
5.2.2 Relative timing of emplacement 133
5.2.3 An Archean greenstone belt host rock 133
5.2.4 Cumulate stratigraphy and mineral paragenesis 137
5.3.5 Mantle source and contamination 140
5.2.6 Estimate of the parent magma composition 149
5.3 Mineralization within the Thunder intrusion 156
5.3.1 Ni-Cu-PGE ± Au, Ag magmatic sulphide mineralization 156
5.3.2 Fractionation controls on Ni-Cu-PGE patterns 158
5.3.3 Sulphur source 161

5.4 The Thunder intrusion and the Midcontinent Rift 167
5.4.1 The emplacement model 167
5.4.2 An early-rift mafic to ultramafic intrusion 169
5.4.3 Relative timing of emplacement of the N-trending gabbroic dikes 170
5.4.4 The cross-cutting mafic dikes 172
6. CONCLUSIONS 174
6.1 Summary of the Thunder intrusion 174
6.1.1 Petrology 174
6.1.2 Mineralization 175
6.2 Closing remarks 176
6.3 Future work 177
REFERENCES 179
APPENDICS
A. Representative petrographic descriptions 196
B. Mineral chemistry from sulphide mineralization analysis 235
C. Mineral chemistry from olivine analysis 258
D. Whole rock geochemistry (major and trace element) 263
E. Whole rock geochemistry (metals) 281

LIST OF FIGURES

Figure 1.1: Geological map of the greater Thunder Bay area 3
Figure 2.1: Geological map showing the regional geology 6
Figure 2.2: Geological map of the Shebandowan greenstone belt 8
Figure 2.3: Bouger gravity field of the Midcontinent Rift, Lake Superior region 13
Figure 2.4: Midcontinent Rift geology, Lake Superior region 14
Figure 2.5: Paleomagnetic polarity and magmatic stages of the Midcontinent Rift..... 18
Figure 2.6: Tectono-magmatic model of the Midcontinent Rift..... 26
Figure 2.7: First vertical magnetic field of the Thunder intrusion region 32
Figure 4.1: Geological map of the Thunder intrusion and vicinity 46
Figure 4.2: Representative photographs of the lower mafic to ultramafic unit 47
Figure 4.3: Representative photographs of the upper gabbroic unit..... 48
Figure 4.4: Representative photographs of the pegmatitic gabbro phase 49
Figure 4.5: Representative photographs contact relationships in the field 50
Figure 4.6: Representative photographs of the country rock..... 52
Figure 4.7: Representative photographs of the eastern N-trending gabbroic dike 55
Figure 4.8: Representative photographs of the western N-trending gabbroic dike 56
Figure 4.9: Lithostratigraphy of diamond drill holes 05TH001, 002 and 003..... 58
Figure 4.10: Representative photographs from diamond drill hole 05TH001..... 60
Figure 4.11: Representative photographs from diamond drill hole 05TH002..... 62
Figure 4.12: Representative photographs from diamond drill hole 05TH003..... 63
Figure 4.13: Lithostratigraphy of diamond drill holes 07TH004, 005, 006 and 007..... 65
Figure 4.14: Representative drill core photos from diamond drill hole 07TH004 66
Figure 4.15: Representative photographs from diamond drill hole 07TH006..... 68
Figure 4.16: Representative photographs from diamond drill hole 07TH007..... 69
Figure 4.17: Geological cross-section of the Thunder intrusion 70
Figure 4.18: Representative photomicrographs of the lower mafic to ultramafic unit..... 72
Figure 4.19: Representative photomicrographs of the upper gabbroic unit 74
Figure 4.20: Representative photomicrographs of the pegmatitic gabbro phase..... 76
Figure 4.21: Summary of petrographic observations..... 78
Figure 4.22: Representative photographs of the secondary alteration features 79

Figure 4.23: Representative photomicrographs of the alteration veins 80
Figure 4.24: Photomicrographs of the basal contact..... 82
Figure 4.25: Sulphide textures in the basal mineralization zone 85
Figure 4.26: Sulphide textures outside the basal mineralization zone and hosted by the lower mafic to ultramafic unit 86
Figure 4.27: Sulphide textures of the chalcopyrite-rich massive sulphide veinlet in diamond drill hole 05TH003 88
Figure 4.28: Sulphide textures of the sulphide stringer veins..... 90
Figure 4.29: Sulphide textures of the upper mineralized zone 92
Figure 4.30: Sulphide textures of the chalcopyrite-rich massive sulphide veins..... 94
Figure 4.31: Sulphide textures of wall rock mineralization..... 96
Figure 4.32: Back-scattered electron images of the basal mineralization zone..... 98
Figure 4.33: Back-scattered electron images of the pyrrhotite-rich massive sulphide veinlet 99
Figure 4.34: Precious metal minerals in the chalcopyrite-rich massive sulphide veinlets 100
Figure. 4.35: Plot of NiO versus % Fo olivine 104
Figure 4.36: Major elements plotted against the depth and simplified lithostratigraphy of diamond drill hole 07TH004 109
Figure 4.37: Harker variation diagrams..... 113
Figure 4.38: Plot of La/Sm_n versus Gd/Yb_n for the intrusive rocks 115
Figure 4.39: Primitive mantle normalized profiles for the intrusive rocks..... 117
Figure 4.40: Plot of whole rock base metals versus total sulphur 122
Figure 4.41: Primitive mantle normalized whole rock Ni-PGE-Cu profiles 125
Figure 4.42: Histogram of $\delta^{34}S$ values..... 128
Figure 4.43: Histogram of $Se/S^T \times 10^6$ ratios 128
Figure 5.1: Primitive mantle normalized profiles plotted against the simplified lithostratigraphy of diamond drill hole 07TH004 134
Figure 5.2: Select high field strength elements, La/Sm_n and Gd/Yb_n plotted against the simplified lithostratigraphy of diamond drill hole 07TH004 135
Figure 5.3: The cumulate stratigraphy of diamond drill hole 07TH004..... 139
Figure 5.4: Primitive mantle normalized profiles for the Thunder intrusion and typical ocean-island basalt 141

Figure 5.5: Primitive mantle normalized profiles for the Seagull and Thunder intrusion 142
Figure 5.6: Plot of La/Sm versus Th 143
Figure 5.7: Plot of εNd_T versus $^{87}Sr/^{86}Sr_i$ for the Thunder intrusion and wall rock 144
Figure 5.8: Plot of εNd_T versus $^{87}Sr/^{86}Sr_i$ for the Thunder intrusion and Nipigon sills 145
Figure 5.9: Plot of εNd_T versus $^{87}Sr/^{86}Sr_i$ for the Thunder intrusion and regional geology 146
Figure 5.10: Plot of εNd_T versus SiO_2, and MgO 148
Figure 5.11: Olivine % Fo plotted against lithostratigraphy of diamond drill hole 07TH004 .. 151
Figure 5.12: Crystallization trends modelled in PELE 153
Figure 5.13: Histogram illustrating the distribution of filtered $Se/S^T \times 10^6$ ratios 166
Figure 5.14: Plot of $Se/S^T \times 10^6$ versus δ34S 166
Figure 5.15: Airborne total magentic field of the Thunder intrusion region 168
Figure 5.16: Plot of La/Sm_n versus Gd/Yb_n for the Thunder intrusion and intrusive rocks of the Nipigon Embayment 170
Figure 5.17: Primitive mantle normalized profiles for the Nipigon Sill Complex, and the eastern and western N-trending gabbroic dike 172
Figure 5.18: Primitive mantle normalized profiles for the Marathon dike swarm, and the eastern and western N-trending gabbroic dike 172

LIST OF TABLES

Table 1.1: Representative grades of the Thunder intrusion and select early-rift mafic to ultramafic intrusions within the Lake Superior region. 4
Table 2.1: Location and depth of diamond drill cores completed in 2005 29
Table 2.2: Location and depth of diamond drill cores completed in 2007 29
Table 2.3: Significant drill intercepts reported by the 2005 drill program 30
Table 2.4: Significant drill intercepts reported by the 2007 drill program 30
Table 3.1: Operating conditions and standards for sulphide chemistry analysis 42
Table 3.2: Operating conditions and standards for olivine analysis 43
Table 4.1: Summary of sulphide minerals identified 83
Table 4.2: Summary of platinum-group minerals and precious-metal minerals identified 100
Table 4.3: Summary of olivine chemistry analysis 102
Table 4.4: Representative whole rock analyses for the intrusive rocks 106
Table 4.5: Whole rock metals and total sulphur analyses from diamond drill hole 07TH004 .. 121
Table 4.6: Summary of sulphur isotope analysis 126
Table 4.7: Whole rock As, Bi, Sb, Se, Te, total S and Se/S^T ratios 127
Table 4.8: Summary of radiogenic isotope analysis 130
Table 5.1: Estimated parent magma composition for the Thunder intrusion 152
Table 5.2: Summary of output data from PELE 156
Table 5.3: Representative metal grades of the basal mineralization zone 157

LIST OF ABBREVIATIONS

Ag-Cp	Silver-rich chalcopyrite
Ag-Pn	Argentian pentlandite
Amph	Amphibole
Apt	Apatite
(Au,Ag)	Electrum
Bt	Biotite
BMZ	Basal mineralization zone
Bn	Bornite
Cal	Calcite
Chl	Chlorite
Cp	Chalcopyrite
Cpx	Clinopyroxene
DDH	Diamond drill hole
DLGC	Dog lake granite chain
Fe-Ox	Iron oxide
Fe-Ti Ox	Iron-titanium oxide
Fm.	Formation
Fo	Forsterite
FWS	Footwall stringers
FWV	Footwall veins
Gn	Galena
Grt	Garnet
Hes	Hessite
HFSE	High field strength element
Ilm	Ilmenite
IPGE	Iridium-platinum group elements

Kt	Kotulskite
LIP	Large igneous province
MagSus	Magnetic susceptibility
Mch	Michenerite
MCR	Midcontinent Rift
Mil	Millerite
Mrc	Marcasite
MNDM	Ministrty of Northern Development and Mines
MSS	Monosulphide solid solution
Mt	Magnetite
Nal	Naldrettite
NiS	Millerite
NLPG	Nothern Lights-Perching Gull
OIB	Ocean island basalt
PGM	Platinum group mineral
Plag	Plagioclase
PMM	Precious metal mineral
Pn	Pentlandite
Po	Pyrrhotite
PPGE	Platinum-platinum group elements
Py	Pyrite
REE	Rare earth element
SGB	Shebandowan greenstone belt
Sp	Sperrylite
Sph	Sphalerite
UMZ	Upper mineralized zone

CHAPTER 1

INTRODUCTION

1.1 Background

The northern Lake Superior region is host to a large segment of the North American Mesoproterozoic Midcontinent Rift (MCR). Although considerable debate has arisen over the past decade in regards to the orgin and evolution of the rifting event, there is a general acceptance that the rifting `was influenced by the impact of a starting mantle plume around 1115 Ma followed by ~ 30 million years of magmatism (Miller and Nicholson, 2013, and references therein). The geological units formed during the evolution of the MCR consist of two major groupings: stratified volcanic and sedimentary rocks collectively known as the Keweenawan Supergroup (Morey and Green, 1982) and an intrusive igneous rock suite termed the Midcontinent Rift Intrusive Supersuite (Miller et al., 2002a, b; Hollings et al., 2007a).

In 2002, high grade massive Ni-Cu-PGE sulphide mineralization was discovered at the Eagle deposit near Marquette, Michigan, stimulating exploration programs in search of small mafic to ultramafic intrusions hosting "conduit-type" magmatic sulphide mineralization associated with the initiation and early stages of the MCR evolution (Ripley and Li, 2011). Since the Eagle discovery, over a half-dozen poorly exposed mineralized early-rift mafic to ultramafic intrusion have been discovered within the Lake Superior region prompting active petrological research (e.g., Heggie, 2005; Hollings et al., 2007a, b; Ding et al., 2010; Goldner, 2011; Foley, 2011) and re-evaluation of the current MCR tectono-magmatic model (Heaman et al., 2007; Hollings et al., 2010; Miller and Nicholson, 2013). However, from an exploration standpoint the small size of these buried mineralized ultramafic intrusions makes them difficult

to locate both on the ground and from regional magnetic survey maps; exploration often requiring a large investment in diamond drilling core programs (Ames et al., 2012).

The Thunder intrusion is a small, mineralized, mafic to ultramafic intrusion located on the outskirts of the City of Thunder Bay, which was explored by Rio Tinto (formerly Kennecott Canada Exploration Inc.) in 2005 and 2007 (Fig. 1.1; Bidwell and Marino, 2007). Early investigations interpreted this intrusive body to be an early-rift occurrence based on geochemical similarities with the mafic to ultramafic intrusive units of the Nipigon Embayment (e.g., Hele intrusion and Shillabeer Sill; Hollings et al., 2007a; Rossell, pers. comm.., 2012). The Thunder intrusion is distinct from other mineralized early-rift intrusions as it is the only known occurrence hosted in the metavolcanic and metasedimentary rocks of the Archean Shebandowan greenstone belt (Ames et al., 2012). Other early-rift intrusions north of the Canada-United States border, including Current Lake and Seagull, intrude the Archean Quetico metasedimentary subprovince and/or Mesoproterozoic Sibley Group (Heggie, 2005; MacTavish, 2013). South of the Canada-United States border, intrusions such as Eagle, Bovine Igneous Complex (BIC) and Tamarack intrude Paleoproterozoic sedimentary rocks of the Animikie and Baraga basin (Ding et al., 2010; Foley, 2011; Goldner, 2011).

The Thunder intrusion is characterized by consistently lower nickel grades than other early-rift intrusions such as Tamarack, Eagle, BIC, Current Lake, Sunday Lake and Seagull (Table 1.1). Nickel grades for the Thunder intrusion from mineralized zones are at least one order of magnitude less than representative grades of the other intrusions (Table 1.1), while Cu, Pd and Pt grades are similar however.

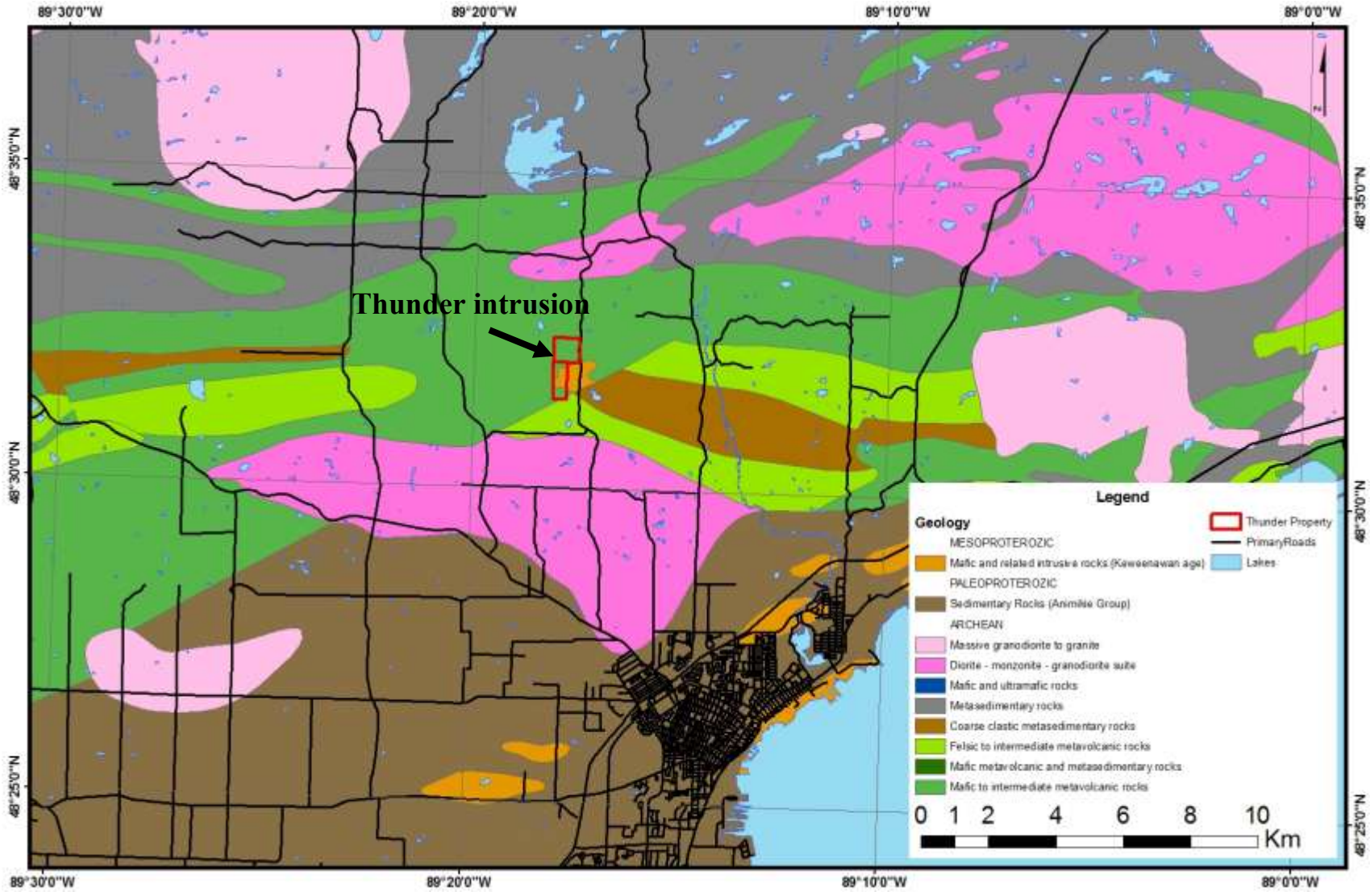

Figure 1.1: Geological map of the greater Thunder Bay area including major road networks and outline of the current mineral claims that enclose the Thunder intrusion. The Thunder intrusion is located on the outskirts of the City of Thunder Bay, within Gorham Township and situated within the eastern limb of the Archean Shebandowan greenstone belt. Geospatial data from OGS (2011).

Table 1.1: Representative grades of select early-rift mafic to ultramafic intrusions hosting Ni-Cu-PGE sulphide mineralization within the Lake Superior region including the Thunder intrusion.

Intrusion	Interval (m)	Ni (%)	Cu (%)	Pd (ppm)	Pt (ppm)	Reference
Thunder	20.0	0.06	0.22	0.25	0.29	Bidwell and Marino (2007)
Current Lake	14.0	1.20	3.50	13.90	16.20	MacTavish et al. (2013)
Sunday Lake	20.2	0.11	0.26	0.95	2.11	Transition Metals (2014)
Seagull	10.5	0.15	0.17	0.37	0.39	Avalon (2001)
Tamarack	10.3	7.01	2.89	0.07	1.51	Rio Tinto (2008)
BIC	16.5	1.00	0.88	0.10	0.68	Rossell (2008)
Eagle*	average	3.57	2.91	0.47	0.73	Rossell and Coombes (2005)

* = Eagle deposit is reported as an average grade for the geologic resource estimate of 4.05 million tonnes.

1.2 Objectives

This MSc study was conducted in collaboration between Lakehead University, the Geological Survey of Canada and the Ontario Geological Survey as part of the TGI-4 Ni-Cu-PGE-Cr project with additional funding provided by the Natural Resources Canada's Research Affiliate Program. The objectives of this study were to 1) characterize the petrology of the Thunder intrusion, 2) define the mineralogical and geochemical signature of the Thunder intrusion and PGE mineralization, 3) characterize the alteration footprint of the intrusion in the surrounding country rocks, and 4) establish practical mineralogical and geochemical exploration criteria for hidden early-rift mafic to ultramafic intrusions hosting magmatic Ni-Cu-PGE sulphide mineralization by relating the characteristics of the intrusion to other fertile and barren intrusive units within the MCR. In addition, this study aimed to establish the age of the intrusion using U-Pb zircon/ baddeleyite and place it within the context of the MCR event. In-kind analytical support was provided by the Ontario Geological Survey Geoscience Laboratories in Sudbury. The mineral claims are currently held by Rio Tinto Exploration Canada Inc. (formerly Kennecott Canada Exploration Inc.), and access for this study was granted by Dean Rossell, Rio Tinto.

CHAPTER 2

REGIONAL GEOLOGY

2.1 The Superior Province

The Superior Province is the world's largest Archean craton covering ~ 1,572,000 km^2 and comprising 23 % of the planet's exposed Archean crust (Thurston, 1991). The formation of the Archean craton has been interpreted to be the result of multiple accretionary events between 2.72 and 2.68 Ga, collectively termed the Kenoran Orogeny (Percival, 2003). Traditionally, the Superior Province has been subdivided into a series of E-trending elongate subprovinces with a general southward younging direction based largely on the dominant lithology present (Card and Ciesielski, 1986). The subdivisions include volcano-plutonic (granite-greenstone), gneissic (plutonic), metasedimentary, and high-grade gneiss terranes, all of which have been metamorphosed to between greenschist and granulite facies (Card and Ciesielski, 1986; Thurston, 1991; Percival, 2003). The margins of the Superior Province are bounded to the north and west by the Trans-Hudson orogeny, to the south by the Penokean orogeny, to the northeast by the New Quebec orogeny, and to the southeast by the Grenville orogeny (Hoffman, 1989). Stott et al. (2010) have recently proposed modifications to the Superior Province tectonic map building on the framework of Card and Ciesielski (1986) and adopting a subdivision scheme based on the concept of terrane and domain boundaries. However, for the purpose of a consistent geologic reference within the Superior Province, the widely accepted subdivisions originally established by Card and Ciesielski (1986) will be used in this thesis.

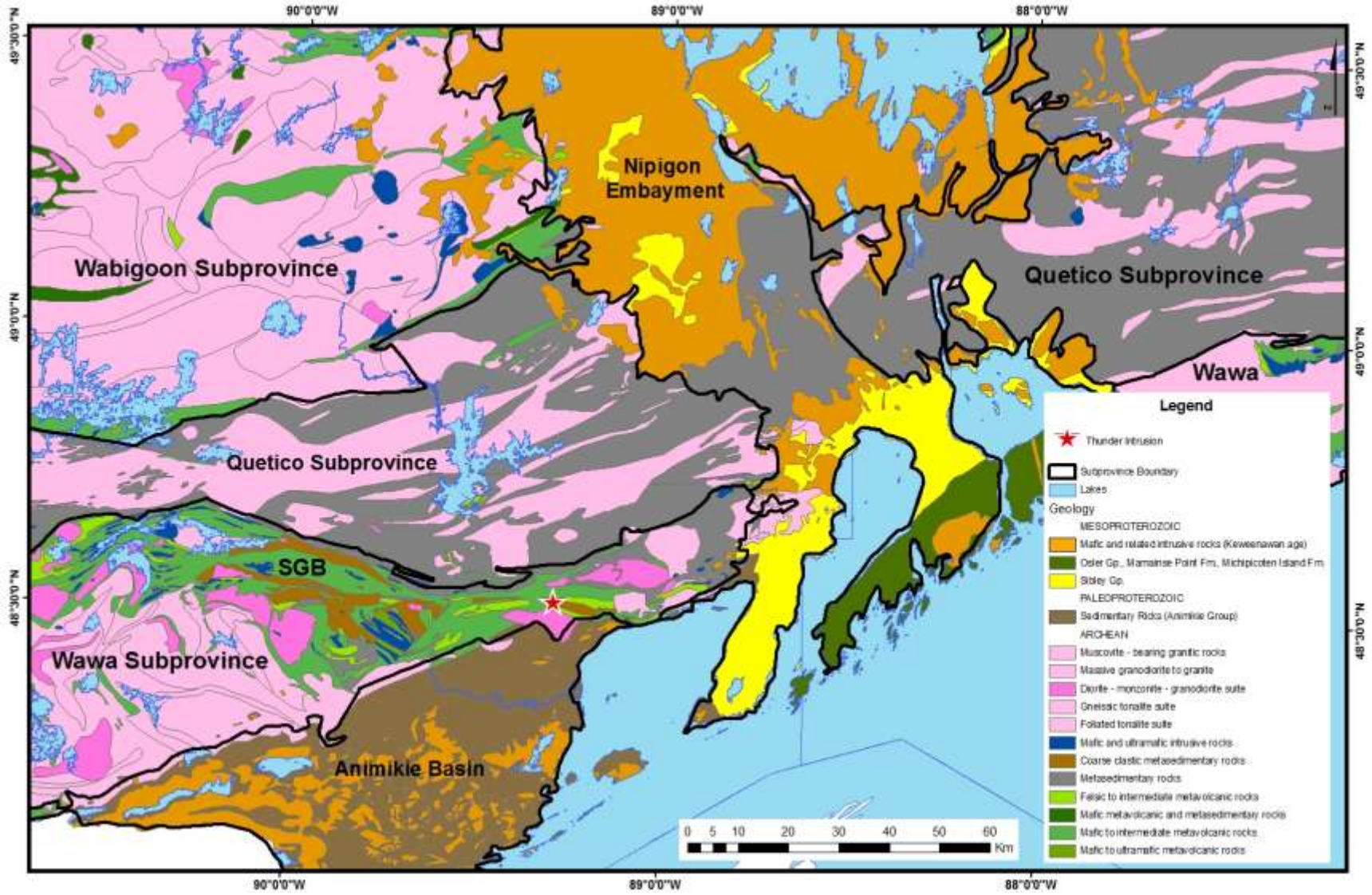

Figure 2.1: Geological map showing the major geological units of the Lake Superior region north of the Canada-USA border and the major subdivisions of the Superior Province. The location of the study area is indicated by the red star. Geospacial data from OGS (2011). Abbreviations: SGB = Shebandowan greenstone belt

2.2 The Shebandowan greenstone belt

The Shebandowan greenstone belt (SGB) comprises the westernmost section of the Wawa Subprovince in Northwestern Ontario and is a semi-continuous chain of two E-NE-trending granite-greenstone belts of similar age: the Shebandowan and Saganagons greenstone belts (Figs. 2.1, 2.2; Williams et al., 1991; Corfu and Stott, 1998). The SGB is located west of the City of Thunder Bay, ON and extends 200 km to northeastern Minnesota, where it is bounded to the north by the Quetico metasedimentary subprovince and to the south by the Northern Lights-Perching Gull Lake (NLPG) batholiths complex and unconformably overlain to the east and southeast by Paleoproterozoic strata of Animikie basin (Fig. 2.2; Williams et al., 1991).

Geochronological studies of the SGB (e.g., Corfu and Stott, 1988; Lodge, 2012) have defined three main supracrustal assemblages: the Greenwater assemblage (ca. 2720 Ma), the Kashabowie assemblage (ca. 2695 Ma) and the Shebandowan assemblage (ca. 2690-2680 Ma). The supracrustal assemblages are represented by mafic metavolcanic rocks that are extensive and variable in texture and composition, intermediate to felsic metavolcanic rocks, and coarse clastic rocks consisting predominantly of turbiditic wackes, sandstones and conglomerate (Fig. 2.2; Lodge 2010, 2011, 2013); interpreted to have been deposited in a submarine island arc to rifted arc tectonic environment (e.g., Osmani, 1996; Corfu and Stott, 1998; Hart and Trebilcock, 2006). These assemblages are structurally deformed and commonly intruded by gabbroic, and locally anorthositic to ultramafic sills (Williams et al., 1991). Metamorphism grades from lower greenschist to lower amphibolite facies with local contact metamorphic aureoles surrounding Archean plutons (Williams et al., 1991).

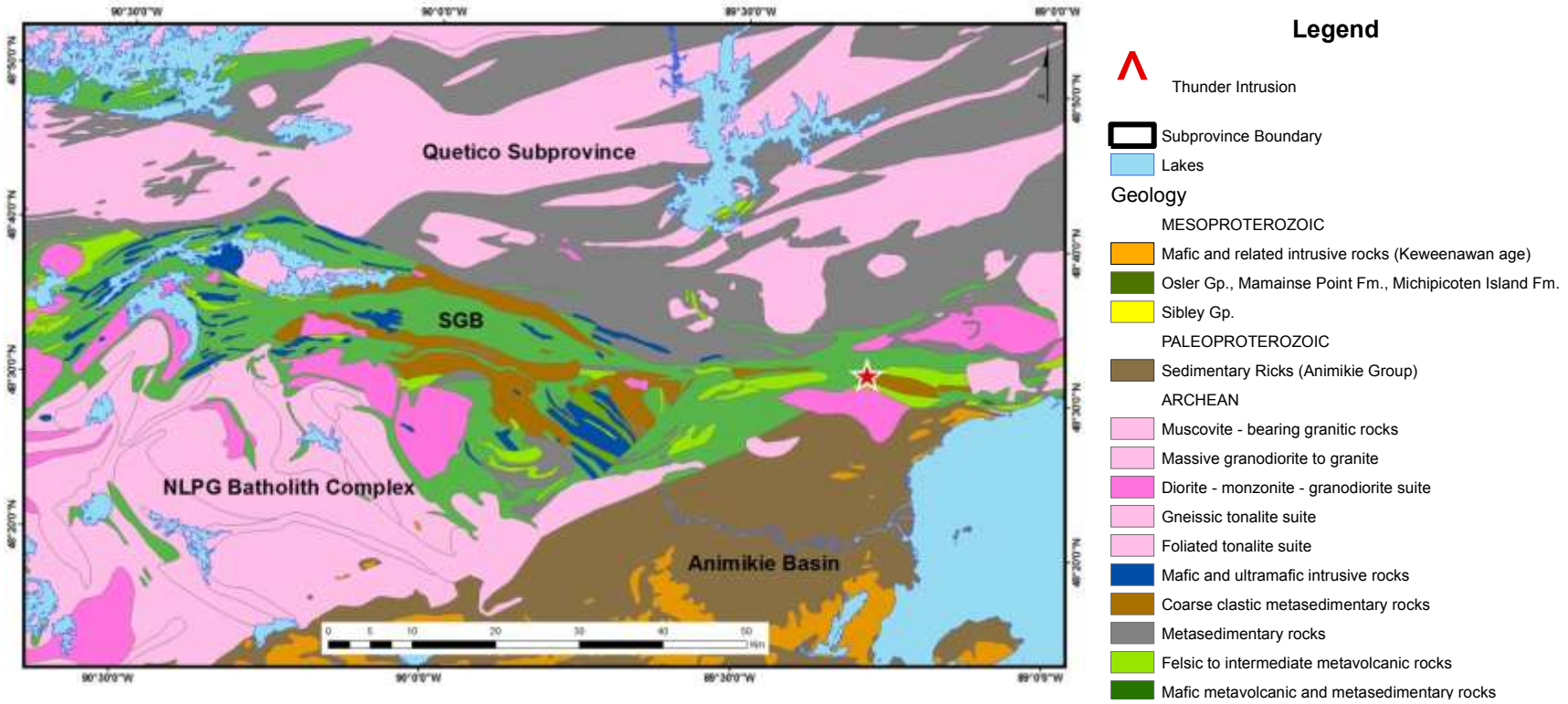

Figure 2.2: Geological map of the Shebandowan greenstone belt. The Thunder intrusion is situated within the eastern limb of the greenstone belt as indicated by the red star. Geospatial data from OGS (2011). Abbreviations: SGB = Shebandowan greenstone belt; NLPG = Northern Light – Perching Gull Lake batholith complex.

2.3 The Quetico Subprovince

The Quetico Subprovince is a metasedimentary subprovince of the Superior Province extending from southwestern Minnesota and eastwards 1000 km across Ontario where it terminates at the Kapuskasing Structural Zone (Fig. 2.1; Williams, 1991). Structurally, the Quetico Subprovince has been interpreted as an accretionary prism wedged between two granite-greenstone subprovinces: the Wawa Subprovince to the south and the Wabigoon Subprovince to the north; however, due to lack of exposure the nature of the boundaries is uncertain (Fig. 2.1; Williams, 1991). Rocks of the westernmost extension of the Quetico Subprovovince are located 5 km north of the study area and as previously discussed, structurally overly rocks of the SGB (Fig. 2.1).

The Quetico Subprovince comprises a supracrustal sequence consisting dominantly of wacke and pelite metamorphosed to schist, paragneiss and migmatite (Card and Ciesielski, 1986). Relict sedimentary features are akin to turbidite fans deposited in a submarine basin of considerable extent (Fralick et al., 2006). The time of deposition is constrained by the youngest U-Pb detrital zircon age at 2698 Ma (Davis et al., 1990) and U-Pb zircon of the oldest intrusion at 2688 Ma (Zaleski et al., 1999).

Abundant S-type granitoids and pegmatites derived from anatexis of sedimentary rock intrude the metasedimentary rocks (Williams et al., 1991); with local I-type granitoids represented by the Dog Lake Granite Chain (DLGC; Kuzmich et al., 2012). The DLGC comprises multiple granitoid plutons including the Shabaqua, Silver Falls, Trout Lake, Barnum Lake, Penasen Lake and White Lily intrusions all of which are located north of the study area (see section 2.7).

2.4 Paleoproterozoic sedimentary rocks

The Penokean Orogeny began at ~ 1880 Ma (lasting until ~ 1830 Ma) when an oceanic arc, the Pembine-Wausau terrane, collided with the southern margin of the Superior Craton (Schulz and Cannon, 2007). During this period of collision, southward dipping subduction led to back arc extension and the development of the Animikie Basin (Fralick et al., 2002). The Animikie Basin is represented by an undeformed, unmetamorphosed Paleoproterozoic sedimentary sequence consisting of iron formation, chert and argillite unconformably overlain by shales and greywackes (Sutcliffe, 1991; Schulz & Cannon, 2007). The rocks are collectively referred to as the Gunflint Formation and Rove Formation, respectively, which together comprise the Animikie Group. The Gunflint Formation reaches a thickness of ~ 130 m (Moorhouse, 1960), whereas the Rove Formation is ~ 500 m thick and thickens southwards to ~ 600 m (Geul, 1973). U-Pb geochronology yielded a detrital zircon age of 1878.3 ± 1.3 Ma using material from a reworked volcanic ash layer in the upper section of the Gunflint Formation (Fralick et al., 2002). The unconformity between the two units is marked by the 1850 Ma Sudbury ejecta layer (Addison et al., 2005). Tuffaceous beds in the basal Rove Formation have yielded U-Pb zircon ages of 1836 ± 5 and 1832 ± 3 Ma and a minimal U-Pb detrital zircon age of ~ 1780 Ma sampled 400 m up-section (Addison et al., 2005; Heaman & Easton, 2006). Rocks of the Animikie Group unconformably overlie Archean basement rocks to the south of the study area forming the bedrock geology of the City of Thunder Bay, ON (Fig 2.1).

2.5 Mesoprotereozoic sedimentary rocks

Mesoproterozoic sedimentary rocks in the northern Lake Superior region are represented by the Sibley Group which unconformably overlie Archean basement rocks and the Paleoproterozoic Animikie Group. The Sibley Group covers an ~ 175 x 400 km surface area and

exceeds a thickness of 950 m exposed from the northwest shore of Lake Superior to the Lake Nipigon region (Fig. 2.1; Rogala et al., 2007). The Sibley Group is a relatively flat-lying sedimentary sequence of siliciclastic and chemical sedimentary rocks consisting of five conformable stratigraphic units from bottom to top: the Pass Lake Formation, the Rossport Formation, the Kama Hill Formation, the Outan Island Formation and the Nipigon Bay Formation (Rogala et al., 2007). Age constraints on the deposition of the Sibley Group obtained through U-Pb detrital zircons and stratigraphic correlations include a maximum age of ~ 1770 Ma for the Pass Lake Fm, a maximum age of ~ 1440 Ma for the Outan Island Fomration and Nipigon Bay Formation. (Rogala et al., 2007), and a minimum age for the Nipigon Bay Formation obtained from the erosively overlying Osler Volcanic Group of the Mesoproterozoic Midcontinent Rift at ~ 1108 Ma (Davis and Sutcliffe, 1985). The current interpretation of the depositional environment holds that the Sibley Group sediments were deposited in a half graben controlled basin inferred to be the result of large-scale subsidence following the ~ 1550 Ma mantle plume event which produce the English Bay Complex (Rogala et al., 2007; Heaman et al., 2007). Climatic conditions fluctuated during deposition, beginning with a lacustrine system (Pass Lake Fm.) that gradually evolved into a saline playa lake environment (Rossport Fm.), and into a sabka-type-environment (Kama Hill Fm.; Rogala, 2003; Rogala et al., 2005; Rogala et al., 2007). The Outan Island Formamation represents the transition from subaqueous to subaerial conditions with the Nipigon Bay Fomation representing an aeolian environment (Rogala, 2003; Rogala et al., 2007).

2.6 The Mesoproterozoic Midcontinent Rift

2.6.1 Overview, geologic setting and structure

The Mesoproterozoic Midcontinent Rift system represents ~ 1100 Ma rifting event within the ancient Laurentian continent. Remnants of the ancient rifting event are traceable through the associated gravity and magnetic anomalies extending along a 2500 km arcuate, segmented length from Kansas, north through Minnesota to Northwestern Ontario, southeast along Lake Superior and south through to Michigan (Fig. 2.3; Kucks, 1999; Bankley et al., 2002). Although the majority of MCR geology is buried beneath Phanerozoic sedimentary rocks in the United States, a large segment is exposed within the northern Lake Superior region (Fig. 2.4; Hutchinson et al., 1990; Cannon, 1992). The major geologic units that comprise the MCR include: 1) thick sequences of stratified subaerial volcanic flows and sedimentary rocks, 2) large local concentrations of plutonic to hypabyssal intrusive rocks, and 3) an upper sequence of sedimentary rocks commonly juxtaposed against volcanic rocks by major faults (Fig. 2.4). Minor geologic units include mafic dikes, mafic to ultramafic intrusions and alkaline to carbonatite intrusions (Fig. 2.4). Exposures of the MCR within the Lake Superior region locally truncate and overly Archean Superior Province basement rock, and/or Mesoproterozoic to Paleoproterozoic sedimentary rock (Figs. 2.1, 2.4).

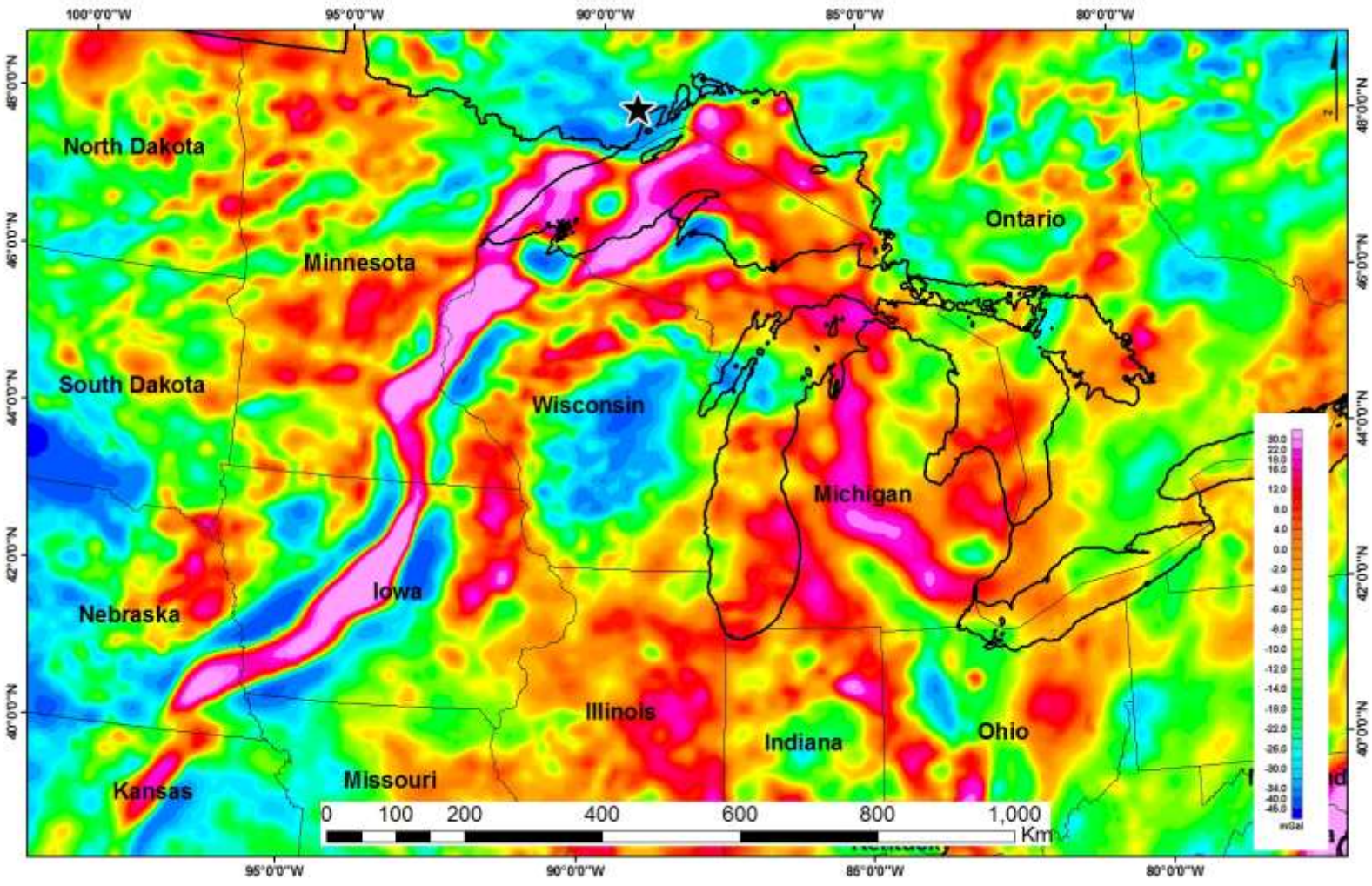

Figure 2.3: The bouger gravity field sampled at 6 km spacing of the Mesoproterozoic Midcontinent Rift preserved in north-central United States and Northwestern Ontario. The MCR is traceable by its magnetic anomaly extending along a 2500 km arcuate, segmented length from Kansas, north through Minnesota to northwestern Ontario, southeast along Lake Superior and south through to Michigan. The location of the Thunder intrusion is denoted by the black star. Geophysical data from the Decade of North American Geology (D-NAG) gravity compilations (Hittelman et al., 1994).

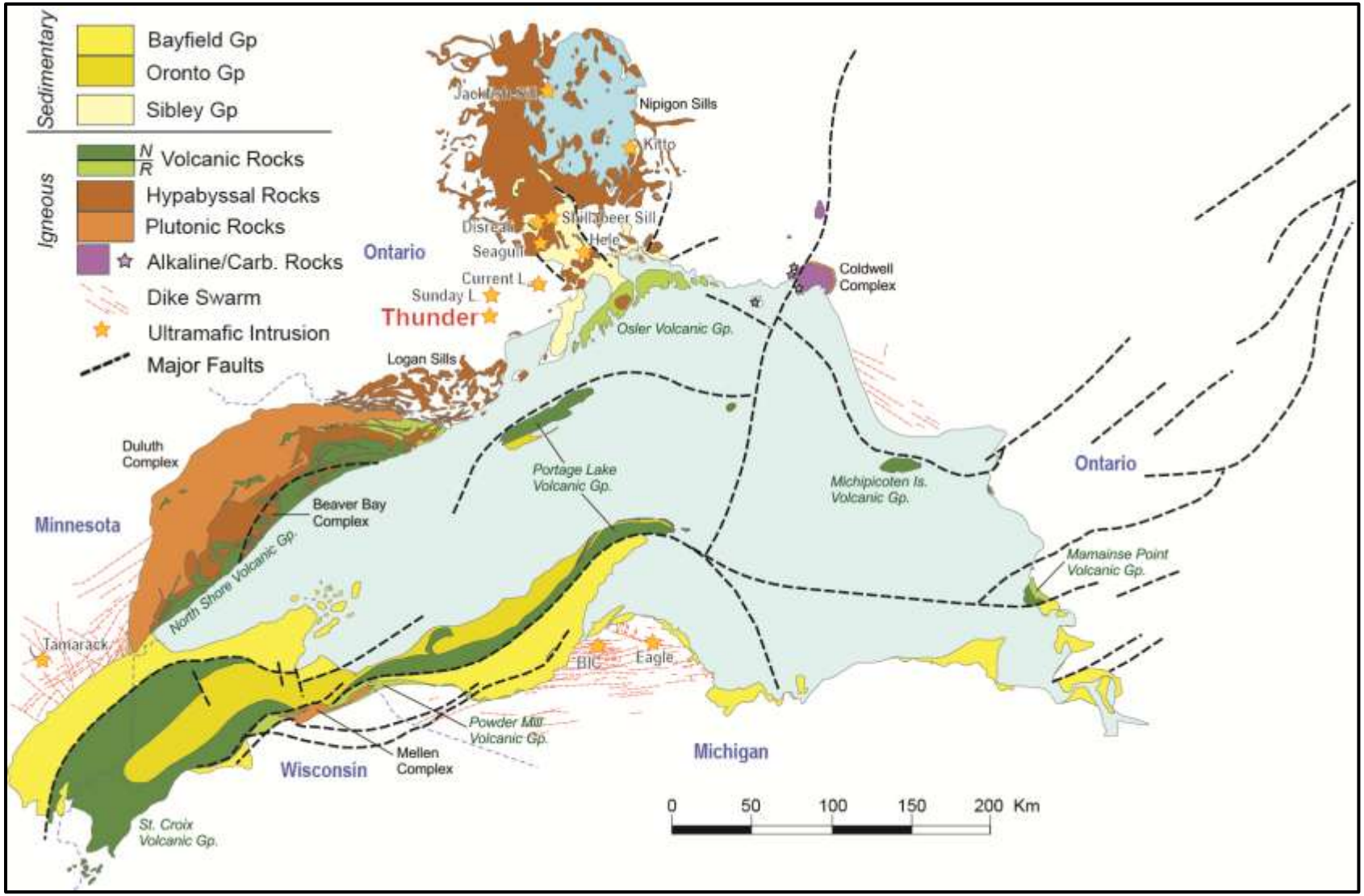

Figure 2.4: Present-day exposure of the Midcontinent Rift geology in the Lake Superior region. Labelled are the major volcanic and intrusive units. Indicated by the yellow stars are locations of the known ultramafic intrusions associated with the early magmatic stages of MCR evolution. Figure modified after Miller and Nicholson (2013).

U-Pb zircon/baddeleyite analyses have constrained MCR magmatism to between 1115 and 1086 Ma, suggesting an ~ 30 million year of magmatism (e.g., Nicholson et al., 1997; Vervoot et al., 2007; Heaman et al., 2007). Heaman et al. (2007) suggested that the intrusions of Northwestern Ontario with U-Pb zircon/baddeleyite ages between 1150 and 1130 Ma may also be related to MCR magmatism. However, integrating these older, compositionally diverse intrusive units into the current model for the MCR (see section 2.6.4) not only doubles the duration of the MCR magmatism but contradicts the current models for its geochemical evolution (Nicholson et al., 1997).

The integration of the MCR's surface exposures and regional geophysical data, especially the seismic reflection profiles across Lake Superior in 1986 for the GLIMPCE project (Great Lake International Multidisciplinary Program on Crustal Evolution; Behrendt et al., 1988), have revealed the three-dimensional structure of the MCR. The GLIMPCE data indicate that the deepest section of the MCR lies beneath the western Lake Superior basin, where a 35 km thick rift-related volcanic sequence has accumulated (Cannon et al., 1989; Trehu et al., 1991; Hinze et al., 1992; Thomas and Teskey, 1994; Allen et al., 1997). It has been estimated that the total volume of MCR-related rocks ranges from 1.3 to 2.0 x 10^6 km^3 which is comparable to many post-Mesoproterozoic, continent-based, large igneous provinces (LIPs; Hutchinson et al., 1990; Cannon, 1992). The major structures involved during the rifting event include a segmented series of en echelon asymmetrical grabens that served as accommodation zones for the outpouring of predominantly mafic magma (Chandler et al., 1989; Cannon et al., 1989; Dickas and Mudrey, 1997). However, these extensional rift structures are more complex, especially after removing the compressional effects of the 1080 Ma Grenville Orogeny where the southwest-trending arm underwent ~ 30 km of shortening (Cannon et al., 1989; Cannon, 1994).

As a result of the Grenville Orogeny, no ocean basin was actually formed during the ancient continental rifting event. Figure 2.4 shows the distribution of major faults that served as generally graben-bounding normal faults during the magmatic phase of the rift.

It is widely recognized by many workers including Hutchinson et al. (1990) and Nicholson and Shirey (1990), that the evolution of the MCR was influenced by the arrival of an anomalously hot mantle plume at the base of the lithosphere at ~ 1115 Ma. Supporting evidence of the mantle plume model includes a high volume of erupted material and underplating of predominantly mafic magma characterized by undepleted mantle radiogenic isotopic signatures and trace element patterns especially in the earliest volcanic products (Nicholson and Shirey, 1990; Shirey, et al., 1994; Nicholson et al., 1997; Shirey, 1997; Hollings et al., 2007b; Hollings et al., 2010; Hollings et al., 2011). The triple junction generated by the mantle plume is thought to have been centered around the Thunder Bay area including the intersection of the two "active" southwest-trending/southeast-trending arms and a "failed" arm segment represented by the Nipigon Embayment as suggested by some (e.g., Franklin et al., 1980; Sutcliffe, 1987; Lightfoot et al., 1991), but questioned by others (e.g., Fralick and Kissin, 1995; Hollings et al., 2004; Rogala, 2007; Hart and MacDonald, 2007).

2.6.2 The Keweenawan Super Group

The stratified volcanic and sedimentary assemblages associated with the MCR magmatism are collectively termed the Keweenawan Super Group (Morey and Green, 1982). The volcanic sequences are predominantly composed of subaerial, tholeiitic flood basalt flows, but also include intermediate and felsic flows and interflow fluvial sedimentary rocks (Green, 1982). Exposures of the Keweenawan Super Group include: Michipicoten Island Formation, Mamainse Point Volcanic Group, Osler Volcanic Group, St. Croix Volcanic Group, Portage

Lake Volcanic Group, Powder Mill Volcanic Group, North Shore Volcanic Group, Oronto Volcanic Group and Bayfield Volcanic Group (Miller and Nicholson, 2013 and references therein). Although as a complete sequence of stratigraphy is not exposed at one locality aside with the exception of the 35km thick sequence buried beneath the western Lake Superior basin floor, a rift-wide chronostratigraphic correlation of the main volcanic sequences and bounding sedimentary units of the Keweenawan Super Group is possible (Nicholson et al., 1997).

Traditionally, the principal means of correlating the MCR volcanic sequences in the Lake Superior region used the magnetic polarity of the rocks (Fig. 2.4; Miller and Nicholson, 2013). The paleomagnetic signatures preserved by the Mamainse Point Volcanic Group exposure suggest multiple magnetic reversals occurred in the order of: reversed → normal → reverse → normal (Fig. 2.5; Swanson-Hysell et al., 2009; Piispa et al., 2014). The age of the first R-N magnetic polarity reversal has been constrained to have occurred between 1105 and 1102 Ma based on U-Pb ages for the uppermost reversely polarized lava in the Olser Volcanic Group: the Agate Point rhyolite (1105.3±2.1 Ma; Davis and Green, 1997), and the oldest normally polarized age for the granitic rocks of the Mellen Complex (1102 ± 2 Ma; Zarman et al., 1997). Unofficially, the second R-N magnetic polarity reversal has been established to have occurred at ~ 1100 Ma based on the U-Pb zircon age for a volcanic tuff layer at the top of the uppermost reversed polarity sequence, just below the Great Conglomerate of the Mamainse Point Volcanic Group (Swanson –Hysell et al., 2014; Fig. 2.5).

Miller and Nicholson (2013) have recently proposed five stages of magmatism during the evolution of the MCR including: the initiation stage (1115 - 1110 Ma), early stage (1110-1106 Ma), hiatus stage (1105 - 1101 Ma), main stage (1101 - 1094) and late stage (1094 - 1086 Ma) incorporating chronostratigraphic correlation of the main volcanic sequences and bounding

sedimentary units of the Lake Superior basin and paleomagnetic polarity (Fig. 2.5). The significance of each magmatic stage within the context of the tectono-magmatic model of the MCR will be discussed in section 2.6.4.

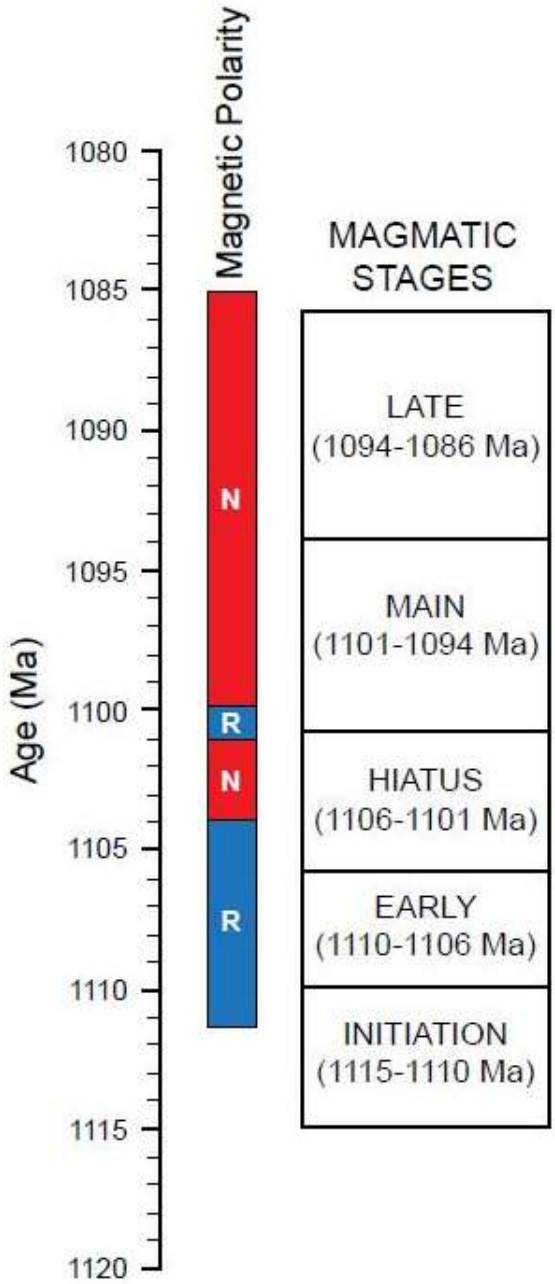

Figure 2.5: Paleomagnetic polarity correlated with the five magmatic stages of the Midcontinent Rift as proposed by Miller and Nicholson (2013). The age of the first R-N magnetic polarity reversal has been constrained to have occurred between 1105 and 1102 Ma and the second R-N magnetic polarity reversal to have occurred at ~ 1100 Ma. Figure modified after Miller and Nicholson (2013).

2.6.3 The Midcontinent Rift Intrusive Supersuite

The intrusive rocks associated with the evolution of the MCR are collectively termed the Midcontinent Rift Intrusive Supersuite (Miller et al., 2002a, b). The supersuite includes four general categories: 1) large subvolcanic intrusive complexes, 2) isolated alkali and carbonatitic intrusions, 3) mafic dike and sill swarms and, 4) small ultramafic to mafic intrusions (Wieblen, 1982; Miller and Nicholson, 2013).

2.6.3.1 Subvolcanic intrusive complexes

The subvolcanic intrusive complexes exposed in the Lake Superior region include the Duluth Complex and Beaver Bay complexes emplaced into the North Shore Volcanic Group of northeastern Minnesota (Miller et al., 2002a, b) and the Mellen Complex emplaced into the Powder Mill Volcanic Group near the Michigan-Wisconsin border (Fitz, 2011; Fig. 2.4). These complexes consist of multiple sheet-like intrusions ranging from mafic to felsic in composition (Miller and Nicholson, 2013 and references therein). U-Pb zircon/baddeleyite ages show that these subvolcanic intrusive complexes were emplaced during the early (1110 - 1105 Ma) and main (1101 - 1094 Ma) magmatic stages of the MCR with the Mellen Complex at 1102 ± 2.8 Ma (Zartman et al., 1997), the Duluth Complex between 1109 and 1106 Ma, and 1099 and 1098 Ma (Paces and Miller, 1993; Vervoort et al., 2007), and the Beaver Bay Complex around 1096 Ma (Paces and Miller, 1993). The Duluth Complex is the largest of the three, with an estimated rock volume between 35,000 and 40,000 km^3, representing the second largest mafic intrusive complex in the world and hosting low-grade, high tonnage Cu-Ni-PGE sulphide mineralization (Allen et al., 1997; Miller et al., 2002a; Eckstrand and Hulbert, 2007).

2.6.3.2 Alkaline and carbonatite intrusions

The isolated alkaline and carbonatite intrusions of the MCR are a unique group of igneous intrusions occurring on the northeast corner of the Lake Superior basin (Fig. 2.4). The largest of this group is the Coldwell Complex, which was emplaced into Archean basement rocks during the early magmatic stages of the MCR with a U-Pb zircon/baddeleyite age of 1108 ± 1 Ma (Heaman and Machado, 1992; Heaman et al., 2007). Other intrusive units within this group of MCR-related intrusive rocks include the Killala Lake alkaline complex, and numerous small lamprophyric, carbonatitic intrusions all clustered in the vicinity of the Coldwell Complex (Fig. 2.4; Sage, 1991). Sage and Watkinson (1995) proposed that these intrusions were structurally controlled by the Trans-Superior Tectonic Zone (TSTZ) and the KSZ which may correspond to the location of maximum lithospheric extension off-axis to the northeast of the central graben (Heaman and Machado, 1992).

2.6.3.3 Mafic dike and sill swarms

Mafic dike swarms oocur within and peripheral to the main magmatic expression of the MCR (Fig. 2.4). The dike swarms generally strike parallel to the trend of the rift axis and likely served as feeder intrusions to basaltic flows and other intrusive units (Green et al., 1987). The average width of these units ranges from 10 to 50 m, but some have been found up to 500 m (Smith and Sutcliffe, 1987; Green et al., 1987). Both normal and reverse polarity dikes occur however, a limited geochronological database imposes a limitation on rift-wide correlation (Green et al., 1987; Miller and Nicholson, 2013). Recent studies by Hollings et al. (2010, 2011) has delineated several dike swarms within the region of the MN-ON border characterized by distinct orientations, magnetic polarities and compositions including the Pigeon River dike swarm, the Cloud River dike swarm and the Mt. Mollie dike. For example, Pigeon River dikes

trend E-NE to NE and dip steeply to the SE, show normal magnetic polarity, characterized by low TiO_2-Gd/Yb_n values, and two U-Pb baddeleyite age dates of 1078 ± 3 Ma and 1141 ± 20 Ma (Heaman et al., 2007; Hollings et al., 2010, 2011). Cloud River dikes are compositionally similar to Pigeon River dikes however; show reverse magnetic polarity and a U-Pb baddeleyite age date of 1109 ± 4.2 Ma (Hollings et al., 2010).

Within the region of the Minnesota-Ontario border and the Lake Nipigon region abundant mafic sills occur and were originally called the Logan Sills (Sutcliffe, 1987; Smith and Sutcliffe, 1989). However, Hollings et al. (2007, 2010) have shown that the sills in the Lake Nipigon region have more diverse compositions and are characterized by relatively low TiO_2 and Gd/Yb_n, whereas the sills south of Thunder Bay are more evolved (mg# < 60) and are characterized by relatively elevated TiO_2 and Gd/Yb_n values. The authors recommend distinguishing Nipigon Sills as those occurring north of Thunder Bay from the Logan sill to the south. U-Pb age dating constrains these intrusions to have been emplaced during the early magmatic stages of the MCR between ~ 1115 and 1100 Ma and show reverse magnetic polarity (Heaman et al., 2007).

2.6.3.4 Mafic to ultramafic intrusions

Lastly, the small mafic to ultramafic intrusions, typically less than 1 km thick and variable in surface area (between 84 and 0.1 km^2); represent the fourth category of the Midcontinent Rift Intrusive Supersuite (e.g., Hollings et al., 2007; Ding et al., 2010). Inspired by the high grade, low tonnage Eagle deposit discovery, an increasing number of small mafic to ultramafic intrusions have been discovered in the Lake Superior region by exploration companies focused on Ni-Cu-PGE mineralization associated with such intrusions (Fig. 2.4; see section 1.1). Within the United States, these intrusions are commonly hosted by Paleoproterozoic sedimentary rocks including the Tamarack intrusion in Minnesota (Goldner, 2011), and the Eagle intrusion

and BIC in northern Michigan (Ding et al., 2010; Foley, 2011). Within the Thunder Bay-Lake Nipigon area these intrusions are commonly hosted by Archean basement and/or Mesoproterozoic sedimentary rocks (i.e., the Sibley Group) including the Current Lake, Seagull, Disraeli, Hele, Kitto, Shillabeer, Jackfish, and Sunday Lake intrusions (Fig. 2.4; Hart and MacDonald, 2007); and the Riverdale sill hosted by Paleoproterozoic sedimentary rock (Puchalski, 2010). U-Pb zircon/baddeleyite analyses show that these intrusions are correlative with the initiation and early magmatic stages of the MCR: 1115 to 1110 Ma; and 1110 to 1106 Ma, respectively (Heaman et al., 2007; Miller and Nicholson, 2013). In addition, Piispa et al. (2014) recently confirmed the early-rift mafic to ultramafic intrusions are characterized by a reverse magnetic polarity signature which is consistent with the initiation and early magmatic stages of the MCR proposed by Miller and Nicholson (2013; Fig. 2.5).

The shape of these intrusions is variable and includes sheet-like (i.e., Shillabeer sill), lopolithic (i.e., Seagull), bowl-shape (i.e., BIC), elliptical cone (i.e., Eagle) and chonolithic (i.e., Current Lake) which has inspired the idea that the magmatic expressions of these intrusion represent portions of a conduit system where multiple pulses of magma have passed en route to the surface (e.g., Heggie, 2005; Goodgame et al., 2010; Ding et al., 2010; Foley, 2011; Goldner, 2011). It has been demonstrated that the picritic lavas of the lower sections of volcanic sequences including Mamainse Point, Powder Mill, North Shore and Osler Volcanic Group are geochemically similar to the estimated parent compositions of some early-rift mafic to ultramafic intrusion including Tamarack (Goldner, 2011) and BIC (Foley, 2011) suggesting co-magmatic and possibly contemporaneous magmatism.

The geochemical patterns of the mafic to ultramafic intrusions listed above indicate ocean island basalt (OIB) characteristics, however, with indications of high field strength element

(HFSE) anomalies (i.e., Nb-Ta, Zr-Hf; Hollings et al., 2007a). The HFSE anomalies and radiogenic isotopes indicate these OIB-like magmas interacted with the continental crust or subcontinental lithospheric mantle (SCLM) en route to surface (Hollings et al., 2007a). Lastly, Hollings et al. (2007) showed that the high Gd/Yb_n values of these mafic to ultramafic intrusions are indicative of a deeper (garnet-bearing) mantle source (Hollings et al., 2007a).

2.6.4 The current tectono-magmatic model of the Midcontinent Rift

Although the role, extent, and existence of mantle plumes continues to be debated (e.g., Campbell, 2007), the ~ 30 million years of recorded magmatism remains the most difficult characteristic to rectify with the proposed mantle plume model for the evolution of the MCR (Hill, 1991; Campbell, 2001, Ernst et al., 2005; Hollings et al., 2014). Hollings et al. (2012) proposed that this prolonged period of magmatism (atypical of the only few million years associated with most Mesozoic and Tertiary LIPs; Coffin and Edholm, 1994; Ernst and Buchan, 2001) could be explained by incorporating the mantle plume cluster theory (Ernst and Buchan, 2002). However, the mantle plume cluster model is refuted by the 20 - 40 cm/yr northeastward drifting rate of the Laurentian continent during the Mesoproterozoic (Swanson-Hysell et al., 2009). Miller and Nicholson (2013) proposed a six stage tectono-magmatic model that attempts to account for the various geochemical, geochronologic and structural attributes of the MCR and is summarized below.

Stage 1 (the initiation stage) involves mafic to ultramafic magmatism between 1115 and 1110 Ma, initiated by a single mantle plume impacting and embedding into the base of the SCLM (Fig. 2.6). No volcanic rocks have been dated older than 1108 ± 2 Ma, which has been attributed to erosion during a period of crustal doming and/or preserved in the keel of the rift basin (Vervoot et al., 2007; Miller and Nicholson, 2013 and references therein). This stage is

represented by the mafic to ultramafic intrusions that occur dominantly in the Thunder Bay-Lake Nipigon region (Heaman et al., 2007), characterized by reverse magnetic polarity signatures (Fig. 2.5).

Stage 2 (the early magmatic stage) represents the progressive embedding of the mantle plume into the SCLM resulting in rapid plateau volcanism, and the onset of crustal underplating between 1110 and 1105 Ma (Fig. 2.6). The volcanic sequences erupted during this stage were reversely polarized (Fig. 2.5) with early primitive basalts (mg# > 50) evolving into more diverse and crustal contaminated compositions ($\varepsilon Nd_T < -2$, Th/Yb > 1; e.g., Mamainse Point Volcanic Group; Nicholson et al., 2007). Structurally, the seismic profile of the early volcanic material and the fluvial and lacustrine sediments preceding the accumulation of the early volcanic sequences suggest that a gentle depression had begun form along the rift axis (Cannon, 1992).

During Stage 3 (the hiatus stage) magmatic activity within the rift reached a temporary volcanic hiatus with the exception of intermittent felsic magmatism and continued crustal underplating from 1105 to 1101 Ma (Fig. 2.6; Miller and Nicholson, 2013). High energy sedimentary sequences correlated to this stage of the MCR's evolution suggest continued vertical subsidence and the development of graben bound faults (Cannon, 1992).

Stage 4 (the main magmatic stage) represents the renewal of volcanic and intrusive activity between 1101 and 1094 Ma at a time of normal magnetic polarity and characterized by rapid to moderate rates of eruption (Figs. 2.5, 2.6; Miller and Nicholson, 2013). The magma compositions correlated to this period ranged from primitive basalts to rhyolites and show little evidence of crustal contamination ($\varepsilon Nd_T < +2$ to -2, Th/Yb < 1; Nicholson et al., 1997). This was a period thought to have included upper crustal separation resulting in rapidly subsiding graben-bound normal faults (Fig. 2.4; Cannon, 1992) and the evacuation of evolved lower crustal

magma chambers accompanied by continued mantle plume melting (Miller and Nicholson, 2013). This stage is represented by the nearly 10 km thickness of normally polarized North Shore Volcanic Group lavas in Minnesota, and at least 5 km of Portage Lake Volcanics in Michigan, as well major parts of the Duluth, Beaver Bay and Mellen intrusive complexes (Fig. 2.4; Miller and Nicholson, 2013).

Stage 5 (the late magmatic stage) encompasses the waning of MCR volcanism due to the thermal collapse of the mantle plume head and detachment from the plume tail accompanied by continued subsidence of the central rift grabens between 1094 and 1080 Ma (Swanson-Hysell et al., 2009; Miller and Nicholson, 2013). Intermediate to felsic volcanism became more localized with the last recorded magmatic event occurring around 1086 Ma, otherwise this period was dominated by thick accumulations of alluvial fan, fluvial and minor lacustrine sediments represented by the Oronto Group infilling the central axis of the rift (Fig. 2.4; Vervoot et al., 2007; Miller and Nicholson, 2013). Towards the end of magmatism, the occurrence of N-MORB-like (normal mid-ocean ridge basalt) compositions with ε_{Nd} values ranging from 0 to +3 from samples of the uppermost sections of the Mamainse Point Volcanic Group stratigraphy (i.e., Group 6 and 7) suggest mixtures of melts from plume and depleted asthenospheric mantle became dominant (Nicholson et al., 1997).

Lastly, stage 6 (the inversion stage) involves the change from principle extensional stresses to compression and the structural inversion of the rift due to the crustal-scale thrusting of the Grenville Orogeny as early as 1080 Ma and may have lasted until 1040 Ma (Fig. 2.6; Cannon, 1994). As a result, areas such as the southwest-trending arm the crust endured ~ 30 km of shortening (Cannon, 1994). During this final stage of the MCR's evolution, flanking sedimentation occurred represented by the Bayfield Group (Fig. 2.4).

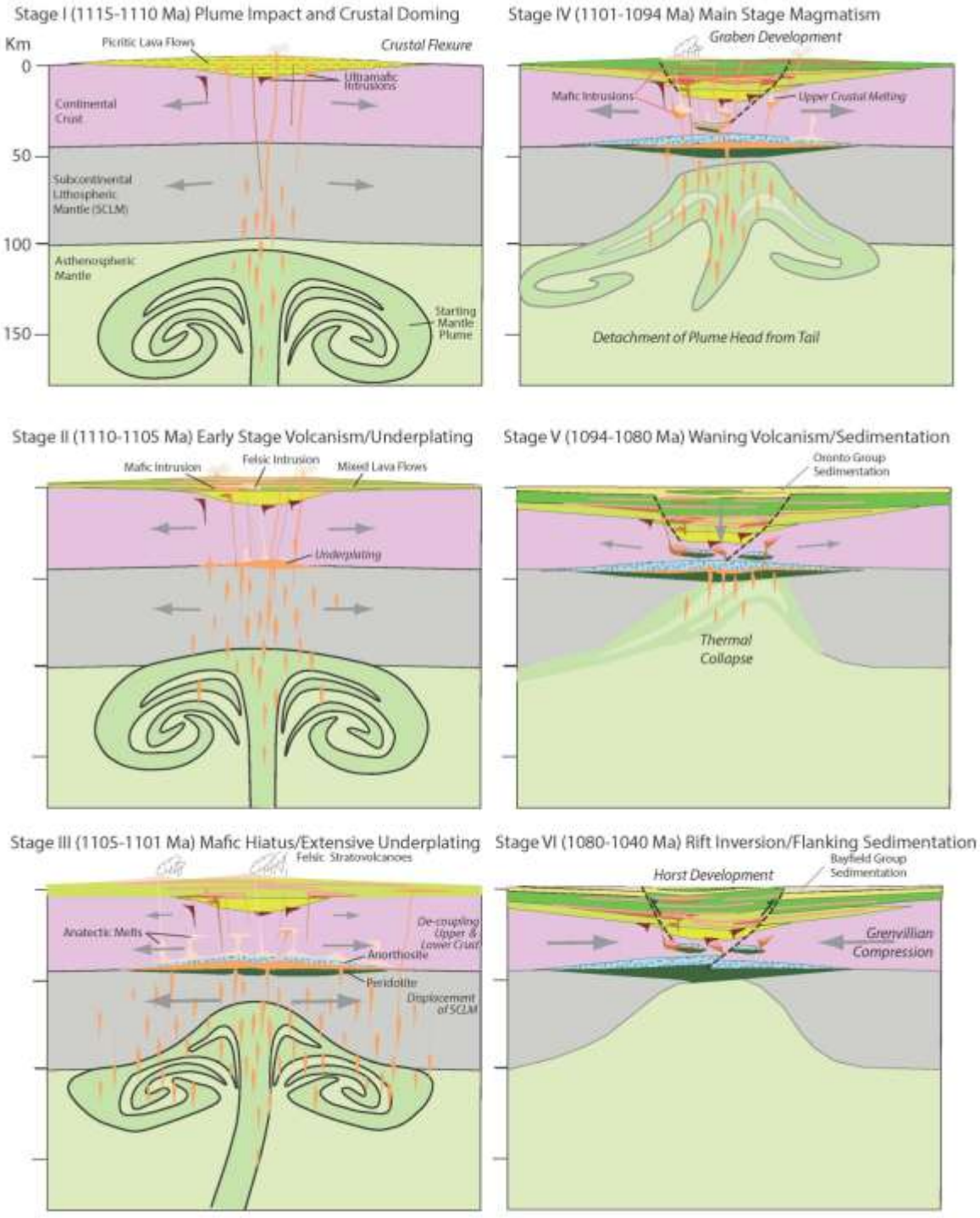

Figure 2.6: The six-stage tectono-magmatic model for the evolution of the Mesoproterozoic Midcontinent Rift proposed by Miller and Nicholson (2013).

A recent counter argument to the "plume paradigm" was discussed by Hollings and Heggie (2014), introducing a passive rifting model to account as the absence of primary ultramafic magmas, and the lack of a radial dike swarm centered in the Thunder Bay area (Ernst et al., 2013a). According to this model, rifting of the ancient Laurentian continent, possibly in response to the widespread 1110 Ma Umkondo LIP event of the Kalahari Craton (Hanson et al., 2003, 2004, 2006; Ernst et al., 2013b) allowed for the upwelling of magma underplated by earlier plume events thought to have been centered in the vicinity of the present-day Lake Superior (e.g., the Marathon LIP; Halls et al., 2008). According to work by Hanson et al. (2003, 2004, 2006), paleomagnetic reconstructions recognized ~ 1100 Ma magmatism in the Congo, the Amazon and India which can be linked to the Umkondo LIP event, which is a separate and distinct event from Keewenawan magmatism (Ernst et al., 2013b). The presence of multiple, broadly contemporaneous LIP events indicates that the Mesoproterozoic may have been a period of significant mantle overturn and atypically increased magmatic activity (Stein and Hofmann, 1994). However, since the passive rifting model is a relatively new and unproven model, the six stage tectono-magmatic model by Miller and Nicholson (2013) will be utilized for this thesis.

2.7 Exploration history of the Gorham Township and vicinity

Exploration within Gorham Township and the vicinity began in the 1800's when quartz ± calcite ± amethyst vein systems within Proterozoic rocks of the greater Thunder Bay area were explored for silver, copper and lead-zinc (Ingall, 1887). Also during this time, the discovery of iron-rich ores in Proterozoic rocks within the Matawin Iron Range of Minnesota prompted exploration efforts in search of an eastern extension of the iron range (Ingall, 1887; MacDonald, 1939a). Although no comparable iron-ores were discovered, exploration within the Gorham Township and vicinity intensified upon the discovery of gold in 1935 (MacDonald, 1939a).

The three main gold occurrences were discovered on the properties of Gorham Gold Mines Ltd., Lake Head Gold Mines Ltd., and Thunderhead Gold Mines Ltd. (MacDonald, 1939a; Thomson, 1989). The mining operations were small scale lasting until the 1960s (MacDonald, 1939a; Thomson, 1989). Of the three gold occurrences in Gorham Township, work at the Thunderhead property led to the initial discovery of Ni-Cu-PGE mineralization at the Thunder intrusion. Thomson (1989) reported exploration efforts during the 1960s focused on a gabbroic unit situated on the southwestern section of the property. A zone of sulphide mineralization up to 12 m wide with 1.77 % Cu and 1.03 % Ni was discovered with subsequent drilling intercepting 5.5 m @ 0.3 % Cu, 0.1 % Ni (Thomson, 1989). The Thunderhead property was optioned to an individual (name not disclosed) in 1980, and since then, no further exploration has taken place on the property (Thomson, 1989; Bidwell and Marino, 2007).

Exploration within the Gorham Township in 2005 focused on the Thunder intrusion. Claims enclosing the Thunder intrusion were acquired in 2005 by Kennecott Canada Exploration Canada (Bidwell and Marino, 2007). There is no record within the public domain of the early investigations conducted by Kennecott, aside from what is reported by Bidwell and Marino (2007). Three diamond drill holes were completed in 2005 totalling ~ 900 m (Table 2.1). Work by Kennecott on the Thunder intrusion was continued by Geoinformatics Exploration Canada Ltd. who targeted a potential higher concentration of sulphide mineralization suggested by a CRONE SQUID ground magnetic survey which indicated a conductor of 50 to 100 siemens located along the basal contact of the intrusion at a vertical depth of ~ 300 m (Bidwell and Marino, 2007). Four diamond drill holes were completed in 2007 totalling 1904 m (Table 2.2; Bidwell and Marino, 2007).

To date, there has been no further work on the Thunder intrusion and vicinity reported within the Ministry of Northern Developement and Mines's (MNDM) public domain except for a brief program conducted by Benton Resources Corp (June 2009). Four claims were acquired by Benton Resources 650 m west of the Thunder intrusion claims (Sims, 2010). Ground investigations, surface sampling and assay results found no gold, nickel or copper mineralization (Sims, 2010).

Table 2.1: Location (UTM NAD83 Zone16) and depth of diamond drill cores completed in 2005 by Kennecott Canada Exploration Inc. (Bidwell and Marino, 2007).

Drill Hole ID	Easting	Northing	Elevation	Dip (°)	Azimuth (°)	Depth (m)
05TH001	329809	5377560	434	90	000	275
05TH002	330435	5378298	421	55	000	291
05TH003	330435	5378298	421	60	180	336

Table 2.2: Location (UTM NAD83 Zone16) and depth of diamond drill cores completed in 2007 by Geoinformatics Exploration Canada Ltd. (Bidwell and Marino, 2007).

Drill Hole ID	Easting	Northing	Elevation	Dip (°)	Azimuth (°)	Depth (m)
07TH004	330319	5377910	455	90	000	518
07TH005	330319	5377910	455	70	000	440
07TH006	330319	5377910	455	75	180	617
07TH007	330161	5378268	461	80	185	329

2.8 The discovery of Ni-Cu-PGE mineralization

A complete record of the assayed intervals from the 2005 drill program conducted by Kennecott Canada Exploration Inc. is not available within the MNDM's public domain records. However, significant intercepts were reported by Bidwell and Marino (2007) and summarized in Table 2.3. The first diamond drill hole (05TH001) targeted a proximal magnetic anomaly to the southwest of the Thunder intrusion intercepting a "garnet-magnetite skarn" yielding anomalous gold values; the next two diamond drill holes (05TH002 and 05TH003) were collared in a layered gabbro-melanocratic gabbro-peridotite intrusion. Significant intercepts of Ni-Cu-PGE

sulphide mineralization were found to be concentrated along the basal contact zone between the Thunder intrusion and wall rock (Table 2.3).

Table 2.3: Significant drill intercepts reported by Bidwell and Marino (2007) from the 2005 drill program on the Thunder intrusion conducted by Kennecott Canada Exploration Inc.

Drill Hole ID	From (m)	To (m)	Width (m)	Cu (%)	Ni (%)	Pt (ppm)	Pd (ppm)	Pt+Pd (ppm)	Au (ppm)
05TH001	58.0	62.0	4.0	0.53	-	-	-	-	1.70
05TH002	-	-	-	-	-	-	-	-	-
05TH003	288.6	300.4	11.8	0.32	0.10	0.30	0.37	0.67	0.04
	292.8	298.3	5.5	0.48	0.14	0.43	0.54	0.97	-

The 2007 drill program conducted by Geoinformatics Exploration Canada Ltd. focused on drill sites within the central portion of the Thunder intrusion. Diamond drill holes 07TH004, 07TH005 and 07TH006 were drilled from the same location and 07TH007 at a nearby location (Table 2.2). The drill holes were collared in a leucogabbro to melanogabbro phase of the intrusion, penetrated an underlying peridotite, and passed through the basal contact into wall rock. Three of the four drill cores intersected greater than 0.50 ppm Pt + Pd (Table 2.4) and mineralization was concentrated along the basal contact of the intrusive rocks with sulphides present as replacements and disseminations up to 8% modal abundance but more typically 1-5%.

Table 2.4: Significant drill intercepts reported by the 2007 drill program on the Thunder intrusion with 0.1% copper cut-off grade conducted by Geoinformatics Exploration Canada Inc. (Bidwell and Marino, 2007).

Drill Hole ID	From (m)	To (m)	Width (m)	Cu (%)	Ni (%)	Pt (ppm)	Pd (ppm)	Pt+Pd (ppm)	Au (ppm)
07TH004	410.0	412.0	2.0	0.14	0.07	0.19	0.19	0.38	0.03
	416.0	418.0	2.0	0.11	0.06	0.14	0.15	0.29	0.02
	424.0	428.0	4.0	0.16	0.08	0.19	0.20	0.39	0.02
	432.0	440.0	8.0	0.23	0.08	0.21	0.34	0.55	0.04
07TH005	362.0	376.0	14.0	0.35	0.07	0.33	0.40	0.73	0.04
	386.0	406.0	20.0	0.22	0.06	0.25	0.29	0.54	0.04
07TH006	181.5	183.3	1.8	0.40	0.07	0.08	0.77	0.85	0.04
	401.5	403.0	1.5	0.16	0.02	0.05	0.07	0.12	0.02
	572.0	576.0	4.0	0.78	0.05	0.36	0.46	0.82	0.12
07TH007	224.0	237.0	13.0	0.15	0.04	0.16	0.17	0.33	0.02
	267.0	270.0	3.0	0.10	0.02	BD	BD	BD	0.02
	283.0	286.0	3.0	0.11	0.01	BD	BD	BD	0.02

Abbreviations: BD = below detection limit

2.9 The Thunder intrusion and vicinity

The discovery of gold within Gorham Township led to the construction of the first bedrock geology map of Gorham Township and vicinity (MacDonald, 1939a, b). The original geological map of the Gorham Township and vicinity (produced by the MNDM) reported olivine gabbro comprising the Thunder intrusion (MacDonald 1939a, b). The original map has been modified as a result of additional mapping in neighbouring townships (Brown, 1995) and has been incorporated into the 1:200 000 scale bedrock geology of Ontario (OGS, 2011). On that map, the Thunder intrusion is listed as Mesoproterozoic mafic dikes and related intrusive rocks (Fig. 1.1). According to the OGS (2011) bedrock geology map, the country rocks surrounding the irregularly shaped margins of the Thunder intrusion include mafic to intermediate metavolcanic rocks, felsic to intermediate metavolcanic rocks and coarse clastic metasedimentary rocks (Fig. 1.1).

The Thunder intrusion is spatially an outlier to the main magmatic expression of the MCR (Fig. 2.4). On a map of the first vertical derivative magnetic field the Thunder intrusion is defined by three isolated magnetic highs surrounded by a magnetic low, producing an overall clover leaf-like shape (Fig. 2.7). The magnetic signature of the intrusive body interrupts the E-trending fabric of the SGB suggesting post-deformation emplacement (Fig. 2.7). Other magnetic anomalies within the vicinity of the Thunder intrusion include two relatively thin N-trending magnetic anomalies that appear to converge on the western and eastern margins of the Thunder intrusion and extend northwards past the DLGC (Fig. 2.7). Their relationship to the Thunder intrusion and the MCR as a whole is uncertain. North of the Thunder intrusion can be seen the large magnetic anomalies of the DLGC previously discussed in section 2.3 (Fig. 2.7).

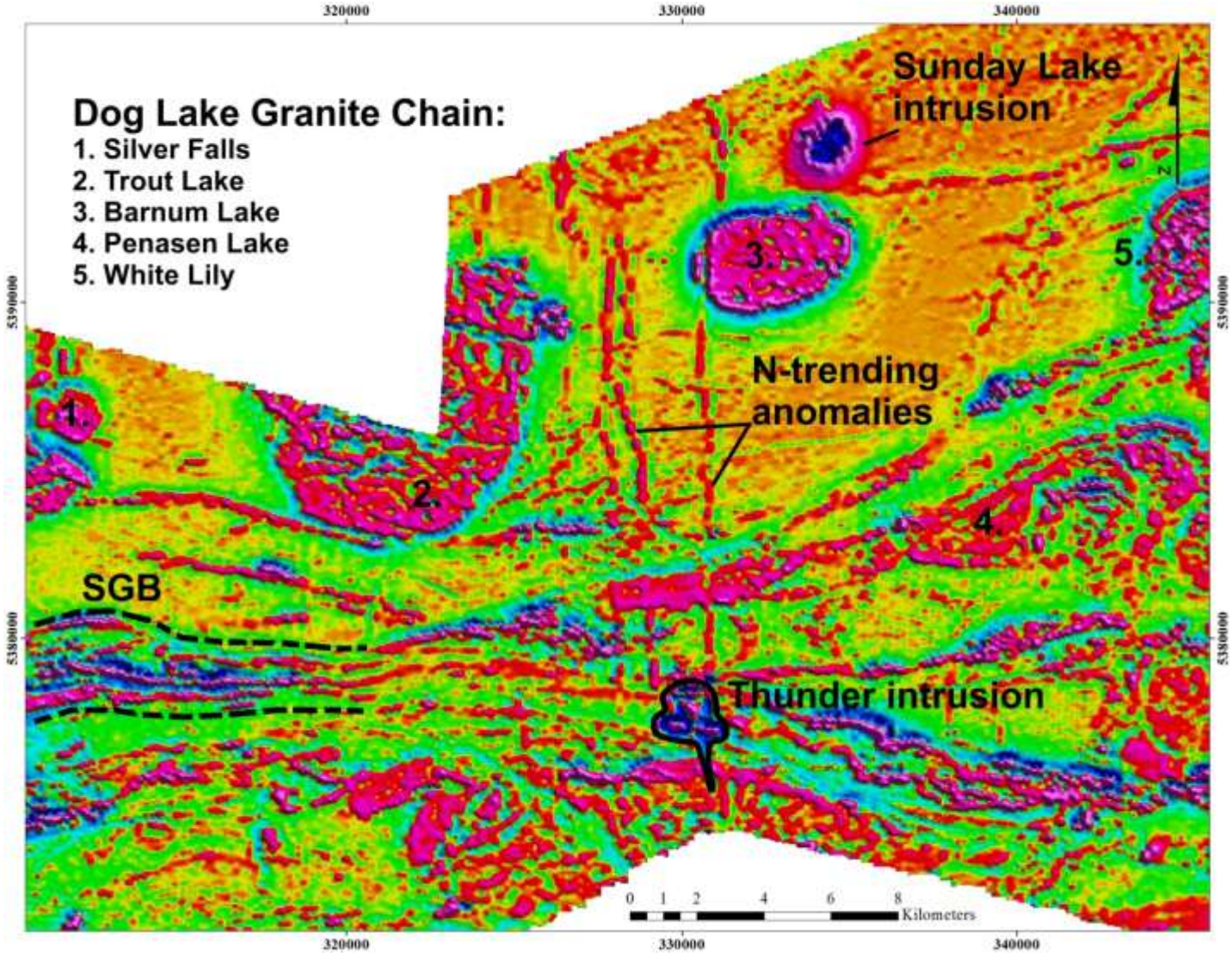

Figure 2.7: The first vertical magnetic field of the Thunder intrusion region. Outlined is the clover leaf-like magnetic expression of the Thunder intrusion, the N-trending magnetic anomalies, the east trending fabric of the Shebadowan greenstone belt (SGB) and select intrusions of the Dog Lake Granite Chain. Geophysical data from OGS (2003a).

The Thunder intrusion is a small, mineralized mafic to ultramafic intrusion interpreted from earlier investigations to be an early-rift occurrence based on geochemical similarities with the mafic to ultramafic intrusive units of the Nipigon Embayment (Rossell, pers. comm., 2012). The Thunder intrusion is distinct from other mineralized early-rift intrusions as it is the only known occurrence hosted in the metavolcanic and metasedimentary rocks of the Archean Shebandowan greenstone belt (Ames et al., 2012). Other early-rift intrusions north of the Canada-United States border, including Current Lake, Seagull and Sunday Lake (north of the Thunder intrusion; see Fig. 2.7), intrude the Archean Quetico metasedimentary subprovince and/or Mesoproterozoic Sibley Group (Heggie, 2005; MacTavish, 2013; Transition Metals Corp., 2014). As this is the first study conducted on the Thunder intrusion, key questions will be addressed as an outcome:

1. The timing, origin and relationship of the Thunder intrusion to other mineralized and barren intrusive complexes, dikes and sills within the MCR
2. The radiogenic Rb/Sr and Sm/Nd isotopic signature of the intrusion and the nature/role of possible contaminants.
3. The role of crustal sulphur assimilation and the observed sulphide mineralization
4. The parent magma composition of the Thunder intrusion and how it compares to other early-rift intrusion compositions.
5. The Ni-Cu-PGE signature and how it compares to the Ni-Cu-PGE signatures of the other known early-rift mineralized intrusion.
6. The alteration footprint thats surrounds the Thunder intrusion

CHAPTER 3

METHODOLOGY

3.1 Location and access

The Thunder intrusion is situated approximately 10 km north-northwest of the City of Thunder Bay, Ontario, within the Gorham Township area (Fig. 1.1). The intrusion is centered at 330319E 5377910N (national topographic sheet 52A/11; UTM NAD83 Zone 16). Two mineral claims currently enclose the Thunder intrusion (claim number 1245457 and 1245452) and are currently held by Rio Tinto Exploration Canada Inc (Fig. 1.1). Access to mineral claims and diamond drill core was granted by Dean Rossell (Principal Geologist, Rio Tinto). Access to the property is achieved by travelling 2 km northwest along HW 102 (locally referred to as Dawson Rd.), 10 km north along Hazelwood Dr. and then 500 m west along Peterson Rd. Exposures of the Thunder intrusion are best observed along access routes including Peterson Rd. which passes through the northern margin of the intrusion, skidder trails which travel to the old diamond drill sites, an E-trending power line which passes through the southern margin of the intrusion and a N-trending pipeline which passes through the eastern margin of the intrusion. The areas in between the access routes are heavily vegetated including swampy lowland running along the northern and eastern margin of the intrusion but nevertheless, outcrops were still found. All lithologies of the intrusion and wall rock were observed at surface; however, outcrops preserving phase and contact relationships were rare. The majority of the diamond drill core is currently stored at the Conmee Core Yard Library located in the Conmee Township and access was facilitated by the Ministry of Northern Development and Mines (MNDM). One of the diamond drill cores is currently stored at the Rio Tinto core logging facility and access was facilitated by Dean Rossell.

3.2 Field work

3.2.1 Introduction

The following section outlines the field work component to this MSc study. Field work including geological mapping, re-logging of available diamond drill core and sampling provided the initial framework on which the remainder of the analytical investigations were based.

3.2.2 Geological mapping of the Thunder intrusion and vicinity

The mineral claims are presently surrounded by multiple private properties. Prior to initiating the mapping component of this MSc study, each private property owner in the vicinity of the mineral claims was visited and provided an introductory letter seeking permission to access the lands. Permission was granted by all surface right owners and positive relations were maintained throughout the study. The majority of mapping was completed during fall 2012 with brief field visits between spring and fall 2013 revisiting key areas of uncertainty.

Each exposure found was recorded as a mapping station in a field notebook. At each mapping station the following was recorded: a UTM coordinate acquired using a handheld Garmin GPS unit, three magnetic susceptibility measurements measured using a handheld Terraplus magnetic susceptibility meter, structural measurements, representative outcrop and hand sample photos, and a description of the outcrop. All mapping station data was then compiled into a master spreadsheet and georeferenced into ArcGIS 10 software.

Two N-trending magnetic anomalies were also investigated as geophysical maps indicate one converging on the Thunder's eastern margin and the other converging on the western margin (Fig. 2.7; OGS, 2003). A suite of locations on the geophysical maps were selected for investigated and visited. Exposures observed to correlate with the magnetic anomaly were treated as a mapping station.

3.2.3 Re-logging of the available diamond drill core

Four of the seven available diamond drill holes (DDH) were logged during fall 2012 and the remaining three completed during summer 2013. While core logging, the available assay interval data from Bidwell and Marino (2007) was used as a guide to detect down hole variations and areas of concentrated mineralization. Data was recorded following an interval format. At each interval the following was recorded: magnetic susceptibility measurements measured using a handheld Terraplus magnetic susceptibility meter, representative core photos, and description. Interval data for each diamond drill core was then compiled into a master spreadsheet. Digital core logs were constructed using Strater 3 software.

3.2.4 Sampling procedure and locations

Sampling focused on collecting a suite of representative lithologies, mineralization and alteration determined by visual examination. Given the medium- to fine-grained nature of the rocks under study, a fist size grab sample was determined representative for whole rock geochemistry. Generally, two clean fist size surface samples were collected at each mapping station. The drill core samples collected were between 30 and 15 cm length to ensure the availability of abundant material for analytical work (>150 g). The drill core samples were split using the saws available at Lakehead University's Lapidary Laboratory and half of the sample was returned to the core boxes.

Most of the samples used for the analytical investigations were from DDH 07TH004 as it was determined to be the most stratigraphically complete representation of the Thunder intrusion and wall rock. Sampling focused on collecting a suite representative of the down-hole variations with the aid of interval data from the 2007 exploration program (Bidwell and Marino, 2007). Down hole variations in zones of mineralization and alteration were small, resulting in tightly

space sample intervals whereas down-hole variations in lithology were relatively large resulting in wider spaced intervals (up to 40 m).

3.3 Analytical methods

3.3.1 Introduction

The following section outlines the analytical techniques and methodologies applied in the investigation of the Thunder intrusion. The initial preparation of all samples used for this MSc study was completed by the author using equipment in Lakehead University's Lapidary Laboratory.

3.3.2 Whole-rock geochemistry

A total of 104 samples were submitted to the Ontario Geological Survey's Geoscience Laboratory (GeoLabs) in Sudbury, ON, to be analyzed for whole-rock geochemistry. The methodology for attaining whole rock geochemistry data followed a similar procedure as outlined by Hollings et al. (2007). Samples were cut, crushed and milled to -200 mesh in an agate ring mill to reduce risk of trace element contamination (Jenner, 1996). Between each sample preparation, the tools and working surfaces were cleaned with acetone. Samples were analyzed for total sulphur (S^T) and carbon (CO_2) by infrared absorption, major elements by X-ray fluorescence (XRF), trace and rare earth elements by inductively coupled plasma mass spectrometry (ICP–MS), and precious metals by nickel sulphide fire-assay combined with ICP-MS. Select trace elements (e.g., Zr and Y) were also analyzed by XRF using a pressed pellet to allow comparison with data generated by ICP–MS. Totals for major element oxide data were generally 100 ± 2% and have been recalculated to a 100% volatile-free basis. Detection limits for major elements are 0.01 weight % and relative standard deviations of duplicate analyses are within 5%.

Trace elements, including the rare earth REE and HFSE analyzed were completed on a Perkin-Elmer Elan 9000 ICP–MS following a variation to the protocol described by Burnham and Schweyer (2004) and Tomlinson et al. (1998). Twenty four trace elements were determined using a 200 mg aliquots of powder digested by a two stage procedure involving an initial decomposition in a closed beaker by a mixture of HF with lesser HCl and $HClO_4$ followed by a second mixture of dilute HCl and $HClO_4$ as described by Burnham et al. (2002). Trace and rare REE data have been recalculated to a 100% volatile-free basis. Detection limits for some trace elements, defined as 3σ of procedural blank, include Th (0.018 ppm), Nb (0.028 ppm), Hf (0.14 ppm), Zr (6.0 ppm), La (0.04 ppm) and Ce (0.12 ppm) (Burham and Schweyer, 2004). Precious metal detection limits, defined as 3σ of procedural blank include Au (0.22 ppb), Ir (0.01 ppb), Pd (0.12 ppb), Pt (0.17 ppb), Rh (0.02 ppb) and Ru (0.08 ppb) (Burham and Schweyer, 2004).

Chondrite-normalized (e.g., La/Sm_n) and primitive mantle-normalized ratios (e.g., La/Sm_n) were calculated from the values of Sun and McDonough (1989), as were the primitive mantle-normalized trace and REE spider diagrams. Primitive mantle-normalized precious metal spider diagrams were calculated from values of Sun and McDonough (1989). The mg# is calculated assuming that 90 % of total iron is as FeO using formula: mg# = $MgO/(MgO+0.9*FeO^T)$, mole %. For quality assurance, the XRF and ICP-MS/AES methods employed by GeoLabs have recently been reviewed by Hargreaves (2012) and Keating and Burnham (2012), respectively. All analyses performed utilized in-house standards, duplicate samples and blanks as part of the normal procedures of GeoLabs.

3.3.3 Rb-Sr and Sm-Nd isotope analysis

Sampling focused on a suite of samples from DDH 07TH004 representative of the Thunder intrusion and wall rock lithologies. Ten samples were submitted to the Isotope

Geochemistry and Geochronology Research Centre at Carleton University (Ottawa, Ontario) to be analyzed for radiogenic isotopes (Sr, Sm-Nd). Sr and Sm-Nd were separated using a Dowex AG50-X8 cation resin. Sr procedural blanks are < 250 pg. Sr samples were loaded onto single Ta filaments with H_3PO_4 for analysis. The isotope ratios were normalised to $^{88}Sr/^{86}Sr = 8.375$ using the NIST SRM987 standard: $^{87}Sr/^{86}Sr = 0.710234 \pm 14$, n = 22. Sm and Nd were separated on Eichrom Ln Resin chromatographic columns containing Teflon powder coated with di-(2-ethylhexyl)-phosphoric acid (HDEHP; Richard et al., 1976). Total procedural blanks for Nd are < 50 picograms and < 6 picograms for Sm. Prior to dissolution, samples were mixed with a $^{148}Nd/^{149}Sm$ spike. Concentrations are precise to ± 1 %, but $^{147}Sm/^{144}Nd$ ratios are reproducible to 0.5 %. Sm and Nd samples were loaded with H_3PO_4 on one side of a Re double filament for analysis. The isotope ratios were normalized to $^{146}Nd/^{144}Nd = 0.72190$. Analyses of the United States Geological Survey (USGS) standard BCR-1 yielded Nd = 29.02 ppm, Sm = 6.68 ppm, and $^{146}Nd/^{144}Nd = 0.512668 \pm 20$ (n = 4). The international La Jolla standard produced: $^{143}Nd/^{144}Nd = 0.511847 \pm 7$, n = 26 (Feb 2005 - June 2007) and an internal lab standard = 0.511818 ± 8, n = 28 (Feb 2005 - June 2007) and 0.511819 ± 10 n = 94 (Feb 2005 - Aug 2009). $^{87}Sr/^{86}Sr_i$ ratios and εNd_T values were calcutlated at time T = 1100 Ma.

3.3.4 S isotope analysis

Sampling focused on a suite of samples from DDH 07TH004 and surface exposures representative of the various styles of visible sulphide mineralization observed at the Thunder intrusion. Twenty samples were submitted to the Indiana University's Department of Geological Sciences. The continuous flow method for sulphur isotope analysis was conducted similar to that of Studley et al. (2002) and recently summarized by Donoghue et al. (2014). Visible sulphide minerals including pyrite, pyrrhotite and chalcopyrite were removed from polished

sections using a 0.75 mm carbide-tip dental drill. Between 0.1 and 0.2 mg of sulphide powder material was then combined with approximately 1.5 to 2.0 mg of vanadium pentoxide (V_2O_5) in tin cups to be prepared in an elemental analyzer by flash combustion at 1800 ºC with a reactor column temperature of 1010 ºC. The subsequent SO_2 gas produced was measured using a Finnigan MAT 252 stable isotope ratio mass spectrometer. Results were reported in per mil (‰) delta notation relative to Vienne-Canyon Diablo Troilite (V-CDT). The analytical uncertainty was < ± 0.05 ‰, and sample reproducibility was within ± 0.2 ‰. Sulfide standards used by the lab were IAEA-S1, IAEA-S2, IAEA-S3, with values of -0.3, 21.7 and -31.3 ‰ respectively, on the SO_2 scale.

The next step to the analysis involves analyzing $\delta^{33}S$ and $\delta^{34}S$ (Donoghue et al., 2014). Sulfide powders were wrapped in aluminum foil, placed in Ni reaction vessels, and then converted to SF_6 by heating at 250 °C for 1 hr and then introduced to excess F_2 derived from a 20% F_2/80% He mixture. The SF_6 mixtures were then heated to 450 °C overnight, condensed from the residual F_2 into a liquid nitrogen cooled trap and subsequently distilled from the trap at −115 °C to the injection loop of gas chromatograph (GC) at −177 °C. GC purification of SF_6 was undertaken using a 1/8" diameter, 12' long Haysep Column with a He carrier flow at 20 mL/min. The SF_6 was registered using a thermoconductivity detector (TCD) and then isolated by freezing into a liquid nitrogen cooled trap. Lastly, purified SF_6 was introduced into a Finnigan MAT 252 mass spectrometer and analyzed using dual inlet methodology. The uncertainty for the measurements includes $\delta^{34}S$ ± 0.2 ‰ and for $\delta^{33}S$ ± 0.1 ‰ based on repeated analyses of sulphide standards IAEA-S1 and IAEA-S2. The $\Delta^{33}S$ values are calculated following the formula from Ono et al. (2012) where $\Delta^{33}S = \ln(\delta^{33}S + 1) - \ln(\delta^{34}S + 1)$ with ± 0.01 ‰ uncertainty.

3.3.5 As, Bi, Sb, Se, Te analysis

A subset of samples from the S-isotope analysis was submitted to Activation Laboratories Ltd. (ActLabs) in Ancaster, Ontario for As, Bi, Sb, Se, Te analysis. The powders were prepared by GeoLabs. The analysis involved digesting a 0.5 g of sample in an aqua regia at 90 °C in a microprocessor-controlled digestion block for two hours. Digested samples were then diluted and analyzed by Perkin-Elmer Elan 9000 ICP–MS. All analyses performed utilized in-house standards, duplicate samples and blanks as part of the normal procedures of ActLabs.

3.3.6 SEM-EDS analysis

Sampling focused on a suite of samples representative of the various styles of sulphide mineralization observed at the Thunder intrusion correlating high assay results. Semi-quantitative mineral analyses were carried using a Zeiss EVO 50 series scanning electron microscope (SEM) including a backscattered electron detector (BSD) and equipped with an Oxford energy dispersive spectrometry (EDS) system at the Geological Survey of Canada, (Ottawa, Ontario). The EDS system was equipped with an X-MAX 150 Silicon Drift Detector, the INCA Energy 450 software and the latest AZtec microanalysis software. Operating conditions included a standard working distance of 8.5 mm, high voltage (EHT) set at 20 kV with a probe current of 400pA to 1nA and filament current set to 2nd peak.

3.3.7 Electron microprobe

Sampling focused on a suite of samples representative of the various styles of mineralization observed for sulphide chemistry on a suite of samples from diamond drill hole 07TH004 to detect down-hole variations in olivine chemistry. Quantitative mineral analyses were carried out with an automated four-spectrometer Cameca Camebax MBX electron microprobe (EMP) by wavelength dispersive x-ray analysis method (WDX) at the Earth Sciences

Department of Carleton University (Ottawa). Raw X-ray data were converted to elemental weight % by the Cameca PAP matrix correction program. Background positions were carefully selected to avoid instances of peak overlap. A suite of well characterized natural and synthetic minerals and compounds were used as calibration standards (see Tables 3.1 and 3.2). Calibration was tested by analyzing known compositions (mineral standards) as unknowns (e.g., olivine and chalcopyrite or pyrrhotite). Operating conditions, X-ray lines and standards for sulphides, tellurides and alloys analyses are outlined in Table 3.1. Operating conditions, X-ray lines and standards for olivine analyses are outlined in Table 3.2. Stoichiometric formula calculations were added to the analyses following the procedures outlined in the appendix of Deer et al. (1992).

Table 3.1: Operating conditions for sulphides, tellurides and alloys analyses were carried out at 20 kV accelerating voltage, 35 nA beam current and a 2 µm diameter focused electron beam. Counting times were 10 seconds or 40,000 accumulated counts. The following tabulates the X-ray lines and standards used.

Element	Line	Standard
S	Kα	synthetic $Fe_{1-x}S$
Fe	Kα	synthetic $Fe_{1-x}S$
Co	Kα	Co
Ni	Kα	synthetic NiAs
Cu	Kα	synthetic $CuFeS_2$
Zn	Kα	synthetic ZnS
As	Lα	synthetic NiAs
Se	Lα	Bi_2Se_3
Ag	Lα	Ag
Cd	Lα	CdS
Sn	Lα	Sn
Sb	Lα	Sb_2S_3
Te	Lα	Te
Au	Mα	Au
Hg	Mα	HgS
Pb	Mα	PbS
Bi	Mα	Bi_2Se_3

Table 3.2: Operating conditions for olivine analyses were carried out at 20 kV accelerating voltage, 25 nA beam current and 2 μm diameter focused electron beam. Counting times were 20 seconds or 40,000 accumulated counts. The following tabulates the X-ray lines and standards used

Element	Line	Standard
Si	Kα	wollastonite
Ti	Kα	synthetic $MnTiO_3$
Al	Kα	synthetic $MgAl_2O_4$
Cr	Kα	synthetic Cr_2O_3
Fe	Kα	synthetic Fe_2SiO_4
Mn	Kα	synthetic $MnTiO_3$
Ni	Kα	synthetic NiO
Co	Kα	synthetic $CoAl_2O_4$
Mg	Kα	olivine (Fo_{92})
Ca	Kα	wollastonite
Na	Kα	albite

CHAPTER 4

RESULTS

4.1 Introduction

This chapter presents the results of geological mapping, core logging, petrography, whole rock geochemistry, mineral chemistry and isotope analyses. The rock classification scheme proposed by Miller et al. (2002c) is utilized in the description of the Thunder intrusion and textural terminology follows the standard definitions established by Battes and Jackson (1987). The modal abundance was estimated by visual examination. The following crystal sizes were used with very fine-grained less than 0.1 mm, fine-grained ranging from 0.1 to 0.1 mm, medium-grained ranging from 1 to 5 mm, and coarse-grained exceeding 5 mm.

4.2 The Thunder intrusion geological map

4.2.1 The Thunder mafic to ultramafic intrusion

Field mapping showed the Thunder intrusion to be a mafic to ultramafic intrusion covering an 800 by 1000 m area at surface (Fig. 4.1). The intrusion is divided into two major lithostratigraphic units: the lower mafic to ultramafic unit and the upper gabbroic unit. The country rock includes mafic to intermediate metavolcanic rocks of the Shebandowan greenstone belt. In addition, outcrops of a N-trending gabbroic dike were identified east of the Thunder intrusion. The magnetic signature of an iron formation present at depth can be traced out with the aid of airborne geophysical data (OGS, 2003a). No major structures were observed in the field surrounding the Thunder intrusion. In addition, contact relationships between the Thunder intrusion and surrounding country rock were rare (see section 4.2.2); the geological boundary of the Thunder intrusion was defined with the aid of airborne geophysical data as there was generally a spatial gap between outcrops of the Thunder intrusion and country rock (Fig. 4.1).

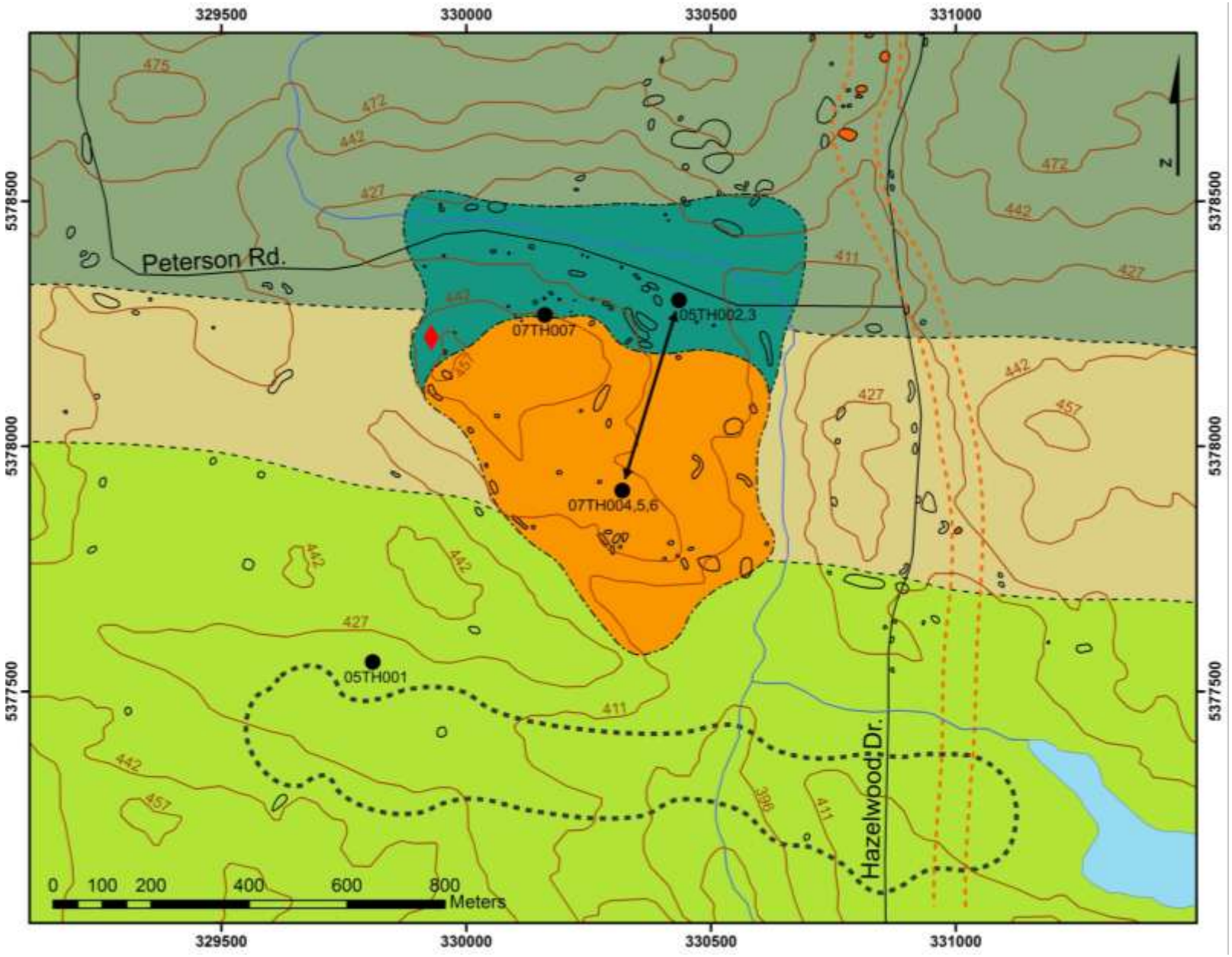
329500
330000
330500
331000
5378500
5378000
5377500
Peterson Rd.
Hazelwood Dr.
05TH002,3
07TH007
07TH004,5,6
05TH001
N
0 100 200 400 600 800
Meters

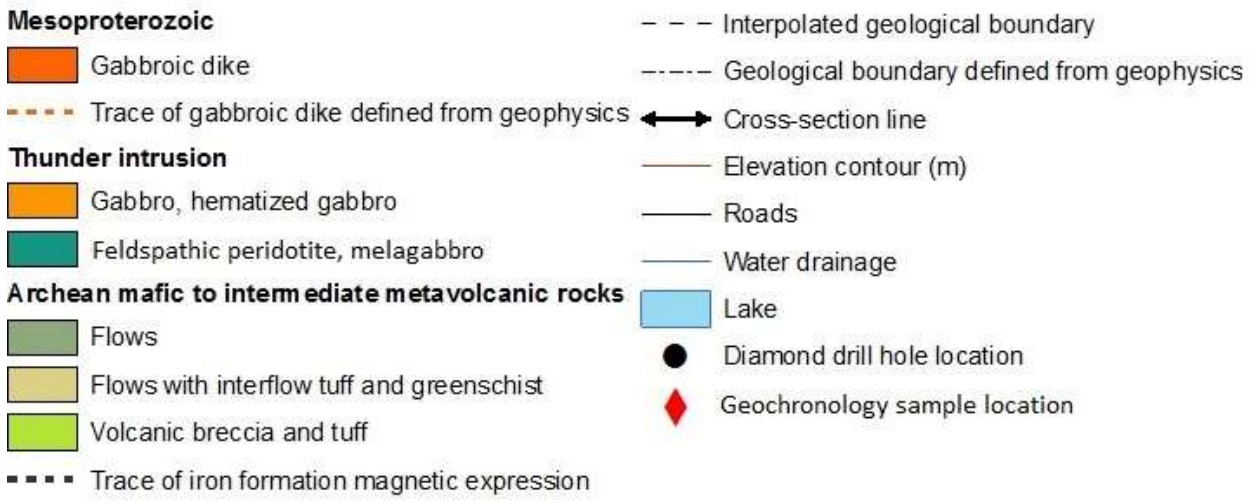

Figure 4.1: Geological map of the Thunder intrusion and vicinity at 1:9000 scale. Included on the geological map are the locations of the diamond drill holes, cross-section line and geochronology sample location. Geophysical interpretations from OGS (2003a).

The lower mafic to ultramafic unit consists dominantly of massive feldspathic peridotite and melagabbro with minor gabbro (Figs. 4.2A, B). This unit is undeformed and unmetamorphosed. All rock types display a characteristic well-developed cumulate texture defined by cumulus fine- to medium-grained olivine and fine- to coarse-grained clinopyroxene, and post-cumulus interstitial to poikilitic plagioclase. Sub-vertical serpentinized fractures up to 1 cm thick were commonly observed (Fig. 4.2C). This unit is poorly exposed and crops out along the northern margin of the Thunder intrusion (Fig. 4.1). The best exposures occur as road side outcrops along Peterson Rd (Figs. 4.1, 4.2D).

The upper gabbroic unit consists dominantly of massive gabbro to hematized gabbro. This unit is undeformed and unmetamorphosed. All rock types display a characteristic subophitic texture defined by medium-to-fine-grained plagioclase and clinopyroxene, and abundant fine- to medium-grained Fe-Ti oxide disseminations (Fig. 4.3A). The hematized gabbro is texturally identical to the gabbro phase except for variable degrees of interstitial overprinting of pinkish-red secondary hematite on plagioclase (Fig. 4.3B). The crystal habit of

plagioclase in the upper gabbroic unit differs from the lower mafic to ultramafic unit in that plagioclase crystals are lath to acicular in shape with a green-tinge and rarely showing primary igneous foliation. Two to four millimeter thick aphanitic sulphide-bearing veins commonly cross-cut outcrops of the upper gabbroic unit (Fig. 4.3C). The upper gabbroic unit forms the bulk of the surface expression of the Thunder intrusion and is best exposed along the east-trending power line which passes through the southern margin of the intrusion (Figs. 4.1, 4.3D).

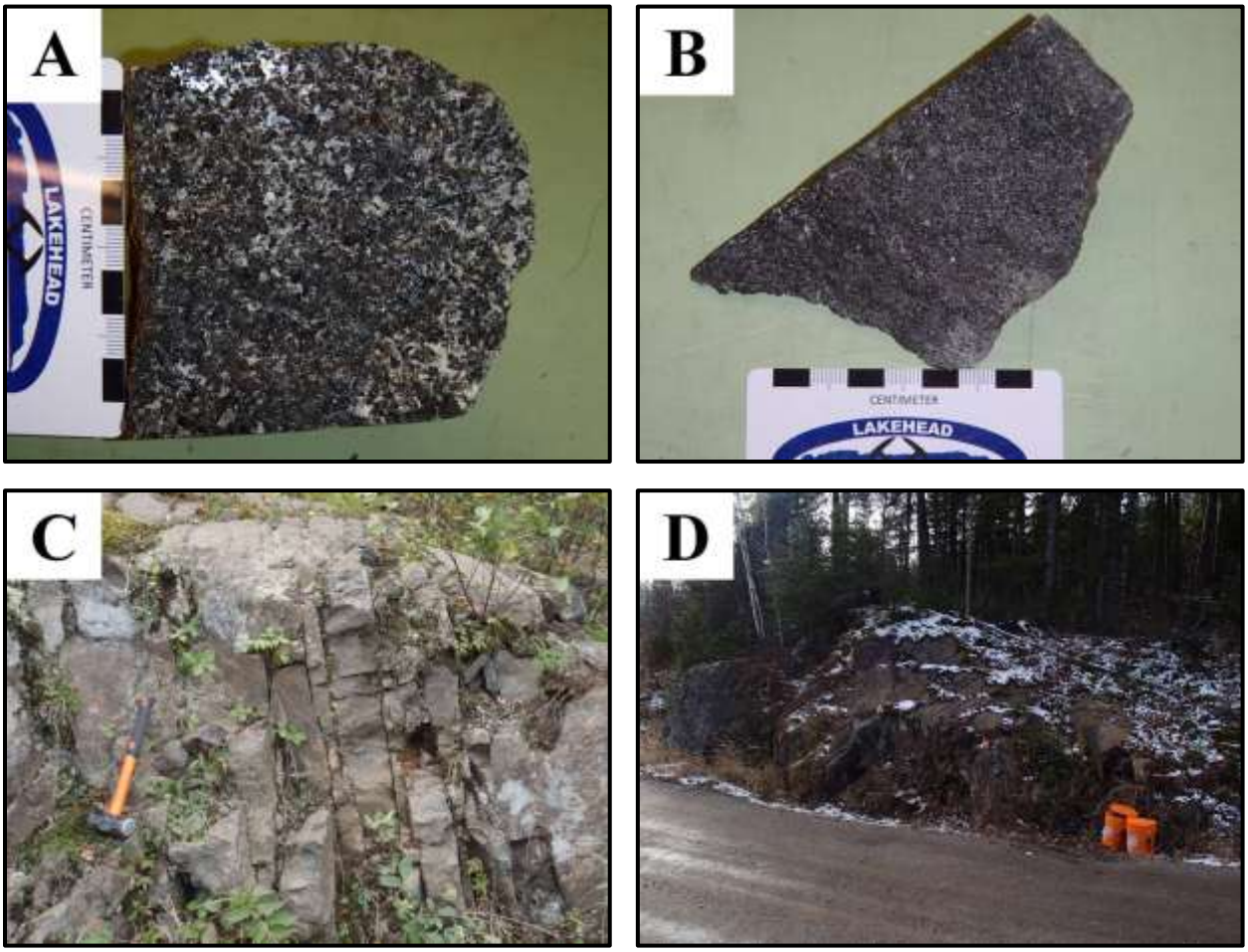

Figure 4.2: Representative photographs of the lower mafic to ultramafic unit, Thunder intrusion. A) Hand sample of melagabbro displaying the characteristic cumulate texture. B) Hand sample of feldspathic peridotite. C) Sub-vertical serpentinized fractures. D) Roadside outcrop exposed along Peterson Rd. Photographs A, C and D location at 16U 330390E 5378301N; photograph B location at 16U 329943E 5378477N.

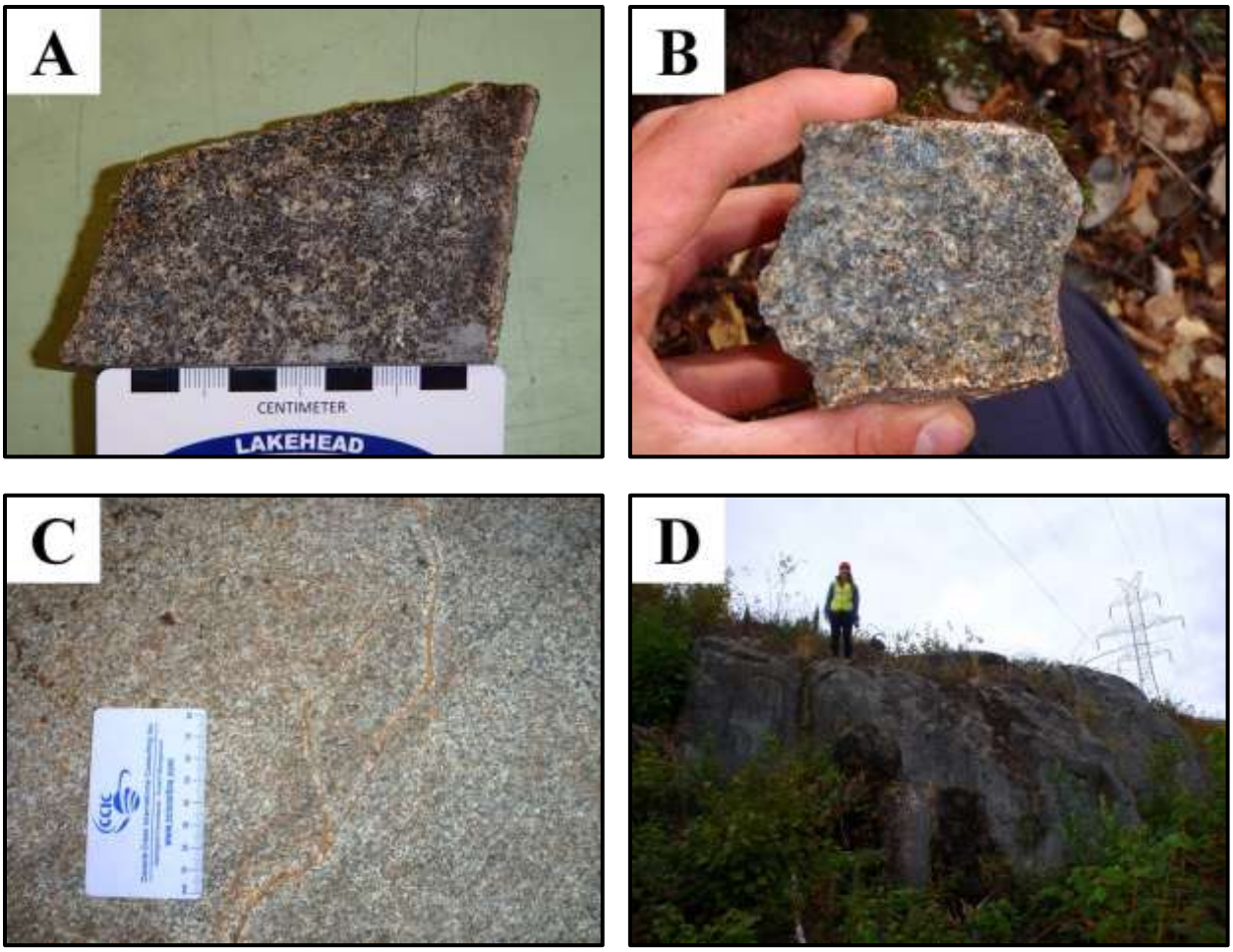

Figure 4.3: Representative photographs of the upper gabbroic unit, Thunder intrusion. A) Hand sample of gabbro displaying the characteristic subophitic texture. B) Hematized gabbro texturally identical to the gabbro. C) Rusty veins cross-cutting gabbro. D) Outcrop exposed along the E-trending power line which passes through the southern margin of the Thunder intrusion. Photographs A and D location at 16U 330283E 5377799N; photograph B location at 16U 330041E 5377062N; photograph C location at 16U 330259E 5378250N.

Rare pegmatitic gabbro sharply cross-cuts the lower mafic to ultramafic unit (Fig. 4.4A), and also occurs as irregular pods in the lower mafic to ultramafic unit (Fig. 4.4B). The pegmatitic gabbro phase consists of medium- to coarse-grained subophitic, subhedral plagioclase and clinopyroxene, and fine- to medium-grained subhedral to anhedral Fe-Ti oxide disseminations. This unit is volumetrically minor and does not appear on the geological map.

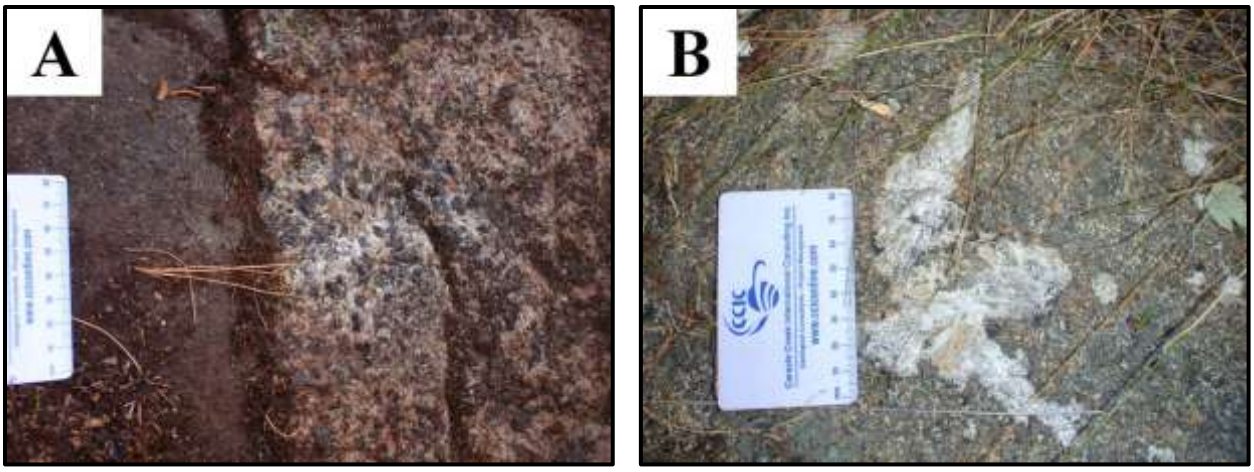

Figure 4.4: Representative photographs of the pegmatitic gabbro phase, Thunder intrusion. A) Pegmatitic gabbro (right) sharply cross-cutting the lower mafic to ultramafic unit (left); location at 16U 329929E 5378222N. B) Irregular pods of pegmatitic gabbro hosted within the lower mafic to ultramafic unit; location at 16U 330140E 5378292N.

4.2.2 Contact relationships

Only three outcrops preserving the sidewall rock contact between the Thunder intrusion and the host rock were observed. Two outcrops showed the sidewall contact between the lower mafic to ultramafic unit and host rock along the northeastern margin of the Thunder intrusion and one outcrop showing the sidewall contact between the upper gabbroic unit and host rock along the southeastern margin of the Thunder intrusion (Fig. 4.1). Both units of the Thunder intrusion have sharp contacts with the wall rock, have poorly developed chill margins and commonly contain pods of granophyre and wall rock fragments (Figs. 4.5A, B, C). Contact metamorphism of the host rock was observed as hornfels alteration displaying conchoidal fracture rather than fracturing along foliation planes. Other indications of a contact metamorphic aureole were not observed in outcrop. The hanging wall rock is poorly exposed along the northern consisting dominantly of mafic to intermediate flows that were not unusual in the sense of an alteration haloe (Fig. 4.1). The southern margins of the Thunder intrusion is a lowland/swampy area and rarely are outcrops observed (Fig. 4.1).

No outcrops were observed preserving the contact or spatial relationship between the lower mafic to ultramafic and upper gabbroic units. However, evidence of the timing relationship between the two intrusive units was observed at one outcrop where gabbro of the upper gabbroic unit was observed to host boulder sized fragments of melagabbro with diffuse reaction rims along the margins (Fig. 4.5D). The melagabbro fragments were found petrographically similar to rocks of the lower mafic to ultrmafic unit.

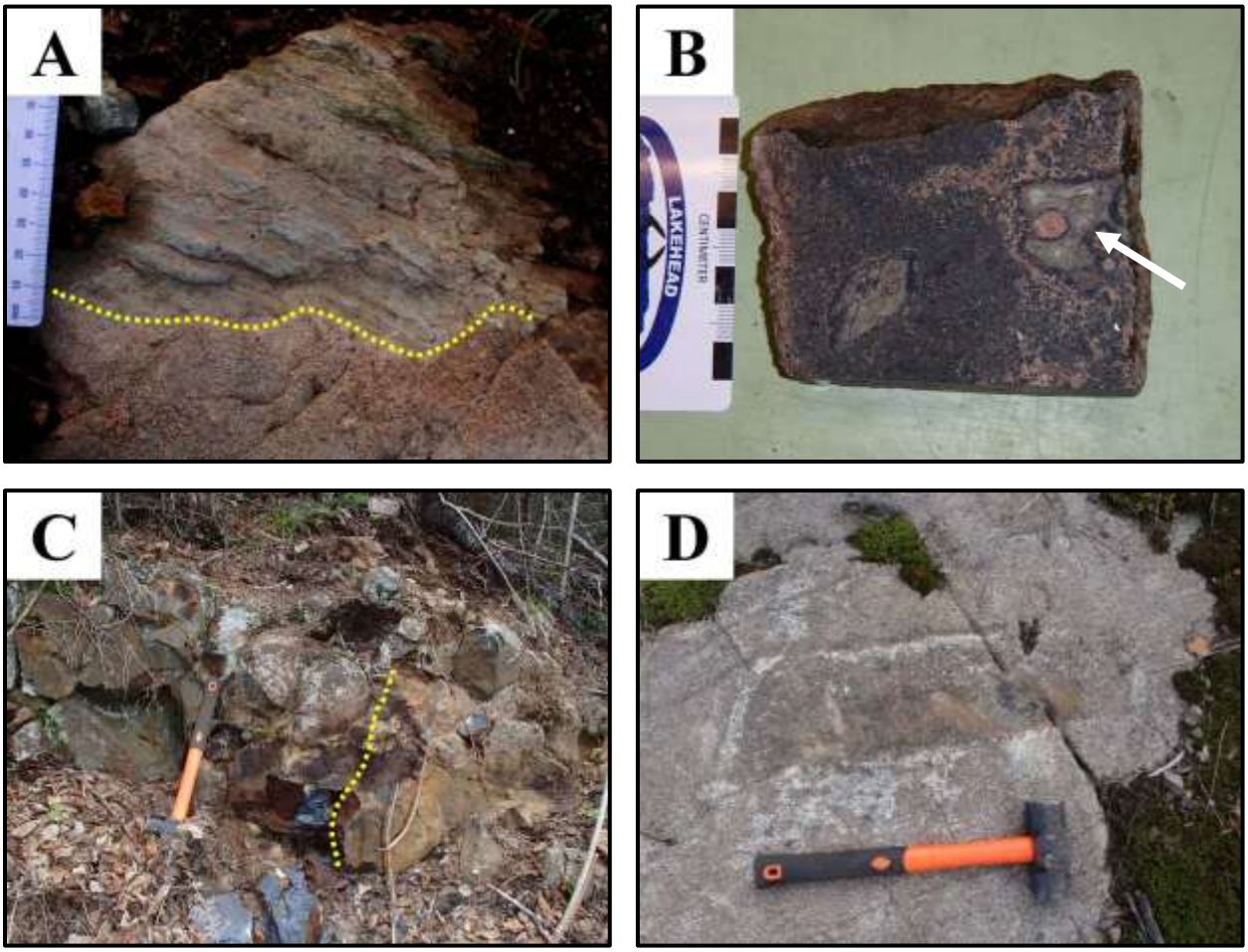

Figure 4.5: Representative photographs of lithologic contacts observed in the field, Thunder intrusion. A) Sharp contact between the upper gabbroic unit (below) and the wall rock (above); location at 16U 330570E 5377742N. B) Hand sample with abundant quartz-rich fragments with black reaction rims surrounded by pods of granophyre hosted by the upper gabbroic unit (sample RTT-BT-142; location at 330569E 5377749N; arrow). C) Sharp contact between the lower mafic to ultramafic unit (right) and the wall rock (left); location at 16U 330537E 5378442N. D) Pods of the lower mafic to ultramafic unit encased by the upper gabbroic unit; location at 16U 330259E 5378250N.

4.2.3 The marginal country rock

The country rock that surrounds the Thunder intrusion was investigated up to ~ 1500 m from the intrusion. Outcrops were generally of good quality along Hazelwood Dr. and the power line. Outcrops in the bush were generally poor and primary textures were difficult to identify due to vegetation cover. The lithologies observed were grouped into three map units: massive flows, flows with interflow tuff and argillite, and volcanic breccia and tuff (Fig. 4.1). The boundaries between the three map units represent major lithological boundaries and parallel the E-trending regional fabric as indicated by geophysical data (Figs. 2.7, 4.1). Bedding and foliation planes dip steeply to the south with a generally eastward strike. All lithologies exhibit up to greenschist facies metamorphism. No major structural boundaries such as faults were observed, however, the majority of rocks are deformed to some degree.

Abundant outcrops of massive flows occur to the northwest of the Thunder intrusion and along Hazelwood Dr., north of the intersection of Hazelwood Dr. and Peterson Rd. (Figs. 4.1, 4.6A, B). The flows consist of mafic to intermediate massive, fine-grained metabasalts with common fine- to medium-grained amphibole phenocrysts. The long-axes of the amphibole phenocrysts were observed parallel to the poorly-developed foliation of the metabasalt. In addition to greenschist facies metamorphism giving the rocks a bluish green color on fresh surfaces, patchy pinkish red potassic alteration, patchy iron-carbonate alteration, greenish yellow epidote alteration and deformed carbonate veins up to a couple of centimeters thick were commonly observed. The flows are interlayered with volumetrically minor tuff and greenschist.

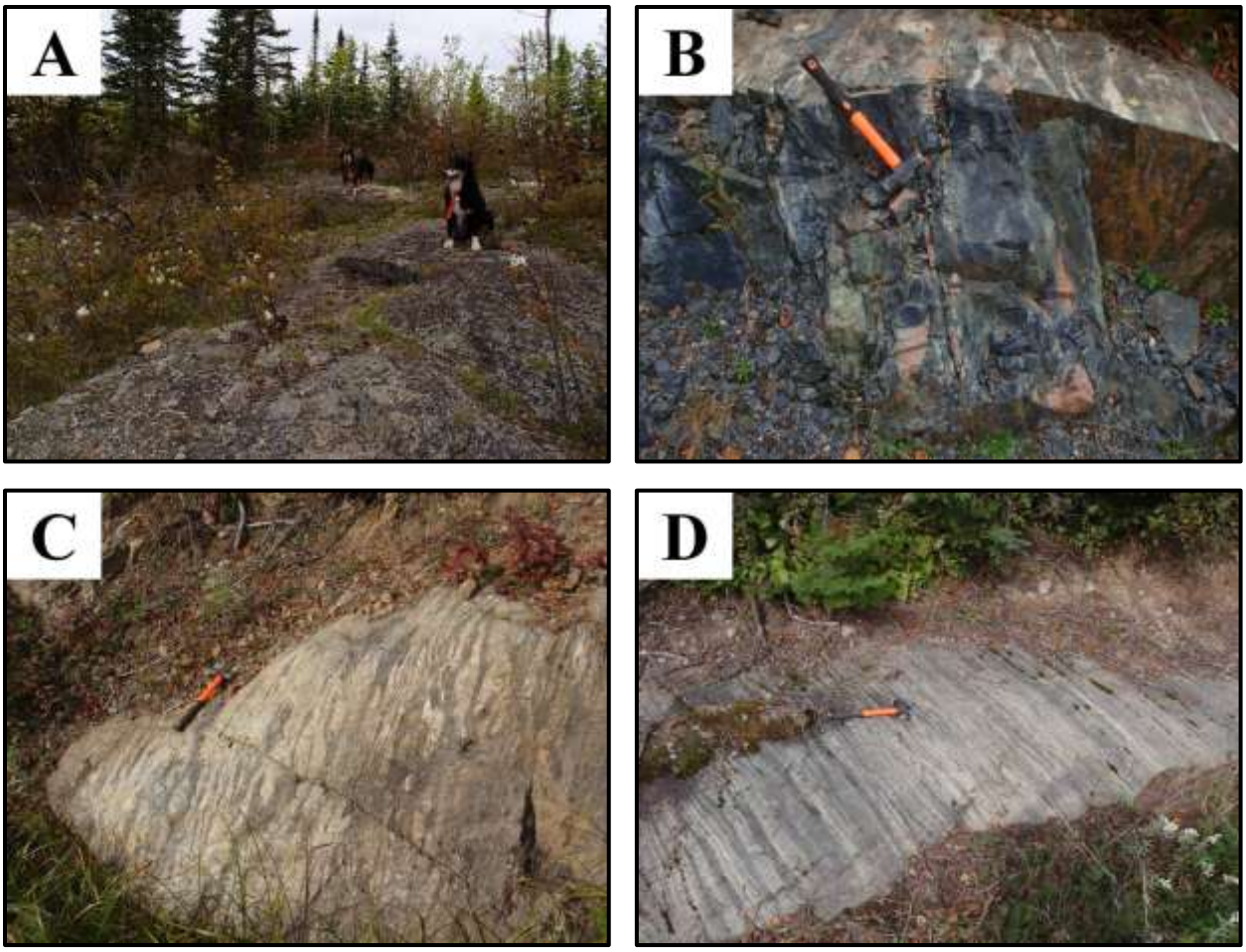

Figure 4.6: Representative photographs of the mafic to intermediate metavolcanic rocks that host the Thunder intrusion. A) Ridge forming outcrop of massive flows northeast of the Thunder intrusion; location at 16U 330520E 5378631N. B) Roadside outcrop along Hazelwood Dr. northeast of the Thunder intrusion consisting of a massive flows with patchy potassic and epidote alteration; location at 16U 330867E 5378553N. C) Roadside outcrop along Hazelwood Dr. east of the Thunder intrusion consisting of sheared pillowed flow selveges; location at 16U 330914E 5378115N. D) Roadside outcrop along Hazelwood Dr. consisting of deformed bedded tuffs with relict planar bedding; location at 16U 330918E 5378034N.

Flows with interflow tuff and greenschist surround the eastern and western margin of the Thunder intrusion (Fig. 4.1). This unit is best exposed along Hazelwood Dr., east of the Thunder intrusion (Figs. 4.6C, D). West of the Thunder intrusion outcrops are rare and poorly exposed. Much of this unit west of the Thunder intrusion was interpolated based on similar lithologies and structural measurements observed in exposures east of the Thunder intrusion. The flows consist of mafic to intermediate, massive, fine-grained metabasalt to sheared fine-grained pillowed metabasalt interlayered with interflow tuff and lapilli tuff and rare greenschist (Fig. 4.6C). In

contrast to the flows along the northern margin of the Thunder intrusion, these flows do not contain fine- to medium-grained amphibole phenocrysts nor patchy potassic and epidote alteration, but still exhibit a weakly developed foliation. The tuffs are mafic to intermediate in composition, aphanitic to very fine-grained, preserve weakly deformed planar bedding ranging from laminations up to beds ~ 12 cm thick, and contain trace to abundant elongated lapilli ranging from 1mm to 8 mm in diameter (Fig. 4.6D). The long axis of the elongated lapilli parallel the east striking bedding and foliation.

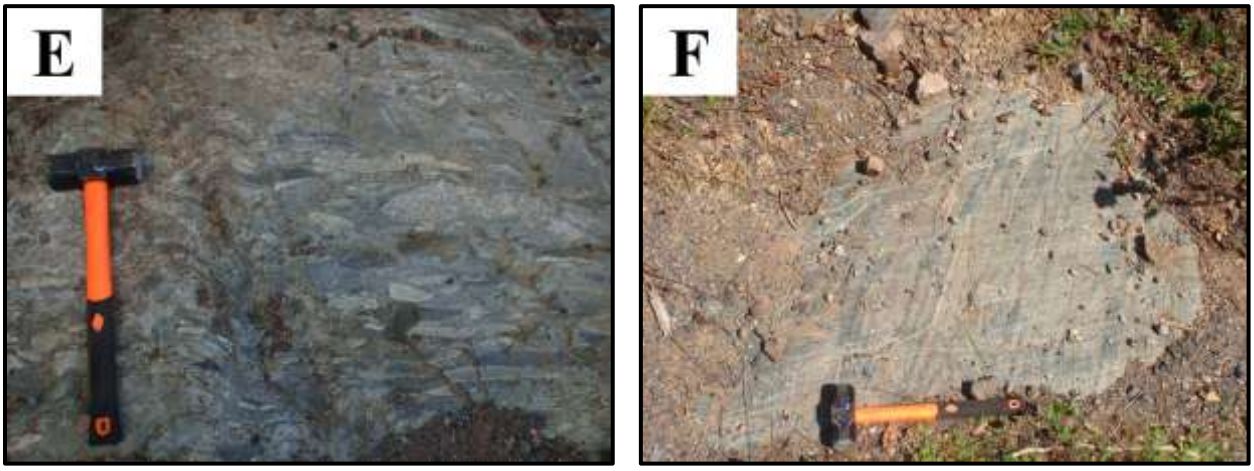

Figure 4.6 (cont.): Representative photographs of the mafic to intermediate metavolcanic rocks that surround the Thunder intrusion. E) Roadside outcrop along Hazelwood Dr. of matrix supported tuff breccias with elongate heterolithic clasts and microfolds; location at 16U 330880E 5377716N. F) Roadside outcrop along Hazelwood Dr. of matrix supported tuff breccias with elongate feldspar-phyric clasts; location at 16U 330874E 5377642N.

Volcanic breccia and tuff surround the southern margin of the Thunder intrusion and are best exposed along Hazelwod Dr., east of the Thunder intrusion and along the E-trending power line that cuts across the southern margin of the Thunder intrusion (Fig. 4.1). Otherwise, outcrops are rare and poorly exposed within the map unit boundaries. This map unit is characterized by volcanic breccia interlayered with mafic to intermediate tuff and lapilli tuff (Figs. 4.6E, F). The tuff breccias range from matrix to clast supported. The matrix is aphanitic to fine-grained with common 1 to 2 mm feldspar crystals. Clasts are heterolithic ranging from lapilli to bomb size (up 24 cm long and 8 cm thick), elongate and are predominantly E-trending. Clast lithologies

include fragments of chert, tuff, lappili tuff and feldspar-phyric clasts. On fresh surfaces, a patchy pinkish red secondary hematite overprint is commonly observed.

4.2.5 North-trending gabbroic dikes

The two N-trending magnetic anomalies discussed in section 2.9 were investigated. The magnetic anomalies were found to correlate with gabbroic dikes and are referred to as the eastern and the western N-trending gabbroic dikes. These rocks are undeformed and unmetamorphosed preserving fresh igneous textures.

The eastern N-trending gabbroic dike is a massive gabbro with a texture defined by well-developed medium-grained ophitic to subophitic plagioclase and clinopyroxene (Figs. 4.7A, B). Scattered outcrops of the eastern N-trending dike were located between 1.8 km south and 13 km north of the Thunder intrusion. No contact relations were observed with the Thunder intrusion. The closest outcrop of the gabbroic dike in relation to the Thunder intrusion was observed ~ 500 m to the east (Fig. 4.1). Outcrops of the dike indicate a maximum width of ~ 40 m. North of the study area the gabbroic dike was observed cross-cutting the Barnum intrusion with a well-developed chill margin (Figs. 2.7, 4.7D; Kuzmich, 2012).

The western N-trending gabbroic dike is a massive gabbro with similar textures to the eastern dike with well-developed medium-grained ophitic to subophitic plagioclase and clinopyroxene including medium- to coarse-grained plagioclase phenocrysts (Fig. 4.8A). Scattered outcrops of the western N-trending gabbroic were difficult to locate due to lack of exposure. The closest outcrop was located ~ 8 km north of the Thunder intrusion (RTT-BT-220) where a ~ 2.5 m fine-grained gabbroic dike with medium-grained plagioclase laths cross-cuts Quetico metasedimentary rock (Fig. 4.8B, C.). A cluster of outcrops were located ~ 24 km north of the Thunder intrusion; the locations of which correlate to the N-trending magnetic anomaly

(Stainton, 2012). The outcrops occur on mineral claims currently held by Glory Resources which are contracted to Clark Exploration Consulting Inc., and permission to access and sample was granted by Steve Siemieniuk, Project Geologist. The gabbroic dike was observed sharply cross-cutting metasedimentary and granitoid rocks of the Quetico subprovince. Field observations at this locality showed a maximum width of 25 m and a minimum width of 1 m (Fig. 4.8D).

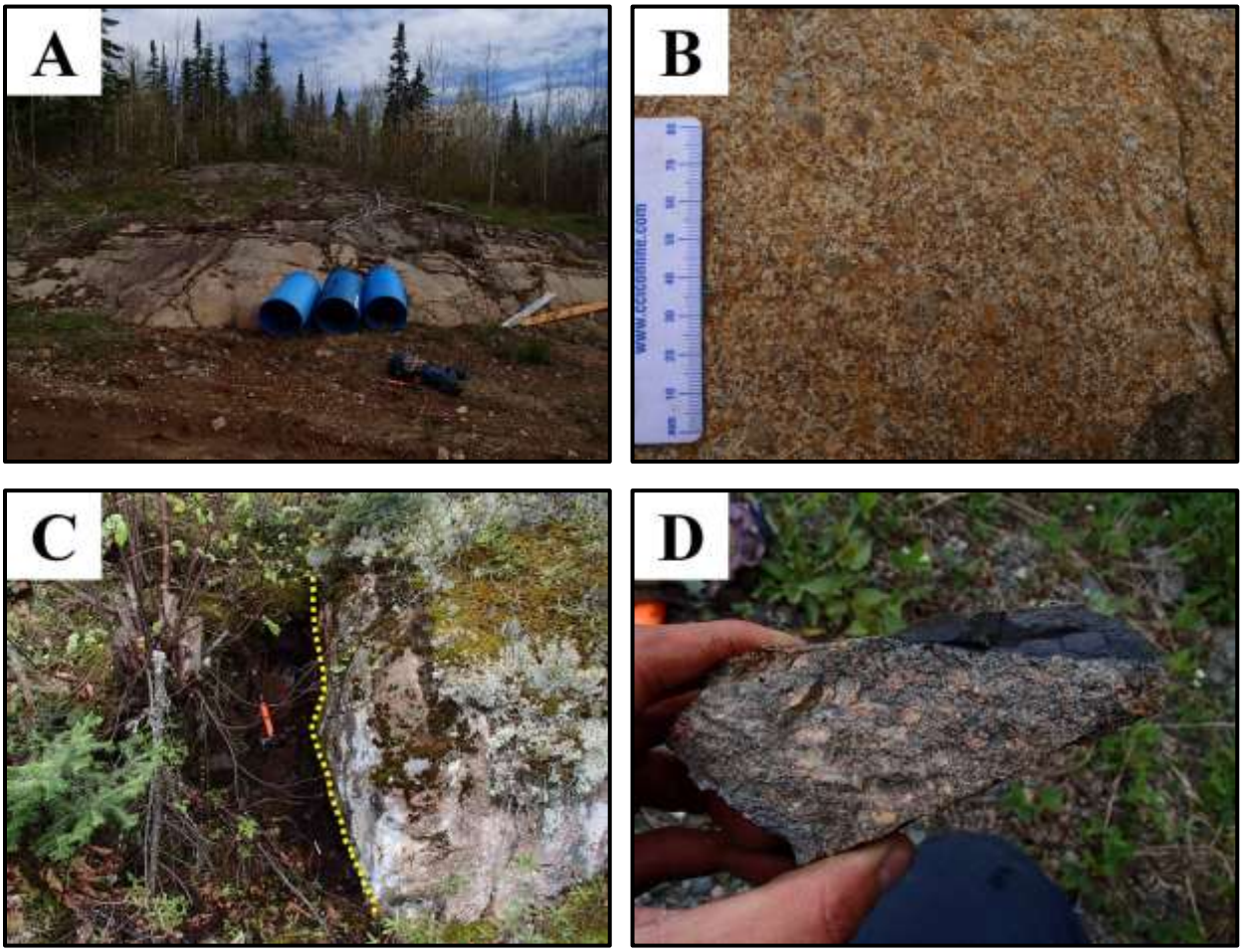

Figure 4.7: Representative photographs of the eastern N-trending gabbroic dike. A) Scattered outcrops reaching up to 40 m width; location at 16U 330803E 5378724N. B) Well-developed ophitic to subophitic texture defined by medium-grained plagioclase and clinopyroxene. C) Sharp cross-cutting relationship in the Barnum intrusion; location at 16U 330587E 5391889N. D) A well-developed chill margin observed in the outcrop in photograph C.

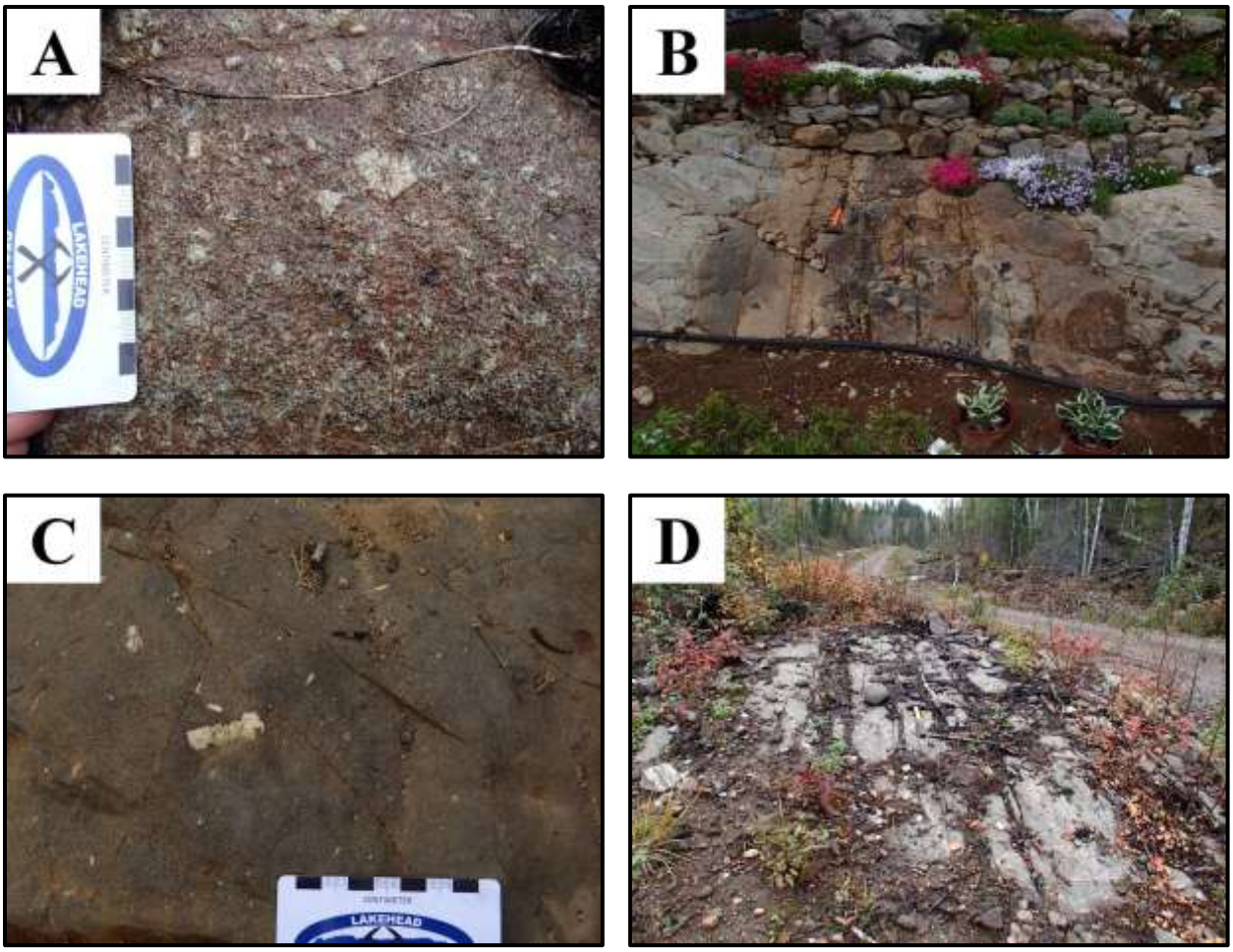

Figure 4.8: Representative photographs of the western N-trending gabbroic dike. A) Well-developed ophitic to subophitic texture defined by medium-grained plagioclase and clinopyroxene including coarse-grained plagioclase phenocrysts; location at 16U 326997 5401169. B) Approximately 2.5 m gabbroic dike sharply cross-cutting metasedimentary rock with characteristic medium- to coarse-gained plagioclase phenocrysts shown in photograph C; location at 16U 328598E 5386506N. D) Outcrops located approximately 24 km north of the Thunder intrusion correlating with the magnetic anomaly; location at 16U 327028 5401620.

4.3 Core logging

A total of 2806 m of diamond drill core was logged from seven holes: 05TH001 (275 m), 05TH002 (291 m), 05TH003 (336 m), 07TH004 (518 m), 07TH005 (440 m), 07TH006 (617 m), and 07TH007 (329 m). Note: rocks of the Thunder intrusion containing visible sulphide disseminations greater than 1 modal % were classified as "mineralized".

4.3.1 Diamond drill hole 05TH001

Diamond drill hole 05TH001is a 275 m long vertical hole that was drilled into the magnetic anomaly located approximately 400 m southwest of the nearest outcrop of the Thunder intrusion (Figs. 2.7, 4.1). The drill core can be subdivided into three major stratigraphic intervals consisting from bottom to top of: ~ 160 m of volcanic breccia and tuff; ~ 50 m of garnet-magnetite-calcite iron formation and ~ 66 m of graphitic heterolithic breccia and schist (Fig. 4.9). Contacts between lithologies are generally gradational. No intrusive rocks of the Thunder intrusion were intersected.

The lower section of DDH 05TH001 consists of matrix supported volcanic breccia of intermediate composition (Fig. 4.10A). The matrix is aphanitic to fine-grained with common 1 to 2 mm feldspar phenocrysts. Clasts are volcaniclastic, heterolithic, lapilli to bomb size and commonly brecciated. Interlayered with the volcanic breccia are bedded and lappilli tuffs similar in composition to the breccia. The overall greyish blue color of the lithologies is commonly overprinted by patchy to interstitial pinkish red secondary hematite alteration (Fig. 4.10B). The fabric of the rock is defined by parallel clast elongation. Overall, these metavolcanic rocks are similar to ones observed along the southern margin of the Thunder intrusion (Fig. 4.1) and in other drill cores.

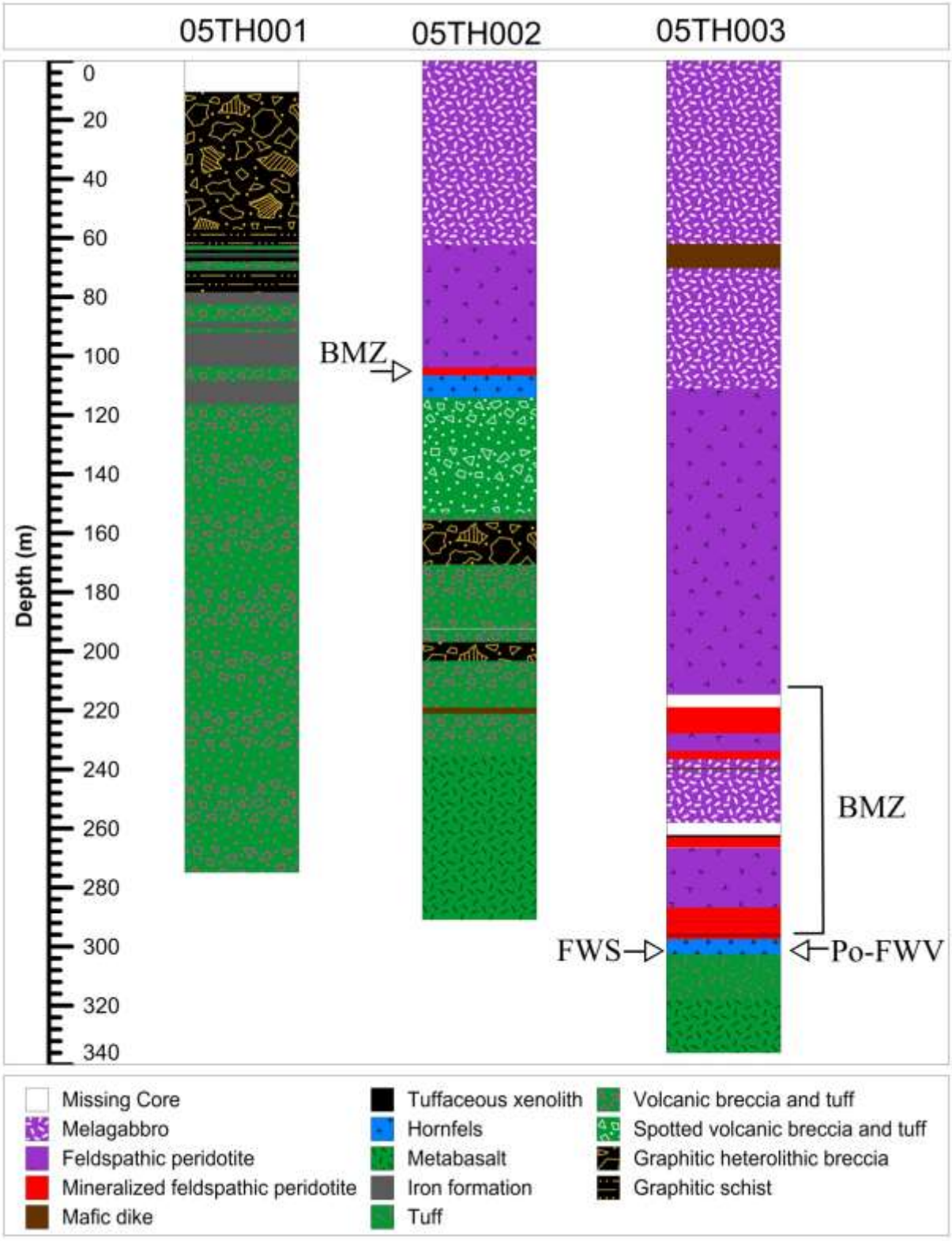

Figure 4.9: Lithostratigraphy of diamond drill holes 05TH001, 002 and 003. Labelled are spatial occurrences of the styles of mineralization discussed in section 4.6. Note: mineralized feldpsathic peridotite contains sulphide disseminations greater than 1 modal %. Refer to Figure 4.1 for collared location.

A garnet-magnetite-calcite iron formation unit comprises the middle section of DDH 05TH001 (Fig. 4.10C). The mineralogy includes andradite-grossular garnet, stilpnomelane, apatite, carbonate, magnetite, pyrite and trace chalcopyrite. Variable fine-grained, granular, pale brown garnet intergrown with fine-grained semi-massive granular magnetite is most abundant, reaching up to 70 modal %. Up to 5 % medium- to fine-grained pyrite-chalcopyrite disseminations and up to 10 % carbonate pods ~ 2 cm in diameter make up the remainder of the visible mineralogy. The bottom section of the iron formation is interlayered with volcanic breccia and tuff, and the upper section interlayered with pyrite-rich graphitic schist (Fig. 4.9). The iron formation unit was not observed in other holes or on surface. Very high magnetic susceptibility measurements taken from the iron-rich interval were determined to correlate with the magnetic anomalies adjacent to the Thunder intrusion's magnetic anomaly in Figure 2.7. The magnetic expression of the unit is traced in Figure 4.1.

Matrix- to clast-supported graphitic heterolithic breccia and graphitic schist comprise the upper section of DDH 05TH001 (Fig. 4.10D). The matrix is aphantic and graphitic in composition giving the rock a blackish gray sheen. Clasts are variable in size ranging from pebble to cobble size and include intermediate volcaniclastic, chert and quartz fragments. The graphitic schists are blackish-blue in color and identical to the matrix of the breccias. Common semi-massive pyrite lenses were observed interlayered with the schists and interstitial to the clasts of the breccias comprising up to 10 %. The fabric of the rock is defined by parallel clast elongation and schistosity. These graphitic rocks were not observed on surface or in other drill cores except DDH 05TH002 (Fig. 4.9).

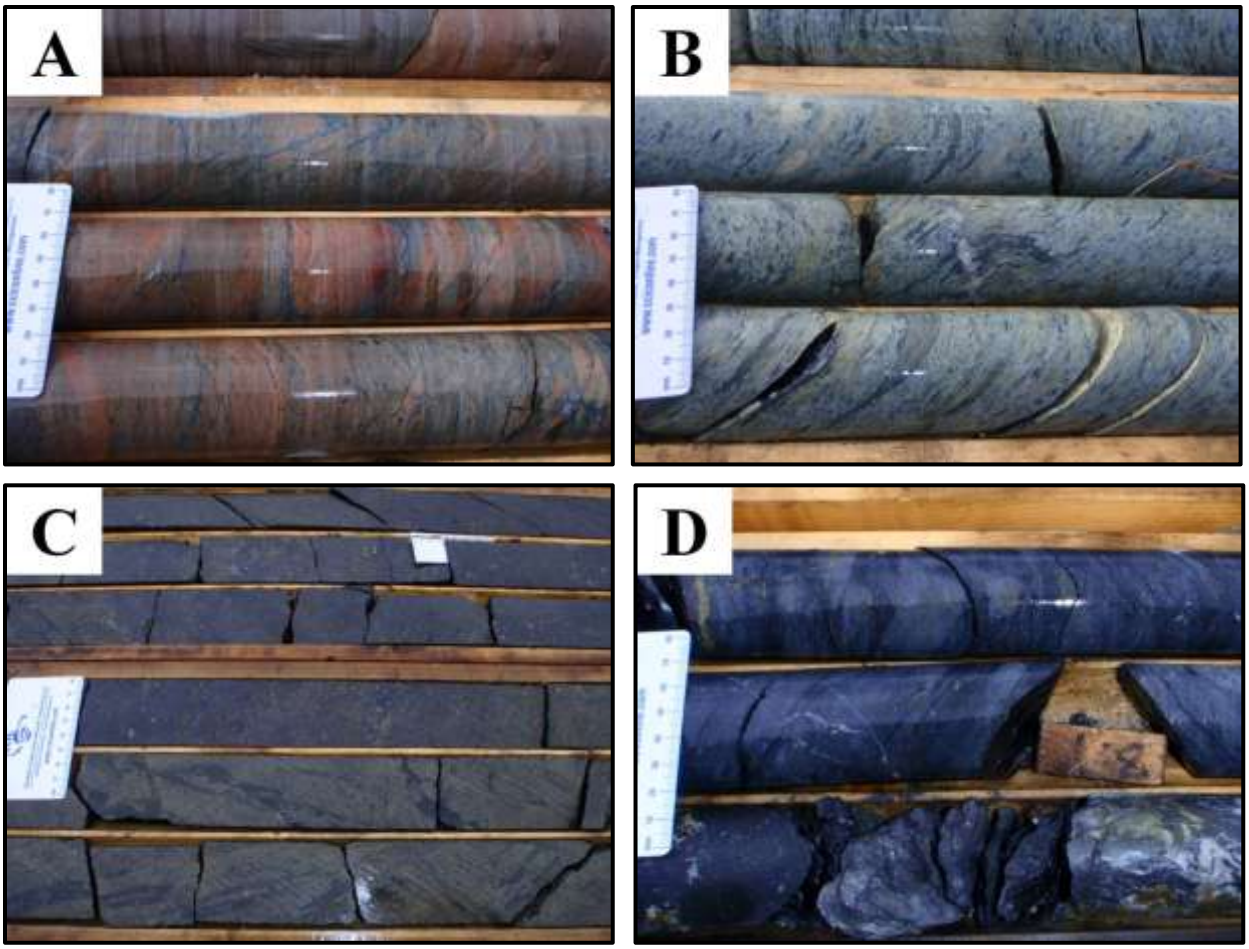

Figure 4.10: Representative photographs of lithologies in diamond drill hole 05TH001. A) Volcanic breccias and tuff with pinkish red secondary hematite overprint at ~ 225 m. B) Volcanic breccias and tuff at ~ 165 m. C) Garnet-magnetite-calcite iron formation at ~ 100 m. D) Graphitic heterolithic breccia and interlayered graphitic schist at ~ 48 m.

4.3.2 The northern margin diamond drill holes

Diamond drill holes located along the northern margin of the Thunder intrusion include 05TH002 and 003 (Fig. 4.1; Table 2.1). Both were collared at the same location with DDH 05TH002 drilled at 55° to the north and DDH 05TH003 drilled at 65° to the south (Table 2.1). The holes generally consist from bottom to top of deformed mafic to intermediate metavolcanic rock and uninterrupted intrusive rocks of the Thunder intrusion (Fig. 4.9). Lithologies of the Thunder intrusion were consistent with surface observations of the lower unit comprising from bottom to top mineralized feldspathic peridotite, feldspathic peridotite and melagabbro (Figs.

4.9, 4.11F, 4.12C, D, E). The uppermost section of the melagabbro interval hosts irregular pods of pegmatitic gabbro up to 5 cm diameter. The wall rock contact is sharp but lacks a well-developed chilled margin.

Although collared at the same location, the wall rock lithologies of DDH 05TH002 and 003 differ. DDH 05TH002 consists from bottom to top of: ~ 56 m of massive fine-grained metabasalt (Fig. 4.11A), ~ 82 m of interlayered volcanic and graphitic breccia (Fig. 4.10B) that is cross-cut by a ~ 2 m thick fine-grained mafic dike between 219.10 and 221.10 m preserving well developed chill margins (Figs. 4.11C), ~ 39 m of spotted kaolinite volcanic breccia and tuff (Fig. 4.10D), and ~ 5 m of hornfels (Figs. 4.9, 4.11E). DDH 05TH003 consists from bottom to top of: ~ 18 m of massive fine-grained, amphibole-phyric metabasalt, ~ 15 m of bedded and lapilli tuffs with patchy pinkish red secondary hematite overprinting and ~ 5 m of (Figs. 4.9, 4.12A, B). An ~ 8 m thick fine-grained mafic dike was observed in 05TH003 where it cross-cuts melagabbro between ~ 62 and 70 m preserving well-developed chilled margins (Figs. 4.9, 4.12F). The contacts between lithologies are generally gradational.

Texturally, the cross-cutting mafic dike occurrences observed in both holes are similar. The mafic dikes are massive, fine- to very fine-grained within the core and aphanitic when proximal to the contact (i.e., the chill margin). The mineralogy consists dominantly of intergranular plagioclase and clinopyroxene. No visible sulphides were observed.

The volcanic breccia and tuffs are similar to those previously discussed; however, the spotted volcanic breccia and tuff is only found in DDH 05TH002. Abundant 1 - 2 mm diameter kaolinite pods overprint a volcanic breccia and tuff unit, as spotted to interstitial clusters interpreted to be kaolinitized feldspar augen (Fig. 4.11D). This rock does not share a direct contact with the Thunder intrusion as it grades upwards into a volcanic breccia and tuff unit

weakly overprinted by contact metamorphism (i.e., hornfels; Figs. 4.9, 4.11E). Hornfels occurs adjacent to the Thunder intrusion contact in both holes (Fig. 4.9).

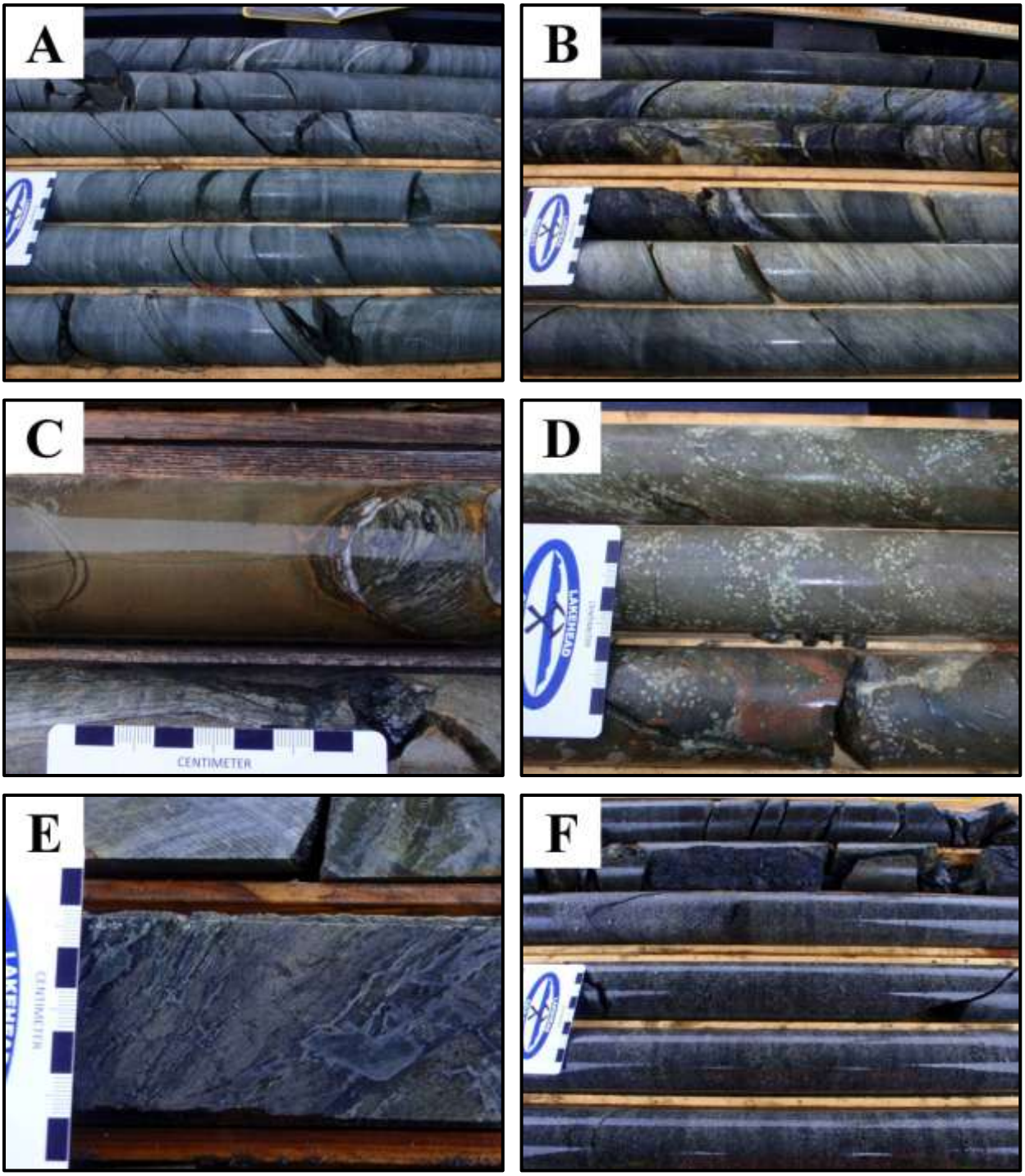

Figure 4.11: Representative photographs of lithologies in diamond drill hole 05TH002. A) Massive fine-grained metabasalt at ~ 260 m. B) Interlayered volcanic breccia and graphitic heterolithic breccia at ~ 205 m. C) Lower contact of a cross-cutting fine-grained mafic dike at ~ 220 m. D) Spotted volcanic breccia and tuff at ~ 150 m. E) Weakly altered rock at ~ 110 m proximal to the wall rock contact. F) Fine-grained feldspathic peridotite at ~ 55 m.

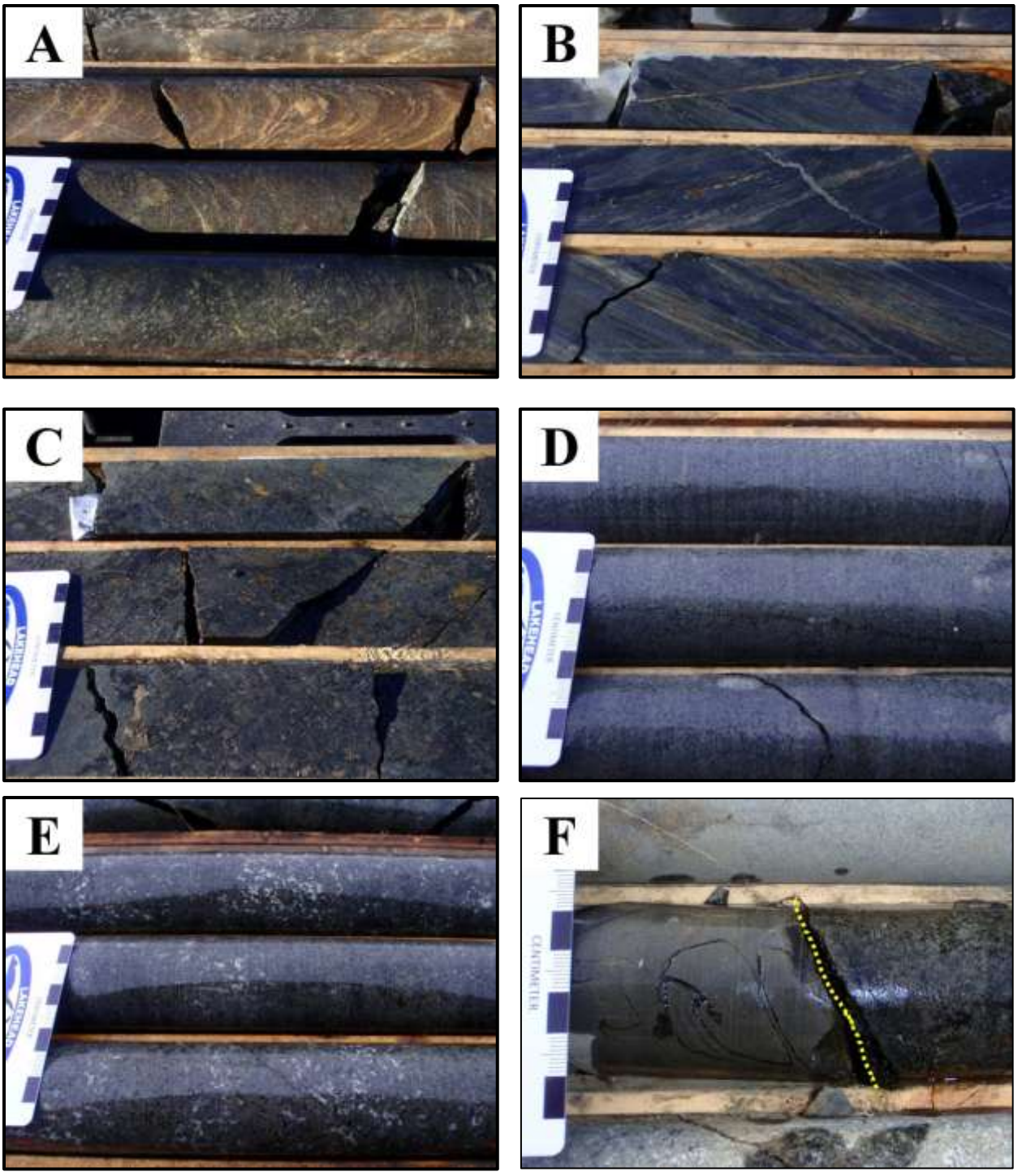

Figure 4.12: Representative photographs of lithologies in diamond drill hole 05TH003. A) Deformed bedded and lapilli tuff at ~ 317 m. B) Bedded tuff weakly overprinted by contact metamorphism at ~ 302 m. C) Sulphide disseminated up to 30% hosted by feldspathic peridotite at ~294 m. D) Fine-grained barren feldspathic peridotite at ~ 210 m. E) Medium- to fine-grained melagabbro at ~ 16 m. F) Lower contact of a fine-grained dike (left) cross-cutting melagabbro (right) at 70.32 m.

4.3.3 Diamond drill holes within the core of the Thunder intrusion

The holes drilled during the 2007 exploration program are located within the center of the Thunder intrusion (Fig. 4.1; Table 2.2). DDHs 07TH004, 005 and 006 were collared at the same location with 07TH004 drilled vertically, 07TH005 drilled at 70° to the north and 07TH006 drilled at 65° to the south; 07TH007 was drilled at 80° to the south at a different location (Fig. 4.1; Table 2.2). Overall, the lithostratigraphy is similar amongst the four holes consisting from bottom to top of deformed mafic to intermediate metavolcanic rock (mostly tuff, lapilli tuff and volcanic breccia), hornfels, mineralized feldspathic peridotite, feldspathic peridotite, melagabbro, gabbro, hematized gabbro and granophyre-bearing hematized gabbro (Figs. 4.13). The thickness of each interval however, varies in the four holes (Fig. 4.13, 4.14, 4.15). Texturally, gabbro, hematized gabbro and granophyre-bearing hematized gabbro are consistent with the upper gabbroic unit, whereas mineralized feldspathic peridotite, feldspathic peridotite and melagabbro are consistent with the lower mafic to ultramafic unit. The contact between the lower mafic to ultramafic unit and the upper gabbroic unit is marked by an abrupt change in plagioclase texture from interstitial and poikilitic to subophitic. The uppermost section of the melagabbro intervals host abundant irregular pods of pegmatitic gabbro up to 10 cm in diameter marking the onset of the contact with the upper gabbroic unit. The contact with the wall rock is sharp but lacks a well-developed chill margin.

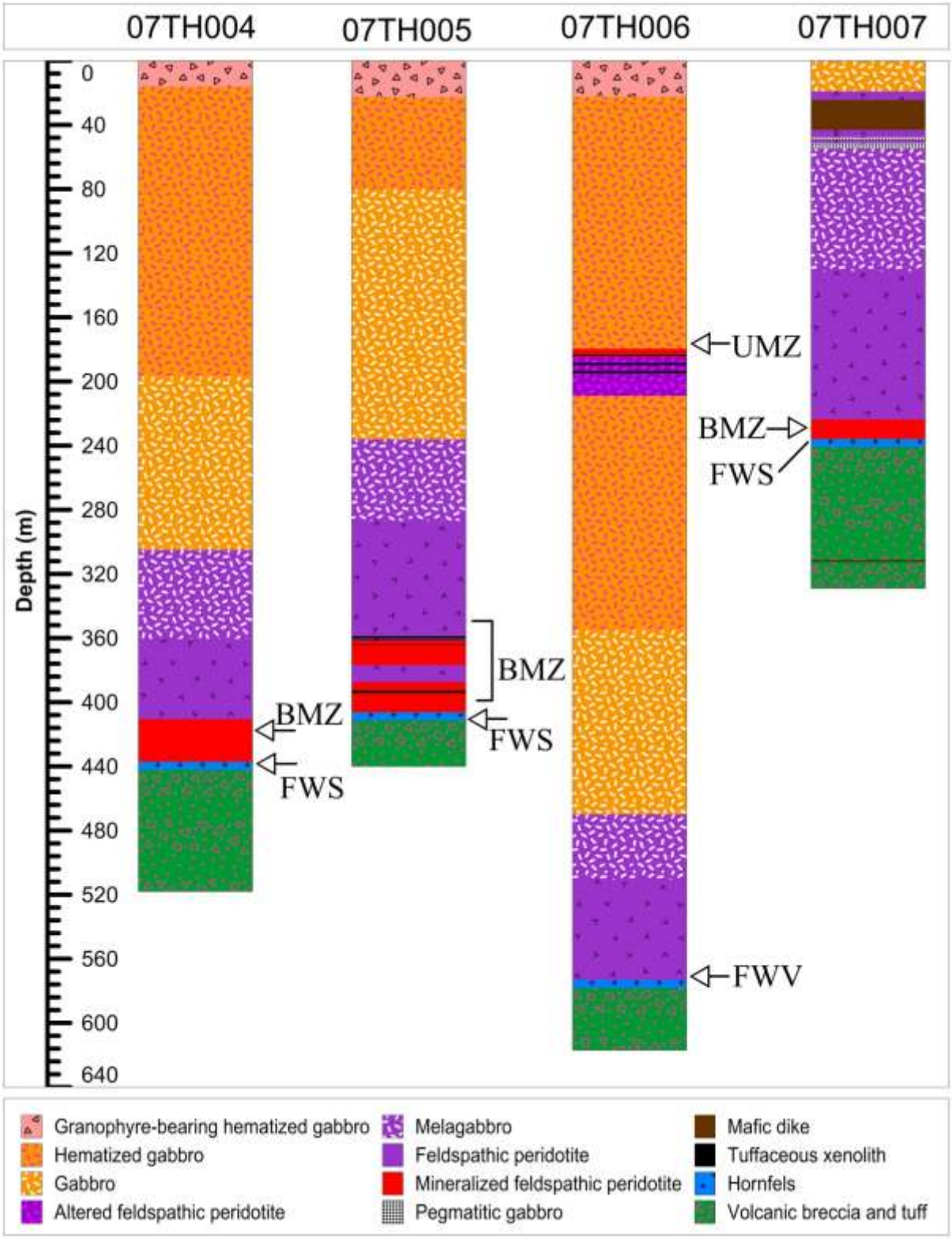

Figure 4.13: Lithostratigraphy of diamond drill holes 07TH004, 005, 006 and 007. Labelled are spatial occurrences of the styles of mineralization discussed in section 4.6. Note: mineralized feldpsathic peridotite contains sulphide disseminations greater than 1 modal %. Refer to Figure 4.1 for collared location

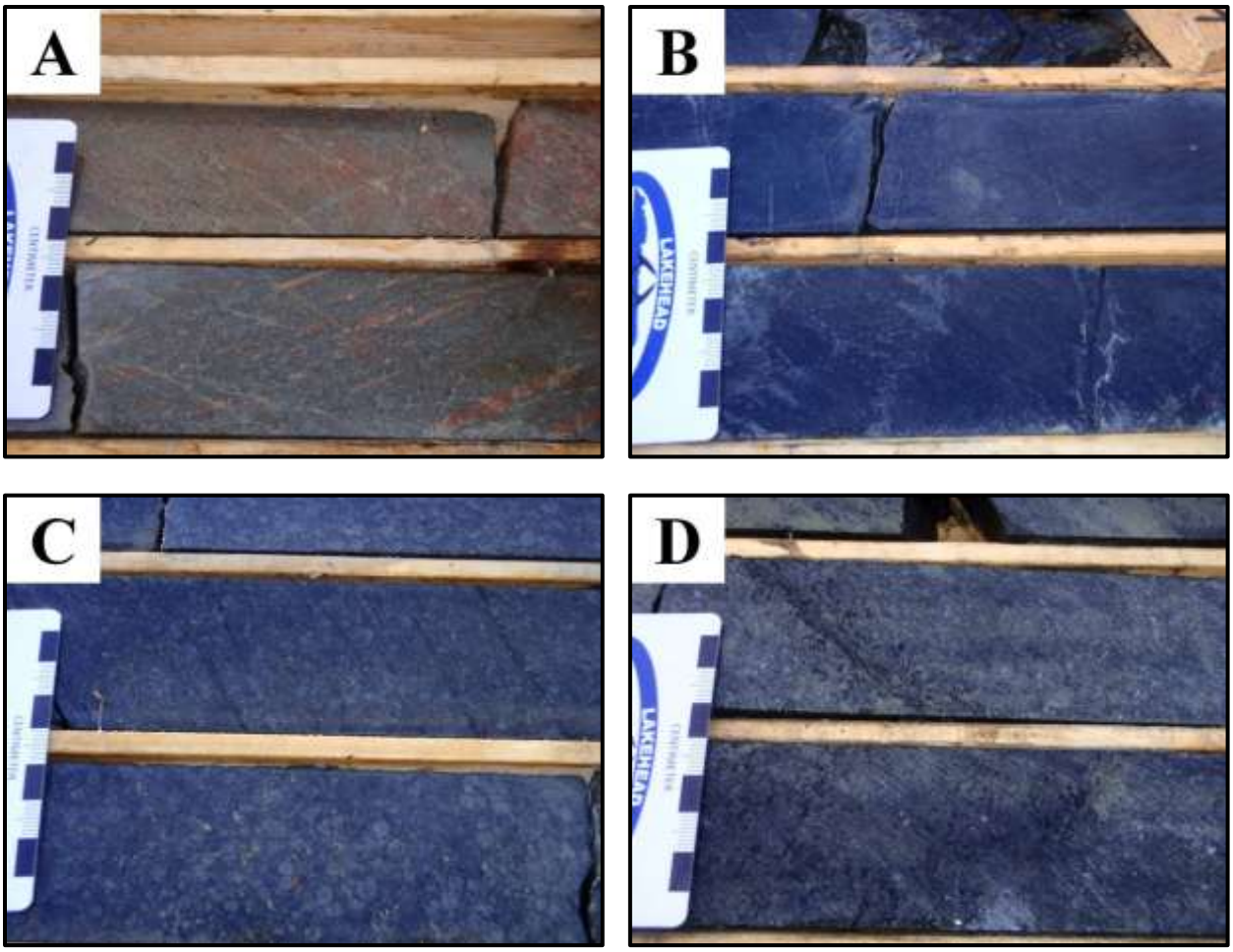

Figure 4.14: Representative photographs of lithologies in diamond drill hole 07TH004. A) Deformed lapilli tuff overprinted by pinkish red secondary hematite alteration at ~ 450 m. B) Hornfels proximal to the Thunder-wall rock contact at ~ 445 m. C) Pyhotite + chalcopyrite disseminations hosted by feldspathic peridotite at ~ 435 m. D) Feldspathic peridotite at ~ 370 m.

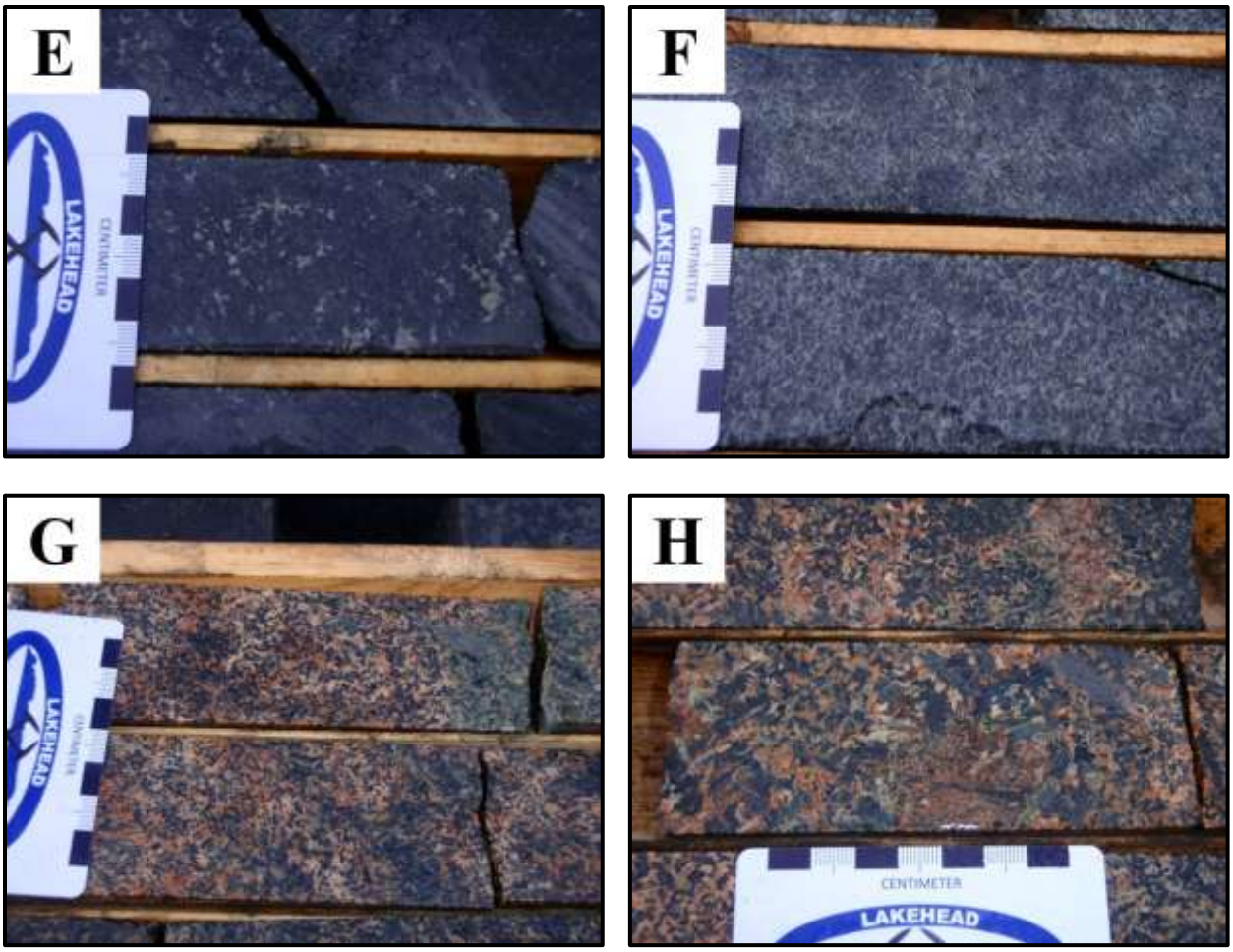

Figure 4.14 (cont.): Representative photographs of lithologies in diamond drill hole 07TH004. E) Melagabbro at ~ 315 m. F) Gabbro at ~ 285 m. G) Hematized gabbro at ~ 30 m. H) Granophyre pods hosted by hematized gabbro at ~ 10 m.

4.3.3.1 Diamond drill hole 07TH006

Between ~ 210 and 180 m within DDH 07TH006, mineralized and altered feldspathic peridotite containing tuffaceous wall rock fragments occur between hematized gabbro (Figs. 4.13, 4.15). The alteration of the feldspathic peridotite consists of patchy pinkish red to purple overprinting on the interstitial plagioclase. The margins of the wall rock fragments are irregular and appear partially melted (Fig. 4.15A**)**. This textural attributes of the mafic rocks throughout this interval are consistent with the lower mafic to ultramafic unit.

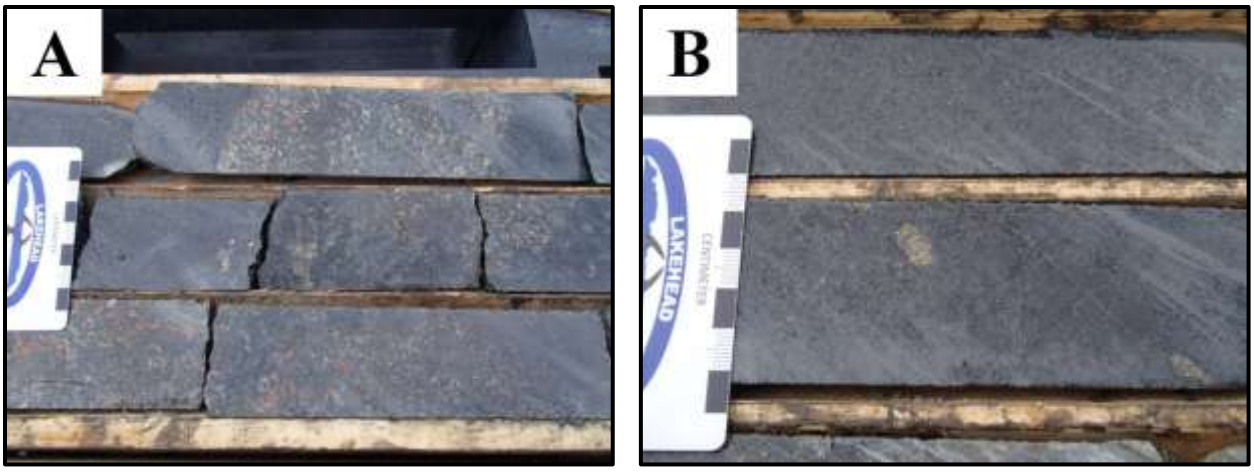

Figure 4.15: Representative photographs of altered feldspathic peridotite with tuffaceous wallrock fragments from diamond drill hole 7TH006. A) Altered feldspathic peridotite at 185 m. B) Trace medium-grained globular sulphide disseminations hosted by fine-grained feldspathic peridotite at 180 m.

4.3.3.2 Other intrusive units

Other intrusive phases intersected by the 2007 diamond drill holes include pegmatitic gabbro and mafic dikes. Within DDH 07TH007 pegmatitic gabbro cross-cuts the lower mafic to ultramafic unit between 45.51 to 47.74 m and 51.60 to 54.64 m (Fig. 4.13). The pegmatitic gabbro exhibits a subophitic texture defined by medium- to coarse-grained subhedral clinopyroxene and plagioclase with scattered pods of interstitial granophyre up to 2 cm (Fig. 4.16A). No chill margin was observed along the contact of the pegmatitic gabbro. This lithology is similar to that of the pegmatitic occurrences on surface (Fig. 4.4).

Also within DDH 07TH007 three mafic dikes were observed two of which cross-cut the lower mafic to ultramafic unit at ~ 25.46 to 43.14 m and 45.40 to 45.51 m (Figs. 4.13, 4.16B, C); the third cross-cutting the metavolcanic wall rock at 311.53 to 312.60 m (Figs. 4.13, 4.16D). Well-developed chill margins in the dikes were observed in all three occurrences. Texturally, these mafic dikes are massive, generally fine- to very fine-grained but aphanitic when proximal to the contact. The mineralogy consists dominantly of intergranular plagioclase and cliopyroxene. No visible sulphides were observed.

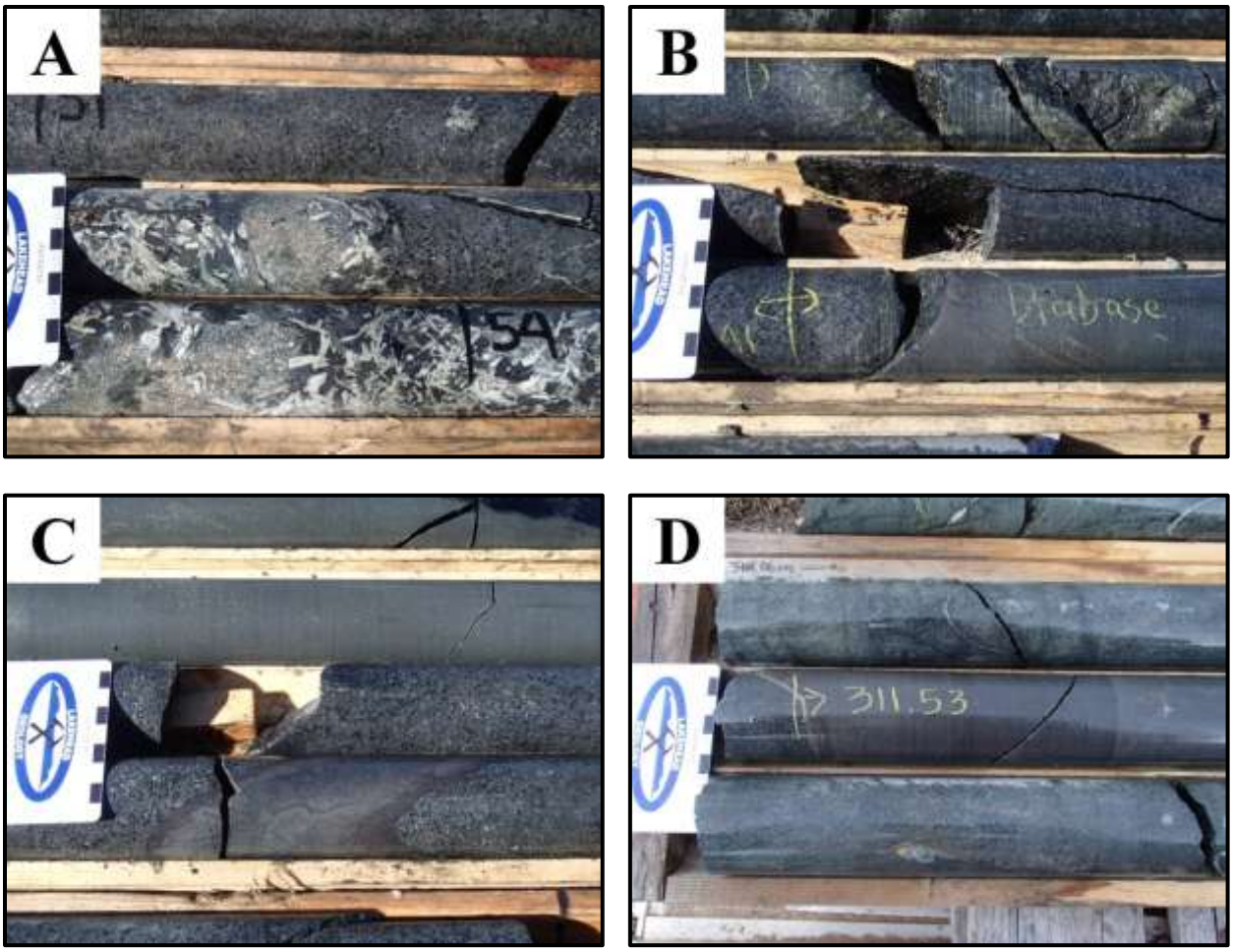

Figure 4.16: Representative photographs of dikes and pegmatitic gabbro in diamond drill hole 07TH007. A) Pegmatitic gabbro cross-cutting feldspathic peridotite at ~ 54 m. B) The upper contact of a fine-grained mafic dike cross-cutting feldspathic peridotite at 24.46 m. C) A small offshoot dike assumed to be associated with the mafic dike in B. D) The upper contact of fine-grained mafic dike sharply cross-cutting metavolcanic wall rock at 311.53 m. Note: drill core markings were done by previous geologists.

4.3.4 Geological cross-section

A simplified lithostratigraphic cross-section of the Thunder intrusion was constructed along a fence of 5 drill holes that lie along a similar azimuth including DDH 05TH002, 003, 07TH004, 005 and 006 (Tables 2.1, 2.2) and the cross-section line of reference illustrated in Figure 4.1 (Fig. 4.17). According to the cross-section, the Thunder intrusion is < 600 m total thickness with a steep southward dip (Fig. 4.17) and a roughly estimated surface area 0.8 km^2 (Fig. 4.1). The lower mafic to ultramafic unit thickens to the northeast whereas the upper

gabbroic unit thickens to the southwest. Evidently, only footwall rocks were intersected by drilling.

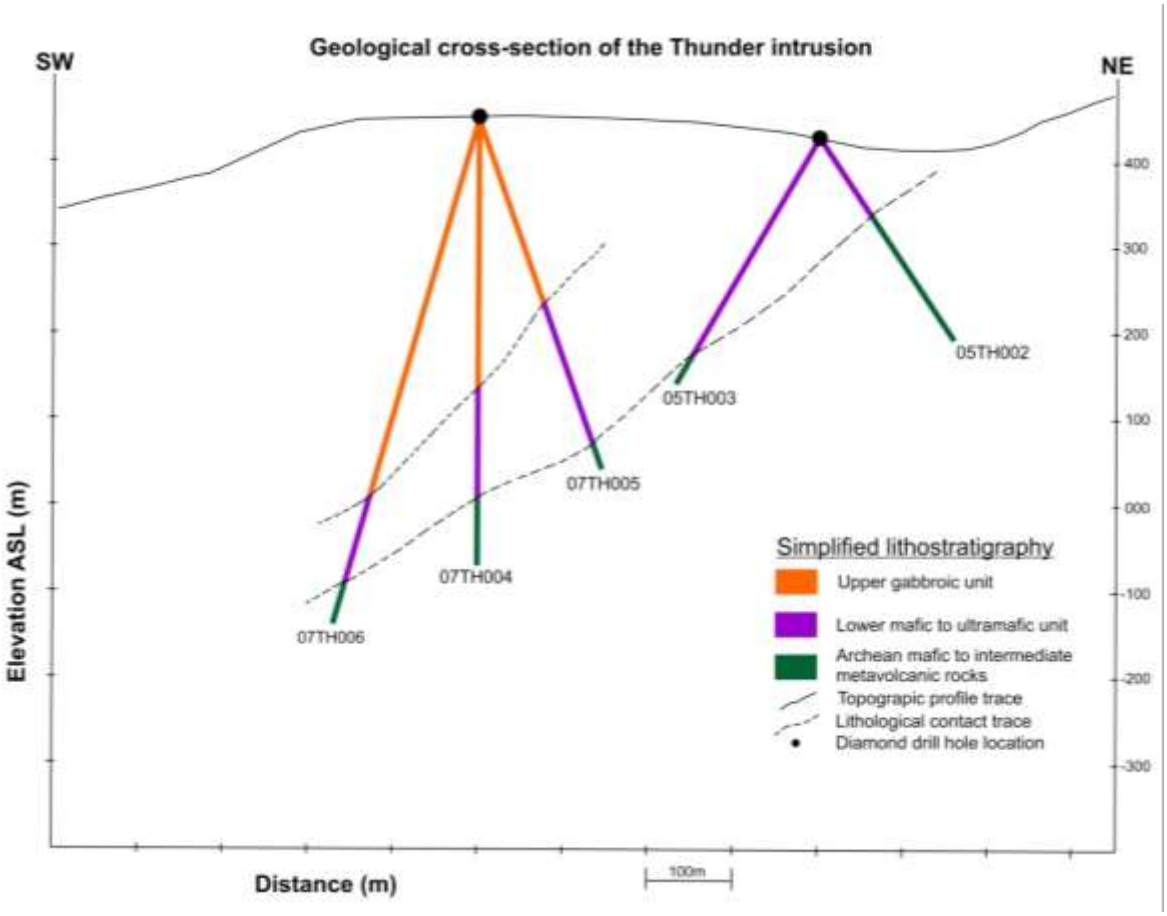

Figure 4.17: Geological cross-section of the Thunder intrusion in accordance with the cross-section line drawn in Figure 4.1.

4.4 Petrography

The petrographic description of representative samples from the lower mafic to ultramafic unit, upper gabbroic unit, pegmatitic gabbro and country rock was completed at Lakehead University in order to characterize the modal mineralogy, textures and alteration. In preparation for the later microprobe analysis, the descriptions were improved, uncertainties resolved and unknown minerals identified with the assistance of Ingrid Kjarsgaard (consulting

mineralogist employed through the Geological Survey of Canada's TGI-4 project). Detailed petrographic descriptions are presented in Appendix A.

4.4.1 Lower mafic to ultramafic unit

In sections 4.2 and 4.3 the lower mafic to ultramafic unit forms the basal section of the Thunder intrusion consisting dominantly of three phases: mineralized feldspathic peridotite, feldspathic peridotite and melagabbro. All rock types are characterized by an orthocumulate texture consisting of cumulus olivine and clinopyroxene and interstitial to poikilitic post-cumulus plagioclase (Fig. 4.18A, B). The transition between phases is gradational and controlled by the post-cumulus plagioclase content. Plagioclase generally increases up-section from more ultramafic compositions (less than 10 %) to more mafic compositions (up to 60 %). Petrographic modal counts found minor feldspathic peridotite from samples collected along the basal section of the lower unit and gabbro from samples collected from the uppermost sections of the lower unit. However, plagioclase content is variable and patchy throughout sections of the lower mafic to ultramafic unit causing the modal mineralogy count and rock name to fluctuate continuously amongst the representative samples collected. Olivine phenocrysts occur rarely up to 30 % (including olivine pseudomorphs), but more typically 5 to 10 modal %. Olivine is most abundant along the basal most sections of the lower mafic to ultramafic unit and drops to minor amounts within the bulk of lower mafic to ultramafic unit. Olivine crystal sizes range from fine- to coarse-grained (typically fine-grained), granular, subhedral phenocrysts to very fine-grained chadacrysts hosted by clinopyroxene oikocrysts (Fig. 4.18A, B). Cumulate clinopyroxene is the most abundant primary mineral phase in samples of the lower mafic to ultramafic unit reaching up to 75 %, but typically 30 to 60 %. Cumulate clinopyroxene phenocrysts range from fine- to coarse-grained (typically medium-grained), are subhedral to euhedral, exhibit common zoning,

lamellar and simple twinning, and commonly poikilitic with very fine-grained biotite inclusions and olivine oikocrysts when proximal to the wall rock contact.

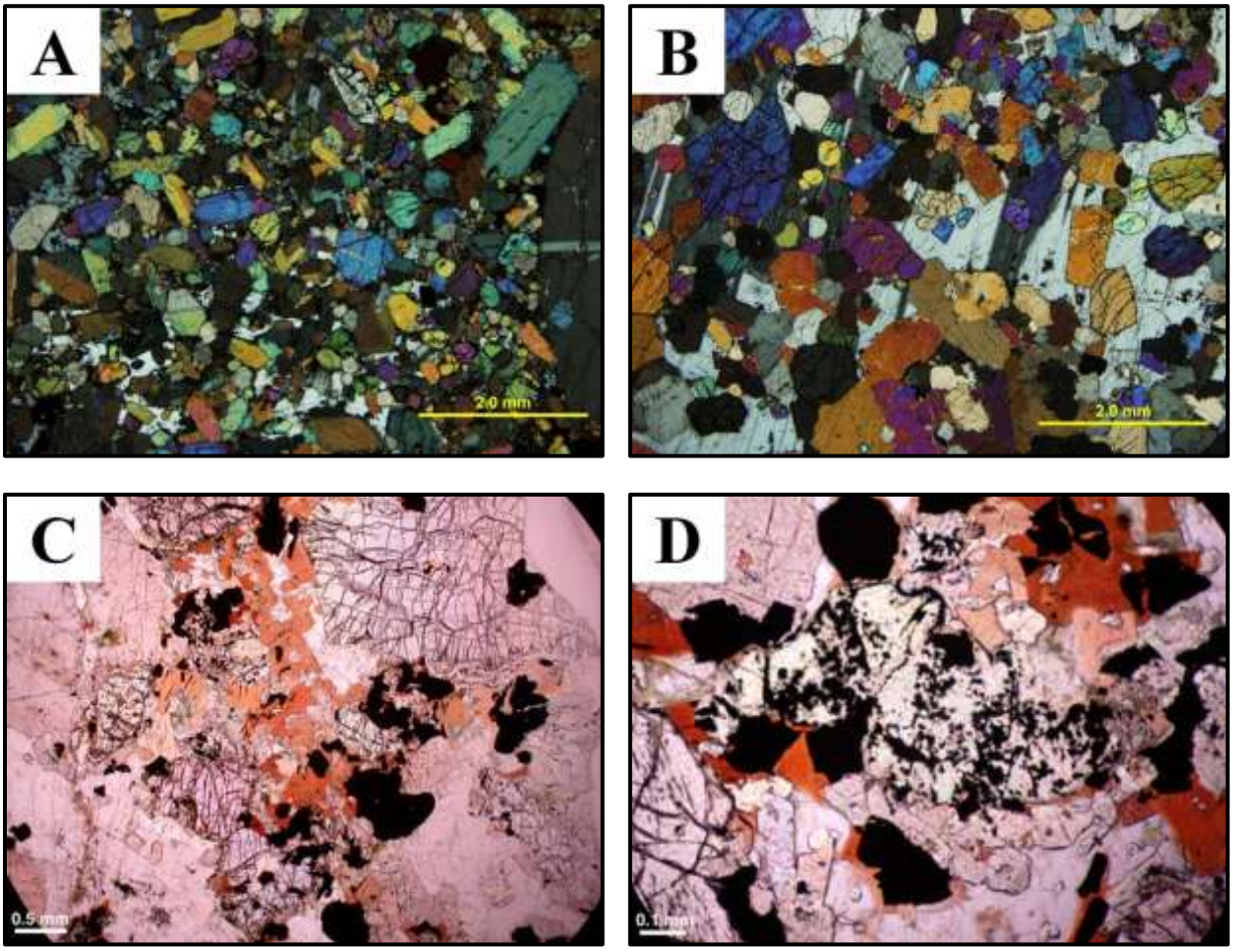

Figure 4.18: Representative photomicrographs of the lithologies comprising the lower mafic to ultramafic unit, Thunder intrusion. A) Feldspathic peridotite under crossed-polarized transmitted light (sample RTT-BT-038). B) Melagabbro under cross-polarized transmitted light (sample RTT-BT-010). C) Red biotite and red hornblende intergrown with cpx, olivine and plagioclase under plan polarized transmitted light (sample RTTC-BT-089). D) Typical talc-magnetite-serpentine pseudomorph after olivine with red biotite and cpx under plane polarized transmitted light (sample RTTC-BT-089).

Accessory primary phases include: medium- to fine-grained, subhedral to euhedral magnetite-ilmenite up to 20 %, but more typically < 5 %; fine- to very fine-grained subhedral to anhedral Ti-rich biotite (reddish brown pleochroism) up to 10 %; and, medium- to fine-grained subhedral to anhedral Ti-rich horneblende (reddish brown pleochroism) up to 10 %. The accessory phases occur as intergrown clusters in the interstitial spaces of the cumulate minerals

(olivine and clinopyroxne) and sulphides, and are most abundant in samples collected proximal to the wall rock contact of the Thunder intrusion (Fig. 4.18C). The Fe-Ti oxides are an exception to this observation as they are also observed at relatively high abundance in the upper most sections of the lower mafic to ultrmafic unit.

At the microscopic scale, rocks of the lower mafic to ultramafic unit are generally fresh. Although abundant fresh olivine phenocrysts are observed, olivine grains are also commonly pseudomorphed by serpentine-talc-magnetite alteration (Fig. 4.18D) and less commonly iddingsite alteration. The secondary minerals comprising the olivine pseudomorphs reach up to 40 % in the most altered samples, but more typically < 5 %. Clinopyroxene phenocrysts are more resistive to secondary replacement but are commonly surrounded by patches of intergrown fine- to very fine-grained secondary chlorite, biotite, serpentine and actinolite. Plagioclase is typically partially replaced by very fine-grained sericite along micro-fractures and as alteration pits (Fig. 4.18D). Note: the alteration described above is observed in all samples and not restricted to a specific horizon.

4.4.2 Upper gabbroic unit

In sections 4.2 and 4.3 the upper gabbroic unit was shown to comprise the upper section of the Thunder intrusion consisting dominantly of three phases: gabbro, hematized gabbro and granophyres-bearing gabbro. All rock types are characterized by a subophitic texture defined by medium- to fine-grained cumulus plagioclase and clinopyroxene and abundant disseminations of magnetite-ilmenite (Fig. 4.19A, B). The modal compositions for all three phases of the upper gabbroic unit are less variable than lower mafic to ultramafic unit. Clinopyroxene ranges from 10 to 20 % and occurs as subhedral to anhedral blocky grains commonly in clusters. Plagioclase ranges from 50 to 70 %, occurs as subhedral laths and intergrown with clinopyroxne. The

accessory phases occur intergrown with clinopyroxne and plagioclase and include: medium-grained, subhedral horneblende up to 5 %; euhedral fine- to very fine-grained (rarely medium-grained) acicular apatite up to 2 % that increases in crystal size and abundance up-section (Fig. 4.19C); subhedral to skeletal fine-grained magnetite-ilmenite disseminations up to 15 % and most abundant within the core of the upper gabbroic unit interval; and, rare medium- to fine-grained subhedral olivine that is typically pseudomorphed by secondary serpentine-actninolite and magnetite.

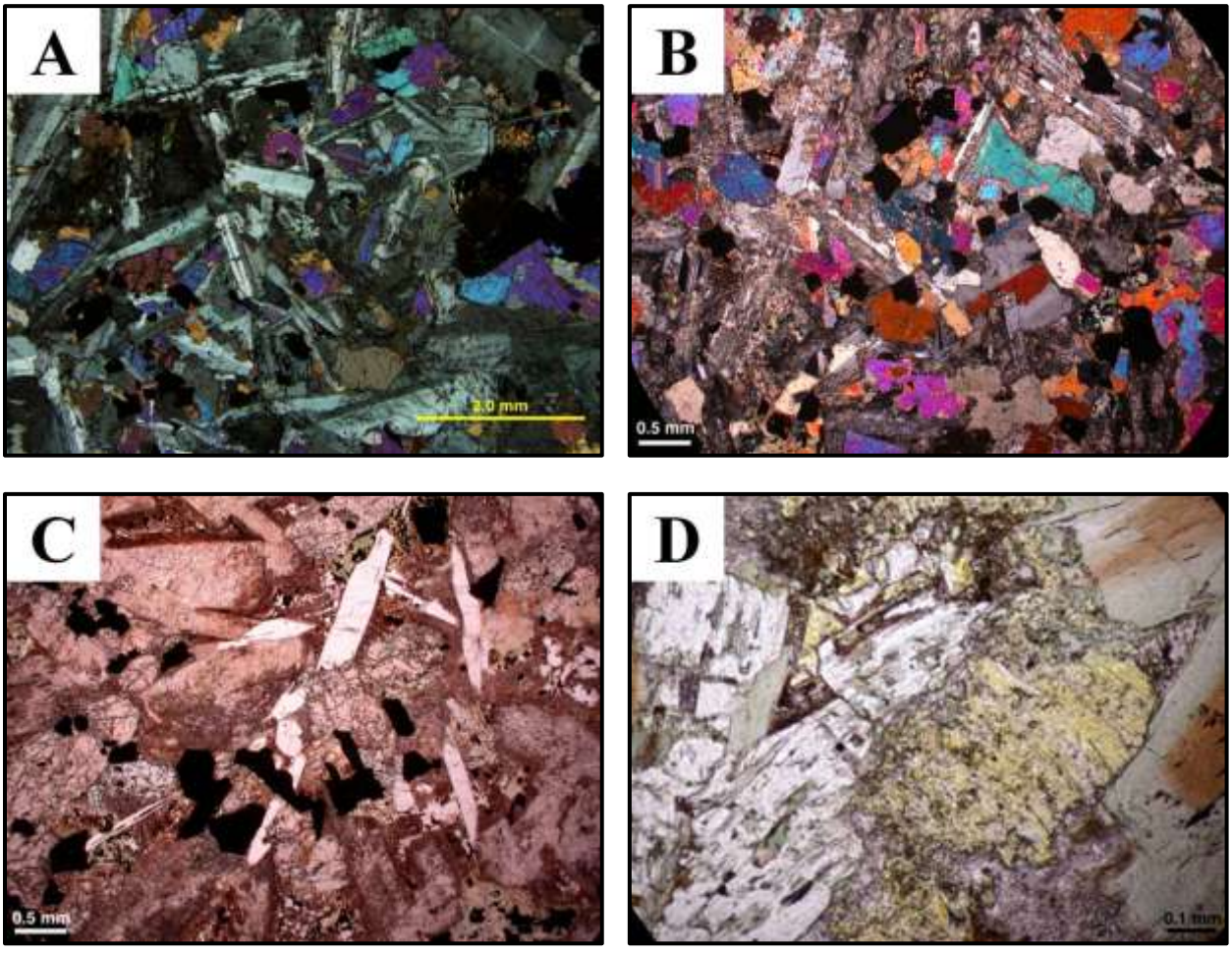

Figure 4.19: Representative photomicrographs of the lithologies comprising the upper gabbroic unit, Thunder intrusion. A) Subophitic gabbro with plagioclase and clinopyroxene cumulates under cross-polarized transmitted light (sample RTT-BT-067). B) Subophitic gabbro with plagioclase, clinopyroxene and abundant magnetite-ilmenite disseminations under crossed polarized transmitted light. Plagioclase is pseudomorphed by sericite (sample RTTC-BT-065A). C) Medium-grained apatite and magnetite-ilmenite intergrown with altered plagioclase in hematized gabbro under plane polarize light (sample RTTC-BT-079). D) Patches of yellowish-green epidote

intergrown with carbonate interstitial to clinopyroxene, altered plagioclase and secondary hornblende in hematized gabbro under plane polarized transmitted light (sample RTTC-BT-079).

The boundaries between phases are gradational, not by plagioclase content as seen in the lower mafic to ultramafic unit, but by a pervasive reddish-pink overprint that increases in intensity up-section (Fig. 4.14G) and the presence of interstitial granophyres (Fig. 4.14H). At the microscopic scale, this pervasive alteration can be characterized as plagioclase rims and interstices overprinted by rusty red altered alkali feldspar up to 25 % with minor secondary quartz (Fig. 4.19C). This alteration style also consists of light-green patches up to 10 cm along the length of the drill core consisting of epidote intergrown with actinolite, carbonate and trace very fine-grained chalcopyrite disseminations (Fig. 4.19D). Other secondary alteration minerals observed include: trace fine-grained, subhedral titanite aggregates in serpentine-actinolite alteration patches; trace very fine-grained rutile altering magnetite-ilmenite and sericite strongly replacing plagioclase. Overall, rocks of the upper gabbroic unit are much more altered than rocks of the lower mafic to ultramafic unit.

4.4.3 Pegmatitic gabbro

In sections 4.2 and 4.3 pegmatitic gabbro was reported as cross-cutting intrusions both in the wall rock and in the lower mafic to ultramafic unit, and as pegmatitic patches within the uppermost sections of the lower mafic to ultramafic unit. This intrusive unit exhibits a characteristic medium- to coarse-grained subophitic texture consisting of intergrown plagioclase and clinopyroxene with magnetite-ilmenite disseminations. Clinopyroxene ranges from 40 to 50 % subhedral to euhedral grains; plagioclase ranges from 20 to 50 % subhedral to euhedral grains but are strongly altered by sericite-kaolinite-serpentine; and, 5 to 10 % skeletal magnetite with ilmenite lamellae (Fig. 4.20A). Traces of very fine-grained chalcopyrite and pyrrhotite occur in the Fe-Ti oxides and plagioclase, and trace very fine- to fine-grained apatite intergrown with

plagioclase and clinopyroxene. Overall, the pegmatitic gabbro is texturally and mineralogically similar to rocks of the upper gabbroic unit. The intrusive contact with the lower mafic to ultramafic unit is sharp and lacks a chilled margin (Fig. 4.20B). In Figure 4.18A the minerals appear intergrown along the margin between the two phases.

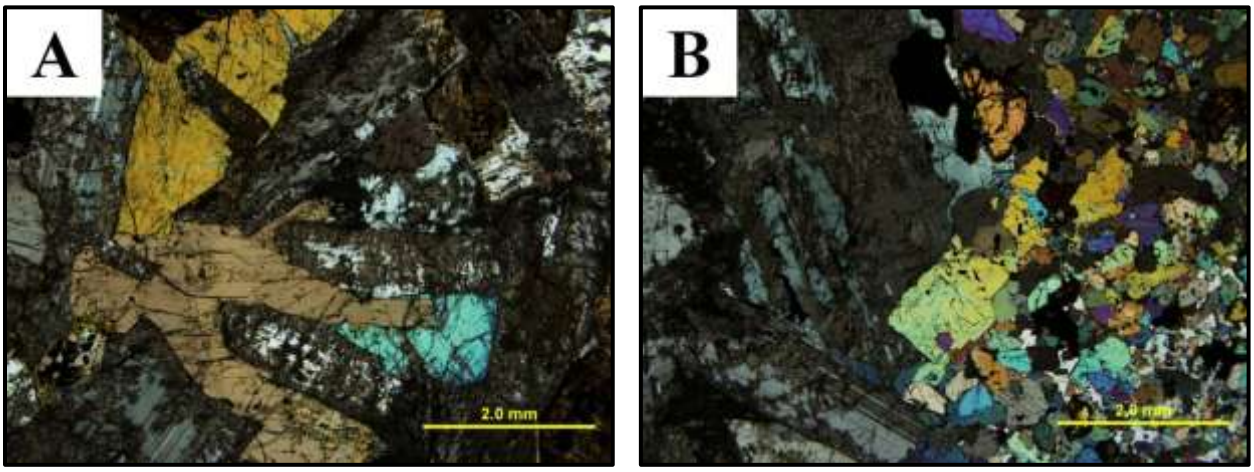

Figure 4.20: Representative photomicrographs of the pegmatitic gabbro phase under crossed-polarized transmitted light, Thunder intrusion. A) Subophitic pegmatitic gabbro with plagioclase and clinopyroxene. B) Sharp contact shared between cross-cutting pegmatitic gabbro (left) and feldspathic peridotite (right) host rock with no developed chill margin. Photomicrographs are from sample RTT-BT-130 collected at the Figure 4.4A outcrop.

4.4.4 Summary of petrographic observations

Diamond drill core 07TH004 was determined to be the most stratigraphical complete representation of the Thunder intrusion and wall rock. At depth, the Thunder intrusion consists of the basal lower mafic to ultramafic unit overlain by the upper gabbroic unit. The lower mafic to ultramafic unit consists generally of three rock types: feldspathic peridotite, melagabbro and gabbro with a texture defined by cumulus olivine and clinopyroxene surrounded by interstitial post-cumulus plagioclase. The upper gabbroic unit consists of gabbro, hematized gabbro and granophyres-bearing gabbro characterized by a subophitic texture defined by cumulus plagioclase and clinopyroxene and abundant disseminations of magnetite-ilmenite. In the uppermost sections of the upper gabbroic unit apatite becomes a more abundant cumulus phase intergrown with plagioclase, clinopyroxene and Fe-Ti oxide. Figure 4.21plots the observed

cumulus mineralogy and stratigraphic position next to the simplified lithostratigraphy of DDH 07TH004. The cumulate stratigraphy follows a bottom-up accumulation sequence of clinopyroxene + olivine, clinopyroxene + olivine + Fe-Ti oxide, plagioclase + clinopyroxene + Fe-Ti oxide and plagioclase + clinopyroxene + Fe-Ti oxide + apatite (Fig. 21). The transition from the lower mafic to ultrmafic unit upwards into the upper gabbroic unit is ultimately marked by the loss of cumulus olivine in the cumulate stratigraphy and the arrival of cumulus plagioclase (i.e., from interstitial to subophitic; Figs. 4.18, 4.19).

4.5 Alteration

4.5.1 Alteration veins within the Thunder intrusion

In addition to primary mineral replacement (e.g., olivine pseudomorphs) shown in section 4.4 (e.g., Figs. 4.18D, 4.19D), secondary alteration commonly occurs as veins internal to the Thunder intrusion. At the macroscopic scale, serpentine veining is commonly observed throughout the lower mafic to ultramafic unit as 2 to 5 mm in-filled subvertical fractures (Fig. 4.22A). The mineralogy of the veins consists mostly of fibrous serpentine with minor actinolite, chlorite and carbonate. Rocks with abundant serpentine veining are often crumbly due to the alteration because of the breakdown of the ferromagnesian minerals (i.e., olivine and clinopyroxene).

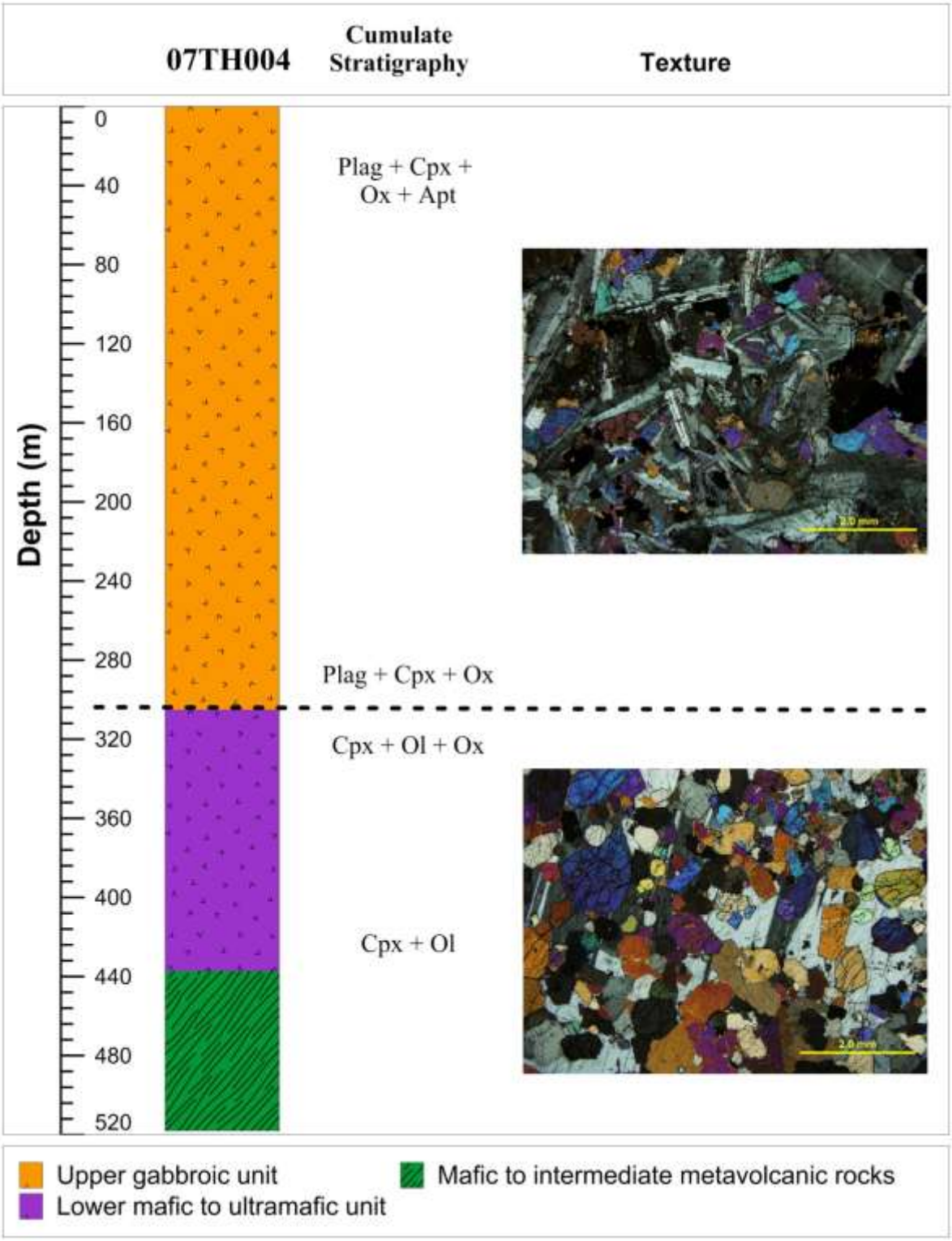

Figure 4.21: Summary of petrographic observations plotting the stratigraphic position of the cumulus minerals next to the simplified lithostratigraphy of diamond drill hole 07TH004. The cumulus stratigraphy follows a bottom-up accumulation sequence. Included are representative petrographic photographs in crossed polarized light illustrating the texture that defines the lower mafic to ultramafic unit and upper gabbroic unit.

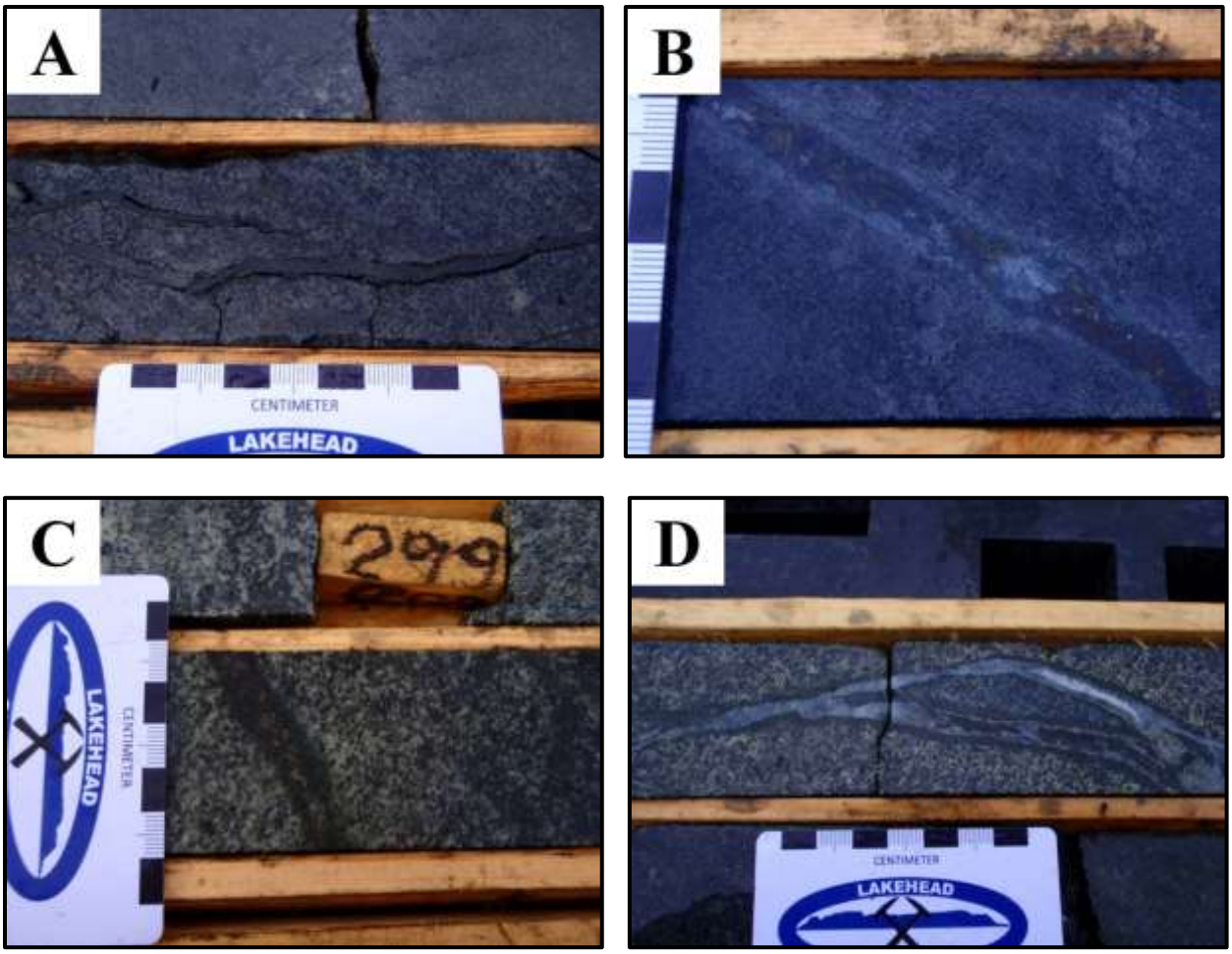

Figure 4.22: Representative photographs of the secondary alteration features commonly observed internal to the Thunder intrusion. All photographs are from diamond drill hole 07TH004. A) Subvertical serpentinized fractures cross-cutting feldspathic peridotite at 308 m. B) Magnetite-pyrite-chalcopyrite vein cross-cutting feldspathic peridotite at ~306 m. C) Magnetite-pyrite-chalcopyrite vein cross-cutting gabbro at ~ 299 m. D) Barren and undeformed subvertical carbonate veins cutting gabbro at~ 274 m.

Subvertical 2 - 5 mm magnetite ± pyrite ± chalcopyrite veins surrounded by serpentinized haloes are also present throughout the upper sections of the lower mafic to ultramafic unit and the bulk of the upper gabbroic unit (Figs. 4.22B, C). At the microscopic scale, the alteration veins consist of a lattice of lath-shaped magnetite intergrown with spongy pyrite and chalcopyrite (Fig. 4.23A, B, C). Minor intergrowths include euhedral apatite, serpentine that is overprinted by acicular actinolite fans and epidote, and carbonate (Fig. 4.23D). Along the margins of the veins, titanite, cummingtonite, serpentine and carbonate are intergrown.

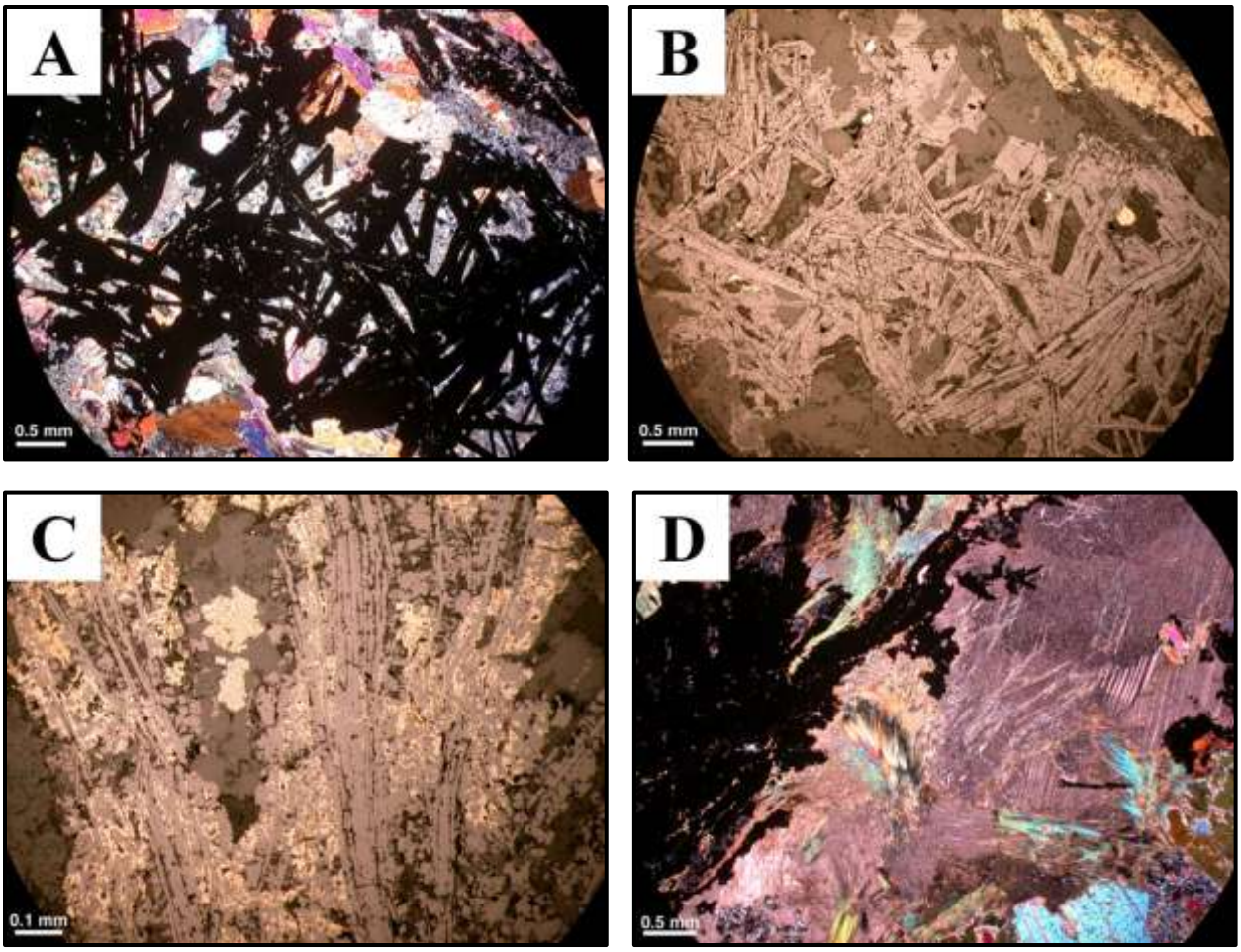

Figure 4.23: Representative photomicrographs of the alteration veins cross-cutting the Thunder intrusion. A), B) Strap-like magnetite with interstitial serpentine, chalcopyrite, titanite, pyrite cross-cutting the upper gabbroic unit under crossed polarized light (sample RTTC-BT-065A), plane polarized light and crossed polarized light respectively. C) Typical magnetite-pyrite-chalcopyrite intergrowth texture under reflected light (sample RTTC-BT-063). D) Actinolite-carbonate-magnetite-pyrite vein cross-cutting the lower mafic to ultramafic unit (sample RTTC-BT-063).

Lastly, subvertical carbonate veins up to 7 cm thick but typically 1 – 2 cm thick with actinolite-chlorite rims are present throughout the Thunder intrusion (Fig. 4.22D). The carbonate veins are internal to the Thunder intrusion, barren of sulphide mineralization and are not associated with the deformed carbonate veins/pods commonly observed in the wall rock lithologies.

4.5.2 Contact metamorphism

Within ~ 5 m of the sharp contact with the lower mafic to ultramafic unit of the Thunder intrusion, contact metamorphism overprints the metavolcanic wall rock. The altered rock was logged as hornfels is dark bluish grey with pre-existing fracture networks overprinted by a pale white color possibly a bleaching effect at the macroscopic scale (Figs. 4.9, 4.11E, 4.12A, 4.13, 4.14B). Texturally, the foliation commonly observed in all wall rock lithologies is absent. At the microscopic scale, the contact between the Thunder intrusion and the wall rock is sharp with a poorly developed chill margin separating the two lithologies (Fig. 4.24A). The hornfels is strongly allotriomorphic i.e., the majority of the mineralogy is strongly poikilitic and anhedral (very jagged shapes) consisting of clinopyroxene, reddish brown biotite, skeletal magnetite ± ilmentite intergrown with very fine-grained granular plagioclase disseminated throughout (Fig. 4.24B, C). Pale white fracture networks consist of pale olive green biotite, dark green actinolite, chlorite, sericite and carbonate. The feldspar grains often exhibit undulose extinction. Outside the contact metamorphic aureole, the wall rock lithologies exhibit a well-developed metamorphic fabric (Fig. 4.24D).

On the Thunder intrusion side of the wall rock contact, the crystal size of the cumulus minerals (i.e, clinopyroxene and olivine) is relatively finer-grained. The crystal habit of plagioclase is also lath-shaped as opposed to the interstitial textre observed throughout the lower mafic to ultramafic unit (Fig. 4.24A). Plagioclase, clinopyroxene and olivine were observed growing outwards into the wall rock rather a chilled liquid (Fig. 4.24A). Away from the sharp contact, the texture is defined by the typical cumulus clinopyroxene and olivine surrounded by interstitial plagioclase with a relatively high abundance of accessory minerals including horneblende, biotite, sulphide, Fe-Ti oxide and secondary replacement minerals (Fig. 4.18C, D).

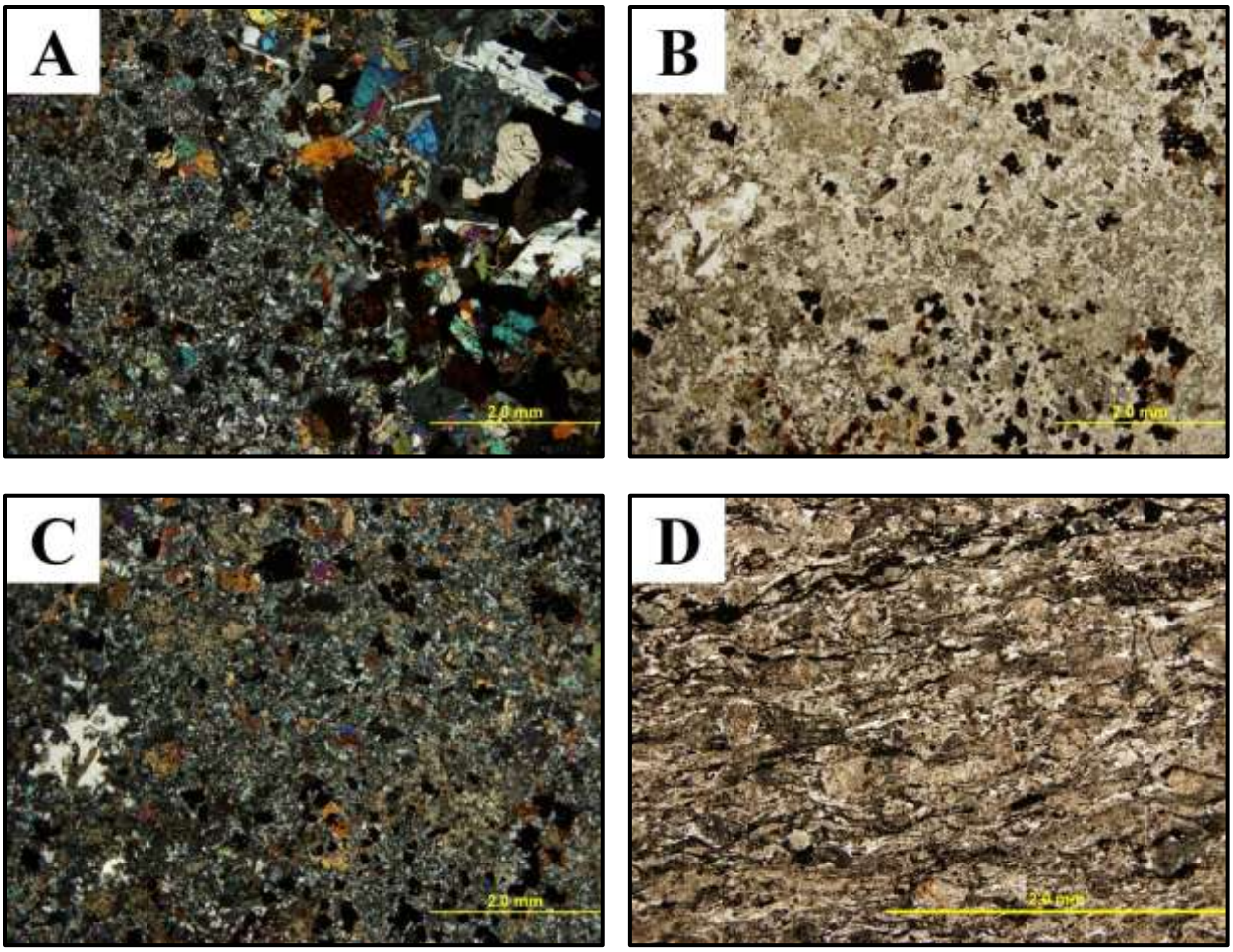

Figure 4.24: A) Photomicrographs showing the contact relationship between the Thunder intrusion (right) and the metavolcanic wall rock (left) (Sample RTTC-BT-173, cross polarized light). B) and C) Photomicrograph of the strong allotriomorphic texture and abundant granular feldspars of the hornfels rock under plane and crossed-polars transmitted light respectively (sample RTTC-BT-090). D) Photomicrograph of the well-developed metamorphic fabric (schistosity) preserved within the wall rocks distal from the Thunder intrusion's contact metamorphic aureole (sample RTTC-BT-088, plane polarized light).

4.6 Mineralization

The petrographic description of representative samples of the various styles of sulphide mineralization observed was completed at Lakehead University in order to characterize the sulphide species, textures and alteration present. In preparation for the later SEM-EDX and microprobe analysis, the descriptions were improved, uncertainties resolved and unknown minerals identified with the assistance of Ingrid Kjarsgaard (consulting mineralogist hired through the Geological Survey of Canada's TGI-4 project). Detailed petrographic descriptions

are presented in Appendix A, sulphide mineral chemistry in Appendix B, sulphide minerals present summarized in Table 4.1 and platinum-group minerals and precious-metal minerals present summarized in Table 4.2. In general, the microprobe analyses on major elements had an error of ± 1-2 %; error on trace elements was up to ± 10 %.

Table 4.1: Sulphide mineralogy of the various styles of mineralization spatially associated with the Thunder intrusion and footwall.

Mineral	Formula
Intrusion-hosted	
Basal mineralization zone	
Bravoite	$(Fe,Ni)S_2$
Chalcopyrite	$CuFeS_2$
Cubanite	Cu_3FeS_4
Galena	PbS
Marcasite	FeS_2
Pentlandite	$(Ni,Fe)_9S_8$
Pyrite	FeS_2
Pyrrhotite	$Fe_{1-x}S$
Siegenite	$(Ni,Co)_3S_4$
Sphalerite	ZnS
Outside the basal mineralization zone	
Bornite	Cu_5FeS_4
Chalcopyrite	$CuFeS_2$
Pentlandite	$(Ni,Fe)_9S_8$
Siegenite	$(Ni,Co)_3S_4$
Sphalerite	ZnS
Alteration veins	
Chalcopyrite	$CuFeS_2$
Galena	PbS
Pyrite	FeS_2
Pyrrhotite	$Fe_{1-x}S$
Upper mineralized zone	
Bornite	Cu_5FeS_4
Chalcopyrite	$CuFeS_2$
Galena	PbS
Millerite	NiS
Pyrite	FeS_2

Mineral	Formula
Footwall-hosted	
Pyrrhotite-rich massive sulphide veinlet	
Chalcopyrite	$CuFeS_2$
Marcasite	FeS_2
Pyrite	FeS_2
Pyrrhotite	$Fe_{1-x}S$
Siegenite	$(Ni,Co)_3S_4$
Chalcopyrite-rich massive sulphide veinlets	
Chalcopyrite	$CuFeS_2$
Galena	PbS
Millerite	NiS
Sphalerite	ZnS
Sulphide stringers	
Chalcopyrite	$CuFeS_2$
Pentlandite	$(Ni,Fe)_9S_8$
Pyrite	FeS_2
Pyrrhotite	$Fe_{1-x}S$
Sphalerite	ZnS
Wall rock	
Chalcopyrite	$CuFeS_2$
Millerite	NiS
Pyrite	FeS_2
Pyrrhotite	$Fe_{1-x}S$
Sphalerite	ZnS

4.6.1 The basal mineralization zone

The most common and significant style of sulphide mineralization occurs along the basal contact between the Thunder intrusion and the wall rock (Fig. 4.9). The basal mineralization consists of 1-5 modal % sulphide, rarely up to 30 modal %, with textures ranging from medium- to fine-grained disseminated, coarse-grained globular and rarely net-textured hosted by feldspathic peridotite of the lower mafic to ultramafic unit (Figs. 4.12C, 4.14C). This zone of mineralization will be referred to as the "basal mineralization zone" (BMZ) in later sections as it hosts high concentrations of chalcophile elements. Sulphide mineralization is most abundant in three drill holes (in DDHs 05TH003, 07TH004 and 005) with DDH 05TH003 hosting the best intercept of the basal mineralization zone. Zones of mineralization reach thicknesses of up to 30 m and are commonly interlayered with barren feldspathic peridotite and melagabbro (Figs. 4.9, 4.13). The primary sulphide mineralogy mainly consists of composite textured pyrrhotite and chalcopyrite (pyrrhotite > chalcopyrite) intergrown with minor euhedral to subhedral magnetite ± ilmenite (Fig. 4.25A, B). Rare inclusions of very fine-grained pentlandite, siegenite ($(Ni,Co)_3S_4$), sphalerite, cobaltite, cubanite and galena are hosted by pyrrhotite and chalcopyrite. Within pyrrhotite and chalcopyrite, extensive secondary, graphic marcasite-pyrite-magnetite intergrowths occur replacing the primary sulphides (Fig. 4.25C). Parachute textured sulphide droplets consisting of pyrrhotite, chalcopyrite and pentlandite also occur interstitial to the silicates and encased in biotite (Fig. 4.25D). The parachute texture has also been recognized by Lightfoot et al. (1984) who interpreted the sulphide globules as the result of fractional crystallization with the settling of a dense, early forming sulphide liquid.

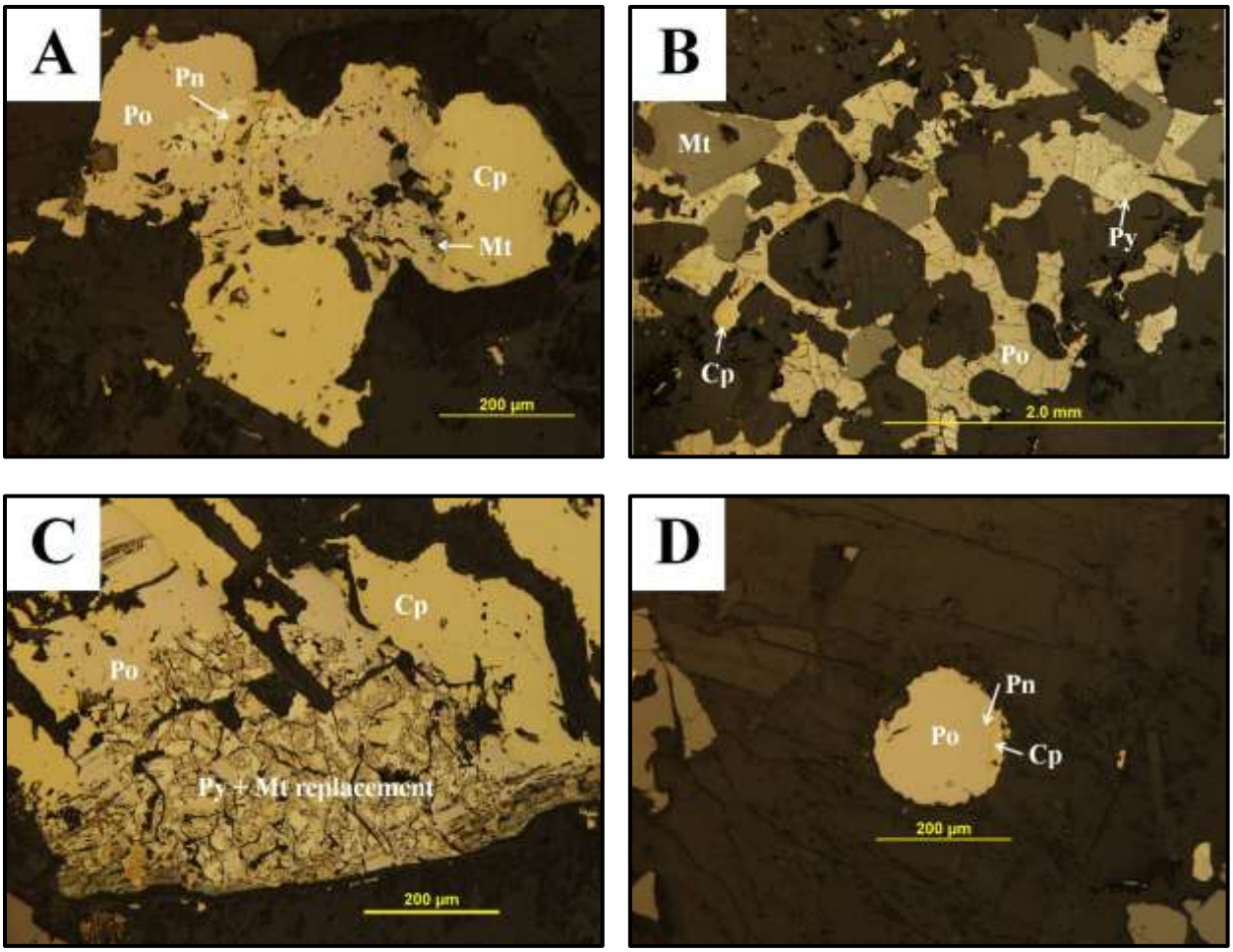

Figure 4.25: Representative photomicrographs of the basal mineralization zone hosted by feldspathic peridotite under reflected light. A) Disseminations of composite sulphides consisting of pyrrhotite, chalcopyrite, pentlandite and magnetite interstitial to the silicate minerals (sample RTTC-BT-089). B) Net-textured magnetite-pyrrhotite-chalcopyrite-pyrite interstitial to the silicate minerals (sample RTTC-BT-173). C) Secondary pyrite + magnetite overprinting marcasite-altered pyrrhotite (sample RTTC-BT-091). D) Sulphide droplet consisting of parachute textured pyrrhotite-chalcopyrite-pentlandite interstitial to the silicate minerals (sample RTTC-BT-089).

Significant trace chalcophile element concentrations occur in pyrite, marcasite and pyrrhotite. Nickel concentrations in pyrite reach up to 6.42 wt. % and cobalt up to 2.58 wt. %. Nickel concentrations in marcasite reach up to 3.61 wt. % and cobalt reaching up to 1.42 wt. % in cobalt. Nickel in pyrrhotite reaches up to 1.36 wt. %.

Outside the basal mineralization zone sulphide abundances decrease to trace amounts hosted by feldspathic peridotite and melagabbro of the lower mafic to ultramafic unit (Fig. 4.12D, 4.14D). The sulphides occur as fine- to very fine-grained crystals consisting dominantly of intergrown chalcopyrite and bornite with grain boundaries typically shared with magnetite and ilmentite (Fig. 4.26). Pyrrhotite does not occur within the primary sulphide assemblage. Rare inclusions of sphalerite, siegenite and pentlandite occur in chalcopyrite and secondary magnetite. Significant trace chalcophile element concentrations occur in pentlandite with cobalt concentrations reaching up to 14.07 wt. %. Overall, the sulphide mineralization hosted within the lower mafic to ultramafic unit outside of the basal mineralization zone is copper-rich and barren of nickeliferous sulphides whereas the sulphide mineralization in the basal mineralization zone is Fe-rich and nickeliferous sulphide bearing.

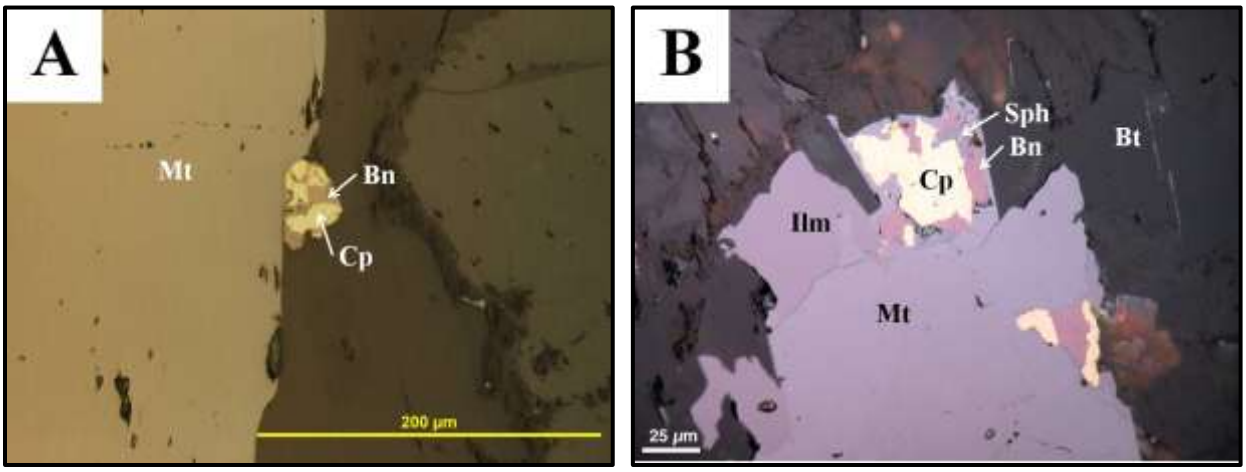

Figure 4.26: Representative photomicrographs under reflected light of the trace copper-rich sulphide mineralization outside the basal mineralization zone hosted by melagabbro of the lower mafic to ultramafic unit. A) Chalcopyrite and bornite along grain boundary of magnetite (sample RTTC-BT-096). B) Chalcopyrite-bornite-sphalerite along the rim of ilmenite-magnetite surrounded by biotite (sample RTTC-BT-097).

4.6.2 Pyrrhotite-rich massive sulphide veinlet

Although no zones of massive sulphide occur in the intrusive rock of the Thunder intrusion or the surrounding wall rocks, a ~ 2 cm pyrrhotite-rich massive sulphide veinlet cross-cuts hornfels within 3 m of the contact with the Thunder intrusion (DDH 05TH003; Figs. 4.9, 4.27A). The sulphide vein mineralogy of the Po-rich footwall veinlet (Po-FWV) is similar to the basal mineralization zone with pyrrhotite containing abundant inclusions of medium-grained, euhedral to lobed magnetite ± ilmenite, intergrowths of chalcopyrite and extensive alteration patches showing graphic intergrowth of secondary marcasite-pyrite-magnetite (Fig. 4.27B). Rare inclusions of bravoite and siegenite occur separately in pyrrhotite (Fig. 4.27C). Along the vein margins, euhedral magnetite crystals are cut by the wall rock (Fig. 4. 27D). The vein is undeformed and cross-cuts relict bedding is observed by the host hornfels rock indicating post-deformation emplacement (Fig, 4.27D).

Significant trace chalcophile element concentrations in pyrite, marcasite and pyrrhotite include nickel and cobalt. Nickel concentrations in pyrite reach up to 3.76 wt. % and cobalt reaching up to 2.09 wt. %. Nickel in marcasite reaches up to 2.04 wt. % whereas cobalt is below detection limit. Nickel in pyrrhotite reach up to 1.44 wt. %. The nickel concentrations in pyrite, marcasite and pyrrhotite are similar to those in the basal mineralization zone (Appendix B).

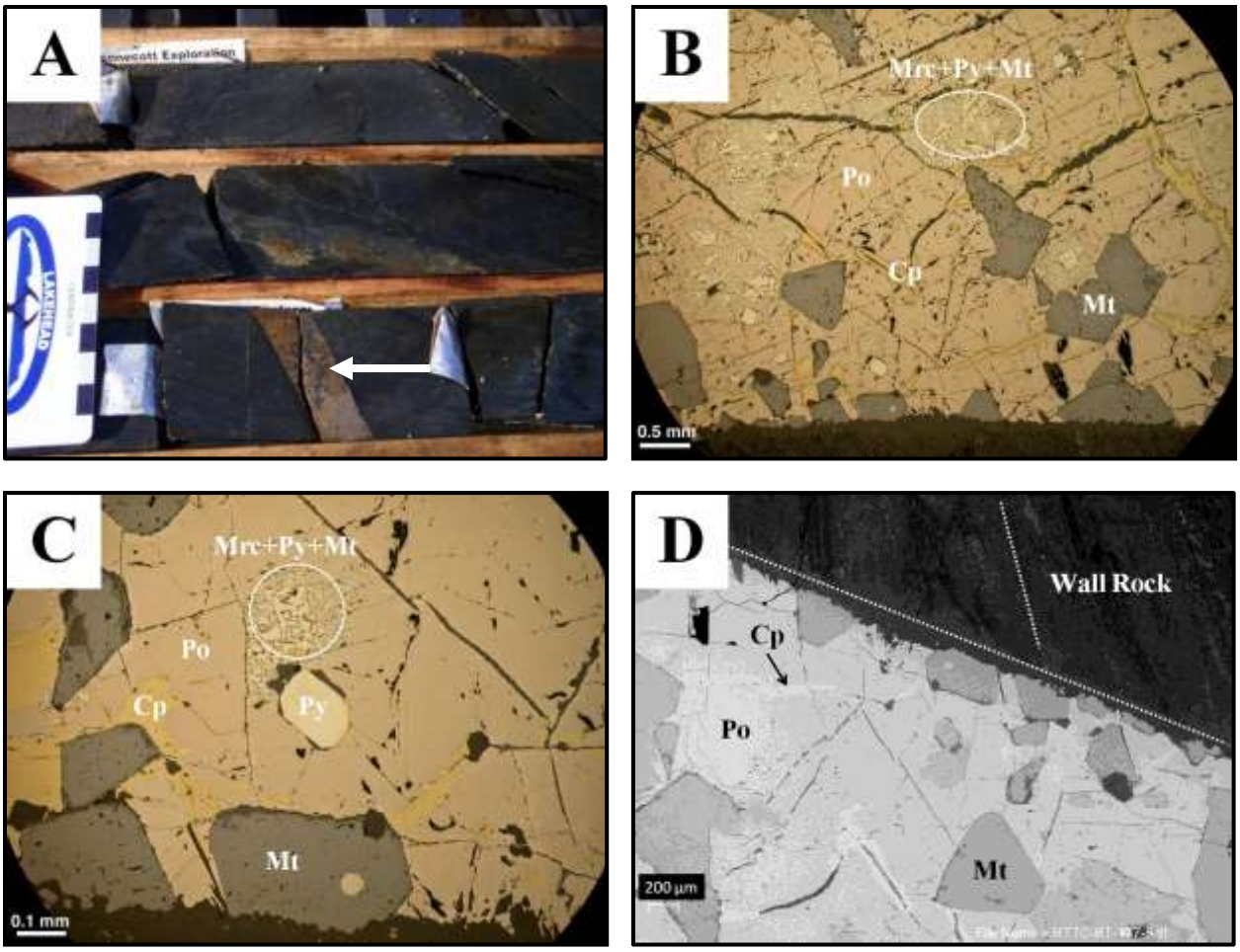

Figure 4.27: A) Photograph of the 0.5 cm thick pyrrhotite-rich massive sulphide veinlet hosted by hornfels (at 300.28 m in diamond drill hole 05TH003; arrow). B) Photomicrograph of massive pyrrhotite with magnetite, chalcopyrite and marcasite-pyrite-magnetite patches. C) Photomicrograph of secondary marcasite-pyrite-magnetite patches and pyrite crystal in massive pyrrhotite. Photographs B and C are under reflected light. D) Back-scattered electron image of the massive sulphide vein cross-cutting the relict bedding of the hornfels host rock. Indicated is the orientation of the vein margin and wall rock bedding. All photomicrographs from sample RTTC-BT-177.

4.6.3 Sulphide stringers

Sulphide stringers < 0.5 cm thick occurring are hosted by hornfels cross-cutting relict bedding and in-filling fractures (4.28A). The footwall sulphide stringers (FWS) occur < 0.5 m from the contact with the Thunder intrusion and are observed in DDH's 07TH004, 005 and 05TH003 (Figs. 4.9, 4.13). The sulphide mineralogy is similar to that of the intrusion-hosted pyrrhotite-rich massive sulphide veinlet and basal mineralization zone, and consists mainly of primary pyrrhotite, chalcopyrite, pentlandite and magnetite (Fig. 4.28B). Accessory silicate phases within the stringers include clinopyroxene and actinolite. Rare inclusions of very fine-grained sphalerite and cobaltite occur in the primary sulphides and very fine grained sperrylite occurs along the grain boundary of chalcopyrite (Fig. 4.28D). The sulphide stringers show extensive graphic pyrite-magnetite intergrowth replacing marcasite alteration in pyrrhotite and chalcopyrite (Fig. 4.28C).

Significant trace chalcophile element concentrations occur only in pyrite and pyrrhotite. Nickel concentrations reach up to 4.97 wt. % and cobalt reaching up to 2.43 wt. % in pyrite. Nickel in pyrrhotite reach up to 1.29 wt. %. The nickel concentrations in pyrite and pyrrhotite are comparable to the basal mineralization zone and pyrrhotite-rich massive sulphide veinlet.

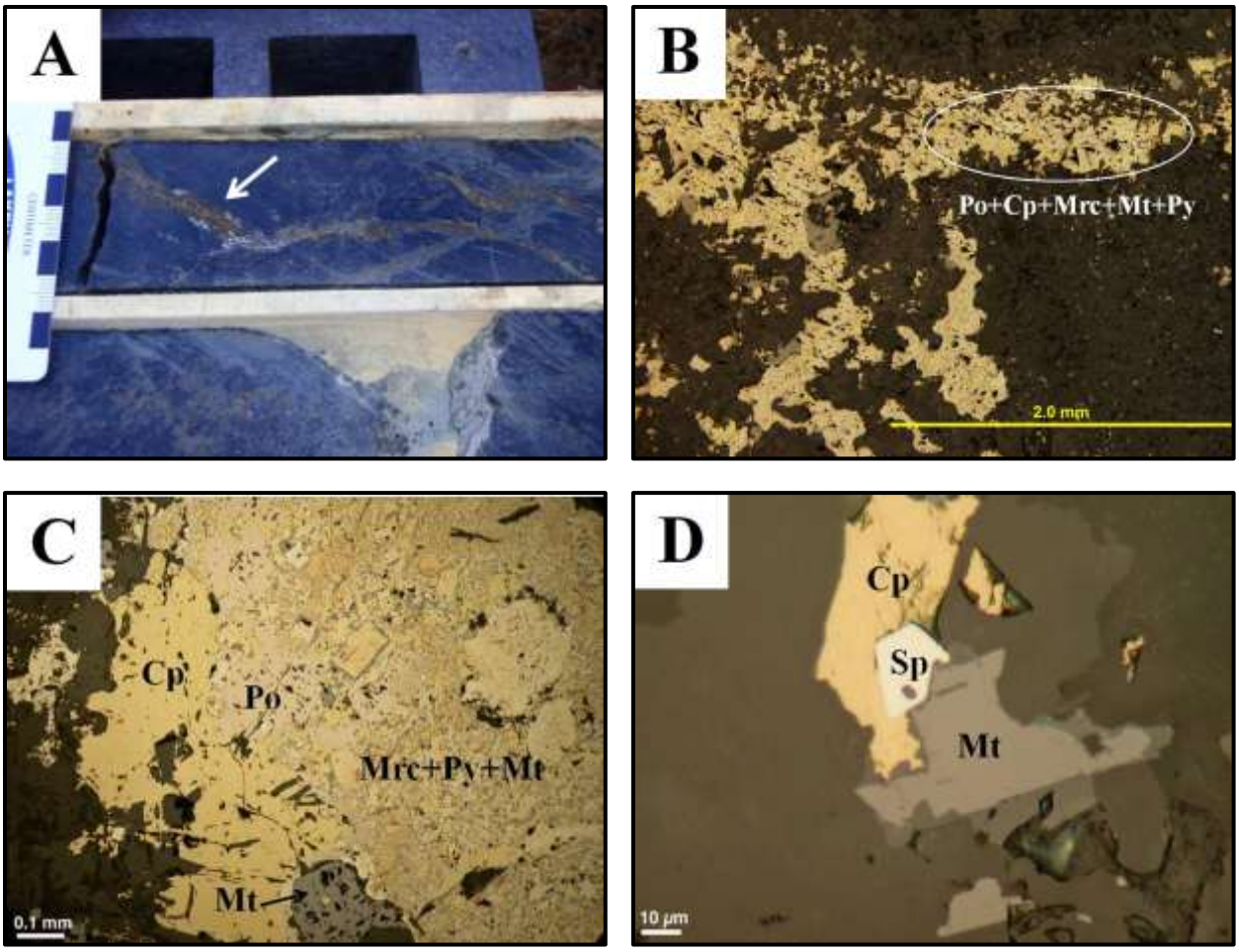

Figure 4.28: A) Photographs of the footwall sulphide stringer veins observed less than 0.5 m of the contact with the Thunder intrusion hosted by hornfels (diamond drill holes 07TH004, 005 and 05TH003; arrow). B) Sulphide stringer vein consisting of intergrown pyrrhotite, chalcopyrite, marcasite, magnetite and trace pyrite. C) Secondary pyrite and magnetite overprinting marcasite-altered pyrrhotite in chalcopyrite. D) Sperrylite along the grain boundary of chalcopyrite and magnetite. Photomicrographs from sample RTTC-BT-090.

4.6.4 The upper mineralized zone

Between ~ 210 and 180 m within DDH 07TH006, mineralized and altered feldspathic peridotite containing tuffaceous wall rock fragments occur between hematized gabbro (Fig. 4.13; see section 4.3.3.1). This upper mineralized zone (UMZ) is a local feature only observed in DDH 07TH006. The spatial extent of this zone is uncertain. Globular sulphides assemblages are interstitial to the silicate assemblage comprising up to 10 modal % in the uppermost sections of this interval (Figs. 4.13, 4.15B). The globular sulphides reach up to coarse-grained diameters consisting dominantly of chalcopyrite-bornite intergrowths with lesser rounded inclusions of fine-grained millerite (Fig. 4.29A, B). Rare very fine-grained inclusions of galena and kotulskite occur in the chalcopyrite-bornite intergrowth (Figs. 4.29C, D). The sulphides are overgrown by spongy aggregates of skeletal secondary magnetite, which also heals former fractures, and is surrounded by secondary chlorite and biotite (Fig. 4.29B). This is in contrast to pyrite-marcasite replacement of the primary base metal sulphide assemblages that occur in the basal mineralization zone. Millerite contains significant cobalt concentrations reaching up to 2.60 wt. %.

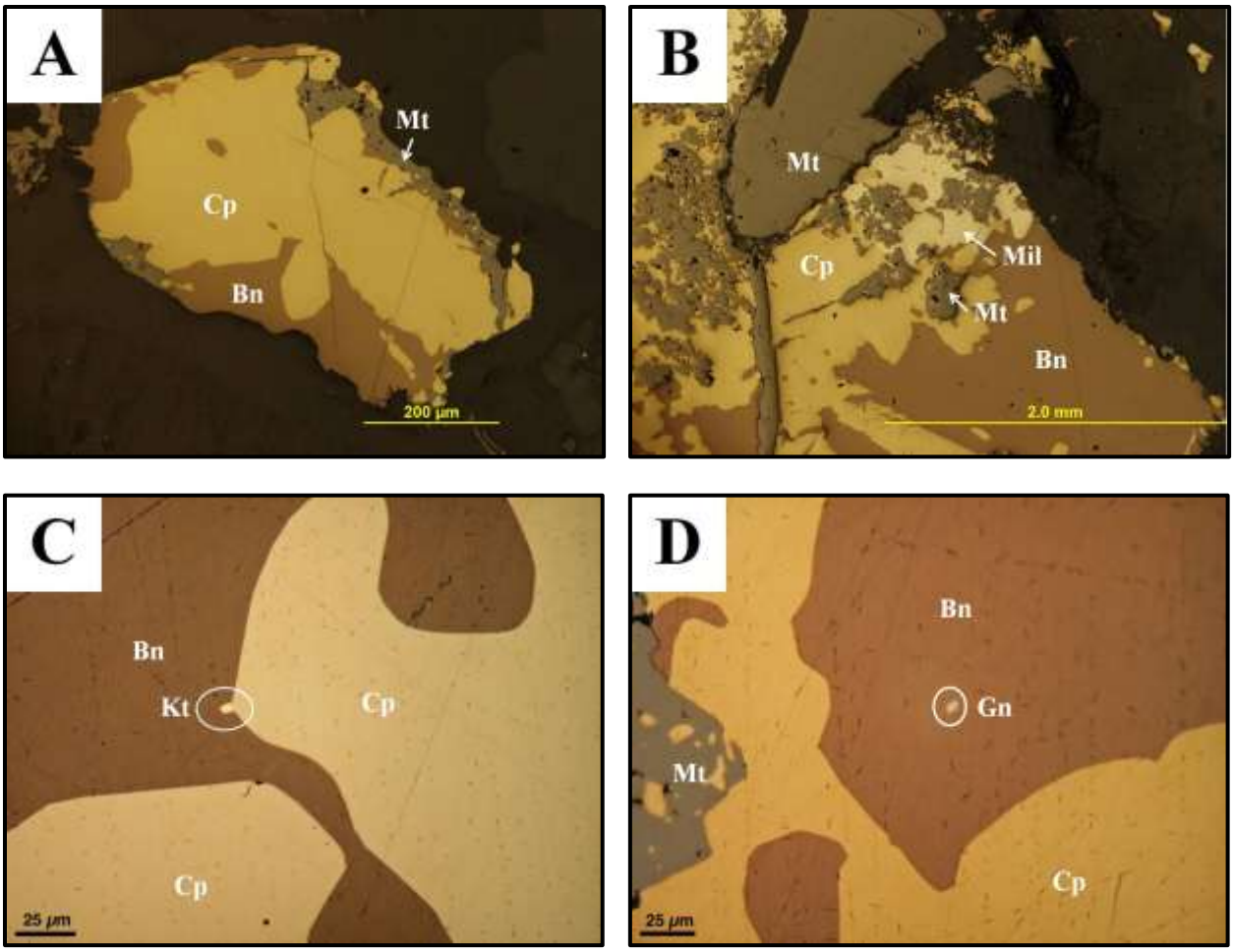

Figure 4.29: Representative textures of the blebby sulphides hosted by feldspathic peridotite of the local upper mineralized zone (diamond drill hole 07TH006). A) Globule consisting of a chalcopyrite and bornite intergrowth overgrown by secondary magnetite. B) Chalcopyrite-bornite intergrowth with cream colored millerite partially replaced by secondary spongy magnetite. C) Very fine-grained kotulskite situated along the grain boundary between bornite and chalcopyrite. D) Very fine-grained galena inclusion in bornite and secondary magnetite partially replacing chalcopyrite. Photomicrographs from sample RTTC-BT-134.

4.6.5 Chalcopyrite-rich massive sulphide veinlets

Within 5 m of the contact with the Thunder intrusion in DDH 07TH006 (between 573.68 and 575.48 m), two chalcopyrite-rich massive sulphide veinlets < 5 cm thick occur conformable to the relict tuffaceous bedding of the wall rock (Figs. 4.13, 4.30A, B). The chalcopyrite-rich footwall veinlets (Cp-FWV) consist dominantly of chalcopyrite and pyrite (chalcopyrite > pyrite) with trace, fine- to very fine-grained subhedral to anhedral inclusions of subhedral millerite, sphalerite, and galena (Fig. 4.30C). Pyrite is commonly euhedral and clustered (Fig. 4.30D). Sulphides are intergrown with chlorite, carbonate, quartz and border strongly altered wall rock that is cut by paragenetically late fractures of carbonate, quartz and chlorite. The pyrite feature is unique to samples of the chalcopyrite-rich massive sulphide veinlets.

Nickel and cobalt are the dominant trace chalcophile elements present in the pyrite cubes with nickel concentrations reaching up to 5.98 wt. % and cobalt concentrations reaching up to 1.46 wt. %. Selenium is high (up to 10.98 wt. %) in galena.

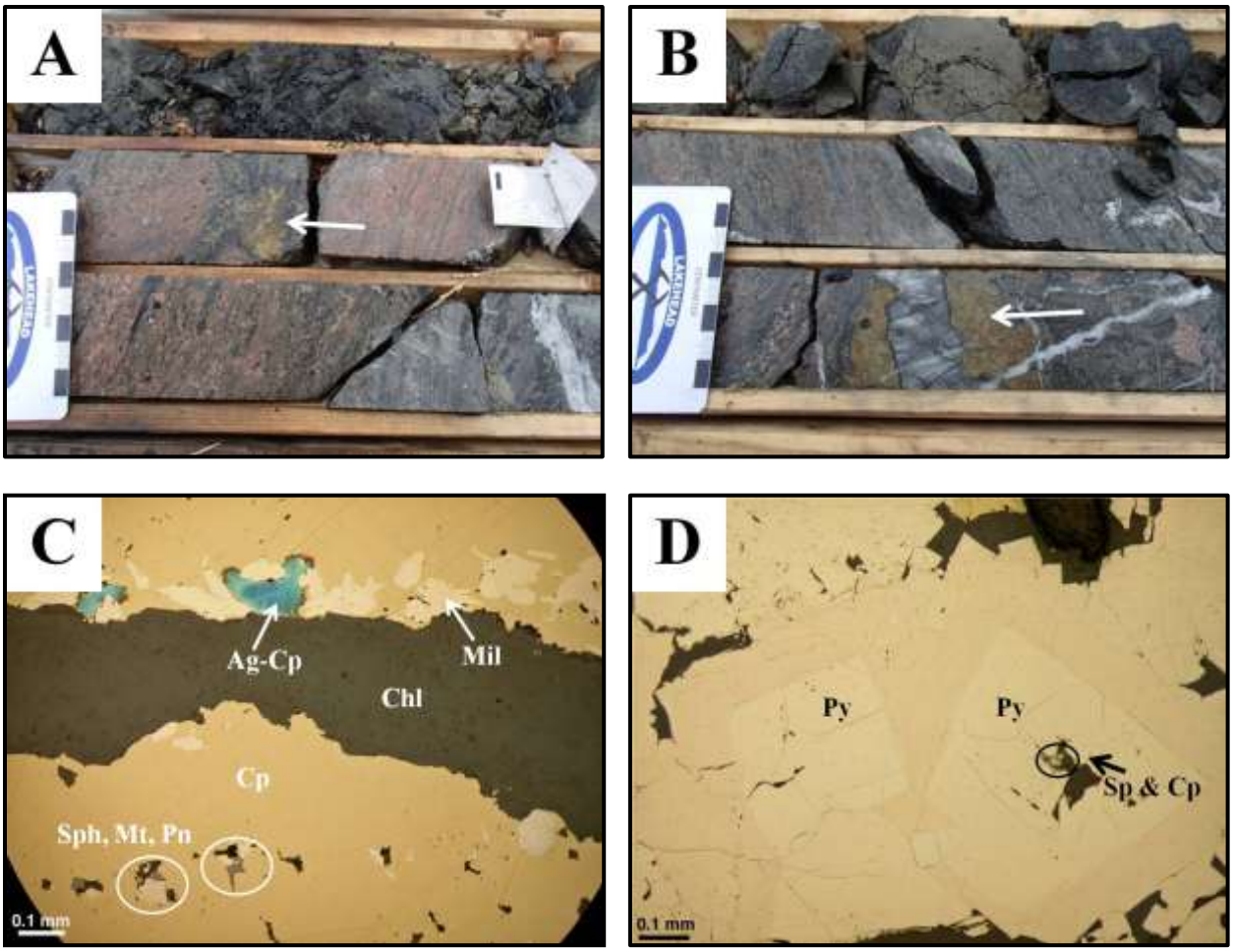

Figure 4.30: Representative textures of the conformable chalcopyrite-rich massive veinlets (diamond drill hole 07TH006). A) Massive chalcopyrite-rich veinlet at 573.68 m conformable with wall rock tuffaceous bedding (arrow). B) Massive chalcopyrite-rich veinlet at 575.48 m parallel to bedding in the wall rock (arrow). Note: multiple generations of carbonate veining cut the sulphides. C) Millerite and turquoise silver-rich chalcopyrite at edge of a chlorite vein through massive chalcopyrite with sphalerite, magnetite and pentlandite inclusions (sample RTTC-BT-163). D) Sphalerite and chalcopyrite inclusions in pyrite (sample RTTC-BT-161).

4.6.6 Sulphide-bearing wall rock

The mafic to intermediate metavolcanic wall rock lithologies surrounding the Thunder intrusion are heterogeneous and generally sulphide-bearing. Pyrite typically forms 1 – 2 % disseminations along with trace chalcopyrite, pyrrhotite, sphalerite, galena and millerite, and locally occurs as lenses with up to 10 % sulphide. Pyrite occurs in: porphyroblast clusters consisting of subhedral poikilitic cubes within the schistose fabric of the host rock (Fig. 4.31A), spongy habit intergrown with quartz-pumpellyite-carbonate veins (Fig. 4.31B) as secondary pyrite overprints (Fig. 4.31C), and in rare cases semi-massive intergrown with magnetite and garnet (Fig. 4.31D). Pyrite hosted in the wallrock is devoid of trace elements (Appendix B).

4.6.7 Platinum-group minerals and Au- Ag-minerals

Platinum-group minerals (PGMs) and precious metal minerals (PMMs) were identified using SEM-EDX and microprobe with assistance provided by Doreen Ames and Pat Hunt (Geological Survey of Canada, Ottawa) and Ingrid Kjarsgaard (consulting mineralogist hired through the Geological Survey of Canada's TGI-4) respectively (Table 4.2). All PGMs identified were PPGE-bearing phases (Pt, Pd, Rh subgroup of the platinum group elements) with the majority being Pd-rich tellurides and bismuthides and minor Pt-rich arsenides; no IPGE-bearing phases (Os, Ir, Ru subgroup of the platinum group elements) were identified. Identification of the PGMs and PMMs focused on a suite of samples representative of the various styles of sulphide mineralization correlating with high assay results (Bidwell and Marino, 2007) including the intrusion-hosted basal mineralization zone (Fig. 4.25) and the upper mineralized zone (Fig. 4.29), and the footwall-hosted pyrrhotite-rich massive sulphide veinlet (Fig. 4.26) and chalcopyrite-rich massive sulphide veinlets (Fig. 4.30). Representative magnetite

± pyrite ± chalcopyrite alteration veins (see section 4.5.1) were studied for PGM identification to test the hypothesis of PGE-mobility. However, no PGMs or PMMs were found.

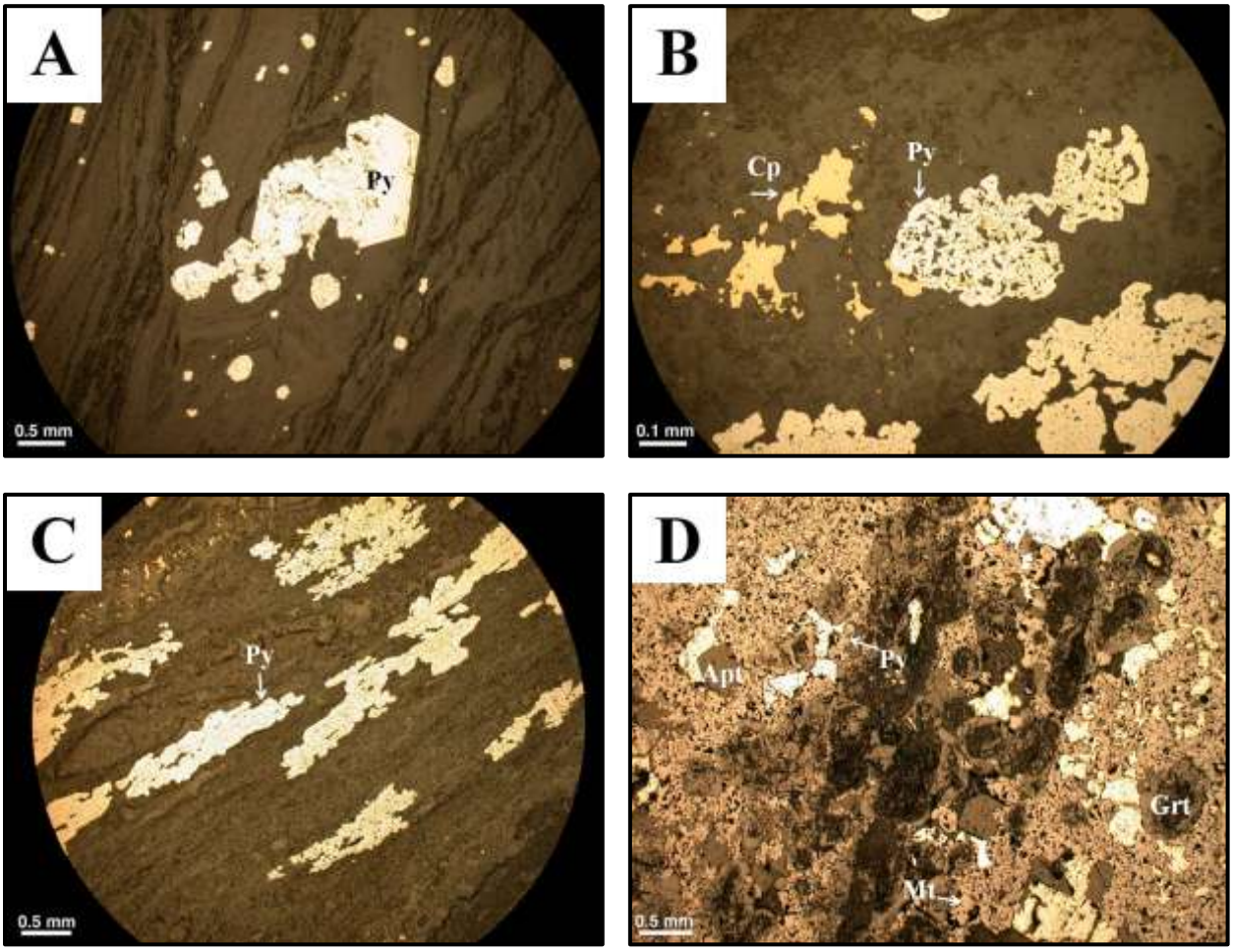

Figure 4.31: Representative textures of the sulphide mineralization in the wall rock surrounding the Thunder intrusion. A) Subhedral and clustered pyrite porphyroblasts in graphite-sericite schist (sample RTTC-BT-187). B) Spongy pyrite with pyrrhotite inclusions intergrown with chalcopyrite in a quartz-pumpellyite-carbonate vein (RTTC-BT-048). C) Secondary pyrite overprinting wall rock fragments and grown parallel to foliation (RTTC-BT-048). D) Garnet-stilpnomelane rosettes and apatite in semi-massive magnetite-pyrrhotite-chalcopyrite-pyrite (RTTC-BT-005).

Most PGMs and PMMs identified were from representative samples of the basal mineralization zone. They typically occur as isolated subhedral grains (rarely clustered) and rarely composite along the grain boundaries of pyrrhotite-chalcopyrite-pentlandite-magnetite and secondary silicates such as amphibole, biotite and chlorite. PGMs were rarely observed as inclusions in pyrrhotite and chalcopyrite. Michenerite is most abundant and the largest PGM identified (up to 9.2 μm x 14.0 μm; Fig. 4.32A) and is the dominant phase (Fig. 4.32B). Other PGMs in the basal mineralization zone include: sperrylite, kotulskite, mereskyite and an unknown mineral with formula Pd_3Pt_3Sn (Fig. 4.32C). Antimony (< 12 wt. %) commonly detected in kotulskite may reflect contamination from surroundings especially in the composite grain occurrences such as antimony from michenerite (Fig. 4.32B). Precious metal minerals identified include hessite, electrum and argentian pentlandite (Fig. 4.32C). Argentian pentlandite was found to be the most abundant and largest PMM identified (up to 20.0 μm x 13.0 μm) observed along grain boundaries of, and encased within, chalcopyrite (Fig. 4.32D).

Antimony-bearing minerals identified in the pyrrhotite-rich massive sulphide veinlet from DDH 05TH003 include naldrettite and stibiopalladinite. They both occur as isolated anhedral to subhedral grains enclosed in pyrrhotite and/or secondary pyrite-marcasite, and occur along sulphide grain boundaries (Fig. 4.33). Naldrettite is the most the abundant and largest PGM (up to 8.3 μm x 8.2 μm) identified.

In the upper mineralized zone, isolated subhedral kotolskite grains are encased by bornite and also occur along the grain boundaries of bornite and chalcopyrite (Fig. 4.29D). The upper mineralized zone is devoid of PMMs (Fig. 4.13; DDH 07TH006).

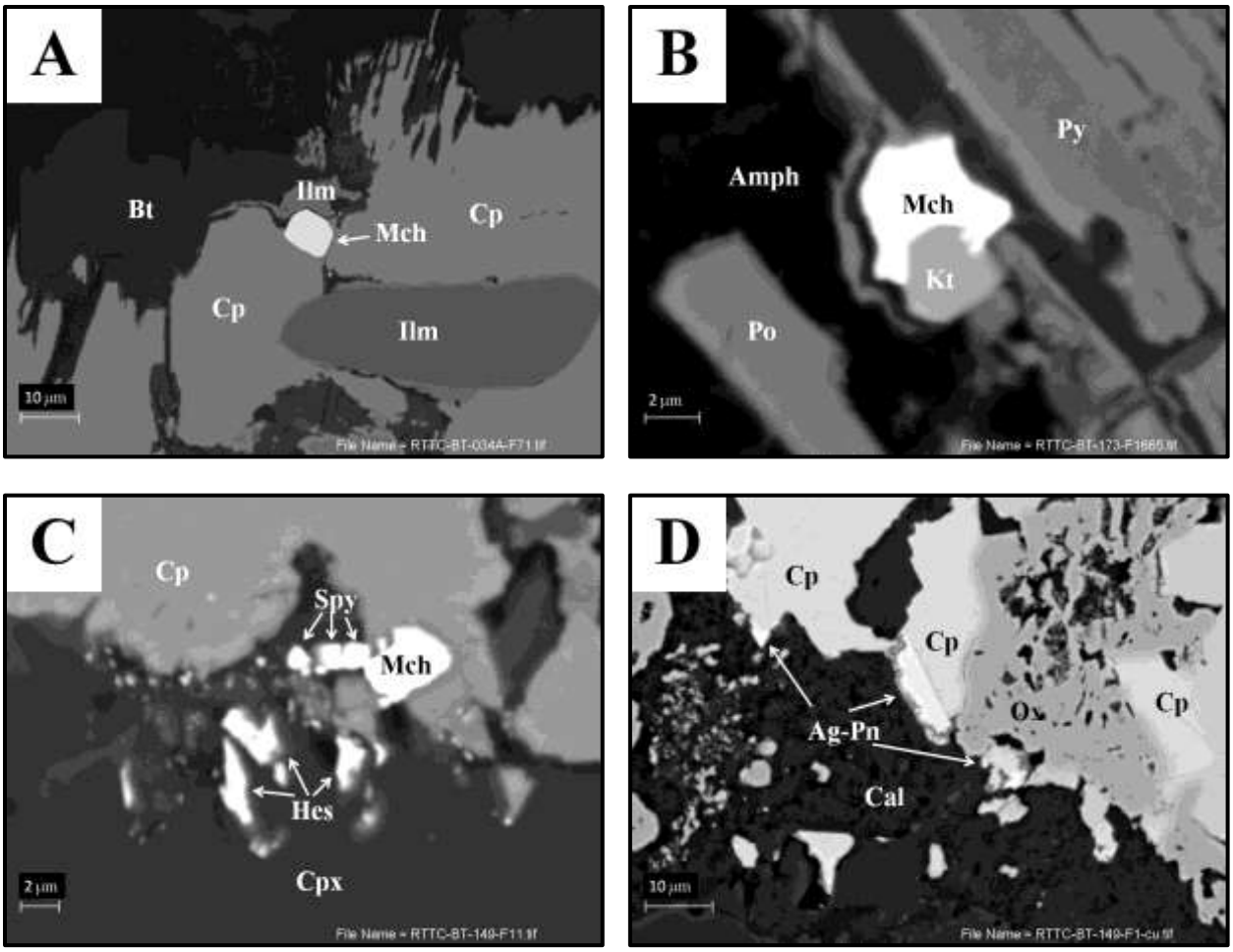

Figure 4.32: Back-scattered electron images of the platinum-group minerals and precious metal minerals identified from the basal mineralization zone, Thunder intrusion. A) An isolated michenerite grain along the grain boundary of chalcopyrite, ilmenite and biotite (sample RTTC-BT-034). Note the cluster of smaller grains of michenerite surrounding the larger grain (arrow). B) Composite grain of michenerite and kotulskite along the grain boundary of pyrite and secondary amphibole (sample RTTC-BT-173). C) A cluster of isolated michenerite, sperryltie and hessite crystals along the grain boundary of chalcopyrite and altered clinopyroxene (sample RTTC-BT-149). D) Argentian pentlandite along the grain boundary of chalcopyrite and calcite (sample RTTC-BT-149).

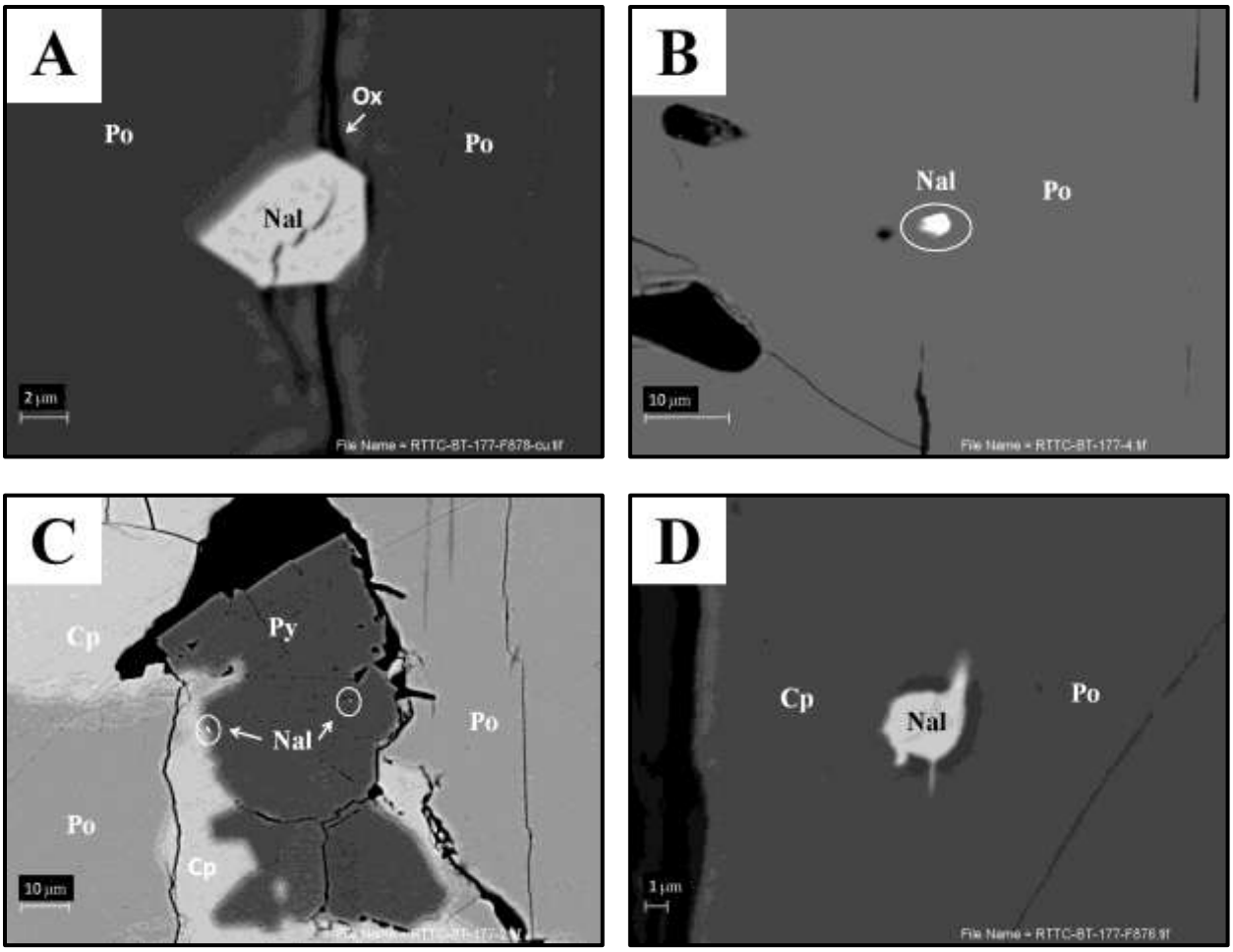

Figure 4.33: Representative back-scattered electron images of the platinum-group minerals and precious metal minerals identified in the footwall-hosted pyrrhotite-rich massive sulphide veinlet (diamond drill hole 07TH003; sample RTTC-BT-177). A) Fractured naldrettite within a Fe-oxide filled fracture in pyrrhotite. B) Naldrettite encased in pyrrhotite. C) Naldrettite enclosed in pyrite and along the grain boundary shared between chalcopyrite and pyrite. D) Anhedral naldrettite along the grain boundary shared between chalcopyrite and pyrrhotite.

Electrum, native silver and gold were found in footwall-hosted chalcopyrite-rich veinlets (DDH 07TH006; Fig. 4.13) as tiny inclusions in chalcopyrite (Fig. 4.34A) however, no PGMs were identified. Silver-bearing chalcopyrite haloes are commonly around the native silver inclusions within chalcopyrite (Fig. 4.34B). Concentrations of Ag within the Ag-bearing chalcopyrite grains ranged from 4.11 to 5.69 wt. %.

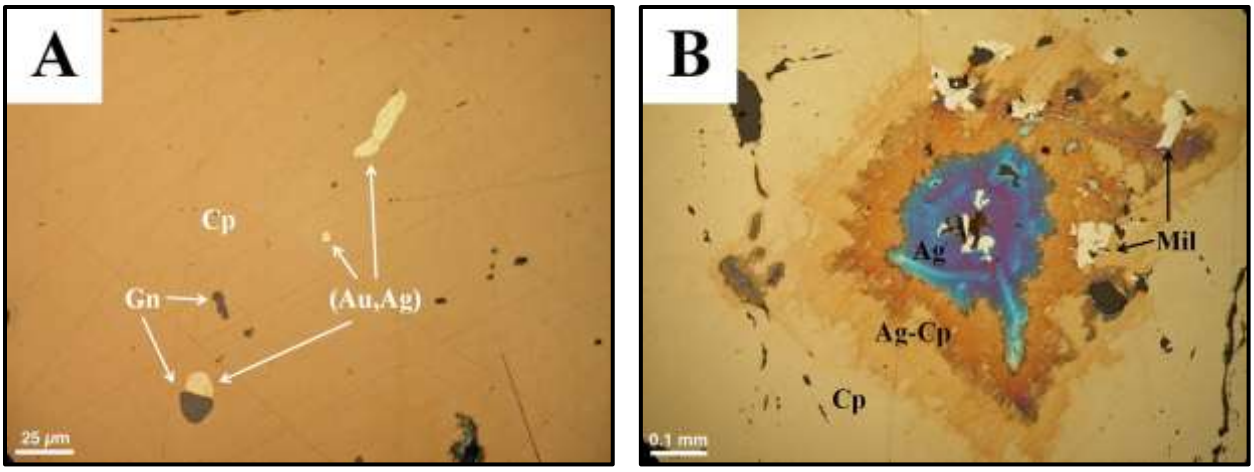

Figure 4.34: Representative photomicrographs of the precious metal minerals identified in samples of the chalcopyrite-rich massive sulphide veinlets (diamond drill hole 07TH006; sample RTTC-BT-163). A) Electrum and galena inclusions in chalcopyrite. B) Patch of silver-bearing chalcopyrite surrounding oxidized silver in chalcopyrite and inclusions of millerite.

Table 4.2: Summary of platinum-group minerals and precious-metal minerals identified in representative samples of the various styles of mineralization observed in the Thunder intrusion and footwall.

Mineral	Formula
Intrusion-hosted	
Basal mineralization zone	
Argentian pentlandite	$(Fe,Ni,Ag)_9S_8$
Electrum	(Au,Ag)
Hessite	Ag_2Te
Kotulskite	Pd(Te,Bi)
Merenskyite	$(Pd,Pt)(Te,Bi)_2$
Michenerite	(Pd,Pt)BiTe
Sperrylite	$PtAs_2$
unknown	Pd_3Pt_3Sn
Upper mineralized zone	
Kotulskite	Pd(Te,Bi)

Mineral	Formula
Footwall-hosted	
Pyrrhotite-rich massive sulphide veinlet	
Naldrettite	Pd_2Sb
Stibiopalladinite	Pd_5Sb_2
Chalcopyrite-rich massive sulphide veinlets	
Electrum	(Au,Ag)
Native silver	Ag

4.7 Olivine chemistry

Olivine analyses focused on samples collected from the lower mafic to ultramafic unit of DDH 07TH004 (n = 10). Additional samples include one surface sample (RTT-BT-149) and one sample from the upper mineralized zone in DDH 07TH007 (RTTC-BT-134). The coarser and least altered olivine crystals enclosed by plagioclase were preferred for analysis as they are expected to have avoided potential exchange with adjacent sulphide minerals (Donoghue et al., 2014). Unfortunately no fresh olivine was found in the upper gabbroic unit thereby restricting the analyses to rocks of the lower mafic to ultramafic unit. Both the core and rim were analyzed for multiple olivine grains in each sample. A summary of results is listed in Table 4.3 with the complete mineral chemistry databases in Appendix C. In general, the microprobe analyses on major elements had an error of ± 1-2 %; error on trace elements was up to ± 10 %. Olivine forsterite compositions range from 56.3 to 86.9 % Fo with an overall average of ~ 65 % Fo. There is little variation between core and rim measurements (typically < 0.5 % Fo) indicating that cumulus olivine was not overly modified by subsolidus re-equilibration with trapped silicate liquid (i.e., the trapped liquid shift; Barnes, 1986). Local variations include sample RTTC-BT-097 with % Fo ~ 56 which differs from majority of samples in DDH 07TH004; and, sample RTTC-BT-089 that shows a wide range in % Fo values from ~ 69 to 86 indicating disequilibrium along the basal contact of the lower mafic to ultramafic unit. Sample RTTC-BT-134 collected from upper mineralized zone yielded % Fo of ~ 68 and surface sample RTT-BT-149 yielded % Fo that ranges from ~ 62 to 66 which together are similar to the average % Fo values from DDH 07TH004 with the exception of sample RTTC-BT-097 and 089. Lastly, plotting NiO versus % Fo exhibits a strong positive correlation with the exception of the isolated values of sample RTTC-BT-097 (Fig. 4.35).

Table 4.3: Summary of olivine analyses by electron microprobe. Refer to Appendix D for a complete listing of the analysis.

Sample ID	Drill core	Depth (m)	Description	% Fo	NiO
RTTC-BT-063	07TH004	306.04	medium olivine, core	61.0	0.10
RTTC-BT-063	07TH004	306.04	medium olivine, rim against cpx	61.4	0.11
RTTC-BT-063	07TH004	306.04	medium olivine, core	60.8	0.09
RTTC-BT-063	07TH004	306.04	medium olivine, rim	60.5	0.07
RTTC-BT-063	07TH004	306.04	fine round olivine, core	64.1	0.10
RTTC-BT-063	07TH004	306.04	fine round olivine, rim	64.2	0.13
RTTC-BT-098	07TH004	317.95	medium rounded olivine, core	63.5	0.15
RTTC-BT-098	07TH004	317.95	medium rounded olivine, rim	63.6	0.13
RTTC-BT-098	07TH004	317.95	coarse rounded olivine, core	63.2	0.14
RTTC-BT-098	07TH004	317.95	coarse rounded olivine, rim	63.4	0.14
RTTC-BT-098	07TH004	317.95	medium olivine, core	66.2	0.15
RTTC-BT-098	07TH004	317.95	medium olivine, rim	66.2	0.14
RTTC-BT-098	07TH004	317.95	coarse olivine, core	63.8	0.18
RTTC-BT-098	07TH004	317.95	coarse olivine, rim	63.6	0.15
RTTC-BT-097	07TH004	323.00	medium subhedral olivine, core	56.8	0.10
RTTC-BT-097	07TH004	323.00	medium subhedral olivine, rim	56.4	0.11
RTTC-BT-097	07TH004	323.00	medium subhedral olivine, core	56.7	0.10
RTTC-BT-097	07TH004	323.00	medium subhedral olivine, rim	56.3	0.09
RTTC-BT-097	07TH004	323.00	coarse euhedral olivine, core	56.8	0.10
RTTC-BT-097	07TH004	323.00	coarse euhedral olivine, rim	56.5	0.09
RTTC-BT-096	07TH004	355.62	coarse olivine, core	67.0	0.14
RTTC-BT-096	07TH004	355.62	coarse olivine, rim	66.9	0.13
RTTC-BT-096	07TH004	355.62	medium olivine, core	67.2	0.14
RTTC-BT-096	07TH004	355.62	medium olivine, rim	67.4	0.13
RTTC-BT-096	07TH004	355.62	medium olivine with Cr-Ti-mt inclusion, core	67.1	0.14
RTTC-BT-096	07TH004	355.62	medium olivine w. Cr-Ti-mt inclusion, rim	67.5	0.14
RTTC-BT-095	07TH004	375.94	medium subhedral olivine, core	67.5	0.17
RTTC-BT-095	07TH004	375.94	medium subhedral olivine, rim	67.0	0.17
RTTC-BT-095	07TH004	375.94	medium subhedral olivine with Cr-mt inclusion, core	67.2	0.17
RTTC-BT-095	07TH004	375.94	medium subhedral olivine with Cr-mt inclusion, rim	67.6	0.16
RTTC-BT-095	07TH004	375.94	large subh. olivine intergrown w. FeTi-oxides, core	67.6	0.18
RTTC-BT-095	07TH004	375.94	large subhedral olivine intergrown with FeTi-oxides, rim	67.8	0.16
RTTC-BT-095	07TH004	375.94	round olivine inclusion in ilmenite	68.5	0.16
RTTC-BT-094	07TH004	404.00	medium euhedral olivine, core	63.2	0.14
RTTC-BT-094	07TH004	404.00	medium euhedral olivine, rim	63.0	0.15
RTTC-BT-094	07TH004	404.00	medium euhedral olivine, core	62.1	0.13
RTTC-BT-094	07TH004	404.00	medium euhedral olivine, rim	61.9	0.16
RTTC-BT-094	07TH004	404.00	medium subhedral olivine, core	61.9	0.12
RTTC-BT-094	07TH004	404.00	medium subhedral olivine, rim	61.7	0.12

Table 4.3 (cont.): Summary of olivine analyses by electron microprobe. Refer to Appendix D for a complete listing of the analysis. Note: sample RTT-BT-149 location at 16U 330412E 5378462N.

Sample ID	Drill core	Depth (m)	Description	% Fo	NiO
RTTC-BT-093	07TH004	409.58	medium subhedral olivine, core	67.5	0.15
RTTC-BT-093	07TH004	409.58	medium subhedral olivine, rim	67.4	0.18
RTTC-BT-093	07TH004	409.58	medium euhedral olivine, core	66.7	0.15
RTTC-BT-093	07TH004	409.58	medium euhedral olivine, rim	66.8	0.16
RTTC-BT-093	07TH004	409.58	small round olivine, core	67.3	0.16
RTTC-BT-093	07TH004	409.58	medium euhedral olivine, core	66.6	0.16
RTTC-BT-093	07TH004	409.58	medium euhedral olivine, rim	66.5	0.17
RTTC-BT-092	07TH004	426.10	medium olivine, core	62.6	0.01
RTTC-BT-092	07TH004	426.10	medium olivine, rim	63.1	0.09
RTTC-BT-092	07TH004	426.10	medium olivine, core	63.9	0.05
RTTC-BT-092	07TH004	426.10	medium olivine, rim	62.2	0.06
RTTC-BT-092	07TH004	426.10	medium euhedral olivine, core	65.0	0.07
RTTC-BT-092	07TH004	426.10	medium euhedral olivine, rim	64.8	0.05
RTTC-BT-091	07TH004	432.18	medium olivine, core	67.2	0.14
RTTC-BT-091	07TH004	432.18	medium olivine, rim	66.0	0.14
RTTC-BT-091	07TH004	432.18	medium olivine, core	66.7	0.15
RTTC-BT-091	07TH004	432.18	medium olivine, rim	66.1	0.12
RTTC-BT-091	07TH004	432.18	medium olivine, core	65.0	0.13
RTTC-BT-091	07TH004	432.18	medium olivine, rim	63.0	0.11
RTTC-BT-089	07TH004	437.00	olivine, core	68.6	0.17
RTTC-BT-089	07TH004	437.00	olivine, rim	68.9	0.19
RTTC-BT-089	07TH004	437.00	fractured olivine, middle	75.3	0.23
RTTC-BT-089	07TH004	437.00	fractured olivine, rim	72.5	0.19
RTTC-BT-089	07TH004	437.00	coarse olivine, core	86.0	0.36
RTTC-BT-089	07TH004	437.00	coarse olivine, rim	74.8	0.28
RTTC-BT-134	07TH006	182.00	medium olivine, core	69.0	0.22
RTTC-BT-134	07TH006	182.00	medium olivine, rim	68.9	0.21
RTTC-BT-134	07TH006	182.00	medium olivine, core	68.7	0.22
RTTC-BT-134	07TH006	182.00	medium olivine, rim	68.5	0.19
RTTC-BT-134	07TH006	182.00	medium euhedral olivine, core	68.9	0.21
RTTC-BT-134	07TH006	182.00	medium euhedral olivine, rim	68.7	0.21
RTT-BT-149	Surface	-	olivine remnants in serpentine alteration	66.1	0.15
RTT-BT-149	Surface	-	olivine remnants in serpentine alteration	65.2	0.15
RTT-BT-149	Surface	-	small olivine	62.0	0.08
RTT-BT-149	Surface	-	small olivine	61.9	0.07
RTT-BT-149	Surface	-	olivine remnant in serpentine	62.8	0.11

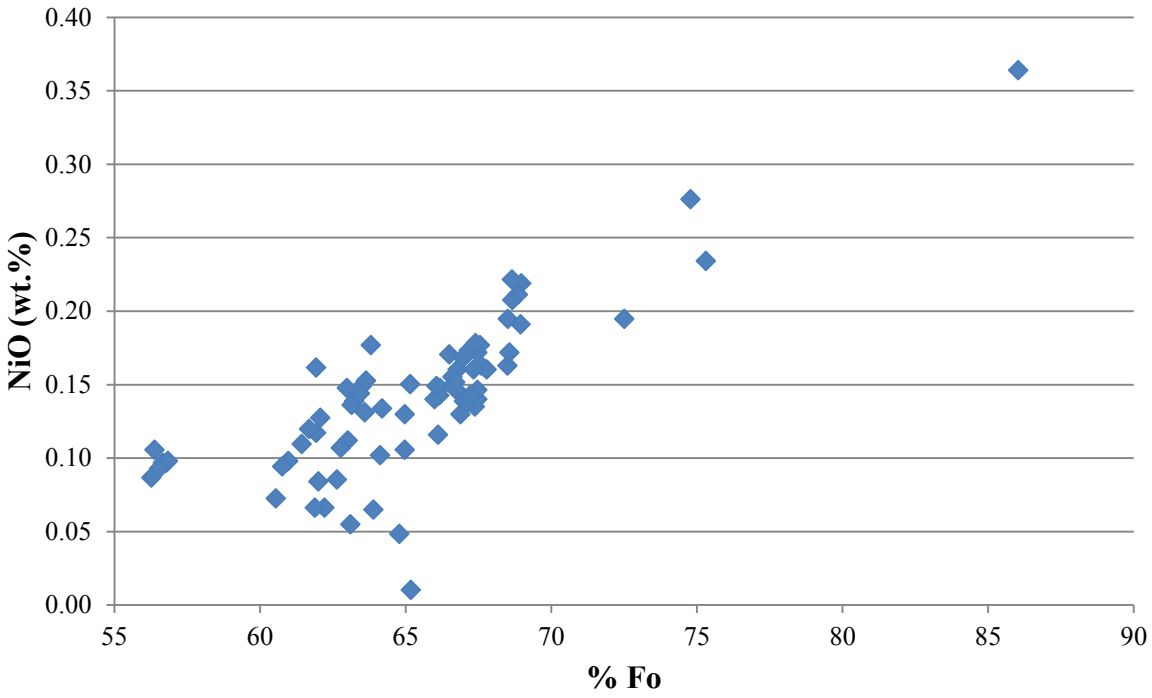

Figure 4.35: Plot of NiO presented as wt. % oxide versus % Fo olivine from the suite lower mafic to ultramafic samples collected from diamond drill hole 07TH004. Results summarized in Table 4.3.

4.8 Whole Rock Geochemistry

Whole rock analyses of 104 samples collected from surface and DDHs 05TH001, 002, 003, 07TH004 and 007 were undertaken. Samples were grouped into the following units: upper gabbroic unit (n = 22), lower mafic to ultramafic unit (n = 28), pegmatitic gabbro (n = 4), eastern N-trending gabbroic dike (n = 6), western N-trending gabbroic dike (n = 5), cross-cutting mafic dike (n = 5), iron formation (n = 2) and metavolcanic rocks (n = 31). The sample groupings is based on the geochemical data presented in the following and and macro/microscopic observations presented in previous sections. The full data set is presented in Appendix D and representative analyses are listed in Table 4.4.

4.8.1 Down-hole variations in major element geochemistry of the Thunder intrusion

Samples of the Thunder intrusion collected from DDH 07TH004 show down-hole variations in major element geochemistry (Fig. 4.36). Diamond drill hole 07TH004 was determined to be the most complete representation of the Thunder intrusion's lithostratigraphy (Fig. 4.13). The lower mafic to ultramafic unit (n = 11) exhibits elevated MgO (13 to 22 wt. %) and CaO (8 to 16 wt. %) contents but low TiO_2 (1 to 3 wt. %), Al_2O_3 (3 to 8 wt. %), total alkali ($Na_2O + K_2O$; 0.6 to 3 wt. %) and P_2O_5 (0.07 to 0.7 wt. %) contents. In contrast, the upper gabbroic unit (n = 22) exhibits relatively elevated TiO_2 (2 to 5 wt. %), Al_2O_3 (10 to 18 wt. %), total alkali (3 to 7 wt. %) and P_2O_5 (0.2 to 0.7 wt. %) contents but low MgO (3 to 6 wt. %) and CaO (6 to 13 wt. %) contents. The mg# differs between the two intrusive units with the lower mafic to ultramafic unit ranging from 55 to 73 and the upper gabbroic unit ranging from 35 to 53. Both units exhibit similar SiO_2, FeO^T and MnO contents; the lower mafic to ultramafic unit SiO_2 ranging from 42 to 49 wt. %, FeO^T ranging from 10 to 22 wt. % and MnO ranging from 0.2 to 0.3 wt. %; the upper gabbroic unit SiO_2 ranging from ~ 43 to 53 wt. %, FeO^T ranging from 10 to 18 wt. % and MnO ranging from 0.1 to 0.2 wt. %. The boundary between the upper gabbroic unit and the lower mafic to ultramafic unit at ~ 300 m marks a zone of significant variation in major element geochemistry including a sharp drop in MgO, CaO and mg# and a sharp spike in Al2O3 moving up section from the lower mafic to ultramafic unit into the upper gabbroic unit. From bottom to top of the Thunder intrusion, there is a general trend of increasing TiO2, P2O5 and total alkali content up section.

Table 4.4: Representative whole rock analyses for the intrusive rocks. All values normalized to be 100% anhydrous. Chondrite-normalizing values from Sun and McDonough (1989). Sample locations are given in NAD83 UTM Zone 16

	Upper gabbroic unit			Lower mafic to ultramafic unit		
Sample ID	RTTC-BT-078	RTTC-BT-074	RTTC-BT-067	RTTC-BT-098	RTTC-BT-095	RTTC-BT-092
SiO_2 (wt. %)	45.88	44.23	47.22	47.61	48.34	48.83
TiO_2	4.96	5.07	3.10	1.39	1.38	1.76
Al_2O_3	12.23	10.50	14.23	6.88	6.01	5.15
FeO^T	16.02	18.32	13.63	12.65	10.47	13.86
MnO	0.22	0.23	0.18	0.20	0.17	0.20
MgO	4.89	5.93	6.33	14.38	14.93	14.19
CaO	9.13	9.97	9.16	13.66	15.67	12.28
Na_2O	3.55	2.73	3.04	1.32	1.31	1.29
K_2O	1.03	0.84	1.39	0.42	0.44	0.70
P_2O_5	0.32	0.23	0.21	0.07	0.11	0.17
LOI	0.62	0.28	1.31	0.36	1.15	1.31
Total	99.26	99.71	99.13	100.29	99.62	99.52
mg#	37.66	39.18	47.89	69.24	73.84	66.97
Th (ppm)	3.17	2.23	2.07	0.69	0.89	2.21
Nb	34.65	22.05	18.86	6.25	10.09	21.07
La	49.56	31.06	25.63	10.66	13.34	26.11
Ce	104.5	73.57	60.80	28.46	33.44	61.58
Pr	13.50	10.28	8.57	4.44	4.96	8.51
Nd	55.64	44.23	36.60	21.03	22.25	36.93
Zr	301.9	231.7	196.6	90.3	100.2	182.4
Hf	7.32	5.90	4.91	2.74	2.81	4.72
Sm	10.52	8.88	7.15	4.83	4.81	7.15
Eu	3.26	2.64	2.19	1.52	1.46	1.98
Ti	30993	30196	19248	8304	8351	11002
Gd	8.12	7.20	5.60	4.07	3.98	5.56
Tb	1.02	0.89	0.70	0.53	0.51	0.70
Dy	5.22	4.52	3.60	2.71	2.73	3.59
Y	22.30	19.39	15.40	11.15	11.39	15.07
Ho	0.87	0.75	0.59	0.45	0.46	0.58
Er	2.16	1.89	1.49	1.11	1.12	1.43
Tm	0.27	0.23	0.18	0.13	0.14	0.18
Yb	1.63	1.36	1.12	0.79	0.83	1.03
Lu	0.23	0.19	0.15	0.11	0.12	0.15
V	403.1	678.2	535.5	236.6	179.4	218.5
Sc	25.16	29.98	24.83	41.05	45.12	38.61
$(La/Sm)_n$	3.04	2.26	2.32	1.43	1.79	2.36
$(Gd/Yb)_n$	4.12	4.38	4.12	4.27	3.95	4.46
Easting	330319	330319	330319	330319	330319	330319
Northing	5377910	5377910	5377910	5377910	5377910	5377910
DDH	07TH004	07TH004	07TH004	07TH004	07TH004	07TH004
Depth (m)	86	182	267	318	376	426

Table 4.4 (cont.): Representative whole rock analyses for the intrusive rocks. All values normalized to be 100% anhydrous. Chondrite-normalizing values from Sun and McDonough (1989). Sample locations are given in NAD83 UTM Zone 16.

	Pegmatitic gabbro			Eastern N-trending gabbroic dike		
Sample ID	RTTC-BT-216	RTT-BT-130	RTTC-BT-062	RTT-BT-055	RTT-BT-180	RTT-BT-222
SiO_2 (wt. %)	50.72	46.82	50.71	48.58	47.53	48.52
TiO_2	3.37	4.14	3.26	1.51	1.44	1.44
Al_2O_3	13.84	12.20	12.04	15.76	15.15	16.38
FeO^T	9.40	12.90	11.48	12.38	12.99	11.33
MnO	0.16	0.16	0.20	0.20	0.20	0.18
MgO	6.53	7.03	5.07	7.37	8.19	7.45
CaO	9.47	11.41	10.22	8.68	9.78	9.48
Na_2O	4.58	2.73	4.97	2.28	2.41	2.63
K_2O	0.49	1.03	0.15	1.71	0.70	1.17
P_2O_5	0.39	0.16	0.61	0.16	0.16	0.16
LOI	1.59	1.04	1.11	1.04	0.64	2.03
Total	100.22	99.36	99.74	99.41	99.31	99.64
mg#	57.91	51.90	46.66	54.11	55.53	56.55
Th (ppm)	4.30	2.14	6.66	1.33	1.27	1.33
Nb	38.48	21.57	54.41	12.00	10.95	11.20
La	45.37	41.61	54.64	14.67	13.62	14.12
Ce	120.1	102.3	151.4	31.43	29.28	29.86
Pr	16.45	13.11	21.27	4.07	3.91	3.95
Nd	67.85	51.39	90.45	17.70	16.90	17.02
Zr	388.2	203.1	565.3	93.98	88.57	92.89
Hf	9.22	5.21	13.13	2.43	2.35	2.38
Sm	12.25	9.04	16.63	3.98	3.84	3.92
Eu	3.61	3.10	4.43	1.50	1.40	1.45
Ti	20900	24890	20203	9230	8643	8827
Gd	9.38	6.84	12.44	3.97	3.85	3.92
Tb	1.16	0.86	1.58	0.60	0.58	0.60
Dy	5.98	4.35	8.02	3.74	3.63	3.67
Y	26.44	18.64	35.83	19.92	18.71	19.52
Ho	1.01	0.71	1.34	0.72	0.71	0.72
Er	2.52	1.77	3.41	2.08	2.04	2.05
Tm	0.32	0.22	0.44	0.29	0.28	0.29
Yb	1.91	1.30	2.62	1.86	1.84	1.88
Lu	0.26	0.18	0.36	0.29	0.27	0.27
V	278.9	570.9	203.5	277.9	264.1	277.0
Sc	25.20	30.22	18.20	31.73	33.21	35.12
$(La/Sm)_n$	2.39	2.97	2.12	2.38	2.29	2.33
$(Gd/Yb)_n$	4.06	4.36	3.93	1.77	1.73	1.73
Easting	330161	329929	330319	331003	330822	331388
Northing	5378268	5378222	5377910	5377824	5384202	5375988
DDH	07TH007	Surface	07TH004	Surface	Surface	Surface
Depth (m)	53	-	311	-	-	-

Table 4.4 (cont.): Representative whole rock analyses for the intrusive rocks. All values normalized to be 100% anhydrous. Chondrite-normalizing values from Sun and McDonough (1989). Sample locations are given in NAD83 UTM Zone 16.

	Western N-trending gabbroic dike			Cross-cutting mafic dikes		
Sample ID	RTT-BT-232	RTT-BT-235	RTT-BT-236	RTTC-BT-101	RTTC-BT-045	RTTC-BT-038
SiO_2 (wt. %)	50.34	49.97	48.60	50.51	50.48	50.00
TiO_2	2.12	1.94	2.21	2.31	2.34	1.00
Al_2O_3	17.27	16.28	15.13	13.39	13.29	14.56
FeO^T	11.22	11.95	13.26	11.97	12.49	11.74
MnO	0.17	0.18	0.20	0.19	0.18	0.21
MgO	3.87	5.70	6.25	6.20	6.20	7.13
CaO	8.14	7.88	8.07	9.77	10.03	11.44
Na_2O	3.34	2.94	2.72	1.86	2.61	2.20
K_2O	1.92	1.52	1.86	2.23	0.74	0.33
P_2O_5	0.36	0.30	0.25	0.24	0.24	0.09
LOI	1.57	1.40	1.30	2.77	0.89	1.50
Total	99.41	98.66	99.25	99.19	99.38	99.59
mg#	40.60	48.55	48.27	50.63	49.58	54.58
Th (ppm)	3.36	2.62	2.27	1.72	1.73	0.80
Nb	18.59	15.57	13.23	12.21	12.58	2.98
La	29.46	24.98	20.39	18.36	18.24	4.72
Ce	61.49	52.42	42.68	40.25	41.63	10.80
Pr	7.93	6.73	5.60	5.61	5.88	1.56
Nd	32.80	28.06	23.37	25.31	26.30	7.38
Zr	168.7	142.0	120.6	183.1	187.7	59.90
Hf	4.14	3.49	3.01	4.63	4.71	1.63
Sm	6.87	5.84	5.07	6.22	6.38	2.23
Eu	2.25	2.06	1.79	2.19	2.12	0.82
Ti	13245	11933	13750	14298	14323	6158
Gd	6.50	5.64	4.86	6.30	6.44	2.82
Tb	0.92	0.81	0.70	0.92	0.95	0.48
Dy	5.43	4.75	4.15	5.40	5.53	3.13
Y	27.82	24.23	21.39	26.26	27.22	15.84
Ho	1.04	0.89	0.80	0.99	1.01	0.63
Er	2.86	2.54	2.22	2.64	2.68	1.84
Tm	0.40	0.35	0.30	0.35	0.36	0.26
Yb	2.49	2.18	1.91	2.15	2.16	1.66
Lu	0.36	0.32	0.28	0.30	0.30	0.24
V	268.8	266.7	414.7	309.6	313.2	287.3
Sc	25.81	27.90	34.86	29.32	29.26	26.80
$(La/Sm)_n$	2.77	2.76	2.60	1.91	1.85	1.37
$(Gd/Yb)_n$	2.16	2.14	2.11	2.43	2.46	1.41
Easting	326984	326997	327028	330435	330435	330435
Northing	5400588	5401169	5401620	5378298	5378298	5378298
DDH	Surface	Surface	Surface	05TH002	05TH003	05TH003
Depth (m)	-	-	-	220	63	240

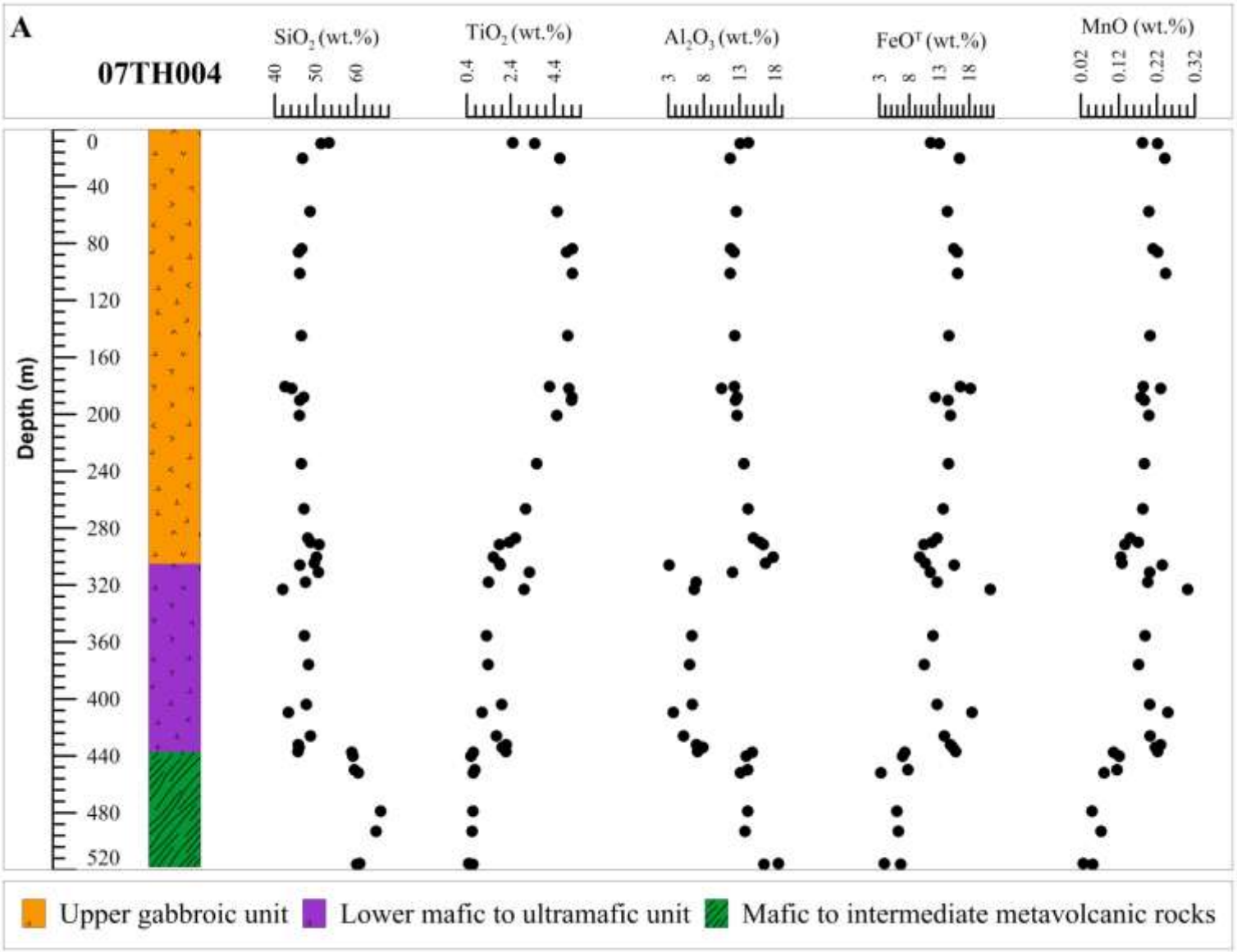

Figure 4.36: A) Select major elements presented as wt.% oxide plotted against the depth and simplified lithostratigraphy of diamond drill hole 07TH004.

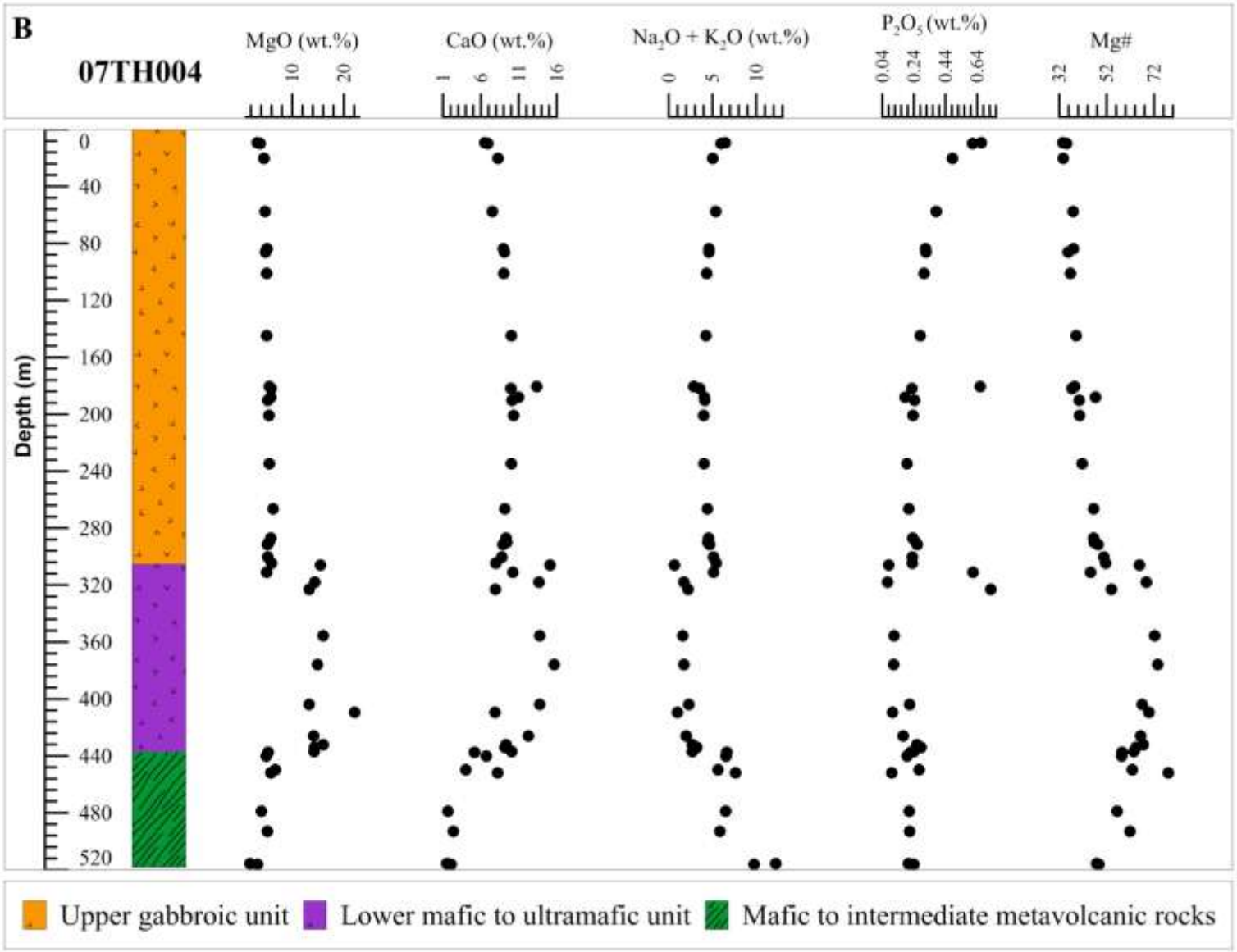

Figure 4.36 (cont.): B) Select major elements presented as wt.% oxide plotted against the depth and simplified lithostratigraphy of diamond drill hole 07TH004.

4.8.2 Harker variation diagrams of the Thunder intrusion

Figure 4.37 shows variations of select major and trace elements plotted against MgO wt. % oxide using all samples of the upper gabbroic unit, lower mafic to ultramafic unit (n = 28) and pegmatitic gabbro. The main feature exhibited by the diagrams includes the linear relationships of selected elements with changing MgO content and the separation of data between the lower mafic to ultramafic unit and the upper gabbroic unit including samples of the pegmatitic gabbro. Rarely do the fields for the upper gabbroic unit and the pegmatitic gabbro overlap with the lower mafic to ultramafic unit. Although there is some variation in the distribution of samples such as CaO, the plots still show broadly coherent trends indicating alteration (i.e., serpentinization) has not significantly affected mobile element abundances.

4.8.3 Trace and rare earth element geochemistry of the intrusive rocks

Chondrite-normalized La/Sm_n vs. Gd/Yb_n values of the intrusive rocks are shown in Figure 4.38 and primitive mantle normalized trace and rare earth element profiles in Figures 4.39A to F. Samples from the upper gabbroic unit have La/Sm_n ranging from 2.15 to 3.42 and Gd/Yb_n ranging from 3.79 to 4.38 which overlap with samples from the lower mafic to ultramafic unit with La/Sm_n ranging from 1.25 to 2.80 and Gd/Yb_n ranging from 3.73 to 5.23. Samples from the pegmatitic gabbro are comparable to those of the upper gabbroic unit with La/Sm_n ranging from 2.12 to 2.98 and Gd/Yb_n ranging from 3.93 to 4.36 but with more variations in LREE and HFSE. The primitive mantle normalized profiles of the upper gabbroic unit, the lower mafic to ultramafic unit and pegmatitic gabbro parallel one another and are characterized by a relative enrichment in light rare earth elements (LREEs), depletion in heavy rare earth elements (HREEs), weak negative Zr-Hf anomalies but in relative trace and REE abundances (Figs. 4.39A, B, C). Samples of the upper gabbroic and pegmatitic gabbro contain

higher LREEs (e.g., La) and HFSEs (e.g., Th) than samples of the lower mafic to ultramafic unit. Samples of the upper gabbroic unit and pegmatitic gabbro both show strong positive and negative Ti and V anomalies whereas samples of the lower mafic to ultramafic unit show weak negative Ti anomalies and strong positive V anomalies. An obvious Nb anomaly is not present amongst the three intrusive units with the exception of one sample collected from the uppermost section of the upper gabbroic unit from DDH 07TH004 that shows a distinct negative Nb anomaly.

Samples of the N-trending gabbroic dikes show a tighter range in LREEs and lower HREE abundances than samples of the upper gabbroic unit, lower mafic to ultramafic unit and pegmatitic gabbro (Fig. 4.38): La/Sm_n values of the eastern N-trending gabbroic dike range from 2.21 to 2.38 and Gd/Yb_n ranging from 1.73 to 1.77 whereas La/Sm_n values of the western N-trending gabbroic dike range from 2.39 to 2.77 and Gd/Yb_n ranging from 1.88 to 2.16. The primitive mantle normalized profiles of the eastern and western gabbroic dike parallel one another and are characterized by a relative enrichment in LREEs and depletion in HREEs, weak negative Zr-Hf anomalies and weak to strong negative Nb anomalies except sample RTT-BT-237 (western N-trending gabbroic dike) which displays no indications of a negative Nb anomaly (Figs. 4.39D, E).

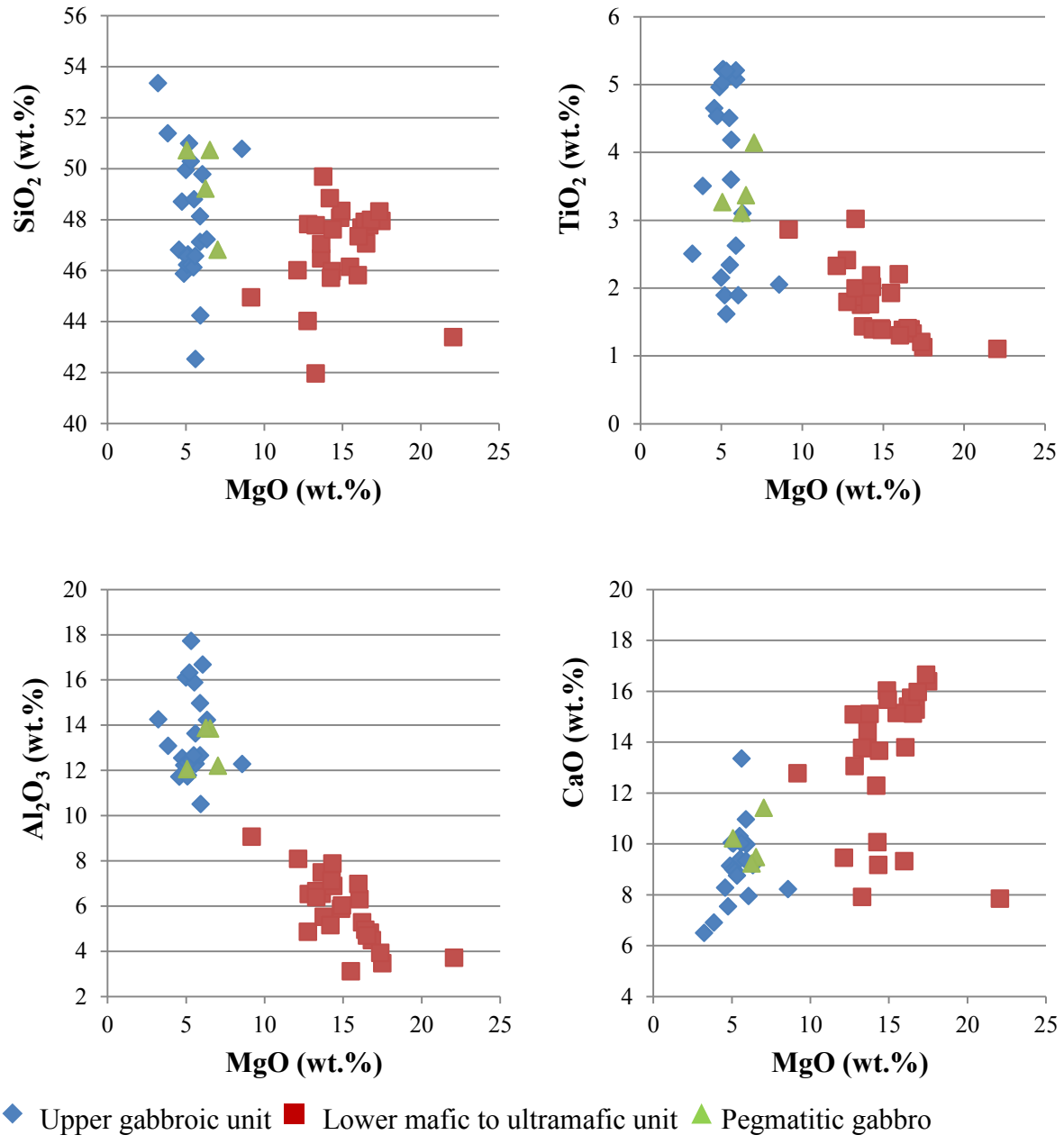

Figure 4.37: Harker variation diagrams of whole rock analyses plotting MgO against selected major elements (wt. % oxide) and trace elements (ppm) using samples of the lower mafic to ultramafic unit, upper gabbroic unit and pegmatitic gabbro.

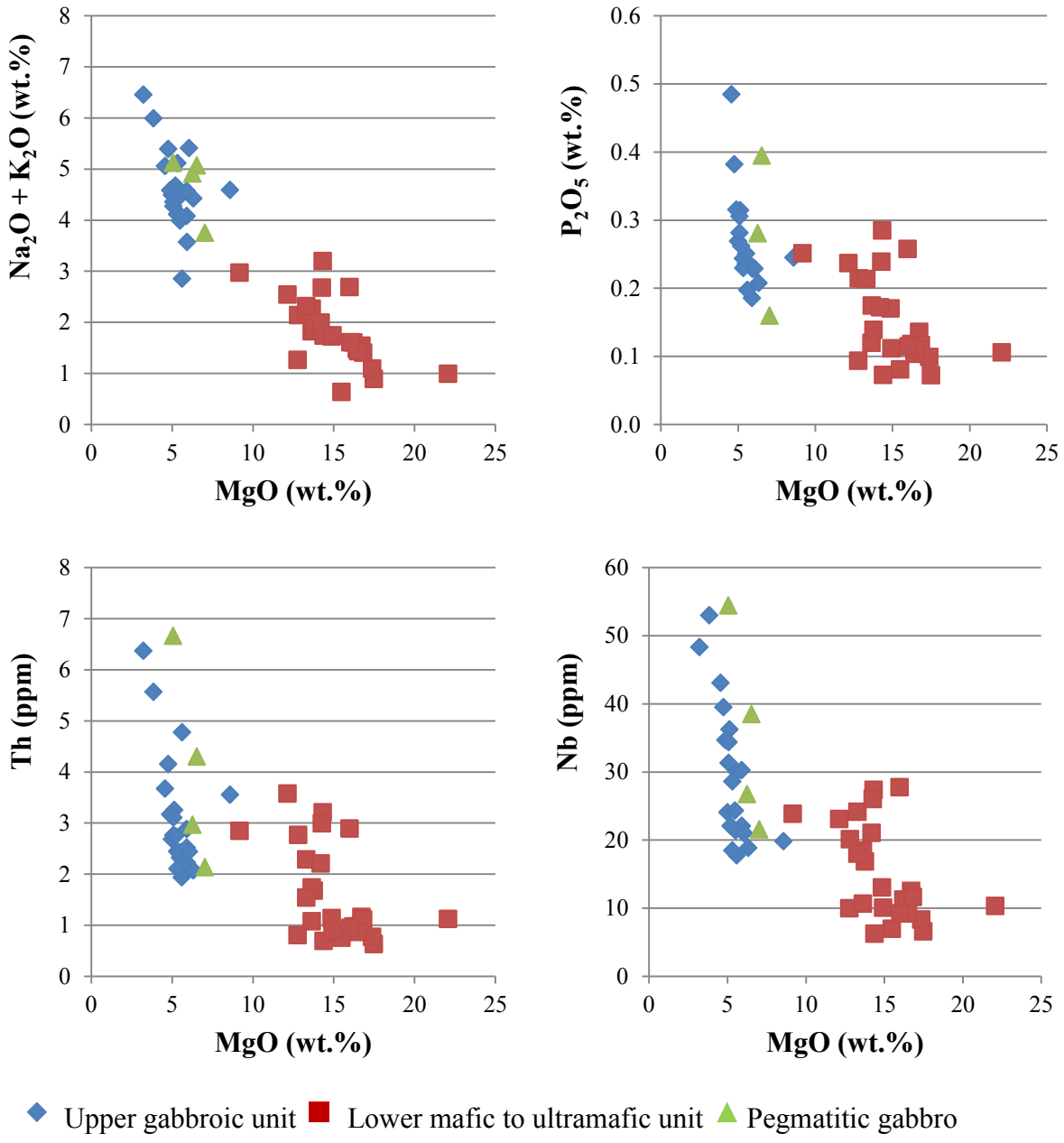

Figure 4.37 (cont.): Harker variation diagrams of whole rock analyses plotting MgO against selected major elements (wt. % oxide) and trace elements (ppm) using samples of the lower mafic to ultramafic unit, upper gabbroic unit and pegmatitic gabbro.

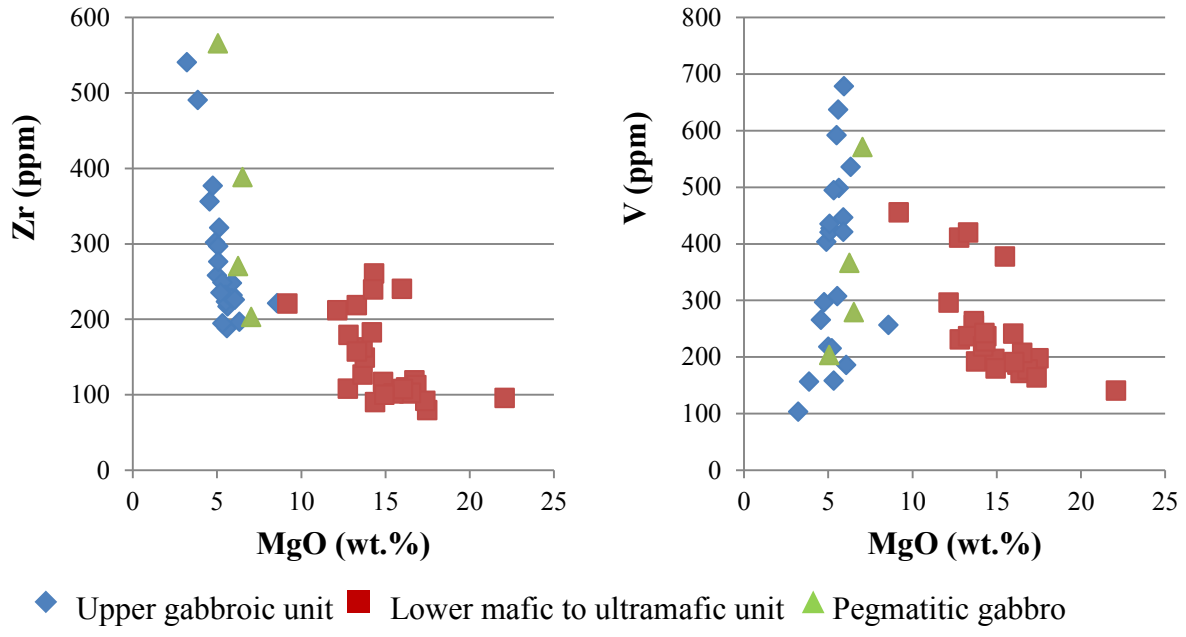

Figure 4.37 (cont.): Harker variation diagrams of whole rock analyses plotting MgO against selected major elements (wt. % oxide) and trace elements (ppm) using samples of the lower mafic to ultramafic unit, upper gabbroic unit and pegmatitic gabbro.

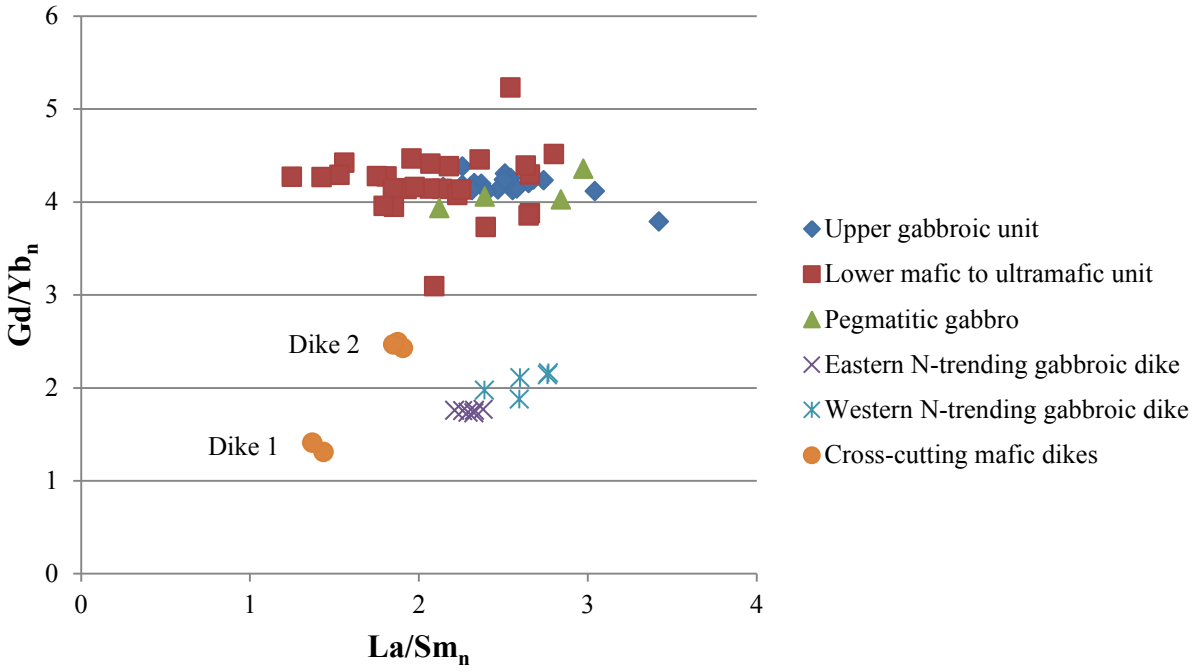

Figure 4.38: Plot of chondrite normalized La/Sm_n versus Gd/Yb_n for all samples of the upper gabbroic unit, lower mafic to ultramafic unit, pegmatitic gabbro, N-trending gabbroic dikes and cross-cutting mafic dikes. Normalizing values from Sun and McDonough (1989). Indicated on the plot are dike 1 and 2 samples.

Samples of the cross-cutting mafic dikes also show a tight range in light rare LREEs and relatively depleted HREEs similar as the N-trending gabbroic dikes when compared to samples of the upper gabbroic unit, lower mafic to ultramafic unit and pegmatitic gabbro (Fig. 4.38). However, these small intrusive units are distinct from the N-trending gabbroic dikes. Within the cross-cutting mafic dikes sample grouping, two distinct sub-units are evident; dike 1 includes samples RTTC-BT-045, -101 and -219; dike 2 includes samples RTTC-BT-038 and -210. Dike 1 samples (n = 2) are characterized by a relative enrichment in LREEs and depletion in HREEs with La/Sm_n values ranging from 1.37 to 1.43 and Gd/Yb_n ranging from 1.31 to 1.41 (Fig. 4.39F). Dike 2 samples (n = 3) are also characterized by a relative enrichment LREEs, depletion HREEs but with higher La/Sm_n values ranging from 1.85 to 1.91and higher Gd/Yb_n ranging from 2.43 to 2.49 (Fig. 4.39F). Both groups of cross-cutting mafic dikes exhibit a moderate negative Nb-anomaly.

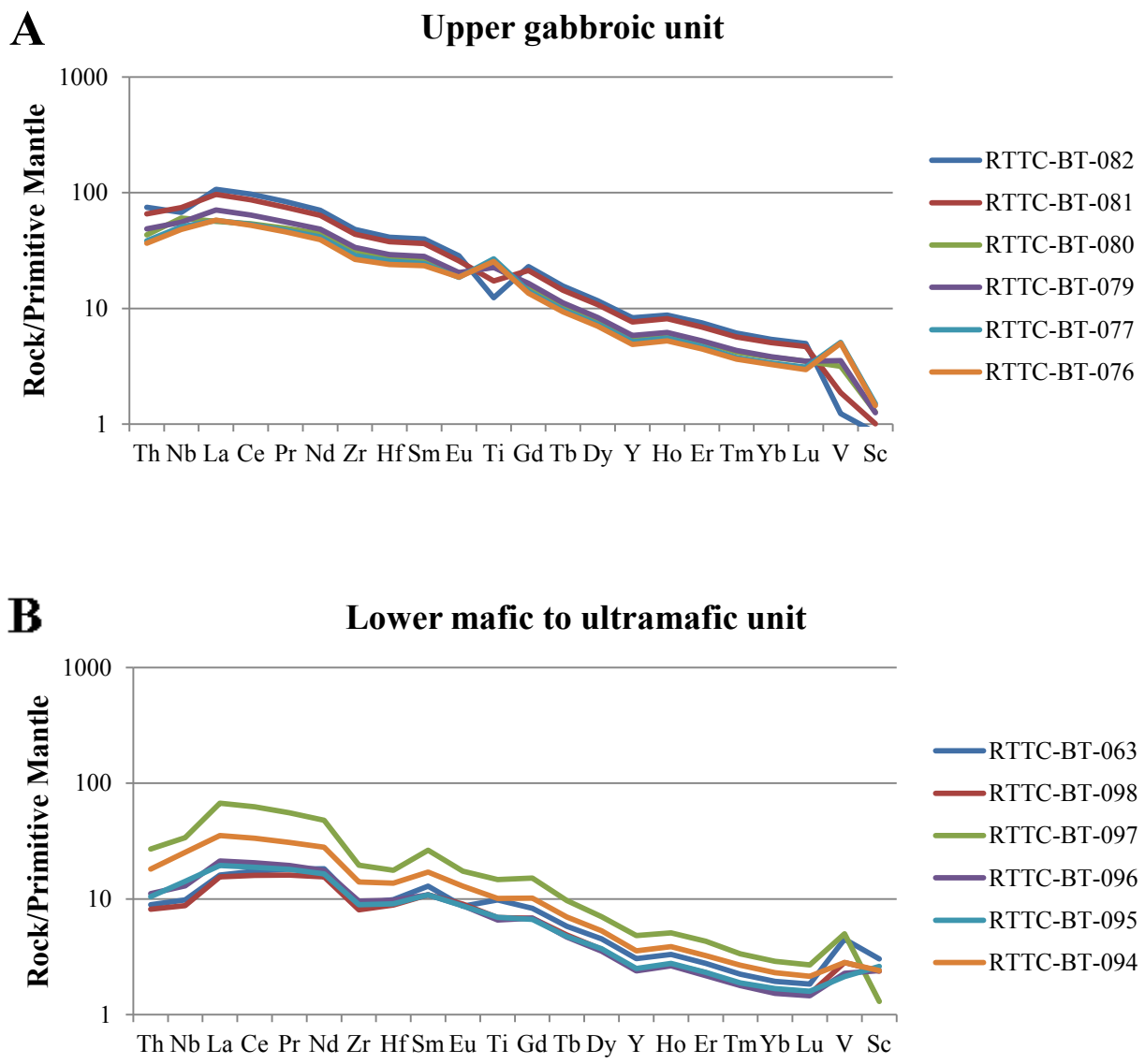

Figure 4.39: Primitive mantle normalized profiles for A) representative samples from the upper gabbroic unit and, B) representative samples from the lower mafic to ultramafic unit. Normalizing values from Sun and McDonough (1989).

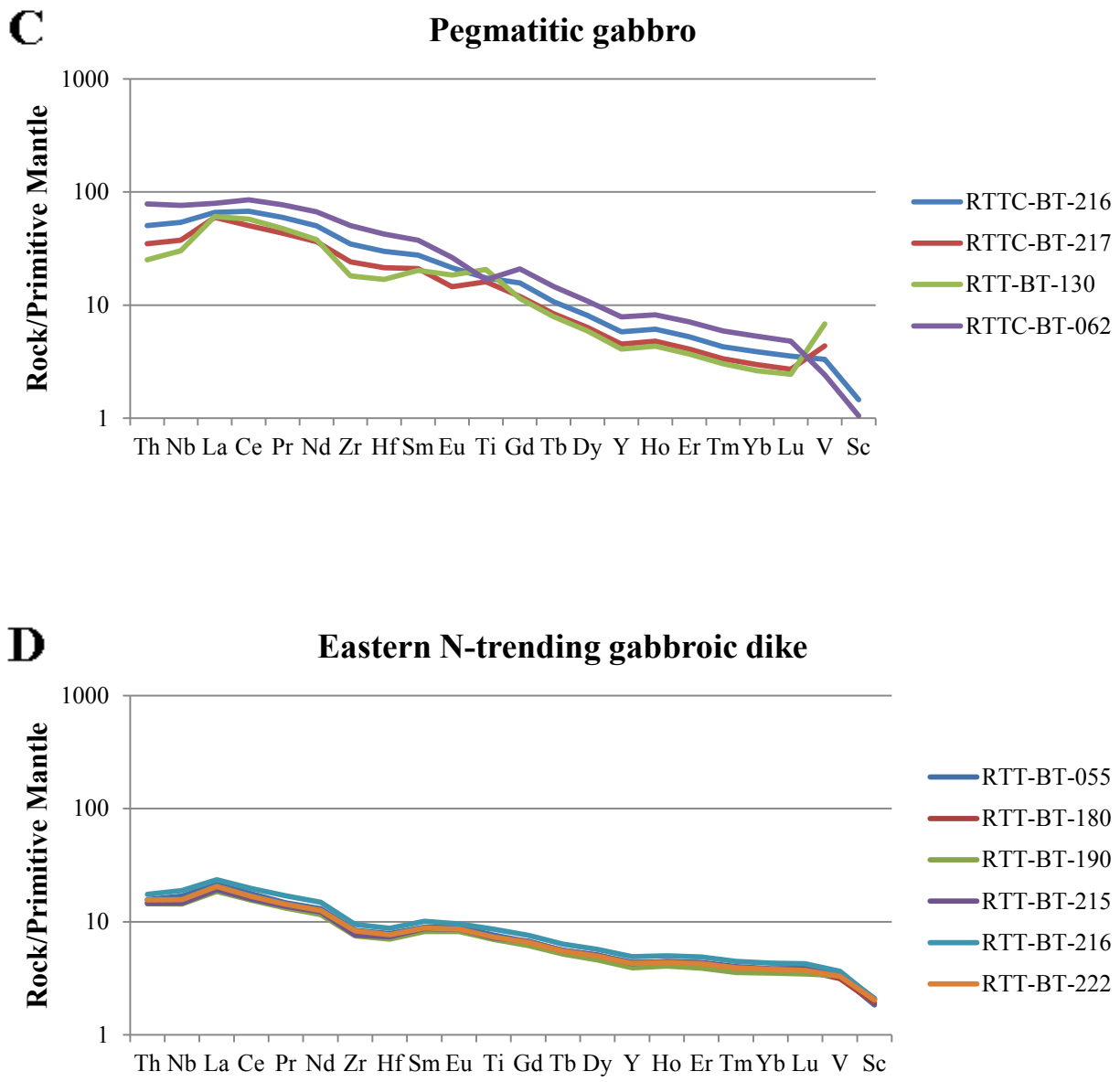

Figure 4.39 (cont.): Primitive mantle normalized profiles for C) all samples from the pegmatitic gabbro and, D) all samples from the eastern N-trending gabbroic dike. Normalizing values from Sun and McDonough (1989).

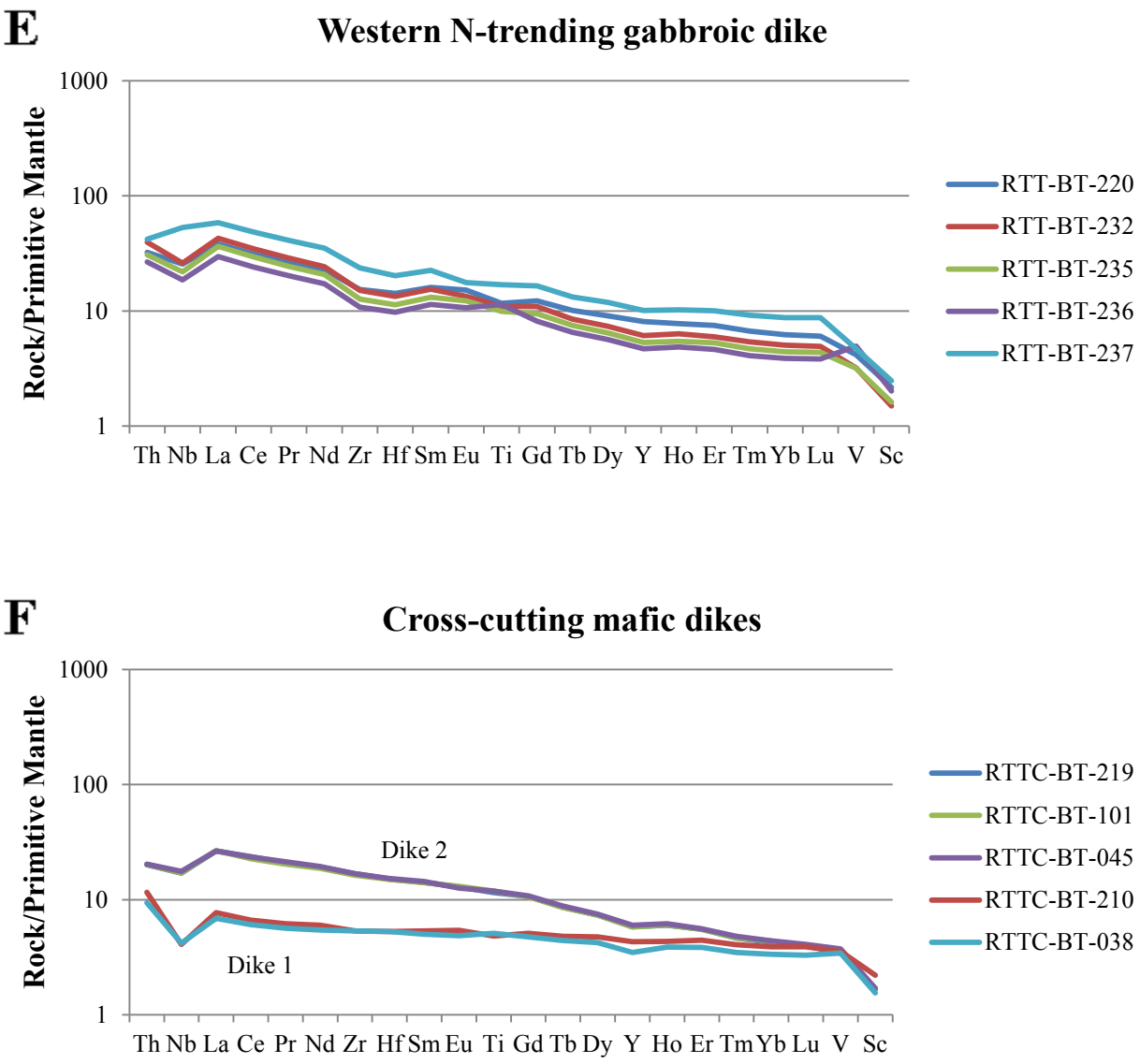

Figure 4.39 (cont.): Primitive mantle normalized profiles for E) all samples from the western N-trending gabbroic dike and, F) all samples from the cross-cutting mafic dikes. Indicated on the diagram plot are dike 1 and 2 sample groupings. Normalizing values from Sun and McDonough (1989).

.

4.8.4 Metal patterns and correlations of the Thunder intrusion

All samples submitted for whole rock geochemistry were analyzed for their base metal, platinum-group element (PGEs) and total sulphur (S^T) concentrations. The full data set is presented in Appendix E and representative base metal analyses from DDH 07TH004 are listed in Table 4.5. Overall, S^T, base metal and PGE concentrations are higher in samples from the lower mafic to ultramafic unit consistent with the observed mineralization. The Pt/Pd ratios for the upper gabbroic unit ranges from 0.12 to 2.15; Pt/Pd ratios for the lower mafic to ultramafic unit ranges from 0.73 and 26.63. The anonymously large Pt/Pd ratios for samples of the lower mafic to ultramafic unit could be a possible bonanza grade effect as the majority of ratios are less than 3 in both cases. Total sulphur concentrations for the upper gabbroic unit range from 0.01 (lower detection limit) to 0.25 wt. %; total sulphur concentrations for the lower mafic to ultramafic unit range from 0.01 (lower detection limit) to 0.82 wt. %. Copper, nickel and cobalt exhibit a weak positive correlation with increasing S^T from samples of the lower mafic to ultramafic unit ($S^T > 0.1$ wt. %) generally collected from the basal mineralization zone (Fig. 4.40). Base metals do not exhibit a positive correlation with increasing S^T for samples of the upper gabbroic unit except for Cu exhibiting a weak positive correlation with $S^T > 0.1$ wt. % (Fig. 4.340).

Table 4.5: Whole rock base metal, platinum-group element and total sulphur analyses for select samples of the upper gabbroic unit and lower mafic to ultramafic unit collected from diamond drill hole 07TH004. All values normalized to be 100% anhydrous.

Sample ID	Depth (m)	Lithological unit	S^T	Co	Cr	Cu	Ni	Zn	Au	Ir	Pd	Pt	Rh	Ru	Pt/Pd
			wt. %	ppm	ppm	ppm	ppm	ppm	ppb	ppb	ppb	ppb	ppb	ppb	
RTTC-BT-082	9.29	Upper gabbroic unit	0.05	47.60	46.62	104.08	113.39	58.78	3.65	0.61	21.08	45.30	0.83	0.15	2.15
RTTC-BT-081	10.00	Upper gabbroic unit	0.11	56.51	78.87	81.70	143.00	54.60	3.69	0.24	16.18	11.73	0.83	0.16	0.73
RTTC-BT-080	20.18	Upper gabbroic unit	0.25	64.41	62.83	86.85	135.98	101.34	3.29	0.16	25.84	10.24	0.80	0.14	0.40
RTTC-BT-079	57.63	Upper gabbroic unit	0.10	56.05	75.73	132.58	77.86	105.01	4.35	0.25	22.72	14.64	0.62	0.19	0.64
RTTC-BT-077	83.78	Upper gabbroic unit	0.03	66.81	33.19	126.31	44.46	132.75	4.23	0.05	30.87	5.30	0.42	0.00	0.17
RTTC-BT-076	101.18	Upper gabbroic unit	0.03	59.61	21.20	76.23	57.79	85.83	3.08	0.02	21.00	4.95	0.22	0.00	0.24
RTTC-BT-075	144.98	Upper gabbroic unit	0.07	53.20	17.13	78.59	33.52	60.45	2.21	0.02	19.14	7.39	0.14	0.00	0.39
RTTC-BT-074	182.00	Upper gabbroic unit	0.02	35.82	18.27	71.06	69.41	49.74	1.68	0.02	22.33	7.15	0.12	0.00	0.32
RTTC-BT-072	188.00	Upper gabbroic unit	0.10	72.15	82.23	143.00	16.58	120.34	5.08	0.13	32.79	9.17	0.20	0.00	0.28
RTTC-BT-071	190.20	Upper gabbroic unit	0.06	51.99	16.13	125.48	30.50	66.52	4.12	0.04	39.31	8.77	0.11	0.00	0.22
RTTC-BT-070	201.05	Upper gabbroic unit	0.01	60.67	12.06	327.59	17.23	179.87	43.21	0.01	49.84	19.80	0.15	0.00	0.40
RTTC-BT-069	234.74	Upper gabbroic unit	0.01	57.21	13.09	258.17	23.60	97.67	26.98	0.02	54.67	17.72	0.13	0.00	0.32
RTTC-BT-067	266.60	Upper gabbroic unit	0.02	36.21	11.14	391.83	29.65	46.57	11.95	0.01	8.30	3.98	0.04	0.00	0.48
RTTC-BT-065	287.00	Upper gabbroic unit	0.06	55.55	9.10	351.09	22.26	78.90	14.06	0.01	28.73	9.21	0.07	0.00	0.32
RTTC-BT-068	288.50	Upper gabbroic unit	0.03	26.17	9.11	529.79	21.65	54.68	11.24	0.01	2.29	0.27	0.02	0.00	0.12
RTTC-BT-100	291.64	Upper gabbroic unit	0.03	23.23	8.11	292.14	12.71	51.68	3.72	0.01	0.77	0.23	0.00	0.00	0.30
RTTC-BT-064	300.30	Upper gabbroic unit	0.02	51.16	56.98	94.73	159.20	54.94	4.67	0.53	24.01	36.22	0.82	0.16	1.51
RTTC-BT-099	304.74	Upper gabbroic unit	0.03	46.94	54.49	111.19	75.12	66.59	3.32	0.27	20.48	17.86	0.67	0.12	0.87
RTTC-BT-063	306.04	Lower mafc to ultramafic unit	0.01	105.97	996.21	51.42	240.18	97.81	2.25	21.07	22.08	587.85	12.81	3.58	26.62
RTTC-BT-098	317.95	Lower mafc to ultramafic unit	0.01	118.61	1260.52	1274.21	1034.03	121.69	12.37	7.12	127.78	93.60	9.03	3.94	0.73
RTTC-BT-097	323.00	Lower mafc to ultramafic unit	0.03	108.07	990.22	196.32	775.06	123.78	3.15	1.90	22.22	41.09	1.41	2.38	1.85
RTTC-BT-096	355.62	Lower mafc to ultramafic unit	0.01	103.68	1562.57	1285.22	771.46	109.44	22.19	1.64	164.16	179.36	1.62	1.64	1.09
RTTC-BT-095	375.94	Lower mafc to ultramafic unit	0.01	153.89	970.89	125.02	2538.57	100.72	5.47	3.26	45.79	111.11	3.54	2.89	2.43
RTTC-BT-094	404.00	Lower mafc to ultramafic unit	0.02	76.39	995.09	96.08	226.96	94.77	5.41	1.82	17.24	33.47	0.96	0.65	1.94
RTTC-BT-093	409.58	Lower mafc to ultramafic unit	0.03	71.86	1444.68	123.32	349.60	79.92	1.27	2.41	5.70	11.53	0.50	0.60	2.02
RTTC-BT-092	426.10	Lower mafc to ultramafic unit	0.82	92.85	1046.31	70.69	147.76	79.33	1.60	2.84	11.65	45.99	1.42	0.80	3.95
RTTC-BT-091	432.18	Lower mafc to ultramafic unit	0.11	125.50	240.94	219.47	234.08	182.47	15.42	3.37	59.78	95.07	2.79	1.49	1.59
RTTC-BT-089	437.00	Lower mafc to ultramafic unit	0.63	87.38	614.20	52.49	115.31	85.31	1.65	1.83	8.70	54.60	1.30	0.54	6.27

Abbreviations: T = total

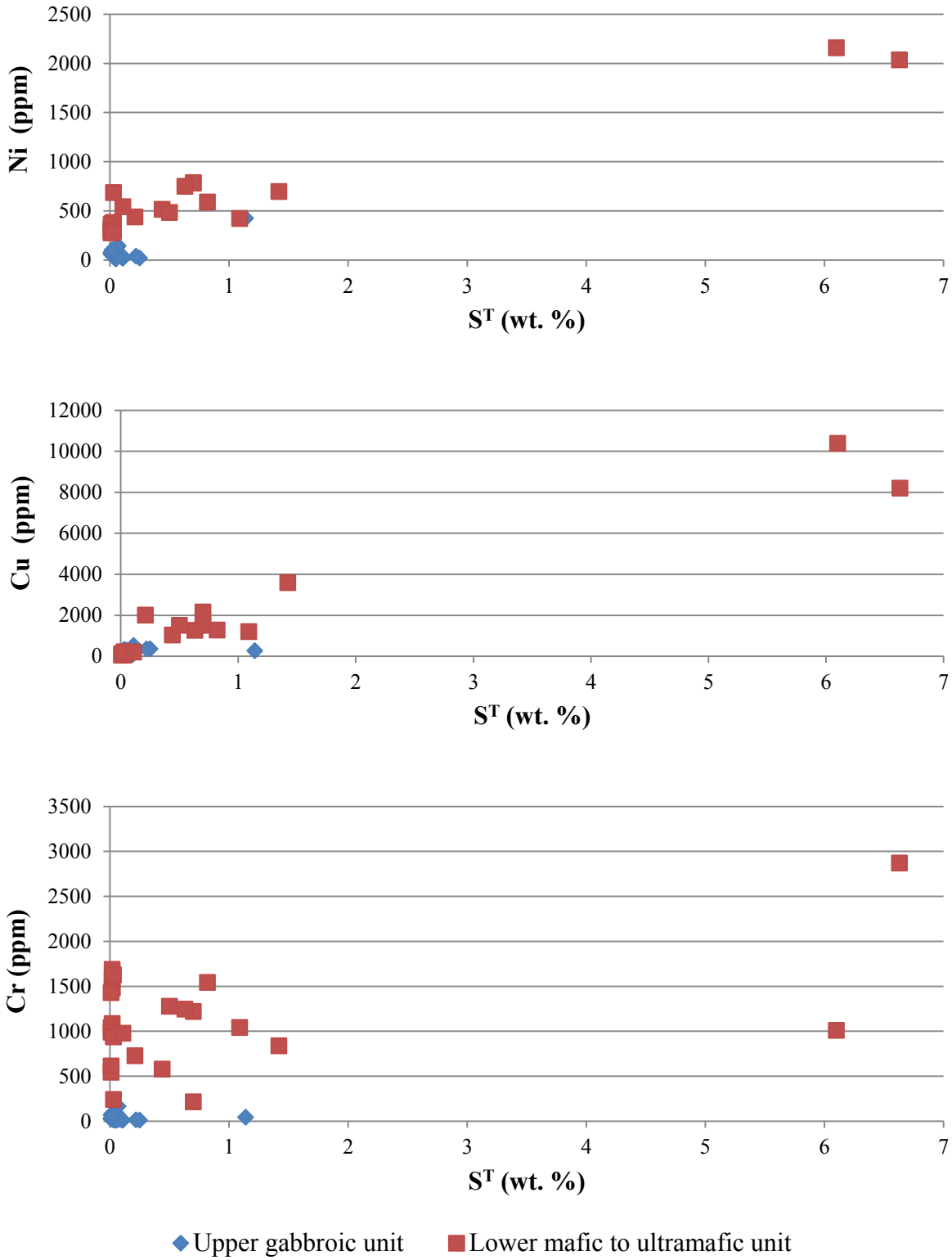

Figure 4.40: Plot of whole rock base metals (Ni, Cu, Cr, Co, Zn) versus total sulphur for samples of the upper gabbroic unit and the lower mafic to ultramafic unit.

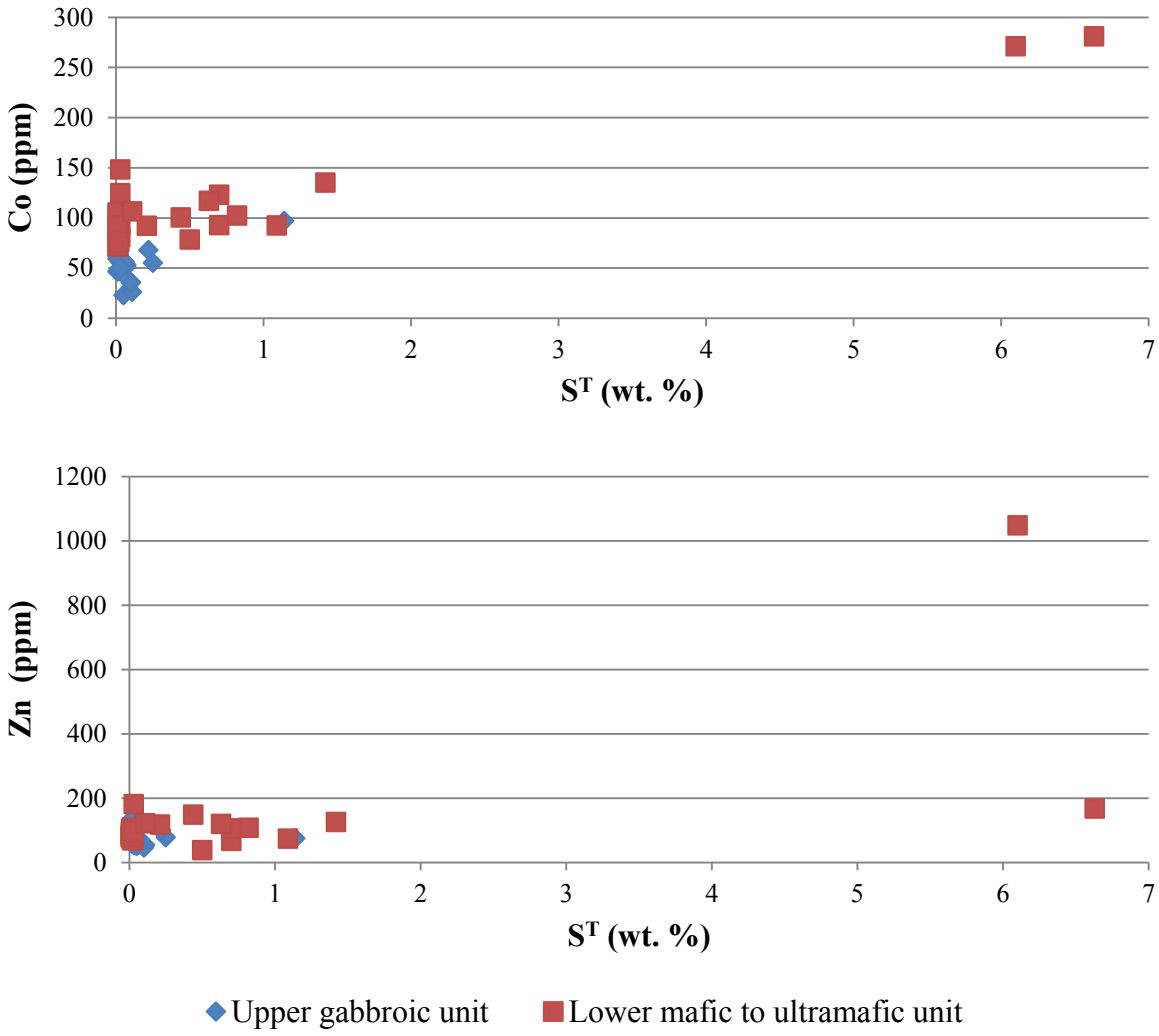

Figure 4.40 (cont.): Plot of whole rock base metals (Ni, Cu, Cr, Co, Zn) versus total sulphur for samples of the upper gabbroic unit and the lower mafic to ultramafic unit.

The primitive mantle normalized Ni-Cu-PGE profiles for samples of the upper gabbroic unit and lower mafic to ultramafic unit are illustrated in Figure 4.41. Overall, samples of the upper gabbroic unit and lower mafic to ultrmafic unit are characterized by a fractionated profile with a depletion in iridium-group platinum group elements (IPGEs) relative to platinum-group platinum group elements (PPGEs). Samples of the upper gabbroic unit can be further characterized by markedly lower Ru and Ir concentrations and low Pt/Pd ratios (no Pt trough) than the samples of the upper gabbroic unit (Fig. 4.41B); samples of the lower mafic to ultramafic unit can be further characterized by relatively higher Pt/Pd ratios with some exhibiting a Pt trough in the Ni-PGE-Cu pattern (Fig. 4.41A).

4.9 Sulphur isotopes and Se/S ratios

Twenty samples from DDH 07TH004 and on surface were analyzed for S isotopic $\delta^{34}S$ compositions to investigate the role of crustal sulphur in the mineralization of the Thunder intrusion with data presented in Table 4.6. Samples were chosen to be representative of each intrusive unit and the metavolcanic wall rock containing visible sulphide mineralization. Figure 4.42 plots ^{34}S values for the upper gabbroic unit (n = 10) range from -2.0 to 4.9 ‰; from -1.3 to 2.9 ‰ for the lower mafic to ultramafic unit (n = 6); and from -3.1 to 2.3 ‰ for the metavolcanic rocks (n = 10). In addition, three samples were analysed for the $\delta^{33}S$ isotopic composition to further investigate the involvement of crustal sulphur during mineralization. Values are presented in delta cap notation (where $\Delta^{33}S = ln(\delta^{33}S + 1) - 0.515*ln(\delta^{34}S + 1)$; Ono et al., 2012; Table 4.6): a surface and drill core sample of the lower mafic to ultramafic unit at 0.122 ‰ and 0.066 ‰, respectively, and a drill core sample of the metavolcanic wall rock at 0.149 ‰.

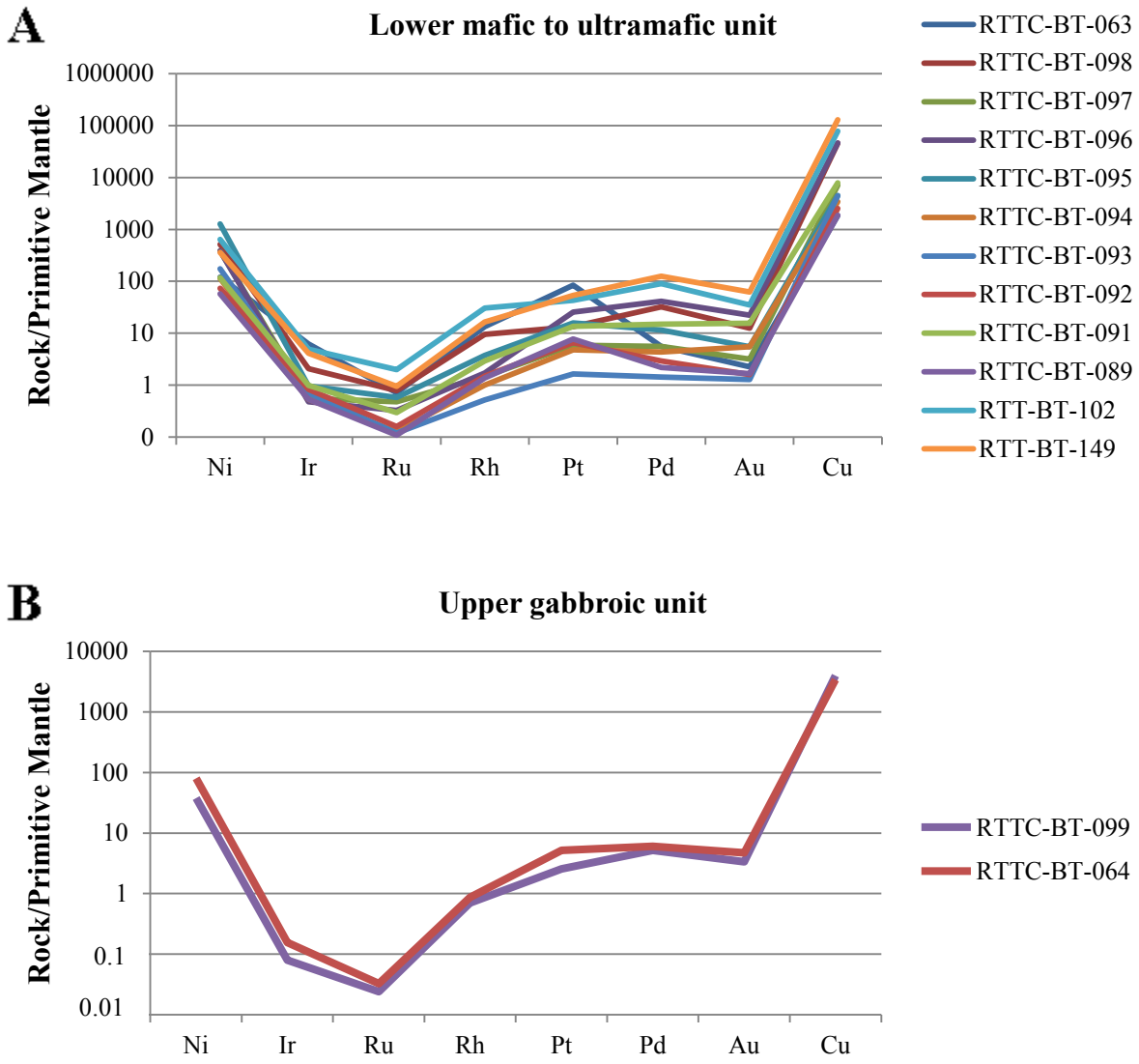

Figure 4.41: Primitive mantle normalized whole rock Ni-PGE-Cu profiles of samples from the A) lower mafic to ultramafic unit and, B) the upper gabbroic unit from diamond drill hole 07TH004. Primitive mantle values are from McDonough and Sun (1995).

Table 4.6: Sulphur isotope values of sulphide minerals from samples of the upper gabbroic unit, lower mafic to ultramafic unit and metavolcanic rocks. Sample locations are given in NAD83 UTM Zone 16.

Sample	Easting	Northing	Depth (m)	Lihtostratigraphic unit	Sulphide type	Mineral(s)	δ34S (V-CDT in ‰)	$\Delta^{33}S$ (in ‰)
Drill hole 07TH004								
RTTC-BT-078	330319	5377910	86.13	Upper gabbroic unit	mt+py+cp vein	pyrite, chalcopyrite	3.8	
RTTC-BT-078	330319	5377910	86.13	Upper gabbroic unit	mt+py+cp vein	pyrite, chalcopyrite	1.3	
RTTC-BT-073	330319	5377910	180.52	Upper gabbroic unit	mt+py+cp vein	pyrite, chalcopyrite	-1.5	
RTTC-BT-072	330319	5377910	188.00	Upper gabbroic unit	disseminated	chalcopyrite	-1.0	
RTTC-BT-072	330319	5377910	188.00	Upper gabbroic unit	disseminated	chalcopyrite	-1.2	
RTTC-BT-069*	330319	5377910	234.74	Upper gabbroic unit	disseminated	chalcopyrite	4.9	
RTTC-BT-065	330319	5377910	287.00	Upper gabbroic unit	mt+py+cp vein	pyrite, chalcopyrite	-1.8	
RTTC-BT-064	330319	5377910	300.30	Upper gabbroic unit	mt+py+cp vein	pyrite, chalcopyrite	-1.1	
RTTC-BT-064	330319	5377910	300.30	Upper gabbroic unit	mt+py+cp vein	pyrite, chalcopyrite	-1.6	
RTTC-BT-063	330319	5377910	306.04	Lower mafic to ultramafic unit	mt+py+cp vein	pyrite, chalcopyrite	-1.3	
RTTC-BT-092	330319	5377910	426.10	Lower mafic to ultramafic unit	disseminated	pyrrhotite, chalcopyrite	0.1	
RTTC-BT-091	330319	5377910	432.18	Lower mafic to ultramafic unit	disseminated	pyrrhotite, chalcopyrite	1.8	0.066
RTTC-BT-089	330319	5377910	437.00	Lower mafic to ultramafic unit	disseminated	pyrhotite, chalcopyrite	1.4	
RTTC-BT-090	330319	5377910	437.38	Metavolcanic rocks	disseminated	pyrrhotite, chalcopyrite	0.2	0.149
RTTC-BT-088	330319	5377910	449.78	Metavolcanic rocks	disseminated	pyrite	-3.1	
RTTC-BT-088	330319	5377910	449.78	Metavolcanic rocks	disseminated	pyrite	-2.7	
RTTC-BT-088	330319	5377910	449.78	Metavolcanic rocks	disseminated	pyrite	-2.4	
RTTC-BT-086	330319	5377910	479.00	Metavolcanic rocks	disseminated	pyrite	-2.0	
RTTC-BT-085	330319	5377910	493.02	Metavolcanic rocks	disseminated	pyrite	-2.3	
RTTC-BT-084	330319	5377910	516.36	Metavolcanic rocks	disseminated	pyrite	-0.6	
Surface								
RTT-BT-142	330569	5377749	-	Upper gabbroic unit	disseminated	chalcopyrite	-2.0	
RTT-BT-102	330445	5378495	-	Lower mafic to ultramafic unit	disseminated	pyrrhotite, chalcopyrite	-1.1	
RTT-BT-149	330411	5378463	-	Lower mafic to ultramafic unit	disseminated	pyrrhotite, chalcopyrite	2.9	0.122
RTT-BT-016	330834	5378246	-	Metavolcanic rocks	disseminated	pyrite	2.3	
RTT-BT-016	330834	5378246	-	Metavolcanic rocks	disseminated	pyrite	1.5	
RTT-BT-141*	330570	5377742	-	Metavolcanic rocks	disseminated	pyrite	-1.0	

Abbreviations: V-CDT = Vienna-Canyon Diablo Troilite, * = undersized sulphide mineral, $\Delta^{33}S = ln\ (\delta^{33}S + 1) - ln\ (\delta^{34}S + 1)$.

Table 4.7: Whole rock As, Bi, Sb, Se, Te, total S and Se/S ratios for samples of the upper gabbroic unit, lower mafic to ultramafic unit and metavolcanic wall rock. Sample locations are given in NAD83 UTM Zone 16 and normalized to be 100 % anhydrous.

Sample	Easting	Northing	Depth (m)	Lithostratigraphic unit	Mineralization	S^T (wt.%)	As (ppm)	Bi (ppm)	Sb (ppm)	Se (ppm)	Te (ppm)	$Se/S^T \times 10^6$
Drill Hole 07TH004												
RTTC-BT-072	330319	5377910	188.00	Upper gabbroic unit	disseminated	0.10	0.7	0.03	0.08	0.4	0.09	400
RTTC-BT-069	330319	5377910	234.74	Upper gabbroic unit	disseminated	0.01	0.8	0.04	0.11	0.2	0.05	2000
RTTC-BT-065	330319	5377910	287.00	Upper gabbroic unit	mt+py+cp vein	0.06	1.2	0.03	0.08	0.4	0.06	667
RTTC-BT-064	330319	5377910	300.30	Upper gabbroic unit	mt+py+cp vein	0.02	1.1	0.03	0.08	0.4	0.12	2000
RTTC-BT-063	330319	5377910	306.04	Lower mafic to ultramafic unit	mt+py+cp vein	0.01	4.3	0.04	0.12	0.3	0.09	3000
RTTC-BT-092	330319	5377910	426.10	Lower mafic to ultramafic unit	disseminated	0.82	1.1	0.24	0.12	1.6	0.34	195
RTTC-BT-091	330319	5377910	432.18	Lower mafic to ultramafic unit	disseminated	0.11	1.1	0.04	0.03	0.2	0.11	182
RTTC-BT-089	330319	5377910	437.00	Lower mafic to ultramafic unit	disseminated	0.63	0.7	0.09	0.03	1.3	0.20	206
RTTC-BT-088	330319	5377910	449.78	Metavolcanic rocks	disseminated	0.03	3.1	0.07	0.36	0.3	0.09	1000
RTTC-BT-086	330319	5377910	479.00	Metavolcanic rocks	disseminated	0.55	4.8	0.12	0.25	0.7	0.16	127
RTTC-BT-085	330319	5377910	493.02	Metavolcanic rocks	disseminated	1.18	2.5	0.17	0.20	0.5	0.34	42
RTTC-BT-084	330319	5377910	516.36	Metavolcanic rocks	disseminated	0.22	10.2	0.05	0.24	0.3	0.15	136
Surface Sample												
RTT-BT-142	330569	5377749	-	Upper gabbroic unit	disseminated	0.07	6.4	0.08	0.50	0.4	0.11	571
RTT-BT-102	330445	5378495	-	Lower mafic to ultramafic unit	disseminated	0.70	1.5	0.09	0.24	2.1	0.46	300
RTT-BT-149	330411	5378463	-	Lower mafic to ultramafic unit	disseminated	1.42	0.6	0.56	0.05	2.9	1.00	204
RTT-BT-016	330834	5378246	-	Metavolcanic rocks	disseminated	0.13	11.3	0.04	0.10	0.6	0.13	462
RTT-BT-141	330570	5377742	-	Metavolcanic rocks	disseminated	0.08	5.3	0.28	0.54	0.4	0.13	500

Abbreviations: T = total sulphur

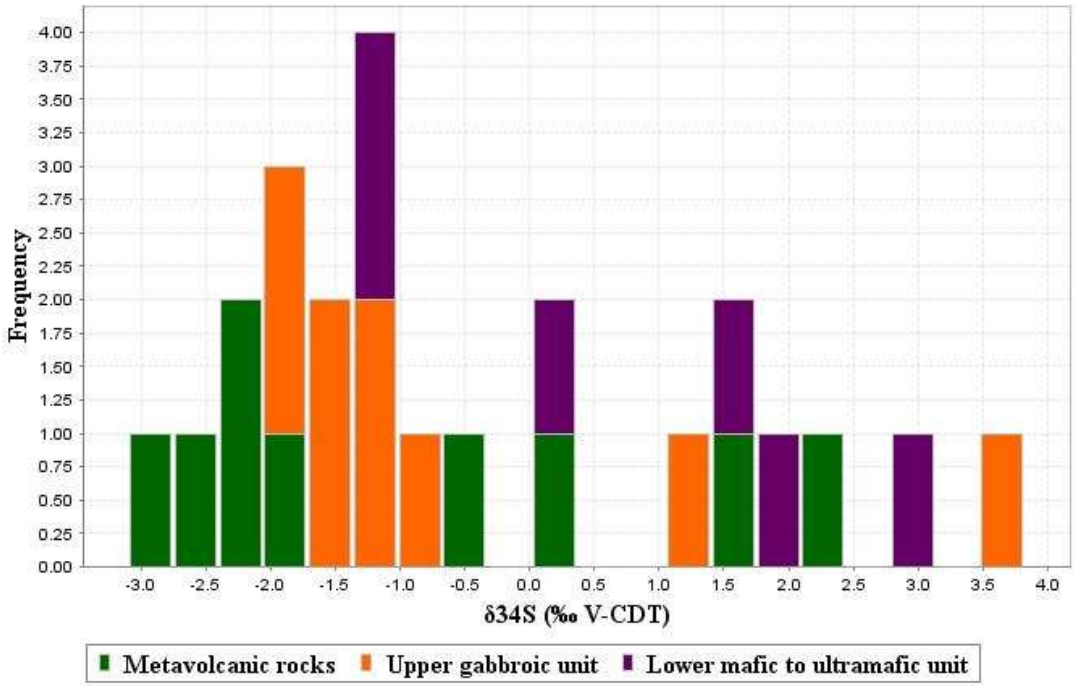

Figure 4.42: Histogram illustrating the distribution of $\delta^{34}S$ values for samples of the upper gabbroic unit, lower mafic to ultramafic unit and metavolcanic rocks. V-CDT = Vienna-Canyon Diablo Troilite.

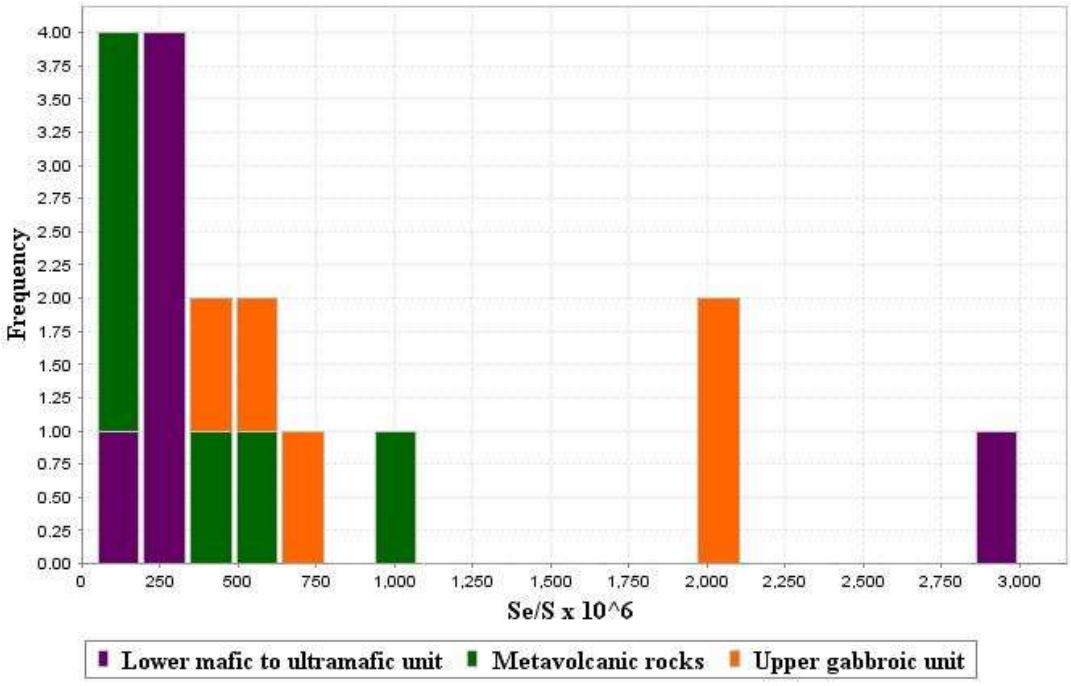

Figure 4.43: Histogram illustrating the distribution of $Se/S^T \times 10^6$ ratios for samples of the upper gabbroic unit, lower mafic to ultramafic unit and metavolcanic wall rock.

The samples used for the S isotope analysis were also analyzed for Se concentrations to further investigate the role of crustal sulphur in the mineralization of the Thunder intrusion and used to calculate $Se/S^T \times 10^6$ ratios (Table 4.7; Fig. 4.43). Only 17 of the 20 samples were analyzed as three sample pulps were not available at time of the analysis. Ratios of $Se/S^T \times 10^6$ range from 400 to 2000 for the upper gabbroic unit (n = 5); from 180 to 3000 for the lower mafic to ultramafic unit (n = 6); and from 40 to 1000 for the metavolcanic rocks (n = 6). Anomalously high values in the dataset include 2000 $Se/S^T \times 10^6$ for the upper gabbroic unit containing mt+py+cp alteration veins (samples RTTC-BT-069 and 064), 3000 $Se/S^T \times 10^6$ for the lower mafic to ultramafic unit containing mt+py+cp alteration veins (sample RTTC-BT-063), and 1000 $Se/S^T \times 10^6$ for the metavolcanic rocks containing S^T concentration near lower detection limit (sample RTTC-BT-088) (Table 4.7; Fig. 4.43).

4.10 Radiogenic isotopes

Rb-Sr and Sm-Nd isotope analyses of ten samples from the upper gabbroic unit, lower mafic to ultramafic unit and the metavolcanic wall rocks from DDH 07TH004 is summarized in Table 4.8. The analysis focused on investigating possible indications of contamination. The upper gabbroic unit (n = 4) is characterized by $^{87}Sr/^{86}Sr_i$ ranging from 0.70313 to 0.70611, $^{143}Nd/^{144}Nd$ ranging from 0.511992 to 0.512127 and εNd_T ranging from -0.7 to 1.0. The lower mafic to ultramafic unit (n = 4) is characterized by $^{87}Sr/^{86}Sr_i$ ranging from 0.7288 to 0.70336, $^{143}Nd/^{144}Nd$ ranging from 0.512065 to 0.512298 and εNd_T ranging from 0.5 to 1.0. The metavolcanic wall rocks (n = 2) are characterized by $^{87}Sr/^{86}Sr_i$ ranging from 0.70712 to 0.70873, $^{143}Nd/^{144}Nd$ ranging from 0.511047 to 0.51186 and εNd_T ranging from -16.8 to -15.8.

Table 4.8: Summary of radiogenic isotope data for the suite of 10 samples collected from diamond drill hole 07TH004 including the upper gabbroic unit, lower mafic to ultramafic unit and the metavolcanic wall rock.

Sample	Depth (m)	Lithostratigraphic unit	$^{87}Rb/^{86}Sr$	$^{87}Sr/^{86}Sr$	±2SE[a]	$(^{87}Sr/^{86}Sr)_i$	$^{147}Sm/^{144}Nd$	$^{143}Nd/^{144}Nd$	±2SE[a]	εNd_T
RTTC-BT-082	9.29	Upper gabbroic unit	0.1810	0.70895	0.00002	0.70611	0.1130	0.512073	0.000004	0.8
RTTC-BT-077	83.78	Upper gabbroic unit	0.1319	0.70635	0.00001	0.70427	0.1178	0.512118	0.000008	1.0
RTTC-BT-072	188.00	Upper gabbroic unit	0.0682	0.70566	0.00001	0.70459	0.1124	0.511992	0.000003	-0.7
RTTC-BT-069	234.74	Upper gabbroic unit	0.0747	0.70431	0.00002	0.70313	0.1208	0.512127	0.000006	0.7
RTTC-BT-063	306.04	Lower mafic to ultramafic unit	0.1401	0.70515	0.00003	0.70294	0.1429	0.512298	0.000008	1.0
RTTC-BT-098	317.95	Lower mafic to ultramafic unit	0.0831	0.70467	0.00001	0.70336	0.1395	0.512266	0.000007	0.8
RTTC-BT-097	323.00	Lower mafic to ultramafic unit	0.1195	0.70476	0.00001	0.70288	0.1104	0.512065	0.000006	1.0
RTTC-BT-094*	404.00	Lower mafic to ultramafic unit	0.0977	0.70486	0.00002	0.70332	0.1229	0.512129	0.000020	0.5
RTTC-BT-088	449.78	Metavolcanic rock	0.5375	0.71559	0.00000	0.70712	0.1078	0.511186	0.000008	-15.8
RTTC-BT-086	479.00	Metavolcanic rock	0.6330	0.71869	0.00001	0.70873	0.0956	0.511047	0.000006	-16.8

Abbreviations: * = poor run, [a] = Uncertainties are presented as ± 2 standard errors (2SE), T = 1100 Ma.

CHAPTER 5

DISCUSSION

5.1 Introduction

The Thunder intrusion is a unique mafic to ultramafic intrusion to the other early-rift mafic to ultramafic intrusions such as Eagle (Ding et al., 2010), Tamarack (Goldner, 2011) and Seagull (Heggie, 2005) as it is the only known occurrence hosted in the metavolcanic and metasedimentary rocks of the Archean Shebandowan greenstone belt hosting economic grades of Ni-Cu-PGE. The distinct greenstone belt host rock, and general lack of knowledge of the Thunder intrusion and how it fits within the context of the MCR brings about the objective of this study: 1) characterize the petrology of the Thunder intrusion, 2) define the mineralogical and geochemical signature of the Thunder intrusion and PGE mineralization, 3) characterize the alteration footprint of the intrusion in the surrounding country rocks, and 4) establish practical mineralogical and geochemical exploration criteria for hidden early-rift mafic to ultramafic intrusions hosting magmatic Ni-Cu-PGE sulphide mineralization by relating the characteristics of the intrusion to other fertile and barren intrusive units within the MCR.

This chapter establishes the relative timing of emplacement of the intrusive units comprising the Thunder intrusion, defines the petrological attributes of the Thunder intrusion, and characterizes the mineralogical signature and its alteration footprint. The Thunder intrusion will be discussed within the regional context of the Midcontinent Rift and compared with other known early-rift lower mafic to ultramafic intrusions. Lastly, the relative timing of emplacement and possible linkages with the Thunder intrusion and the other intrusive units within the study area will be discussed. The lithostratigraphy of the Thunder intrusion will be simplified into a lower mafic to ultramafic unit overlain by an upper gabbroic unit. A full description of the lower

mafic to ultramafic unit and upper gabbroic can be found in the preceding chapter (section 4.2 and 4.4 and a description of DDH 07TH004 can be found in section 4.3).

5.2 Petrology of the Thunder intrusion

5.2.1 Correlation of the intrusive units comprising the Thunder intrusion

Czamanske et al. (1994, 1995) used the presence of abrupt jumps in major and trace element contents to identify distinct magmatic pulses that formed the Noril'sk-Talnakh deposits of Siberia, Russia. Following a similar rationale, the internal lithostratigraphy of the Thunder intrusion was examined to see whether or not multiple pulses of magma with distinct compositions were emplaced. The boundary between the lower mafic to ultramafic unit and upper gabbroic unit at ~ 300 m in DDH 07TH004 marks an abrupt change in texture from a cumulate to subophitic texture (Figs. 4.21) and major element geochemistry including a sharp drop in MgO and CaO, and a sharp increase in Al_2O_3 moving up-section from the lower unit into the upper unit (Fig. 4.36). However, the trace element geochemistry suggests the two intrusive units comprising the Thunder intrusion were sourced from the same parental magma on the basis of sub-parallel primitive mantle normalised trace and rare earth element profiles across the lithostratigraphy (Figs. 5.1, 5.2), a gradual increase in HFSE concentrations up-hole (e.g., Ti, V, Zr, Th; Fig. 5.2), and similar La/Sm_n and Gd/Yb_n ratios that undergo minimal fluctuations across stratigrphy (Fig. 5.2). The pegmatitic gabbro is interpreted as a late pegmatitic phase of the Thunder intrusion as evidenced by overlapping REE ratios (Fig. 4.38), similar rare and trace element profiles to the upper gabbroic unit (Figs. 4.39A, C), and cross-cutting relationships with the lower mafic to ultramafic unit (e.g., Fig. 4.4A).

5.2.2 Relative timing of emplacement

The coarse-grained nature of the pegmatitic gabbro and geochemical similarity with the lower mafic to ultramafic and upper gabbroic unit (Fig. 4.38) made it suitable material for U-Pb age dating to determine the crystallization age. It yielded a concordant $^{207}Pb/^{206}Pb$ zircon age of 1108.0 ± 1.0 Ma for the Thunder intrusion (Geological Survey of Canada, Rayner pers. comm.., 2014). Considering the recently proposed tectono-magmatic model from Miller and Nicholson (2013; Fig. 2.6) the Thunder intrusion fits between the initial (1115 – 1110 Ma) to early (1110 – 1105 Ma) tectono-magmatic stages of the MCR evolution and falls within range of the other fertile early-rift mafic to ultramafic intrusions such as the Eagle at 1107.20 ± 5.7 Ma (Ding et al. 2010), Tamarack at 1105.6 ± 1.2 Ma (Goldner, 2011), and Seagull at 1112.80 ± 1.4 Ma (Heaman et al., 2007).

5.2.3 An Archean greenstone belt host rock

The characterization of the alteration footprint in the wall rock surrounding the Thunder intrusion was an integral component of this study in effort to indentify a potential vector(s) for targeting buried mineralization. Field mapping and core logging showed that the dominant lithologies comprising the wall rock are volcanic breccias and tuffs that have undergone greenschist facies metamorphism. The wall rocks were also observed to have undergone pre-Thunder ductile deformation evidenced by clast elongation parallel to foliation (e.g., Figs. 4.6E, F), micro-folding (e.g., Fig. 4.6E) and deformed pillow selvages (e.g., Fig. 4.6C). Comparing the macro and microscopic scale observations to the regional scale fabric, first vertical derivative magnetic field images suggest that the Thunder intrusion is situated within an east-trending shear zone of the Archean Shebandowan greenstone belt that pre-dates the emplacement of the Mesoproterozoic emplacement of the Thunder intrusion (Fig. 2.7).

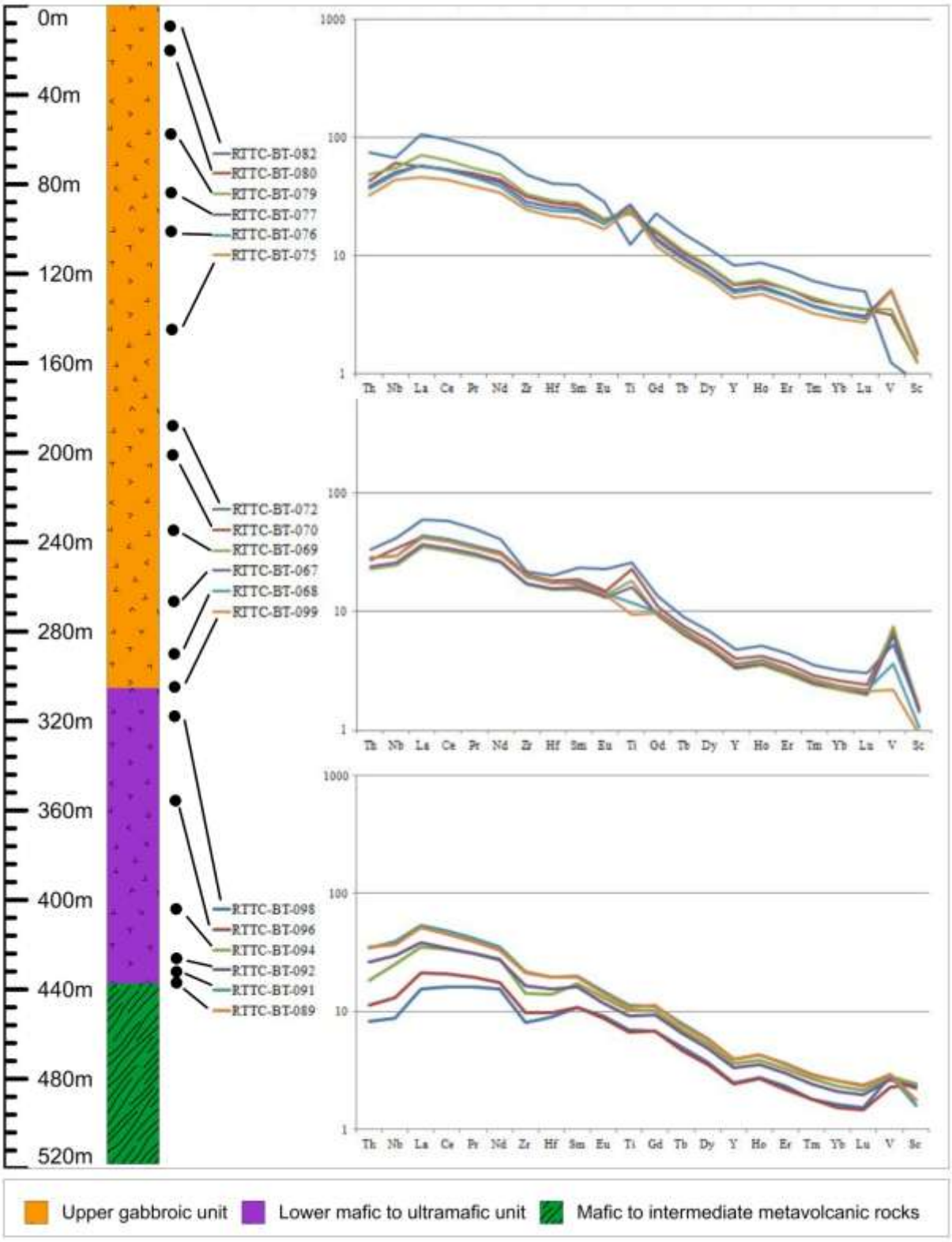

Figure 5.1: Primitive mantle normalized profiles plotted against the simplified lithostratigraphy of diamond drill hole 07TH004. Normalizing values of Sun and McDonough (1989).

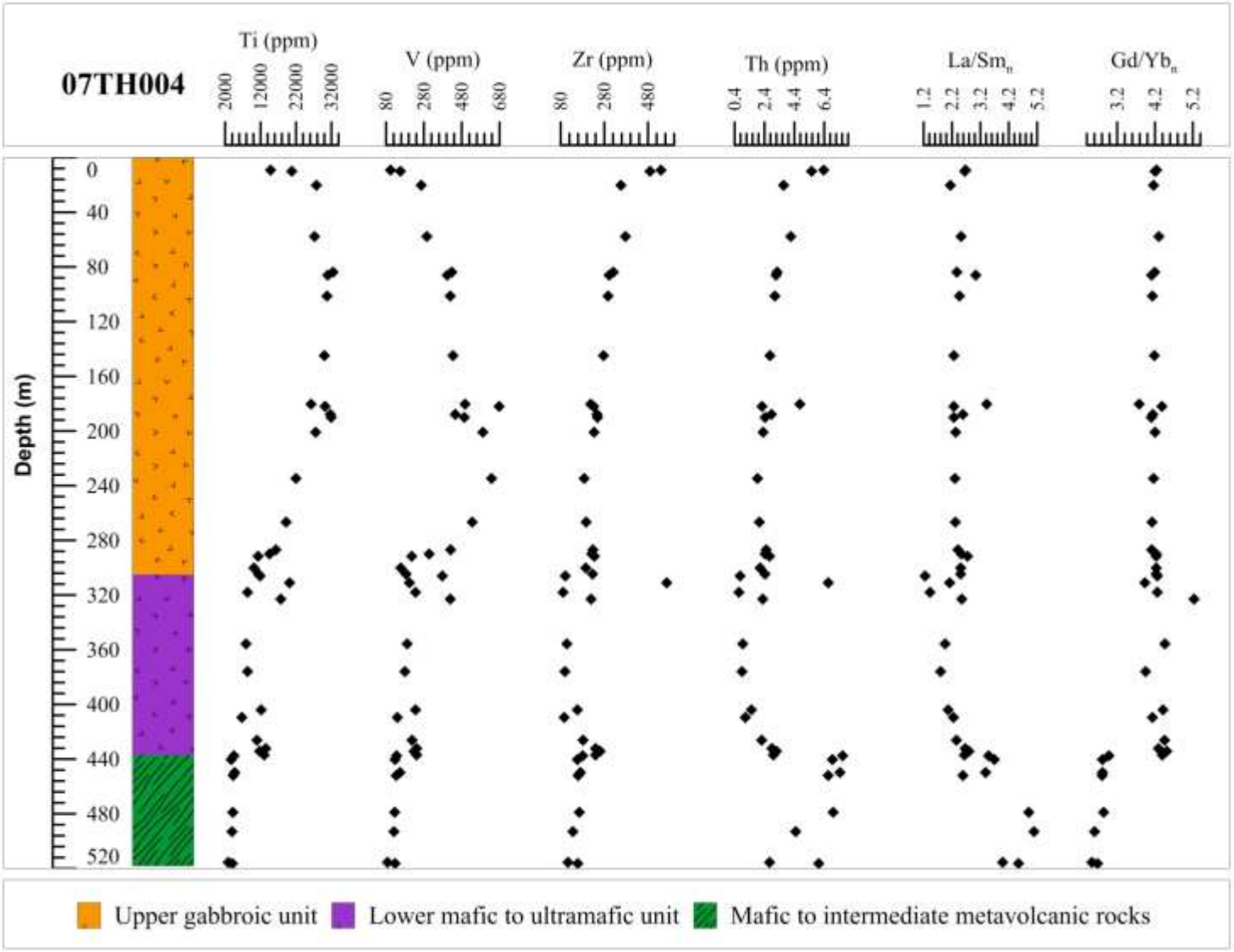

Figure 5.2: Select high field strength elements (Ti, V, Zr, Th) and chondrite-normalized rare earth element ratios (La/Sm_n, Gd/Yb_n) plotted against the simplified lithostratigraphy of diamond drill hole 07TH004. Normalizing values of Sun and McDonough (1989).

The contact metamorphic aureole produced by the emplacement of the Thunder intrusion is neglible and limited to 5 m that was characterized by static annealing textures that overprint the metamorphic fabric (Fig. 4.24). Possible explanations for the lack of extensive contact metamorphic effects include the small size of the intrusion (e.g., 800 m x 1000 m x 500 m; Figs. 4.1, 4.17), the poor permeability of the wall rock (i.e., the rocks are sealed shut to permeating magmatic fluids due to ductile deformation), the lack of highly contrasting compositions (i.e., ultramafic to mafic intrusive rock juxtaposed to mafic to intermediate volcanic rock) and pre-existing metamorphosed wall rock (i.e., low grade metamorphic overprint) resulting in a cold "unreactive" host rock. In addition, no hanging wall rocks are preserved at the Thunder intrusion (Fig. 4.17) unlike other early-rift mafic to ultramafic intrusions that are typically buried thereby limiting the investigation of the alteration footprint and the development of vectoring techniques for targeting buried mineralization (e.g., Sunday Lake; Transition Metals, 2014).

Bidwell and Marino (2007) reported the iron formation unit intercepted by DDH 05TH001 as a garnet-magnetite skarn which lead to the hypothesis of a possible contact metamorphic aureole linkage with the Thunder intrusion. According to Meinert (2005), the majority of skarns are associated with relatively shallow magmatic systems emplaced within or near carbonate rocks, but can also form in other rock types including shale, sandstone, granite, iron formation, basalt and komatiite. Zonation is a key characteristic feature in skarns where there is the general pattern of proximal garnet and distal pyroxene and including zonation in the mineralogy such as systematic color or compositional variations (Meinert, 2005). However, although the iron formation unit contains some calc-silicate mineralogy and zonation (i.e., andradite-grossular garnets; sample RTTC-BT-005 and 006 (Appendix A), clear contact relationships between the iron formation unit and the Thunder intrusion were not found in the

seven drill holes. Projecting the iron formation unit to surface puts it ~ 400 m south east of the nearest outcrop of the Thunder intrusion which greatly exceeds the 5 m contact metamorphic aureole established here. Therefore, until further drilling has proven otherwise, the relationship between the iron formation unit and the Thunder intrusion and the possible genetic link to skarn formation during emplacement remains uncertain.

5.2.4 Cumulate stratigraphy and mineral paragenesis

The lower mafic to ultramafic unit is a suite of orthocumulate mafic to ultramafic rocks characterized by cumulus olivine and clinopyroxene predominating over interstitial minerals (i.e., plagioclase, biotite, amphibole, and Fe-Ti oxide) that crystallized later from the magma and were entrapped between the cumulus minerals. In contrast, the upper gabbroic unit consists of gabbroic rocks characterized by subophitic plagioclase and clinopyroxene, abundant disseminationed Fe-Ti oxide and trace to no olivine pseudomorphs with the addition of apatite in the uppermost sections (~ 60 m in DDH 07TH004). Using the classic cumulate nomenclature, first proposed by Wager et al. (1960) and redefined by Irvine (1982), the textural and mineralogical distinction between the two intrusive units (e.g., Fig. 4.21) combined with the whole rock geochemistry (e.g., Fig. 4.36) and magnetic susceptibility measurements (DDH 07TH004), and acknowledging that multiple saturated cumulus phases will occur at approximately cotectic proportions as predicted from experimental data (e.g., McCallum et al., 1980), defines a four stage cumulus mineral paragenesis for the Thunder intrusion (Fig. 5.3).

The first stage of cumulus mineral paragenesis corresponds to the development of the lower mafic to ultramafic unit, characterized by the accumulation of cumulus clinopyroxene + olivine (Fig. 5.6). It is interpreted to the most primitive stage of the Thunder intrusion. Clinopyroxene is the dominant cumulus phase whereas olivine occurs in minor modal

proportions (5 – 10 %) except in some drill core samples collected along the basal section where it reaches up to 30 %. Plagioclase becomes more abundant up-section but displays an intercumulus texture with the exception of the pegmatitic pods in the upper most section of the lower unit that mark the onset of the boundary between the two intrusive units. The dominance of clinopyroxene and olivine is consistent with the higher CaO and MgO concentrations of the lower mafic to ultramafic unit (Fig. 4.36A).

Prior to the crystallization of the upper gabbroic unit, an increase in magnetic susceptibility and TiO_2 concentration along the upper most section of the lower mafic to ultramafic unit (~ 320 m) indicates that Fe-Ti oxide is becoming more abundant (Fig. 5.3). The second stage in the mineral paragenesis involves cumulus clinopyroxene + olivine + Fe-Ti oxide. Note: the high magnetic susceptibility measurements along the basal contact of the lower unit are related to the presence of Fe-sulphides of the basal mineralization zone.

At ~ 300 m a significant change in major element geochemistry (Fig. 4.36) and texture (i.e., cumulate to subophitic; Figs. 4.16 and 4.18, respectively) is evident. The abrupt increase in Al_2O_3, an abrupt drop in MgO, a change in plagioclase habit from interstitial to subophitic, an abrupt increase in magnetic susceptibility indicates that this is the stage at which plagioclase reached saturation (Fig. 5.3). In addition the steep trend on a Harker variation diagram of MgO vs. TiO_2 (Fig. 4.37), positive Ti and V trough on the primitive mantle normalized plots (Fig. 5.2), and higher abundance of Fe-Ti oxides (Fig. 4.19) indicates that Fe-Ti oxide becomes a significant cumulus phase in the paragenesis. In a natural system, the arrival of Fe-Ti oxide as a crystallizing phase would cause a depletion in silica activity and the disappearance of olivine (Wager and Brown, 1967) which is consistent with the lack of olivine observed in the upper gabbroic unit. The loss of olivine, arrival of cumulus plagioclase and increase Fe-Ti oxide

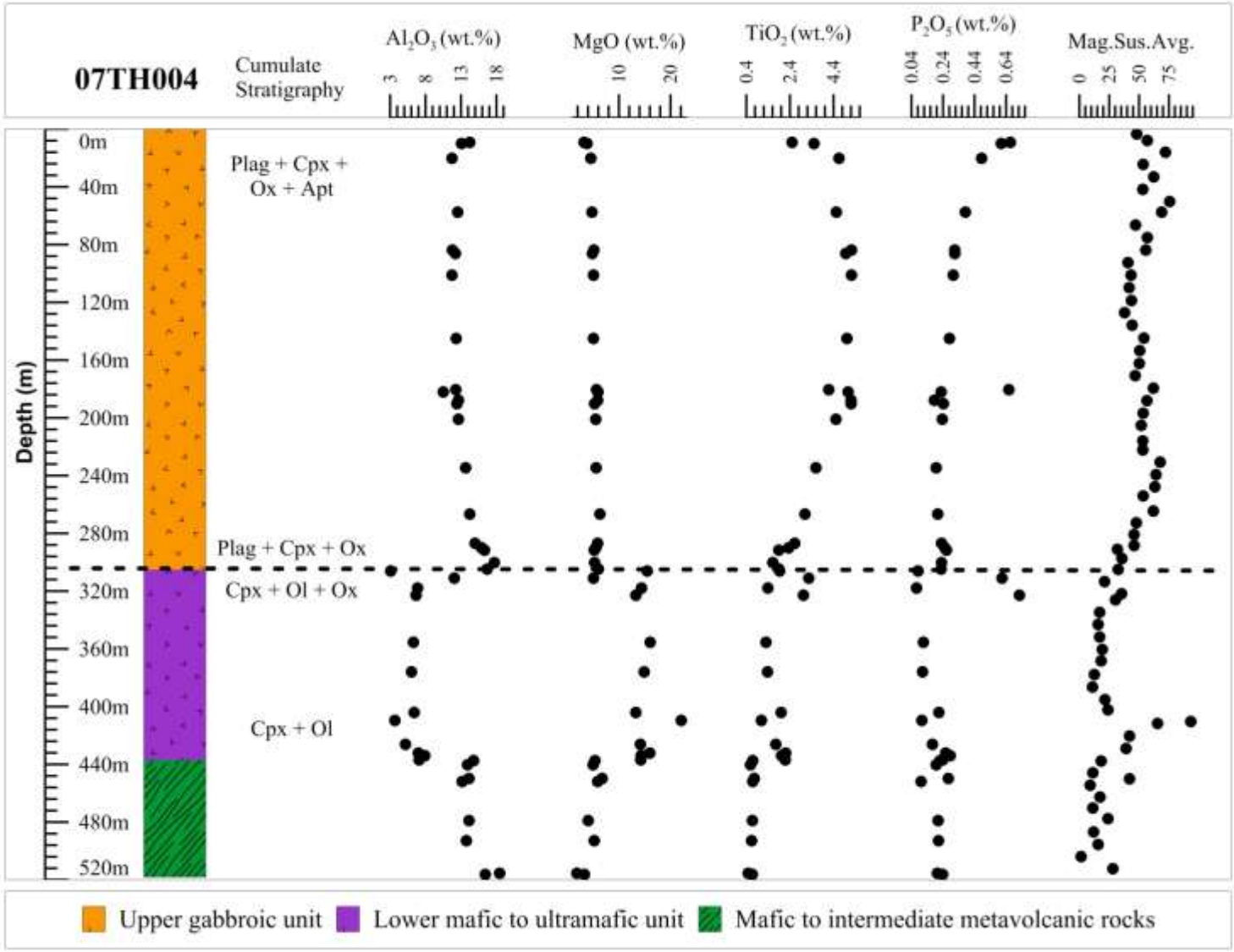

Figure 5.3: The cumulate stratigraphy of diamond drill hole 07TH004 interpreted from petrographic observations, correlated with whole rock major element geochemistry notably Al_2O_3, MgO, TiO_2 and P_2O_5, and magnetic susceptibility.

defines the third stage of the mineral parageneis consisting of plagioclase + clinopyroxene + Fe-Ti oxide (Fig. 5.3). The variations in the HFSE and REE ratios (Fig. 5.2) at the boundary between the lower and upper unit, is interpreted as the disruption of element distribution as plagioclase reaches saturation.

In the uppermost section (~ 60 m depth) of the upper gabbroic unit, the crystal size and abundance of apatite increases (Fig. 4.19C). It's not until ~ 10 m depth where there is a noticeable drop in TiO_2 and increase in P_2O_5 marking the stage at which apatite becomes a cumulus phase (Fig. 5.3). Magnetic susceptibility is still relatively high in the upper most section implying that the accumulation of Fe-Ti oxide is ongoing (Fig. 5.3). However, the overall abundance of Fe-Ti oxide is decreasing which is consistent with the negative Ti trough and depletion in V on the primitive mantle normalized profiles (Fig. 5.2). This defines the fourth stage of the mineral paragenesis consisting of plagioclase + clinopyroxene + Fe-Ti oxide + apatite and is representative of the most evolved stage of the crystallization history (Fig. 5.3).

5.3.5 Mantle source and contamination

The primitive mantle normalized profiles of the Thunder intrusion characterized by LREE enrichment and fractionated HREE (Figs. 4.39A, B) are broadly comparable to Sun and McDonough's (1989) modern plume-derived oceanic island basalts (OIB; Fig. 5.4) and other MCR early-rift mafic to ultramafic intrusions exhibiting OIB-like signatures within the MCR such as the Seagull intrusion (Fig. 5.5; Heggie, 2005; Nicholson et al., 1997; Hollings et al., 2007a). Nicholson et al. (1997) showed that the early-rift basalts were derived from small degrees of partial melting at depth of an enriched OIB-type plume mantle source. Since the incompatible element abundances of the more primitive samples of the Thunder intrusion (i.e., the lower mafic to ultramafic unit) are systematically lower than typical OIB (Fig. 5.4B), it

possibly formed at higher degrees of melting than typical OIB or by variations in the composition of the source region (Hollings et al., 2007a). In contrast, the fact that the incompatible element abundances of the more evolved samples of the Thunder intrusion (i.e., the upper gabbroic unit) are systematically higher than typical OIB (e.g., Fig. 5.4A) is likely the result of the evolving residual melt during fractionation.

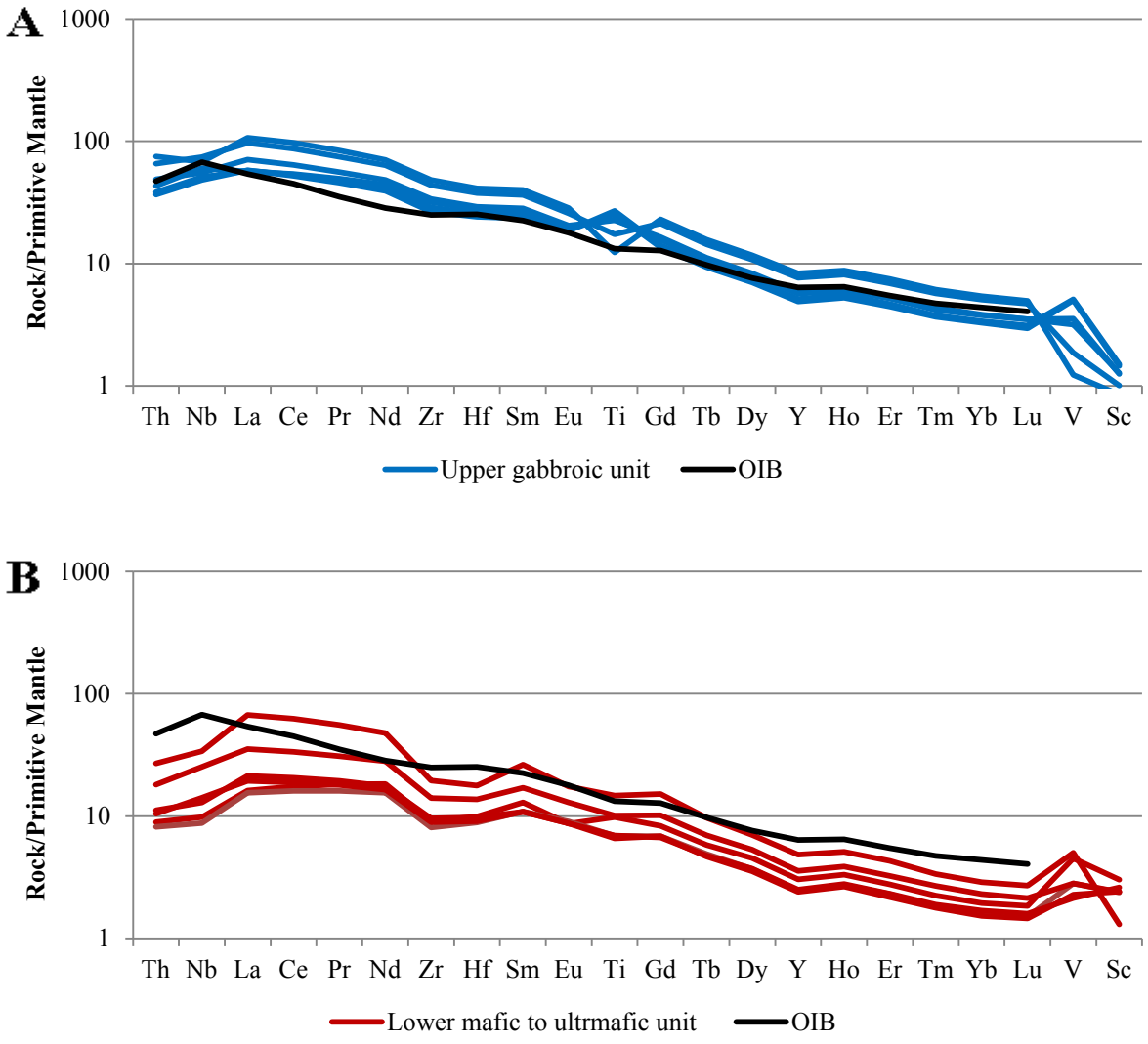

Figure 5.4: Primitive mantle normalized profiles comparing the Thunder intrusive units with ocean-island basalt (OIB). A) Representative samples of the upper gabbroic unit. B) Representative samples of the lower mafic to ultramafic unit. Normalizing values and ocean-island basalt data from Sun and McDonough (1989).

The presence of a negative Nb anomaly in the upper most section of the upper gabbroic unit (e.g., sample no. RTTC-BT-082; Figs. 4.39B and 5.4A), the up-hole increase in Th concentrations (Fig. 5.2) and a strong positive correlation of Th with La/Sm (Fig. 5.6) show that the Thunder parental magma is not typical of OIB-type composition. Rather, the geochemical signature of the Thunder intrusion is consistent with OIB-type signature that has undergone contamination during emplacement (Hollings et al., 2007a). To evaluate the origin and nature of the contaminant(s), the Sm-Nd and Rb-Sr radiogenic isotope signature of the Thunder intrusion and the Archean basement rocks that immediately underlie the intrusion were analyzed (Table 4.8).

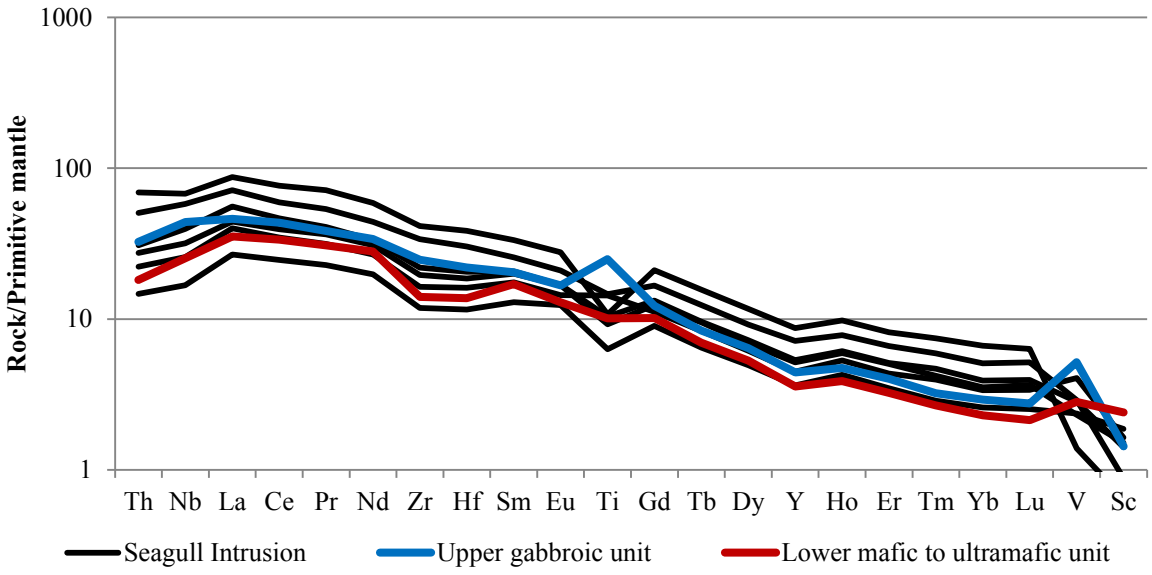

Figure 5.5: Primitive mantle normalized profiles for six representative samples of the Seagull intrusion, one of the lower mafic to ultramafic unit (RTT-BT-095), and one of the upper gabbroic unit (RTTC-BT-075). Normalizing values from Sun and McDonough (1989). Seagull intrusion data from Heggie (2005).

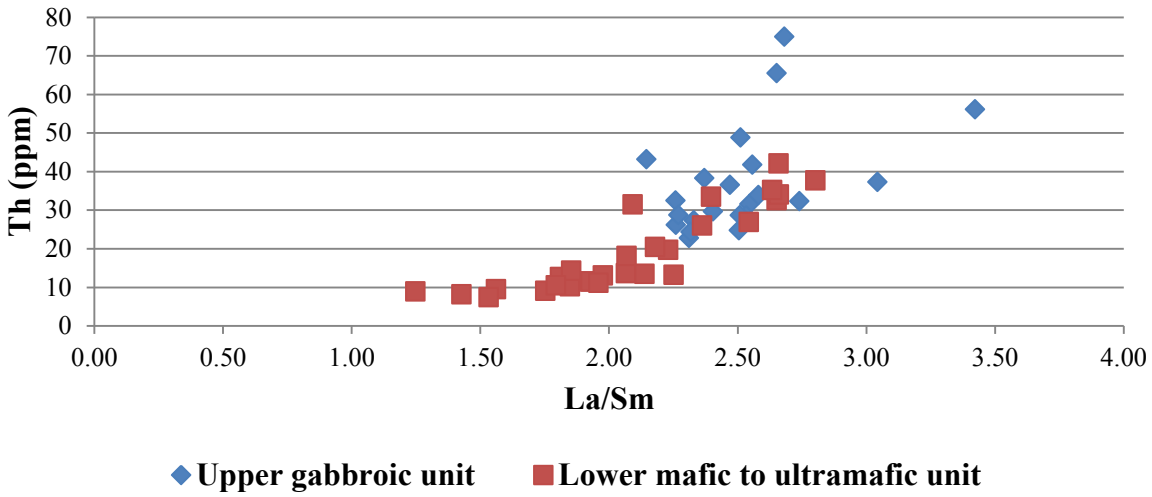

Figure 5.6: Plot of Th versus La/Sm versus Th (ppm) of the two Thunder intrusive units.

The lower mafic to ultramafic unit, upper gabbroic unit and metavolcanic wall rock are shown on a plot of εNd_T versus $^{87}Sr/^{86}Sr_i$ (Fig. 5.7) to distinguish the radiogenic isotope signatures. Nicholson and Shirey (1990) proposed that a primitive mantle source would have had a εNd_T value of 0 and an $^{87}Sr/^{86}Sr_i$ value between 0.7032 (Fig. 5.7). The Sr_i values of the lower mafic to ultramafic unit cluster around that of a primitive mantle source, whereas samples of the upper gabbroic unit trend toward wall rock values and span a relatively large range; εNd_T values for both intrusive units exhibit minimal variation and are close to a primitive mantle composition of zero with majority being slightly positive (Fig. 5.7). Since the Thunder intrusion Sr_i values deviate from a primitive mantle composition and trend towards values of the adjacent wall rock and one point exhibits a slightly negative εNd_T values, the data are consistent with contamination from an older crustal source (Hollings et al., 2007b). However, the lack of correlation between Sr_i and in εNd_T ($r = -0.28$) implies that the metavolcanic rocks that immediately underlie the Thunder intrusion were not a likely contaminant to the magma.

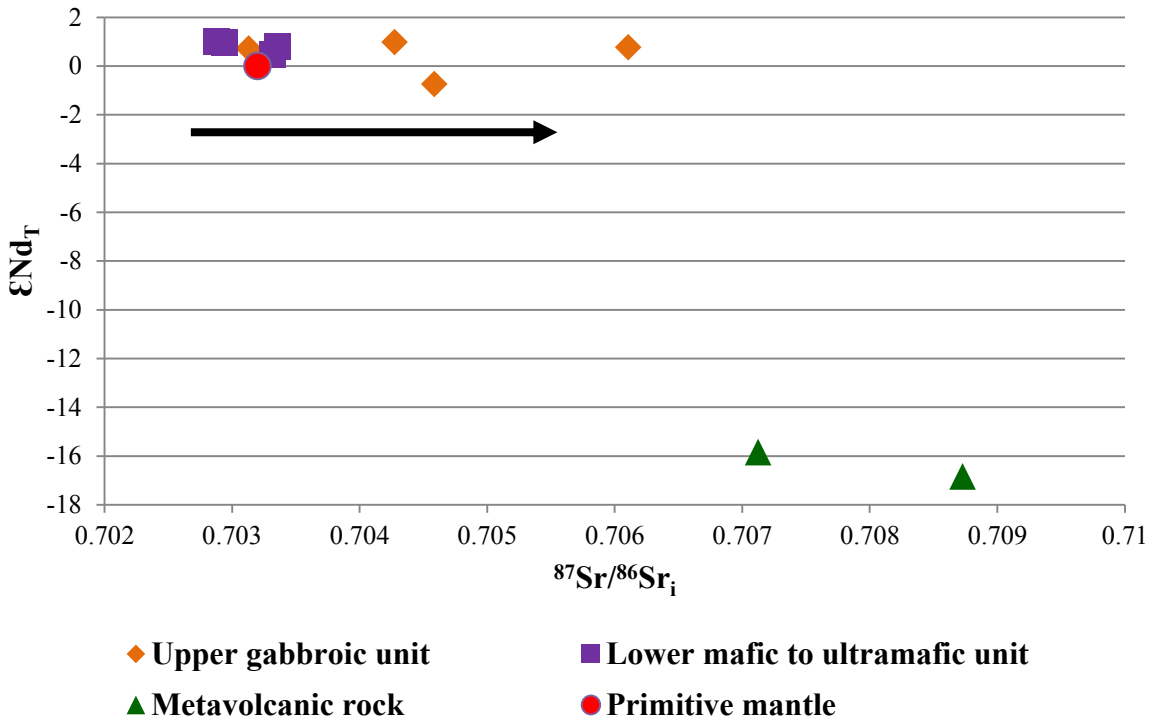

Figure 5.7: Plot of εNd_T versus $^{87}Sr/^{86}Sr_i$ at 1100 Ma for the intrusive units of the Thunder intrusion and its host rocks (diamond drill hole 07TH004). Primitive mantle values from Nicholson and Shirey (1990) where $\varepsilon Nd_T = 0$ and $^{87}Sr/^{86}Sr_i$ 0.7030 at 1100 Ma denoted by the red dot.

Other possible contaminants to consider within the Shebandowan greenstone belt include lithologies sampled by Henry et al. (1998) including metavolcanic, metasedimentary and granitic rocks. However, even those samples are characterized by similarly strong negative εNd_T values ranging from calc. -13.7 to -21.0 (Henry et al., 1998). The Rb-Sr radiogenic isotope signature was not measured by Henry et al. (1998). However, it is unlikely that the Shebandowan greenstone belt lithologies are not potential contaminants to the Thunder intrusion. The Archean granitoid and iron formation unit that occurs ~ 2 km and 400 m south, respectively, of the Thunder intrusion should be considered in the future as the down-dip direction of the intrusion suggests possible interaction at depth (see section 5.4.4).

The Rb-Sr and Sm-Nd radiogenic isotope signature of the Thunder intrusion was compared to that of other intrusive rocks of the MCR (Fig. 5.8). The horizontal trend due to the

lack of correlation between Sr_i and in εNd_T for the Thunder intrusion is similar to that reported for the three groupings of Nipigon Sills (Fig. 5.8; Hollings et al., 2007b). This was interpreted as different degrees of contamination in the Nipigon sills. Only one Thunder sample falls within falls within range of the slightly negative εNd_T Nipigon Sill grouping (i.e., group 1; Fig. 5.8). Shallow crustal contamination by a Sibley Group component with εNd_T similar to the sills, but with strongly enriched Sr_i could produced this effect (Fig. 5.8; Hollings et al., 2007b). However, contamination from the Sibley Group sedimentary rocks does not explain the isotope signature of the Thunder intrusion. The Thunder intrusion could not have penetrated the shallow basin-filling level of the Sibley Group as no outcrops in the vicinity of the Thunder intrusion are Mesoproterozoic in age (e.g., Fig. 2.1; Rogola et al., 2007). What is presently preserved of the Thunder intrusion indicates that the magma only intruded Archean rocks.

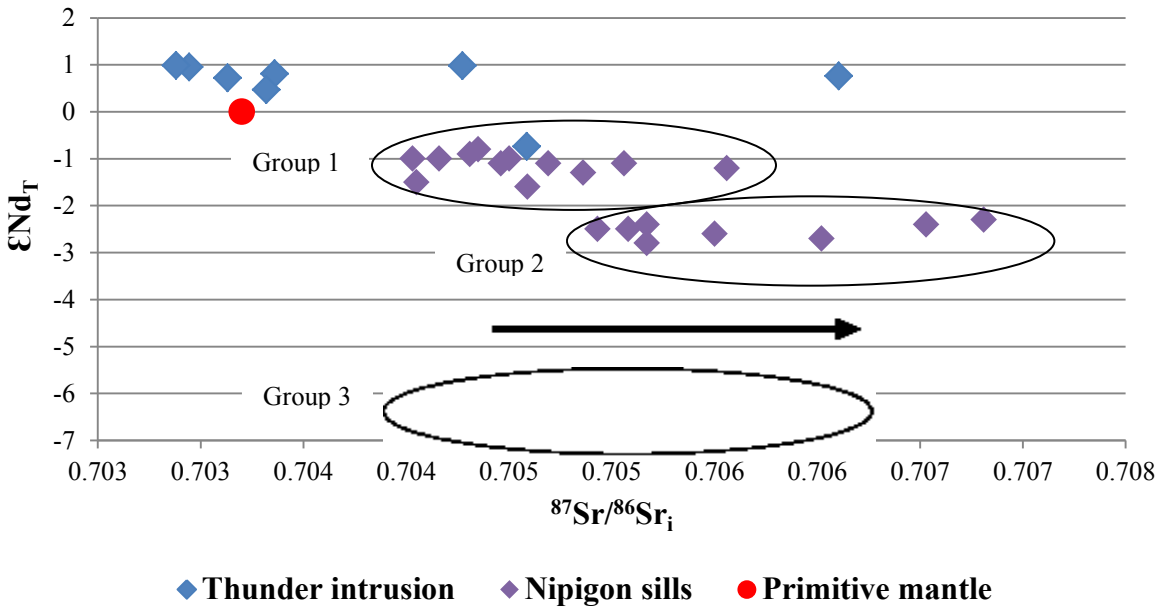

Figure 5.8: Plot of εNd_T versus $^{87}Sr/^{86}Sr_i$ at 1100 Ma for the units of Thunder intrusion (diamond drill hole 07TH004) and the Nipigon sills. Data sources include: primitive mantle values from Nicholson and Shirey (1990), and Nipigon Sill data and groupings from Hollings et al. (2007b). Denoted are group 1 less contamination, group 2 moderation contamination and group 3 most contamination for the Nipigon sills.

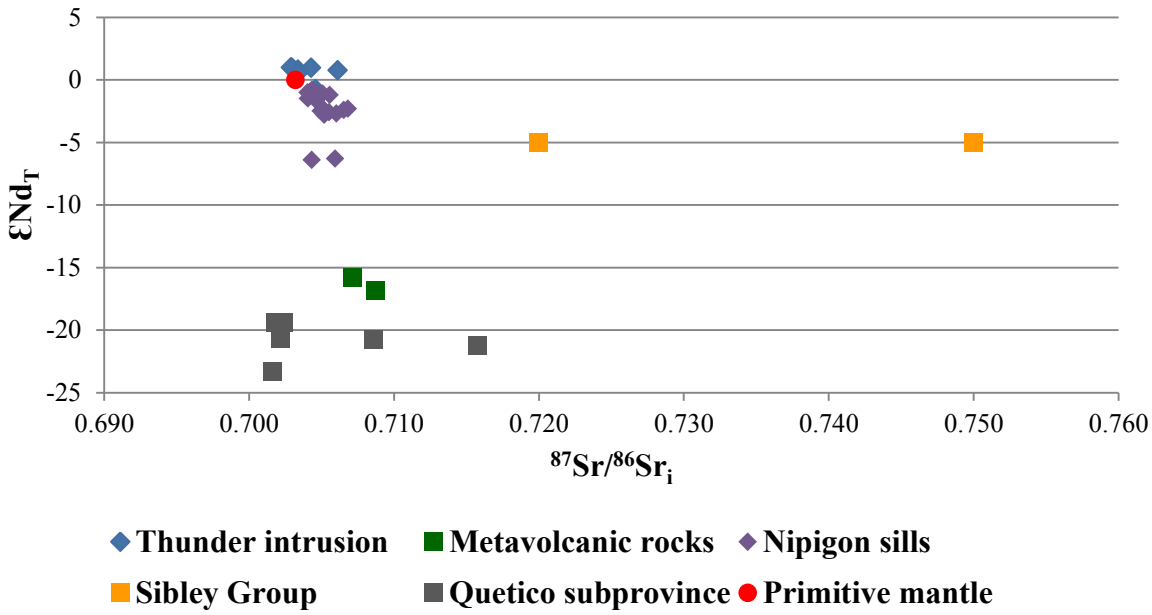

Figure 5.9: Plot of εNd_T versus $^{87}Sr/^{86}Sr_i$ at 1100 Ma for the host rocks and units of the Thunder intrusion (diamond drill hole 07TH004), the Nipigon Sills, Quetico subprovince metasedimentary rocks and Sibley Group sedimentary rocks. Data sources include: primitive mantle values from Nicholson and Shirey (1990), Nipigon sill data from Hollings et al. (2007b), Quetico subprovince data from Pan et al. (1999) and Sibley Group data from Metasaranta et al., pers. comm., 2005).

Other Archean rocks within the region include metasedimentary rocks of the Quetico Subprovince north of the study area (Fig. 2.1). According to data obtained Pan et al. (1999), rocks of the Quetico subprovince are characterized by strongly negative εNd_T values ranging from calc. ~ -19.0 to – 23.0 and Sr_i values ranging from calc. ~ 0.702 to 0.716 (Fig. 5.9). The high εNd_T values are also comparable to those of the metavolcanic rocks of the SGB both obtained from this study and from Pan et al. (1999). Rocks of the Quetico subprovince have been proposed as a possible contaminant to the Nipigon Sills (Hollings et al., 2007b) and the early-rift Seagull intrusion (Heggie, 2005) to account for negative εNd_T signatures. However, rocks of the Quetico subprovince are an unlikely contaminant to the Thunder intrusion as the southern dip direction of the Thunder intrusion's basal contact suggests unlikely interaction (see section 5.4.4). The Animikie Group rocks that occur south of the study area (Fig. 2.1) are not considered as they are Paleoproterozoic in age (Fralick et al., 2002) and do not occur at depth.

The last contaminant to consider includes contamination from a deeper, more wide-spread contaminant such as the subcontinental lithospheric mantle (SCLM) which has been proposed for contamination signatures observed in rocks of the Mamainse Point Volcanic Group (Shirey et al., 1994). Shirey et al. (1994) explained that the assimilation of refractory, melt-depleted SCLM would allow the mafic to ultramafic rocks of the MCR to retain their elevated MgO contents whilst acquiring a negative εNd_T signature from the SCLM. Nicholson et al. (1997) argued that negative Nb anomalies present in most magma types in the MCR reflect a contribution from SCLM which is consistent with observations of Hollings et al. (2007a) who showed that there is a widespread negative Nb anomaly in the mafic to ultramafic intrusions of the Nipigon Embayment. Hollings et al. (2007b) also observes that SiO_2 contents do not increase as εNd_T become more negative for the intrusive rocks of the Nipigon Embayment. Using this rationale, εNd_T is plotted against whole rock SiO_2 and MgO compositions of the respective samples from the Thunder intrusion (Fig. 5.10). The fact that SiO_2 does not increase with decreasing εNd_T for samples for the Thunder intrusion (Fig. 5.10A) and the presence of a negative Nb anomaly (e.g., Fig. 5.1) is consistent with contamination from the SCLM. The MgO contamination relationship does not appear to hold true for the samples of the Thunder intrusion as a whole as the negative εNd_T values are not accompanied by a corresponding increase in MgO (Fig. 5.10B). Samples of the upper gabbroic (which was the only intrusive unit of the Thunder intrusion to have a negative εNd_T signature), show the relationship holds true as the MgO contents of the upper gabbroic unit remain relatively elevated as εNd_T values become more negative. The data therefore suggests that contamination at depth by possibly the SCLM could account for the geochemical signature of the Thunder intrusion as oppose to in situ contamination.

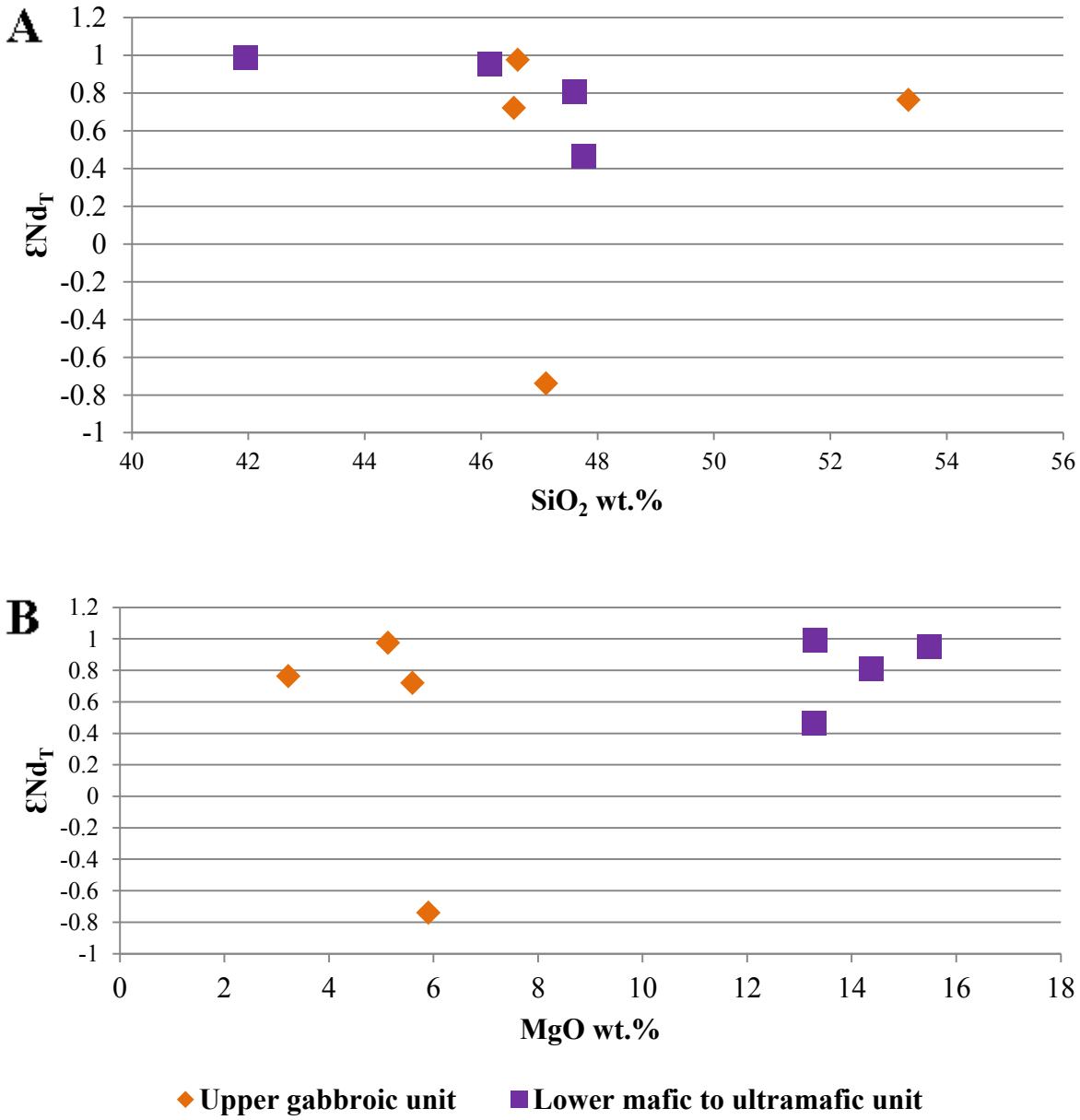

Figure 5.10: Plot of εNd_T at 1100 Ma versus A) SiO_2, and B) MgO presented as wt. % oxide for upper gabbroic unit and lower mafic to ultramafic unit.

It is evident that the Thunder intrusion underwent some degree of contamination during emplacement. The data shown here supports contamination by the SCLM to account for the negative εNd_T signature. However, the comparable Sr_i and εNd_T relationship between the Thunder intrusion and Nipigon Sills indicates contamination at shallow crustal levels possibly from basin filling sedimentary rocks. Therefore, expansion of the Rb-Sr, Sm-Nd radiogenic

isotope study is required in effort to either further support or rule out contamination from the SCLM and to investigate other possible shallow crustal level contaminants. Other rocks to consider for analysis within the study area include the iron formation unit intercepted by DDH 05TH001 (see section 4.3.1) and granitoid south of the Thunder intrusion (Fig. 1.1). Both rock types occur in the down-dip direction of the Thunder intrusion's bottom contact (Fig. 4.17).

5.2.6 Estimate of the parent magma composition

Goldner (2011), Foley (2010) and Ding et al. (2010) have estimated the parent magma composition of Tamarack, BIC and Eagle intrusions, respectively, by seeking samples of the basal contact that show textural and geochemical indications of rapid cooling (i.e., quenched texture) and subtracting the weighted olivine core composition from the bulk rock composition using the mass balance equation of Roeder and Emslie (1970) (Eqn. 1). The olivine chemistry used by Goldner (2011), Foley (2010) and Ding et al. (2010) were assumed to represent the olivine composition at first saturation with the parental liquid.

$X_{Whole\ Rock} = X_{Olivine} * \%Olivine + X_{Magma} * \%Magma$, or

$X_{Magma} = (X_{Whole\ Rock} - (X_{Olivine} * \%\ Olivine)) / \%Magma$ (Eqn. 1)

A quenched, mafic to ultramafic sample collected ~ 20 cm above the wall rock contact (Sample RTTC-BT-089) was selected for the calculation as it preserves textural characteristics of a quenched liquid including disequilibrium amongst the cumulate minerals (e.g., zoning in clinopyroxene; Appendix A), a high concentration of incompatible trace and rare earth elements relative to samples further from the contact (Fig. 5.2), a high proportion of interstitial post-cumulus minerals that tend to concentrate the incompatible elements (i.e., biotite, amphibole and plagioclase; see section 4.4.1) and a wide range of % Fo olivine measurements including the highest % Fo olivine measurement of Fo_{86} (Fig. 5.11). The Fo_{86} olivine is interpreted as residual

evidence of the primitive olivines that were the first to equilibrate with the parental liquid of the Thunder intrusion (Barnes, 1986). The high concentration of NiO in the Fo_{86} olivine is consistent with a primitive olivine composition preserved in sample RTTC-BT-089 (Fig. 4.35; Roeder and Emslie, 1970).

The modal percent of olivine in sample RTTC-BT-089 is approximately 10 % (Appendix A). As a first approximation, it will be assumed that the parent liquid contained 10 modal % of Fo_{86} in order to calculate the magmatic component using Eqn. 1. The occurrence of primary amphibole and biotite indicates that the parent magma was not completely dry, so the LOI was also included in the calculation. A summary of the calculations performed is shown in Table 5.1.

The calculated mg# of ~ 57 for the estimated parent magma composition of the Thunder intrusion is less than those calculated for the Tamarack (68.5; Goldner, 2011) and BIC (67.7; Foley, 2011), and of those calculated by Sutcliffe (1987) who demonstrated that primary mafic magmas in equilibrium with residual mantle olivine compositions of Fo_{88} to Fo_{94} (Carter 1970; Basaltic Volcanism Study Project (BVSP), 1981) should have mg#s of 68 to 83. The lower mg# suggests that the estimated parent magma composition for the Thunder intrusion is representative of a more evolved magma than the other early-rift mafic to ultramafic intrusions. This indicates that not all early-rift mafic to ultramafic intrusions found in proximity to Lake Superior basin hosting Ni-Cu-PGE mineralization were emplaced as primitive melts.

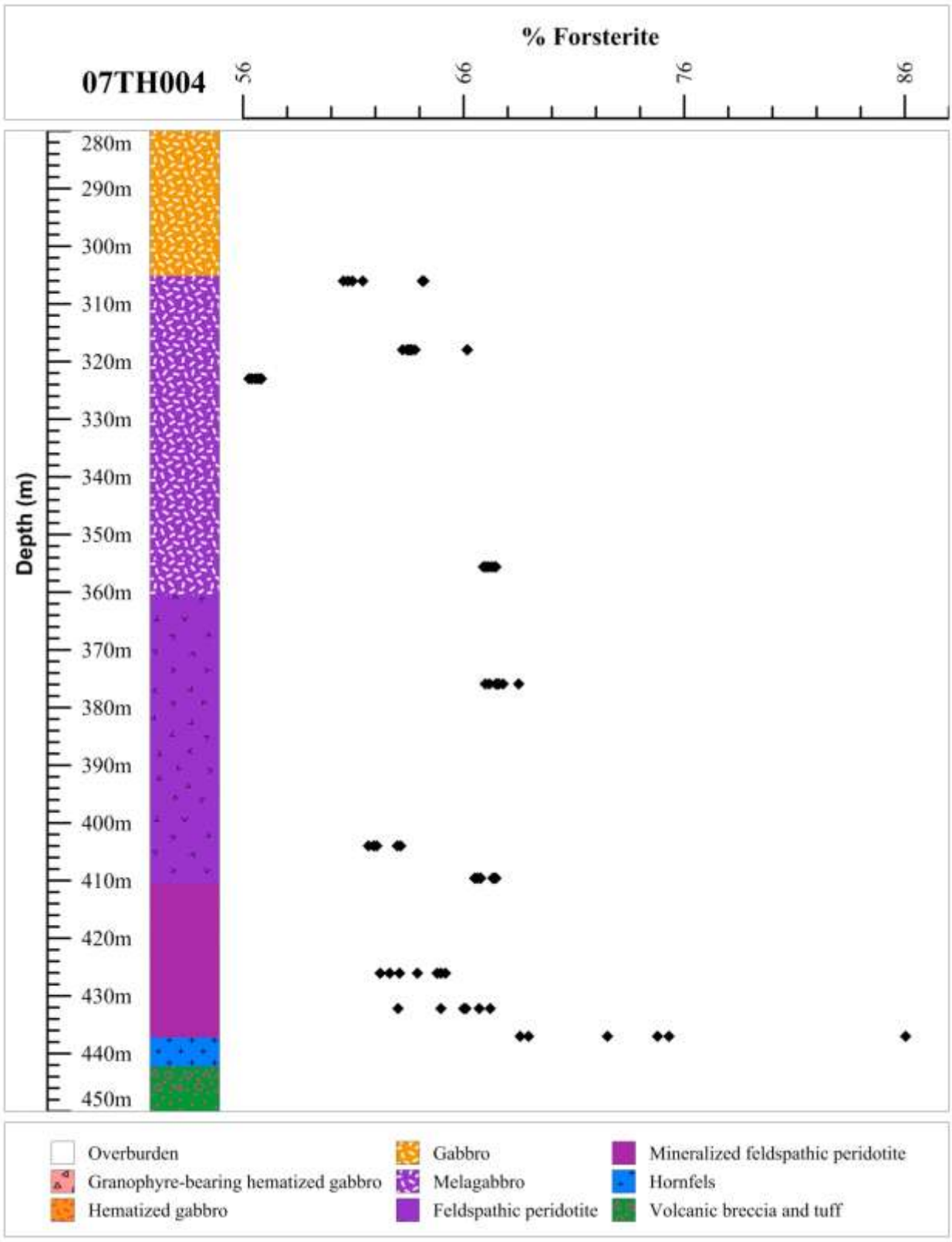

Figure 5.11: Olivine % Fo compositions plotted against lithostratigraphy from samples of diamond drill hole 07TH004. See Table 4.3 for olivine chemistry.

Table 5.1: Data and calculations used to estimate the Thunder intrusion's parent magma using the most primitive olivine measured (RTTC-BT-089 from diamond drill hole 07TH004). Both analyzes are normalized to 100 %. The primary composition is calculated by subtracting 10 % of Fo_{86} olivine from the whole rock composition. The mg# is calculated assuming that 90% of total iron is as FeO using formula: mg# = MgO/(MgO+0.9*FeO^T), mole %.

	Fo_{86} Olivine	RTTC-BT-089	RTTC-BT-089 - 10% Fo_{86} Ol
SiO_2	40.23	45.87	46.50
Al_2O_3	0.00	7.14	7.94
FeO^T	13.32	15.82	16.09
MnO	0.19	0.22	0.23
MgO	46.07	14.32	10.79
CaO	0.14	10.10	11.20
Na_2O	0.02	1.87	2.07
K_2O	0.00	0.82	0.91
TiO_2	0.03	2.19	2.43
P_2O_5	0.00	0.24	0.27
LOI	0.00	1.41	1.57
Total	100.00	100.00	100.00
mg#	86.0	64.2	57.0

Abbreviations: FeO^T = all Fe has been converted to FeO by 0.8998*Fe_2O_3, Ol = olivine

As an independent test of the calculated parent magma composition for the Thunder intrusion (Table 5.1), the estimate was modelled in the PELE software developed by Boudreau (1999). This program adapts the thermodynamic-based phase equilibrium algorithm of Ghiorso and Sack's (1995) MELTS software to a PC platform with an interface that allows for the simulation of equilibrium and fractional crystallization of an input magma composition at selected temperature intervals, pressure and oxygen fugacities. Five equilibrium crystallization models were run with oxygen fugacities buffered in the quartz-fayalite-magnetite (QFM) system including QFM + 2, QFM + 1, QFM, QFM -1 and QFM -2 (Fig. 5.12) which stands for log units above/below the QFM. Pressure was assumed to be 2 kbar for shallow crustal emplacement and a temperature interval of 5 °C starting at the olivine's liquidus temperature. PELE requires a selection of oxide types available for crystallization with a choice of two spinel groups (either

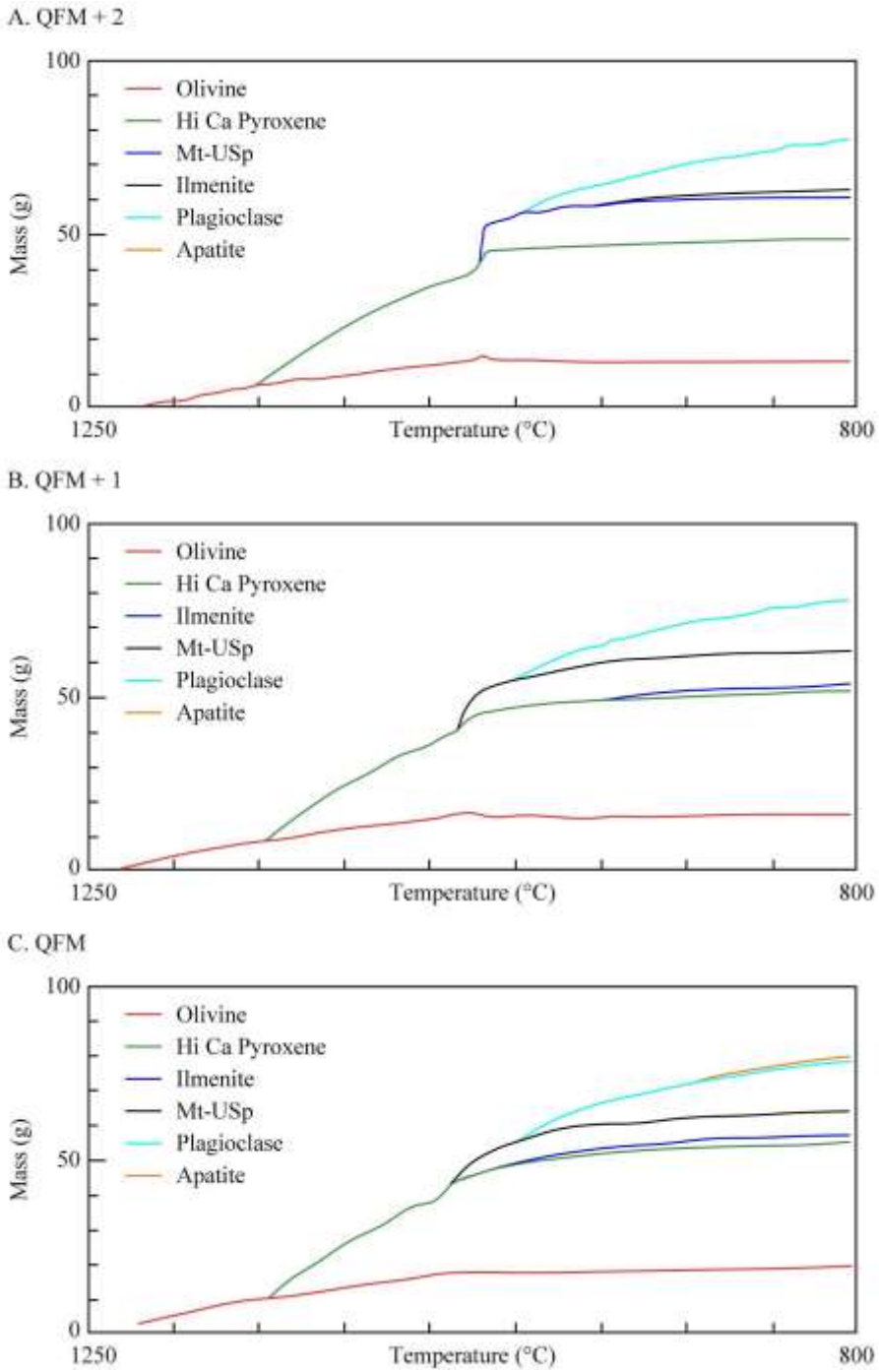

Figure 5.12: Mineral paragenesis calculated from equilibrium crystallization of parental magma estimated by the removal of 10 % Fo_{86} olivine modelled using PELE with five different oxygen fugacities of the quartz-fayalite-magnetite buffering system including A) QFM +2, B) QFM + 1, and C) QFM.

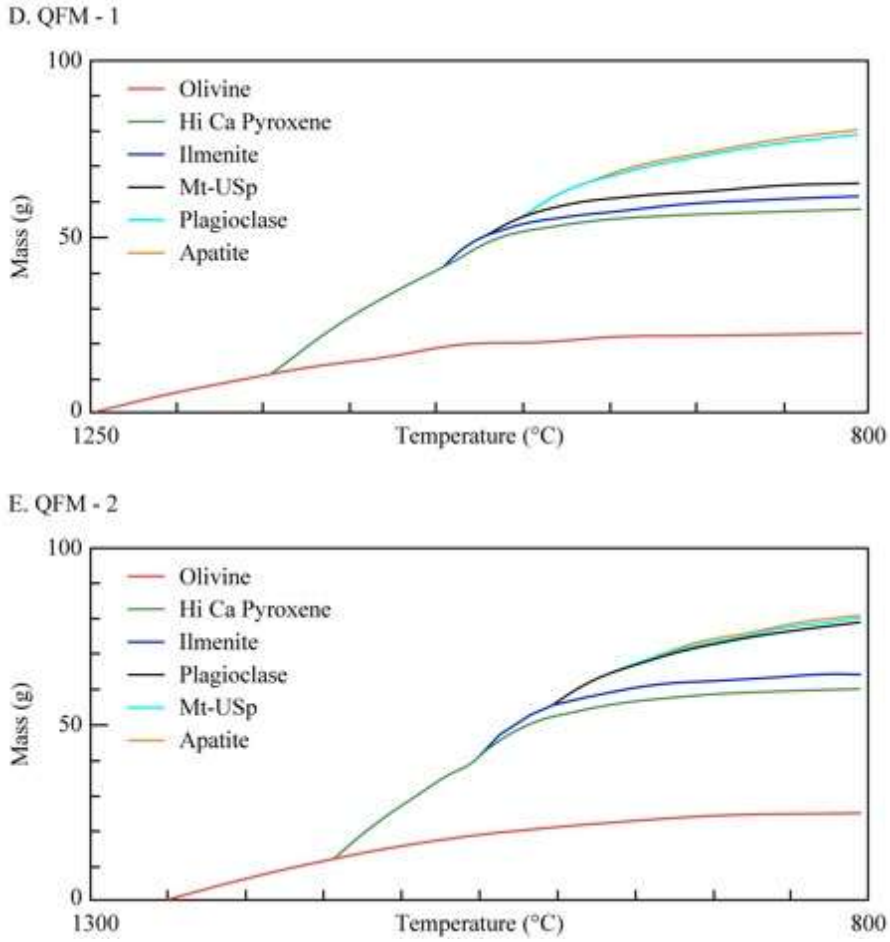

Figure 5.12 (cont.): Mineral paragenesis calculated from equilibrium crystallization of parental magma estimated by the removal of 10 % Fo_{86} olivine modelled using PELE with five different oxygen fugacities of the quartz-fayalite-magnetite buffering system including D) QFM -1 and, E) QFM – 2.

eight components or magnetite-ulvospinel only) and three rhombohedral oxide models (either four components, hematite-ilmenite, or ilmenite). Given the observed oxide mineralogy, magnetite-ulvospinel (mt-usp) and ilmenite were selected for the Thunder intrusion.

Four out of five equilibrium crystallization models (Fig. 5.12) produce a mineral paragenesis order of olivine → clinopyroxene → Fe-Ti oxide → plagioclase → apatite. Differences amongst the four plots include the arrival order of ilmenite and magnetite, for example under QFM + 2 conditions, magnetite occurs first prior to ilmenite whereas under QFM conditions ilmenite occurs before magnetite. QFM – 2 conditions produced a mineral

paragenesis of olivine → clinopyroxene → ilmenite → plagioclase → magnetite → apatite. The general order of cumulate phases under more oxidizing conditions is similar to the observed mineral paragenesis discussed in section 5.3.1 with the exception of the differing arrival times of ilmenite and magnetite-ulvospinel.

An additional test of the estimated parent magma composition for the Thunder intrusion compared the % Fo compositions of the first saturated olivine phase in equilibrium with the liquidus under the six buffering conditions in PELE (Table 5.2). Under more oxidizing conditions produced an olivine composition of ~ Fo_{86} which is consistent with the assumed primitive olivine first to equilibrate with the liquidus of the Thunder intrusion parent magma (sample RTTC-BT-089; Table 5.1). An oxidizing environment during the emplacement of the Thunder intrusion is consistent with the observed pervasive hematite overprint that increases up-hole in the upper gabbroic (DDH 07TH004; e.g., Fig. 4.14G)) interpreted as deutric alteration from the upward migration of residual fluids (e.g., Fig. 4.22). Although the estimated primary composition for the Thunder intrusion is more evolved than other mafic to ultramafic units within the MCR, modelling gave a comparable mineral paragenesis and olivine composition suggesting that the estimated primary composition is a reasonable one.

The estimated parent compositions may reflect the involvement of multiple staging chambers during the accent of the Thunder intrusion magma to account for the relatively more evolved composition. The involvement of magmatic staging chambers has been similarly proposed for the conduit system that formed the Noril'sk-Talnakh deposits (Arndt, 2005). In addition, the more evolved composition might explain the low nickel grades when compared to the other early-rift intrusions with primitive compostions such as Eagle, Tamarack and BIC

(Table 1.1). Evidently, primitive mafic to ultramafic magmatism is required to form sulphide mineralization with high nickel grades within the MCR.

Table 5.2: Output data from PELE including the olivine composition in equilibrium with the liquidus temperature at differing oxygen fugacities.

Buffer	% Fo Olivine in equilibrium with the liquid
QFM + 2	86.73
QFM + 1	85.48
QFM	83.36
QFM - 1	83.55
QFM - 2	82.97

5.3 Mineralization within the Thunder intrusion

5.3.1 Ni-Cu-PGE ± Au, Ag magmatic sulphide mineralization

The basal mineralization zone along the basal contact of the lower mafic to ultramafic unit is the primary mineralization style hosted by the Thunder intrusion. The parachute textured sulphide droplets consisting of pyrrhotite, chalcopyrite and pentlandite occur interstitial to the silicates and encased in biotite (Fig. 4.25D) and are interpreted as evidence of the accumulation of immiscible sulphide droplets via gravitational settling (Lightfoot et al., 1984). Since sulphides were not observed as inclusions in the cumulus minerals of the lower mafic to ultrmafic unit (i.e., olivine and clinopyroxene) and always interstitial to the cumulus minerals, it is interpreted that parent magma was emplaced undersaturated in sulphide and reached sulphide saturation during fractional crystallization of the lower mafic to ultramafic unit. The upper gabbroic unit exhibits weak to no mineralization indicating that the residual magma was depleted in sulphide following the crystallization of the lower mafic to ultramafic unit.

The thickest intercepts of the basal mineralization zone were from DDH 05TH003, 07TH004 and 005 (Figs. 4.9, 4.13; Appendix E; Bidwell and Marino, 2007). The thickness of the BMZ and abundance of visible sulphide was also observed to thicken and increase

respectively upwards along the dip of the intrusion (Fig. 4.17) from ~ 30 m thick and 1-5 % sulphide (DDH 07TH004; Fig. 4.13) to ~ 80 m thick and up to 30 % sulphide (DDH 05TH003; Fig. 4.9). Note: only sulphides greater than 1 modal % were considered for determining the thickness of the BMZ and sulphides were most abundant along the basal most sections of the BMZ sharply decreasing up-depth. The grades of the BMZ were also observed to increase upwards along the dip of the intrusion (Fig. 4.17; Table 5.3). In addition, Cu grades are consistently higher than Ni throughout the BMZ. Considering the distribution of the basal mineralization zone (Figs. 4.9, 4.13) and the basal contact (Fig. 4.17), it appears that sulphide segregation was greatest in the area of the DDH 05TH003 intercept possibly due to a change in slope of the basal contact (i.e., sulphide trap; Naldrett, 2011). Additional drilling will help elucidate the structure of the basal contact, distribution of the BMZ and possible wall rock control. As of now, understanding of the basal contact and BMZ is limited by the fence of five diamond drill holes (05TH002, 003, 07TH004, 005 and 006; Fig. 4.17).

Table 5.3: Metal grades from representative samples collected from the basal mineralization zone of diamond drill hole 03TH005 and 07TH004. Note: samples RTTC-BT-233 and 234 are not duplicates and were collected < 1 m apart.

Sample	Hole ID	Depth	Cu ppm	Co ppm	Ni ppm	Au ppb	Ir ppb	Pd ppb	Pt ppb	Rh ppb	Ru ppb
RTTC-BT-233	05TH003	297	10381	271	2057	115	42	1032	937	59	37
RTTC-BT-234	05TH003	297	8198	281	1843	85	37	932	638	64	30
RTTC-BT-229	07TH004	434	1488	103	699	15	9	174	126	13	7
RTTC-BT-089	07TH004	437	1575	100	708	12	7	126	92	9	4

In addition to the Pt- and Pb-bearing tellurides, bismuthides and arsenides indentified in the BMZ and found spatially associated with pyrrhotite and chalcopyrite (Fig. 4.32), PMMs including argentian pentlandite (Fig. 4.32D), hessite (Fig. 4.32C) and electrum was observed spatially associated with the magmatic sulphide mineralization. The PMMs identified in the BMZ have not been reported in the mineralized zones of other MCR early-rift mafic to

ultramafic intrusions such as BIC (e.g., Foley, 2011), Tamarack (e.g., Goldner, 2011), and Eagle (e.g., Ding et al., 2011) but have been reported in the Seagull intrusion (e.g., Heggie, 2005). As this intrusion is hosted by metavolcanic rocks bearing Ag and Au mineralization (see section 2.7), it is possible that wall rock assimilation could account for the precious metal mineralogy observed in the basal mineralization zone.

Mineralization within the footwall rocks is limited to ~ 2 m thickness consisting of rare < 0.5 cm sulphide stringers (DDH 05TH003, 07TH004, 005), ~ 2 cm thick massive pyrrhotite-rich massive sulphide veinlet (DDH 07TH003) and two < 5 cm thick massive chalcopyrite-rich massive sulphide veinlets (DDH 07TH006; Table 4.1). However, the footwall-hosted sulphide mineralization is not all genetically related to the Thunder intrusion. The pyrrhotite-rich massive sulphide veinlet and sulphide stringers were determined related to the Thunder intrusion on the basis on similar sulphide mineralogy (Table 4.1), PGM mineralogy (Table 4.2) and cross-cutting relationships (Figs. 4.27D, 4.28A). The chalcopyrite-rich massive sulphide veinlets (DDH 07TH006) were determined unrelated to the Thunder intrusion on the basis of conformable contact relationships with relict tuffaceous bedding (Figs. 4.30A, B), the absence of PGMs (Table 4.2), unique PMM mineralogy including electrum, native silver, gold and Ag-bearing chalcopyrite (DDH 07TH006; Fig. 4.13 (Table 4.1), recrystallized pyrite (Fig. 4.30D) and sulphide mineralogy (Table 4.1; e.g., no pyrrhotite). Therefore, the chalcopyrite-rich massive sulphide veinlets were ruled out as a local wall rock mineralization feature.

5.3.2 Fractionation controls on Ni-Cu-PGE patterns

To evaluate the metal distribution in a magmatic system (Barnes and Maier, 1999) the whole rock primitive mantle normalized Ni-Cu-PGE profiles of the Thunder intrusion upper gabbroic and lower mafic to ultramafic unit which are characterized by depletion in IPGEs (Ir,

Ru, Rh) relative to PPGEs (Pt, Pd, Au) were considered (Fig. 4.41). Two possible explanations for the fractionated PGE pattern observed in the Thunder intrusion include: the IPGEs may have partitioned into an earlier silicate phase deeper in the magmatic system. Phases that have been shown to sequester IPGEs include chromite (Capobianco and Drake, 1990; Capobianco et al., 1994; Righter et al., 2004), olivine (Brugman et al., 1987; Brenan et al., 2005), monosulphide solid solution (MSS; i.e., magmatic pyrrhotite; Ballhaus et al., 2006) and discrete PGE phases (Borisov and Palme, 2000; O'Hara et al., 2001). Of these the partitioning of the IPGEs into an olivine-rich rock type (i.e., peridotite) is the most likely possibility as the other phases were not observed in the Thunder intrusion.

The second alternative is the formation of an earlier magmatic sulphide liquid phase deeper in the system that concentrated the IPGEs such as MSS that represents the Fe-rich sulphide liquid phase first to equilibrate in a mafic magma (Naldrett, 1969). According to Ballhaus et al. (2006) Pt, Pd, Au and Cu are invariably incompatible in the MSS whereas Ir, Ru and Rh are highly compatible. As sulphide magma crystallizes, the residual sulphide liquid will become highly enriched in Cu, Pt, Pd, and Au but depleted in Ir, Ru, Rh. During late stage cooling of the sulphide magma, migration of Cu-rich residual sulphide liquid is a common phenomenon; particularly when of large pools of massive sulphide are formed (e.g., Eagle footwall Cu-rich sulphide veins, Ding et al., 2011). This separation of the Cu-rich residual sulphide liquid typically occurs as veins or disseminations rich in chalcopyrite, commonly containing significant amounts of rare minerals including cubanite and bornite (e.g., Naldrett et al., 1994) and unique precious metal mineral such as argentian pentlandite (Mandziuk and Scott, 1977). Chalcopyrite, cubanite, bornite and argentian pentlandite were observed in the lower mafic to ultramafic unit both within and outside the basal mineralization zone (see section 4.6).

In addition, there is an overall lack of Ni-bearing sulphides in the basal mineralization zone including pentlandite, siegenite and bravoite (Table 4.1), most of which have undergone secondary replacement producing marcasite + pyrite + magnetite intergrowths (e.g., 4.25C). The pyrrhotite-rich massive sulphide veinlet cross-cutting the wall rock (DDH 05TH003; Fig. 4.27) with similar sulphide species as the basal mineralization zone (Fig. 4.25; Table 4.1) and the disrupted grain boundaries of euhedral magnetite along the veinlet's boundary (Fig. 4.27D) is evidence for a migrating sulphide liquid. If the mineralization observed in lower mafic to ultramafic unit is representative of this Cu-rich residual sulphide liquid, then it is reasonable to suggest that the Fe-rich MSS massive sulphide horizon may occur deeper in the system.

The Eagle Ni-Cu-PGE deposit serves as an analogue for MCR-related mafic to ultramafic magmatism hosting high-grade Ni-Cu-PGE massive sulphide (e.g., Ripley and Li, 2007). In the Eagle Deposit of northern Michigan, the disseminated, semi-massive and massive sulphide mineralization broadly show unfractionated IPGE-PPGE patterns (Ding et al., 2011). The PPGE-rich sulphide zones, such as the upper massive and semi-massive zones, can be explained by fractional crystallization of the MSS (Ding et al., 2011). In addition, Cu-rich veins in the footwall rocks of the Eagle deposit are characterized by relatively PPGE-rich Ni-Cu-PGE patterns which are generally consistent with highly fractionated sulphide liquids expelled from crystallizing sulphide liquid as previously discussed (Ding et al., 2011). The Ni-Cu-PGE patterns for the disseminated sulphide mineralization hosted by the Thunder intrusion's lower mafic to ultramafic unit are similar to the upper massive and semi-massive sulphide zones and Cp-rich veins of the Eagle deposit and thereby support the second alternative proposed for Thunder's fractionated patterns involving the formation of an earlier sulphide liquid phase deeper in the system that has concentrated the IPGEs.

5.3.3 Sulphur source

According to Naldrett (2011) and references therein, the controlling factors in the development of a magmatic sulphide deposit hosting economic grades of Ni, Cu and PGE are the solubility of sulfur in silicate melts, the partitioning behaviour of chalcophile metals between sulfide and silicate liquids, and the mechanisms that drive that silicate melt to sulfide saturation. Mavrogenes and O'Neil (1999) and Holzheid and Grove (2002) have shown that with decreasing pressure, the solubility of sulfur increase exponentially. In order for sulfide saturation to be achieved in a low-pressure environment, either extensive fractional crystallization or the introduction of external sulfur is required by the models. In general, sulphide saturation is achieved by fractional crystallization after Ni has been depleted due to olivine crystallization (Ripley and Li, 2013). Several researchers have shown that the assimilation of sulphur-bearing country rock and/or SiO_2-rich wall rocks are effective means to achieve early sulphide saturation which is critical in the generation of Ni-rich magmatic sulphide deposits (e.g., Keays, 1995; Naldrett, 1999; Lesher and Burnham, 2001; Ripley and Li, 2003; Li and Ripley, 2005, Ripley and Li, 2013). In the MCR, the presence of sulphide-bearing Archean and Proterozoic country rocks hosting the conduits and local environment of mafic to ultramafic intrusions of the MCR makes for a favorable exploration environment for Ni-Cu-PGE magmatic sulphide (e.g., Donoghue et al., 2014).

To investigate the involvement of crustal derived sulphur in the formation of mineralization in the Thunder intrusion, $\delta^{34}S$ measurements were made. If the sulfur was mantle derived the $\delta^{34}S$ values should fall within a range of 0 ± 2 ‰ (Ripley, 1999). Whereas if the $\delta^{34}S$ values of the magmatic sulphides are higher than mantle values and are similar to those found in the marginal country rocks, then it is reasonable to suggest crustal sulfur assimilation (Ripley &

Li, 2003). The $\delta^{34}S$ values for mt+py+po veins and cp disseminations in the upper gabbroic unit, and the po + cp disseminations in the lower mafic to ultramafic unit range from -2.0 to +3.8 ‰ and fall within range of upper mantle values (Fig. 4.42; Table 4.6). Values for the py-bearing metavolcanic host rock range from -3.1 to +2.3 ‰ are not strongly anomalous, and are isotopically similar to those of Thunder which in turn, fall within range of typical upper mantle (Fig. 4.42). This is problematic as the detection of a crustal sulphur component is limited by the lack of anomalous values in the metavolcanic host rocks.

A similar scenario was found at the Seagull intrusion where $\delta^{34}S$ values for sulphides from the intrusion-hosted mineralization that ranged from -2.3 to +2.6 ‰ (Kissin et al., 2007). Values for the host rock include sulphides from the Quetico subprovince metapelites ranging from -2.3 to +1.1 ‰ and sulphides for the Sibley Group sedimentary rocks range from +7.7 to +9.0 ‰ (Kissin et al., 2007). Kissin et al. (2007) indicated that the similarity between the sulphur isotope data from samples of the Seagull intrusion and Quetico subprovince metapelites provide plausible evidence for the incorporation of Quetico subprovince sulphides in the intrusion. However, the isotopic compositions are very close to a mantle composition as is the case with the Thunder intrusion.

The lack of anomalous values in the Archean rocks both the metavolcanic rocks hosting the Thunder intrusion and the Quetico subprovince hosting the Seagull intrusion could be attributed to the lack of bacterial processes responsible for much of the present day S isotope fractionation (e.g., biologically mediated reduction of sulphate; Chambers and Trudinger, 1979; Habicht and Canfield, 1997), or simply that the sulphur utilized was isotopically similar to mantle sulphur and fractionations were small (Ripley and Li, 2003). To test this hypothesis, $\delta^{33}S$

measurements of the sulphide mineralization in the Thunder intrusion and wall rock were undertaken.

Deviations from the isotope fractionation relationship between $\delta^{33}S$ and $\delta^{34}S$ ($\delta^{33}S = 0.515\ \delta^{34}S$) is thought to have occurred during the Archean via mass independent fractionation as bacterial processes responsible for much of the sulfur isotopic fractionation were not yet operative (Farquhar et al., 2000). Farquhar and Wing (2003) showed that anomalous $\Delta^{33}S$ signals for Archean rocks older than 2.45 Ga are characteristically within a range extending to values greater than +/- 1.0 ‰ that incorporated in sulphate- and sulphur-bearing species, and felsic intrusions. Pyrrhotite + chalcopyrite bearing samples from the basal mineralization zone for $\Delta^{33}S$ yielding values 0.066 and 0.122 ‰ (Table 4.6). Another analysis from the pyrite-bearing metavolcanic wall rock yielded a $\Delta^{33}S$ values of 0.149 ‰. Overall, the three values are not strongly anomalous. Rather, the lower mafic to ultramafic unit and metavolcanic wall rock are again isotopically similar and close to 0.

On the Canadian side of the MCR (i.e., Ontario), the ^{33}S isotope value has not been analyzed for the wall rocks surrounding the other early-rift mafic to ultramafic intrusions. On the American side of the MCR (e.g., Michigan); however, $\Delta^{33}S$ has been investigated in conjunction with $\delta^{34}S$ (e.g., BIC, (Donoghue et al., 2014); Eagle deposit, (Ding et al., 2012)). Both $\delta^{34}S$ and $\Delta^{33}S$ were analyzed for the mineralization and host rocks including the Paleoproterozoic Baraga Group sedimentary rocks including the Goodrich quartzite, chert-carbonate unit, and the Michigamme Formation (generally considered to be correlative with the Rove Formation; Johnston et al., 2006), and the Archean quartz monodiorite basement rocks (Ding et al., 2012). In summary, values for $\Delta^{33}S$ were not to be found strongly anomalous for the units analyzed, but isotopic similarity was observed between the semi-massive sulphide and

the Archean quartz monodiorite; the disseminated and massive sulphide showed similarity with the Paleoproterozoic rocks (Ding et al., 2012). Ding et al. (2012) indicated that multiple sources of sulphur were involved in the generation of the Eagle deposit likely the results of different magma pathways in a conduit environment. This conclusion is similar to the one from Donoghue et al. (2014) for the multiple sulphur isotope study done on BIC.

Ripley and Li (2003) and Fiorentini et al. (2012) have suggested that crustal signatures have the potential of being reduced by isotope exchange and mixing in a magmatic system. This might explain why results from the multiple S-isotope study do not provide strong confirmation of the involvement of crustal sulphur in the Thunder intrusion. Another possible explanation could include the nature of the Thunder intrusion`s host rock being dominantly volcanic in origin and characterized by weak S-isotope signatures. An expansion of the S isotope study is required for the Thunder intrusion as the distribution of samples collected $\Delta^{33}S$ is small and likely not representative, and that the database for $\Delta^{33}S$ values for rocks on the northern side of the MCR is limited. Additional work should sample lithologies such as the graphitic heterolithic breccias and schists observed in DHH's 05TH001 and 002.

Typical Se/S values assigned to mantle-derived rocks range from 230 to 350 x 10^6 (Eckstrand and Hubert, 1987). However, many samples at Thunder contain very low concentrations of S^T which introduces error in the calculation. For example: samples with Se/S ratios greater than 1000 contain S^T concentrations near that of the detection limit (0.01 %). Therefore, Figure 5.13 filters the data from Table 4.6 with a S^T cut-off of 0.1 %. After the modification of Figure 4.43, the majority of samples from the lower mafic unit (n =3) plot below values of mantle-derived rocks as well samples of the metavolcanic rocks (n = 2); one sample of the upper gabbroic unit plots above values of mantle-derived rocks as well one sample of

metavolcanic rocks (Fig. 5.13). Values for the Thunder intrusion appear to be pulled toward values of the metavolcanic wall rock indicating possible crustal sulphur assimilation.

For a regional comparison, Se/S ratios for the Seagull intrusion and Quetico metasedimentary rocks show a similar range from ~ 26 to 628 x 10^6 (Kissin et al., 2007). It should be noted that Kissin et al. (2007) analyzed sulphide minerals for the Se/S ratio rather whole rock composition. Plotting Se/S versus $\delta^{34}S$, Kissin et al. (2007) observed much scatter in the magmatic sulphides some lying outside the field for mantle sulphide (Eckstrand and Hubert, 1987). As a result, Kissin et al. (2007) proposed that contamination by the Quetico metapelite sulphide was involved in the mineralization of Seagull. Following a similar approach, Se/S versus $\delta^{34}S$ for this study's data is plotted in Figure 5.14. As was the case for the Seagull intrusion, there is much scatter in the data with the majority plotting outside the field of Eckstrand and Hubert (1987) and Ripley (1999) for mantle Se/S and $\delta^{34}S$ respectively. However, the data still falls within close range of typical upper mantle values as was the case for the S-istopes discussed above. Therefore, although the S-isotope signatures and Se/S ratios are consistent with a mantle origin and the Archean wall rocks have S-isotopes that cannot be distinguished; the involvement of crustal sulphur remains speculative.

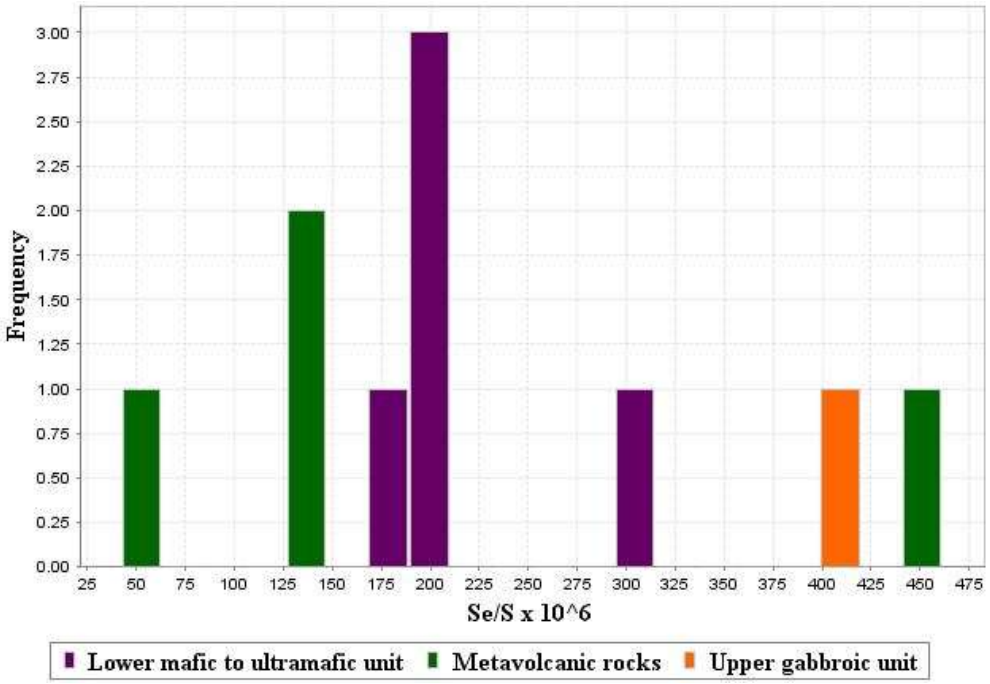

Figure 5.13: Histogram illustrating the distribution of whole rock $Se/S^T \times 10^6$ ratios for the upper gabbroic unit, lower mafic to ultramafic unit and metavolcanic wall rock containing sulphide mineralization. Total sulphur cut-off at less than 0.1 % (n = 11).

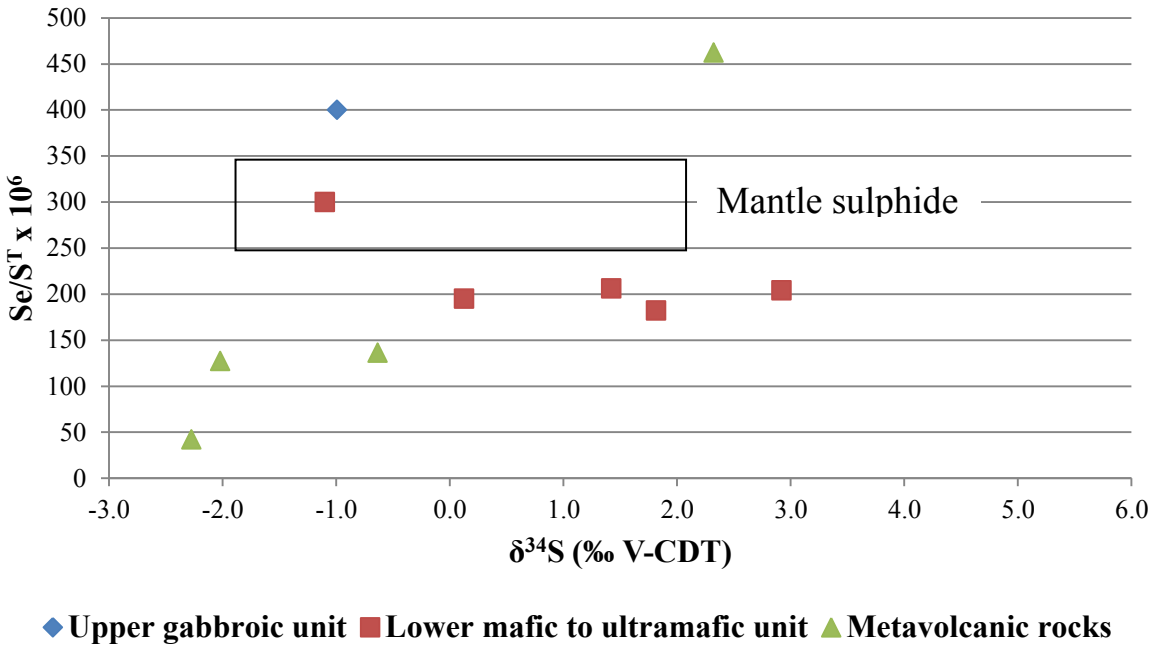

Figure 5.14: Plot of $Se/S^T \times 10^6$ versus $\delta^{34}S$ ‰ for samples from Figure 5.16. The rectangle represents the range of composition of mantle sulphides after Eckstrand and Hubert (1987) and Ripley (1999) for Se/S and $\delta^{34}S$ respectively. V-CDT = Vienna-Canyon Diablo Troilite.

5.4 The Thunder intrusion and the Midcontinent Rift

5.4.1 The emplacement model

The Wawa and Quetico subprovince boundary is roughly outlined by granitoid bodies of the Dog Lake Granite Chain and Nipigon Bay granites emplaced along crustal-scale faults that formed the terrane boundaries as "stitching plutons" (e.g., Hollings and Kuzmich, 2014). The close spatial proximity of early-rift mafic to ultrmafic intrusions such Thunder, Sunday Lake and Current Lake (Fig. 5.15) and granitoid bodies of the DLGC suggests a possible structural control on the distribution of mafic to ultramafic intrusions containing Ni-Cu-PGE sulphide mineralization in the northern Lake Superior region north of the Canada-USA border. The Thunder parent magma likely travelled along a conduit through reactivated subprovince boundary deep-seated structures during the Mesoproterozoic rifting event. The structural control on the primary distribution of mafic to ultrmafic intrusions containing Ni-Cu-PGE sulphide mineralization in the roots of large igneous provinces has been observed elsewhere such as the Huangshandong, Huanshang and Jinchuan intrusion in China (Lightfoot and Evans-Lamswood; 2014). The low mg# (57) estimate for the parent magma represents a more evolved magma than the other early-rift mafic to ultramafic intrusions in the MCR. The involvement of multiple staging chambers during the accent of the Thunder intrusion may account for the evolved composition possibly reflecting a conduit system similar to the one proposed for the Noril'sk-Talnakh deposits (Arndt, 2005).

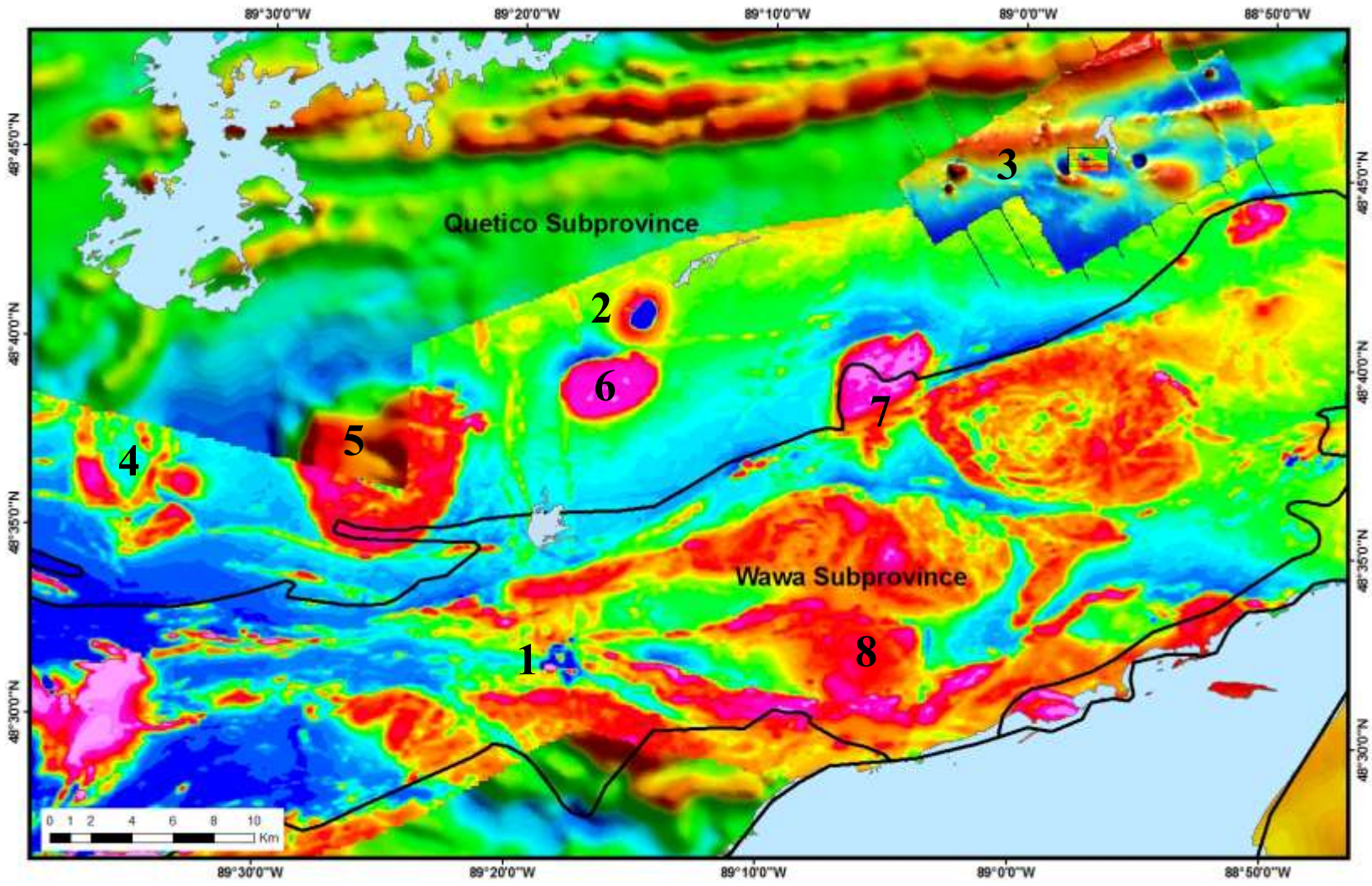

Figure 5.15: Airborne total magnatic field of the region north of the Thunder intrusion including the outline of the Wawa and Quetico Subprovince boundary. Geophysical data from OGS (2003 a,b) and Geoteck Ltd. (2011). Indiacted on the map are mafic to ultramafic intrusions including 1 = Thunder, 2 = Sunday Lake and 3 = Current Lake, and granitoid intrusions of the Dog Lake Granite Chain including 4 = Silver Falls, 5 = Trout Lake, 6 = Barnum Lake, 7 = White Lily, and 8 = Penasen Lake.

5.4.2 An early-rift mafic to ultramafic intrusion

Hollings et al. (2007a) showed that a plot of La/Sm_n versus Gd/Yb_n can be used to discriminate the intrusive units of the MCR (Fig. 5.16). On this diagram the upper gabbroic unit and lower mafic to ultramafic unit of the Thunder intrusion lie slightly above the field of the lower mafic to ultramafic intrusions and sills of the Nipigon Embayment on the Gd/Yb_n axis (e.g., Hele Intrusion and Shillabeer Sill respectively) and within range on the La/Sm_n axis (i.e., between 1.00 and 3.00). The high Gd/Yb_n values are consistent with the interpretation of Hollings et al. (2007a) that the parent magmas of the mafic to ultramafic intrusions of the Nipigon Embayment were derived from a deeper source than the diabase sills (e.g., Nipigon sills).

With OIB-like characteristics and εNd_T and $^{87}Sr/^{86}Sr_i$ values similar to that of a mantle plume source (Nicholson and Shirey, 1990), the Thunder intrusion is broadly another example of MCR early-rift mafic to ultramafic magmatism in the Lake Superior region. The relatively evolved composition of the Thunder intrusion indicates that not all early-rift mafic to ultramafic intrusions hosting Ni-Cu-PGE mineralization were emplaced as primitive melts. In the case of the Thunder intrusion, this may reflect the involvement of multiple staging chambers during the accent of the parent magma. Evidence for contamination of the parent magma is evident with possible contaminants including SCLM and/or an upper crustal unit. On the plot of La/Sm_n versus Gd/Yb_n (Fig. 5.16) both intrusive units of the Thunder intrusion plot slightly above the field of the mafic to ultramafic intrusions and sills of the Nipigon Embayment (e.g., Hele Intrusion and Shillabeer Sill respectively). The high Gd/Yb_n values are consistent with the interpretation of Hollings et al. (2007a) that the parent magmas of the mafic to ultramafic

intrusions of the Nipigon Embayment were derived from a deeper source than the diabase sills (e.g., Nipigon sills).

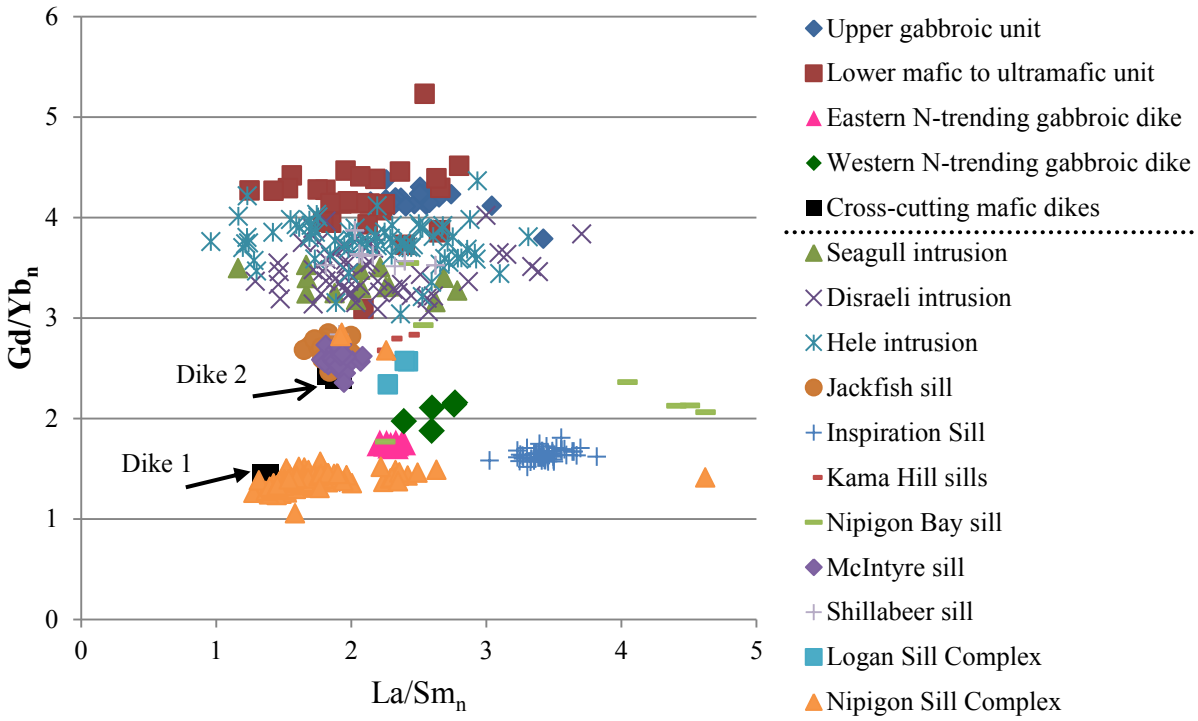

Figure 5.16: Plot of La/Sm$_n$ vs. Gd/Yb$_n$ for the upper gabbroic unit and lower mafic to ultramafic unit of the Thunder intrusion, N-trending gabbroic dikes, cross-cutting mafic dikes and intrusions of the Nipigon Embayment. Chondrite-normalized rare earth element ratios calculated from the values of Sun and McDonough (1989). Nipigon Embayment data from Cundari et al. (2013). Black lines denotes data collected from this study (above) and data from Cundari et al. (2013; below). Indicated on the plot are dike 1 and 2 of cross-cutting mafic dike sample groupings.

5.4.3 Relative timing of emplacement of the N-trending gabbroic dikes

Through mapping, core logging, petrography and whole rock geochemistry multiple distinctive intrusive units have been identified in the Thunder intrusion area that post-date the metavolcanic lithologies of the Archean Shebandowan greenstone belt. The intrusive rocks are easily distinguishable from each other by their incompatible element abundances when plotted on a La/Sm$_n$ vs Gd/Yb$_n$ plot (Fig. 4.38). Three grouping are shown in Figure 4.38: the lower mafic to ultramafic unit + upper gabbroic unit + pegmatitic gabbro, the N-trending gabbroic

dikes, and Group 1 and 2 cross-cutting mafic dikes. The N-trending gabbroic dikes were of interest as they represent possible feeder intrusions to the Thunder intrusion or possible linkages between with other intrusions in the region such as Sunday Lake (Fig. 2.7). The cross-cutting mafic dikes were of interest as they may also represent feeder intrusions to the Thunder intrusion (Figs. 4.9, 4.13). The following will establish a chronological order of emplacement for the intrusive units within the study area.

The N-trending gabbroic dikes are geochemically distinct from the Thunder intrusion (Figs. 4.38, 4.39). Minor differences exist between the two N-trending gabbroic dikes as samples of the western gabbroic dike exhibit an obvious negative Nb anomaly (except sample RTT-BT-237; Fig. 4.39E); whereas samples of the eastern gabbroic dike do not (Fig. 4.39D). However, the relative timing of emplacement is uncertain as there are no direct field relationships observed between the gabbroic dikes and the Thunder intrusion. It is speculated that the gabbroic dikes are MCR-related as they cross-cut the Archean rocks (e.g., Figs. 4.6C, D), are geochemical similar to the Nipigon sills (Figs. 5.16 and 5.17), similar orientation of other north-trending dikes west of the Lake Nipigon that carry MCR signatures (Halls and Stott, 2003; Halls et al., 2005) that have been observed to cross-cut the Nipigon sills (Osmani, 1991), and have no major metamorphic overprint (Appendix C).

These N-trending dikes were also compared to the N-trending 2125 – 2100 Ma, N-trending Marathon dike swarm that occur east of the Lake Nipigon (Ernst et al., 2006). Marathon dikes are characterized by a pronounced negative Eu anomaly which is distinct from the N-trending gabbroic dikes proximal to the study (Fig. 5.18). Therefore, although it is likely that the N-gabbroic dikes are MCR-related, additional geochronology and paleomagnetism is required for the correlation with the other dikes of the MCR.

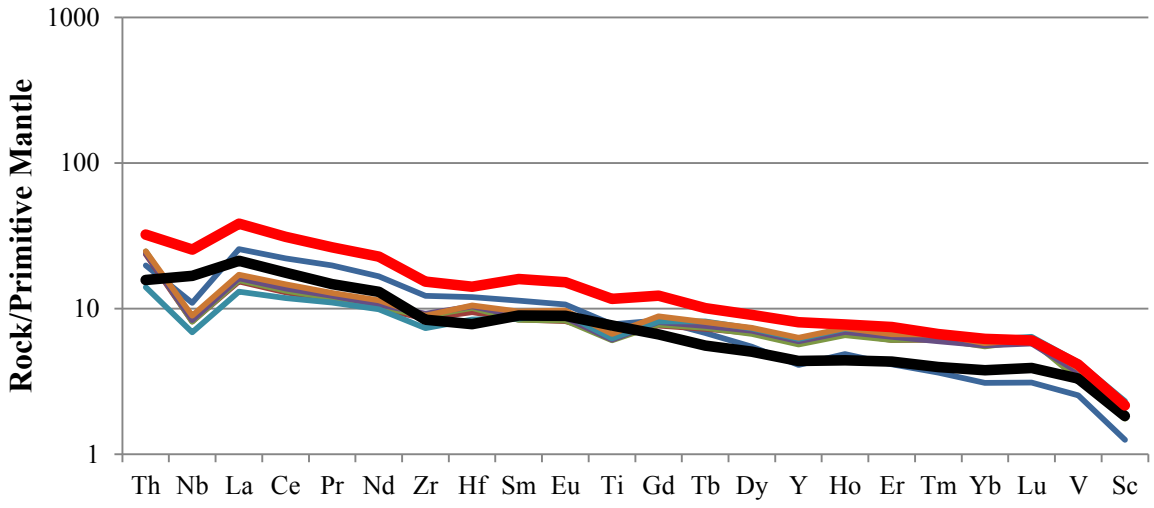

Figure 5.17: Primitive mantle normalized profiles for six representative samples of the Nipigon Sill Complex, one sample of the eastern N-trending gabbroic dike (black; RTT-BT-055) and one sample of the western N-trending gabbroic dike (red; RTT-BT-220). Normalizing values from Sun and McDonough (1989). Nipigon Sill Complex data from Cundari et al. (2013).

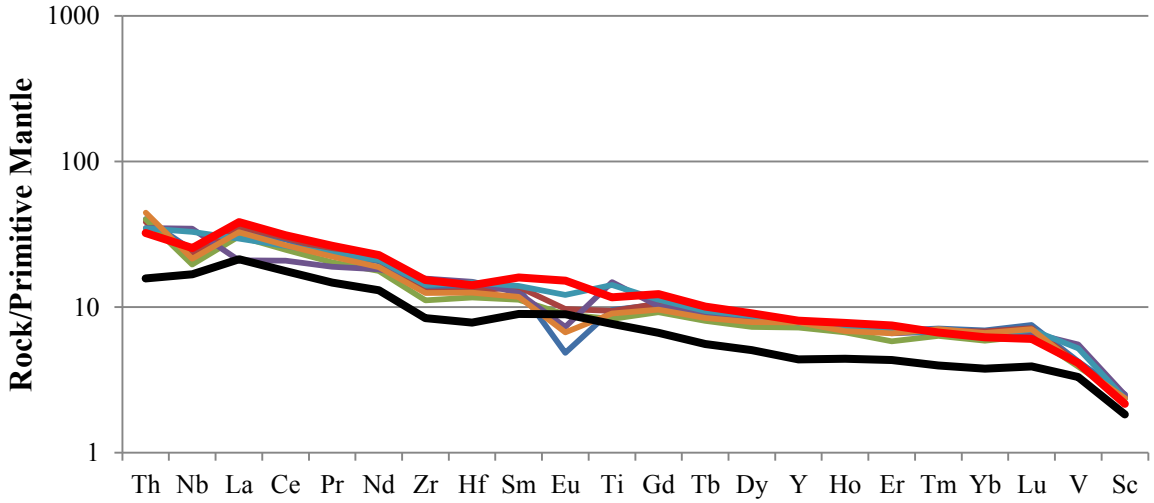

Figure 5.18: Primitive mantle normalized profiles for six representative samples of the Marathon dike swarm, one sample of the eastern N-trending gabbroic dike (black; RTT-BT-055) and one sample of the western N-trending gabbroic dike (red; RTT-BT-220). Normalizing values from Sun and McDonough (1989). Marathon dike data from Halls et al. (2008).

5.4.4 The cross-cutting mafic dikes

The northern margin of the Thunder intrusion is cross-cut by two geochemically distinct mafic dikes (DDHs 05TH002, 003 (Fig. 4.9); 07TH007 (Fig. 4.13). Dike 1 is characterized by relatively low Gd/Yb_n ratios and group 2 dike have relatively high Gd/Yb_n ratios (Figs. 4.38,

5.16). The orientation of the dikes is not well constrained; however, correlating the occurrences from the three drill holes and projected location on surface suggests a steep dip for both dikes and a west to southwest trend. On the regional MCR intrusive plot of La/Sm_n vs. Gd/Yb_n (Fig. 5.16), dike 1 is geochemically similar to the Nipigon Sill Complex and group 1 is geochemically similar to the McIntyre sill and Jackfish sill (Fig. 5.16) suggesting that these mafic dikes were sourced from different parental magmas than the Thunder intrusion but likely travelled along the same conduit. Without confirmation from geochronology or cross-cutting relationships between the two mafic dikes, establishing the relative timing of emplacement for these units is not possible.

CHAPTER 6

CONCLUSIONS

6.1 Summary of the Thunder intrusion

This study has characterized the petrology, mineralization and alteration footprint of the Thunder intrusion within the context of the MCR. To do this, a number of analytical techniques such as petrography, mineral chemistry, whole rock geochemistry and isotopes have been applied to the lithologies and mineralized zones recognized in the Thunder intrusion to develop an emplacement model.

6.1.1 Petrology

Overlapping REE ratios suggest that the upper gabbroic unit and lower mafic to ultramafic unit were sourced from the same parent magma that underwent subsequent differentiation through a combination of fractionation and cumulate processes. Petrological observations are consistent with a four stage cumulus mineral paragenetic sequence: clinopyroxene + olivine, clinopyroxene + olivine + Fe-Ti oxide, plagioclase + clinopyroxene + Fe-Ti oxide and plagioclase + clinopyroxene + Fe-Ti oxide + apatite.

The trace and rare earth element profiles are characterized by LREE enrichment and fractionated HREE, which are broadly comparable to Sun and McDonough (1989)'s modern plume-derived OIB and other early rift mafic to ultramafic intrusions (e.g., Seagull. The presence of a negative Nb anomaly in the upper most section of the upper gabbroic unit, assimilation features including irregular quartz-rich fragments surrounded by pods of granophyre, and an up-hole increase in Th concentrations are all consistent with contamination by older crustal material. The radiogenic Sm-Nd and Rb-Sr isotope signature is similar to the contamination trends of the Nipigon Sills interpreted to be the result of contamination by shallow

basin filling sedimentary rocks (Hollings et al., 2007b). The lack of correlation between Sr_i and in εNd_T ($r = -0.28$) implies that the metavolcanic rocks that immediately underlie the Thunder intrusion were not a likely contaminant to the magma. Expansion of the radiogenic isotope study is required to rule out contamination at depth by a source such as the SCLM or another local rock unit such as the iron formation located in the down-dip direction of the Thunder intrusion.

On a plot of La/Sm_n versus Gd/Yb_n both intrusive units of the Thunder intrusion plot slightly above the field of the mafic to ultramafic intrusions and sills of the Nipigon Embayment (e.g., Hele Intrusion and Shillabeer Sill respectively; Fig. 5.16). The high Gd/Yb_n values are consistent with the interpretation of Hollings et al. (2007a) that the parent magmas of the mafic to ultramafic intrusions of the Nipigon Embayment were derived from a deeper source than the diabase sills (e.g., Nipigon sills). The relatively evolved composition may reflect the involvement of multiple staging chambers during the accent of the parent magma. The parent magma to the Thunder intrusion likely travelled along a conduit through reactivated subprovince boundary deep-seated structures during the Mesoproterozoic rifting event.

6.1.2 Mineralization

The mineralization zone along the basal contact of the lower mafic to ultramafic unit is the primary mineralization in the Thunder intrusion and is interpreted to be the accumulation of immiscible sulphide droplets via gravitational settling. The upper gabbroic unit exhibits weak to no mineralization. Ni-Cu-PGE grades are highest in DDHs 07TH004, 005 and 05TH003, but are poor in 07TH006 and 05TH002. Sulphides typically occur 1 – 5 modal %, rarely up to 30 modal %, and occur as medium- to fine-grained disseminated, coarse-grained globular and rarely net-textured. Pyrrhotite, chalcopyrite and rare pentlandite with common secondary marcasite-pyrite replacement are present, along with trace tellurides, bismuthides, arsenides and unique Ag- and

Au-bearing phases such as argentian pentlandite. As this intrusion is hosted by metavolcanic rocks bearing Ag and Au mineralization, it is possible that wall rock assimilation could account for the precious metal mineralogy observed in the basal mineralization zone.

Whole rock geochemistry indicates fractionated Ni-Cu-PGE patterns consisting of depletion in IPGEs relative to PPGEs for the disseminated sulphide mineralization hosted by the lower mafic to ultramafic unit are similar to the upper massive and semi-massive sulphide zones and Cp-rich veins of the Eagle deposit (Ding et al., 2011). The similarity is consistent with an earlier sulphide liquid phase forming deeper in the system that has concentrated the IPGEs.

The sulphur source appears to be of mantle origin, however, the assimilation of crustal sulphur is a possibility but hard to distinguish as the wall rock S isotope and S/Se^T signature is similar to that of upper mantle.

6.2 Closing remarks

Findings from this study have provided further insight to early-rift mafic to ultramafic magmatism. Regardless of host rock, the Thunder intrusion's geochemical signature is consistent with the other known early-rift mafic to ultramafic intrusions including relatively high Gd/Yb_n values that are consistent with Hollings et al. (2007a) discrimination plot for the intrusions of the Nipigon Embayment and OIB-like characteristics with indications of crustal contamination that are comparable to other early-rift intrusions (e.g., Heggie, 2005; and Hollings et al., 2007b). However, an average % Fo olivine composition of 65 and a calculated mg# of 57 demonstrates that the parent magma that formed the Thunder intrusion is representative of a more evolved magma than other early-rift mafic to ultramafic intrusions such as BIC, Tamarack and Eagle (e.g., Ding et al., 2010; Foley, 2011; Goldner, 2011). This indicates that not all early-rift mafic to ultramafic intrusions found in proximity to Lake Superior basin hosting Ni-Cu-PGE

mineralization were emplaced as primitive melts. In the case of the Thunder intrusion, this may reflect the involvement of multiple staging chambers during the accent of the parent magma. The Thunder parent magma likely travelled along a conduit through reactivated deep-seated structures during the Mesoproterozoic rifting event. The subprovince boundary between the Quetico and Wawa subprovince outlined by the Dog Lake Granite Chain and Nipigon Bay batholiths (Hollings and Kuzmich, 2014) and the relative proximity of early-rift mafic to ultrmafic intrusions such Thunder, Sunday Lake and Current Lake (Fig. 5.15) indicates possible structural control on the distribution of mafic to ultramafic intrusions containing Ni-Cu-PGE sulphide mineralization in the northern Lake Superior region north of the Canada-USA border.

6.3 Future work

Future work on the Thunder intrusion should be carried out as a number of questions remain to be resolved:

- There is an uneven distribution of the basal mineralization zone in the six drill holes that intercept the Thunder intrusion. If additional drilling were to commence, an in-depth petrographic and chemostratigraphic investigation of samples collected at a set interval in other drill holes may provide illumination on the magma chamber dynamics (e.g., R factor; Campbell and Naldrett, 1979), the basal structure and possible wall rock control, additional sulphide horizons, and the potential to host PGE reef.
- Expansion of the S-isotope study as there is a general lack of knowledge regarding S isotope systematics in Archean rocks on the northern side of the Lake Superior (Ripley pers. comm., 2014). Incorporating other lithologies in the surrounding country rock such as the graphitic units (metasedimentary) and the iron formation unit is recommended as

samples collected for this study focused on metavolcanic lithologies from DDH 07TH004 and on surface.

- Additional radiogenic isotope work (Sm-Nd, Rb-Sr, Pb) and geochemical modelling would further elucidate the role of contamination and assimilation during emplacement. Additional lithologies is suggested as samples collected focused only on the lithologies of DDH 07TH004. The Archean granitoid and iron formation unit that occurs south of the Thunder intrusion should be considered as the down-dip direction of the intrusion suggests possible interaction at depth.

REFERENCES

Addison, W.D., Brumpton, G.R., Vallini, D.A., McNaughton, N.J., Davis, D.W., Kissin, S.A., Fralick, P.W. and Hammond, A.L., 2005, Discovery of distal ejecta from the 1850 Ma Sudbury impact event: Geology, v. 33, p. 193-196.

Allen, D.J., Hinze, W.J., Dickas, A.B., and Mudrey, M.G., Jr., 1997, Integrated geophysical modeling of the North American Midcontinent Rift System: New interpretations for western Lake Superior, northwestern Wisconsin, and eastern Minnesota, *in* Ojakangas, R.J., Dickas, A.B., and Green, J.C., eds., Middle Proterozoic to Cambrian Rifting, Central North America: Geological Society of America Special Paper, v. 312, p.47-72.

Amdt, N.T., 2005, The conduits of magmatic ore deposits, *in* Mungall, J.E., ed., exploration for platinum-group element deposits: Mineralogical Association of Canada Short Course, v. 35, p. 181-201.

Ames, D.E., Dare, S.A.S., Hanley, J.J., Hollings, P., Jackson, S.E., Jugo, P.J., Kontak, D.J., Linnen, R.L., and Samson, I.M., 2012., Update on research activities in the targeted geoscience initiative 4 magmatic-hydrothermal nickel-copper-platinum group elements ore system subproject: system fertility and ore vectors, *in* summary of field work and other activities 2012: Ontario Geological Survey, Open File Report 6280.

Avalon Ventures Ltd., 2001, Diamond Drill logs: Thunder Bay Resident Geologist's Office, Assessment File 52H02SW2001, 2.21989.

Ballhaus, C., Bockrath, C., Wohlgemuth-Ueberwasser, C., Laurenc, V., and Berndt, J., 2006, Fractionation of the noble metals by physical processes: Contributions to Mineralogy and Petrology, v. 152, p. 667-684.

Bankey, V., Cuevas, A, Daniels, D., Finn, C.A., Hernandez, I., Hill, P, Kucks, R., Miles, W., Pikington, M., Roberts, C., Roest, W., Rystrom, V., Shearer, S., Snyder, S., Sweeney, R., Velez, J., Philips, J.D., and Ravat, D., 2002, Digital data grids for the magnetic anomaly map of North America: U. S. Geological Survey, Open File Report 02-414.

Barnes, S.J., 1986, The effect of trapped liquid shift crystallization on cumulus mineral compositions in layered intrusions: Contributions to Mineralogy and Petrology, v. 93, p. 524-531.

Barnes, S. J., and Maier, W. D., 1999, The fractionation of Ni, Cu and the noble metals in silicate and sulfide liquids in dynamic processes, *in* Keays, R.R., Lesher, C.M., and Lightfoot, P.C., eds., magmatic ore deposits and their application in mineral exploration: Geological Association of Canada Short Course, v. 13, p. 69-106.

Basaltic Volcanism Study Project., 1981. Basaltic volcanism on the terrestrial planets: New York, Pergamon Press Inc.

Bates, R.L., and Jackson, J.A., eds., 1987, Glossary of geology, 3rd ed: Alexandria, American Geological Institute, 788 p.

Behrendt, J.C., Green, A.G., Cannon, W.F., Hutchinson, D.R., Lee, M.W., Milkereit, B., Agena, W.F., and Spencer, C., 1988, Crustal structure of the Midcontinent rift system—results from GLIMPCE deep seismic reflection profiles: Geology, v. 16, p. 81-85.

Bidwell, G. E., and Marino, F., 2007, Thunder Project: 2007 Field program diamond drilling on the 1245457 claim: Thunder Bay Regional Geologist office, Assessment Files 2.34638.

Borisov, A., and Palme, H., 2000, Solubilities of noble metals in Fe-containing silicate melts as derived from experiments in Fe-free systems: American Mineralogist, v. 85, p. 1665–1673.

Boudreau, A.E., 1999, PELE - A version of the MELTS software program for the PC platform: Computers and Geosciences, v. 25, p. 21-203.

Brenan, J.M., McDonough, W.F., and Ash, R., 2005, An experimental study of the solubility and partitioning of iridium, osmium and gold between olivine and silicate melt: Earth Planet Science Letter, v. 237, p. 855–872.

Brown, G.H., 1995, Precambrian geology, Oliver and Ware townships: Ontario Geological Survey Report 294, 48 p.

Brugmann, G.E., Arndt, N.T., Hofmann, A.W., and Tobschall, H.J., 1987, Noble metal abundances in komatiite suites from Alexo, Ontario, and Gorgona-Island Colombia: Geochimica et Cosmochimic Acta, v. 51, p. 2159–2169.

Burnham, O.M., Hechler, J.H., Semenyna, L., and Schweyer, J., 2002, Mineralogical controls on the determination of trace elements following mixed acid dissolution, *in* Summary of Field Work and Other Activities 2002: Ontario Geological Survey, Open File Report 6100, p. 36-1-36-12.

Burnham, O.M., and Schweyer, J., 2004. Trace element analysis of geological samples by ICP-MS at the Geoscience Laboratories: revised capabilities due to improvements to instrumentation, in Summary of Field Work and Other Activities 2004: Ontario Geological Survey, Open File Report 6145, p. 54-1 to 54-20.

Campbell, I.H., 2001, Identification of ancient mantle plumes, in Ernst, R.E., and Buchan, K.L., eds., Mantle Plumes: Their Identification Through Time: Geological Society of America Special Paper, v. 352, p. 5-21.

Campbell, I.H., 2007, Testing the plume theory: Chemical Geology, v. 241, p. 153-176.

Campbell, I.H., and Naldrett, A.J., 1979, The influence of silicate:sulfide ratios on the geochemistry of magmatic sulfides. Economic Geology, v. 74, p. 1503-1506.

Cannon, W.F., 1994, Closing the Midcontinental Rift—a far-field effect of Grenvillian compression: Geology, v. 22, p. 155–158.

Cannon, W.F., and Hinze, W.J., 1992, Speculations on the origin of the North American Midcontinent Rift: Tectonophysics, v. 213, 49-55.

Cannon, W.F., Green, A.C., Hutchinson, D.R., Lee, M.W., Milkereit, B., Behrendt, J.C., Halls, H.C., Green, J.C., Dickas, A.B., Morey, G.B., Sutcliffe, R.H., and Spencer, C., 1989, The North American Midcontinent Rift beneath Lake Superior from GLIMPCE seismic reflection profiling: Tectonics, v. 8, p. 305-332.

Card, K.D., and Cielsielski, A. 1986, DNAG #1 Subdivisions of the Superior Province of the Canadian Shield: Geoscience Canada, v. 13, p. 5-14.

Chandler, V.W., McSwiggen, P.L., Morey, G.B., Hinze, W.J., and Anderson, R.R., 1989, Interpretation of seismic reflection, gravity and magnetic data across Middle Proterozoic Midcontinent Rift, northwestern Wisconsin, eastern Minnesota and central Iowa: American Association of Petroleum Geology Bulletin, v. 73, p. 261-275.

Chambers, L.A. and Trudinger, P.A., 1979, Microbiological fractionation of stable sulfur isotopes: a review and critique: Journal of Geomicrobiology, v. 1, p. 249–293.

Capobianco, C.J., and Drake, M.J., 1990, Partitioning of ruthenium, rhodium, and palladium between spinel and silicate melt and implications for platinum group element fractionation trends: Geochimica et Cosmochimic Acta, v. 54, p. 869–874.

Capobianco, C.J., Hervig, R.L., and Drake, M.J., 1994, Experiments on crystal liquid partitioning of Ru, Rh and Pd for magnetite and hematite solid-solutions crystallized from silicate melt: Chemical Geology, v. 113, p. 23–43.

Carter, J.L., 1970, Mineralogy and chemistry of the Earth's upper mantle based on the partial fusion – partial crystallization mode: Geological Society of America, Bulletin, v. 81, p. 2021–2034.

Coffin, M.F., and Eldholm, O., 1994, Large igneous provinces: Crustal structure, dimensions, and external consequences: Reviews of Geophysics, v. 32, p. 1–36.

Corfu, F. and Stott, G.M. 1998, Shebandowan greenstone belt, western Superior Province: U-Pb ages, tectonic implications, and correlations: Geological Society of American Bulletin, v. 110, p.1467-1484.

Cundari, R.M., Carl, C.F.J., Hollings, P. and Smyk, M.C. 2013, New and compiled whole-rock geochemical and isotope data of Midcontinent Rift-related rocks, Thunder Bay area: Ontario Geological Survey, Miscellaneous Release Data 308.

Czamanske, G.K., Wooden, J.L., Zientek, M.L., Fedorenko, V.A., Zen'ko, T.E., Kent, J., King, B.S., Knight, R.L., and Siems, D.F., 1994, Geochemical and isotopic constraints on the petrogenesis of the Noril'sk-Talnakh ore-forming systems, *in* Lightfoot, P.C., and Naldrett, A.J. (eds.), Proceedings of the Sudbury-Noril'sk Symposium, Sudbury: Ontrario Geological Survey, Special Volume 5, p. 313-342.

Czamanske, G.K., Zen'ko, T.E., Fedorenko, V.A., Calk, L.C., Budahn, J.R., Bullock, J.H., Jr., Fries, T.L., King, B.S., and Siems, D.F., 1995, Petrography and geochemical characterization of ore-bearing intrusions of the Noril'sk type, Siberia; with discussion of their origin: Resource Geology, Special Issue 18, p. 1-48.

Davis, D.W., and Green, J.C., 1997, Geochronology of the North American Midcontinent rift in western Lake Superior and implications for its geodynamic evolution: Canadian Journal of Earth Science, v. 34, p. 476-488.

Davis, D.W., and Sutcliffe, R.H. 1985, U–Pb ages from the Nipigon Plate and Northern Lake Superior: Geological Society of America Bulletin, v. 96, p. 1572–1579.

Davis, D.W., Pezzuto, F., and Ojakangas, R.W. 1990, The age and provenance of metasedimentary rocks in the Quetico subprovince, Ontario, from single zircon analysis: implications for Archean sedimentation and tectonics in the Superior Province: Earth and Planetary Science Letters, v. 99, p. 195-205.

Deer, W.A., Howie, R.A. & Zussman, J., 1992, An introduction to the rock-forming minerals, 2nd ed.: Harlow, Pearson Education Ltd.

Dickas, A.B., and Mudrey, M.G., Jr., 1997, Segmented structure of the Middle Proterozoic Midcontinent Rift System, North America, *in* Ojakangas, R.J., Dickas, A.B., Green, J.C., eds., Middle Proterozoic to Cambrian rifting, Central North America: Geological Society of America Special Paper, v. 312, p.37-46.

Ding, X., Li, C., Ripley, E. M., Rossell, D., and Kamo, S., 2010, The Eagle and East Eagle sulfide ore-bearing maficultramafic intrusions in the Midcontinent Rift System, upper Michigan: geochronology and petrologic evolution: Geochemisty Geophysics Geosystems, v.11, p. 1-22.

Ding, X., Ripley, E. M., and Li, C., 2011, PGE geochemistry of the Eagle Ni-Cu-(PGE) deposit, upper Michigan: constraints on ore genesis in a dynamic magma conduit: Mineral Deposita, v. 47, p. 89-104.

Ding, X., Ripley, E. M., Shirey, S. B., and Li, C. 2012, Os, Nd, O and S isotope constraints on country rock contamination in the conduit-related Eagle Cu-Ni-(PGE) deposit, Midcontinent Rift System, upper Michingan: Geochimica et Cosmochimic Acta, v. 89, p. 10-30.

Donoghue, K.A., Ripley, E.M., and Li, C., 2014, Sulfur isotope and mineralogical studies of Ni-Cu sulfide mineralization in the Bovine Igneous Complex (BIC Intrusion), Baraga Basin, Northern Michigan: Economic Geology, v. 109, p. 325-341.

Eckstrand, O.R., and Hulbert, L.J., 1987, Selenium and the source of sulphur in magmatic nickel and platinum deposits: Geological Association of Canada-Mineralogical Association of Canada Program with Abstracts, v. 12, p. 40.

Eckstrand, O.R., and Hulbert, L.J., 2007, Magmatic nickel-copper-platinum group element deposits, *in* Goodfellow, W.D., ed., mineral deposits of canada: a synthesis of major deposits types, district metallogeny, the evolution of geological provinces, and exploration methods: Geological Association of Canada, Mineral Deposits Division, Special Publication No. 5, p. 205-222.

Ernst, R.E. and Buchan, K.L., 2001, Large mafic magmatic events through time and links to mantle-plume heads, in Ernst, R.E., and Buchan, K.L., eds., mantle plumes: their identification through time: Boulder, Colorado: Geological Society of America, Special Paper 352, p. 483–575.

Ernst, R.E., and Buchan, K.L., 2002, Maximum size and distribution in time and space of mantle plumes: evidence from large igneous provinces: Journal of Geodynamics, v. 34, p. 309–342.

Ernst, R.E., Buchanan, K.L., and Campbell, I.H., 2005, Frontiers in large igneous province research: Lithos, v. 79, p. 271–297.

Ernst, R.E., Buchan, K.L., Heaman, L.M., Hart, T.R. and Morgan, J., 2006, Multidisciplinary study of north- to north-northeast-trending dikes in the region west of the Nipigon Embayment: Lake Nipigon Region Geoscience Initiative: Ontario Geological Survey, Miscellaneous Release Data 194.

Ernst, R.E., Bleeker, W., Soderlund, U., and Kerr, A., 2013a, Large igneous provinces and supercontinents: toward completing the plate tectonic revolution: Lithos, v. 174, p. 1-14.

Ernst, R.E., Pereirac, E., Hamilton, M., Pisarevsky, S.,Rodriques, J., Tassinari, C., Teixeirah, W., and Van Dunemi, V., 2013b, Mesoproterozoic intraplate magmatic 'barcode' record of the Angola portion of the Congo Craton: newly dated magmatic events at 1505 and 1101 Ma and implications for Nuna (Colombia) supercontinent reconstructions: Precambrian Research, v. 230, p. 103-118.

Farquhar, J., Bao, H., and Thiemens, M., 2000, Atmospheric influences of Earth's sulfur-cycle: Science, v. 289, p. 756-758.

Farquhar, J. and Wing, B.A., 2003, Multiple sulfur isotopes and the evolution of the atmosphere: Earth and Planetary Science Letters, v. 213, p. 1-13.

Fitz, T., 2011, Field Trip 9 - granitic, gabbroic, and ultramafic rocks of the Mellen Intrusive Complex in northern Wisconsin: Institute on Lake Superior Geology Annual Meeting, 57th, Ashland, WI, Proceedings and Abstracts, Part 2, p.166-186.

Fiorentini, M.L., Bekker, A., Rouxel, O., Wing, B., Maier, W., and Rumble, D., 2012, Multiple sulfur and iron isotope composition of magmatic Ni-Cu-(PGE) sulfide mineralization from eastern Botswana: Economic Geology, v. 107, p. 105-116.

Foley, D.J., 2011. Petrology and Cu-Ni-PGE Mineralization of the Bovine Igneous Complex, Baraga County, Northern Michigan: Unpublished M.Sc. Thesis, Duluth, MN, University of Minnesota, Duluth, 211 p.

Franklin, J.M., Mcllwaine, W.H., Poulsen, K.H. and Wanless, R.K., 1980, Stratigraphy and depositional setting of the Sibley Group, Thunder Bay District, Ontario, Canada: Canadian Journal of Earth Sciences, v.17, p. 633-651.

Fralick, P, and Kissin, S.A., 1995, Mid-Proterozoic basin development in central North America: implications of Sibley Group volcanism and sedimentation, in petrology and metallogeny of volcanic and intrusive rocks of the Midcontinent Rift System: International Geological Correlation Program, Project 336, Proceedings, p. 51-52.

Fralick, P., Davis, D.W., Kissin, S.A., 2002, The age of the Gunflint Formation, Ontario, Canada: single zircon U–Pb age determinations from reworked volcanic ash: Canadian Journal of Earth Sciences, v. 39, p. 1085-1091.

Fralick, P., Purdon, R.H., and Davis, D.W., 2006, Neoarchean trans-subprovince sediment transport in western Superior Province: Canadian Journal of Earth Sciences, v. 43, p. 1055-1070.

Geotech Ltd., 2011, Report on a helicopter-borne Z-axis tipper electromagnetic (ZTEM) and aeromagnetic geophysical survey, Thunder Bay North Block for Magma Metals Limited: Thunder Bay Regional Geologist office, Assessment File 2.53477-Revised.

Geul, J.J.C., 1973, Geology of Crooks Township, Jarvis and Prince locations and offshore islands, District of Thunder Bay: Ontario Division of Mines, Geological Report 102, 46 p.

Ghiorso, M.S., and Sack, R.O., 1995, Chemical mass transfer in magmatic processes. IV. A revised and internally consistent thermodynamic model for the interpolation and extrapolation of liquid-solid equilibria in magmatic systems at elevated temperatures and pressures: Contributions to Mineralogy and Petrology, v. 119, p. 197-212.

Goldner, B.D., 2011, Igneous Petrology of the Ni-Cu-PGE Mineralized Tamarack Intrusion, Aitkin and Carlton Counties, Minnesota: Unpublished M.Sc. thesis, Duluth, MN, University of Minnesota, Duluth, 166 p.

Goodgame, V.R., Johnson, J.R., MacTavish, A.D., Stone, W.E., Watkins, K.P., and Wilson, G.C., 2010, The Thunder Bay North Deposit: chonolith-hosted Pt-Pd-Cu-Ni mineralization related to the Midcontinent Rift [abs]: International Platinum Symposium, 11th, Sudbury, Ontario, Abstract Volume, Ontario Geological Survey, Miscellaneous Release Data 269.

Green, J.C., 1982, Geology of the Keweenawan extrusive rocks, in Wold, R.J., and Hinze, W.J., eds., Geology and tectonics of the Lake Superior basin: Geological Society of America Memoir, v. 156, p. 47-56.

Green, J.C., Bornhorst, T.J., Chandler, V.W., Mudrey, M.J., Jr., Myers, P.E., Pesonen, L.J., and Wilband, J.T., 1987, Keweenawan dykes of the Lake Superior region: evidence of evolution of the middle Proterozoic Midcontinent Rift of North America, *in* Hall, H.C. and Farhig, W.F., eds., mafic dyke swarms: Geological Association of Canada, Special Paper, v. 34, p. 289-302.

Habicht, K. and Canfield, D.E., 1997, Sulfur isotope fractionation during bacterial sulfate reduction in organic-rich sediments: Geochimica et Cosmochimica Acta, v. 61, p. 5351–5361.

Halls, H.C. and Stott, G.M., 2003, Paleomagnetic studies of mafic dikes in the vicinity of Lake Nipigon, northwestern Ontario, in summary of field work and other activities 2003: Ontario Geological Survey, Open File Report 6120, p.11-1 to 11-7.

Halls, H.C., Stott, G.M. and Davis, D.W., 2005, Paleomagnetism, geochronology and geochemistry of several Proterozoic mafic dike swarms in northwestern Ontario: Ontario Geological Survey, Open File Report 6171, 59 p.

Halls, H.C., Davis, D.W., Stott, G.M., Ernst, R.E., Hamilton, M.A., 2008, The Paleoproterozoic Marathon large igneous province: new evidence for a 2.1 Ga long-lived mantle plume event along the southern margin of the North American Superior Province: Precambrian Research, v. 162, p. 327–353.

Hanson, R.E., 2003, Proterozoic geochronology and tectonic evolution of southern Africa, in Yoshida, M., Windly, B., and Dasgupta, S., eds., Proterozoic East Gondwana: supercontinent assembly and breakup: Geological Society of London, Special. Publication, v. 206, p. 428-463.

Hanson, R.E., Crowley, J.L., Bowring, S,A., Ramezani, J., Gose, W.A., Dalziel, I.W.D. Pancake, J.A., Seidel, E.K., Blenkinshop, T.G., and Mukwakwami, J., 2004, Coeval large-scale magmatism in the Kalahari and Laurentian cratons during Rodinia assembly: Science, v. 304, p. 1126-1129.

Hanson, R.E., Harmer, R.E., Blenkinshop, T.G., Buller, D.S., Dalziel, I.W.D., Gose, W.A., Hall, R.P., Kampunzu, A.B., Key, R.M., Mukwakwami, J., Munyanyiwa, H., Pancake, J.A., Seidel, E.K., and Ward, E.K., 2006, Mesoproterozoic intraplate magmatism in the Kalahari craton: a review: Journal of African Earth Sciences, v. 44, p. 1055-1086.

Hargreaves, J., 2012, QA/QC: summary of 2010-2012 quality-control data at the Geoscience Laboratories, *in* summary of field work and other activities 2012: Ontario Geological Survey, Open File Report 6280, p.40-1-40-5.

Hart, T.R., and MacDonald, C.A., 2007, Geology and structure of the western margin of the Nipigon Embayment: Canadian Journal of Earth Sciences, v. 44, p. 1021–1040.

Hart, T.M., and Trebilcock, D.M., 2006, Geology of the Hamlin and Wye lakes area, Shebandowan greenstone belt, Thunder Bay, *in* summary of field work and other activities 2006: Ontario Geological Survey, Open File Report 6192, p. 9-1-9-9.

Heaman, L.M., and Easton, R.M., 2006, Preliminary U/Pb geochronology results: Lake Nipigon Region Geoscience Initiative: Ontario Geologic Survey, Miscellaneous Release Data 191, 86 p.

Heaman, L.M. and Machado, 1992, Timing and origin of Midcontinent Rift alkaline magmatism, North America: evidence from the Coldwell Complex: Contributions to Mineralogy and Petrology, v. 110, p. 289-303.

Heaman, L.M., Easton, M., Hart, T.R., Hollings, P., MacDonald, C.A., Smyk, M., 2007, Further refinement to the timing of Mesoproterozoic magmatism, Lake Nipigon Region, Ontario: Canadian Journal of Earth Sciences, v. 44, p. 1055–1086.

Heggie, G.J., 2005, Whole rock geochemistry, mineral chemistry, petrology and Pt, Pd mineralization of the Seagull intrusion, Northwestern Ontario: Unpublished M.Sc. Thesis, Thunder Bay, ON, Lakehead University, 364 p.

Henry, P., Stevenson, R.K., and Gariepy, C., 1998, Late Archean mantle composition and crustal growth in the Western Superior Province of Canada; neodymium and lead isotopic evidence from the Wawa, Quetico, and Wabigoon subprovinces: Geochimica et Cosmochimica Acta, v. 62: p. 143–157.

Hill, R.I., 1991, Starting plumes and continental break-up: Earth and Planetary Science Letters, v. 104, p. 398–416.

Hittelman, A.M, Kinsfather, J.O, and Meyers, H., 1994, Geophysics of North America, DNAG Bouger Gravity (http://dap.geosoft.com/Flamingo/).

Hinze, W.J., Allen, D.J., Fox, A.J., Sunwood, D., Woelk, T., and Green, A.J., 1992, Geophysical investigations and crustal structure of the North American Midcontinent Rift system: Tectonophysics, v. 213, p. 17-32.

Hoffman, P.F., 1989, Precambrian geology and tectonic history of North America, *in* the geology of North America: an overview, volume A: Geological Society of America, p.447-512.

Hollings, P., and Heggie, G., 2014, Rethinking the Midcontinent Right – Puncturing the "Plume Paradigm": Institute on Lake Superior Geology Annual Meeting, 60th, Hibbing, MN, Proceedings and Abstracts, p. 57-58.

Hollings. P., and Kuzmich, B., 2014, Preliminary geochemical analysis of the Nipigon Bay granites, northern Lake Superior: Geological Association of Canada-Mineralogical Association of Canada Program with Abstracts, v. 37, p. 119-120.

Hollings, P., Fralick, P.W., and Kissin, S.A., 2004, Geochemistry and geodynamic implications of the Mesoproterozoic English Bay granite–rhyolite complex, northwestern Ontario: Canadian Journal of Earth Sciences, v. 41, p. 1329–1338.

Hollings, P., Hart, T., Richardson, A., MacDonald, C.A., 2007a, Geochemistry of the Mesoproterozoic intrusive rocks of the Nipigon Embayment, northwestern Ontario: evaluating the earliest phases of rift development: Canadian Journal of Earth Sciences, v. 44, p. 1087–1110.

Hollings, P., Richardson, A., Creaser, R.A., and Franklin, J.M., 2007b, Radiogenic isotope characteristics of the Mesoproterozoic intrusive rocks of the Nipigon Embayment, northwestern Ontario: Canadian Journal of Earth Sciences, v. 44, p. 1111-1129.

Hollings, P., Smyk, M., Heaman, L,M., and Halls, H., 2010, The geochemistry, geochronology, and paleomagnetism of dikes and sills associated with the Mesoproterozoic Midcontinent Rift near Thunder Bay, Ontario, Canada: Precambrian Research, v. 183, p. 553-571.

Hollings, P., Smyk, M., and Cousens, B., 2011, The radiogenic isotope characteristics of dikes and sills associated with the Mesoproterozoic Midcontinent Rift near Thunder Bay, Ontario, Canada: Precambrian Research, v. 214-215, p. 269-279.

Holzheid, A., and Grove, T.L., 2002, Sulfur saturation limits in silicate melts and their implications for core formation scenarios for terrestrial planets: American Mineralogist, v. 87, p. 227-237.

Hutchinson, D.R., White, R.S., Cannon, W.F., and Schulz, K.J., 1990, Keweenawan hot spot: Geophysical evidence for a 1.1 Ga mantle plume beneath the Midcontinent Rift system: Journal of Geophysical Research, v. 95, p. 10869-10844.

Ingall, E.D., 1887, Report of mines and mining on Lake Superior: Geological Survey of Canada, Annual Report, Part H, 124 p.

Irvine, T. N., 1982, Terminology for layered intrusions: Journal of Petrology, v. 23, p. 127-162.

Jenner, G.A., 1996, Trace element geochemistry of igneous rocks: geochemical nomenclature and analytical geochemistry*, in* trace element geochemistry of volcanic rocks: applications for massive sulphide exploration: Geological Association of Canada Short Course, v. 12, p. 51–77.

Johnston D. T., Poulton S. W., Fralick P. W., Wing B. A., Canfield D. E. and Farquhar J., 2006, Evolution of the oceanic sulfur cycle at the end of the Paleoproterozoic: Geochimica et Cosmochimic Acta, v. 70, p. 5723–5739.

Keating, G.L., and Burnham, O.M., 2012, Revision of the calibration for major element analysis of geological samples by wavelength dispersive X-ray fluorescence at the Geoscience Laboratories, *in* summary of field work and other activities 2012: Ontario Geological Survey, Open File Report 6280, p. 39-1-39-4.

Keays, R. R., 1995, The role of komatiitic and picritic magmatism and S-saturation in the formation of ore deposits: Lithos, v. 34, p. 1-18.

Kissin, S. A., Heggie, G. J., Franklin, J. M., and Somarin, A. K., 2007, Sulfide saturation mechanisms in gabbroic intrusions in the Nipigon Embayment: Canadian Journal of Earth Science, v. 44, p. 1203-1214.

Kucks, R.P., 1999, Bouguer gravity anomaly data grid for the conterminous US (http://mrdata.usgs.gov/services/gravity?request=getcapabilities&service=WMS&version=1.1.1).

Kuzmich, B., 2012, Geochemistry and petrology of the Dog Lake Granite Chain, Quetico Basin, Northwestern Ontario: Unpublished B.Sc thesis, Thunder Bay, ON, Lakehead University, 136 p.

Lesher, C.M., and Burnham, O.M., 2001, Multicomponent elemental and isotopic mixing in Ni-Cu-(PGE) ores at Kambalda, Western Australia: Canadian Mineralogist. v. 39, p. 421-446.

Li, C., and Ripley, E.M., 2005, Empirical equations to predict the sulfur content of mafic magmas at sulfide saturation and applications to magmatic sulfide deposits: Mineral Deposita, v. 40, p. 218-230.

Lightfoot, P.C., and Evans-Lamswood, D., 2014, Structural controls on the primary distributrion of mafic-ultramafic intrusions containing Ni-Cu-Co-(PGE) sulfide mienralization in the roots of large igneous provinces: Ore Geology Reviews, v. 64, p. 354-386.

Lightfoot, P.C., Naldrett, A.J., and Hawkesworth, C.J., 1984, The geology and geochemistry of the Waterfall Gorge section of the Insizwa Complex with particular reference to the origin of the nickel sulfide deposits: Economic Geology, v. 79, p. 1857-1879.

Lightfoot, P.C., Sutcliffe, R.H., and Doherty, W., 1991, Crustal contamination identified in Keweenawan Osler Group tholeiites, Ontario: A trace element perspective: Journal of Geology, v. 99, p. 739-760.

Lodge, R.W.D., 2010, Volcanology and lithofacies of the Shebandowan Greenstone Belt, Wawa Subprovince, *in* summary of field work and other activities 2010: Ontario Geological Survey, Open File Report 6260, p. 16-1-16-22.

Lodge, R.W.D., 2011, A progress report on the volcanology, stratigraphy and geodynamic setting of greenstone belts of age 2720 Ma near the Wawa-Quetico Subprovincial boundary, *in* summary of field work and other activities 2011: Ontario Geological Survey, Open File Report 6270, p. 11-1-11-13.

Lodge, R.W.D., 2012, Preliminary results of uranium-lead geochronology from the Shebandowan greenstone belt, Wawa Subprovince, *in* summary of field work and other activities: Ontario Geological Survey, Open File Report 6280, p. 10-1-10-10.

Lodge, R.W.D., 2013, Geology and mineral potential of Aldina Township, Wawa Subprovince, *in* summary of field work and other activities 2013: Ontario Geological Survey, Open File Report 6290, p. 6-1-6-13.

MacDonald, R.D., 1939a, Geology of Gorham Township and Vicinity: Ontario Geological Survey, Annual Report, Part 3, v. 49, p. 1-8.

MacDonald, R.D., 1939b, Gorham Township and vicinity, District of Thunder Bay, Ontario: Ontario Geological Survey, Annual Report, Map 48c, scale 1 inch = 1 mile.

MacTavish, A.D., Heggie, G.J., and Johnson, J.R., 2013, The Thunder Bay North Pt-Pd-Cu-Ni Deposits, *in* proceedings of the 2013 workshop on Ni-Cu-PGE deposits of the Lake Superior region: Precambrian Research Center Short Course, v. 13-01, p. 177-179.

Mandzuik, Z. I., and Scott, S. D., 1997, Synthesis, stability, and phase relations of argentian pentlandite in the system Ag-Fe-Ni-S: Canadian Mineralogist, v. 15, p. 349-364.

Mavrogenes, J.A., and O'Neil, H., 1999, The relative effects of pressure, temperature and oxygen fugacity on the solubility of sulphide in mafic magmas: Geochimica et Cosmochimic Acta, v. 63, p. 1173-1180.

McDonough, W.F., and Sun, S.S., 1995, The composition of the Earth: Chemical Geology, v. 120, p. 223-253.

Meinert, L. D., Dipple, G. M., and Nicolescu, S., 2005, World skarn deposits: Society of Economic Geologists 100th Anniversary Volume, p. 299-336.

Miller, J.D., and Green, J.C., 2002a, Geology of the Beaver Bay Complex and related hypabyssal intrusions, *in* Miller, J.D. Jr., Green, J.C., Severson, M.J., Chandler, V.W., Hauck, S.A., Peterson, D.E., and Wahl, T.E., eds., geology and mineral potential of the Duluth Complex and related rocks of northeastern Minnesota: Minnesota Geological Survey, Report of Investigations, v. 58, p. 144-163.

Miller, J., and Nicholson, S., 2013, Geology and mineral deposits of the1.1Ga Midcontinent Rift in the Lake Superior region: an overview, in field guide to copper-nickel-platinim group element deposits of the Lake Superior region: Precambrian Research Center, Guidebook, v. 13-01, p. 1-50.

Miller, J.D., and Severson, M.J., 2002b, Geology of the Duluth Complex, *in* Miller, J.D. Jr., Green, J.C., Severson, M.J., Chandler, V.W., Hauck, S.A., Peterson, D.E., and Wahl, T.E., eds., Geology and mineral potential of the Duluth Complex and related rocks of northeastern Minnesota: Minnesota Geological Survey, Report of Investigations, v. 58, p. 106-143.

Miller, J.D. Jr., Green, J.C., Severson, M.J., 2002c, Terminology, nomenclature, and classification of Keweenawan igneous rocks of northeastern Minnesota, *in* Miller, J.D. Jr., Green, J.C., Severson, M.J., Chandler, V.W., Hauck, S.A., Peterson, D.E., and Wahl, T.E., eds., geology and mineral potential of the Duluth Complex and related rocks of northeastern Minnesota: Minnesota Geological Survey, Report of Investigations, v. 58, p. 5-20.

Moorhouse, W.W., 1960, Gunflint iron range in the vicinity of Port Authur: Ontario Department of Mines, Annual Report, Part 7, v. 69, p. 1-40.

Morey, G.B., and Green, J.C., 1982, Status of the Keweenawan as a stratigraphic unit in the Lake Superior region, *in* Wold, R.J., and Hinz, W.J., eds., geology and tectonics of the Lake Superior basin: Geological Society of America Memoir, v. 156, p.15-26.

Mungall, J.E., 2005, Geochemistry of the PGE, *in* Mungall, J.E., ed., exploration for platinum-group element deposits: Mineralogical Association of Canada Short Course, v. 35, p. 1-34.

Mungall, J.E., 2014, Geochemistry of Magmatic Ore Deposits: Treatise on Geochemistry 2nd ed., p. 195-217.

Naldrett, A.J., 1969, A portion of the system Fe-S-O between 900 and 1080 °C and its application to sulfide ore magmas: Journal of Petrology, v. 10, p. 171-202.

Naldrett, A.J., 1999, World-class Ni-Cu-PGE deposits: key factors in their genesis. Mineral Deposita, v. 34, p. 227-240.

Naldrett, A.J., 2011, Fundamentals of magmatic sulfide deposits: Reviews in Economic Geology, v. 17, p. 1-50.

Nicholson, S.W. and Shirey, S.B., 1990, Midcontinent Rift volcanism in the Lake Superior Region: Sr, Nd and Pb isotopic evidence for a mantle plume origin: Journal of Geophysical Research, v. 95, p. 10851-10868.

Nicholson, S.W., Shirey, S., Schulz, K., and Green, J., 1997, Rift-wide correlation of 1.1 Ga Midcontinent Rift System basalts: implications for multiple mantle sources during rift development: Canadian Journal of Earth Sciences, v. 34, p. 504–520.

O'Hara, M. J., Fry, N., and Prichard, H. M., 2001, Minor phases as carriers of trace elements in non-modal crystal-liquid separation processes II: illustrations and bearing on behaviour of REE, U, Th and the PGE in igneous processes: Journal of Petrology, v. 42, p. 1887–1910.

Ono, S., Keller, N.S., Rouxel, O., and Alt, J.C., 2012, Sulfur-33 constraints on the origin of secondary pyrite in altered oceanic basement: Geochimica et Cosmochimica Acta, v. 87, p. 323−340.

Ontario Geological Survey, 2003a, Shebandowan area, Ontario airborne magnetic and electromagnetic surveys: Ontario Geological Survey, Geophysical Data Set 1021 - Revised.

Ontario Geological Survey 2003b. Ontario airborne geophysical surveys, single master gravity and aeromagnetic data for Ontario: Ontario Geological Survey, Geophysical Data Set 1036.

Ontario Geological Survey, 2011, 1:250 000 scale bedrock geology of Ontario: Ontario Geological Survey, Miscellaneous Release Data 126 - Revision 1.

Osmani, I.A., 1991, Proterozoic mafic dike swarms in the Superior Province of Ontario, *in* Geology of Ontario: Ontario Geological Survey, Special Volume 4, Part I, p. 661-682.

Osmani, I.A., 1996, Geology and mineral potential of the upper and middle Shebandowan lakes area, west-central Shebandowan greenstone belt: Ontario Geological Survey, Open File Report 5938, 82 p.

Paces, J.B. and Miller, J.D., 1993, Precise U-Pb ages of Duluth Complex and related mafic intrusions, northeastern, Minnesota: new insights for physical, petrogenetic,

paleomagnetic and tectono-magmatic processes associated with 1.1 Ga Midcontinent rifting: Journal of Geophysical Research, v.98, p. 13997-14013.

Pan, Y., Fleet, M.E., and Longstaffe, F.J., 1999, Melt-related metasomatism in mafic granulites of the Quetico Subprovince, Ontario: constraints from O–Sr–Nd isotopic and fluid inclusion data: Canadian Journal of Earth Sciences, v. 36, p. 1449–1462.

Percival, J.A., 2003, Orogenic framework for the Superior Province: dissection of the "Kenoran Orogeny" Geological Survey of Canada, Western Superior NARMAP working group, Online Abstract (http://www.lithoprobe.ca/Contributed%20Abstracts/Oral%20 Presentation/Percival-abstract.pdf).

Piispa, E. J., Smirnov, A.V., and Pesonen, J.P., 2014, Mesoproterozoic Midcontinent Rift intrusives in the Thunder Bay area (Ontario, Canada): a paleomagnetic review: Institute on Lake Superior Geology Annual Meeting, 60th, Hibbing, MN, Proceedings and Abstracts, p. 99-100.

Puchalski, R., 2010, The petrography and geochemistry of the Riverdale Sill: Unpublished B.Sc thesis, Thunder Bay, ON, Lakehead University, 65 p.

Richard, P., Shimizu, N., and Allegre, C.J., 1976, $^{143}Nd/^{146}Nd$, a natural tracer: an application to oceanic basalts: Earth and Planetary Science Letters, v. 31, p. 269-278.

Righter, K., Campbell, A.J., Humayun, M., and Hervig, R.L., 2004, Partitioning of Ru, Rh, Pd, Re, Ir, and Au between Cr-bearing spinel, olivine, pyroxene and silicate melt: Geochimica et Cosmochimic Acta, v. 68, p. 867–880.

Rio Tinto, 2008. Nickel-copper exploration target at Tamarack (Minnesota, USA): Press Release.

Ripley, E.M., 1999, Systematics of sulphur and oxygen isotopes in mafic igneous rocks and Cu-Ni-PGE mineralization in dynamic processes, *in* magmatic ore deposits and their applications in mineral exploration: Geological Association of Canada Short Course, v. 13, p. 111-158.

Ripley, E.M., and Li., C., 2003, Sulfur isotope exchange and metal enrichment in the formation of magmatic Cu-Ni-(PGE) deposits: Economic Geology, v. 98, p. 635-641.

Ripley, E.M., and Li, C., 2011, A review of conduit-related Ni-Cu-(PGE) sulfide mineralization at the Voisey's Bay Deposit, Labrador, and the Eagle Deposit, Northern Michigan, *in* Ripley, E.M. and Li, C., eds., magmatic Ni-Cu and PGE deposits: geology, geochemistry, and genesis: Reviews in Economic Geology, v. 17. p. 181-197.

Ripley, E.M., and Li, C., 2013, Sulfide saturation in mafic magmas: is external sulfur required for the magmatic Ni-Cu-(PGE) ore genesis?: Economic Geology, v. 108, p. 45-58.

Roeder, P. L., and Emslie, R. F., 1970, Olivine-liquid equilibrium: Contributions to Mineralogy and Petrology, v. 29, p. 275-289.

Rogala, B., 2003, The Sibley Group: a lithostratigraphic, geochemical, and paleomagnetic study: Unpublished M.Sc thesis, Thunder Bay, ON, Lakehead University, 254 p.

Rogala, B., Fralick, P.W., and Metsaranta, R., 2005, Stratigraphy and sedimentology of the Mesoproterozoic Sibley Group and related igneous intrusions, northwestern Ontario: Lake Nipigon Region Geoscience Initiative: Ontario Geological Survey, Open File Report 6174.

Rogala, B., Fralick, P.W., Heaman, L.M., Metsaranta, R., 2007, Lithostratigraphy and chemostratigraphy of the Mesoproterozoic Sibley Group, northerwestern Ontario, Canada: Canadian Journal of Earth Sciences, v. 44, p. 1131-1149.

Rossell, D., and Coombes, S., 2005, The geology of the Eagle nickel-copper deposit Michigan, USA: Kennecott Exploration report to Kennecott Minerals Company, 34 p.

Rossell, D., 2008, Geology of the Keweenawan BIC Intrusion: Institute on Lake Superior Geology Annual Meeting, 54th, Marquette, MI, Proceedings and Abstracts, Part 2, p. 181-199.

Sage, R.P., 1991, Alkalic rock, carbonatite and kimberlite complexes of Ontario, Superior Province, *in* Geology of Ontario: Ontario Geological Survey, Special Volume 4, Part I, p. 683-709.

Sage, R.P. and Watkinson, D.H., 1995, Alkalic rocks of the Midcontinent Rift: Institute on Lake Superior Geology, 41st, Marathon, ON, Proceedings and Abstracts, Part 2, p. 1-79.

Schulz, K.J., and Cannoon, W.F., 2007, The Penokean Orogeny in the Lake Superior region: Precambrian Research, v. 157, p. 4-25.

Shirey, S.B., 1997, Re–Os isotopic compositions of Midcontinent Rift System picrites: implications for plume-lithosphere interaction and enriched mantle sources: Canadian Journal of Earth Sciences, v. 34, p. 489–503.

Shirey, S., Klewin, K., Berg, J., and Carlson, R., 1994, Temporal changes in the sources of flood basalts: isotopic and trace element evidence from the 1100 Ma old Keweenawan Mamainse Point Formation, Ontario, Canada: Geochimica et Cosmochimica Acta, v. 58, p. 4475–4490.

Sims, N.P.A., 2010, Assessment Report on 2009 Prospecting on the Gorham Town Property: Ontario Geologic Survey, Assessment Files 2.45681.

Smith, A.R. And Sutcliffe, R.H., 1987, Keweenawan intrusive rocks of the Thunder Bay, *in* summary of field work 1987: Ontario Geological Survey, Miscellaneous Paper 137, p. 248-255.

Stein, M. and Hofmann, A.W., 1994, Mantle plumes and episodic crustal growth: Nature, v. 372, p. 63-68.

Stott, G.M., Corkery, M.T., Percival, J.A., Simard, M., and Goutier, J., 2010, A revised terrane subdivision of the Superior Province, *in* summary of field work and other activities 2010: Ontario Geological Survey, Open File Report 6260, p. 20-1-20-10.

Studley, S.A., Ripley, E.M., Elswick, E.R., Dorais, M.J., Fong, J., Finkelstein, D., and Pratt, L.M., 2002, Analysis of sulfides in whole rock matrices by elemental analyzer-continuous flow isotope ratio mass spectrometry: Chemical Geology, v. 192, p. 141−148.

Sun, S.S., and McDonough, W.F., 1989, Chemical and isotopic systematics of oceanic basalts: implications for mantle composition and processes, *in* magmatism in the ocean basins: Geological Society, Special Publication, v. 42, p. 313-345.

Sutcliffe, R.H., 1987, Petrology of middle Proterozoic diabases and picrites from Lake Nipigon, Canada: Contributions to Mineralogy and Petrology, v. 96, p. 201–211.

Sutcliffe, R.H., 1991, Proterozoic geology of the Lake Superior Area, *in* Geology of Ontario: Ontario Geological Survey, Special Volume 4, Part I, p. 627-658.

Swanson-Hysell, N.L., Maloof, A. C., Weiss, B.P., and Evans, D.A.D., 2009, No asymmetry in geomagnetic reversals recorded by 1.1-billion-year-old Keweenawan basalts: Nature Geoscience, v. 2, p. 713-717.

Swanson-Hysell, N.L., Burgess, S.D., Maloof, A.C., and Bowring, S.A., 2014, Magmatic activity and plate motion during the latent stage of Midcontinent Rift development: Geology, v. 42, p. 475-478.

Thomson, K., 1989, Noranda Exploration Company Limited, report of Gorham Township properties: Ontario Geologic Survey, Assessment File 2.12687.

Thomas, M.D., and Teskey, D.J., 1994, An interpretation of gravity anomalies over the Midcontinent rift, Lake Superior, constrained by GLIMPCE seismic and aeromagnetic data: Canadian Journal of Earth Sciences, v. 31, p. 682-697.

Thurston, P.C., 1991, Archean geology of Ontario: Introduction, *in* Geology of Ontario: Ontario Geological Survey, Special Volume 4, Part I, p. 73-78.

Tomlinson, K.Y., Bowins, R., and Heshler, J., 1998, Refinement of hafnium (Hf) and zirconium (Zr) analysis by improvement in the sample digestion procedure: Ontario Geological Survey, Miscellaneous Paper 169, p. 189–192.

Transition Metals Corp., 2014, Transition Metals and Implats make platinum discovery at Sunday Lake, intersecting 20.2 meters grading 3.22 combined PGM's: Press Release, January 27, 2014.

Trehu, A., Morel-a-l'Huissier, P., Meyer, R., Hajnal, Z., Karl, J., Mereu, R., Sexton, J., Shay, J., Chan, W.-K., Epili, D., Jefferson, T., Shih, X.-R., Wending, S., Milkereit, B., Green, A., and Hutchinson, D., 1991. Imaging the Midcontinent Rift beneath Lake Superior using large aperture seismic data: Geophysical Research Letters, v. 18, p. 625-628.

Vervoort, J.D., Wirth, K., Kennedy, B., Sandland, T., and Harpp, K.S., 2007, The magmatic evolution of the Midcontinent Rift: new geochronologic and geochemical evidence from felsic magmatism: Precambrian Research, v. 157, p. 235-268.

Wager, L.R., and Brown, G.M., 1967, Layered Igneous Rocks: Edinburgh, Oliver and Boyd Ltd. 588 p.

Wager, L.R., Brown, G.M., and Wadsworth, W.J., 1960, Types of igneous cumulates: Journal of Petrology, v. 1, p. 73-85.

Williams, H. R., 1991, Quetico Subprovince, *in* Geology of Ontario: Ontario Geological Survey, Special Volume 4, Part I, p. 383-403.

Williams, H.R., Stott, G.M., Heather, K.B., Muir, T.L., and Sage, R.P., 1991, Wawa Subprovince, *in* Geology of Ontario: Ontario Geological Survey, Special Volume 4, Part I, p. 485-539.

Zaleski, E., van Breemen, O., and Peterson, V.L., 1999, Geological evolution of the Manitouwadge greenstone belt and Wawa-Quetico subprovince boundary, Superior Province, Ontario, constrained by U-Pb zircon dates of supracrustal and plutonic rocks: Canadian Journal of Earth Science, v. 36, p. 945-966.

Zartman, R.E., Nicholson, S.W., Cannon, W.F., and Morey, G.B., 1997, U-Th-Pb zircon ages of some Keweenawan Supergroup rocks from the south shore of Lake Superior: Canadian Journal of Earth Sciences, v. 34, p. 549-561.

APPENDIX A

Representative petrographic descriptions

UTM datum NAD83 Zone 16

Sample: RTTC-BT-005
UTM: 330319E 5377910N
DDH: 05TH001
Depth: 112 m
Lithology: Uncertain
Unit: Iron formation
Description:

Sample consists mostly of semi-massive granular magnetite intergrown with abundant inclusions and rosette-like andradite-grossular garnet with stilpnomelane core. The minerals are intergrown with minor amounts of anhedral pyrrhotite, chalcopyrite, patches of semi-massive pyrite and abundant medium-grained euhedral to subhedral apatite. Empty cavities in thin section observed.

Primary/secondary minerals:

- **Quartz:** trace, fine- to medium-grained, intergrown with carbonate.
- **Garnet:** 22%, fine-grained, subhedral to euhedral, andradite-grossular composition, concentrically zoned, pale brown color in plane polarized light, rosette-like cores of dark brown stipnomelane.
- **Stilpnomelane:** 10%, fine-grained, anhedral, dark brown acicular aggregates comprising the cores of garnets and interstitial to the sulphides and apatite.
- **Actinolite:** 2%, fine-grained, acicular aggregates, intergrown with stilpnomelane.
- **Apatite:** 4%, fine- to medium-grained, subhedral to euhedral, elongate habit, abundant inclusions of stilpnomelane (?).
- **Carbonate:** 2%, fine-grained, anhedral, lining voids filled with quartz, interstitial to the intergrowth of garnet and magnetite.

Opaque minerals:

- **Pyrite:** 10%, very fine- to fine-grained, anhedral to suhbedral, granular and semi-massive texture (recrystallization?), intergrown with garnet and magnetite.
- **Chalcopyrite:** 1%, very fine- to fine-grained, anhedral, rimming/intergrown with pyrite and magnetite.
- **Pyrrhotite:** 4%, fine-grained to very fine-grained, intergrown with magnetite, pyrite and chalcopyrite.
- **Magnetite:** 45%, very fine- to fine-grained, granular and pitted forming semi-massive texture, intergrown with all minerals.
- **Sphalerite:** trace, very fine-grained, translucent orange grains, intergrown with pyrite.

Sample: RTTC-BT-006
UTM: 330319E 5377910N
DDH: 05TH001
Depth: 111 m
Lithology: Uncertain
Unit: Iron formation
Description:

Sample similar to RTTC-BT-005 except more garnet and less magnetite. The sample consists of abundant andradite-grossular garnet intergrown with and rimmed by aggregates of stilpnomelane and minor carbonate, and intergrown with fine-grained granular magnetite and coarse-grained apatite. Anhedral pyrrhotite, chalcopyrite and pyrite fill some of the carbonate-rimmed interstices.

Primary/secondary minerals:

- **Garnet:** 60%, fine-grained, subhedral to euhedral, andradite-grossular composition, concentrically zoned, pale brown color in plane polarized light, commonly clustered into large masses.
- **Stilpnomelane:** 8%, fine-grained, anhedral, dark brown acicular aggregates intergrown with garnet and rimming interstices between sulphides and apatite.
- **Actinolite:** 2%, fine-grained, acicular aggregates, intergrown with stilpnomelane.
- **Apatite:** 13%, coarse-grained, anhedral crystals forming large masses intergrown with garnet and stilpnomelane, abundant inclusions of stilpnomelane (?).
- **Carbonate:** 3%, fine-grained, anhedral, lining or filling voids and intergrown with sulphides.

Opaque minerals:

- **Pyrite:** 2%, very fine- to fine-grained, anhedral to suhbedral, granular masses in interstices.
- **Chalcopyrite:** 1%, very fine- to fine-grained, anhedral, intergrown with pyrrhotite and carbonate in interstices.
- **Pyrrhotite:** 1%, very fine- to fine-grained, patches intergrown with magnetite.
- **Magnetite:** 10%, very fine- to fine-grained, granular and clustered, commonly surrounding garnet.

Sample: RTTC-BT-034
Location: 330435E 5378298N
DDH: 05TH**003**
Depth: 296 m
Lithology: Mineralized feldspathic peridotite
Unit: Thunder intrusion - lower mafic to ultramafic unit
Description:

Feldspathic peridotite consisting of fine-grained cumulus olivine pseudomorphs and medium-grained cumulus clinopyroxene, surrounded by interstitial plagioclase, biotite and hornblende. Olivine pseudomorphs consist of talc + serpentine + magnetite; plagioclase with common sericite and serpentine alteration pits; clinopyroxene more resistive to alteration. Disseminated sulphides consisting of intergrown pyrrhotite + chalcopyrite + pentlandite. Pyrrhotite commonly replaced by patchy graphic intergrowth of pyrite + marcasite + secondary sulphide.

Primary minerals:

- **Olivine:** 20%, very fine- to fine-grained, subhedral, cumulus mineral and chadacrysts in clinopyroxene, complete replacement by talc + serpentine + magnetite.
- **Clinopyroxene:** 30%, medium-grained, subhedral, cumulus mineral, lamellar twinning, hosts olivine chadacrysts.
- **Plagioclase:** 10%, interstitial and poikilitic with biotite, chlorite, Fe-Ti oxide and sulphide inclusions, modal percent varies throughout slide, common alteration patches of sericite and serpentine.
- **Biotite:** 10%, very fine- to fine-grained, subhedral to anhedral, interstitial to the cumulus minerals, commonly clustered, pleochroic brown to reddish brown (Ti-bearing), commonly rimming Fe-Ti oxide.
- **Hornblende:** 1%, fine-grained, anhedral, pleochroic brown, interstitial to the cumulatus minerals, commonly rimming biotite and Fe-Ti oxide.
- **Apatite:** trace, very fine-grained, euhedral, elongate crystal, inclusions in plagioclase and piercing into biotite grains, also as inclusions in biotite.

Secondary minerals:

- **Talc:** very fine-grained, associated with olivine alteration, makes up a large percentage of the 20% olivine.
- **Serpentine:** 5%, very fine-grained, alteration patches in plagioclase and rimming clinopyroxene.
- **Actinolite:** trace, observed in patches in plagioclase and associated with hydrous mineral clusters
- **Sericite:** trace, very fine-grained, alteration pits in plagioclase

Opaque minerals:

- **Pyrrhotite:** 8%, medium- to fine-grained, anhedral, intergrown with chalcopyrite and Fe-Ti oxide, hosts pentlandite flames, common marcasite + pyrite + secondary magnetite alteration patches.
- **Chalcopyrite:** 4%, fine-grained, anhedral, intergrown with pyrrhotite.
- **Pentlandite**: trace, very fine-grained, flames in pyrrhotite.
- **Pyrite/Marcasite:** 6%, fine-to medium-grained, anhedral to subhedral, graphic intergrowth with secondary magnetite occurring as alteration patches in pyrrhotite.
- **Fe-Ti oxide:** 6%, fine-grained, anhedral interstitial grains to the silicates and subhedral lobes intergrown with sulphides, commonly rimmed by biotite and hornblende, consists of magnetite with ilmenite lamellae and magnetite intergrown with ilmenite.
- **Secondary Magnetite:** trace, very fine-grained, anhedral grains associated with olivine alteration.

Sample: RTTC-BT-048
Location: 330435E 5378298N
DDH: 07TH002
Depth: 155 m
Lithology: Volcanic breccias and tuff
Unit: Footwall rocks
Description:

A foliated, fragmental volcanic rock consisting of lenticular fragments of various lithologies including very fine-grained intergrown quartz and feldspar fragments and angular feldspar-rich fragments. The fragments are angular and elongated parallel to foliation. The lenticular fragments are surrounded by veins consisting of intergrown quartz + carbonate + chlorite that are also parallel to foliation. The rock is overprinted by epidote + chlorite + actinolite + pyrite (greenschist metamorphism). The pyrite occurs as very fine- to fine-grained disseminations to clusters that are commonly poikiloblastic. The clusters are also elongated parallel to foliation.

Primary/secondary minerals:

- **Quartz:** 10%, very fine-grained in veins intergrown with carbonate and quartz; very fine-grained intergrown with feldspar in fragments.
- **Feldspar:** 20%, very fine-grained, anhedral intergrown with quart in fragments; medium- to coarse-grained fragments with a pitted texture overprinted by epidote + chlorite + actinolite.
- **Actinolite:** 12%, very fine-grained, overprinting the protolith.
- **Chlorite:** 2%, very fine-grained, intergrown with carbonate and quartz in veins.
- **Carbonate:** 2%, very fine-grained, intergrown with chlorite and quartz in veins.

- **Epidote:** 36%, very fine-grained, overprinting the protolith.

Opaque minerals:

- **Pyrite:** 18%, very fine-grained, subhedral to eubhedral granular disseminations to clusters, elongated in direction of the foliation, overprinting the protolith, commonly poikiloblastic.
- **Chalcopyrite:** trace, very fine-grained, anhedral, intergrown in the quartz + carbonate + chlorite veins.

Sample: RTTC-BT-049
Location: 330435E 5378298N
DDH: 07TH002
Depth: 147 m
Lithology: Spotted volcanic breccias and tuff
Unit: Footwall rocks
Description:

A foliated rock consisting of layers of very fine-grained clinopyroxene and titanite aggregates in a matrix composed dominantly of kaolinite (formerly feldspar?) giving the rock a pervasive pale brownish grey color. Throughout the rock, medium-grained kaolinitized feldspar augen and lenses/veinlets of carbonate, clinopyroxene, titanite, actinolite and pyrite occur.

Primary/secondary minerals:

- **Clinopyroxene:** 35%, very fine-grained and overprinting kaolinite/feldspathic matrix; fine-grained and subhedral in lenses/veinlets.
- **Titanite:** 3%, very fine-grained, granular aggregates overprinting kaolinite/feldspathic matrix; very fine-grained crystals in lenses/veinlets.
- **Carbonate:** 1%, very fine-grained, infilling lenses/veinlets.
- **Actinolite:** trace, very fine-grained, intergrown with carbonate in lenses/veinlets.
- **Quartz:** 10%, very fine-grained, anhedral, deformed in veins and fragments.
- **Feldspar:** 50%, very fine-grained comprising the matrix of the rock and strongly kaolinitized, also as kaolinitized augen.

Opaque minerals:

- **Pyrite:** 8%, very fine-grained, micro-vein filling, disseminations in lenses,
- **Chalcopyrite:** trace, very fine-grained, intergrown with carbonate and pryrite in veins

---

Sample: RTTC-BT-062
Location: 330319E 5377910N
DDH: 07TH004
Depth: 311 m
Lithology: Pegmatitic gabbro
Unit: Thunder intrusion – pegmatitic pod in the lower mafic to ultramafic unit
Description:

Coarse-grained intergrown plagioclase and clinopyroxene producing a weakly developed subophitic texture. Altered Fe-Ti oxide occurs as disseminations with skeletal texture preserving the ilmenite lamellae. Plagioclase is partially to completely replaced by kaolinite; clinopyroxene more resistant to alteration but commonly rimmed by actinolite and hornblende. Abundant, fine-grained euhedral apatite crystals pierce into the above primary minerals. The interstitial space between plagioclase and clinopyroxene is commonly infilled with very fine-grained actinolite, titanite and secondary magnetite. Trace disseminated very fine-grained chalcopyrite occurs throughout the alteration and very fine-grained spongy pyrite in plagioclase.

Primary minerals:

- **Clinopyroxene:** 10% coarse-grained, subhedral, partial replacement by actinolite, intergrown with plagioclase.
- **Plagioclase:** 85%, medium-grained to coarse grained laths, complete replacement by kaolinite.
- **Apatite:** trace%, fine-grained, subhedral to euhedral, abundant inclusions in plagioclase and piercing into clinopyroxene and Fe-Ti oxide.

Alteration minerals:

- **Actinolite:** 1%, very fine-grained, anhedral, rimming clinopyroxene and intergrown with hornblende, infilling interstitial spaces of altered primary minerals.
- **Hornblende:** trace, fine-grained, rimming clinopyroxene and intergrown with actinolite.
- **Titanite**: trace, very fine-grained, within the interstitial spaces of plagioclase and clinopyroxene and associated with alteration.

Opaque minerals:

- **Chalcopyrite:** trace, very fine-grained, anhedral, disseminations.
- **Pyrite:** trace, very fine-grained, spongy textured, associated with plagioclase replacement.
- **Fe-Ti oxide**: 4%, fine- to medium-grained, anhedral (skeletal), disseminated, altered with only the ilmenite lamellae remaining, magnetite completely altered/dissolved.
- **Secondary magneite:** trace, associated with the alteration.

Sample: RTTC-BT-063
DDH: 07TH004
DDH UTM: 330319E 5377910N
Depth: 306 m
Lithology: Clinopyroxenite with alteration vein
Unit: Thunder intrusion – lower mafic to ultramafic unit
Description:

Clinopyroxenite consisting of cumulus clinopyroxene and olivine intergrown with magnetite and interstitial plagioclase. Olivine occurs partially to completely replaced by serpentine + magnetite alteration whereas clinopyroxene more resistant to alteration. The clinopyroxenite is cross-cut by a diffuse alteration vein consisting of dominantly of magnetite, carbonate, pyrite + chalcopyrite and actinolite. Actinolite occurs along the margins of the vein as fans of curvy acicular aggregates piercing into the carbonate core. Vein magnetite forms stringy to granular pseudomorphs replacing an unknown mineral and is intergrown with carbonate and the sulphides. Along the margins of the vein clinopyroxene crystals are coarse-grained while plagioclase and olivine are completely replaced by serpentine + carbonate alteration and primary magnetite is partially replaced by titanite (a thin alteration halo). Outside of the vein, patches of carbonate ± pyrite associated with olivine replacement occur.

Primary minerals:

- **Olivine:** 3%, fine- to very fine-grained, subhedral, cumulus to chadacrysts in clinopyroxene, partial to complete replacement serpentine + magnetite alteration.
- **Clinopyroxene:** 70%, mostly fine- to medium-grained and coarse-grained along margin of alteration vein, subhedral to anhedral, cumulus, common simple and lamellar twinning, rarely poikilitc with olivine chadacrysts.
- **Plagioclase:** 2%, interstitial to clinopyroxene and olivine, replaced by serpentine proximal to vein margin.
- **Biotite:** trace, very fine-grained, pleochroic reddish brown, intergrown with clinopyroxene.

Alteration minerals:

- **Serpentine:** 3%, very fine-grained, replacing olivine and along clinopyroxene fractures, replacing plagioclase in vicinity of the alteration vein.
- **Carbonate:** 6%, coarse-grained, anhedral, intergrown with actinolite, magnetite, chlorite, pyrite and chalcopyrite in the alteration vein.
- **Actinolite:** 4%, fine-grained, fans of curved acicular aggregates along the margins of the vein, intergrown with carbonate.
- **Magnetite:** 4%, fine- to medium-grained, elongate stringy to granular pseudomorphs in vein replacing unknown mineral, intergrown with carbonate and the sulphides.
- **Chlorite:** 1%, fine-grained, intergrown with actinolite in vein.

- **Epidote:** 1%, fine-grained, intergrown with actinolite and magnetite in vein.
- **Titanite:** 1%, fine-grained, anhedral to subhedral, replacing primary magnetite in vicinity of vein.

Opaque minerals:

- **Magnetite:** 2%, fine- to medium-grained, anhedral to poikilitic intergrown with clinopyroxene, disseminated.
- **Chalcopyrite:** trace, fine-grained, anhedral, intergrown with pyrite in the sulphide patches of the alteration vein, rare inclusions in clinopyroxene.
- **Pyrite-pyrrhoitite:** 3%, fine-grained, intergrown with secondary magnetite in vein.

Sample: RTTC-BT-065A
DDH: 07TH004
DDH UTM: 330319E 5377910N
Depth: 287 m
Lithology: Gabbro with alteration vein
Unit: Thunder intrusion – upper gabbroic unit
Description:

Altered gabbro consisting of abundant plagioclase laths intergrown with clinopyroxene clusters and Fe-Ti oxide disseminations with a subophitic texture. Plagioclase is almost completely replaced by sericite. Fe-Ti oxide disseminations consisting of magnetite with abundant ilmenite lamellae. The gabbro is cross-cut by a diffuse alteration vein consisting dominantly of secondary magnetite with a lath-like crystal habit, coarse-grained euhedral apatite and anhedral pyrite + chalcopyrite intergrowths. The vein margin consists of cummingtonite intergrown the host rock (a thin alteration halo).

Primary minerals:

- **Olivine:** 3%, fine-grained, relicts, subhedral to anhedral, replaced by serpentine + magnetite pseudomorphs.
- **Clinopyroxene:** 20%, medium- to fine-grained, subhedral to anhedral, commonly clusters, common lamellar twinning, common alteration pits and biotite and secondary magnetite inclusions.
- **Plagioclase:** 55%, medium- to fine-grained, lath-shaped, relicts, completely replaced by sericite, intergrown with clinopyroxene.
- **Biotite:** trace, very fine-grained, pleochroic reddish brown, inclusions in clinopyroxene.

Alteration minerals:

- **Sericite:** complete replacement of plagioclase.
- **Actinolite:** trace, fine-grained, intergrown with serpentine in alteration vein.

- **Cummingtonite:** 2%, medium-grained, anhedral, intergrown with clinopyroxene at vein margin.
- **Epidote:** trace, fine-grained, replacing plagioclase and serpentine.
- **Titanite:** 1%, fine-grained, intergrown with magnetite at the alteration vein margin.
- **Carbonate:** trace, fine-grained, intergrown with actinolite, serpentine and magnetite at the alteration vein margin, intergrown with magnetite and apatite in vein core.
- **Apatite:** 1%, coarse-grained, euhedral, intergrown with alteration vein minerals, very fine-grained intergrowths in the host rock.

Opaque minerals:

- **Fe-Ti oxide:** 5%, fine- to medium-grained, subhedral to anhedral, disseminated to clusters, intergrown with plagioclase and clinopyroxene, magnetite with ilmenite lamellae.
- **Magnetite:** 10%, fine- to medium-grained, lath-shaped replacing altered plagioclase, intergrown with pyrite, also associated with olivine pseudomorphs.
- **Pyrite:** 3%, very fine-grained, anhedral, spongy to lath shaped replacing altered plagioclase, intergrown with alteration vein minerals.
- **Chalcopyrite:** trace, fine- to very fine-grained, intergrown with pyrite.

Sample: RTTC-BT-065B
DDH: 07TH004
DDH UTM: 330319E 5377910N
Depth: 287 m
Lithology: Gabbro with alteration vein
Unit: Thunder intrusion – upper gabbroic unit
Description:

Similar to RTTC-BT-065A but sampling a different alteration vein in the gabbro. Altered gabbro consisting of abundant plagioclase laths intergrown with clinopyroxene clusters and Fe-Ti oxide disseminations producing an overall subophitic texture. Plagioclase is almost completely replaced by sericite. Fe-Ti oxide disseminations consisting of magnetite with abundant ilmenite lamellae. The gabbro is cross-cut by a diffuse alteration vein consisting dominantly of secondary magnetite with a lath-like crystal habit, coarse-grained euhedral apatite and anhedral pyrite + chalcopyrite intergrowths. The vein margin consists of cummingtonite intergrown the host rock (a thin alteration halo).

Primary minerals:

- **Olivine:** 3%, fine-grained, relict crystals, subhedral to anhedral, replaced by serpentine + magnetite pseudomorphs.

- **Clinopyroxene:** 25%, medium- to fine-grained, subhedral to anhedral, commonly clusters, common lamellar twinning, common alteration pits and biotite and secondary magnetite inclusions.
- **Plagioclase:** 50%, medium- to fine-grained, lath-shaped, relicts, completely replaced by sericite, intergrown with clinopyroxene.
- **Biotite:** trace, very fine-grained, pleochroic reddish brown, inclusions in clinopyroxene.

Alteration minerals:

- **Sericite:** complete replacement of plagioclase.
- **Actinolite:** trace, fine-grained, intergrown with serpentine in alteration vein.
- **Cummingtonite:** 1%, medium-grained, anhedral, intergrown with clinopyroxene at alteration vein margin.
- **Epidote:** trace, fine-grained, replacing plagioclase and serpentine.
- **Titanite:** 1%, fine-grained, intergrown with magnetite at the alteration vein margin.
- **Carbonate:** trace, fine-grained, intergrown with actinolite, serpentine and magnetite at the alteration vein margin, intergrown with magnetite and apatite in vein core.
- **Apatite:** 2%, coarse-grained, euhedral, intergrown with alteration vein minerals, very fine-grained intergrowths in the host rock.

Opaque minerals:

- **Fe-Ti oxide:** 5%, fine- to medium-grained, subhedral to anhedral, disseminated to clusters, intergrown with plagioclase and clinopyroxene, magnetite with ilmenite lamellae.
- **Magnetite:** 10%, fine- to medium-grained, lath-shaped replacing altered plagioclase, intergrown with pyrite, also associated with olivine pseudomorphs.
- **Pyrite:** 3%, very fine-grained, anhedral, spongy to lath shaped replacing altered plagioclase, intergrown with alteration vein minerals.
- **Chalcopyrite:** trace, fine- to very fine-grained, intergrown with pyrite.

Sample: RTTC-BT-077
DDH: 07TH004
DDH UTM: 330319E 5377910N
Depth: 84 m
Lithology: Hematized gabbro
Unit: Thunder intrusion – upper gabbroic unit
Description:

Gabbro consisting of abundant plagioclase laths intergrown with clinopyroxene clusters, commonly rimmed by hornblende and Fe-Ti oxide disseminations producing an overall subophitic texture. Plagioclase is almost completely replaced sericite. Fe-Ti oxide disseminations consisting of magnetite with abundant ilmenite lamellae. Plagioclase is

completely replaced by sericite. The altered plagioclase is also rimmed by and interstices filled are filled with reddish stained (hematite overprint) alkali feldspar in graphic intergrowth with minor quartz giving the rock a pinkish tint. Rare olivine pseudomorphs consisting of serpentine + actinolite + magnetite.

Primary minerals:

- **Olivine:** trace, fine-grained, relicts, subhedral to anhedral, replaced by serpentine + actinolite + magnetite pseudomorphs.
- **Clinopyroxene:** 20%, medium- to fine-grained, subhedral to anhedral, commonly clusters, common lamellar twinning, commonly rimmed by hornblende.
- **Plagioclase:** 50%, medium- to fine-grained, lath-shaped, relicts, completely replaced by sericite and overprinted by a rusty red alkali feldspar (hematized), intergrown with clinopyroxene.
- **Hornblende:** 4%, medium-grained, anhedral, commonly intergrown/rimming clinopyroxene.
- **Biotite:** trace, very fine-grained, pleochroic reddish brown, altered by chlorite, intergrown with primary minerals.
- **Apatite:** trace, fine-grained, euhedral to subhedral, piercing into primary minerals

Alteration minerals:

- **Alkali feldspar:** 10%, very fine-grained, rusty red color overprinting plagioclase along the rims and interstices, intergrown with quartz.
- **Quartz:** 1%, very fine-grained, graphic intergrowth with alkali feldspar and interstitial to altered plagioclase.
- **Actinolite:** 6%, very fine-grained, replacing clinopyroxene and hornblende.
- **Serpentine:** 2%, very fine-grained, replacing olivine along with secondary magnetite.
- **Epidote:** trace, fine-grained, associated with plagioclase alteration.
- **Titanite:** trace, very fine-grained aggregates intergrown with serpentine + magnetite alterations.

Opaque minerals:

- **Fe-Ti oxide:** 6%, fine- to medium-grained, subhedral to anhedral, disseminated to clusters, intergrown with plagioclase and clinopyroxene, magnetite with ilmenite lamellae, magnetite intergrown with ilmenite.
- **Magnetite:** 1%, fine- to very fine-grained, associated with olivine pseudomorphs.
- **Pyrite:** trace, very fine-grained, associated with epidote replacement.
- **Chalcopyrite:** trace, fine- to very fine-grained, inclusions in Fe-Ti oxides and altered plagioclase.

Sample: RTTC-BT-079
DDH: 07TH004
DDH UTM: 330319E 5377910N
Depth: 58 m
Lithology: Hematized gabbro
Unit: Thunder intrusion – upper gabbroic unit
Description:

Gabbro consisting of abundant plagioclase laths intergrown with clinopyroxene clusters, commonly rimmed by hornblende and Fe-Ti oxide disseminations producing an overall subophitic texture. Fe-Ti oxide disseminations consisting of magnetite with abundant ilmenite lamellae. Plagioclase is almost completely replaced sericite. The altered plagioclase is also rimmed by and interstices filled are filled with reddish stained (hematite overprint) alkali feldspar in graphic intergrowth with minor quartz giving the rock a pinkish tint. Rare olivine pseudomorphs consisting of chlorite + actinolite + magnetite. Patches of epidote intergrown with amphibole, carbonate and chalcopyrite. Common fine-to medium-grained apatite intergrown with plagioclase and clinopyroxene.

Primary minerals:

- **Olivine:** trace, fine-grained, relicts, subhedral to anhedral, replaced by serpentine + actinolite + magnetite pseudomorphs.
- **Clinopyroxene:** 20%, medium- to fine-grained, subhedral to anhedral, commonly clusters, common lamellar twinning, commonly rimmed by hornblende.
- **Plagioclase:** 50%, medium- to fine-grained, lath-shaped, relicts, completely replaced by sericite and overprinted by a rusty red alkali feldspar (hematized), intergrown with clinopyroxene.
- **Hornblende:** 5%, medium-grained, anhedral, commonly intergrown/rimming clinopyroxene.
- **Biotite:** trace, very fine-grained, pleochroic reddish brown, altered by chlorite, intergrown with primary minerals.
- **Apatite:** 1%, fine- to medium-grained, euhedral to subhedral, piercing into primary minerals

Alteration minerals:

- **Alkali feldspar:** 20%, very fine-grained, rusty red color overprinting plagioclase along the rims and interstices, intergrown with quartz.
- **Quartz:** 1%, very fine-grained, graphic intergrowth with alkali feldspar and interstitial to altered plagioclase.
- **Actinolite:** 1%, very fine-grained, replacing clinopyroxene and hornblende.
- **Serpentine:** 2%, very fine-grained, replacing olivine along with secondary magnetite.
- **Epidote:** 2%, fine-grained, interstitial to plagioclase and hornblende, intergrown with carbonate and chalcopyrite.

- **Titanite:** trace, very fine-grained aggregates intergrown with serpentine + magnetite alteration.
- **Chlorite:** 4%, fine-grained, associated with plagioclase and clinopyroxene alteration.
- **Carbonate:** trace, fine-grained, anhedral, associated with epidote replacement.

Opaque minerals:

- **Fe-Ti oxide:** 5%, fine- to medium-grained, subhedral to anhedral, disseminated to clusters, intergrown with plagioclase and clinopyroxene, magnetite with ilmenite lamellae, magnetite intergrown with ilmenite.
- **Magnetite:** 1%, fine- to very fine-grained, associated with olivine pseudomorphs.
- **Pyrite:** trace, very fine-grained, associated with epidote replacement.
- **Chalcopyrite:** trace, fine- to very fine-grained, anhedral, inclusions in amphibole surrounding magnetite-ilmenite, and intergrown with epidote.

Sample: RTTC-BT-089
DDH: 07TH004
Location: 330319E 5377910N
Depth: 437 m
Lithology: Feldspathic peridotite
Unit: Thunder intrusion - lower mafic to ultramafic unit
Description:

Feldspathic peridotite consisting of coarse-grained, zoned, cumulus clinopyroxene and medium-grained cumulus olivine surrounded by interstitial plagioclase, biotite and amphibole. The feldspathic peridotite hosts disseminations of pyrrhotite + chalcopyrite + magnetite + trace pentlandite. Olivine partially replaced by talc + serpentine + magnetite alteration; clinopyroxene resistant to alteration. Alteration patches of chlorite + actinolite and veins permeate plagioclase. Rare sulphide liquid droplets consisting of intergrown pyrrhotite, chalcopyrite and trace pentlandite hosted by interstitial plagioclase and biotite.

Primary minerals:

- **Olivine:** 10%, fine- to medium-grained, subhedral, cumulus mineral, heavily fractured, dusted with very fine-grained magnetite inclusions, common partial replacement by talc + serpentine + magnetite, occurs as a cumulate mineral encased by interstitial plagioclase to clustering with pyroxenes, rarely enclosed by pyroxenes.
- **Clinopyroxene:** 55%, fine- to coarse-grained, subhedral, cumulus mineral, commonly zoned, simple and lamellar twinning, poikilitic with biotite, olivine and magnetite chadacrysts.
- **Plagioclase:** 20%, interstitial and variable distribution, hosts clusters of amphibole and biotite, sericite alteration pits, patches of actinolite + chlorite alteration.

- **Biotite:** 2%, fine- to very fine-grained, subhedral to anhedral, pleochroic reddish brown (Ti-bearing), rimming Fe-Ti oxide, commonly chadacrysts in clinopyroxene, commonly rimmed by chlorite.
- **Horneblende:** 1%, fine-grained, anhedral, pleochroic brown to reddish brown (Ti-bearing), intergrown with Fe-Ti oxide, sulphides and apatite.
- **Apatite:** trace, very fine-grained, subhedral to euhedral, elongate crystals, observed within interstitial plagioclase and piercing into biotite grains.

Alteration minerals:

- **Sericite:** trace, very fine-grained, occurs as alteration pits in interstitial plagioclase.
- **Talc:** 3%, very fine-grained, associated with olivine replacement, intergrown with talc.
- **Serpentine:** 2%, very fine-grained, associated with olivine replacement, intergrown with talc.
- **Actinolite:** trace, fine-grained, intergrown with serpentine and chlorite and occurs as alteration patches in plagioclase.
- **Chlorite:** 1%, fine-grained, anhedral, intergrown with serpentine and actinolite and occurs as alteration patches in plagioclase, also rimming biotite.

Opaque minerals:

- **Pyrrhotite**: 1%, fine- to medium-grained, intergrown with chalcopyrite, sphalerite and Fe-Ti oxide, hosts pentlandite flames and blocks.
- **Chalcopyrite**: 1%, fine-grained, intergrown with pyrrhotite, sphalterite and Fe-Ti odixde.
- **Pentlandite**: trace, very fine-grained, intergrown with pyrrhotite and chalcopyrite, rimmed by secondary magnetite.
- **Sphalerite**: trace, very fine-grained, intergrown with pyrrhotite and chalcopyrite, rimming pentlandite.
- **Galena**: trace, very fine-grained, inclusions in pyrrhotite.
- **Fe-Ti oxide:** 4%, fine-grained, subhedral to anhedral, magnetite with ilmenite lamellae, and magnetite + ilmenite intergrowths.
- **Secondary magnetite:** 1%, very fine-grained grained, associated with serpentine + talc alteration of olivine.

Sample: RTTC-BT-090
Locations: 330319E 5377910N
DDH: 07TH004
Depth: 437 m
Lithology: Hornfels with sulphide stringers
Unit: Footwall rocks
Description:

Very fine-grained gabbroic rock consisting of anhedral grains of clinopyroxene, biotite and hornblende, surrounded by interstitial feldspar that is commonly pierced by euhedral acicular apatite. Overall rock has a allotriomorphic texture. The hornfels hosts a diffuse vein consisting of very fine-grained anhedral clinopyroxene + actinolite. The vein appears to have introduced sulphide stringers consisting of intergrown pyrrhotite + chalcopyrite + pentlandite + magnetite. Sulphide patches consisting of a similar mineralogy also occur throughout the hornfels. Primary sulphide minerals are replaced by patches of a graphic intergrowth of pyrite + marcasite + secondary magnetite. Plagioclase grains display undulose extinction indicating strain.

Secondary minerals:

- **Feldspar:** 45%, very fine-grained, anhedral, interstitial to clinopyroxene and biotite, pierced by euhedral acicular apatite, displays undulose extinction.
- **Clinopyroxene:** 35%, very fine-grained, anhedral, granular, intergrown with sulphides and feldspar.
- **Biotite:** 4%, very fine-grained, anhedral, intergrown with plagioclase and clinopyroxene.
- **Hornblende:** 5%, very fine-grained, anhedral, intergrown with plagioclase and clinopyroxene.
- **Apatite:** trace, very fine-grained, euhedral, acicular, piercing into feldspar.
- **Chlorite:** 1%, very fine-grained, anhedral, intergrown with the other secondary minerals.
- **Actinolite:** 2%, very fine-grained, anhedral, intergrown with clinopyroxene in the vein and interstitial to the sulphides.
- **Titanite:** trace, very fine-grained, anhedral, associated with the actinolite + clinopyroxene vein.

Opaque minerals:

- **Pyrite:** 2%, very fine-grained, associated with patchy sulphide alteration consisting of a graphic intergrowth of pyrite + marcasite + secondary magnetite, also disseminated in the host rock.
- **Marcasite:** trace, very fine-grained, anhedral, associated with patchy sulphide alteration consisting of a graphic intergrowth of pyrite + marcasite + secondary magnetite
- **Pyrrhotite:** 1%, very fine- to fine-grained, anhedral, intergrown with chalcopyrite and Fe-Ti oxide.
- **Chalcopyrite:** 2%, very fine- to fine-grained, anhedral, intergrown with pyrrhotite and Fe-Ti oxide.

- **Pentlandite:** trace, very fine-grained, anhedral, remnants observed along the grain boundary of pyrrhotite and chalcopyrite.
- **Sphalerite:** trace, very fine-grained, inclusions in chalcopyrite
- **Cobaltite:** trace, very fine-grained, anhedral, occurring along the grain boundaries of pyrrhotite, chalcopyrite and pentlandite.
- **Fe-Ti oxide:** 1%, very fine-grained, anhedral aggregates to lobed, intergrown with sulphides, magnetite with exsollution lamellae.
- **Secondary magnetite:** 1%, very fine-grained, anhedral, aggregates, scattered throughout the hornfels rock and associated with sulphide alteration.

Sample: RTTC-BT-091
DDH: 07TH004
DDH UTM: 330319E 5377910N
Depth: 432 m
Lithology: Olivine melagabbro
Unit: Thunder intrusions - lower mafic to ultramafic unit
Description:

Olivine melagabbro consisting of coarse-grained, zoned, cumulus clinopyroxene and coarse-grained cumulus olivine surrounded by interstitial plagioclase, biotite and amphibole. The olivine melagabbro hosts disseminations of pyrrhotite + chalcopyrite + magnetite + trace pentlandite. Olivine partially replaced by talc + serpentine + magnetite alteration; clinopyroxene resistant to alteration. Alteration patches of chlorite + actinolite in plagioclase. Rare sulphide liquid droplets consisting of intergrown pyrrhotite, chalcopyrite and trace pentlandite hosted by interstitital plagioclase, biotite and amphibole. Pyrrhotite commonly replaced by secondary marcasite patches.

Primary minerals:

- **Olivine:** 4%, fine- to medium-grained, subhedral, cumulus mineral, heavily fractured, common partial to complete replacement by talc + serpentine + magnetite, rarely chadacrystics in clinopyroxene.
- **Clinopyroxene:** 30%, fine- to medium-grained, subhedral, cumulus mineral, commonly zoned, simple and lamellar twinning, poikilitic with biotite, olivine and magnetite chadacrysts.
- **Plagioclase:** 40%, interstitial and variable distribution, hosts clusters of amphibole and biotite, sericite alteration pits, patches of actinolite + chlorite alteration.
- **Biotite:** 6%, fine- to very fine-grained, subhedral to anhedral, pleochroic reddish brown (Ti-bearing), rimming Fe-Ti oxide, commonly chadacrysts in clinopyroxene, commonly rimmed by chlorite.

- **Horneblende:** 2%, fine-grained, anhedral, pleochroic brown to reddish brown (Ti-bearing), intergrown with Fe-Ti oxide, sulphides and apatite.
- **Apatite:** trace, very fine-grained, subhedral to euhedral, elongate crystals, observed within interstitial plagioclase and piercing into biotite grains.

Alteration minerals:

- **Sericite:** trace, very fine-grained, occurs as alteration pits in interstitial plagioclase.
- **Talc:** 1%, very fine-grained, associated with olivine replacement, intergrown with serpentine.
- **Serpentine:** 8%, very fine-grained, associated with olivine replacement, intergrown with talc.
- **Actinolite:** 2%, fine-grained, intergrown with serpentine and chlorite and occurs as alteration patches in plagioclase.
- **Chlorite:** 1%, fine-grained, anhedral, intergrown with serpentine and actinolite and occurs as alteration patches in plagioclase, also rimming biotite.

Opaque minerals:

- **Pyrrhotite**: 1%, fine- to medium-grained, anhedral, intergrown with chalcopyrite, Fe-Ti oxide and very fine-grained pentlandite flames/blocks.
- **Chalcopyrite**: 1%, fine-grained, anhedral, intergrown with pyrrhotite and pentlandite.
- **Pentlandite**: trace, very fine-grained, intergrown with pyrrhotite and chalcopyrite, rimmed by secondary magnetite.
- **Marcasite:** trace, very fine-grained, anhedral, replacing pyrrhotite.
- **Fe-Ti oxide:** 3%, fine-grained, subhedral to anhedral, magnetite with ilmenite lamellae, and magnetite + ilmenite intergrowths.
- **Secondary magnetite:** 1%, very fine-grained grained, associated with serpentine + talc alteration of olivine.

Sample: RTTC-BT-092
DDH: 07TH004
DDH UTM: 330319E 5377910N
Depth: 426 m
Lithology: Feldspathic peridotite
Unit: Thunder intrusion - lower mafic to ultramafic unit
Description:

Feldspathic peridotite consisting of coarse-grained, zoned, cumulus clinopyroxene and coarse-grained cumulus olivine surrounded by interstitial plagioclase, biotite and amphibole. The feldspathic peridotite hosts < 1 % disseminations of pyrrhotite + chalcopyrite + magnetite + trace pentlandite. Olivine partially replaced by talc + serpentine + magnetite alteration; clinopyroxene resistant to alteration. Alteration patches of chlorite + actinolite in plagioclase.

Rare sulphide liquid droplets consisting of intergrown pyrrhotite, chalcopyrite and trace pentlandite hosted by interstitital plagioclase, biotite and amphibole. Pyrrhotite commonly replaced by secondary marcasite patches.

Primary minerals:

- **Olivine:** 8%, fine- to medium-grained, subhedral, heavily fractured, cumulus mineral, common partial to complete replacement by talc + serpentine + magnetite, rarely chadacrysts in clinopyroxene.
- **Clinopyroxene:** 70%, fine- to medium-grained, subhedral, cumulus mineral, commonly zoned and simple twinning, poikilitic with biotite, olivine and magnetite chadacrysts.,
- **Plagioclase:** 10%, interstitial and variable distribution, hosts clusters of amphibole and biotite, sericite alteration pits, patches of actinolite + chlorite alteration.
- **Biotite:** 4%, fine- to very fine-grained, subhedral to anhedral, pleochroic reddish brown (Ti-bearing), rimming Fe-Ti oxide, commonly chadacrysts in clinopyroxene, commonly rimmed by chlorite.
- **Hornblende:** 2%, fine-grained, anhedral, pleochroic brown to reddish brown (Ti-bearing), intergrown with Fe-Ti oxide, sulphides and apatite.
- **Apatite:** trace, very fine-grained, subhedral to euhedral, elongate crystals, observed within interstitial plagioclase and piercing into biotite grains.

Alteration minerals:

- **Sericite:** trace, very fine-grained, occurs as alteration pits in interstitial plagioclase.
- **Talc:** trace, very fine-grained, associated with olivine replacement, intergrown with talc.
- **Serpentine:** 1%, very fine-grained, associated with olivine replacement, intergrown with talc.
- **Actinolite:** trace, fine-grained, intergrown with serpentine and chlorite and occurs as alteration patches in plagioclase.
- **Chlorite:** trace, fine-grained, anhedral, intergrown with serpentine and actinolite and occurs as alteration patches in plagioclase, also rimming biotite.

Opaque minerals:

- **Pyrrhotite**: trace, fine- to medium-grained, anhedral, intergrown with chalcopyrite, Fe-Ti oxide, very fine-grained pentlandite and trace blocky pyrite.
- **Chalcopyrite**: trace, fine-grained, anhedral, intergrown with pyrrhotite and pentlandite.
- **Pentlandite**: trace, very fine-grained, intergrown with pyrrhotite and chalcopyrite, rimmed by secondary magnetite.
- **Pyrite**: trace, very fine-grained, blocky aggregates in pyrrhotite and rimmed by magnetite.
- **Fe-Ti oxide:** 4%, fine-grained, subhedral to anhedral, magnetite with ilmenite lamellae, and magnetite + ilmenite intergrowths.

- **Secondary magnetite:** 1%, very fine-grained, associated with serpentine + talc alteration of olivine.

Sample: RTTC-BT-093
DDH: 07TH004
DDH UTM: 330319E 5377910N
Depth: 410 m
Lithology: Feldspathic peridotite
Unit: Thunder intrusion - lower mafic to ultramafic unit
Description:

Feldspathic peridotite consisting of medium-grained olivine enclosed in coarse-grained clinopyroxene, hornblende and plagioclase. Multiple fine-grained parallel ribbons of fine-grained secondary magnetite occur in serpentine, clinopyroxene and hornblende but not in olivine or plagioclase, and faint layering of the mafic minerals gives the rock a banded appearance. Olivine commonly pseudomorphed by serpentine + magnetite. Very fine-grained chalcopyrite and bornite observed intergrown with the secondary magnetite ribbons.

Primary minerals:

- **Olivine:** 15%, fine- to medium-grained, subhedral, partial to complete replacement by serpentine + magnetite, commonly chadacrysts in plagioclase, clinopyroxene and amphibole.
- **Clinopyroxene:** 25%, medium- to coarse grained, subhedral to anhedral, poikilitic with olivine chadacrysts, intergrown with plagioclase, hornblende and olivine
- **Plagioclase:** 14%, interstitial, oikocrystic and enclosing olivine, clinopyroxene and hornblende, rare patches of chlorite alteration.
- **Biotite:** 1%, very fine- to fine-grained, anhedral, pleochroic reddish brown (Ti-bearing), rare inclusions in clinopyroxenes, interstitial to mafic minerals, cleavage planes lined with secondary magnetite.
- **Hornblende:** 15%, medium- to coarse-grained, pleochroic pale orange, oikocrystic and intergrown with olivine, plagioclase and clinopyroxene.
- **Apatite**: trace, very fine-grained, subhedral to euhedral, elongate crystals, encased in plagioclase.

Alteration minerals:

- **Serpentine:** 25%, very fine-grained, partial to complete replacement of olivine + secondary magnetite
- **Chlorite:** trace, very fine-grained, alteration patches in plagioclase.

Opaque minerals:

- **Chalcopyrite:** trace, very fine-grained, anhedral, patches that are intergrown with bornite and magnetite.
- **Pyrite:** trace, very fine-grained, anhedral, lace-like in serpentine.
- **Bornite:** trace, very fine-grained, anhedral, patches that are intergrown with chalcopyrite and magnetite.
- **Fe-Ti oxide:** 1%, fine- to very fine-grained, anhedral and interstitial to the silicate minerals.
- **Secondary Magnetite:** 4%, very fine-grained, anhedral, parallel ribbons occurring in serpentine, clinopyroxene and hornblende but not in olivine or plagioclase, fracture infill.

Sample: RTTC-BT-094
Location: 330319E 5377910N
DDH: 07TH004
Depth: 404 m
Lithology: Melagabbro
Unit: Thunder intrusion - lower mafic to ultramafic unit
Description:

Melagabbro consisting of medium-grained, cumulus clinopyroxene and fine-grained, cumulus olivine surrounded by interstitial plagioclase, biotite and hornblende. Olivine partially replaced by talc + serpentine + magnetite alteration; clinopyroxene resistant to alteration. Abundant sericite alteration patches in plagioclase. Traces disseminated sulphides consisting of intergrown chalcopyrite and bornite, and commonly rimming Fe-Ti oxide in the interstitial.

Primary minerals:

- **Olivine:** 8%, fine-grained, subhedral, cumulus mineral, pseudomorphed by serpentine + chlorite + magnetite rarely goethite (iddingsite), fine to very fine grained, subhedral, heavily fractured, cumulate to inclusions in pyroxenes.
- **Clinopyroxene:** 46%, medium- to fine-grained clusters, subhedral, cumulus mineral, rarely zoned, simple and lamellar twinning, poikilitc with biotite, hornblende and olivine chadacrysts.
- **Plagioclase:** 36%, interstitial and poikilitic with cumulus mineral chadacrysts, abundant sericite alteration patches and minor chlorite alteration patches.
- **Biotite:** 3%, very fine- to fine-grained, subhedral to anhedral, pleochroic reddish brown (Ti-bearing), commonly intergrown with hornblende, and Fe-Ti oxide.
- **Hornblende:** 2%, medium- to fine-grained, anhedral to subhedral, pleochroic orange brown to reddish brown (Ti-bearing), intergrown with biotite and Fe-Ti oxide.
- **Apatite:** trace, very fine-grained, subhedral to euhedral, elongate crystals, piercing into plagioclase and biotite.

Alteration minerals:

- **Serpentine:** 2%, very fine-grained, associated with olivine replacement.
- **Chlorite:** trace, very fine-grained, anhedral, intergrown with actinolite and occurring as alteration patches in plagioclase.
- **Actinolite:** trace, very fine-grained, anhedral, intergrown with chlorite and occurring as alteration patches in plagioclase.
- **Sericite**: very fine-grained, 75% of the plagioclase altered by patches of sericite alteration.

Ore minerals:

- **Chalcopyrite**: trace, very fine-grained, anhedral, inclusions in clinopyroxene and as disseminations in the interstitial, commonly intergrown with bornite.
- **Bornite**: trace, very fine-grained, intergrown with chalcopyrite.
- **Fe-Ti oxide:** 3%, fine-grained, subhedral to anhedral, magnetite with ilmenite lamellae and magnetite intergrown with ilmenite, interstitial to silicates, commonly rimmed by biotite and hornblende.
- **Secondary magnetite:** trace, very fine-grained, associated with olivine replacement.

Sample: RTTC-BT-095
Location: 330319E 5377910N
DDH: 07TH004
Depth: 376 m
Lithology: Feldspathic peridotite
Unit*:* Thunder intrusion – lower mafic to ultramafic unit.
Description:

Feldspathic peridotite consisting of medium-grained, cumulus clinopyroxene and fine-grained, cumulus olivine surrounded by interstitial plagioclase, biotite and hornblende. Olivine partially replaced by talc + serpentine + magnetite alteration; clinopyroxene resistant to alteration. Abundant sericite alteration patches and minor patches of chlorite in plagioclase. Trace disseminated sulphides consisting of intergrown chalcopyrite and bornite, and commonly rimming Fe-Ti oxide in the interstitial.

Primary minerals:

- **Olivine:** 8%, fine- to very fine-grained, subhedral, pseudomorphed by serpentine + talc + magnetite, cumulus mineral and as chadacrysts in clinopyroxene..
- **Clinopyroxene:** 65%, medium- to fine-grained are rare fine- to very fine-grained clusters, subhedral, cumulus mineral, simple and lamellar twinning, rare zoning, poikilitc with biotite, amphibole, and olivine chadacrysts.
- **Plagioclase:** 20%, interstitial and poikilitic enclosing cumulus minerals, ¾ of the plagioclase is overprinted by sericite alteration patches, common apatite inclusions.

- **Biotite:** 1%, very fine-grained, anhedral, pleochroic reddish brown (Ti-bearing), interstitial and rarely inclusion in clinopyroxenes, commonly clustered and rimming hornblende, and Fe-Ti oxide.
- **Hornblende:** trace, fine to very fine-grained, anhedral and rarely subhedral, strong pleochroic orange brown (Ti-bearing), commonly rimming Fe-Ti oxide, common clustered with biotite.
- **Apatite:** trace, very fine-grained, subhedral to euhedral, elongate crystals, piercing into plagioclase and biotite.

Alteration minerals:

- **Serpentine:** 6%, very fine-grained, associated with olivine replacement.
- **Chlorite:** trace, very fine-grained, anhedral, rimming biotite.
- **Sericite**: very fine grained, 75% of the plagioclase altered by patches of sericite alteration.

Opaque minerals:

- **Chalcopyrite**: trace, very fine-grained, anhedral, disseminated, interstitial the cumulus minerals.
- **Bornite**: trace, very fine-grained, intergrown with chalcopyrite.
- **Fe-Ti oxide:** 2%, fine-grained, subhedral to anhedral, magnetite with ilmenite lamellae and magnetite intergrown with ilmenite, interstitial to silicates, commonly rimmed by biotite and hornblende.
- **Secondary magnetite:** trace, very fine-grained, associated with olivine replacement.

Sample: RTTC-BT-096
Location: 330319E 5377910N
DDH: 07TH004
Depth: 356 m
Lithology: Feldspathic peridotite
Unit: Thunder intrusion - lower mafic to ultramafic unit
Description:

Feldspathic peridotite consisting of medium-grained, cumulus clinopyroxene and fine-grained, cumulus olivine surrounded by interstitial plagioclase, biotite and hornblende. Olivine partially replaced by talc + serpentine + magnetite alteration; clinopyroxene resistant to alteration. Abundant sericite alteration patches and minor patches of chlorite in plagioclase. Trace disseminated sulphides consisting of intergrown chalcopyrite and bornite, and commonly rimming Fe-Ti oxide in the interstitial.

Primary minerals:

- **Olivine:** 8%, fine- to medium-grained, subhedral, cumulus mineral to very fine-grained chadacrysts in clinopyroxene, commonly pseudomorphed by serpentine + talc + magnetite.
- **Clinopyroxene:** 65%, medium-grained to fine-grained clusters, subhedral, cumulus mineral, simple and lamellar twinning, rarely poikilitc with biotite and olivine chadacrysts.
- **Plagioclase:** 20%, interstitial and poikilitic with cumulus mineral inclusions, patches of sericite alteration, common apatite inclusions.
- **Biotite:** 2%, very fine- to fine-grained, anhedral, pleochroic reddish brown (Ti-bearing), interstitial and rarely inclusion in clinopyroxene, rimming Fe-Ti oxide.
- **Hornblende:** trace, fine- to very fine-grained, anhedral and rarely subhedral, strong pleochroic orange brown, rimming biotite and Fe-Ti oxide.
- **Apatite:** trace, very fine-grained, subhedral to euhedral, elongate crystals, piercing into plagioclase and biotite.

Alteration minerals:

- **Talc:** trace, very fine-grained, associated with olivine replacement.
- **Serpentine:** 3%, very fine-grained, associated with olivine replacement.
- **Chlorite:** trace, very fine-grained, anhedral, rimming biotite.
- **Actinolite:** trace, very fine-grained, rimming hornblende.
- **Sericite**: very fine-grained, abundant alteration patches in plagioclase.

Opaque minerals:

- **Chalcopyrite**: trace, very fine-grained, anhedral, disseminations in the interstitial.
- **Bornite**: trace, very fine-grained, intergrown with chalcopyrite.
- **Fe-Ti oxide:** 2%, fine-grained, subhedral to anhedral, magnetite with ilmenite lamellae and magnetite intergrown with ilmenite, interstitial to silicates, commonly rimmed by biotite and hornblende.
- **Secondary magnetite:** trace, very fine-grained, associated with olivine replacement.

Sample: RTTC-BT-097
Location: 330319E 5377910N
DDH: 07TH004
Depth 323 m
Lithology: Melagabbro
Unit: Thunder intrusion - lower mafic to ultramafic unit
Description:

Melagabbro consisting of medium-grained, cumulus clinopyroxene and fine-grained, cumulus olivine surrounded by interstitial plagioclase, biotite and hornblende. Olivine partially

to completely replaced by serpentine + magnetite alteration. Patches of intense alteration of clinopyroxene consisting of intergrown actinolite and chlorite along with serpentized olivine. Abundant sericite alteration patches and minor patches of chlorite in plagioclase. Traces disseminated sulphides consisting of intergrown chalcopyrite and bornite, and commonly rimming Fe-Ti oxide in the interstitial.

Primary minerals:

- **Olivine:** 10%, fine- to very fine-grained, subhedral, cumulus mineral to very fine-grained chadacrysts in clinopyroxene, common psuedomorphs consisting of serpentine + magnetite.
- **Clinopyroxene:** 40%, medium- to fine-grained, subhedral, cumulus minerals, simple and lamellar twinning, rare olivine chadacrysts.
- **Plagioclase:** 20%, interstitial, patches of sericite alteration.
- **Biotite:** 6%, very fine- to fine-grained, anhedral, pleochroic reddish brown (Ti-bearing), interstitial and rarely inclusion in clinopyroxene, commonly intergrown and chlorite and rimming Fe-Ti oxides.
- **Apatite:** trace, fine- to very fine-grained, subhedral, elongate crystals, piercing into plagioclase and biotite.

Alteration minerals:

- **Serpentine:** 4%, very fine-grained, associated with olivine replacement.
- **Chlorite:** 3%, very fine-grained, anhedral, associated with actinolite and clinopyroxene replacement.
- **Actinolite:** 9%, very fine-grained, associated with chlorite and clinopyroxene replacement.
- **Sericite**: 3%, very fine-grained, alteration patches in plagioclase.
- **Titanite**: trace, very fine-grained, aggregates in alteration patches.

Opaque minerals:

- **Chalcopyrite**: trace, very fine-grained, anhedral, disseminations in the interstitial and rimming Fe-Ti oxide.
- **Bornite**: trace, very fine-grained, intergrown with chalcopyrite.
- **Fe-Ti oxide**: 5%, fine- to very fine-grained, subhedral to anhedral, magnetite with ilmenite lamellae and magnetite intergrown with ilmenite, interstitial to silicates, commonly rimmed by biotite and hornblende.
- **Secondary magnetite:** trace, very fine-grained, associated with olivine replacement.

Sample: RTTC-BT-098
Location: 330319E 5377910N
DDH: 07TH004
Depth: 318 m
Lithology: Melagabbro
Unit: Thunder intrusion - lower mafic to ultramafic unit
Description:

Melagabbro consisting of medium-grained, cumulus clinopyroxene and fine-grained, cumulus olivine surrounded by interstitial plagioclase. Olivine partially replaced by serpentine + magnetite alteration; clinopyroxene resistant to alteration. Common sericite alteration patches in plagioclase. Serpentinized fractures observed cross-cut the rock. Trace disseminated sulphides consisting of intergrown chalcopyrite + bornite + pyrite, and are commonly rimming Fe-Ti oxide in the interstitial.

Primary minerals:

- **Olivine:** 10%, fine- to medium-grained, subhedral, cumulus mineral, rarely very fine-grained chadacrysts in clinopyroxene, common partial replacement by serpentine + magnetite.
- **Clinopyroxene:** 55%, medium-grained, subhedral, cumulus mineral, simple and lamellar twinning, rarely zoned, rare olivine and biotite chadocryts, cross-cut by serpentinized fractures.
- **Plagioclase:** 30%, interstitial, patches to fractures of sericite alteration, serpentinized fractures, trace apatite inclusions.
- **Biotite:** trace, very fine-grained, anhedral, reddish brown pleochroism (Ti-bearing), rimming Fe-Ti oxides.
- **Apatite:** trace, very fine-grained, subhedral, inclusions in plagioclase and piercing into biotite grains.

Alteration minerals:

- **Serpentine**: 3%, very fine-grained, associated with olivine replacement and serpentinized fractures.
- **Chlorite:** trace, very fine grained, observed in areas of alteration mantling the cumulus minerals.
- **Sericite:** 1%, very fine-grained, patches of plagioclase replacement.
- **Chlorite:** trace, very fine-grained, rimming biotite.

Opaque minerals:

- **Chalcopyrite**: trace, very fine-grained, intergrown with bornite and pyrite and rimming Fe-Ti oxide.
- **Bornite**: trace, very fine-grained, anhedral, intergrown with chalcopyrite and pyrite and rimming Fe-Ti oxide.

- **Pyrite**: trace, very fine-grained, intergrown with chalcopyrite and bornite and rimming Fe-Ti oxide.
- **Fe-Ti oxide:** 1%, fine- to very fine-grained, subhedral to anhedral, magnetite with ilmenite lamellae and magnetite intergrown with ilmenite, interstitial to silicates.
- **Secondary magnetite:** trace, very fine-grained, associated with olivine replacement

---

Sample: RTTC-BT-134
Location: 330319E 5377910N
DDH: 07TH**006**
Depth: 182 m
Lithology: Mineralized feldspathic peridotite
Unit: Thunder intrusion – lower mafic - ultramafic unit/upper mineralized zone
Description:

Feldspathic peridotite consisting of fine-grained cumulus olivine and medium-grained cumulus clinopyroxene, and interstitial plagioclase, biotite, Fe-Ti oxide and apatite. All silicate minerals show parallel microfractures. Olivine is commonly partially to completely replaced by serpentine + magnetite alteration; clinopyroxene is more resistant to alteration; abundant sericite alteration patches throughout interstitial plagioclase. The melagabbro hosts up to coarse-grained blebby sulphides consisting of intergrown chalcopyrite, bornite, millerite and lobed Fe-Ti oxide. The sulphides are intergrown with spongy textured secondary magnetite.

Primary minerals:

- **Olivine:** 15%, fine- to very fine-grained, subhedral, cumulus mineral to chadacrysts in clinopyroxene, parallel micro-fractures, partial to complete replacement by serpentine + magnetite.
- **Clinopyroxene:** 55%, medium-grained, cumulus mineral, subhedral, lamellar twinning, rare very fine-grained olivine and biotite chadacrysts, common parallel micro-fractures.
- **Plagioclase:** 20%, interstitial, abundant sericite alteration pits, parallel microfractures.
- **Biotite:** trace, fine to very-fine grained, subhedral to anhedral, interstitial, commonly clustered and rimmed by chlorite, pleochroic reddish brown (Ti-bearing).
- **Apatite:** trace, very fine-grained, euhedral, commonly inclusions in plagioclase and piercing into biotite grains, also as inclusions in biotite.

Alteration minerals:

- **Chlorite:** trace, very fine-grained, anhedral, rimming biotite and sulphide blebs.
- **Serpentine:** 1%, very fine-grained, associated with olivine replacement.
- **Sericite:** 5%, very fine-grained, alteration pits in plagioclase.

Opaque minerals:

- **Chalcopyrite:** 1%, intergrown with bornite and millerite
- **Bornite:**1 %, intergrown with chalcopyrite and millerite

- **Millerite:** trace, intergrown with chalcopyrite and bornite
- **Fe-Ti oxide:** 2%, fine-grained, subhedral to anhedral aggregates to lobes, disseminated and interstitial, commonly rimmed by biotite and intergrown with sulphides, magnetite with ilmenite lamellae to magnetite intergrown with ilmenite.
- **Secondary Magnetite:** 1%, very fine-grained, associated with olivine replacement and infilling fractures in sulphide blebs with a spongy texture.

Sample: RTTC-BT-161
DDH Location: 330319E 5377910N
DDH: 07TH006
Depth: 575 m
Lithology: Tuffaceous rock hosting chalcopyrite-rich massive sulphide veinlet
Unit: Footwall rock
Description:

Tuffaceous rock consisting of very fine- to fine-grained anhedral feldspar matrix intergrown with chlorite, actinolite, titanite clinozoisite, and quartz. The tuffaceous rock hosts a massive sulphide veinlet consisting of semi-massive anhedral to euhedral pyrite intergrown with chalcopyrite. The sulphides are in turn intergrown with patches of anhedral carbonate and chlorite. Carbonate and chlorite also infill fractures in the sulphide veinlet. Euhedral pyrite cubes suggest recrystallization. The sulphide vein appears conformable to relict bedding of the tuffaceous host rock. Empty cavities observed both in the host rock and vein.

Primary/secondary minerals:

- **Feldspar**: 35%, very fine- to fine-grained, anhedral, undulose extinction (evidence of strain), anhedral, comprises the matrix of the host rock, partial replacement by kaolinite.
- **Quartz:** 2%, very fine-grained, anhedral to subhedral, undulose extinction, intergrown with feldspar producing a graphic to myrmekitic intergrowth texture with feldspar present in both the host rock and vein..
- **Carbonate**: 12%, medium-grained, anhedral, patches intergrown with sulphides in the vein.
- **Chlorite:** 20%, very fine-grained, anhedral, patches intergrown with the sulphide vein and infilling fractures.
- **Titanite**: trace, fine to very fine grained, subhedral, within the matrix.
- **Actinolite**: 1%, very fine-grained, anhedral, intergrown with feldspare matrix.
- **Titanite:** trace, very fine-grained, anhedral, intergrown in feldspar matrix.
- **Clinozoisite:** trace, very fine-grained, anhedral, intergrown in feldspar matrix.
- **Apatite:** trace, very fine-grained, euhdral elongate crystals, intergrown in feldspar matrix.

Opaque minerals:

- **Pyrite**: 16%, very fine- to medium-grained, comprises the vein as anhedral masses to euhedral disseminated cubes intergrown with carbonate + chlorite.
- **Chalcopyrite**: 14%, very fine- to medium-grained, anhedral masses, intergrown with pyrite, pyrite inclusions, intergrown with carbonate + chlorite.
- **Sphalerite**: trace, very fine-grained, inclusions in pyrite.
- **Galena**: trace, very fine-grained, inclusions in pyrite.
- **Secondary magnetite:** trace, very fine-grained, anhedral, disseminated in feldspar matrix.

Sample: RTTC-BT-163
Location: 330319E 5377910N
DDH: 07TH006
Depth: 574 m
Lithology: Tuffaceous rock hosting chalcopyrite-rich massive sulphide veinlet
Unit: Footwall rock
Description:

Sulphide veinlet consisting of massive chalcopyrite and fine-grained inclusions of subhedral millerite, sphalerite and galena. The sulphides are intergrown with very fine- to fine-grained chlorite + carbonate + quartz infill permeating fractures. The sulphide veinlet margin is shared with a host rock consisting of fine-grained quartz and pods of actinolite.

Primary/secondary minerals:

- **Quartz:** 18%, in the host rock the quartz is subhedral and equigranular (fine-grained) with polygonal grain boundaries; in the vein quartz is very fine-grained, anhedral and intergrown with carbonate and chlorite.
- **Carbonate**: 2%, fine- to medium-grained, anhedral to subhedral, intergrown with quartz and chlorite infilling permeating fractures in the sulphide veinlet.
- **Chlorite:** 8%, very fine-grained, anhedral fans, intergrown with carbonate and quartz inflling permeating fractures in the sulphide veinlet, pods with radiating acicular crystals along the grain boundaries of polygonal quartz in the host rock.
- **Titanite:** trace, very fine-grained, anhedral, remnants in the vein and host rock.

Opaque minerals:

- **Chalcopyrite**: 70%, massive with inclusions of millerite, spherite and galena.
- **Pyrite:** 1%, very fine-grained, anhedral to subhedral, disseminated to clustered in the host rock.
- **Millerite:** trace, very fine-grained, anhedral, inclusions in chalcopyrite.
- **Galena:** trace, very fine-grained, anhedral, inclusions in chalcopyrite.
- **Sphalerite:** trace, very fine-grained, anhedral, inclusions in chalcopyrite.

- **Magnetite:** trace, very fine-grained, anhedral, inclusions in chalcopyrite.

Sample: RTTC-BT-173
Location: 330435E 5378298N
DDH: 05TH003
Depth: 298 m
Lithology: Mineralized feldspathic peridotite sharing sharp contact with footwall hornfels
Unit: Thunder intrusion – lower mafic to ultramafic unit
Description:

Mineralized feldspathic peridotite consisting of fine- to medium-grained cumulus olivine pseudomorphs and fine- to medium-grained cumulus clinopyroxene surrounded by interstitial plagioclase, biotite and net-like sulphides + magnetite. Olivine pseudomorphs consists of serpentine + magnetite that in turn are being replaced by deep red stilpnomelane(?); clinopyroxene more resistant to alteration; common sericite alteration pits in plagioclase. Sulphide mineralization is characterized by net-like intergrowths of Fe-Ti oxide, pyrrhotite, chalcopyrite and pentlandite. Pyrrhotite is commonly altered by patches of a graphic intergrowth of marcasite + pyrite + secondary magnetite.

The mineralized feldspathic peridotite shares a sharp contact with a gabbroic hornfels rock. The crystal habit of plagioclase is tabular along the contact. The hornfels footwall rock is characterized by an allotriomorphic texture consisting of very fine-grained feldspar matrix intergrown with very fine-grained cliopyroxene, biotite and Fe-Ti oxide. Alteration minerals include actinolite, chlorite, sericite and talc overprinting the primary(?) minerals. A pyrite-rich veinlet was observed cross-cutting the hornfels.

Note: modal count for the mineralized feldspathic peridotite only.

Primary minerals:

- **Olivine:** 20% (5% unaltered), fine- to medium-grained, cumulus mineral and very fine-grained chadacrysts in clinopyroxene, subhedral, pseudomorphs consisting of serpentine + secondary magnetite (the serpentine is commonly replaced by deep red stilpnomelane and pyrite),
- **Clinopyroxene:** 30%, fine-grained, subhedral, lamellar twinning and zoning, hosts olivine chadacrysts.
- **Plagioclase:** 10%, interstitial to the cumulate minerals highly altered, poikilitic with biotite, chlorite, oxide, and sulphide inclusions, replacement by sericite, chlorite, serpentine.
- **Biotite:** trace, fine- to very fine-grained, anhedral, interstitial to the cumulus minerals, commonly clustered, pleochroic brown to reddish brown, commonly rimming the Fe-Ti oxides.

- **Hornblende:** trace, fine-grained, anhedral, pleochroic brown, intergrown with the other primary minerals
- **Apatite:** trace, very fine-grained, euhedral elongate crystals encased in plagioclase and piercing into the other silicates.

Secondary minerals:

- **Chlorite**: trace, very fine-grained, rimming biotite.
- **Sericite:** trace, very fine grained, alteration pits in plagioclase
- **Serpentine:** 5%, very fine-grained, anhedral, associated with olivine replacement, commonly replaced by deep red stilpnomelane, also occurs in veinlets
- **Stilpnomelane:** 10%, very fine-grained, associated with serpentine replacement of olivine and replacement of pyrrhotite.

Opaque minerals:

- **Pyrrhotite**: 10%, medium- to fine-grained, anhedral, intergrown with chalcopyrite and hosting pentlandite flames, commonly replaced by patchy pyrite + marcasite + secondary magnetite.
- **Chalcopyrite**: 4%, fine-grained, intergrown with pyrrhotite.
- **Penntlandite**: trace, very fine-grained, flames in pyrrhotite.
- **Pyrite/Marcasite:** 5%, very fine- to fine-grained, patches of graphic intergrowth with secondary magnetite and replacing pyrrhotite, pyrite also occurs as subhedral to euhedral cubes in pyrrhotite.
- **Magnetite:** 20%, fine- to medium-grained, subhedral to anhedral aggregates and lobes, interstitial to the cumulus minerals and intergrown with the sulpphides producing a net-like texture, commonly rimmed by biotite, rare ilmenite lamellae in magentite.
- **Secondary magnetite:** 1%, very fine-grained, anhedral aggregates associated with olivine replacement.

Sample: RTTC-BT-176
Location: 330435E 5378298N
DDH: 05TH003
Depth: 298 m
Lithology: Mineralized feldspathic clinopyroxenite cross-cutting wall rock
Unit: Footwall
Description:

A mineralized feldspathic clinopyroxenite cross-cutting wall rock (finger injection?). In hand sample the mineralization is described as sulphide stringers. The feldspathic clinopyroxenite consists of abundant very fine- to fine-grained clinopyroxene intergrown with interstitial plagioclase and biotite. Clinopyroxene crystals are also medium-grained intergrown with the sulphide stringers. Plagioclase is variably altered by intergrown chlorite and actinolite

patches and host veins of serpentine. The sulphides consist of intergrown pyrrhotite, chalcopyrite, pentlandite flames and lobed Fe-Ti oxide. Patchy pyrite-marcasite alteration replaces pyrrhotite. The feldspathic cinopyroxenite shares a sharp contact with the wall rock and lacks a chill margin. The wall rock appears to be a metasedimentary rock with relict bedding consisting dominantly of granular grains of magnetite, feldspar, chlorite, clinopyroxene. Wall rock contains trace amounts of very fine-grained pyrrhotite, chalcopyrite and pyrite (sulphide-bearing wall rock). The contact is marked by several dark green pseudomorphs intergrown with opaques.

Note: modal counts based on the feldspathic clinopyroxenite.

Primary minerals:

- **Clinopyroxene:** 56%, very fine- to fine-grained, subhedral, intergrown with plagioclase and biotite.
- **Plagioclase:** 20%, interstitital and intergrown with clinopyroxene and biotite
- **Biotite:** 2%, fine-grained, pleochroic reddish brown (Ti-bearing), intergrown with clinopyroxene and plagioclase.
- **Apatite:** trace, very fine-grained, elongate crystals piercing into plagioclase.

Secondary minerals:

- Intergrown actinolite, chlorite and serpentine replacing plagioclase and clinopyroxene in the wall rock. These minerals are only in trace amounts in the feldspathic clinopyroxenite.

Opaque minerals:

- **Pyrrhotite:** 8%, fine-grained, anhedral masses intergrown with lobed Fe-Ti oxide, chalcopyrite
- **Chalcopyrite:** 2%, very fine-grained, anhedral, intergrown with pyrrhotite and lobed Fe-Ti oxide.
- **Pentlandite:** trace, very fine-grained, anhedral, flames intergrown along margins of pyrrhotite and chalcopyrite.
- **Marcastite-Pyrite:** trace, very fine-grained, replacement patches of pyrrhotite.
- **Fe-Ti oxide:** 2%, fine-grained, subhedral aggregates to lobed and intergrown with sulphides, magnetite with ilmenite lamellae and magnetite intergrown with ilmenite.

Sample: RTTC-BT-177
Location: 330435E 5378298N
DDH: 05TH003
Depth: 300 m
Lithology: Pyrrhotite-rich massive sulphide veinlet cross-cut wall rock
Unit: Wall Rock
Description:

Pyrrhotite-rich massive sulphide veinlet cross-cutting wall rock hornfels. The hornfels rock is foliated and slightly banded consisting of lenses and schlieren of very fine- to fine-grained granular magnetite, biotite, serpentine/chlorite, feldspar and quartz. The sulphide vein consists of massive pyrrhotite with abundant inclusions of medium-grained, ehedral to lobed magnetite, veins of chalcopyrite, and extensive alteration patches of a graphic intergrowth consisting of pyrite + marcasite + secondary magnetite. Discrete subhedral to euhedral grains of pyrite also occurs throughout the massive pyrrhotite. Along the sharp vein sharp the euhedral crystals of magnetite are disrupted.

Note: modal counts only for the massive sulphide veinlet.

Opaque minerals:

- **Pyrrhotite:** 90%, dominant mineral in the massive sulphide, common fractures infilled with gangue, hosts chalcopyrite veinlets, disseminated magnetite grains, pentlandite flames, patches of marcasite + pyrite + secondary magnetite alteration and discrete subhedral to euhedral pyrite.
- **Chalcopyrite:** 2%, veins in pyrrohite.
- **Pentlandite:** trace, flames in pyrrhotite.
- **Pyrite:** 3%, occurs as pyrite + marcasite + secondary magnetite alteration patches in pyrrhotite and as discrete subhedral to euhdral grains in pyrrhotite.
- **Marcasite:** 1%, occurs as pyrite + marcasite + secondary magnetite alteration patches in pyrrhotite.
- **Magnetite:** 4%, fine grained, subhedral to euhedral aggregates to lobes in pyrrhotite, grain boundaries disrupted along vein margin.
- **Secondary magnetite:** trace, very fine-grained, occurs as pyrite + marcasite + secondary magnetite alteration patches in pyrrhotite.

Sample: RTTC-BT-187
Location: 330435E 5378298N
DDH: 07TH002
Depth: 169 m
Lithology: Graphitic schist
Unit: Footwall rocks
Description

A graphitic, fragmental rock with well-developed schistosity consisting of feldspathic fragments that are cross-cut by multiple generations of quartz + chlorite veins. The graphite comprises the matrix surrounding the feldspathic fragments and is strongly deformed (i.e., abundant microfolding). The graphite also infills micro-fractures of the feldspathic fragments. The rock is overprinted by subhedral to euhedral pyrite disseminations to clusters that are also part of the foliation. Pyrite is commonly poikiloblastic and the clusters are elongated parallel to foliation. Chlorite pervasively overprints the rocks (greenschist facies metamorphism).

Primary/secondary minerals:

- **Quartz:** 4%, very fine-grained, anhedral, intergrown with feldspar in the fragments and intergrown with chlorite and sericite in veins.
- **Feldspar:** 20%, very fine-grained, anhedral, intergrown with quartz; medium- to coarse-grained angular, elongated fragments.
- **Graphite:** 40%, very fine-grained, comprises the matrix surrounding the feldspathic fragments and infilling microfractures, abundant microfolding.
- **Sericite:** 4%, very fine-grained, deformed and intergrown with quartz in vein and overprinting the feldspathic fragments.
- **Kaolinite:** 12%, very fine-grained, intergrown with graphite and feldspar, overprinting the feldspathic fragments.
- **Chlorite:** 2%, very fine-grained, intergrown with quartz in veins and as patches overprinting feldspathic fragments.

Opaque minerals:

- **Pyrite:** 18%, very fine-grained, subhedral to eubhedral granular clusters and disseminations, clusters elongated in direction of the foliation, overprinting the protolith, commonly poikiloblastic.
- **Chalcopyrite:** trace, very fine-grained, anhedral, intergrown with quartz + chlorite in veins.
- **Pyrrhotite:** trace, very fine-grained, anhedral, intergrown with quartz + chlorite in veins.

Sample: RTT-BT-102A
Location: 330445E 5378495N
Lithology: Melagabbro
Unit: Thunder intrusion – lower mafic to ultramafic unit
Description:

Outcrop sample collected along the north-eastern margin of the Thunder intrusion. A very uneven textured melagabbro/feldspathic pyroxenite with a large sulphide bleb patch in the middle of the slide and pervasive alteration throughout. Host rock consists of very fine- to medium-grained cumulus clinopyroxene and fine-grained pseudomorphs of cumulus olivine completely serpentinized. Interstitial to the cumulus minerals consists of strongly altered plagioclase, biotite, Fe-Ti oxide and trace apatite. Plagioclase is completely replaced by kaolinite with abundant patches of intergrown serpentine and actinolite. The sulphide bleb consists of fine-grained pyrite intergrown with chalcopyrite and minor goethite and cuprite. Disseminated throughout the slide are anhedral grains of intergrown pyrite and chalcopyrite rimmed by goethite and cuprite. The Fe-Ti oxides are also heavily altered with only the ilmenite lamellae preserved while the magnetite has been dissolved.

Primary minerals:

- **Olivine:** relicts, fine-grained, subhedral, cumulus mineral, rarely chadacrystic hosted within clinopyroxene, complete replacement by serpentine.
- **Clinopyroxene**: 40%, fine- to medium-grained, cumulus mineral, lamellar and simple twinning, rare zoning, rarely oikocrystic hosting olivine pseudomorph chadacryst.
- **Plagioclase:** 30%, interstitial to fully encasing olivine and clinopyroxene, complete replaced by kaolinite with abundant intergrown actinolite and serpentine alteration patches.
- **Biotite:** 4%, fine-grained, anhedral, pleochroic reddish brown (Ti-bearing), rimming Fe-Ti oxide.
- **Apatite:** trace, very fine-grained, elongate anhedral crystals intergrown with and encased by biotite and plagioclase.

Alteration minerals:

- **Serpentine/Chlorite:** 20%, very fine-grained, associated with olivine replacement and as alteration patches in plagioclase.
- **Actinolite:** 1%, very fine-grained, partial replacement of clinopyroxene as radiating crystals along the rims, intergrown with chlorite + serpentine patches.
- **Carbonate:** 1%, fine-grained, associated with alteration patches throughout plagioclase (breakdown of mafic minerals) and interstitial to altered sulphides.

Opaque minerals:

- **Chalcopyrite**: trace, fine-grained, anhedral, intergrown with pyrite in the sulphide patches, rimmed by goethite/cuprite.

- **Pyrite**: 2%, fine-grained, anhedral, intergrown with chalcopyrite.
- **Fe-Ti oxide:** 2%, fine- to medium-grained, anhedral, occurs as remnants of magnetite with ilmenite lamellae but the magnetite has been altered away and remnants of the lamellae remain.
- **Secondary magnetite:** trace, very fine-grained, associated with serpentine alteration of olivine.

Sample: RTT-BT-102B
Location: 330445E 5378495N
Lithology: Melagabbro
Unit: Thunder intrusion – lower mafic to ultramafic unit
Description:

Outcrop sample collected along the north-eastern margin of the Thunder intrusion. Same rock sample as RTT-BT-102A but thin section cut away from the large alteration/sulphide bled patch. Melagabbro consisting of abundant fine- to medium-grained cumulus clinopyroxene and fine-grained cumulus olivine pseudomorphs surrounding by interstitial altered plagioclase, biotite, Fe-Ti oxide and trace apatite. Olivine pseudomorphs consists of intergrown serpentine and chlorite. Plagioclase is completely replaced by kaolinite with abundant patches of intergrown serpentine, chlorite and actinolite. Disseminated fine-grained chalcopyrite + pyrite occurring in alteration patches.

Primary minerals:

- **Olivine:** relicts, fine-grained, subhedral, cumulus mineral, rarely chadacrystic hosted within clinopyroxene, complete replacement by serpentine.
- **Clinopyroxene**: 50%, fine- to medium-grained, cumulus mineral, lamellar and simple twinning, rare zoning, rarely oikocrystic hosting olivine pseudomorph chadacryst.
- **Plagioclase:** 30%, interstitial to fully encasing olivine and clinopyroxene, complete replaced by kaolinite with abundant intergrown actinolite and serpentine alteration patches.
- **Biotite:** 6%, fine-grained, anhedral, pleochroic reddish brown (Ti-bearing), rimming Fe-Ti oxide.
- **Apatite:** trace, very fine-grained, elongate anhedral crystals intergrown with and encased by biotite and plagioclase.

Alteration minerals:

- **Serpentine/Chlorite:** 5%, very fine-grained, associated with olivine replacement and as alteration patches in plagioclase.
- **Actinolite:** 3%, very fine-grained, partial replacement of clinopyroxene as radiating crystals along the rims, intergrown with chlorite + serpentine patches.

Opaque minerals:

- **Chalcopyrite**: trace, fine-grained, anhedral, intergrown with pyrite in the sulphide patches, rimmed by goethite/cuprite.
- **Pyrite**: trace%, fine-grained, anhedral, intergrown with chalcopyrite.
- **Fe-Ti oxide:** 6%, fine- to medium-grained, anhedral, occurs as remnants of magnetite with ilmenite lamellae but the magnetite has been partially altered away and remnants of the lamellae remain.
- **Secondary magnetite:** trace, very fine-grained, associated with serpentine alteration of olivine.

Sample: RTT-BT-130
Location: 329929E 5378222N
Lithology: Pegmatitic gabbro
Unit: Thunder intrusion – pegmatitic gabbro
Description:

Sample collected along the western margin of the Thunder. Sample chosen for U/Pb age dating analysis. Pegmatitic gabbro consisting of coarse- to medium-grained clinopyroxene intergrown with coarse- to medium-grained plagioclase producing a well developed subophitic texture. Abundant disseminated fine- to medium-grained altered Fe-Ti oxide where mostly the ilmenite lamellae remain. Plagioclase is partially replaced by sericite and commonly pierced by fine-grained euhedral apatite; clinopyroxene more resistant to alteration; trace olivine pseudomorphs consisting of actinolite + serpentine + secondary magnetite. Trace chalcopyrite intergrown with Fe-Ti oxide.

Primary minerals:

- **Olivine:** trace, fine-grained, anhedral, completely replaced by serpentine + magnetite.
- **Clinopyroxene:** 30%, medium- to coarse-grained, subhedral to anhedral, intergrown with plagioclase laths.
- **Plagioclase**: 50%, medium- to coarse-grained, subhedral to anhedral, lath shaped, intergrown with clinopyroxene, common sericite alteration pits.
- **Biotite:** trace, very fine-grained, intergrown with serpentine.
- **Apatite:** trace, very fine- to fine-grained, euhedral, piercing into plagioclase laths.

Alteration minerals:

- **Sericite:** trace, very fine-grained, alteration pits in plagioclase.
- **Actinolite:** 1%, very fine-grained, anhedral, associated with olivine replacement.
- **Serpentine:** 8%, very fine-grained, anhedral, associated with olivine replacement.
- **Chlorite:** 1%, very fine-grained, anhedal, associated with mafic mineral alteration.

Opaque minerals:

- **Chalcopyrite:** trace, very fine-grained, intergrown with Fe-Ti oxide.
- **Fe-Ti oxide:** 10%, fine- to medium-grained, anhedral to subhedral, skeletal, altered magnetite with ilmenite lamellae.
- **Secondary magnetite:** trace, very fine-grained, associated with olivine replacement.

Sample: RTT-BT-149
Location: 330412E 5378462N
Lithology: Mineralized feldspathic peridotite
Unit: Thunder intrusion – lower mafic to ultramafic unit
Description:

Sample collected from a trench outcrop located along the north-eastern margin of the Thunder intrusion. Feldspathic peridotite consisting of abundant fine-grained cumulus olivine and fine- to medium-grained cumulus clinopyroxene, interstitial post-cumulus plagioclase, biotite and amphibole, and disseminated magnetite + pyrrhotite + chalcopyrite mineralization. Olivine occurs partially to completely replaced by serpentine + talc + magnetite alteration. Clinopyroxene more resistant to alteration with minor chlorite + serpentine + actinolite replacement along rims. Micro-fractures observed throughout thin section and traced through all minerals.

Primary minerals:

- **Olivine:** 10%, relicts, fine-grained, subhedral, cumulate, rarely chadacrystic hosted within clinopyroxene, partial to complete replacement by talc + serpentine + magnetite.
- **Clinopyroxene**: 65%, fine- to-medium-grained, rarely very fine-grained, subhedral, rarely anhedral, cumulate, lamellar and simple twinning, rare zoning, rarely oikocrystic hosting olivine chadacryst, partial replacement along margins by chlorite + serpentine + actinolite but more resistant to alteration than olivine.
- **Plagioclase:** 15 % but variable distribution, interstitial to fully encasing olivine and clinopyroxene, common sericite alteration pits and fractures.
- **Horneblende:** 5%, medium-grained, anhedral to subhedral, pleochroic brown to deep reddish brown (Ti-bearing), partial replacement by chlorite, intergrown with magnetite and apatite.
- **Biotite:** 1%, fine-grained, anhedral, pleochroic reddish brown (Ti-bearing), rimming magnetite.
- **Apatite:** trace, very fine-grained, elongate anhedral crystals intergrown with and encased by biotite.

Alteration minerals:

- **Chlorite:** 1%, very fine-grained, partial replacement of olivine, intergrown with talc and serpentine, along the rims of amphibole and biotite.

- **Actinolite:** 2%, very fine-grained, partial replacement of clinopyroxene as radiating crystals along the rims, intergrown with chlorite + serpentine patches.
- **Talc:** 1%, very fine-grained, partial to complete replacement of olivine, intergrown with serpentine and chlorite.
- **Serpentine:** 1%, very fine-grained, partial to complete replacement of olivine, intergrown with talc and chlorite.
- **Magnetite:** trace, very fine-grained, associated with alteration of olivine.
- **Carbonate:** trace, intergrown with serpentine and actinolite alteration.

Opaque minerals:

- **Pyrrhotite:** 2%, fine- to medium-grained, anhedral, intergrown with chalcopyrite and magnetite, rare very fine-grained pentlandite flames.
- **Chalcopyrite**: 2%, fine-grained, anhedral, intergrown with pyrrhotite and magnetite.
- **Fe-Ti oxide:** 5%, fine- to medium-grained, anhedral to subhedral lobed grains, intergrown with sulphides, amphibole and biotite, magnetite with lamellae lamellae and magnetite intergrown with ilmenite.
- **Pentlandite:** trace, very fined-grained, occurs as flames in pyrrhotite.
- **Sphalerite:** trace, very fine-grained, inclusions

APPENDIX B

Mineral chemistry from sulphide mineralization analysis

Sample ID	DDH	Depth	Description	Mineral
Basal mineralization zone				
RTTC-BT-089	07TH004	437	cp interstitial to gangue	chalcopyrite
			f. gr. po integrrown w. sec. mt	pyrrhotite
			anh. poikilitic py	pyrrhotite
			f. gr. cp incl in serpentine	chalcopyrite
			anh. cp intergrown w. gangue	chalcopyrite
			anh. po intergrown w. cp	pyrrhotite
			pn intergrown w. po, cp	pentlandite
			tiny white spec at boundary of pn and po	*galena*
			po integrrown w. pn	pyrrhotite
			f. gr. pn incl. in po-cp	pentlandite
			f. gr. sph incl. in po-cp	sphalerite
RTTC-BT-091	07TH004	432	coarse cp integrrown w. low-Al chlorite and po-pn	chalcopyrite
			anh. po integrrown w. cp and low-Al chlorite	pyrrhotite
			altered pn remnants intergrown w. po	pentlandite
			altered pn remnants intergrown w. po	pentlandite
			tiny (1-2µm) Pd-telluride incl in po	merenskyite
			tiny (1-2µm) Pd-telluride incl in po, rep	merenskyite
			Ag-pn at tip of cp	Ag-pentlandite
			elongate euh. PdTeSbBi in gangue	Sb-kotulskite?
			elongate euh. PdTeSbBi in gangue, other spot	Sb-kotulskite?
			cp	chalcopyrite
			coarse round po	pyrrhotite
			bladed po intergrown w. gangue	pyrrhotite
			bladed po intergrown w. gangue	pyrrhotite
			po droplet in a,mphibole	pyrrhotite
RTTC-BT-034	07TH003	297	pyrrhotite	Pyrrhotite
			cp	Chalcopyrite
			PdTe at tip of marcasite alteration (F115)	kotulskite
			marcasite alteration	Marcasite
			large cp	Chalcopyrite
			py or mc outlining serpentine in fsp	Pyrite 2
			euh bravoite in marcasite alteration	Pyrite
			pyrrhotite host	Pyrrhotite
			siegenite flames in pyrrhotite	Siegenite
			marcasite alteration	Marcasite

Sample ID	S	Mn	Fe	Co	Ni	Cu	Zn	As	Se	Pd	Ag	Cd	Sn	Sb	Te	Pt	Au	Hg	Pb	Bi	Total
Basal mineralization zone																					
RTTC-BT-089	34.19	0.01	31.23	0.01	0.02	35.01	0.03	0.01	0.04	0.00	0.00	0.00	0.00	0.00	0.02	0.00	0.08	0.00	0.00	0.07	100.73
	40.79	0.02	57.80	0.03	1.09	0.00	0.00	0.00	0.01	0.00	0.02	0.00	0.00	0.00	0.00	0.04	0.00	0.04	0.00	0.17	100.00
	39.10	0.01	59.81	0.03	0.93	0.01	0.05	0.00	0.00	0.00	0.01	0.02	0.01	0.00	0.00	0.00	0.00	0.00	0.01	0.02	100.02
	34.18	0.03	30.39	0.02	0.08	34.14	0.05	0.00	0.00	0.02	0.03	0.00	0.01	0.00	0.00	0.03	0.00	0.01	0.05	0.06	99.11
	34.41	0.01	30.96	0.03	0.13	34.45	0.05	0.00	0.01	0.07	0.00	0.00	0.00	0.00	0.04	0.00	0.03	0.00	0.08	0.09	100.36
	39.25	0.02	59.63	0.05	0.81	0.05	0.04	0.00	0.03	0.01	0.00	0.03	0.00	0.00	0.00	0.13	0.02	0.00	0.01	0.12	100.21
	32.77	0.00	27.91	3.12	36.48	0.03	0.00	0.00	0.03	0.00	0.00	0.11	0.01	0.00	0.04	0.00	0.00	0.00	0.00	0.04	100.51
	32.93	*0.01*	*43.42*	*0.55*	*7.19*	*0.08*	*0.03*	*0.01*	*0.10*	*0.00*	*0.00*	*0.00*	*0.01*	*0.00*	*0.03*	*0.04*	*0.03*	*0.02*	*11.44*	*0.05*	*95.92*
	39.18	0.00	59.00	0.04	1.13	0.00	0.01	0.02	0.01	0.00	0.00	0.00	0.01	0.00	0.00	0.06	0.03	0.04	0.00	0.12	99.66
	32.39	0.00	27.87	3.45	35.62	0.03	0.06	0.04	0.02	0.01	0.06	0.00	0.01	0.00	0.00	0.00	0.00	0.00	0.05	0.07	99.67
	32.45	0.02	8.90	0.02	0.00	1.30	56.07	0.00	0.00	0.00	0.00	0.57	0.03	0.00	0.00	0.00	0.02	0.03	0.02	0.14	99.57
RTTC-BT-091	34.77	0.00	30.31	0.00	0.00	35.34	0.04	0.00	0.01	0.00	0.08	0.00	0.04	0.00	0.02	0.00	0.00	0.13	0.00	0.08	100.81
	39.38	0.00	59.25	0.01	1.08	0.07	0.03	0.00	0.01	0.02	0.00	0.00	0.01	0.00	0.01	0.00	0.00	0.01	0.00	0.06	99.92
	33.05	0.00	28.51	1.37	36.96	0.01	0.00	0.03	0.01	0.00	0.05	0.00	0.01	0.00	0.00	0.00	0.08	0.09	0.00	0.16	100.33
	33.43	0.03	28.72	1.20	36.73	0.02	0.00	0.03	0.02	0.00	0.01	0.00	0.00	0.00	0.02	0.03	0.04	0.00	0.00	0.00	100.26
	30.18	0.01	43.91	0.00	0.74	0.13	0.04	0.00	0.01	6.95	0.00	0.00	0.01	0.24	11.90	0.05	0.08	0.00	0.02	3.43	97.68
	28.87	0.00	42.30	0.01	0.76	0.04	0.00	0.00	0.01	7.61	0.00	0.00	0.00	0.31	13.64	0.00	0.00	0.02	0.04	3.80	97.42
	31.63	0.00	33.57	0.00	21.57	0.71	0.04	0.00	0.00	0.00	12.65	0.13	0.02	0.00	0.05	0.00	0.00	0.00	0.03	0.00	100.41
	0.00	0.00	0.84	0.00	0.00	0.43	0.00	0.00	0.01	41.18	0.00	0.00	0.06	12.29	30.60	0.00	0.00	0.00	0.00	15.89	101.29
	0.01	0.00	0.94	0.00	0.00	0.47	0.05	0.00	0.00	40.28	0.00	0.00	0.07	12.34	30.53	0.00	0.00	0.00	0.03	15.46	100.20
	34.45	0.00	30.15	0.00	0.00	35.27	0.06	0.00	0.03	0.01	0.03	0.03	0.01	0.00	0.00	0.00	0.01	0.00	0.00	0.05	100.08
	39.72	0.01	58.72	0.04	1.24	0.21	0.00	0.00	0.00	0.01	0.00	0.00	0.00	0.00	0.00	0.00	0.00	0.02	0.00	0.16	100.13
	38.26	0.01	58.53	0.06	1.07	0.00	0.00	0.00	0.02	0.03	0.03	0.00	0.01	0.00	0.01	0.01	0.00	0.00	0.02	0.20	98.26
	39.55	0.01	59.41	0.03	0.96	0.00	0.00	0.03	0.00	0.02	0.00	0.01	0.03	0.00	0.02	0.00	0.00	0.00	0.01	0.12	100.19
	39.27	0.00	58.47	0.03	1.36	0.00	0.00	0.00	0.00	0.06	0.00	0.00	0.00	0.00	0.00	0.00	0.04	0.00	0.00	0.13	99.36
RTTC-BT-034	39.48	0.03	58.59	0.03	1.12	0.00	0.00	0.03	0.00	0.01	0.04	0.00	0.00	0.00	0.00	0.08	0.06	0.00	0.00	0.02	99.46
	34.41	0.00	30.27	0.00	0.04	34.83	0.05	0.00	0.00	0.00	0.02	0.00	0.00	0.00	0.00	0.10	0.00	0.00	0.00	0.00	99.71
	0.06	0.03	1.38	0.03	0.00	0.05	0.04	0.00	0.02	40.47	0.00	0.00	0.03	1.53	34.72	0.06	0.02	0.00	0.00	24.21	102.64
	53.29	0.02	47.13	0.00	0.12	0.05	0.06	0.00	0.00	0.00	0.01	0.00	0.03	0.00	0.00	0.00	0.06	0.00	0.00	0.15	100.92
	34.03	0.00	30.65	0.02	0.02	34.79	0.00	0.00	0.00	0.00	0.00	0.02	0.02	0.00	0.01	0.00	0.00	0.06	0.00	0.13	99.74
	38.92	0.09	39.81	0.00	0.01	0.05	0.01	0.00	0.00	0.05	0.01	0.00	0.03	0.00	0.00	0.02	0.00	0.00	0.14	0.11	79.24
	53.45	0.01	40.21	0.22	6.42	0.00	0.00	0.03	0.04	0.00	0.00	0.00	0.01	0.00	0.02	0.06	0.00	0.05	0.00	0.06	100.58
	39.51	0.00	58.63	0.06	0.74	0.02	0.03	0.00	0.03	0.00	0.03	0.00	0.00	0.00	0.00	0.03	0.00	0.02	0.01	0.08	99.18
	42.20	0.01	13.42	18.88	24.76	0.08	0.00	0.02	0.00	0.00	0.00	0.00	0.04	0.00	0.00	0.03	0.08	0.08	0.00	0.14	99.75
	53.30	0.00	43.80	0.28	3.11	0.02	0.00	0.01	0.00	0.00	0.02	0.02	0.00	0.00	0.00	0.00	0.00	0.00	0.00	0.25	100.82

Sample ID	S	Mn	Fe	Co	Ni	Cu	Zn	As	Se	Pd	Ag	Cd	Sn	Sb	Te	Pt	Au	Hg	Pb	Bi	TOTAL
Basal mineralization zone																					
RTTC-BT-089	1.957	0.000	1.027	0.000	0.001	1.011	0.001	0.000	0.001	0.000	0.000	0.000	0.000	0.000	0.000	0.000	0.001	0.000	0.000	0.001	4.000
	1.093	0.000	0.889	0.000	0.016	0.000	0.000	0.000	0.000	0.000	0.000	0.000	0.000	0.000	0.000	0.000	0.000	0.000	0.000	0.001	2.000
	1.057	0.000	0.928	0.000	0.014	0.000	0.001	0.000	0.000	0.000	0.000	0.000	0.000	0.000	0.000	0.000	0.000	0.000	0.000	0.000	2.000
	1.981	0.001	1.011	0.001	0.003	0.999	0.002	0.000	0.000	0.000	0.000	0.000	0.000	0.000	0.000	0.000	0.000	0.000	0.000	0.001	4.000
	1.973	0.000	1.019	0.001	0.004	0.997	0.001	0.000	0.000	0.001	0.000	0.000	0.000	0.000	0.001	0.000	0.000	0.000	0.001	0.001	4.000
	1.060	0.000	0.924	0.001	0.012	0.001	0.001	0.000	0.000	0.000	0.000	0.000	0.000	0.000	0.000	0.001	0.000	0.000	0.000	0.001	2.000
	7.903	0.000	3.865	0.409	4.806	0.003	0.000	0.000	0.002	0.000	0.000	0.007	0.001	0.000	0.002	0.000	0.000	0.000	0.000	0.002	17.000
	1.029	0.000	0.779	0.009	0.123	0.001	0.000	0.000	0.001	0.000	0.000	0.000	0.000	0.000	0.000	0.000	0.000	0.000	0.055	0.000	2.000
	1.062	0.000	0.919	0.001	0.017	0.000	0.000	0.000	0.000	0.000	0.000	0.000	0.000	0.000	0.000	0.000	0.000	0.000	0.000	0.001	2.000
	7.885	0.000	3.896	0.457	4.737	0.003	0.007	0.004	0.001	0.001	0.005	0.000	0.001	0.000	0.000	0.000	0.000	0.000	0.002	0.003	17.000
	0.984	0.000	0.155	0.000	0.000	0.020	0.834	0.000	0.000	0.000	0.000	0.005	0.000	0.000	0.000	0.000	0.000	0.000	0.000	0.001	2.000
RTTC-BT-091	1.984	0.000	0.993	0.000	0.000	1.018	0.001	0.000	0.000	0.000	0.001	0.000	0.001	0.000	0.000	0.000	0.000	0.001	0.000	0.001	4.000
	1.063	0.000	0.919	0.000	0.016	0.001	0.000	0.000	0.000	0.000	0.000	0.000	0.000	0.000	0.000	0.000	0.000	0.000	0.000	0.000	2.000
	7.976	0.000	3.951	0.180	4.873	0.001	0.000	0.003	0.001	0.000	0.004	0.000	0.000	0.000	0.000	0.000	0.003	0.003	0.000	0.006	17.000
	8.038	0.004	3.965	0.157	4.824	0.003	0.000	0.003	0.002	0.000	0.001	0.000	0.000	0.000	0.001	0.001	0.001	0.000	0.000	0.000	17.000
	1.470	0.000	1.228	0.000	0.020	0.003	0.001	0.000	0.000	0.102	0.000	0.000	0.000	0.003	0.146	0.000	0.001	0.000	0.000	0.026	3.000
	1.443	0.000	1.215	0.000	0.021	0.001	0.000	0.000	0.000	0.115	0.000	0.000	0.000	0.004	0.171	0.000	0.000	0.000	0.000	0.029	3.000
	8.038	0.000	4.899	0.000	2.995	0.091	0.005	0.000	0.000	0.000	0.956	0.009	0.002	0.000	0.003	0.000	0.000	0.000	0.001	0.000	17.000
	0.000	0.000	0.073	0.000	0.000	0.032	0.000	0.000	0.000	1.874	0.000	0.000	0.003	0.489	1.161	0.000	0.000	0.000	0.000	0.368	4.000
	0.001	0.000	0.082	0.000	0.000	0.036	0.004	0.000	0.000	1.848	0.000	0.000	0.003	0.495	1.168	0.000	0.000	0.000	0.001	0.361	4.000
	1.979	0.000	0.995	0.000	0.000	1.022	0.002	0.000	0.001	0.000	0.000	0.000	0.000	0.000	0.000	0.000	0.000	0.000	0.000	0.000	4.000
	1.070	0.000	0.908	0.001	0.018	0.003	0.000	0.000	0.000	0.000	0.000	0.000	0.000	0.000	0.000	0.000	0.000	0.000	0.000	0.001	2.000
	1.055	0.000	0.926	0.001	0.016	0.000	0.000	0.000	0.000	0.000	0.000	0.000	0.000	0.000	0.000	0.000	0.000	0.000	0.000	0.001	2.000
	1.065	0.000	0.919	0.000	0.014	0.000	0.000	0.000	0.000	0.000	0.000	0.000	0.000	0.000	0.000	0.000	0.000	0.000	0.000	0.000	2.000
	1.067	0.000	0.912	0.000	0.020	0.000	0.000	0.000	0.000	0.001	0.000	0.000	0.000	0.000	0.000	0.000	0.000	0.000	0.000	0.001	2.000
RTTC-BT-034	1.070	0.000	0.912	0.000	0.017	0.000	0.000	0.000	0.000	0.000	0.000	0.000	0.000	0.000	0.000	0.000	0.000	0.000	0.000	0.000	2.000
	1.982	0.000	1.001	0.000	0.001	1.013	0.001	0.000	0.000	0.000	0.000	0.000	0.000	0.000	0.000	0.001	0.000	0.000	0.000	0.000	4.000
	0.005	0.002	0.061	0.001	0.000	0.002	0.001	0.000	0.001	0.938	0.000	0.000	0.001	0.031	0.671	0.001	0.000	0.000	0.000	0.286	2.000
	1.985	0.000	1.008	0.000	0.003	0.001	0.001	0.000	0.000	0.000	0.000	0.000	0.000	0.000	0.000	0.000	0.000	0.000	0.000	0.001	3.000
	1.966	0.000	1.016	0.001	0.000	1.014	0.000	0.000	0.000	0.000	0.000	0.000	0.000	0.000	0.000	0.000	0.000	0.001	0.000	0.001	4.000
	1.885	0.003	1.107	0.000	0.000	0.001	0.000	0.000	0.000	0.001	0.000	0.000	0.000	0.000	0.000	0.000	0.000	0.000	0.001	0.001	3.000
	1.998	0.000	0.863	0.004	0.131	0.000	0.000	0.000	0.001	0.000	0.000	0.000	0.000	0.000	0.000	0.000	0.000	0.000	0.000	0.000	3.000
	1.073	0.000	0.914	0.001	0.011	0.000	0.000	0.000	0.000	0.000	0.000	0.000	0.000	0.000	0.000	0.000	0.000	0.000	0.000	0.000	2.000
	4.001	0.001	0.731	0.974	1.283	0.004	0.000	0.001	0.000	0.000	0.000	0.000	0.001	0.000	0.000	0.001	0.001	0.001	0.000	0.002	7.000
	1.990	0.000	0.939	0.006	0.063	0.000	0.000	0.000	0.000	0.000	0.000	0.000	0.000	0.000	0.000	0.000	0.000	0.000	0.000	0.001	3.000

Sample ID	DDH	Depth	Description	Mineral
Basal mineralization zone				
RTTC-BT-092	07TH004	426	cp inclusion in anh. po	Chalcopyrite
			anh. po rimmed by cp	Pyrrhotite
			anh. sph in cp rimming po	Sphalerite
			small anh. po intergrown with cp	Pyrrhotite
			tiny michenerite in po attached to mt	Michenerite
			intergrown w. tiny michenerite in po attached to mt	Ni-merenskyite
			po host	Pyrrhotite
			cp	Chalcopyrite
			py-mt alteration in po	Pyrite
			po	Pyrrhotite
			pn integrrown w. po	pentlandite
RTTC-BT-149	surface	-	coarse po w. pn flames	pyrrhotite
			v. f. gr. pn flames in po	pentlandite
			cp intergr. w. po	chalcopyrite
			po w. pn and mt flames	pyrrhotite
			anh cubanite in cp	cubanite
			cp	chalcopyrite
			pn flame in po	pentlandite
			cp in gangue	chalcopyrite
			po intergrown w. cp	pyrrhotite
			cubanite intergrown w. cp	cubanite
			Ag-pn attached to cp	Ag-pentlandite
			PtPdSn	Pd3Pt3Sn
			PtPdSn, repeat	Pd3Pt3Sn
			michenerite	Pd6Bi3(Te,Sb)
			michenerite	Pd6Bi3(Te,Sb)
RTT-BT-102	surface	-	anh cp in sulphide patch	Chalcopyrite
			euh py in sulphide patch	Pyrite
			euh py in sulphide patch, core	Pyrite
			remobilized cp	Chalcopyrite
			py veining remobilized cp	Pyrite
			michenerite	mixture?

Sample ID	S	Mn	Fe	Co	Ni	Cu	Zn	As	Se	Pd	Ag	Cd	Sn	Sb	Te	Pt	Au	Hg	Pb	Bi	Total
Basal mineralization zone																					
RTTC-BT-092	34.19	0.00	30.94	0.04	0.01	34.50	0.03	0.02	0.01	0.03	0.01	0.00	0.00	0.00	0.00	0.06	0.00	0.00	0.00	0.11	99.95
	39.84	0.01	60.29	0.04	0.85	0.00	0.09	0.01	0.00	0.01	0.00	0.03	0.00	0.00	0.01	0.03	0.00	0.04	0.11	0.17	101.52
	32.60	0.03	8.83	0.05	0.20	1.51	55.14	0.00	0.00	0.00	0.00	0.04	0.00	0.00	0.00	0.00	0.00	0.01	0.00	0.04	98.46
	39.50	0.03	59.71	0.00	0.76	0.17	0.02	0.00	0.00	0.00	0.00	0.00	0.00	0.00	0.00	0.00	0.00	0.05	0.00	0.13	100.37
	0.49	0.01	3.18	0.02	0.12	0.04	0.00	0.06	0.00	23.86	0.00	0.00	0.00	1.16	27.46	0.00	0.00	0.02	0.02	45.09	101.52
	0.53	0.00	2.84	0.03	4.43	0.02	0.03	0.00	0.01	19.39	0.00	0.00	0.00	0.74	60.27	0.00	0.00	0.01	2.64	10.23	101.16
	39.42	0.02	60.00	0.05	0.90	0.03	0.00	0.03	0.00	0.07	0.00	0.00	0.00	0.00	0.00	0.08	0.00	0.00	0.00	0.02	100.63
	34.18	0.02	30.94	0.01	0.02	34.82	0.02	0.00	0.01	0.03	0.00	0.00	0.00	0.00	0.04	0.05	0.00	0.02	0.00	0.08	100.23
	53.41	0.01	44.55	0.09	3.49	0.00	0.02	0.00	0.00	0.02	0.00	0.00	0.01	0.00	0.03	0.00	0.00	0.00	0.00	0.10	101.72
	39.35	0.02	59.90	0.07	0.94	0.02	0.00	0.00	0.00	0.00	0.00	0.02	0.00	0.00	0.01	0.02	0.01	0.03	0.00	0.06	100.45
	32.80	0.01	27.86	0.90	37.22	0.27	0.00	0.01	0.01	0.03	0.07	0.02	0.00	0.00	0.02	0.00	0.00	0.00	0.00	0.00	99.20
RTTC-BT-149	39.02	0.00	60.29	0.02	0.45	0.03	0.01	0.00	0.01	0.00	0.03	0.00	0.02	0.00	0.00	0.00	0.00	0.01	0.00	0.18	100.05
	33.23	0.00	30.47	4.16	31.95	0.63	0.03	0.00	0.02	0.02	0.00	0.00	0.01	0.00	0.04	0.00	0.00	0.00	0.02	0.12	100.70
	34.38	0.00	31.05	0.02	0.05	35.65	0.04	0.00	0.01	0.00	0.01	0.00	0.00	0.00	0.03	0.00	0.00	0.09	0.00	0.12	101.48
	39.04	0.00	60.13	0.00	0.57	0.00	0.02	0.00	0.00	0.00	0.00	0.01	0.00	0.00	0.05	0.01	0.00	0.00	0.00	0.18	100.00
	34.82	0.01	41.95	0.00	0.00	23.73	0.07	0.00	0.02	0.04	0.12	0.00	0.00	0.00	0.03	0.07	0.00	0.00	0.00	0.00	100.85
	34.07	0.03	30.72	0.00	0.06	35.42	0.01	0.03	0.02	0.00	0.06	0.00	0.01	0.00	0.00	0.00	0.00	0.03	0.00	0.08	100.53
	33.73	0.02	30.48	3.44	33.34	0.55	0.00	0.00	0.00	0.06	0.04	0.00	0.00	0.00	0.04	0.00	0.04	0.12	0.00	0.09	101.94
	33.60	0.02	30.27	0.01	0.14	34.65	0.00	0.01	0.03	0.07	0.00	0.02	0.02	0.00	0.00	0.01	0.00	0.00	0.05	0.21	99.11
	39.09	0.00	60.41	0.02	0.43	0.00	0.00	0.00	0.00	0.00	0.02	0.00	0.03	0.00	0.00	0.01	0.00	0.08	0.00	0.12	100.21
	34.72	0.01	41.37	0.01	0.00	23.74	0.00	0.00	0.02	0.00	0.04	0.00	0.02	0.00	0.00	0.00	0.00	0.03	0.00	0.02	99.96
	28.48	0.07	33.11	0.04	17.18	2.25	0.00	0.00	0.00	0.01	13.06	0.01	0.00	0.00	0.00	0.04	0.00	0.00	0.00	0.08	94.32
	14.97	0.01	15.93	0.02	0.04	14.45	0.01	0.00	0.06	17.81	0.00	0.00	6.21	0.00	0.00	32.72	0.00	0.00	0.15	0.06	102.43
	17.58	0.01	7.56	0.00	0.06	19.88	0.01	0.07	0.00	21.12	0.00	0.00	7.62	0.00	0.00	34.75	0.00	0.02	0.00	0.10	108.76
	8.69	0.02	7.62	0.02	0.02	7.18	0.03	0.00	0.01	33.33	0.00	0.00	0.05	0.93	5.63	0.01	0.09	0.07	0.00	32.44	96.12
	10.02	0.00	10.24	0.04	0.14	7.66	0.00	0.00	0.03	30.18	0.00	0.00	0.02	0.34	5.72	0.00	0.00	0.07	0.00	32.84	97.30
RTT-BT-102	34.00	0.00	30.75	0.00	0.00	35.23	0.06	0.00	0.00	0.00	0.00	0.00	0.02	0.00	0.00	0.03	0.00	0.06	0.00	0.10	100.24
	53.44	0.00	46.62	0.71	0.65	0.05	0.00	0.01	0.01	0.00	0.00	0.00	0.00	0.00	0.00	0.00	0.00	0.00	0.00	0.03	101.50
	53.50	0.00	42.75	0.48	5.08	0.06	0.00	0.00	0.02	0.00	0.10	0.00	0.02	0.00	0.03	0.00	0.00	0.12	0.00	0.03	102.19
	34.08	0.00	31.03	0.00	0.02	34.89	0.06	0.00	0.01	0.00	0.00	0.00	0.00	0.00	0.00	0.03	0.00	0.03	0.00	0.12	100.26
	53.81	0.00	47.53	0.38	0.12	0.47	0.02	0.02	0.02	0.02	0.00	0.03	0.05	0.00	0.00	0.00	0.00	0.01	0.00	0.14	102.61
	0.05	0.02	2.35	0.05	0.01	0.05	0.09	0.00	0.00	40.57	0.00	0.00	7.52	2.12	6.88	0.00	0.00	0.00	0.00	35.58	95.29

Sample ID	S	Mn	Fe	Co	Ni	Cu	Zn	As	Se	Pd	Ag	Cd	Sn	Sb	Te	Pt	Au	Hg	Pb	Bi	TOTAL
Basal mineralization zone																					
RTTC-BT-092	1.969	0.000	1.023	0.001	0.000	1.003	0.001	0.000	0.000	0.001	0.000	0.000	0.000	0.000	0.000	0.001	0.000	0.000	0.000	0.001	4.000
	1.062	0.000	0.922	0.001	0.012	0.000	0.001	0.000	0.000	0.000	0.000	0.000	0.000	0.000	0.000	0.000	0.000	0.000	0.000	0.001	2.000
	0.993	0.000	0.154	0.001	0.003	0.023	0.824	0.000	0.000	0.000	0.000	0.000	0.000	0.000	0.000	0.000	0.000	0.000	0.000	0.000	2.000
	1.063	0.001	0.922	0.000	0.011	0.002	0.000	0.000	0.000	0.000	0.000	0.000	0.000	0.000	0.000	0.000	0.000	0.000	0.000	0.001	2.000
	0.061	0.001	0.230	0.002	0.008	0.002	0.000	0.003	0.000	0.908	0.000	0.000	0.000	0.039	0.871	0.000	0.000	0.000	0.000	0.874	3.000
	0.058	0.000	0.176	0.002	0.261	0.001	0.002	0.000	0.000	0.631	0.000	0.000	0.000	0.021	1.635	0.000	0.000	0.000	0.044	0.169	3.000
	1.059	0.000	0.925	0.001	0.013	0.000	0.000	0.000	0.000	0.001	0.000	0.000	0.000	0.000	0.000	0.000	0.000	0.000	0.000	0.000	2.000
	1.965	0.001	1.021	0.000	0.001	1.010	0.000	0.000	0.000	0.001	0.000	0.000	0.000	0.000	0.001	0.001	0.000	0.000	0.000	0.001	4.000
	1.978	0.000	0.948	0.002	0.071	0.000	0.000	0.000	0.000	0.000	0.000	0.000	0.000	0.000	0.000	0.000	0.000	0.000	0.000	0.001	3.000
	1.059	0.000	0.925	0.001	0.014	0.000	0.000	0.000	0.000	0.000	0.000	0.000	0.000	0.000	0.000	0.000	0.000	0.000	0.000	0.000	2.000
	7.988	0.002	3.896	0.119	4.952	0.033	0.000	0.001	0.001	0.002	0.005	0.001	0.000	0.000	0.001	0.000	0.000	0.000	0.000	0.000	17.000
RTTC-BT-149	1.055	0.000	0.936	0.000	0.007	0.000	0.000	0.000	0.000	0.000	0.000	0.000	0.000	0.000	0.000	0.000	0.000	0.000	0.000	0.001	2.000
	7.976	0.000	4.199	0.544	4.190	0.076	0.003	0.000	0.002	0.002	0.000	0.000	0.001	0.000	0.002	0.000	0.000	0.000	0.001	0.004	17.000
	1.956	0.000	1.014	0.001	0.002	1.023	0.001	0.000	0.000	0.000	0.000	0.000	0.000	0.000	0.000	0.000	0.000	0.001	0.000	0.001	4.000
	1.056	0.000	0.934	0.000	0.008	0.000	0.000	0.000	0.000	0.000	0.000	0.000	0.000	0.000	0.000	0.000	0.000	0.000	0.000	0.001	2.000
	2.943	0.000	2.036	0.000	0.000	1.012	0.003	0.000	0.001	0.001	0.003	0.000	0.000	0.000	0.001	0.001	0.000	0.000	0.000	0.000	6.000
	1.956	0.001	1.012	0.000	0.002	1.026	0.000	0.001	0.000	0.000	0.001	0.000	0.000	0.000	0.000	0.000	0.000	0.000	0.000	0.001	4.000
	7.999	0.002	4.151	0.444	4.320	0.066	0.000	0.000	0.000	0.004	0.003	0.000	0.000	0.000	0.003	0.000	0.001	0.005	0.000	0.003	17.000
	1.958	0.001	1.013	0.000	0.004	1.019	0.000	0.000	0.001	0.001	0.000	0.000	0.000	0.000	0.000	0.000	0.000	0.000	0.000	0.002	4.000
	1.055	0.000	0.937	0.000	0.006	0.000	0.000	0.000	0.000	0.000	0.000	0.000	0.000	0.000	0.000	0.000	0.000	0.000	0.000	0.001	2.000
	2.955	0.000	2.022	0.000	0.000	1.020	0.000	0.000	0.001	0.000	0.001	0.000	0.000	0.000	0.000	0.000	0.000	0.000	0.000	0.000	6.000
	7.812	0.011	5.215	0.006	2.574	0.311	0.000	0.000	0.000	0.001	1.065	0.001	0.000	0.000	0.000	0.002	0.000	0.000	0.000	0.003	17.000
	2.386	0.000	1.457	0.002	0.003	1.162	0.001	0.000	0.004	0.855	0.000	0.000	0.267	0.000	0.000	0.857	0.000	0.000	0.004	0.002	7.000
	2.665	0.001	0.658	0.000	0.005	1.521	0.000	0.004	0.000	0.965	0.000	0.000	0.312	0.000	0.000	0.866	0.000	0.000	0.000	0.002	7.000
	2.598	0.003	1.307	0.003	0.003	1.083	0.004	0.000	0.001	3.002	0.000	0.000	0.004	0.073	0.422	0.001	0.004	0.003	0.000	1.488	10.000
	2.817	0.000	1.654	0.006	0.022	1.087	0.000	0.000	0.003	2.559	0.000	0.000	0.002	0.025	0.404	0.000	0.000	0.003	0.000	1.417	10.000
RTT-BT-102	1.957	0.000	1.016	0.000	0.000	1.023	0.002	0.000	0.000	0.000	0.000	0.000	0.000	0.000	0.000	0.000	0.000	0.001	0.000	0.001	4.000
	1.980	0.000	0.992	0.014	0.013	0.001	0.000	0.000	0.000	0.000	0.000	0.000	0.000	0.000	0.000	0.000	0.000	0.000	0.000	0.000	3.000
	1.977	0.000	0.907	0.010	0.103	0.001	0.000	0.000	0.000	0.000	0.001	0.000	0.000	0.000	0.000	0.000	0.000	0.001	0.000	0.000	3.000
	1.959	0.000	1.024	0.000	0.001	1.012	0.002	0.000	0.000	0.000	0.000	0.000	0.000	0.000	0.000	0.000	0.000	0.000	0.000	0.001	4.000
	1.976	0.000	1.002	0.008	0.002	0.009	0.000	0.000	0.000	0.000	0.000	0.000	0.001	0.000	0.000	0.000	0.000	0.000	0.000	0.001	3.000
	0.023	0.005	0.574	0.011	0.003	0.010	0.019	0.000	0.000	5.198	0.000	0.000	0.864	0.237	0.735	0.000	0.000	0.000	0.000	2.321	10.000

Sample ID	DDH	Depth	Description	Mineral
Basal mineralization zone				
RTTC-BT-173	07TH003	298	po repl silicate alteration (stilpn?)	Pyrrhotite
			po repl silicate alteration (stilpn?), lighter area	Pyrrhotite
			cp	Chalcopyrite
			po	Pyrrhotite
			kotulskite ? intergrown w. cobaltite in marcasite alteration	kotulskite
			cobaltite intergr. w. kotulskite	cobaltite
			marcasite alteration	Marcasite
			po	Pyrrhotite
			cp	Chalcopyrite
			kotulskite (F358)	kotulskite
Upper mineralized zone				
RTTC-BT-134	07TH006	182	tiny bornite ass. w. sec. mt in serpentine alteration	Bornite
			tiny ? ass. w. sec. mt in serpentine alteration	mixture ?
			tiny ? ass. w. sec. mt in serpentine alteration	mixture ?
			rounded millerite in cp-bn	Millerite
			tiny round white incl in bn	kotulskite?
			bornite	Bornite
			cp	Millerite
			cp	Chalcopyrite
			Pd(BiTe) in bn	kotulskite?
			tiny gn in other bn	Galena
			bornite	Bornite
			millerite	Millerite
			millerite	Millerite
Sulphide stringers				
RTTC-BT-176	05TH003	298	massive po	Pyrrhotite
			stringy marcasite alteration in massive po	Marcasite
			f. gr. euhedral bravoite in "moat" in massive po	Bravoite
			cp in massive po	Chalcopyrite
			tiny grain [Pd(Te,Bi,Sb)]in gangue	kotulskite
			pn flame protruding into gangue	Siegenite
			filigree pyrite altering plagioclase	Pyrite
			pyrite aggregates in cp in po	Pyrite
			cp surr. py	Chalcopyrite
			massive po	Pyrrhotite
			euh. bravoite in massive po	Pyrite
			siegeneite flame in massive po	Siegenite
			tiny oval inclusion in rim of massive po	Ni-merenskyite?
			massive po	Pyrrhotite
			tiny spec Pd(Te,Bi,Sb) in cp	Kotulskite
			cp	Chalcopyrite

Sample ID	S	Mn	Fe	Co	Ni	Cu	Zn	As	Se	Pd	Ag	Cd	Sn	Sb	Te	Pt	Au	Hg	Pb	Bi	Total
Basal mineralization zone																					
RTTC-BT-173	40.96	0.00	58.48	0.01	0.38	0.00	0.00	0.00	0.02	0.01	0.00	0.00	0.00	0.00	0.02	0.01	0.00	0.05	0.00	0.13	100.05
	40.45	0.00	59.29	0.01	0.17	0.00	0.00	0.01	0.02	0.07	0.00	0.00	0.00	0.00	0.03	0.00	0.08	0.05	0.00	0.13	100.31
	34.24	0.00	30.82	0.00	0.00	34.62	0.04	0.00	0.00	0.00	0.00	0.05	0.01	0.00	0.00	0.06	0.00	0.02	0.00	0.08	99.93
	40.98	0.03	58.09	0.02	0.71	0.01	0.00	0.00	0.00	0.01	0.00	0.04	0.00	0.00	0.03	0.00	0.08	0.05	0.00	0.08	100.12
	0.11	0.02	2.10	0.04	0.08	0.02	0.09	0.00	0.00	40.17	0.00	0.00	0.00	1.94	36.98	0.00	0.00	0.06	0.00	22.09	103.69
	18.59	0.00	8.02	16.94	6.54	0.04	0.05	43.26	0.23	4.23	0.34	0.00	0.00	0.00	0.44	0.00	0.00	0.00	0.00	0.33	99.01
	53.81	0.00	44.40	0.12	3.61	0.02	0.05	0.00	0.02	0.03	0.01	0.09	0.00	0.00	0.00	0.00	0.09	0.00	0.01	0.06	102.29
	39.54	0.00	59.96	0.06	0.92	0.03	0.01	0.00	0.03	0.00	0.07	0.00	0.02	0.00	0.02	0.05	0.05	0.06	0.00	0.10	100.93
	34.66	0.01	30.74	0.00	0.00	34.91	0.04	0.00	0.00	0.00	0.00	0.00	0.02	0.00	0.01	0.00	0.07	0.00	0.00	0.06	100.51
	0.21	0.00	4.19	0.02	0.02	0.38	0.00	0.01	0.01	38.16	0.00	0.00	0.00	2.97	30.82	0.13	0.00	0.00	0.02	24.11	101.05
Upper mineralized zone																					
RTTC-BT-134	25.07	0.00	11.07	0.00	0.02	61.97	0.02	0.00	0.01	0.00	0.00	0.00	0.00	0.00	0.00	0.00	0.00	0.00	0.00	0.06	98.22
	0.01	0.06	2.68	0.01	0.04	0.00	0.02	0.00	0.04	0.00	0.00	0.04	0.05	0.00	0.00	8.86	19.79	0.22	0.13	0.06	31.99
	0.01	0.05	3.49	0.01	0.07	0.00	0.01	0.00	0.04	0.02	0.00	0.00	0.01	0.03	0.00	7.36	12.21	0.11	0.00	0.00	23.41
	34.72	0.00	0.32	2.54	60.79	0.05	0.02	0.01	0.02	0.00	0.00	0.00	0.02	0.00	0.07	0.04	0.00	0.06	0.00	0.11	98.76
	4.65	0.02	1.53	0.04	0.16	18.71	0.02	0.00	0.00	40.50	0.00	0.00	0.00	0.26	30.00	0.00	0.00	0.96	0.11	7.83	104.79
	25.45	0.00	11.38	0.00	0.05	61.91	0.01	0.00	0.02	0.00	0.00	0.00	0.02	0.00	0.00	0.00	0.03	0.00	0.00	0.08	98.96
	35.22	0.00	0.33	2.60	61.25	0.37	0.03	0.00	0.01	0.00	0.00	0.00	0.00	0.01	0.06	0.00	0.06	0.10	0.00	0.06	100.07
	34.21	0.02	30.00	0.00	0.01	34.48	0.04	0.00	0.02	0.02	0.00	0.00	0.00	0.00	0.00	0.03	0.05	0.00	0.00	0.09	98.96
	5.12	0.01	2.49	0.01	0.01	17.06	0.00	0.00	0.01	38.41	0.00	0.00	0.01	0.26	33.10	0.03	0.10	0.68	0.01	8.92	106.21
	12.50	0.02	1.53	0.00	0.06	8.13	0.06	0.00	3.65	0.02	0.00	0.06	0.00	0.00	0.00	0.00	0.00	0.00	81.70	0.00	107.72
	25.73	0.00	11.36	0.00	0.00	62.13	0.06	0.00	0.04	0.00	0.00	0.00	0.00	0.00	0.01	0.02	0.01	0.00	0.00	0.13	99.50
	34.57	0.02	0.35	3.92	59.44	0.36	0.02	0.01	0.03	0.00	0.00	0.03	0.00	0.00	0.05	0.05	0.00	0.00	0.00	0.06	98.88
	35.08	0.01	0.07	2.37	61.72	0.00	0.04	0.02	0.04	0.00	0.00	0.00	0.01	0.00	0.01	0.03	0.11	0.00	0.00	0.01	99.50
Sulphide stringers																					
RTTC-BT-176	39.74	0.01	58.75	0.07	1.29	0.00	0.02	0.01	0.00	0.01	0.00	0.00	0.00	0.00	0.01	0.01	0.00	0.00	0.00	0.14	100.06
	53.28	0.00	44.21	1.41	1.94	0.00	0.00	0.01	0.00	0.00	0.00	0.00	0.02	0.00	0.01	0.00	0.03	0.00	0.00	0.05	100.95
	53.58	0.01	43.32	0.41	3.59	0.01	0.00	0.02	0.02	0.00	0.00	0.00	0.00	0.00	0.00	0.00	0.00	0.00	0.00	0.10	101.05
	34.26	0.00	30.70	0.01	0.00	34.47	0.00	0.00	0.01	0.02	0.00	0.00	0.02	0.00	0.04	0.00	0.00	0.00	0.00	0.13	99.65
	0.04	0.03	6.63	0.04	0.03	0.00	0.03	0.00	0.01	27.10	0.00	0.00	0.05	3.35	22.82	0.08	0.00	0.00	0.00	13.90	74.12
	42.39	0.01	13.94	18.28	25.67	0.10	0.02	0.00	0.01	0.00	0.00	0.05	0.02	0.00	0.00	0.01	0.07	0.04	0.00	0.14	100.72
	50.60	0.01	45.53	0.01	0.08	0.00	0.03	0.00	0.01	0.01	0.00	0.00	0.03	0.00	0.00	0.00	0.00	0.00	0.16	0.01	96.46
	53.67	0.02	43.99	3.58	0.01	0.00	0.03	0.00	0.00	0.00	0.00	0.00	0.03	0.00	0.00	0.00	0.00	0.00	0.00	0.13	101.45
	34.44	0.00	30.59	0.00	0.00	34.64	0.09	0.00	0.03	0.00	0.00	0.00	0.00	0.00	0.00	0.00	0.00	0.00	0.00	0.05	99.84
	39.56	0.02	58.63	0.08	1.29	0.02	0.00	0.00	0.02	0.00	0.00	0.00	0.02	0.00	0.01	0.04	0.07	0.00	0.00	0.09	99.84
	53.92	0.01	47.48	0.03	0.12	0.01	0.00	0.00	0.00	0.00	0.00	0.00	0.02	0.00	0.00	0.04	0.04	0.00	0.00	0.09	101.77
	42.00	0.02	12.40	20.29	25.58	0.00	0.07	0.01	0.01	0.00	0.00	0.00	0.00	0.00	0.00	0.00	0.00	0.00	0.00	0.05	100.41
	24.21	0.00	33.00	0.00	0.73	0.11	0.02	0.00	0.00	12.60	0.00	0.00	0.04	0.11	20.23	0.00	0.00	0.00	0.00	7.78	98.81
	39.83	0.00	58.38	0.00	1.23	0.02	0.00	0.02	0.00	0.00	0.00	0.00	0.04	0.00	0.03	0.06	0.00	0.00	0.00	0.07	99.68
	9.07	0.00	9.87	0.00	0.01	9.59	0.01	0.00	0.00	27.06	0.00	0.00	0.04	3.84	24.81	0.00	0.00	0.00	0.02	13.37	97.70
	34.48	0.00	30.68	0.02	0.01	34.64	0.01	0.00	0.02	0.04	0.00	0.00	0.01	0.00	0.00	0.06	0.05	0.05	0.00	0.21	100.27

Sample ID	S	Mn	Fe	Co	Ni	Cu	Zn	As	Se	Pd	Ag	Cd	Sn	Sb	Te	Pt	Au	Hg	Pb	Bi	TOTAL
Basal mineralization zone																					
RTTC-BT-173	1.095	0.000	0.898	0.000	0.005	0.000	0.000	0.000	0.000	0.000	0.000	0.000	0.000	0.000	0.000	0.000	0.000	0.000	0.000	0.001	2.000
	1.083	0.000	0.912	0.000	0.003	0.000	0.000	0.000	0.000	0.001	0.000	0.000	0.000	0.000	0.000	0.000	0.000	0.000	0.000	0.001	2.000
	1.972	0.000	1.019	0.000	0.000	1.006	0.001	0.000	0.000	0.000	0.000	0.001	0.000	0.000	0.000	0.001	0.000	0.000	0.000	0.001	4.000
	1.096	0.000	0.892	0.000	0.010	0.000	0.000	0.000	0.000	0.000	0.000	0.000	0.000	0.000	0.000	0.000	0.000	0.000	0.000	0.000	2.000
	0.008	0.001	0.090	0.001	0.003	0.001	0.003	0.000	0.000	0.905	0.000	0.000	0.000	0.038	0.695	0.000	0.000	0.001	0.000	0.253	2.000
	0.993	0.000	0.246	0.492	0.191	0.001	0.001	0.989	0.005	0.068	0.005	0.000	0.000	0.000	0.006	0.000	0.000	0.000	0.000	0.003	3.000
	1.982	0.000	0.939	0.002	0.073	0.000	0.001	0.000	0.000	0.000	0.000	0.001	0.000	0.000	0.000	0.000	0.001	0.000	0.000	0.000	3.000
	1.060	0.000	0.923	0.001	0.013	0.000	0.000	0.000	0.000	0.000	0.001	0.000	0.000	0.000	0.000	0.000	0.000	0.000	0.000	0.000	2.000
	1.981	0.000	1.009	0.000	0.000	1.007	0.001	0.000	0.000	0.000	0.000	0.000	0.000	0.000	0.000	0.000	0.001	0.000	0.000	0.000	4.000
	0.015	0.000	0.181	0.001	0.001	0.014	0.000	0.000	0.000	0.865	0.000	0.000	0.000	0.059	0.583	0.002	0.000	0.000	0.000	0.278	2.000
Upper mineralized zone																					
RTTC-BT-134	3.996	0.000	1.014	0.000	0.002	4.985	0.001	0.000	0.001	0.000	0.000	0.000	0.000	0.000	0.000	0.000	0.000	0.000	0.000	0.001	10.000
	0.005	0.015	0.722	0.002	0.009	0.000	0.004	0.000	0.008	0.000	0.000	0.005	0.006	0.000	0.000	0.683	1.511	0.016	0.009	0.005	3.000
	0.003	0.015	1.128	0.003	0.022	0.000	0.004	0.000	0.008	0.003	0.000	0.000	0.001	0.004	0.000	0.680	1.118	0.010	0.000	0.000	3.000
	0.998	0.000	0.005	0.040	0.954	0.001	0.000	0.000	0.000	0.000	0.000	0.000	0.000	0.000	0.001	0.000	0.000	0.000	0.000	0.000	2.000
	0.256	0.000	0.048	0.001	0.005	0.520	0.001	0.000	0.000	0.673	0.000	0.000	0.000	0.004	0.416	0.000	0.000	0.008	0.001	0.066	2.000
	4.021	0.000	1.033	0.000	0.004	4.936	0.001	0.000	0.002	0.000	0.000	0.000	0.001	0.000	0.000	0.000	0.001	0.000	0.000	0.002	10.000
	0.999	0.000	0.005	0.040	0.949	0.005	0.000	0.000	0.000	0.000	0.000	0.000	0.000	0.000	0.000	0.000	0.000	0.000	0.000	0.000	2.000
	1.986	0.001	1.000	0.000	0.000	1.010	0.001	0.000	0.000	0.000	0.000	0.000	0.000	0.000	0.000	0.000	0.000	0.000	0.000	0.001	4.000
	0.279	0.000	0.078	0.000	0.000	0.470	0.000	0.000	0.000	0.632	0.000	0.000	0.000	0.004	0.454	0.000	0.001	0.006	0.000	0.075	2.000
	0.789	0.001	0.056	0.000	0.002	0.259	0.002	0.000	0.094	0.000	0.000	0.001	0.000	0.000	0.000	0.000	0.000	0.000	0.798	0.000	2.000
	4.040	0.000	1.024	0.000	0.000	4.923	0.005	0.000	0.003	0.000	0.000	0.000	0.000	0.000	0.000	0.000	0.000	0.000	0.000	0.003	10.000
	0.993	0.000	0.006	0.061	0.933	0.005	0.000	0.000	0.000	0.000	0.000	0.000	0.000	0.000	0.000	0.000	0.000	0.000	0.000	0.000	2.000
	0.999	0.000	0.001	0.037	0.961	0.000	0.001	0.000	0.000	0.000	0.000	0.000	0.000	0.000	0.000	0.000	0.000	0.000	0.000	0.000	2.000
Sulphide stringers																					
RTTC-BT-176	1.070	0.000	0.908	0.001	0.019	0.000	0.000	0.000	0.000	0.000	0.000	0.000	0.000	0.000	0.000	0.000	0.000	0.000	0.000	0.001	2.000
	1.985	0.000	0.946	0.029	0.040	0.000	0.000	0.000	0.000	0.000	0.000	0.000	0.000	0.000	0.000	0.000	0.000	0.000	0.000	0.000	3.000
	1.992	0.000	0.925	0.008	0.073	0.000	0.000	0.000	0.000	0.000	0.000	0.000	0.000	0.000	0.000	0.000	0.000	0.000	0.000	0.001	3.000
	1.977	0.000	1.017	0.000	0.000	1.003	0.000	0.000	0.000	0.000	0.000	0.000	0.000	0.000	0.001	0.000	0.000	0.000	0.000	0.001	4.000
	0.004	0.002	0.365	0.002	0.002	0.000	0.002	0.000	0.000	0.783	0.000	0.000	0.001	0.084	0.550	0.001	0.000	0.000	0.000	0.204	2.000
	3.984	0.000	0.752	0.935	1.318	0.005	0.001	0.000	0.000	0.000	0.000	0.001	0.000	0.000	0.000	0.000	0.001	0.001	0.000	0.002	7.000
	1.975	0.000	1.021	0.000	0.002	0.000	0.000	0.000	0.000	0.000	0.000	0.000	0.000	0.000	0.000	0.000	0.000	0.000	0.001	0.000	3.000
	1.989	0.000	0.936	0.072	0.000	0.000	0.000	0.000	0.000	0.000	0.000	0.000	0.000	0.000	0.000	0.000	0.000	0.000	0.000	0.001	3.000
	1.981	0.000	1.010	0.000	0.000	1.005	0.003	0.000	0.001	0.000	0.000	0.000	0.000	0.000	0.000	0.000	0.000	0.000	0.000	0.000	4.000
	1.069	0.000	0.909	0.001	0.019	0.000	0.000	0.000	0.000	0.000	0.000	0.000	0.000	0.000	0.000	0.000	0.000	0.000	0.000	0.000	2.000
	1.989	0.000	1.006	0.001	0.002	0.000	0.000	0.000	0.000	0.000	0.000	0.000	0.000	0.000	0.000	0.000	0.000	0.000	0.000	0.001	3.000
	3.963	0.001	0.672	1.042	1.318	0.000	0.003	0.000	0.000	0.000	0.000	0.000	0.000	0.000	0.000	0.000	0.000	0.000	0.000	0.001	7.000
	1.352	0.000	1.058	0.000	0.022	0.003	0.001	0.000	0.000	0.212	0.000	0.000	0.001	0.002	0.284	0.000	0.000	0.000	0.000	0.067	3.000
	1.075	0.000	0.905	0.000	0.018	0.000	0.000	0.000	0.000	0.000	0.000	0.000	0.000	0.000	0.000	0.000	0.000	0.000	0.000	0.000	2.000
	0.489	0.000	0.306	0.000	0.000	0.261	0.000	0.000	0.000	0.440	0.000	0.000	0.001	0.055	0.336	0.000	0.000	0.000	0.000	0.111	2.000
	1.980	0.000	1.011	0.000	0.000	1.003	0.000	0.000	0.000	0.001	0.000	0.000	0.000	0.000	0.000	0.001	0.000	0.000	0.000	0.002	4.000

Sample ID	DDH	Depth	Description	Mineral
Sulphide stringers				
RTTC-BT-090	07TH004	437	cp	Chalcopyrite
			anh. pn in cp	Pentlandite
			anh. py veining cp	Pyrite
			sperrylite fragment	sperrylite
			py intergrown w. mt	Pyrite
			pn	Pentlandite
			cp	Chalcopyrite
			small sph incl. in cp	sphalerite
			spongy mc-py alteration	Pyrite
			small euh sperrylite	sperrylite
			po (in vein?) w. cp lenses	Pyrrhotite
			trace anh py attached to round mt	Pyrite
			po host	Pyrrhotite
			py overgrowing stringy marcasite alteration	Pyrite
			coarse pn	Pentlandite
			small subh py at edge of po-cp	Pyrite
			coarse pn	Pentlandite
			po	Pyrrhotite
			spongy pyrite patches in py-mt intergrowth	Pyrite
			anh. po	Pyrrhotite
Po-rich massive sulphide veinlet				
RTTC-BT-177	05TH003	300	py aggregate surr. by cp	Pyrite
			py in graphic intergrowth w. mt (previous was in 2)	Pyrite
			massive po	Pyrrhotite
			cp rimming py 1	Chalcopyrite
			Pd5Sb2 in gangue filled crack in massive po	Stibiopalladinite
			massive po	Pyrrhotite
			euh. Pd2Sb in crack in po (F878)	Naldrettite
			Pd2Sb in crack in po (F876)	Naldrettite
			bravoite in po	Pyrite
			massive po	Pyrrhotite
			siegenite flame in po	Siegenite
			stringy marcasite alteration	Marcasite
			remobilized cp	Chalcopyrite

Sample ID	S	Mn	Fe	Co	Ni	Cu	Zn	As	Se	Pd	Ag	Cd	Sn	Sb	Te	Pt	Au	Hg	Pb	Bi	Total
Sulphide stringers																					
RTTC-BT-090	33.93	0.00	30.23	0.00	0.02	34.52	0.01	0.02	0.01	0.00	0.00	0.00	0.03	0.00	0.00	0.00	0.00	0.01	0.00	0.10	98.88
	32.74	0.01	23.91	0.00	42.56	0.28	0.05	0.00	0.01	0.00	0.02	0.00	0.15	0.00	0.00	0.00	0.04	0.02	0.00	0.19	99.99
	53.64	0.00	47.28	0.00	0.16	0.42	0.00	0.00	0.02	0.04	0.00	0.00	0.00	0.00	0.00	0.00	0.00	0.04	0.00	0.06	101.65
	0.38	0.01	0.55	0.01	0.00	0.56	0.00	42.20	0.28	0.08	0.02	0.00	0.00	0.08	0.00	55.12	0.00	0.03	0.26	0.00	99.57
	53.73	0.02	42.53	0.01	4.65	0.07	0.00	0.00	0.01	0.00	0.00	0.02	0.03	0.00	0.00	0.02	0.00	0.00	0.00	0.09	101.17
	34.26	0.00	25.75	0.24	40.23	0.06	0.00	0.02	0.00	0.03	0.00	0.00	0.00	0.00	0.03	0.03	0.00	0.08	0.01	0.18	100.92
	34.46	0.00	30.50	0.03	0.05	34.76	0.00	0.01	0.03	0.04	0.01	0.01	0.03	0.00	0.02	0.00	0.00	0.09	0.00	0.10	100.12
	32.26	0.03	6.97	0.07	0.02	1.55	57.66	0.01	0.00	0.00	0.00	0.22	0.04	0.00	0.00	0.00	0.06	0.08	0.00	0.13	99.10
	53.27	0.00	42.49	0.09	4.97	0.04	0.08	0.00	0.01	0.00	0.00	0.00	0.05	0.00	0.01	0.01	0.00	0.00	0.00	0.13	101.13
	0.39	0.00	0.65	0.01	0.05	0.30	0.03	42.29	0.23	0.07	0.01	0.00	0.00	0.10	0.00	56.84	0.00	0.00	0.25	0.14	101.34
	39.21	0.00	60.20	0.02	1.22	0.07	0.00	0.00	0.02	0.02	0.00	0.02	0.00	0.00	0.04	0.08	0.00	0.00	0.00	0.14	101.05
	53.40	0.00	45.56	2.14	0.02	0.07	0.05	0.00	0.01	0.07	0.03	0.00	0.00	0.00	0.00	0.02	0.00	0.15	0.00	0.13	101.64
	39.48	0.00	59.19	0.00	1.18	0.00	0.00	0.03	0.01	0.00	0.00	0.00	0.00	0.00	0.01	0.03	0.00	0.00	0.00	0.12	100.05
	53.81	0.00	45.49	2.26	0.05	0.10	0.00	0.00	0.03	0.00	0.00	0.00	0.00	0.00	0.00	0.00	0.00	0.00	0.00	0.10	101.84
	32.64	0.00	28.38	1.00	38.06	0.02	0.00	0.00	0.02	0.01	0.03	0.03	0.00	0.00	0.00	0.00	0.00	0.05	0.00	0.00	100.24
	53.98	0.00	44.63	2.43	0.04	0.48	0.04	0.00	0.01	0.02	0.00	0.00	0.00	0.00	0.02	0.00	0.00	0.00	0.00	0.05	101.71
	32.78	0.00	28.50	1.04	37.41	0.04	0.00	0.02	0.00	0.00	0.00	0.00	0.00	0.00	0.04	0.01	0.00	0.00	0.09	0.06	99.99
	39.01	0.00	59.11	0.01	1.29	0.03	0.00	0.00	0.02	0.00	0.00	0.00	0.00	0.00	0.00	0.00	0.00	0.03	0.00	0.03	99.53
	53.45	0.00	45.41	2.58	0.07	0.00	0.09	0.00	0.02	0.03	0.01	0.00	0.00	0.00	0.00	0.05	0.00	0.00	0.00	0.03	101.73
	39.20	0.00	59.89	0.05	0.79	0.00	0.00	0.00	0.00	0.00	0.00	0.00	0.00	0.00	0.02	0.00	0.00	0.07	0.00	0.16	100.17
Po-rich massive sulphide veinlet																					
RTTC-BT-177	53.36	0.00	45.29	2.09	0.02	0.05	0.03	0.01	0.00	0.02	0.00	0.00	0.00	0.00	0.00	0.05	0.00	0.04	0.00	0.18	101.14
	53.08	0.00	44.11	0.17	3.51	0.00	0.01	0.01	0.01	0.00	0.00	0.00	0.01	0.00	0.01	0.00	0.11	0.11	0.00	0.12	101.25
	39.83	0.00	58.47	0.08	1.44	0.01	0.00	0.00	0.00	0.00	0.00	0.01	0.01	0.00	0.02	0.00	0.00	0.00	0.00	0.05	99.91
	34.17	0.00	30.36	0.00	0.02	34.26	0.01	0.02	0.00	0.00	0.00	0.00	0.00	0.00	0.00	0.08	0.05	0.00	0.04	0.12	99.12
	0.00	0.00	0.00	0.03	0.00	0.04	0.03	0.13	0.00	69.44	0.00	0.00	0.14	30.30	0.00	0.00	0.00	0.00	0.00	0.05	100.15
	36.16	0.00	58.35	0.07	1.35	0.00	0.02	0.00	0.01	0.00	0.00	0.00	0.01	0.00	0.00	0.02	0.00	0.04	0.00	0.07	96.10
	0.39	0.00	3.08	0.00	0.09	0.03	0.03	0.13	0.04	61.44	0.00	0.00	0.10	34.31	0.00	0.00	0.00	0.00	0.00	0.00	99.65
	0.00	0.00	0.00	0.03	0.10	0.66	0.07	0.12	0.01	64.60	0.00	0.00	0.10	33.49	1.04	0.00	0.00	0.00	0.00	0.50	100.71
	54.77	0.00	42.17	1.44	3.76	0.00	0.02	0.03	0.02	0.03	0.00	0.01	0.01	0.00	0.00	0.07	0.00	0.00	0.00	0.09	102.41
	38.77	0.00	58.83	0.09	1.24	0.00	0.00	0.03	0.03	0.04	0.00	0.00	0.02	0.00	0.00	0.00	0.00	0.04	0.00	0.11	99.20
	41.26	0.00	18.21	12.41	27.03	0.00	0.03	0.00	0.02	0.00	0.00	0.01	0.01	0.00	0.00	0.00	0.00	0.03	0.00	0.09	99.09
	52.62	0.02	45.20	0.01	2.04	0.00	0.01	0.00	0.01	0.00	0.00	0.00	0.03	0.00	0.00	0.00	0.01	0.01	0.00	0.22	100.18
	34.29	0.00	30.83	0.00	0.01	34.63	0.01	0.00	0.00	0.04	0.00	0.00	0.00	0.00	0.00	0.00	0.03	0.02	0.00	0.11	99.96

Sample ID	S	Mn	Fe	Co	Ni	Cu	Zn	As	Se	Pd	Ag	Cd	Sn	Sb	Te	Pt	Au	Hg	Pb	Bi	TOTAL
Sulphide stringers																					
RTTC-BT-090	1.974	0.000	1.010	0.000	0.001	1.013	0.000	0.000	0.000	0.000	0.000	0.000	0.001	0.000	0.000	0.000	0.000	0.000	0.000	0.001	4.000
	7.953	0.001	3.335	0.001	5.648	0.035	0.006	0.000	0.001	0.000	0.002	0.000	0.010	0.000	0.000	0.000	0.001	0.001	0.000	0.007	17.000
	1.984	0.000	1.004	0.000	0.003	0.008	0.000	0.000	0.000	0.000	0.000	0.000	0.000	0.000	0.000	0.000	0.000	0.000	0.000	0.000	3.000
	0.040	0.000	0.033	0.001	0.000	0.030	0.000	1.913	0.012	0.003	0.001	0.000	0.000	0.002	0.000	0.960	0.000	0.000	0.004	0.000	3.000
	1.996	0.000	0.907	0.000	0.094	0.001	0.000	0.000	0.000	0.000	0.000	0.000	0.000	0.000	0.000	0.000	0.000	0.000	0.000	0.001	3.000
	8.173	0.000	3.527	0.031	5.244	0.008	0.000	0.002	0.000	0.002	0.000	0.000	0.000	0.000	0.001	0.001	0.000	0.003	0.000	0.007	17.000
	1.980	0.000	1.006	0.001	0.002	1.007	0.000	0.000	0.001	0.001	0.000	0.000	0.000	0.000	0.000	0.000	0.000	0.001	0.000	0.001	4.000
	0.985	0.000	0.122	0.001	0.000	0.024	0.863	0.000	0.000	0.000	0.000	0.002	0.000	0.000	0.000	0.000	0.000	0.000	0.000	0.001	2.000
	1.985	0.000	0.909	0.002	0.101	0.001	0.001	0.000	0.000	0.000	0.000	0.000	0.000	0.000	0.000	0.000	0.000	0.000	0.000	0.001	3.000
	0.040	0.000	0.039	0.001	0.003	0.016	0.001	1.899	0.010	0.002	0.000	0.000	0.000	0.003	0.000	0.980	0.000	0.000	0.004	0.002	3.000
	1.052	0.000	0.927	0.000	0.018	0.001	0.000	0.000	0.000	0.000	0.000	0.000	0.000	0.000	0.000	0.000	0.000	0.000	0.000	0.001	2.000
	1.981	0.000	0.970	0.043	0.000	0.001	0.001	0.000	0.000	0.001	0.000	0.000	0.000	0.000	0.000	0.000	0.000	0.001	0.000	0.001	3.000
	1.065	0.000	0.917	0.000	0.017	0.000	0.000	0.000	0.000	0.000	0.000	0.000	0.000	0.000	0.000	0.000	0.000	0.000	0.000	0.000	2.000
	1.986	0.000	0.964	0.045	0.001	0.002	0.000	0.000	0.000	0.000	0.000	0.000	0.000	0.000	0.000	0.000	0.000	0.000	0.000	0.001	3.000
	7.890	0.000	3.940	0.132	5.027	0.002	0.000	0.000	0.002	0.001	0.002	0.002	0.000	0.000	0.000	0.000	0.000	0.002	0.000	0.000	17.000
	1.993	0.000	0.946	0.049	0.001	0.009	0.001	0.000	0.000	0.000	0.000	0.000	0.000	0.000	0.000	0.000	0.000	0.000	0.000	0.000	3.000
	7.936	0.000	3.962	0.138	4.949	0.004	0.000	0.002	0.000	0.000	0.000	0.000	0.000	0.000	0.003	0.000	0.000	0.000	0.003	0.002	17.000
	1.059	0.000	0.921	0.000	0.019	0.000	0.000	0.000	0.000	0.000	0.000	0.000	0.000	0.000	0.000	0.000	0.000	0.000	0.000	0.000	2.000
	1.979	0.000	0.965	0.052	0.001	0.000	0.002	0.000	0.000	0.000	0.000	0.000	0.000	0.000	0.000	0.000	0.000	0.000	0.000	0.000	3.000
	1.058	0.000	0.928	0.001	0.012	0.000	0.000	0.000	0.000	0.000	0.000	0.000	0.000	0.000	0.000	0.000	0.000	0.000	0.000	0.001	2.000
Po-rich massive sulphide veinlet																					
RTTC-BT-177	1.986	0.000	0.968	0.042	0.000	0.001	0.001	0.000	0.000	0.000	0.000	0.000	0.000	0.000	0.000	0.000	0.000	0.000	0.000	0.001	3.000
	1.978	0.000	0.944	0.003	0.071	0.000	0.000	0.000	0.000	0.000	0.000	0.000	0.000	0.000	0.000	0.000	0.001	0.001	0.000	0.001	3.000
	1.073	0.000	0.904	0.001	0.021	0.000	0.000	0.000	0.000	0.000	0.000	0.000	0.000	0.000	0.000	0.000	0.000	0.000	0.000	0.000	2.000
	1.982	0.000	1.011	0.000	0.000	1.003	0.000	0.000	0.000	0.000	0.000	0.000	0.000	0.000	0.000	0.001	0.000	0.000	0.000	0.001	4.000
	0.000	0.000	0.000	0.003	0.000	0.004	0.003	0.014	0.000	5.042	0.000	0.000	0.009	1.922	0.000	0.000	0.000	0.000	0.000	0.002	7.000
	1.026	0.000	0.951	0.001	0.021	0.000	0.000	0.000	0.000	0.000	0.000	0.000	0.000	0.000	0.000	0.000	0.000	0.000	0.000	0.000	2.000
	0.039	0.000	0.178	0.000	0.005	0.002	0.001	0.006	0.002	1.858	0.000	0.000	0.003	0.907	0.000	0.000	0.000	0.000	0.000	0.000	3.000
	0.000	0.000	0.000	0.001	0.006	0.034	0.003	0.005	0.000	2.004	0.000	0.000	0.003	0.908	0.027	0.000	0.000	0.000	0.000	0.008	3.000
	2.007	0.000	0.887	0.029	0.075	0.000	0.000	0.000	0.000	0.000	0.000	0.000	0.000	0.000	0.000	0.000	0.000	0.000	0.000	0.001	3.000
	1.057	0.000	0.921	0.001	0.018	0.000	0.000	0.000	0.000	0.000	0.000	0.000	0.000	0.000	0.000	0.000	0.000	0.000	0.000	0.000	2.000
	3.941	0.000	0.999	0.645	1.411	0.000	0.001	0.000	0.001	0.000	0.000	0.000	0.000	0.000	0.000	0.000	0.000	0.000	0.000	0.001	7.000
	1.979	0.000	0.976	0.000	0.042	0.000	0.000	0.000	0.000	0.000	0.000	0.000	0.000	0.000	0.000	0.000	0.000	0.000	0.000	0.001	3.000
	1.973	0.000	1.019	0.000	0.000	1.006	0.000	0.000	0.000	0.001	0.000	0.000	0.000	0.000	0.000	0.000	0.000	0.000	0.000	0.001	4.000

Sample ID	DDH	Depth	Description	Mineral
Cp-rich massive sulphide veinlet				
RTTC-BT-161	07TH006	575	zoned py cubes in calcite	Pyrite
			zoned py cubes in calcite, spomgy rim	Pyrite ± millerite
			tiny round inclusion in py core	Galena
			cp	Chalcopyrite
			coarse py	Pyrite
			tiny millerite inclusions in py	Millerite
			sph triangle in py	Sphalerite
			zoned euh py, core (w. sph incl.)	Pyrite
			sph incl.	sphalerite
			py rim	Pyrite
			cp intertsitial to py	Chalcopyrite
			cp intertsitial to py	Chalcopyrite
			tiny Ag inclusion	Silver ± S, Cl
			tiny gn inclusion in py rim (w. millerite)	Galena
			py streaks repl chlorite	Pyrite
			cp in f. gr. wall rock	Chalcopyrite
RTTC-BT-163	07TH006	574	massive cp	Chalcopyrite
			millerite inclusion sin cp	Millerite
			Ag (±S, Cl)	Silver ± S, Cl
			turquoise Ag-cp	Ag-chalcopyrite
			brighter area in millerite	Millerite
			darker area in millerite	Millerite
			f. gr. sph attached to cp	Sphalerite
			small subh pyrite inclusion in cp at edge of circle	Pyrite
			small euh pyrite inclusion in cp	Pyrite
			tiny gn incl in cp-millerite	galena
			sph	Sphalerite
			electrum in cp	Electrum
			sph intergrown w. electrum in cp	Sphalerite
			Se-galena in cp	Se-galena
			galena at edge of cp	mixture
			electrum w. sph in cp	electrum
			RTTC-BT-163A (8)	Chalcopyrite
			oxidized Ag in centre of Ag-cp	Silver
			Ag-cp	Ag-chalcopyrite
			bravoite, core	Pyrite

Sample ID	S	Mn	Fe	Co	Ni	Cu	Zn	As	Se	Pd	Ag	Cd	Sn	Sb	Te	Pt	Au	Hg	Pb	Bi	Total
Cp-rich massive sulphide veinlet																					
RTTC-BT-161	54.80	0.00	47.33	0.00	0.10	0.03	0.07	0.00	0.01	0.02	0.03	0.00	0.00	0.00	0.00	0.03	0.00	0.07	0.00	0.18	102.67
	53.21	0.00	37.60	0.95	8.80	0.07	0.00	0.00	0.04	0.00	0.00	0.00	0.00	0.00	0.01	0.00	0.00	0.00	0.04	0.08	100.81
	41.10	0.00	29.93	0.16	2.88	0.20	0.06	0.00	0.81	0.00	0.02	0.00	0.00	0.00	0.02	0.00	0.00	0.00	24.61	0.03	99.81
	34.64	0.02	30.25	0.00	0.02	34.70	0.06	0.00	0.00	0.03	0.00	0.00	0.00	0.00	0.00	0.05	0.01	0.00	0.03	0.20	100.01
	54.04	0.00	47.28	0.00	0.02	0.02	0.00	0.02	0.00	0.02	0.00	0.00	0.00	0.00	0.00	0.02	0.03	0.00	0.00	0.19	101.64
	35.32	0.01	3.83	0.03	60.17	0.00	0.00	0.00	0.15	0.00	0.07	0.00	0.00	0.00	0.06	0.00	0.02	0.03	0.01	0.11	99.81
	32.11	0.13	9.98	0.05	0.00	0.00	55.66	0.01	0.01	0.00	0.00	0.04	0.00	0.00	0.00	0.00	0.00	0.00	0.00	0.17	98.15
	52.90	0.00	46.67	0.00	0.00	0.03	0.05	0.01	0.03	0.06	0.00	0.00	0.01	0.00	0.02	0.00	0.00	0.04	0.00	0.19	99.99
	32.27	0.12	10.00	0.06	0.00	0.03	55.09	0.00	0.02	0.00	0.00	0.09	0.00	0.02	0.00	0.00	0.09	0.00	0.00	0.12	97.92
	52.70	0.00	42.04	1.46	3.40	0.00	0.04	0.00	0.03	0.00	0.00	0.00	0.00	0.00	0.03	0.00	0.02	0.04	0.00	0.15	99.92
	34.18	0.00	30.32	0.00	0.03	33.72	0.00	0.00	0.00	0.00	0.00	0.00	0.00	0.00	0.00	0.00	0.08	0.06	0.00	0.09	98.47
	34.27	0.03	30.20	0.00	0.00	34.41	0.00	0.00	0.01	0.00	0.06	0.00	0.01	0.00	0.00	0.07	0.00	0.08	0.00	0.09	99.23
	0.89	0.01	1.41	0.01	0.00	1.58	0.05	0.00	0.02	0.00	84.20	0.00	0.00	0.00	0.16	0.01	0.01	0.00	0.04	0.00	88.39
	28.26	0.00	17.01	0.26	1.41	0.24	0.00	0.01	1.01	0.00	0.08	0.09	0.03	0.00	0.05	0.01	0.03	0.00	50.38	0.09	98.94
	52.94	0.01	41.83	0.54	4.27	0.01	0.01	0.02	0.04	0.08	0.00	0.00	0.00	0.00	0.00	0.00	0.00	0.00	0.00	0.13	99.86
	34.38	0.01	30.05	0.00	0.03	34.31	0.00	0.01	0.00	0.00	0.03	0.00	0.04	0.00	0.00	0.00	0.00	0.00	0.00	0.05	98.91
RTTC-BT-163	34.77	0.00	30.51	0.00	0.04	34.91	0.01	0.00	0.02	0.02	0.01	0.00	0.02	0.00	0.06	0.01	0.00	0.02	0.07	0.10	100.57
	34.46	0.00	0.32	0.29	63.93	0.12	0.06	0.64	0.06	0.00	0.06	0.00	0.00	0.01	0.06	0.00	0.06	0.04	0.00	0.10	100.20
	4.66	0.03	1.08	0.00	1.24	1.10	0.01	0.00	0.00	0.00	86.04	0.00	0.00	0.00	0.13	0.00	0.03	0.20	0.02	0.03	94.56
	33.09	0.00	28.40	0.00	0.34	33.16	0.07	0.00	0.00	0.03	4.11	0.03	0.01	0.00	0.01	0.03	0.11	0.01	0.00	0.06	99.46
	35.16	0.01	1.50	0.35	63.96	0.45	0.00	0.03	0.02	0.00	0.00	0.00	0.00	0.00	0.02	0.00	0.00	0.15	0.00	0.00	101.63
	34.93	0.00	1.25	0.35	63.66	0.40	0.01	0.00	0.03	0.00	0.00	0.02	0.00	0.00	0.11	0.00	0.01	0.02	0.00	0.12	100.92
	32.89	0.00	3.57	0.03	0.00	2.32	61.12	0.03	0.02	0.00	0.06	0.15	0.00	0.00	0.00	0.00	0.00	0.05	0.00	0.01	100.25
	54.29	0.01	47.12	0.02	0.02	0.02	0.06	0.01	0.00	0.00	0.01	0.02	0.00	0.00	0.02	0.09	0.00	0.00	0.00	0.08	101.76
	54.24	0.00	41.80	0.28	5.15	0.20	0.74	0.05	0.01	0.01	0.00	0.00	0.02	0.00	0.02	0.00	0.05	0.00	0.00	0.11	102.67
	20.38	0.00	10.65	0.05	5.98	11.89	0.00	0.00	0.15	0.00	0.02	0.06	0.05	0.00	0.05	0.00	0.02	0.00	53.05	0.24	102.58
	32.64	0.02	3.42	0.00	0.03	0.02	62.90	0.00	0.05	0.00	0.01	0.25	0.00	0.00	0.00	0.00	0.06	0.09	0.04	0.00	99.54
	0.00	0.00	0.00	0.00	0.00	0.00	0.00	0.00	0.01	0.00	24.94	0.00	0.00	0.00	0.11	0.00	76.56	0.00	0.00	0.00	101.62
	32.10	0.01	3.01	0.02	0.00	2.23	61.36	0.00	0.01	0.00	0.07	0.37	0.00	0.01	0.04	0.02	0.15	0.01	0.00	0.08	99.50
	8.44	0.00	0.00	0.00	0.00	0.00	0.00	0.00	10.98	0.03	0.07	0.09	0.02	0.00	0.10	0.04	0.00	0.00	82.16	0.11	102.05
	30.36	0.02	17.81	0.08	12.92	23.27	0.00	0.00	1.08	0.00	0.06	0.00	0.01	0.00	0.03	0.00	0.01	0.00	14.60	0.04	100.28
	0.00	0.00	0.00	0.03	0.00	0.00	0.00	0.00	0.00	0.00	27.46	0.00	0.00	0.00	0.08	0.01	74.02	0.00	0.00	0.00	101.59
	34.42	0.00	30.25	0.00	0.01	34.66	0.00	0.00	0.01	0.00	0.00	0.00	0.01	0.00	0.00	0.04	0.00	0.00	0.04	0.13	99.57
	1.48	0.00	0.84	0.00	0.32	0.90	0.06	0.00	0.00	0.00	92.75	0.00	0.00	0.00	0.16	0.00	0.01	0.00	0.00	0.00	96.52
	32.76	0.00	27.92	0.02	1.21	31.94	0.00	0.01	0.05	0.00	5.69	0.00	0.00	0.00	0.00	0.09	0.00	0.07	0.00	0.09	99.84
	53.84	0.00	47.48	0.03	0.05	0.02	0.00	0.00	0.02	0.00	0.01	0.03	0.02	0.00	0.03	0.00	0.00	0.02	0.00	0.09	101.64

Sample ID	S	Mn	Fe	Co	Ni	Cu	Zn	As	Se	Pd	Ag	Cd	Sn	Sb	Te	Pt	Au	Hg	Pb	Bi	TOTAL
Cp-rich massive sulphide veinlet																					
RTTC-BT-161	2.001	0.000	0.993	0.000	0.002	0.001	0.001	0.000	0.000	0.000	0.000	0.000	0.000	0.000	0.000	0.000	0.000	0.000	0.000	0.001	3.000
	1.990	0.000	0.808	0.019	0.180	0.001	0.000	0.000	0.001	0.000	0.000	0.000	0.000	0.000	0.000	0.000	0.000	0.000	0.000	0.000	3.000
	1.280	0.000	0.535	0.003	0.049	0.003	0.001	0.000	0.010	0.000	0.000	0.000	0.000	0.000	0.000	0.000	0.000	0.000	0.119	0.000	2.000
	1.990	0.001	0.998	0.000	0.001	1.006	0.002	0.000	0.000	0.001	0.000	0.000	0.000	0.000	0.000	0.000	0.000	0.000	0.000	0.002	4.000
	1.995	0.000	1.002	0.000	0.000	0.000	0.000	0.000	0.000	0.000	0.000	0.000	0.000	0.000	0.000	0.000	0.000	0.000	0.000	0.001	3.000
	1.002	0.000	0.062	0.001	0.932	0.000	0.000	0.000	0.002	0.000	0.001	0.000	0.000	0.000	0.000	0.000	0.000	0.000	0.000	0.000	2.000
	0.984	0.002	0.176	0.001	0.000	0.000	0.836	0.000	0.000	0.000	0.000	0.000	0.000	0.000	0.000	0.000	0.000	0.000	0.000	0.001	2.000
	1.989	0.000	1.007	0.000	0.000	0.000	0.001	0.000	0.000	0.001	0.000	0.000	0.000	0.000	0.000	0.000	0.000	0.000	0.000	0.001	3.000
	0.990	0.002	0.176	0.001	0.000	0.001	0.828	0.000	0.000	0.000	0.000	0.001	0.000	0.000	0.000	0.000	0.000	0.000	0.000	0.001	2.000
	1.987	0.000	0.910	0.030	0.070	0.000	0.001	0.000	0.001	0.000	0.000	0.000	0.000	0.000	0.000	0.000	0.000	0.000	0.000	0.001	3.000
	1.991	0.000	1.014	0.000	0.001	0.991	0.000	0.000	0.000	0.000	0.000	0.000	0.000	0.000	0.000	0.000	0.001	0.001	0.000	0.001	4.000
	1.985	0.001	1.004	0.000	0.000	1.006	0.000	0.000	0.000	0.000	0.001	0.000	0.000	0.000	0.000	0.001	0.000	0.001	0.000	0.001	4.000
	0.032	0.000	0.029	0.000	0.000	0.029	0.001	0.000	0.000	0.000	0.906	0.000	0.000	0.000	0.001	0.000	0.000	0.000	0.000	0.000	1.000
	1.193	0.000	0.412	0.006	0.032	0.005	0.000	0.000	0.017	0.000	0.001	0.001	0.000	0.000	0.000	0.000	0.000	0.000	0.329	0.001	2.000
	1.994	0.000	0.905	0.011	0.088	0.000	0.000	0.000	0.001	0.001	0.000	0.000	0.000	0.000	0.000	0.000	0.000	0.000	0.000	0.001	3.000
	1.993	0.000	1.000	0.000	0.001	1.004	0.000	0.000	0.000	0.000	0.000	0.000	0.001	0.000	0.000	0.000	0.000	0.000	0.000	0.000	4.000
RTTC-BT-163	1.987	0.000	1.001	0.000	0.001	1.006	0.000	0.000	0.000	0.000	0.000	0.000	0.000	0.000	0.001	0.000	0.000	0.000	0.001	0.001	4.000
	0.982	0.000	0.005	0.004	0.995	0.002	0.001	0.008	0.001	0.000	0.001	0.000	0.000	0.000	0.000	0.000	0.000	0.000	0.000	0.000	2.000
	0.145	0.000	0.019	0.000	0.021	0.017	0.000	0.000	0.000	0.000	0.795	0.000	0.000	0.000	0.001	0.000	0.000	0.001	0.000	0.000	1.000
	1.957	0.000	0.964	0.000	0.011	0.990	0.002	0.000	0.000	0.001	0.072	0.001	0.000	0.000	0.000	0.000	0.001	0.000	0.000	0.001	4.000
	0.984	0.000	0.024	0.005	0.978	0.006	0.000	0.000	0.000	0.000	0.000	0.000	0.000	0.000	0.000	0.000	0.000	0.001	0.000	0.000	2.000
	0.986	0.000	0.020	0.005	0.981	0.006	0.000	0.000	0.000	0.000	0.000	0.000	0.000	0.000	0.001	0.000	0.000	0.000	0.000	0.001	2.000
	0.994	0.000	0.062	0.000	0.000	0.035	0.906	0.000	0.000	0.000	0.001	0.001	0.000	0.000	0.000	0.000	0.000	0.000	0.000	0.000	2.000
	2.000	0.000	0.996	0.000	0.000	0.000	0.001	0.000	0.000	0.000	0.000	0.000	0.000	0.000	0.000	0.001	0.000	0.000	0.000	0.000	3.000
	1.991	0.000	0.881	0.006	0.103	0.004	0.013	0.001	0.000	0.000	0.000	0.000	0.000	0.000	0.000	0.000	0.000	0.000	0.000	0.001	3.000
	0.923	0.000	0.277	0.001	0.148	0.272	0.000	0.000	0.003	0.000	0.000	0.001	0.001	0.000	0.001	0.000	0.000	0.000	0.372	0.002	2.000
	0.995	0.000	0.060	0.000	0.000	0.000	0.940	0.000	0.001	0.000	0.000	0.002	0.000	0.000	0.000	0.000	0.000	0.000	0.000	0.000	2.000
	0.000	0.000	0.000	0.000	0.000	0.000	0.000	0.000	0.000	0.000	0.372	0.000	0.000	0.000	0.001	0.000	0.626	0.000	0.000	0.000	1.000
	0.984	0.000	0.053	0.000	0.000	0.035	0.922	0.000	0.000	0.000	0.001	0.003	0.000	0.000	0.000	0.000	0.001	0.000	0.000	0.000	2.000
	0.656	0.000	0.000	0.000	0.000	0.000	0.000	0.000	0.347	0.001	0.002	0.002	0.000	0.000	0.002	0.001	0.000	0.000	0.988	0.001	2.000
	0.977	0.000	0.329	0.001	0.227	0.378	0.000	0.000	0.014	0.000	0.001	0.000	0.000	0.000	0.000	0.000	0.000	0.000	0.073	0.000	2.000
	0.000	0.000	0.000	0.001	0.000	0.000	0.000	0.000	0.000	0.000	0.403	0.000	0.000	0.000	0.001	0.000	0.595	0.000	0.000	0.000	1.000
	1.986	0.000	1.002	0.000	0.000	1.009	0.000	0.000	0.000	0.000	0.000	0.000	0.000	0.000	0.000	0.000	0.000	0.000	0.000	0.001	4.000
	0.049	0.000	0.016	0.000	0.006	0.015	0.001	0.000	0.000	0.000	0.912	0.000	0.000	0.000	0.001	0.000	0.000	0.000	0.000	0.000	1.000
	1.946	0.000	0.952	0.001	0.039	0.957	0.000	0.000	0.001	0.000	0.101	0.000	0.000	0.000	0.000	0.001	0.000	0.001	0.000	0.001	4.000
	1.989	0.000	1.007	0.001	0.001	0.000	0.000	0.000	0.000	0.000	0.000	0.000	0.000	0.000	0.000	0.000	0.000	0.000	0.000	0.001	3.000

Sample ID	DDH	Depth	Description	Mineral
Outside the basal mineralizarion zone				
RTTC-BT-094	07TH004	404	tiny white grain intergrown w. sec. mt in serpentine p	Co-pentlandite
			tiny white grain intergrown w. sec. mt in serpentine,	Co-pentlandite
			small cp	Chalcopyrite
			small pn inclusion in cp	Pentlandite
			tiny sph beside small pn inclusion in cp	Sphalerite
			anh cp	Chalcopyrite
			tiny bn intergrown w. cp	Bornite
			tiny bn intergrown w. cp	Bornite
			tiny square white grain in sec. mt	Co-pentlandite
RTTC-BT-097	07TH004	323	tiny square white grain in sec. mt in serpentine pseudomorph	Siegenite
			tiny square cp w. sph incl.	Chalcopyrite
			bn rimming tiny square cp w. sph incl.	Bornite
			sph rimming tiny square cp w. sph incl.	sphalerite
			other bn rimmed by cp	Bornite
			cp	Chalcopyrite
			sph intergrown w. bn	sphalerite
Mt+Py+Cp alteration veins				
RTTC-BT-065A	07TH004	287	small cp droplet in serpentine	chalcopyrite
			subhedral py intergrown w. serpentine	pyrite
			lace py repl. plag	pyrite
			lace py repl. plag, outside circle	pyrite
			anh cp intertsitial to chl, between (2) and (5-6)	chalcopyrite
			v. f. gr. galena intergrown w. pyrite intergrown . cp	galena
			inhong. pyrite intergrown . cp	pyrite
			cp	chalcopyrite
			f. gr. galena in gangue	galena
			pyrite intergrown w. cp	pyrite
RTTC-BT-065B	07TH004	287	lace-pyrite and chl repl plag	pyrite
			cp w. py intertsitial to strap mt in vein	chalcopyrite
			py w. cp interstitial to strap mt in vein	pyrite
RTTC-BT-063	07TH004	306	spongy pyrite intergrown w. mt	pyrrhotite
			spongy pyrite intergrown w. mt	pyrite
			spongy po intergrown w. mt	pyrrhotite
			spongy py intergrown w. mt	pyrrhotite
			pyrite intergrown w. cp, core	pyrite

Sample ID	S	Mn	Fe	Co	Ni	Cu	Zn	As	Se	Pd	Ag	Cd	Sn	Sb	Te	Pt	Au	Hg	Pb	Bi	Total
Outside the basal mineralizarion zone																					
RTTC-BT-094	31.32	0.02	16.72	14.07	33.59	0.17	0.11	0.00	0.01	0.00	0.00	0.00	0.02	0.00	0.00	0.00	0.10	0.00	0.11	0.13	96.36
	30.83	0.02	16.44	13.60	33.47	0.17	0.02	0.00	0.03	0.00	0.00	0.00	0.00	0.00	0.01	0.00	0.01	0.01	0.08	0.00	94.66
	33.30	0.02	30.27	0.01	0.13	34.14	0.04	0.00	0.08	0.01	0.00	0.00	0.02	0.00	0.00	0.05	0.09	0.09	0.00	0.11	98.34
	32.52	0.01	22.14	4.68	39.75	0.67	0.03	0.16	0.05	0.00	0.00	0.01	0.00	0.00	0.03	0.00	0.03	0.00	0.00	0.20	100.27
	31.58	0.00	5.50	0.04	0.16	2.99	57.99	0.00	0.07	0.00	0.00	0.17	0.01	0.01	0.01	0.00	0.00	0.02	0.00	0.04	98.58
	33.97	0.00	31.29	0.02	0.00	34.57	0.01	0.03	0.00	0.02	0.00	0.00	0.00	0.00	0.00	0.00	0.04	0.00	0.00	0.04	99.98
	24.72	0.04	12.30	0.00	0.04	60.77	0.04	0.02	0.06	0.09	0.00	0.03	0.00	0.00	0.00	0.03	0.08	0.02	0.00	0.01	98.24
	25.47	0.04	11.50	0.00	0.00	61.16	0.04	0.00	0.06	0.00	0.00	0.00	0.06	0.00	0.00	0.00	0.03	0.04	0.00	0.00	98.40
	31.17	0.01	16.95	14.07	33.93	0.16	0.00	0.00	0.01	0.00	0.00	0.00	0.00	0.00	0.02	0.00	0.00	0.00	0.08	0.02	96.41
RTTC-BT-097	36.96	0.03	7.53	15.44	31.04	6.08	0.03	0.00	0.00	0.01	0.00	0.00	0.00	0.00	0.00	0.03	0.00	0.01	0.11	0.13	97.40
	34.20	0.00	30.99	0.00	0.01	34.82	0.65	0.00	0.00	0.02	0.00	0.00	0.01	0.00	0.00	0.00	0.00	0.00	0.00	0.08	100.76
	25.89	0.02	13.24	0.01	0.00	62.64	0.53	0.00	0.05	0.00	0.00	0.00	0.00	0.00	0.02	0.00	0.09	0.06	0.00	0.11	102.66
	31.66	0.01	3.76	0.00	0.02	3.53	60.89	0.00	0.01	0.00	0.00	0.13	0.02	0.00	0.00	0.00	0.01	0.00	0.00	0.00	100.04
	25.85	0.03	12.33	0.00	0.02	63.32	0.05	0.00	0.05	0.00	0.00	0.04	0.00	0.00	0.00	0.00	0.00	0.05	0.00	0.00	101.74
	34.62	0.04	30.42	0.00	0.03	34.93	0.02	0.00	0.02	0.05	0.00	0.00	0.00	0.00	0.00	0.06	0.00	0.00	0.01	0.06	100.24
	32.07	0.02	2.67	0.11	0.00	2.44	61.86	0.00	0.06	0.00	0.00	0.09	0.01	0.00	0.00	0.00	0.06	0.00	0.00	0.19	99.60
Mt+Py+Cp alteration veins																					
RTTC-BT-065A	34.23	0.00	30.83	0.00	0.02	34.17	0.06	0.03	0.00	0.00	0.04	0.01	0.00	0.00	0.00	0.10	0.00	0.00	0.00	0.17	99.66
	53.19	0.02	47.69	0.15	0.12	0.02	0.04	0.01	0.01	0.01	0.08	0.01	0.01	0.00	0.00	0.03	0.00	0.00	0.00	0.06	101.45
	52.21	0.00	47.26	0.04	0.00	0.00	0.07	0.00	0.00	0.02	0.00	0.00	0.03	0.00	0.00	0.13	0.06	0.00	0.14	0.16	100.12
	52.20	0.00	46.28	1.02	0.13	0.02	0.01	0.00	0.03	0.00	0.00	0.00	0.00	0.00	0.00	0.06	0.00	0.06	0.21	0.20	100.22
	34.40	0.01	31.00	0.00	0.00	34.58	0.00	0.00	0.02	0.00	0.01	0.00	0.00	0.00	0.01	0.03	0.00	0.00	0.00	0.13	100.19
	13.14	0.01	0.00	0.03	0.03	0.00	0.06	0.00	0.67	0.06	0.01	0.06	0.01	0.00	0.01	0.10	0.02	0.00	85.00	0.00	99.20
	53.31	0.01	47.79	0.07	0.16	0.04	0.04	0.00	0.00	0.00	0.00	0.00	0.01	0.00	0.00	0.00	0.02	0.07	0.05	0.08	101.64
	34.14	0.00	30.78	0.05	0.01	35.05	0.02	0.02	0.02	0.00	0.05	0.00	0.03	0.00	0.00	0.00	0.02	0.00	0.00	0.05	100.23
	13.40	0.00	2.12	0.00	0.00	0.12	0.00	0.00	0.03	0.05	0.00	0.01	0.02	0.00	0.00	0.02	0.00	0.00	83.61	0.01	99.38
	53.54	0.01	47.47	0.29	0.10	0.00	0.05	0.00	0.02	0.00	0.00	0.00	0.05	0.00	0.02	0.00	0.00	0.00	0.00	0.13	101.67
RTTC-BT-065B	52.34	0.02	47.35	0.06	0.06	0.01	0.02	0.01	0.02	0.00	0.06	0.02	0.01	0.00	0.00	0.00	0.05	0.00	0.00	0.11	100.13
	34.06	0.00	30.76	0.02	0.00	34.64	0.03	0.00	0.00	0.02	0.08	0.00	0.02	0.00	0.00	0.03	0.00	0.00	0.00	0.08	99.73
	53.64	0.00	47.59	0.15	0.02	0.02	0.02	0.00	0.02	0.00	0.00	0.00	0.01	0.00	0.00	0.01	0.00	0.00	0.00	0.13	101.59
RTTC-BT-063	38.60	0.03	57.03	0.08	0.09	0.07	0.05	0.00	0.03	0.00	0.01	0.00	0.00	0.00	0.00	0.00	0.06	0.09	0.00	0.02	96.13
	52.00	0.00	47.22	0.00	0.01	0.03	0.01	0.01	0.02	0.04	0.00	0.00	0.03	0.00	0.00	0.00	0.01	0.06	0.00	0.16	99.61
	38.20	0.01	55.58	0.11	0.07	0.00	0.01	0.03	0.00	0.03	0.00	0.00	0.02	0.00	0.04	0.04	0.00	0.02	0.08	0.08	94.31
	36.28	0.00	55.94	0.11	0.08	0.00	0.06	0.00	0.01	0.04	0.00	0.00	0.02	0.00	0.02	0.00	0.00	0.00	0.03	0.19	92.76
	53.54	0.00	47.25	0.14	0.24	0.00	0.00	0.00	0.03	0.00	0.01	0.00	0.01	0.00	0.00	0.01	0.00	0.00	0.00	0.05	101.29

Sample ID	S	Mn	Fe	Co	Ni	Cu	Zn	As	Se	Pd	Ag	Cd	Sn	Sb	Te	Pt	Au	Hg	Pb	Bi	TOTAL
Outside the basal mineralizarion zone																					
RTTC-BT-094	7.929	0.003	2.431	1.939	4.647	0.021	0.014	0.000	0.001	0.000	0.000	0.000	0.001	0.000	0.000	0.000	0.004	0.000	0.004	0.005	17.000
	7.931	0.003	2.429	1.903	4.704	0.021	0.003	0.000	0.003	0.000	0.000	0.000	0.000	0.000	0.001	0.000	0.000	0.000	0.003	0.000	17.000
	1.956	0.001	1.021	0.000	0.004	1.012	0.001	0.000	0.002	0.000	0.000	0.000	0.000	0.000	0.000	0.000	0.001	0.001	0.000	0.001	4.000
	7.899	0.002	3.087	0.618	5.276	0.082	0.003	0.016	0.004	0.000	0.000	0.000	0.000	0.000	0.002	0.000	0.001	0.000	0.000	0.007	17.000
	0.974	0.000	0.097	0.001	0.003	0.046	0.877	0.000	0.001	0.000	0.000	0.002	0.000	0.000	0.000	0.000	0.000	0.000	0.000	0.000	2.000
	1.957	0.000	1.035	0.001	0.000	1.005	0.000	0.001	0.000	0.000	0.000	0.000	0.000	0.000	0.000	0.000	0.000	0.000	0.000	0.000	4.000
	3.949	0.004	1.128	0.000	0.004	4.898	0.003	0.001	0.004	0.004	0.000	0.001	0.000	0.000	0.000	0.001	0.002	0.001	0.000	0.000	10.000
	4.041	0.003	1.048	0.000	0.000	4.897	0.003	0.000	0.004	0.000	0.000	0.000	0.003	0.000	0.000	0.000	0.001	0.001	0.000	0.000	10.000
	7.884	0.002	2.462	1.937	4.690	0.020	0.000	0.000	0.001	0.000	0.000	0.000	0.000	0.000	0.001	0.000	0.000	0.000	0.003	0.001	17.000
RTTC-BT-097	3.707	0.002	0.434	0.843	1.701	0.307	0.001	0.000	0.000	0.000	0.000	0.000	0.000	0.000	0.000	0.000	0.000	0.000	0.002	0.002	7.000
	1.957	0.000	1.018	0.000	0.000	1.005	0.018	0.000	0.000	0.000	0.000	0.000	0.000	0.000	0.000	0.000	0.000	0.000	0.000	0.001	4.000
	3.956	0.001	1.162	0.001	0.000	4.830	0.040	0.000	0.003	0.000	0.000	0.000	0.000	0.000	0.001	0.000	0.002	0.001	0.000	0.003	10.000
	0.966	0.000	0.066	0.000	0.000	0.054	0.911	0.000	0.000	0.000	0.000	0.001	0.000	0.000	0.000	0.000	0.000	0.000	0.000	0.000	2.000
	3.978	0.003	1.090	0.000	0.002	4.918	0.003	0.000	0.003	0.000	0.000	0.002	0.000	0.000	0.000	0.000	0.000	0.001	0.000	0.000	10.000
	1.984	0.001	1.001	0.000	0.001	1.010	0.000	0.000	0.000	0.001	0.000	0.000	0.000	0.000	0.000	0.001	0.000	0.000	0.000	0.001	4.000
	0.982	0.000	0.047	0.002	0.000	0.038	0.929	0.000	0.001	0.000	0.000	0.001	0.000	0.000	0.000	0.000	0.000	0.000	0.000	0.001	2.000
Mt+Py+Cp alteration veins																					
RTTC-BT-065A	1.976	0.000	1.022	0.000	0.001	0.996	0.002	0.001	0.000	0.000	0.001	0.000	0.000	0.000	0.000	0.001	0.000	0.000	0.000	0.002	4.000
	1.975	0.000	1.017	0.003	0.002	0.000	0.001	0.000	0.000	0.000	0.001	0.000	0.000	0.000	0.000	0.000	0.000	0.000	0.000	0.000	3.000
	1.970	0.000	1.024	0.001	0.000	0.000	0.001	0.000	0.000	0.000	0.000	0.000	0.000	0.000	0.000	0.001	0.000	0.000	0.001	0.001	3.000
	1.970	0.000	1.003	0.021	0.003	0.000	0.000	0.000	0.000	0.000	0.000	0.000	0.000	0.000	0.000	0.000	0.000	0.000	0.001	0.001	3.000
	1.974	0.000	1.022	0.000	0.000	1.001	0.000	0.000	0.001	0.000	0.000	0.000	0.000	0.000	0.000	0.000	0.000	0.000	0.000	0.001	4.000
	0.984	0.000	0.000	0.001	0.001	0.000	0.002	0.000	0.020	0.001	0.000	0.001	0.000	0.000	0.000	0.001	0.000	0.000	0.985	0.000	2.000
	1.975	0.000	1.017	0.001	0.003	0.001	0.001	0.000	0.000	0.000	0.000	0.000	0.000	0.000	0.000	0.000	0.000	0.000	0.000	0.000	3.000
	1.962	0.000	1.016	0.002	0.000	1.017	0.001	0.000	0.000	0.000	0.001	0.000	0.001	0.000	0.000	0.000	0.000	0.000	0.000	0.000	4.000
	0.969	0.000	0.088	0.000	0.000	0.004	0.000	0.000	0.001	0.001	0.000	0.000	0.000	0.000	0.000	0.000	0.000	0.000	0.936	0.000	2.000
	1.981	0.000	1.008	0.006	0.002	0.000	0.001	0.000	0.000	0.000	0.000	0.000	0.001	0.000	0.000	0.000	0.000	0.000	0.000	0.001	3.000
RTTC-BT-065B	1.971	0.000	1.024	0.001	0.001	0.000	0.000	0.000	0.000	0.000	0.001	0.000	0.000	0.000	0.000	0.000	0.000	0.000	0.000	0.001	3.000
	1.967	0.000	1.020	0.001	0.000	1.009	0.001	0.000	0.000	0.000	0.001	0.000	0.000	0.000	0.000	0.000	0.000	0.000	0.000	0.001	4.000
	1.984	0.000	1.011	0.003	0.000	0.000	0.000	0.000	0.000	0.000	0.000	0.000	0.000	0.000	0.000	0.000	0.000	0.000	0.000	0.001	3.000
RTTC-BT-063	1.079	0.000	0.915	0.001	0.001	0.001	0.001	0.000	0.000	0.000	0.000	0.000	0.000	0.000	0.000	0.000	0.000	0.000	0.000	0.000	2.000
	1.969	0.000	1.027	0.000	0.000	0.001	0.000	0.000	0.000	0.001	0.000	0.000	0.000	0.000	0.000	0.000	0.000	0.000	0.000	0.001	3.000
	1.087	0.000	0.908	0.002	0.001	0.000	0.000	0.000	0.000	0.000	0.000	0.000	0.000	0.000	0.000	0.000	0.000	0.000	0.000	0.000	2.000
	1.058	0.000	0.937	0.002	0.001	0.000	0.001	0.000	0.000	0.000	0.000	0.000	0.000	0.000	0.000	0.000	0.000	0.000	0.000	0.001	2.000
	1.985	0.000	1.006	0.003	0.005	0.000	0.000	0.000	0.000	0.000	0.000	0.000	0.000	0.000	0.000	0.000	0.000	0.000	0.000	0.000	3.000

Sample ID	DDH	Depth	Description	Mineral
Iron formation				
RTTC-BT-005	05TH001	112	sph	sphalerite
			py surrounding sph	Pyrite
			med. rounded po intergr. w. mt	Pyrrhotite
			anh cpintergr. w. mt	Chalcopyrite
			anh po intergr. w. mt	Pyrrhotite
			anh cp	Chalcopyrite
			anh po intergr. w. grt (previous was in2)	Pyrrhotite
			coarse py integrrown w. mt	Pyrite
RTTC-BT-006	05TH001	111	anh. po	Pyrrhotite
			anh. py intergr. w. stilpnomelane	Pyrite
			coarser euh py	Pyrite
			cp rimmed by acicualr stilpnomelane fringe	Chalcopyrite
			anh po	Pyrrhotite
			coarse anh po, rimmed by cp	Pyrrhotite
			euh py rimming zoned grt	Pyrite
			euh py rimming zoned grt, other area	Pyrite
Wall rock				
RTTC-BT-048	05TH002	155	spongy py intergrown w. cp	Pyrite
			po incl. in spongy py intergrown w. cp	Pyrrhotite
			cp	Chalcopyrite
			spongy py overprinting altered fragment	Pyrite
			cp intergrown w. cc and chl in vein	Chalcopyrite
			tiny millerite in cp	Millerite
RTTC-BT-187	05TH002	169	poikilitic pyrite aggregate	Pyrite

Sample ID	S	Mn	Fe	Co	Ni	Cu	Zn	As	Se	Pd	Ag	Cd	Sn	Sb	Te	Pt	Au	Hg	Pb	Bi	Total
Iron formation																					
RTTC-BT-005	32.51	0.02	6.93	0.03	0.00	0.01	60.26	0.02	0.00	0.00	0.00	0.34	0.00	0.00	0.00	0.07	0.00	0.00	0.00	0.11	100.28
	52.10	0.00	44.27	0.00	0.01	0.00	4.89	0.00	0.00	0.00	0.00	0.01	0.00	0.00	0.03	0.01	0.04	0.00	0.00	0.07	101.44
	39.22	0.00	61.04	0.04	0.13	0.00	0.09	0.00	0.01	0.03	0.00	0.00	0.04	0.00	0.00	0.09	0.00	0.00	0.00	0.12	100.80
	34.13	0.01	30.70	0.00	0.02	35.31	0.02	0.00	0.03	0.03	0.00	0.00	0.02	0.00	0.00	0.02	0.00	0.04	0.01	0.07	100.41
	39.12	0.02	60.91	0.04	0.12	0.00	0.00	0.00	0.00	0.00	0.00	0.01	0.03	0.00	0.00	0.00	0.00	0.00	0.00	0.02	100.27
	34.22	0.01	31.00	0.01	0.00	34.98	0.01	0.00	0.03	0.02	0.00	0.01	0.00	0.00	0.01	0.00	0.05	0.00	0.00	0.01	100.35
	39.08	0.01	60.62	0.05	0.13	0.00	0.00	0.03	0.02	0.00	0.00	0.00	0.00	0.00	0.00	0.00	0.00	0.02	0.00	0.02	99.99
	53.24	0.00	47.80	0.08	0.11	0.02	0.00	0.00	0.01	0.03	0.00	0.02	0.00	0.00	0.00	0.00	0.00	0.00	0.00	0.16	101.47
RTTC-BT-006	39.40	0.00	60.64	0.03	0.41	0.00	0.01	0.00	0.00	0.00	0.00	0.00	0.01	0.00	0.00	0.00	0.02	0.10	0.01	0.13	100.76
	53.81	0.00	47.82	0.00	0.00	0.00	0.00	0.00	0.00	0.00	0.00	0.00	0.01	0.00	0.03	0.00	0.00	0.00	0.00	0.08	101.75
	53.36	0.01	47.46	0.05	0.54	0.00	0.00	0.00	0.02	0.02	0.00	0.00	0.00	0.00	0.00	0.08	0.07	0.02	0.00	0.23	101.85
	33.91	0.00	30.68	0.02	0.00	34.91	0.00	0.00	0.00	0.00	0.00	0.00	0.01	0.00	0.02	0.06	0.00	0.01	0.00	0.15	99.76
	38.89	0.00	60.09	0.05	0.40	0.05	0.04	0.00	0.02	0.05	0.00	0.00	0.00	0.00	0.03	0.07	0.00	0.03	0.00	0.04	99.77
	38.49	0.00	60.27	0.08	0.42	0.00	0.05	0.01	0.04	0.00	0.00	0.00	0.00	0.00	0.00	0.00	0.04	0.00	0.00	0.10	99.51
	53.79	0.00	48.20	0.06	0.04	0.02	0.00	0.00	0.00	0.00	0.00	0.00	0.02	0.00	0.00	0.01	0.04	0.00	0.02	0.14	102.34
	53.70	0.02	47.37	0.17	0.04	0.00	0.04	0.00	0.02	0.05	0.00	0.00	0.00	0.00	0.00	0.13	0.00	0.00	0.00	0.10	101.62
Wall rock																					
RTTC-BT-048	53.72	0.00	47.79	0.08	0.28	0.04	0.00	0.00	0.03	0.00	0.00	0.00	0.00	0.00	0.00	0.00	0.00	0.01	0.00	0.14	102.08
	38.25	0.00	60.40	0.02	0.74	0.02	0.01	0.00	0.00	0.02	0.00	0.00	0.01	0.00	0.00	0.00	0.00	0.04	0.00	0.02	99.53
	34.38	0.01	30.52	0.00	0.02	34.87	0.04	0.00	0.03	0.01	0.00	0.01	0.00	0.00	0.00	0.00	0.00	0.00	0.00	0.00	99.90
	54.05	0.00	48.21	0.00	0.03	0.01	0.00	0.02	0.00	0.02	0.03	0.00	0.00	0.00	0.00	0.00	0.00	0.02	0.00	0.15	102.54
	33.97	0.03	30.68	0.00	0.02	35.19	0.02	0.02	0.00	0.00	0.02	0.00	0.00	0.00	0.00	0.00	0.12	0.00	0.00	0.03	100.10
	34.67	0.01	0.85	0.00	63.34	0.11	0.06	0.00	0.02	0.04	0.01	0.00	0.00	0.00	0.03	0.00	0.00	0.00	0.00	0.07	99.21
RTTC-BT-187	53.58	0.01	47.39	0.03	0.01	0.00	0.02	0.14	0.01	0.00	0.01	0.00	0.01	0.00	0.02	0.00	0.00	0.00	0.00	0.16	101.38

Sample ID	S	Mn	Fe	Co	Ni	Cu	Zn	As	Se	Pd	Ag	Cd	Sn	Sb	Te	Pt	Au	Hg	Pb	Bi	TOTAL
Iron formation																					
RTTC-BT-005	0.982	0.000	0.120	0.000	0.000	0.000	0.893	0.000	0.000	0.000	0.000	0.003	0.000	0.000	0.000	0.000	0.000	0.000	0.000	0.001	2.000
	1.955	0.000	0.954	0.000	0.000	0.000	0.090	0.000	0.000	0.000	0.000	0.000	0.000	0.000	0.000	0.000	0.000	0.000	0.000	0.000	3.000
	1.053	0.000	0.941	0.001	0.002	0.000	0.001	0.000	0.000	0.000	0.000	0.000	0.000	0.000	0.000	0.000	0.000	0.000	0.000	0.000	2.000
	1.960	0.000	1.012	0.000	0.001	1.023	0.001	0.000	0.001	0.001	0.000	0.000	0.000	0.000	0.000	0.000	0.000	0.000	0.000	0.001	4.000
	1.054	0.000	0.943	0.001	0.002	0.000	0.000	0.000	0.000	0.000	0.000	0.000	0.000	0.000	0.000	0.000	0.000	0.000	0.000	0.000	2.000
	1.963	0.000	1.021	0.000	0.000	1.013	0.000	0.000	0.001	0.000	0.000	0.000	0.000	0.000	0.000	0.000	0.000	0.000	0.000	0.000	4.000
	1.056	0.000	0.940	0.001	0.002	0.000	0.000	0.000	0.000	0.000	0.000	0.000	0.000	0.000	0.000	0.000	0.000	0.000	0.000	0.000	2.000
	1.976	0.000	1.019	0.002	0.002	0.000	0.000	0.000	0.000	0.000	0.000	0.000	0.000	0.000	0.000	0.000	0.000	0.000	0.000	0.001	3.000
RTTC-BT-006	1.058	0.000	0.935	0.000	0.006	0.000	0.000	0.000	0.000	0.000	0.000	0.000	0.000	0.000	0.000	0.000	0.000	0.000	0.000	0.001	2.000
	1.986	0.000	1.013	0.000	0.000	0.000	0.000	0.000	0.000	0.000	0.000	0.000	0.000	0.000	0.000	0.000	0.000	0.000	0.000	0.000	3.000
	1.976	0.000	1.009	0.001	0.011	0.000	0.000	0.000	0.000	0.000	0.000	0.000	0.000	0.000	0.000	0.000	0.000	0.000	0.000	0.001	3.000
	1.960	0.000	1.018	0.001	0.000	1.018	0.000	0.000	0.000	0.000	0.000	0.000	0.000	0.000	0.000	0.001	0.000	0.000	0.000	0.001	4.000
	1.055	0.000	0.936	0.001	0.006	0.001	0.001	0.000	0.000	0.000	0.000	0.000	0.000	0.000	0.000	0.000	0.000	0.000	0.000	0.000	2.000
	1.048	0.000	0.942	0.001	0.006	0.000	0.001	0.000	0.000	0.000	0.000	0.000	0.000	0.000	0.000	0.000	0.000	0.000	0.000	0.000	2.000
	1.978	0.000	1.018	0.001	0.001	0.000	0.000	0.000	0.000	0.000	0.000	0.000	0.000	0.000	0.000	0.000	0.000	0.000	0.000	0.001	3.000
	1.986	0.000	1.006	0.003	0.001	0.000	0.001	0.000	0.000	0.001	0.000	0.000	0.000	0.000	0.000	0.001	0.000	0.000	0.000	0.001	3.000
Wall rock																					
RTTC-BT-048	1.980	0.000	1.011	0.002	0.006	0.001	0.000	0.000	0.000	0.000	0.000	0.000	0.000	0.000	0.000	0.000	0.000	0.000	0.000	0.001	3.000
	1.042	0.000	0.945	0.000	0.011	0.000	0.000	0.000	0.000	0.000	0.000	0.000	0.000	0.000	0.000	0.000	0.000	0.000	0.000	0.000	2.000
	1.977	0.000	1.008	0.000	0.001	1.012	0.001	0.000	0.001	0.000	0.000	0.000	0.000	0.000	0.000	0.000	0.000	0.000	0.000	0.000	4.000
	1.982	0.000	1.015	0.000	0.001	0.000	0.000	0.000	0.000	0.000	0.000	0.000	0.000	0.000	0.000	0.000	0.000	0.000	0.000	0.001	3.000
	1.957	0.001	1.015	0.000	0.001	1.023	0.001	0.000	0.000	0.000	0.000	0.000	0.000	0.000	0.000	0.000	0.001	0.000	0.000	0.000	4.000
	0.992	0.000	0.014	0.000	0.990	0.002	0.001	0.000	0.000	0.000	0.000	0.000	0.000	0.000	0.000	0.000	0.000	0.000	0.000	0.000	2.000
RTTC-BT-187	1.986	0.000	1.009	0.001	0.000	0.000	0.000	0.002	0.000	0.000	0.000	0.000	0.000	0.000	0.000	0.000	0.000	0.000	0.000	0.001	3.000

Standard	FNS4	FNS4	FNS4	FNS4	FNS4	FNS4	FNS4	FNS4
Mineral	Pyrrhotite	Pyrrhotite	Pyrrhotite	Pyrrhotite	Pyrrhotite	Pyrrhotite	Pyrrhotite	Pyrrhotite
S	38.43	38.13	38.86	38.40	38.57	38.21	38.87	38.73
Mn	0.03	0.03	0.03	0.00	0.02	0.00	0.03	0.03
Fe	57.79	57.28	57.35	57.56	57.12	56.76	57.94	57.42
Co	1.36	1.36	1.35	1.31	1.30	1.36	1.28	1.34
Ni	1.38	1.34	1.30	1.26	1.38	1.40	1.27	1.33
Cu	1.37	1.47	1.33	1.34	1.31	1.43	1.30	1.32
Zn	0.00	0.05	0.03	0.00	0.05	0.04	0.00	0.00
As	0.02	0.00	0.02	0.01	0.00	0.01	0.02	0.00
Se	0.00	0.02	0.00	0.00	0.02	0.03	0.00	0.01
Pd	0.03	0.07	0.02	0.03	0.04	0.04	0.00	0.00
Ag	0.00	0.00	0.07	0.00	0.00	0.05	0.00	0.00
Cd	0.00	0.00	0.00	0.05	0.00	0.00	0.04	0.00
Sn	0.01	0.00	0.02	0.00	0.00	0.00	0.01	0.00
Sb	0.00	0.00	0.00	0.00	0.00	0.00	0.00	0.00
Te	0.00	0.02	0.00	0.00	0.01	0.05	0.00	0.00
Pt	0.00	0.00	0.00	0.00	0.03	0.09	0.00	0.00
Au	0.00	0.02	0.02	0.06	0.00	0.00	0.00	0.00
Hg	0.00	0.00	0.04	0.00	0.00	0.00	0.00	0.00
Pb	0.00	0.00	0.00	0.00	0.05	0.00	0.00	0.00
Bi	0.00	0.08	0.12	0.18	0.12	0.11	0.09	0.00
Total	100.42	99.86	100.56	100.20	100.01	99.56	100.86	100.18
S	1.198	1.189	1.050	1.044	1.048	1.045	1.047	1.049
Mn	0.001	0.001	0.001	0.000	0.000	0.000	0.000	0.000
Fe	1.035	1.026	0.890	0.898	0.892	0.891	0.896	0.893
Co	0.023	0.023	0.020	0.019	0.019	0.020	0.019	0.020
Ni	0.024	0.023	0.019	0.019	0.020	0.021	0.019	0.020
Cu	0.022	0.023	0.018	0.018	0.018	0.020	0.018	0.018
Zn	0.000	0.001	0.000	0.000	0.001	0.001	0.000	0.000
As	0.000	0.000	0.000	0.000	0.000	0.000	0.000	0.000
Se	0.000	0.000	0.000	0.000	0.000	0.000	0.000	0.000
Pd	0.000	0.001	0.000	0.000	0.000	0.000	0.000	0.000
Ag	0.000	0.000	0.001	0.000	0.000	0.000	0.000	0.000
Cd	0.000	0.000	0.000	0.000	0.000	0.000	0.000	0.000
Sn	0.000	0.000	0.000	0.000	0.000	0.000	0.000	0.000
Sb	0.000	0.000	0.000	0.000	0.000	0.000	0.000	0.000
Te	0.000	0.000	0.000	0.000	0.000	0.000	0.000	0.000
Pt	0.000	0.000	0.000	0.000	0.000	0.000	0.000	0.000
Au	0.000	0.000	0.000	0.000	0.000	0.000	0.000	0.000
Hg	0.000	0.000	0.000	0.000	0.000	0.000	0.000	0.000
Pb	0.000	0.000	0.000	0.000	0.000	0.000	0.000	0.000
Bi	0.000	0.000	0.000	0.001	0.001	0.000	0.000	0.000
TOTAL	2.303	2.287	2.000	2.000	2.000	2.000	2.000	2.000

APPENDIX C

Mineral chemistry from olivine analysis

Sample ID	Easting	Northing	DDH	Depth (m)	SiO2	TiO2	Al2O3	Cr2O3	FeO	MnO	CoO	NiO	MgO	CaO	Na2O	Total
CAMARGO Olivine Standard (Fo91)					40.84	0.00	0.02	0.02	8.39	0.13	0.04	0.41	49.69	0.07	0.00	99.60
CAMARGO Olivine standard values					40.80	0.04	0.00	0.04	8.61	0.13	0.02	0.38	49.77	0.20	0.00	99.97
RTTC-BT-089	330319	5377910	07TH004	437	37.10	0.03	0.02	0.02	27.84	0.54	0.03	0.17	34.06	0.08	0.01	99.90
					37.07	0.10	0.00	0.07	27.54	0.50	0.03	0.19	34.31	0.06	0.02	99.88
					38.13	0.04	0.00	0.03	22.29	0.34	0.07	0.23	38.14	0.09	0.02	99.38
					37.91	0.03	0.03	0.01	24.66	0.41	0.04	0.19	36.49	0.10	0.00	99.87
					39.99	0.03	0.00	0.00	13.24	0.19	0.04	0.36	45.79	0.14	0.02	99.80
					38.19	0.01	0.03	0.00	22.96	0.34	0.06	0.28	38.21	0.08	0.03	100.18
RTTC-BT-063	330319	5377910	07TH004	306	36.21	0.04	0.00	0.00	33.56	0.52	0.05	0.10	29.41	0.23	0.05	100.17
					36.20	0.06	0.01	0.00	33.24	0.46	0.00	0.11	29.71	0.24	0.04	100.07
					36.14	0.04	0.03	0.00	33.48	0.46	0.04	0.09	29.08	0.23	0.12	99.71
					36.19	0.02	0.02	0.00	33.45	0.51	0.04	0.07	28.80	0.22	0.25	99.58
					36.90	0.02	0.02	0.02	31.48	0.43	0.06	0.10	31.57	0.23	0.04	100.86
					36.78	0.05	0.01	0.00	31.43	0.45	0.09	0.13	31.61	0.22	0.02	100.79
RTTC-BT-091	330319	5377910	07TH004	432	36.79	0.02	0.03	0.06	28.95	0.54	0.03	0.14	33.29	0.11	0.02	99.98
					36.65	0.03	0.03	0.00	29.72	0.54	0.05	0.14	32.35	0.17	0.02	99.69
					36.92	0.02	0.01	0.00	29.03	0.57	0.03	0.15	32.64	0.21	0.01	99.60
					36.89	0.05	0.02	0.01	29.53	0.52	0.00	0.12	32.32	0.14	0.03	99.61
					36.37	0.03	0.00	0.01	30.49	0.59	0.01	0.13	31.72	0.09	0.03	99.47
					36.63	0.05	0.00	0.00	31.79	0.71	0.05	0.11	30.39	0.09	0.03	99.86
RTTC-BT-092	330319	5377910	07TH004	426	36.50	0.03	0.01	0.00	32.48	0.54	0.03	0.09	30.55	0.15	0.02	100.39
					36.96	0.02	0.00	0.00	31.95	0.59	0.03	0.05	30.65	0.24	0.04	100.53
					36.56	0.02	0.01	0.01	31.10	0.56	0.05	0.06	30.88	0.19	0.01	99.45
					36.62	0.04	0.00	0.00	32.47	0.58	0.03	0.07	29.99	0.09	0.00	99.89
					36.96	0.02	0.02	0.01	30.80	0.54	0.01	0.11	32.05	0.21	0.01	100.73
					36.70	0.05	0.02	0.00	30.65	0.52	0.00	0.05	31.64	0.13	0.00	99.76
RTTC-BT-093	330319	5377910	07TH004	410	36.96	0.05	0.00	0.00	28.28	0.48	0.01	0.15	32.90	0.24	0.00	99.06
					37.49	0.03	0.03	0.00	28.42	0.39	0.06	0.18	32.97	0.19	0.03	99.78
					36.99	0.03	0.00	0.01	28.90	0.46	0.04	0.15	32.54	0.23	0.02	99.36
					37.12	0.04	0.00	0.02	29.27	0.41	0.05	0.16	33.01	0.19	0.00	100.27
					36.85	0.04	0.02	0.00	28.72	0.42	0.05	0.16	33.21	0.20	0.02	99.71
					37.30	0.05	0.01	0.00	29.16	0.42	0.03	0.16	32.63	0.19	0.03	99.98
					36.30	0.03	0.05	0.00	29.23	0.45	0.07	0.17	32.55	0.15	0.04	99.03
RTTC-BT-094	330319	5377910	07TH004	404	36.37	0.03	0.04	0.01	32.06	0.53	0.03	0.14	30.83	0.21	0.00	100.24
					36.11	0.04	0.03	0.01	32.29	0.48	0.05	0.15	30.83	0.20	0.04	100.23
					37.01	0.04	0.01	0.00	32.79	0.49	0.05	0.13	30.11	0.22	0.02	100.87
					36.37	0.03	0.01	0.01	33.16	0.49	0.05	0.16	30.26	0.18	0.00	100.73
					36.31	0.03	0.00	0.00	33.00	0.56	0.05	0.12	30.12	0.27	0.02	100.47
					36.29	0.05	0.04	0.02	32.99	0.48	0.04	0.12	29.80	0.17	0.00	100.02

Sample ID	Si	Ti	Al	Cr	Fe	Mn	Co	Ni	Mg	Ca	Na	∑ cations	Fo
	1.000	0.000	0.000	0.000	0.172	0.003	0.001	0.008	1.814	0.002	0.000	3.000	**91.3**
	0.997	0.001	0.000	0.001	0.176	0.003	0.000	0.007	1.812	0.005	0.000	3.002	**91.2**
RTTC-BT-089	0.995	0.001	0.001	0.000	0.625	0.012	0.001	0.004	1.363	0.002	0.000	3.004	**68.6**
	0.994	0.002	0.000	0.002	0.617	0.011	0.001	0.004	1.371	0.002	0.001	3.004	**68.9**
	1.000	0.001	0.000	0.001	0.489	0.008	0.001	0.005	1.491	0.003	0.001	2.999	**75.3**
	1.000	0.001	0.001	0.000	0.544	0.009	0.001	0.004	1.436	0.003	0.000	2.999	**72.5**
	1.000	0.000	0.000	0.000	0.277	0.004	0.001	0.007	1.707	0.004	0.001	3.000	**86.0**
	0.997	0.000	0.001	0.000	0.501	0.007	0.001	0.006	1.487	0.002	0.002	3.004	**74.8**
RTTC-BT-063	0.997	0.001	0.000	0.000	0.773	0.012	0.001	0.002	1.207	0.007	0.003	3.003	**61.0**
	0.996	0.001	0.000	0.000	0.765	0.011	0.000	0.002	1.219	0.007	0.002	3.004	**61.4**
	1.000	0.001	0.001	0.000	0.774	0.011	0.001	0.002	1.199	0.007	0.007	3.002	**60.8**
	1.003	0.000	0.001	0.000	0.775	0.012	0.001	0.002	1.190	0.007	0.013	3.003	**60.5**
	0.997	0.000	0.001	0.000	0.711	0.010	0.001	0.002	1.272	0.007	0.002	3.003	**64.1**
	0.995	0.001	0.000	0.000	0.711	0.010	0.002	0.003	1.275	0.006	0.001	3.004	**64.2**
RTTC-BT-091	0.992	0.000	0.001	0.001	0.653	0.012	0.001	0.003	1.339	0.003	0.001	3.007	**67.2**
	0.995	0.001	0.001	0.000	0.675	0.012	0.001	0.003	1.310	0.005	0.001	3.004	**66.0**
	1.000	0.000	0.000	0.000	0.658	0.013	0.001	0.003	1.318	0.006	0.001	3.000	**66.7**
	1.001	0.001	0.001	0.000	0.670	0.012	0.000	0.003	1.307	0.004	0.001	2.999	**66.1**
	0.994	0.001	0.000	0.000	0.697	0.014	0.000	0.003	1.293	0.003	0.002	3.006	**65.0**
	1.003	0.001	0.000	0.000	0.728	0.016	0.001	0.002	1.241	0.003	0.001	2.997	**63.0**
RTTC-BT-092	0.997	0.001	0.000	0.000	0.742	0.012	0.001	0.002	1.243	0.004	0.001	3.003	**62.6**
	1.004	0.000	0.000	0.000	0.726	0.014	0.001	0.001	1.242	0.007	0.002	2.996	**63.1**
	1.002	0.000	0.000	0.000	0.713	0.013	0.001	0.001	1.261	0.006	0.001	2.998	**63.9**
	1.004	0.001	0.000	0.000	0.745	0.013	0.001	0.001	1.226	0.003	0.000	2.995	**62.2**
	0.997	0.000	0.001	0.000	0.695	0.012	0.000	0.002	1.288	0.006	0.000	3.003	**65.0**
	0.999	0.001	0.000	0.000	0.698	0.012	0.000	0.001	1.284	0.004	0.000	3.000	**64.8**
RTTC-BT-093	1.002	0.001	0.000	0.000	0.641	0.011	0.000	0.003	1.330	0.007	0.000	2.997	**67.5**
	1.008	0.001	0.001	0.000	0.639	0.009	0.001	0.004	1.322	0.005	0.002	2.992	**67.4**
	1.003	0.001	0.000	0.000	0.655	0.011	0.001	0.003	1.315	0.007	0.001	2.997	**66.7**
	0.998	0.001	0.000	0.000	0.658	0.009	0.001	0.003	1.324	0.005	0.000	3.001	**66.8**
	0.995	0.001	0.001	0.000	0.649	0.010	0.001	0.003	1.337	0.006	0.001	3.004	**67.3**
	1.005	0.001	0.000	0.000	0.657	0.010	0.001	0.003	1.311	0.006	0.002	2.995	**66.6**
	0.991	0.001	0.002	0.000	0.668	0.010	0.002	0.004	1.325	0.004	0.002	3.008	**66.5**
RTTC-BT-094	0.993	0.001	0.001	0.000	0.732	0.012	0.001	0.003	1.255	0.006	0.000	3.005	**63.2**
	0.988	0.001	0.001	0.000	0.739	0.011	0.001	0.003	1.258	0.006	0.002	3.011	**63.0**
	1.006	0.001	0.000	0.000	0.745	0.011	0.001	0.003	1.220	0.006	0.001	2.994	**62.1**
	0.993	0.001	0.000	0.000	0.758	0.011	0.001	0.004	1.232	0.005	0.000	3.006	**61.9**
	0.994	0.001	0.000	0.000	0.756	0.013	0.001	0.003	1.229	0.008	0.001	3.006	**61.9**
	0.998	0.001	0.001	0.001	0.758	0.011	0.001	0.003	1.221	0.005	0.000	3.001	**61.7**

Sample ID	Easting	Northing	DDH	Depth (m)	SiO2	TiO2	Al2O3	Cr2O3	FeO	MnO	CoO	NiO	MgO	CaO	Na2O	Total
RTTC-BT-095	330319	5377910	07TH004	376	37.05	0.02	0.02	0.00	28.83	0.46	0.03	0.17	33.55	0.36	0.00	100.50
					37.13	0.04	0.01	0.00	29.07	0.49	0.03	0.17	33.07	0.26	0.01	100.28
					37.20	0.01	0.02	0.01	28.91	0.50	0.03	0.17	33.18	0.32	0.00	100.36
					37.02	0.04	0.02	0.00	28.53	0.45	0.01	0.16	33.39	0.24	0.02	99.89
					36.86	0.02	0.00	0.00	28.64	0.50	0.02	0.18	33.45	0.31	0.01	99.99
					37.06	0.07	0.00	0.00	28.20	0.46	0.05	0.16	33.29	0.27	0.00	99.57
					37.21	0.05	0.00	0.00	27.94	0.46	0.02	0.16	34.09	0.27	0.00	100.21
RTTC-BT-096	330319	5377910	07TH004	356	37.25	0.03	0.00	0.01	29.23	0.47	0.04	0.14	33.30	0.17	0.00	100.63
					36.96	0.03	0.01	0.02	29.12	0.40	0.03	0.13	33.01	0.17	0.00	99.87
					37.02	0.04	0.00	0.00	29.12	0.41	0.07	0.14	33.54	0.21	0.02	100.57
					37.28	0.03	0.02	0.00	28.81	0.44	0.02	0.13	33.38	0.09	0.00	100.21
					36.79	0.01	0.00	0.01	29.11	0.42	0.05	0.14	33.30	0.22	0.00	100.05
					37.29	0.04	0.01	0.00	28.53	0.41	0.06	0.14	33.19	0.12	0.00	99.79
RTTC-BT-097	330319	5377910	07TH004	323	35.30	0.05	0.00	0.03	36.57	0.56	0.09	0.10	26.95	0.26	0.00	99.89
					35.49	0.05	0.02	0.01	36.93	0.57	0.08	0.11	26.78	0.21	0.01	100.25
					35.58	0.04	0.00	0.01	36.97	0.58	0.09	0.10	27.13	0.23	0.00	100.72
					35.47	0.06	0.01	0.02	37.26	0.60	0.06	0.09	26.89	0.22	0.01	100.69
					35.75	0.05	0.01	0.01	36.57	0.56	0.06	0.10	27.01	0.26	0.00	100.39
					35.68	0.08	0.02	0.01	36.57	0.59	0.08	0.09	26.70	0.18	0.00	99.99
RTTC-BT-098	330319	5377910	07TH004	318	36.85	0.04	0.01	0.00	31.71	0.42	0.05	0.15	30.95	0.26	0.03	100.48
					36.64	0.04	0.02	0.01	31.79	0.41	0.01	0.13	31.16	0.20	0.02	100.43
					36.62	0.06	0.01	0.00	32.18	0.47	0.05	0.14	31.05	0.28	0.01	100.85
					36.76	0.02	0.03	0.01	31.65	0.45	0.04	0.14	30.81	0.20	0.01	100.12
					37.07	0.05	0.01	0.01	29.70	0.42	0.04	0.15	32.60	0.21	0.01	100.27
					37.15	0.04	0.02	0.01	29.88	0.42	0.04	0.14	32.77	0.17	0.01	100.65
					36.67	0.04	0.01	0.00	31.58	0.47	0.05	0.18	31.24	0.22	0.01	100.47
					36.73	0.04	0.01	0.00	31.82	0.42	0.09	0.15	31.25	0.17	0.00	100.67
RTT-BT-149	330411	5378463	Surface	-	36.49	0.01	0.02	0.01	29.55	0.53	0.08	0.15	32.27	0.38	0.02	99.50
					36.86	0.01	0.00	0.00	30.34	0.55	0.01	0.15	31.84	0.36	0.01	100.12
					36.14	0.04	0.00	0.00	32.47	0.65	0.03	0.08	29.72	0.28	0.02	99.43
					35.91	0.03	0.04	0.00	32.74	0.62	0.06	0.07	29.82	0.33	0.03	99.66
					36.21	0.03	0.01	0.00	32.03	0.66	0.01	0.11	30.30	0.33	0.01	99.70
RTTC-BT-149	330319	5377910	07TH006	182	37.32	0.04	0.01	0.00	27.41	0.38	0.08	0.22	34.19	0.24	0.00	99.88
					37.69	0.04	0.02	0.02	27.61	0.36	0.03	0.21	34.25	0.21	0.02	100.47
					37.07	0.03	0.00	0.00	27.65	0.37	0.05	0.22	33.98	0.22	0.01	99.60
					37.23	0.03	0.01	0.01	27.74	0.40	0.04	0.19	33.86	0.19	0.00	99.70
					37.45	0.02	0.01	0.00	27.81	0.35	0.03	0.21	34.49	0.24	0.00	100.60
					36.84	0.04	0.04	0.00	27.56	0.38	0.02	0.21	33.89	0.22	0.01	99.21
CAMARGO Olivine Standard (Fo91)					40.97	0.00	0.01	0.02	8.40	0.12	0.01	0.41	49.62	0.06	0.00	99.63
CAMARGO Olivine standard values					40.80	0.04	0.00	0.04	8.61	0.13	0.02	0.38	49.77	0.20	0.00	99.99

Sample ID	Si	Ti	Al	Cr	Fe	Mn	Co	Ni	Mg	Ca	Na	∑ cations	Fo
RTTC-BT-095	0.993	0.000	0.000	0.000	0.646	0.011	0.001	0.004	1.341	0.010	0.000	3.006	**67.5**
	0.998	0.001	0.000	0.000	0.653	0.011	0.001	0.004	1.325	0.007	0.001	3.001	**67.0**
	0.998	0.000	0.000	0.000	0.649	0.011	0.001	0.004	1.328	0.009	0.000	3.001	**67.2**
	0.997	0.001	0.001	0.000	0.642	0.010	0.000	0.004	1.340	0.007	0.001	3.003	**67.6**
	0.993	0.000	0.000	0.000	0.645	0.011	0.001	0.004	1.343	0.009	0.000	3.007	**67.6**
	1.000	0.001	0.000	0.000	0.636	0.011	0.001	0.003	1.339	0.008	0.000	2.999	**67.8**
	0.996	0.001	0.000	0.000	0.625	0.010	0.000	0.004	1.360	0.008	0.000	3.004	**68.5**
RTTC-BT-096	0.998	0.001	0.000	0.000	0.655	0.011	0.001	0.003	1.330	0.005	0.000	3.002	**67.0**
	0.998	0.001	0.000	0.000	0.657	0.009	0.001	0.003	1.328	0.005	0.000	3.002	**66.9**
	0.992	0.001	0.000	0.000	0.653	0.009	0.001	0.003	1.340	0.006	0.001	3.007	**67.2**
	1.000	0.001	0.001	0.000	0.646	0.010	0.000	0.003	1.335	0.003	0.000	2.999	**67.4**
	0.992	0.000	0.000	0.000	0.656	0.009	0.001	0.003	1.339	0.006	0.000	3.008	**67.1**
	1.004	0.001	0.000	0.000	0.642	0.009	0.001	0.003	1.332	0.003	0.000	2.995	**67.5**
RTTC-BT-097	0.992	0.001	0.000	0.001	0.859	0.013	0.002	0.002	1.129	0.008	0.000	3.007	**56.8**
	0.994	0.001	0.001	0.000	0.865	0.014	0.002	0.002	1.118	0.006	0.000	3.004	**56.4**
	0.992	0.001	0.000	0.000	0.862	0.014	0.002	0.002	1.127	0.007	0.000	3.007	**56.7**
	0.991	0.001	0.000	0.000	0.870	0.014	0.001	0.002	1.120	0.007	0.000	3.008	**56.3**
	0.998	0.001	0.000	0.000	0.853	0.013	0.001	0.002	1.124	0.008	0.000	3.001	**56.8**
	1.000	0.002	0.000	0.000	0.857	0.014	0.002	0.002	1.115	0.005	0.000	2.998	**56.5**
RTTC-BT-098	1.001	0.001	0.000	0.000	0.720	0.010	0.001	0.003	1.253	0.008	0.001	2.999	**63.5**
	0.996	0.001	0.001	0.000	0.723	0.009	0.000	0.003	1.263	0.006	0.001	3.003	**63.6**
	0.994	0.001	0.000	0.000	0.730	0.011	0.001	0.003	1.256	0.008	0.001	3.005	**63.2**
	1.002	0.000	0.001	0.000	0.721	0.010	0.001	0.003	1.252	0.006	0.001	2.997	**63.4**
	0.999	0.001	0.000	0.000	0.669	0.009	0.001	0.003	1.310	0.006	0.001	3.000	**66.2**
	0.998	0.001	0.000	0.000	0.671	0.010	0.001	0.003	1.312	0.005	0.001	3.001	**66.2**
	0.996	0.001	0.000	0.000	0.718	0.011	0.001	0.004	1.265	0.007	0.000	3.003	**63.8**
	0.996	0.001	0.000	0.000	0.722	0.010	0.002	0.003	1.264	0.005	0.000	3.003	**63.6**
RTT-BT-149	0.994	0.000	0.001	0.000	0.673	0.012	0.002	0.003	1.310	0.011	0.001	3.007	**66.1**
	0.999	0.000	0.000	0.000	0.688	0.013	0.000	0.003	1.287	0.010	0.001	3.001	**65.2**
	0.999	0.001	0.000	0.000	0.750	0.015	0.001	0.002	1.224	0.008	0.001	3.001	**62.0**
	0.992	0.001	0.001	0.000	0.756	0.015	0.001	0.001	1.228	0.010	0.002	3.007	**61.9**
	0.996	0.001	0.000	0.000	0.737	0.015	0.000	0.002	1.242	0.010	0.000	3.004	**62.8**
RTTC-BT-149	0.999	0.001	0.000	0.000	0.614	0.009	0.002	0.005	1.365	0.007	0.000	3.000	**69.0**
	1.002	0.001	0.001	0.000	0.614	0.008	0.001	0.005	1.358	0.006	0.001	2.997	**68.9**
	0.997	0.001	0.000	0.000	0.622	0.008	0.001	0.005	1.362	0.006	0.000	3.003	**68.7**
	1.000	0.001	0.000	0.000	0.623	0.009	0.001	0.004	1.356	0.005	0.000	2.999	**68.5**
	0.996	0.000	0.000	0.000	0.619	0.008	0.001	0.005	1.368	0.007	0.000	3.003	**68.9**
	0.995	0.001	0.001	0.000	0.622	0.009	0.000	0.005	1.364	0.006	0.000	3.004	**68.7**
	1.002	0.000	0.000	0.000	0.172	0.003	0.000	0.008	1.810	0.002	0.000	2.997	**91.3**
	0.997	0.001	0.000	0.001	0.176	0.003	0.000	0.007	1.812	0.005	0.000	3.002	**91.2**

APPENDIX D

Whole rock geochemistry (major and trace element)

UTM datum NAD83 Zone 16

	Eastern N-trending gabbroic dike					
Sample ID	RTT-BT-055	RTT-BT-180	RTT-BT-190	RTT-BT-215	RTT-BT-216	RTT-BT-222
SiO_2 (wt.%)	47.79	46.90	47.28	47.69	47.94	47.36
TiO_2	1.49	1.42	1.28	1.42	1.66	1.41
Al_2O_3	15.50	14.95	15.62	15.20	15.31	15.99
Fe_2O_3	13.53	14.24	13.16	13.82	13.68	12.29
MnO	0.192	0.202	0.190	0.202	0.206	0.171
MgO	7.25	8.08	7.70	7.55	6.92	7.27
CaO	8.539	9.653	9.791	9.969	9.810	9.250
Na_2O	2.24	2.38	2.33	2.47	2.60	2.57
K2O	1.68	0.69	1.23	0.79	0.69	1.14
P_2O_5	0.161	0.155	0.139	0.151	0.186	0.159
LOI	1.04	0.64	1.06	0.54	0.80	2.03
Total	99.41	99.31	99.78	99.80	99.80	99.64
Ti (ppm)	9133	8587	8350	8640	10278	8647
Rb	50.55	15.01	39.12	20.07	17.46	47.81
Sr	497.5	350.3	393.0	347.2	333.0	515.5
Cs	3.011	1.241	2.663	1.718	2.169	3.494
Ba	675.0	281.7	309.6	306.6	327.0	527.4
Sc	31.4	33.0	35.5	36.1	35.5	34.4
V	275.0	262.4	277.7	294.8	304.3	271.4
Ta	0.712	0.677	0.615	0.639	0.822	0.664
Nb	11.879	10.883	10.151	10.358	13.333	10.972
Zr	93	88	83	85	105	91
Hf	2.40	2.33	2.15	2.26	2.68	2.33
Th	1.321	1.259	1.216	1.227	1.476	1.299
U	0.260	0.256	0.241	0.237	0.290	0.344
Y	19.71	18.59	17.65	19.32	22.19	19.12
La	14.52	13.53	12.63	13.14	16.10	13.83
Ce	31.10	29.09	27.18	28.13	34.75	29.25
Pr	4.024	3.880	3.616	3.768	4.638	3.867
Nd	17.51	16.79	15.52	16.45	19.99	16.67
Sm	3.938	3.813	3.609	3.837	4.463	3.839
Eu	1.4882	1.3935	1.3669	1.4364	1.5963	1.4163
Gd	3.931	3.823	3.639	4.000	4.493	3.838
Tb	0.5973	0.5810	0.5543	0.5998	0.6789	0.5837
Dy	3.699	3.603	3.362	3.734	4.177	3.596
Ho	0.7172	0.7056	0.6596	0.7308	0.8164	0.7029
Er	2.059	2.022	1.852	2.089	2.328	2.008
Tm	0.2904	0.2820	0.2605	0.2953	0.3290	0.2848
Yb	1.840	1.824	1.716	1.884	2.115	1.838
Lu	0.286	0.272	0.254	0.284	0.314	0.269
Tl	0.282	0.087	0.186	0.098	0.101	0.263
Pb	2.6	2.5	2.3	2.4	37.0	3.3
Sn	0.76	0.74	0.63	0.68	0.95	0.64
Sb	<0.04	<0.04	<0.04	<0.04	0.04	0.07
Easting	331003	330822	330803	330593	330587	331388
Northing	5377824	5384202	5378724	5391886	5391889	5375988
DDH	Surface	Surface	Surface	Surface	Surface	Surface
Depth (m)	-	-	-	-	-	-

	Western N-trending gabbroic dike					Mafic dikes
Sample ID	RTT-BT-220	RTT-BT-232	RTT-BT-235	RTT-BT-236	RTT-BT-237	RTTC-BT-219
SiO_2 (wt.%)	41.31	49.25	48.60	47.60	44.00	49.10
TiO_2	2.06	2.07	1.89	2.16	3.26	2.22
Al_2O_3	15.78	16.90	15.83	14.82	12.29	13.22
Fe_2O_3	10.66	12.20	12.92	14.43	18.60	13.78
MnO	0.347	0.165	0.177	0.195	0.163	0.161
MgO	4.35	3.79	5.54	6.12	5.20	7.17
CaO	10.810	7.960	7.662	7.906	6.414	8.762
Na_2O	1.98	3.27	2.86	2.66	1.88	2.96
K2O	3.21	1.88	1.48	1.82	2.68	0.54
P_2O_5	0.269	0.353	0.296	0.241	0.555	0.232
LOI	8.65	1.57	1.40	1.30	3.92	1.88
Total	99.43	99.41	98.66	99.25	98.96	100.03
Ti (ppm)	12827	13036	11764	13570	19593	13621
Rb	69.91	60.73	42.17	57.74	164.00	12.02
Sr	244.9	466.3	382.1	413.9	210.8	358.3
Cs	1.835	3.825	2.219	1.875	4.915	2.143
Ba	601.7	656.6	654.3	602.7	880.4	165.4
Sc	34.2	25.4	27.5	34.4	41.0	28.3
V	317.8	264.6	262.9	409.3	377.2	285.7
Ta	1.021	1.070	0.899	0.764	2.103	0.768
Nb	16.594	18.298	15.348	13.060	36.344	11.907
Zr	157	166	140	119	255	185
Hf	4.00	4.07	3.44	2.97	6.00	4.57
Th	2.509	3.306	2.584	2.238	3.430	1.673
U	0.461	0.552	0.455	0.400	0.774	0.413
Y	33.53	27.38	23.89	21.11	44.06	25.94
La	24.01	28.99	24.63	20.12	38.61	17.87
Ce	50.50	60.52	51.68	42.12	82.86	41.26
Pr	6.647	7.807	6.633	5.525	10.865	5.662
Nd	28.18	32.28	27.66	23.06	45.56	25.52
Sm	6.492	6.765	5.761	5.002	9.608	6.153
Eu	2.3268	2.2177	2.0297	1.7695	2.8432	2.1335
Gd	6.676	6.396	5.556	4.792	9.424	6.223
Tb	0.9964	0.9008	0.7949	0.6946	1.3700	0.9122
Dy	6.100	5.347	4.678	4.099	8.401	5.332
Ho	1.1641	1.0201	0.8813	0.7862	1.6097	0.9660
Er	3.284	2.817	2.508	2.195	4.616	2.607
Tm	0.4515	0.3910	0.3412	0.2981	0.6507	0.3362
Yb	2.799	2.451	2.148	1.882	4.151	2.067
Lu	0.408	0.359	0.319	0.279	0.623	0.288
Tl	0.524	0.308	0.204	0.270	0.983	0.058
Pb	5.7	6.7	3.4	4.2	5.7	4.0
Sn	1.24	1.13	0.98	0.90	0.95	1.58
Sb	0.30	0.06	<0.04	<0.04	0.04	0.10
Easting	328598	326984	326997	327028	327159	330161
Northing	5386506	5400588	5401169	5401620	5402611	5378268
DDH	Surface	Surface	Surface	Surface	Surface	07TH007
Depth (m)	-	-	-	-	-	43

	Cross-cutting mafic dikes				Iron formation	
Sample ID	RTTC-BT-210	RTTC-BT-101	RTTC-BT-045	RTTC-BT-038	RTTC-BT-006	RTTC-BT-005
SiO_2 (wt.%)	49.06	48.70	49.72	49.05	20.00	10.58
TiO_2	0.96	2.23	2.30	0.98	0.05	0.07
Al_2O_3	14.89	12.91	13.09	14.28	2.08	1.46
Fe_2O_3	13.03	12.83	13.67	12.80	53.93	75.29
MnO	0.201	0.188	0.179	0.205	0.224	0.182
MgO	7.24	5.98	6.11	6.99	0.99	0.84
CaO	10.638	9.416	9.883	11.222	18.449	7.245
Na_2O	2.10	1.79	2.57	2.16	0.03	0.03
K2O	0.69	2.15	0.73	0.32	0.07	0.07
P_2O_5	0.085	0.229	0.239	0.086	2.066	1.328
LOI	1.70	2.77	0.89	1.50	0.53	1.76
Total	100.59	99.19	99.38	99.59	98.42	98.86
Ti (ppm)	5717	13899	14195	6065	318	241
Rb	24.83	61.35	17.05	6.29	2.71	2.95
Sr	147.7	281.2	358.4	134.3	17.3	11.3
Cs	0.824	2.618	2.141	1.333	0.536	0.459
Ba	196.4	464.1	219.4	105.2	12.7	15.0
Sc	37.5	28.5	29.0	26.4	1.4	<1.1
V	294.0	301.0	310.4	283.0	197.2	112.9
Ta	0.176	0.754	0.786	0.183	0.058	0.061
Nb	2.864	11.872	12.467	2.937	4.518	5.868
Zr	59	178	186	59	22	15
Hf	1.61	4.50	4.67	1.61	0.52	0.32
Th	0.971	1.669	1.716	0.789	2.796	1.230
U	0.269	0.398	0.421	0.259	4.366	3.100
Y	19.33	25.53	26.98	15.60	3.62	3.22
La	5.20	17.85	18.08	4.65	131.83	98.37
Ce	11.59	39.13	41.26	10.64	280.18	185.20
Pr	1.677	5.452	5.832	1.537	30.951	16.761
Nd	7.96	24.60	26.06	7.27	94.51	38.41
Sm	2.341	6.048	6.318	2.193	3.443	1.094
Eu	0.8953	2.1296	2.0974	0.8054	7.1138	2.4215
Gd	2.987	6.127	6.383	2.781	0.793	0.508
Tb	0.5115	0.8974	0.9395	0.4686	0.1072	0.0807
Dy	3.444	5.252	5.476	3.081	0.429	0.349
Ho	0.7015	0.9622	1.0040	0.6242	0.0789	0.0690
Er	2.101	2.569	2.660	1.816	0.225	0.182
Tm	0.2953	0.3356	0.3530	0.2529	0.0278	0.0271
Yb	1.888	2.089	2.143	1.633	0.184	0.176
Lu	0.283	0.288	0.300	0.240	0.028	0.028
Tl	0.116	0.207	0.057	0.083	0.092	0.282
Pb	0.9	8.6	2.3	2.1	4.5	4.5
Sn	0.64	1.04	1.21	<0.16	2.90	2.93
Sb	0.17	1.37	0.06	0.04	0.25	0.11
Easting	330161	330435	330435	330435	329809	329809
Northing	5378268	5378298	5378298	5378298	5377560	5377560
DDH	07TH007	05TH002	05TH003	05TH003	05TH001	05TH001
Depth (m)	312	220	63	240	111	112

	Pegmatitic gabbro				Upper gabbroic unit	
Sample ID	RTTC-BT-216	RTTC-BT-217	RTT-BT-130	RTTC-BT-062	RTT-BT-074	RTT-BT-142
SiO_2 (wt.%)	50.03	48.62	46.03	50.02	49.01	49.33
TiO_2	3.32	3.07	4.07	3.22	2.11	1.99
Al_2O_3	13.65	13.71	11.99	11.88	15.80	11.93
Fe_2O_3	10.30	12.76	14.09	12.58	11.56	12.56
MnO	0.160	0.207	0.158	0.199	0.210	0.325
MgO	6.44	6.19	6.91	5.00	4.91	8.34
CaO	9.345	9.120	11.222	10.076	9.853	7.985
Na_2O	4.52	4.06	2.68	4.90	3.24	2.26
K2O	0.48	0.79	1.01	0.15	1.17	2.20
P_2O_5	0.389	0.277	0.157	0.606	0.264	0.238
LOI	1.59	1.26	1.04	1.11	0.72	1.84
Total	100.22	100.06	99.36	99.74	98.85	99.00
Ti (ppm)	20568	19177	24629	19978	12873	12150
Rb	13.49	23.97	29.05	2.99	33.56	71.86
Sr	531.8	709.4	792.2	192.8	1104.1	544.4
Cs	0.257	0.734	0.913	0.173	1.447	1.402
Ba	90.4	145.0	343.8	22.4	382.8	627.7
Sc	24.8	26.9	29.9	18.0	19.7	24.7
V	274.5	361.6	564.9	201.2	216.6	251.5
Ta	2.544	1.757	1.325	3.433	1.555	1.252
Nb	37.874	26.390	21.345	53.802	23.876	19.466
Zr	382	267	201	559	256	217
Hf	9.07	6.53	5.16	12.98	6.12	5.34
Th	4.229	2.931	2.113	6.587	2.665	3.487
U	2.131	0.985	1.361	2.709	0.879	1.026
Y	26.02	20.34	18.44	35.43	18.16	17.31
La	44.65	40.54	41.17	54.03	33.35	31.07
Ce	118.22	88.32	101.20	149.73	79.31	73.34
Pr	16.189	11.753	12.976	21.036	10.674	10.005
Nd	66.77	48.67	50.85	89.44	45.59	41.60
Sm	12.060	9.218	8.942	16.446	8.466	7.854
Eu	3.5492	2.4098	3.0683	4.3816	2.6312	2.1404
Gd	9.232	7.041	6.773	12.298	6.517	6.250
Tb	1.1415	0.8979	0.8485	1.5619	0.8084	0.7639
Dy	5.890	4.627	4.301	7.931	4.154	3.972
Ho	0.9915	0.7751	0.7026	1.3287	0.6870	0.6561
Er	2.483	1.942	1.752	3.373	1.707	1.671
Tm	0.3117	0.2448	0.2219	0.4318	0.2148	0.2111
Yb	1.882	1.447	1.286	2.587	1.267	1.253
Lu	0.258	0.198	0.179	0.352	0.179	0.178
Tl	0.030	0.050	0.087	0.024	0.213	0.339
Pb	2.0	1.7	1.6	8.6	2.5	6.3
Sn	3.37	0.95	1.96	3.26	1.03	1.82
Sb	0.17	0.09	0.16	0.52	0.09	0.89
Easting	330161	330161	329929	330319	330576	330569
Northing	5378268	5378268	5378222	5377910	5377761	5377749
DDH	07TH007	07TH007	Surface	07TH004	Surface	Surface
Depth (m)	53	71	-	311	-	-

	Upper gabbroic unit					
Sample ID	RTTC-BT-082	RTTC-BT-081	RTTC-BT-080	RTTC-BT-079	RTTC-BT-077	RTTC-BT-078
SiO_2 (wt.%)	52.42	50.20	46.01	47.59	45.98	45.25
TiO_2	2.46	3.42	4.57	4.43	5.15	4.89
Al_2O_3	14.01	12.78	11.52	12.26	11.62	12.06
Fe_2O_3	12.65	14.13	17.88	15.59	16.89	17.56
MnO	0.179	0.217	0.237	0.195	0.207	0.219
MgO	3.17	3.77	4.49	4.65	5.06	4.82
CaO	6.383	6.747	8.130	7.371	8.866	9.006
Na_2O	4.78	4.66	4.02	4.29	3.46	3.50
K2O	1.56	1.19	0.95	0.98	1.06	1.02
P_2O_5	0.656	0.597	0.476	0.373	0.310	0.311
LOI	1.31	1.23	1.13	1.22	0.68	0.62
Total	99.58	98.94	99.41	98.95	99.28	99.26
Ti (ppm)	14678	20606	27407	26854	32199	30799
Rb	39.86	31.77	22.05	28.68	29.21	27.08
Sr	637.4	597.7	390.1	682.0	640.5	689.8
Cs	0.252	0.220	0.133	0.305	0.425	0.308
Ba	658.3	570.0	233.0	229.2	255.1	240.7
Sc	14.5	17.2	21.7	21.4	25.8	25.0
V	101.9	154.7	262.4	293.1	424.1	400.6
Ta	2.887	3.245	2.775	2.621	2.480	2.390
Nb	47.675	52.329	42.573	39.011	35.987	34.435
Zr	533	484	352	372	319	300
Hf	12.54	11.53	8.46	8.89	7.86	7.27
Th	6.286	5.498	3.631	4.100	3.234	3.152
U	2.151	1.984	1.241	1.424	1.114	1.364
Y	37.27	34.39	25.56	26.20	23.23	22.16
La	72.48	65.58	38.39	48.04	39.38	49.25
Ce	170.04	152.48	94.83	112.13	94.06	103.83
Pr	22.846	20.380	13.472	15.204	12.962	13.412
Nd	94.18	85.08	59.27	64.60	55.71	55.29
Sm	17.472	15.981	11.565	12.364	10.736	10.457
Eu	4.7225	4.2661	3.3114	3.3841	3.0983	3.2444
Gd	13.517	12.520	9.242	9.687	8.368	8.072
Tb	1.6692	1.5301	1.1383	1.1924	1.0492	1.0089
Dy	8.479	7.833	5.889	6.065	5.349	5.191
Ho	1.4182	1.3186	0.9745	1.0052	0.9021	0.8610
Er	3.548	3.263	2.466	2.483	2.228	2.147
Tm	0.4469	0.4157	0.3058	0.3177	0.2764	0.2711
Yb	2.637	2.466	1.838	1.861	1.650	1.622
Lu	0.362	0.342	0.256	0.255	0.229	0.224
Tl	0.216	0.184	0.107	0.159	0.153	0.142
Pb	2.0	2.2	4.9	1.3	2.5	4.9
Sn	2.47	1.73	1.78	1.55	1.60	1.69
Sb	0.20	0.20	0.25	0.19	0.26	0.30
Easting	330319	330319	330319	330319	330319	330319
Northing	5377910	5377910	5377910	5377910	5377910	5377910
DDH	07TH004	07TH004	07TH004	07TH004	07TH004	07TH004
Depth (m)	9	10	20	58	84	86

	Upper gabbroic unit					
Sample ID	RTTC-BT-076	RTTC-BT-075	RTTC-BT-073	RTTC-BT-074	RTTC-BT-072	RTTC-BT-071
SiO_2 (wt.%)	45.54	45.98	41.58	43.98	45.97	45.54
TiO_2	5.14	4.96	4.09	5.04	5.08	5.12
Al_2O_3	11.55	12.19	12.01	10.44	12.35	12.27
Fe_2O_3	17.59	16.04	17.92	20.15	13.38	15.88
MnO	0.240	0.200	0.180	0.229	0.174	0.185
MgO	5.01	5.02	5.50	5.90	5.76	5.24
CaO	8.862	9.880	13.054	9.915	10.688	9.993
Na_2O	3.05	3.41	2.10	2.71	3.36	3.29
K2O	1.24	0.81	0.69	0.84	0.62	0.76
P_2O_5	0.301	0.278	0.644	0.227	0.181	0.240
LOI	0.48	0.78	1.86	0.28	1.48	0.74
Total	99.00	99.55	99.63	99.71	99.04	99.26
Ti (ppm)	30587	29752	25743	30111	31197	31722
Rb	29.66	19.39	13.26	20.38	19.45	19.05
Sr	800.3	743.1	588.4	733.2	825.1	814.7
Cs	1.023	0.384	0.369	0.733	0.653	0.342
Ba	373.4	224.5	247.8	264.9	154.5	222.1
Sc	25.0	24.6	19.6	29.9	25.8	25.9
V	418.1	431.4	489.2	676.3	439.8	490.6
Ta	2.391	2.144	1.900	1.462	2.035	1.951
Nb	34.218	31.085	29.435	21.990	29.806	28.405
Zr	295	274	213	231	244	247
Hf	7.39	6.72	5.50	5.88	6.15	6.10
Th	3.093	2.739	4.683	2.221	2.838	2.427
U	1.068	1.115	1.589	0.804	2.079	1.012
Y	22.12	19.93	27.71	19.34	21.36	18.76
La	39.48	31.47	62.74	30.97	41.16	29.65
Ce	92.21	76.58	141.75	73.36	102.55	70.98
Pr	12.584	10.509	17.528	10.252	13.693	9.847
Nd	52.89	45.58	68.15	44.11	55.54	42.62
Sm	10.329	9.005	11.845	8.858	10.307	8.443
Eu	3.1230	2.7817	3.5817	2.6349	3.8070	2.4766
Gd	8.031	7.236	9.170	7.183	7.860	6.565
Tb	1.0040	0.8997	1.1363	0.8852	0.9650	0.8204
Dy	5.144	4.686	6.073	4.511	5.013	4.276
Ho	0.8565	0.7710	1.0361	0.7461	0.8285	0.7156
Er	2.132	1.914	2.595	1.884	2.088	1.777
Tm	0.2695	0.2370	0.3368	0.2315	0.2586	0.2223
Yb	1.608	1.432	2.003	1.357	1.569	1.324
Lu	0.218	0.202	0.285	0.193	0.221	0.182
Tl	0.117	0.106	0.053	0.085	0.104	0.101
Pb	1.9	3.6	7.5	3.7	3.5	3.0
Sn	1.67	1.28	4.33	1.36	2.81	1.29
Sb	0.22	0.22	0.25	0.15	0.16	0.22
Easting	330319	330319	330319	330319	330319	330319
Northing	5377910	5377910	5377910	5377910	5377910	5377910
DDH	07TH004	07TH004	07TH004	07TH004	07TH004	07TH004
Depth (m)	101	145	181	182	188	190

	Upper gabbroic unit					
Sample ID	RTTC-BT-070	RTTC-BT-069	RTTC-BT-068	RTTC-BT-067	RTTC-BT-065	RTTC-BT-100
SiO_2 (wt.%)	45.57	45.98	48.01	46.19	47.36	50.39
TiO_2	4.45	3.55	2.30	3.03	2.58	1.87
Al_2O_3	12.50	13.46	15.63	13.92	14.73	16.13
Fe_2O_3	16.29	15.94	12.94	14.82	13.86	11.46
MnO	0.197	0.185	0.169	0.179	0.148	0.135
MgO	5.43	5.53	5.44	6.19	5.81	5.15
CaO	10.178	9.897	9.248	8.957	9.191	8.812
Na_2O	3.15	3.00	3.23	2.97	3.28	3.52
K2O	0.79	1.01	1.18	1.36	1.22	1.10
P_2O_5	0.233	0.195	0.247	0.203	0.228	0.259
LOI	0.96	0.56	0.96	1.31	1.10	0.89
Total	99.75	99.31	99.35	99.13	99.51	99.72
Ti (ppm)	27290	21850	14356	18994	16119	11229
Rb	20.86	24.41	34.89	43.67	40.31	32.00
Sr	820.6	944.6	1057.0	904.5	1045.8	1088.9
Cs	0.502	1.160	1.319	1.275	0.862	1.002
Ba	225.4	297.0	294.5	543.0	245.3	276.6
Sc	26.2	25.3	18.1	24.5	20.4	14.7
V	585.8	633.3	304.1	528.5	416.5	213.4
Ta	1.626	1.176	1.347	1.187	1.409	1.414
Nb	24.081	17.641	21.197	18.606	21.829	21.861
Zr	230	187	221	194	225	233
Hf	5.67	4.69	5.34	4.85	5.42	5.70
Th	2.300	1.926	2.407	2.044	2.494	2.721
U	0.914	0.674	0.840	0.749	0.951	1.041
Y	17.91	14.96	16.45	15.20	16.42	16.46
La	29.76	24.28	30.60	25.29	28.38	33.55
Ce	71.66	58.54	72.39	60.00	67.44	77.59
Pr	9.918	8.156	9.890	8.456	9.229	10.397
Nd	42.60	35.13	41.42	36.12	39.81	43.42
Sm	8.256	6.791	7.805	7.054	7.627	7.912
Eu	2.5108	2.3108	2.3859	2.1657	2.2651	2.4376
Gd	6.514	5.426	5.938	5.529	5.845	6.045
Tb	0.8127	0.6788	0.7415	0.6865	0.7368	0.7594
Dy	4.203	3.521	3.802	3.556	3.790	3.855
Ho	0.6911	0.5812	0.6309	0.5856	0.6373	0.6364
Er	1.722	1.428	1.551	1.475	1.564	1.646
Tm	0.2145	0.1797	0.1943	0.1822	0.1995	0.2031
Yb	1.283	1.077	1.160	1.109	1.176	1.182
Lu	0.178	0.146	0.160	0.148	0.166	0.169
Tl	0.097	0.102	0.128	0.197	0.142	0.108
Pb	3.1	2.0	6.8	2.0	4.1	2.4
Sn	1.18	1.19	1.39	0.76	1.36	1.45
Sb	0.16	0.14	0.16	0.15	0.23	0.20
Easting	330319	330319	330319	330319	330319	330319
Northing	5377910	5377910	5377910	5377910	5377910	5377910
DDH	07TH004	07TH004	07TH004	07TH004	07TH004	07TH004
Depth (m)	201	235	290	267	287	292

	Upper gabbroic unit		Lower mafic to ultramafic unit			
Sample ID	RTTC-BT-064	RTTC-BT-099	RTT-BT-102	RTT-BT-149	RTT-BT-158	RTT-BT-001
SiO_2 (wt.%)	49.44	48.70	43.85	42.74	44.72	46.12
TiO_2	1.59	1.85	2.79	2.34	2.26	1.74
Al_2O_3	17.43	16.32	8.84	4.72	7.86	7.43
Fe_2O_3	10.64	11.63	17.28	18.71	18.44	13.97
MnO	0.123	0.126	0.242	0.220	0.219	0.190
MgO	5.24	5.93	8.95	12.40	11.80	13.54
CaO	8.608	7.778	12.455	14.646	9.184	14.327
Na_2O	3.57	3.39	2.08	0.97	1.31	1.40
K2O	1.46	1.90	0.82	0.26	1.16	0.41
P_2O_5	0.226	0.224	0.245	0.091	0.230	0.119
LOI	1.32	1.71	1.65	1.03	1.77	0.50
Total	99.65	99.56	99.20	98.13	98.95	99.75
Ti (ppm)	10051	11290	16904	14267	13433	10176
Rb	45.92	67.09	21.23	6.20	34.58	11.24
Sr	1225.4	1105.5	211.9	333.1	496.0	444.0
Cs	1.118	1.080	0.841	0.929	2.364	1.234
Ba	272.2	295.2	241.3	81.2	294.8	121.5
Sc	14.4	15.8	37.2	46.1	32.0	43.5
V	155.8	182.5	447.8	406.2	290.9	255.2
Ta	1.174	1.245	1.519	0.611	1.481	0.703
Nb	18.228	20.649	23.457	9.905	22.669	10.602
Zr	192	222	217	107	208	126
Hf	4.63	5.38	5.60	3.19	5.42	3.81
Th	2.077	2.398	2.798	0.797	3.514	1.072
U	0.725	0.842	0.894	0.257	1.164	0.322
Y	14.81	15.91	19.74	12.41	18.54	12.57
La	27.50	28.87	29.57	12.90	34.29	15.84
Ce	64.68	68.58	69.12	33.36	77.06	39.42
Pr	8.780	9.329	9.523	5.083	10.338	5.975
Nd	37.26	40.10	40.39	24.16	43.56	26.79
Sm	7.095	7.438	7.972	5.342	8.335	5.656
Eu	2.3494	2.2686	2.1640	1.5690	2.2966	1.6749
Gd	5.348	5.671	6.517	4.542	6.550	4.661
Tb	0.6668	0.7115	0.8342	0.5723	0.8189	0.5898
Dy	3.446	3.707	4.386	2.954	4.267	3.052
Ho	0.5696	0.6037	0.7335	0.4927	0.7192	0.5094
Er	1.443	1.527	1.894	1.178	1.833	1.240
Tm	0.1782	0.1896	0.2465	0.1462	0.2311	0.1512
Yb	1.044	1.108	1.446	0.850	1.398	0.902
Lu	0.148	0.156	0.212	0.121	0.194	0.127
Tl	0.147	0.219	0.135	0.129	0.331	0.065
Pb	2.6	1.9	4.9	4.1	2.4	1.9
Sn	1.15	1.33	1.24	1.33	1.51	0.84
Sb	0.18	0.20	0.45	0.05	0.68	0.71
Easting	330319	330319	330445	330411	330537	330390
Northing	5377910	5377910	5378495	5378463	5378442	5378301
DDH	07TH004	07TH004	Surface	Surface	Surface	Surface
Depth (m)	300	305	-	-	-	-

	Lower mafic to ultramafic unit					
Sample ID	RTTC-BT-059	RTTC-BT-058	RTTC-BT-181	RTTC-BT-057	RTTC-BT-055	RTTC-BT-044
SiO_2 (wt.%)	47.66	47.56	47.39	47.75	48.60	47.58
TiO_2	1.39	1.38	1.38	1.12	1.40	1.34
Al_2O_3	5.83	5.26	4.78	3.45	5.40	4.91
Fe_2O_3	11.56	12.11	12.06	12.37	11.98	11.79
MnO	0.193	0.182	0.183	0.198	0.167	0.180
MgO	14.74	16.18	16.58	17.42	13.47	16.31
CaO	15.890	15.353	15.156	16.323	14.782	15.637
Na_2O	1.27	1.22	1.13	0.69	1.50	1.14
K2O	0.44	0.38	0.40	0.20	0.38	0.33
P_2O_5	0.169	0.118	0.135	0.072	0.136	0.103
LOI	0.75	0.54	0.90	0.86	1.46	0.64
Total	99.89	100.28	100.09	100.45	99.28	99.96
Ti (ppm)	8972	8649	8026	6962	8690	8252
Rb	11.82	8.66	9.72	4.84	12.62	8.76
Sr	412.7	387.0	273.6	174.5	123.3	323.5
Cs	1.702	0.948	1.172	0.740	0.728	1.166
Ba	157.6	126.9	107.9	55.1	61.2	97.5
Sc	48.8	48.7	49.1	57.0	47.7	49.0
V	195.3	185.6	187.5	195.9	189.2	170.4
Ta	0.799	0.702	0.799	0.419	1.015	0.695
Nb	12.964	11.190	12.423	6.536	16.614	10.810
Zr	116	109	118	79	147	101
Hf	3.08	3.02	3.24	2.35	3.88	2.78
Th	1.135	0.972	1.151	0.629	1.651	0.973
U	0.353	0.301	0.371	0.203	0.609	0.305
Y	12.94	11.91	11.64	9.68	15.28	11.14
La	18.05	15.10	16.13	9.63	23.45	13.85
Ce	43.41	36.83	38.27	24.63	56.09	33.18
Pr	6.121	5.256	5.547	3.803	7.897	4.800
Nd	26.37	23.75	24.22	17.76	34.01	21.50
Sm	5.456	5.112	5.047	4.063	6.797	4.641
Eu	1.6042	1.5192	1.4685	1.2045	1.7742	1.3686
Gd	4.468	4.189	4.166	3.501	5.336	3.948
Tb	0.5722	0.5364	0.5221	0.4462	0.6793	0.4976
Dy	2.971	2.826	2.734	2.290	3.524	2.626
Ho	0.5025	0.4612	0.4648	0.3854	0.5878	0.4383
Er	1.201	1.147	1.137	0.920	1.444	1.069
Tm	0.1546	0.1424	0.1427	0.1144	0.1813	0.1333
Yb	0.893	0.836	0.832	0.675	1.084	0.789
Lu	0.125	0.116	0.118	0.095	0.146	0.111
Tl	0.061	0.029	0.060	0.080	0.058	0.043
Pb	8.6	4.6	1.3	1.3	2.8	1.7
Sn	0.80	0.67	0.70	0.30	1.57	0.68
Sb	0.06	<0.04	0.12	0.04	0.30	0.04
Easting	330435	330435	330435	330435	330435	330435
Northing	5378298	5378298	5378298	5378298	5378298	5378298
DDH	05TH002	05TH002	05TH002	05TH002	05TH002	05TH003
Depth (m)	54	65	87	98	104	72

	Lower mafic to ultramafic unit					
Sample ID	RTTC-BT-170	RTTC-BT-171	RTTC-BT-039	RTTC-BT-037	RTTC-BT-172	RTTC-BT-233
SiO_2 (wt.%)	47.79	47.71	46.20	46.91	46.62	37.73
TiO_2	1.32	1.19	1.38	1.86	1.75	1.46
Al_2O_3	4.47	3.88	4.61	6.52	6.36	5.64
Fe_2O_3	11.65	11.03	13.20	14.46	14.97	25.06
MnO	0.177	0.171	0.212	0.206	0.280	0.394
MgO	16.76	17.15	16.22	13.61	12.49	10.00
CaO	15.900	16.433	14.839	13.719	12.729	11.278
Na_2O	1.00	0.82	0.90	1.82	1.57	1.10
K2O	0.40	0.26	0.51	0.44	0.52	0.50
P_2O_5	0.116	0.098	0.108	0.174	0.209	0.149
LOI	0.79	0.89	1.29	0.32	1.87	4.11
Total	100.37	99.63	99.47	100.04	99.37	97.42
Ti (ppm)	8207	7324	8279	12311	10942	9069
Rb	10.72	6.56	12.67	10.84	14.77	15.96
Sr	264.5	274.7	250.0	621.8	324.5	222.8
Cs	1.080	1.144	1.262	2.369	1.020	1.263
Ba	98.4	96.4	140.2	179.9	126.8	150.1
Sc	51.1	53.6	49.0	46.3	39.6	23.2
V	176.3	162.6	204.6	262.5	226.5	249.3
Ta	0.741	0.527	0.609	1.184	1.266	0.954
Nb	11.576	8.286	9.127	18.372	19.763	12.410
Zr	112	91	101	162	176	157
Hf	3.05	2.57	2.87	4.31	4.47	4.08
Th	1.105	0.764	0.857	1.734	2.716	2.566
U	0.353	0.254	0.294	0.537	1.198	0.913
Y	11.59	10.20	10.69	15.73	17.98	23.05
La	15.09	11.87	13.07	24.87	30.11	23.16
Ce	36.14	29.98	32.13	59.17	67.23	54.23
Pr	5.183	4.373	4.767	8.390	8.949	7.574
Nd	23.36	20.18	21.31	36.00	37.29	32.94
Sm	4.933	4.376	4.570	7.377	7.339	7.153
Eu	1.4064	1.2894	1.3679	2.2118	2.0541	1.9850
Gd	4.114	3.636	3.792	5.876	5.798	6.057
Tb	0.5228	0.4674	0.4835	0.7485	0.7456	0.8259
Dy	2.701	2.372	2.450	3.777	3.858	4.597
Ho	0.4447	0.3970	0.4085	0.6299	0.6674	0.8137
Er	1.107	0.964	1.023	1.548	1.691	2.067
Tm	0.1375	0.1182	0.1232	0.1921	0.2123	0.2711
Yb	0.818	0.703	0.757	1.109	1.245	1.621
Lu	0.112	0.098	0.103	0.152	0.176	0.228
Tl	0.063	0.118	0.077	0.076	0.985	1.277
Pb	1.4	1.6	6.0	2.4	3.4	189.7
Sn	0.68	0.56	0.63	0.84	1.56	1.51
Sb	0.09	<0.04	0.07	0.05	0.40	0.70
Easting	330435	330435	330435	330435	330435	330435
Northing	5378298	5378298	5378268	5378298	5378298	5378268
DDH	05TH003	05TH003	05TH003	05TH003	05TH003	05TH003
Depth (m)	167	206	226	242	287	297

	Lower mafic to ultramafic unit					
Sample ID	RTTC-BT-234	RTTC-BT-063	RTTC-BT-098	RTTC-BT-097	RTTC-BT-096	RTTC-BT-095
SiO_2 (wt.%)	33.58	45.52	47.58	41.27	46.98	47.60
TiO_2	2.30	1.90	1.39	2.97	1.29	1.36
Al_2O_3	4.23	3.07	6.88	6.55	6.25	5.92
Fe_2O_3	32.50	16.99	14.05	23.50	13.20	11.46
MnO	0.232	0.231	0.196	0.296	0.188	0.170
MgO	10.78	15.28	14.37	13.08	15.92	14.70
CaO	9.617	14.936	13.652	7.784	13.685	15.425
Na_2O	0.87	0.48	1.32	1.54	1.21	1.29
K2O	0.50	0.15	0.42	0.65	0.39	0.43
P_2O_5	0.095	0.080	0.073	0.714	0.114	0.110
LOI	3.05	0.82	0.36	0.80	0.41	1.15
Total	97.75	99.46	100.29	99.15	99.64	99.62
Ti (ppm)	14762	11725	8274	17602	7902	8255
Rb	14.33	5.66	13.07	18.82	10.22	10.20
Sr	216.3	116.9	455.1	455.7	427.5	404.9
Cs	1.174	1.200	0.972	2.048	0.879	1.155
Ba	92.9	39.0	107.7	231.1	119.1	128.3
Sc	28.1	51.9	40.9	22.3	41.5	44.6
V	483.0	374.5	235.8	416.3	190.2	177.3
Ta	0.707	0.454	0.423	1.612	0.611	0.638
Nb	7.684	6.947	6.225	23.940	9.196	9.975
Zr	118	101	90	217	107	99
Hf	3.28	3.03	2.73	5.44	3.00	2.78
Th	1.176	0.751	0.691	2.272	0.942	0.880
U	0.428	0.254	0.236	0.796	0.304	0.276
Y	11.23	13.75	11.11	21.78	10.86	11.26
La	13.41	10.99	10.62	45.74	14.55	13.19
Ce	32.37	30.68	28.36	109.88	36.28	33.05
Pr	4.801	4.966	4.421	15.230	5.335	4.905
Nd	22.02	24.50	20.95	64.22	23.72	21.99
Sm	4.675	5.691	4.813	11.620	4.801	4.753
Eu	1.3516	1.4408	1.5122	2.9049	1.4617	1.4461
Gd	3.712	4.907	4.054	8.935	4.055	3.931
Tb	0.4851	0.6235	0.5272	1.0392	0.5032	0.5063
Dy	2.537	3.306	2.704	5.123	2.607	2.700
Ho	0.4277	0.5400	0.4458	0.8302	0.4333	0.4502
Er	1.049	1.320	1.102	2.050	1.039	1.103
Tm	0.1320	0.1641	0.1336	0.2459	0.1314	0.1379
Yb	0.778	0.951	0.786	1.413	0.751	0.822
Lu	0.110	0.135	0.112	0.198	0.107	0.117
Tl	0.673	0.043	0.031	0.059	0.067	0.212
Pb	11.7	<0.6	1.2	4.4	1.4	3.2
Sn	0.92	0.71	0.64	1.37	0.80	0.71
Sb	0.32	0.25	<0.04	0.16	0.04	0.04
Easting	330435	330319	330319	330319	330319	330319
Northing	5378268	5377910	5377910	5377910	5377910	5377910
DDH	05TH003	07TH004	07TH004	07TH004	07TH004	07TH004
Depth (m)	297	306	318	323	356	376

	Lower mafic to ultramafic unit					
Sample ID	RTTC-BT-094	RTTC-BT-093	RTTC-BT-092	RTTC-BT-091	RTTC-BT-229	RTTC-BT-089
SiO_2 (wt.%)	47.22	41.82	47.96	44.98	44.72	44.76
TiO_2	1.97	1.06	1.73	2.16	1.96	2.14
Al_2O_3	6.31	3.57	5.06	6.84	7.66	6.97
Fe_2O_3	13.88	19.80	15.13	16.23	16.48	17.15
MnO	0.199	0.240	0.199	0.226	0.210	0.218
MgO	13.14	21.28	13.94	15.69	13.93	13.97
CaO	13.611	7.561	12.063	9.151	8.922	9.851
Na_2O	1.63	0.63	1.27	1.88	2.26	1.82
K2O	0.66	0.33	0.69	0.76	0.85	0.80
P_2O_5	0.211	0.102	0.169	0.253	0.277	0.234
LOI	0.81	3.70	1.31	1.43	1.37	1.38
Total	99.64	100.09	99.52	99.60	98.64	99.29
Ti (ppm)	12054	6516	10857	13321	11611	12867
Rb	17.39	10.02	20.54	19.01	21.51	19.83
Sr	514.7	224.4	392.9	653.9	656.6	604.6
Cs	1.145	2.167	1.130	1.747	1.552	1.296
Ba	176.4	91.0	183.2	247.9	333.2	231.1
Sc	41.3	25.5	38.1	26.9	26.8	29.7
V	234.5	135.3	215.6	238.0	224.4	239.0
Ta	1.110	0.639	1.332	1.722	1.773	1.564
Nb	17.861	9.962	20.793	27.368	27.003	25.652
Zr	156	92	180	237	257	236
Hf	4.21	2.45	4.66	5.94	6.34	5.95
Th	1.527	1.082	2.181	2.853	3.162	2.951
U	0.490	0.341	0.752	0.921	1.058	0.937
Y	16.08	8.41	14.87	17.51	19.87	17.64
La	24.07	13.47	25.77	35.98	42.11	34.48
Ce	59.04	32.03	60.77	83.59	95.98	79.47
Pr	8.431	4.474	8.402	11.187	12.865	10.637
Nd	37.61	19.21	36.44	46.45	52.72	44.12
Sm	7.519	3.867	7.052	8.742	9.714	8.461
Eu	2.1514	1.1130	1.9538	2.4458	2.7281	2.3614
Gd	5.999	3.007	5.484	6.413	7.450	6.564
Tb	0.7470	0.3841	0.6935	0.8318	0.9297	0.8036
Dy	3.879	2.006	3.544	4.218	4.618	4.156
Ho	0.6294	0.3306	0.5752	0.6872	0.7691	0.6856
Er	1.540	0.825	1.407	1.690	1.863	1.668
Tm	0.1968	0.1042	0.1779	0.2144	0.2332	0.2097
Yb	1.125	0.602	1.018	1.235	1.365	1.237
Lu	0.157	0.088	0.144	0.171	0.184	0.169
Tl	0.058	0.037	0.232	0.111	0.168	0.206
Pb	2.0	1.2	6.4	10.3	7.2	4.6
Sn	0.84	0.37	1.97	1.27	1.56	1.24
Sb	0.04	0.05	0.25	0.13	0.11	0.09
Easting	330319	330319	330319	330319	330319	330319
Northing	5377910	5377910	5377910	5377910	5377910	5377910
DDH	07TH004	07TH004	07TH004	07TH004	07TH004	07TH004
Depth (m)	404	410	426	432	434	437

	Mafic to intermediate metavolcanic rocks					
Sample ID	RTTC-BT-230	RTTC-BT-231	RTTC-BT-088	RTTC-BT-087	RTTC-BT-086	RTTC-BT-085
SiO_2 (wt.%)	58.12	58.15	57.10	59.71	63.88	61.82
TiO_2	0.69	0.59	0.74	0.69	0.65	0.62
Al_2O_3	14.58	13.68	13.56	12.96	13.67	13.12
Fe_2O_3	7.92	7.48	8.24	3.57	6.36	6.53
MnO	0.105	0.119	0.110	0.080	0.048	0.070
MgO	5.28	4.94	6.51	5.79	3.90	4.97
CaO	5.076	6.570	3.845	8.104	1.632	2.261
Na_2O	5.02	3.66	3.67	6.03	4.65	3.88
K2O	1.53	2.78	1.73	1.50	1.66	1.70
P_2O_5	0.218	0.193	0.262	0.099	0.203	0.202
LOI	0.99	1.51	3.04	1.28	2.94	3.76
Total	99.53	99.67	98.81	99.81	99.59	98.93
Ti (ppm)	4420	3694	4565	4273	4046	3846
Rb	43.49	75.41	57.15	41.34	44.67	48.31
Sr	616.5	450.5	307.9	157.7	204.4	238.3
Cs	1.631	1.215	2.183	0.080	0.674	1.443
Ba	665.8	735.8	405.9	150.5	282.6	329.4
Sc	17.2	17.3	21.6	20.7	14.9	16.5
V	134.1	125.1	148.1	131.4	121.4	117.7
Ta	0.437	0.359	0.360	0.373	0.379	0.298
Nb	6.526	5.109	5.930	6.408	5.866	4.826
Zr	179	155	165	159	161	131
Hf	4.40	3.91	4.25	4.02	4.02	3.29
Th	7.570	6.855	7.217	6.589	6.794	4.324
U	1.953	1.741	1.868	1.618	1.708	1.255
Y	16.54	15.44	18.16	17.31	15.07	11.77
La	38.24	34.38	36.72	24.19	49.74	36.78
Ce	81.20	71.95	80.64	58.19	97.88	69.56
Pr	10.131	8.828	10.031	7.727	11.490	7.939
Nd	39.95	33.92	39.47	31.26	41.98	30.08
Sm	7.086	6.018	7.021	6.046	6.551	4.666
Eu	1.6777	1.4647	1.5398	1.5554	1.7560	1.0399
Gd	4.987	4.367	5.276	4.914	4.591	3.272
Tb	0.6100	0.5489	0.6634	0.6278	0.5633	0.4146
Dy	3.200	2.925	3.540	3.354	2.998	2.208
Ho	0.5714	0.5303	0.6403	0.6005	0.5295	0.4087
Er	1.566	1.432	1.781	1.663	1.444	1.133
Tm	0.2154	0.2009	0.2421	0.2287	0.2045	0.1628
Yb	1.382	1.283	1.553	1.449	1.335	1.038
Lu	0.205	0.194	0.235	0.213	0.197	0.166
Tl	0.326	0.344	0.203	0.091	0.139	0.139
Pb	11.4	10.8	3.0	0.8	2.1	1.5
Sn	1.44	1.27	0.84	2.18	1.00	1.04
Sb	0.55	0.86	0.60	0.37	0.36	0.34
Easting	330319	330319	330319	330319	330319	330319
Northing	5377910	5377910	5377910	5377910	5377910	5377910
DDH	07TH004	07TH004	07TH004	07TH004	07TH004	07TH004
Depth (m)	437	440	450	452	479	493

	Mafic to intermediate metavolcanic rocks					
Sample ID	RTTC-BT-083	RTTC-BT-084	RTTC-BT-053	RTTC-BT-050	RTTC-BT-052	RTTC-BT-185
SiO_2 (wt.%)	59.81	58.49	50.59	47.19	54.71	48.60
TiO_2	0.48	0.66	0.95	1.11	1.17	0.98
Al_2O_3	18.11	15.97	15.66	14.74	16.22	14.36
Fe_2O_3	4.18	7.06	9.55	5.36	6.09	5.21
MnO	0.026	0.050	0.185	0.107	0.146	0.099
MgO	1.84	3.21	6.25	5.08	7.46	5.50
CaO	1.465	2.022	9.567	20.298	4.866	20.541
Na_2O	4.56	4.65	3.25	2.28	6.18	2.01
K2O	7.43	4.85	1.64	0.17	0.61	0.10
P_2O_5	0.201	0.232	0.092	0.029	0.112	0.149
LOI	1.56	1.88	2.04	3.89	2.49	2.78
Total	99.66	99.07	99.77	100.25	100.05	100.33
Ti (ppm)	2892	4024	5959	6594	7305	6023
Rb	184.64	128.16	57.40	3.02	17.86	1.14
Sr	228.8	216.6	220.1	513.9	278.6	58.5
Cs	0.728	0.580	2.540	0.040	0.674	0.054
Ba	991.4	761.0	276.0	18.5	152.1	10.2
Sc	10.2	15.2	45.6	38.5	48.4	38.6
V	86.1	125.6	276.2	213.9	315.9	240.3
Ta	0.214	0.335	0.255	0.302	0.318	0.281
Nb	3.295	5.469	4.025	6.837	4.855	6.011
Zr	112	155	90	101	115	96
Hf	2.91	3.85	2.49	2.81	3.15	2.66
Th	2.693	5.911	0.491	0.915	0.615	0.631
U	0.928	1.803	0.145	1.367	0.626	1.698
Y	9.51	14.28	29.47	31.03	29.58	28.14
La	22.56	40.43	5.87	26.02	8.78	34.12
Ce	45.61	78.81	15.26	58.58	20.52	73.83
Pr	5.493	9.254	2.396	7.278	2.838	8.145
Nd	21.40	35.16	11.94	27.63	13.00	28.04
Sm	3.656	5.751	3.623	5.542	3.842	4.810
Eu	1.3096	1.6038	1.1162	1.7248	1.0809	1.8855
Gd	2.677	4.058	4.577	5.649	4.699	4.687
Tb	0.3336	0.5116	0.7808	0.8906	0.8074	0.7672
Dy	1.848	2.713	5.224	5.690	5.353	4.949
Ho	0.3434	0.4969	1.0976	1.1240	1.0883	1.0186
Er	0.976	1.394	3.313	3.327	3.285	2.973
Tm	0.1323	0.1939	0.4848	0.4766	0.4718	0.4389
Yb	0.873	1.251	3.222	3.070	3.071	2.982
Lu	0.132	0.187	0.479	0.443	0.452	0.449
Tl	0.496	0.383	0.177	0.011	0.063	0.021
Pb	1.6	1.7	1.4	1.0	0.9	2.2
Sn	0.97	1.19	1.02	2.40	0.95	2.92
Sb	0.36	0.53	1.20	1.32	0.70	0.60
Easting	330319	330319	330435	330435	330435	330435
Northing	5377910	5377910	5378298	5378298	5378298	5378298
DDH	07TH004	07TH004	05TH002	05TH002	05TH002	05TH002
Depth (m)	516	516	111	122	134	139

	Mafic to intermediate metavolcanic rocks					
Sample ID	RTTC-BT-049	RTTC-BT-048	RTTC-BT-186	RTTC-BT-187	RTTC-BT-046	RTTC-BT-189
SiO_2 (wt.%)	49.33	55.41	68.42	56.62	50.73	60.02
TiO_2	1.23	0.44	0.36	0.38	1.05	0.43
Al_2O_3	13.49	11.12	11.21	11.56	15.49	14.70
Fe_2O_3	8.90	16.69	8.42	11.18	13.23	5.20
MnO	0.132	0.082	0.022	0.013	0.173	0.073
MgO	6.65	3.51	1.75	1.26	5.53	4.35
CaO	13.192	2.383	0.495	0.696	3.484	3.676
Na_2O	3.67	2.90	2.40	2.35	3.70	3.78
K2O	0.36	0.78	2.16	4.00	3.06	2.03
P_2O_5	0.284	0.125	0.095	0.111	0.099	0.163
LOI	2.58	5.14	3.99	11.08	3.44	4.53
Total	99.82	98.58	99.32	99.25	99.99	98.95
Ti (ppm)	7682	2830	2110	2494	6494	2609
Rb	6.90	20.43	89.46	105.30	91.13	68.26
Sr	106.7	125.1	84.7	161.1	174.1	439.8
Cs	0.078	0.769	2.236	1.748	0.655	2.517
Ba	75.4	175.0	168.7	812.4	644.3	629.1
Sc	43.0	11.8	6.5	11.7	43.6	11.3
V	343.0	72.6	44.7	67.3	274.1	88.1
Ta	0.340	0.389	0.416	0.491	0.283	0.241
Nb	5.917	6.049	6.103	6.835	4.488	3.632
Zr	126	135	145	145	102	109
Hf	3.46	3.38	3.64	3.68	2.77	2.87
Th	0.629	2.584	2.710	5.775	0.557	2.678
U	2.461	1.632	0.888	1.719	0.160	0.777
Y	35.21	15.83	12.00	15.90	28.94	11.14
La	31.83	13.82	14.82	20.91	6.29	19.36
Ce	67.33	27.10	30.53	46.57	14.84	40.83
Pr	7.096	3.055	3.741	5.836	2.359	5.071
Nd	23.88	11.98	14.89	22.60	12.14	19.76
Sm	4.723	2.514	2.634	3.837	3.859	3.495
Eu	2.2340	0.9793	0.4805	0.7655	1.2454	1.0096
Gd	5.298	2.529	2.121	2.979	4.602	2.617
Tb	0.8883	0.3938	0.3023	0.4246	0.8041	0.3521
Dy	5.939	2.563	1.938	2.726	5.336	1.961
Ho	1.2498	0.5371	0.4155	0.5615	1.1051	0.3784
Er	3.800	1.664	1.283	1.703	3.301	1.058
Tm	0.5612	0.2501	0.1934	0.2551	0.4759	0.1493
Yb	3.713	1.700	1.289	1.742	3.104	0.987
Lu	0.561	0.259	0.200	0.274	0.464	0.151
Tl	0.077	0.093	0.572	0.971	0.206	0.277
Pb	11.0	9.9	5.7	22.1	2.2	3.8
Sn	6.18	1.36	0.43	0.55	1.09	0.67
Sb	1.17	0.34	0.38	3.77	0.90	0.27
Easting	330435	330435	330435	330435	330435	330435
Northing	5378298	5378298	5378298	5378298	5378298	5378298
DDH	05TH002	05TH002	05TH002	05TH002	05TH002	05TH002
Depth (m)	147	155	159	169	194	258

	Mafic to intermediate metavolcanic rocks					
Sample ID	RTTC-BT-235	RTTC-BT-178	RTTC-BT-031	RTTC-BT-033	RTTC-BT-026	RTT-BT-016
SiO_2 (wt.%)	46.68	46.64	50.79	67.12	48.29	50.44
TiO_2	1.45	1.55	1.71	0.45	1.40	0.99
Al_2O_3	13.71	14.24	14.52	15.49	12.26	13.22
Fe_2O_3	18.78	16.89	14.48	3.30	9.00	12.88
MnO	0.214	0.224	0.196	0.044	0.121	0.249
MgO	8.13	8.99	2.89	1.74	6.66	4.94
CaO	6.087	7.551	8.362	2.538	11.484	10.308
Na_2O	2.81	1.51	4.48	5.61	4.64	4.00
K2O	0.44	0.40	0.49	1.69	0.17	0.30
P_2O_5	0.163	0.167	0.169	0.111	0.175	0.098
LOI	1.33	1.46	1.44	1.71	3.55	1.66
Total	99.79	99.62	99.53	99.80	97.75	99.09
Ti (ppm)	9327	9752	10987	2849	8894	
Rb	10.50	16.95	17.01	44.31	3.65	6.76
Sr	156.2	152.7	190.0	354.0	127.6	262.9
Cs	2.065	2.625	1.680	0.703	0.070	0.698
Ba	59.6	73.0	90.3	349.2	10.8	131.6
Sc	31.0	36.2	37.7	7.5	42.1	38.8
V	245.1	278.5	286.3	61.2	293.1	264.4
Ta	0.432	0.353	0.370	0.178	0.330	0.262
Nb	6.667	5.438	5.758	2.295	5.150	4.310
Zr	110	121	127	103	130	97
Hf	2.94	3.23	3.40	2.53	3.43	2.66
Th	0.713	0.638	0.660	1.272	0.648	0.538
U	0.285	0.177	0.188	0.363	1.581	0.153
Y	31.93	39.17	33.81	8.31	38.51	30.16
La	9.13	8.33	6.94	8.87	25.64	6.65
Ce	22.44	20.87	18.65	18.97	48.84	16.88
Pr	3.272	3.155	2.961	2.381	5.031	2.574
Nd	15.58	15.80	14.71	9.51	17.98	12.52
Sm	4.198	4.653	4.442	1.906	4.426	3.688
Eu	1.3640	1.5779	1.5527	0.6457	2.2737	1.3055
Gd	4.986	5.886	5.392	1.752	5.664	4.644
Tb	0.8180	0.9899	0.9035	0.2438	0.9691	0.7900
Dy	5.449	6.549	6.005	1.443	6.548	5.336
Ho	1.1313	1.3626	1.2424	0.2747	1.3798	1.0934
Er	3.367	4.096	3.757	0.811	4.083	3.244
Tm	0.4888	0.5980	0.5542	0.1113	0.6012	0.4785
Yb	3.239	3.928	3.595	0.722	3.913	3.106
Lu	0.501	0.602	0.547	0.107	0.586	0.464
Tl	0.564	0.257	0.076	0.129	0.034	0.055
Pb	12.5	3.2	6.0	1.0	1.4	0.9
Sn	1.76	1.37	1.14	0.53	4.27	1.26
Sb	0.28	0.40	0.83	0.28	0.58	0.38
Easting	330435	330435	330435	330435	330435	330834
Northing	5378268	5378298	5378298	5378298	5378298	5378246
DDH	05TH003	05TH003	05TH003	05TH003	05TH003	Surface
Depth (m)	298	300	306	315	330	-

	Mafic to intermediate metavolcanic rocks					
Sample ID	RTT-BT-036	RTT-BT-037	RTT-BT-053	RTT-BT-103	RTT-BT-104	RTT-BT-140
SiO_2 (wt.%)	49.64	49.90	52.86	49.01	49.54	58.76
TiO_2	2.15	0.94	1.61	0.60	0.54	0.69
Al_2O_3	13.54	13.08	11.85	17.51	17.79	14.97
Fe_2O_3	15.05	11.96	13.31	8.37	9.26	6.76
MnO	0.215	0.187	0.226	0.219	0.114	0.148
MgO	5.12	8.20	5.67	6.22	8.05	6.32
CaO	6.574	8.197	6.357	7.906	5.053	2.384
Na_2O	4.22	2.05	4.92	2.51	3.02	3.83
K2O	0.57	2.44	0.22	4.21	4.22	1.96
P_2O_5	0.232	0.084	0.189	0.336	0.243	0.223
LOI	2.34	2.41	2.11	2.53	1.25	3.24
Total	99.65	99.45	99.32	99.42	99.08	99.29
Ti (ppm)	12856	5781	10042	3726	3369	
Rb	12.13	38.30	4.55	140.00	92.68	45.22
Sr	221.5	359.1	131.0	1125.3	638.6	303.2
Cs	1.765	0.409	0.281	6.793	3.191	1.562
Ba	114.9	335.8	48.2	1124.3	964.4	459.4
Sc	35.1	35.7	41.4	23.7	22.1	15.5
V	276.7	247.3	366.0	219.0	165.4	129.4
Ta	0.375	0.188	0.395	0.083	0.168	0.429
Nb	5.805	2.903	6.305	1.534	2.714	6.784
Zr	123	66	144	38	64	208
Hf	3.31	1.82	3.86	1.00	1.69	5.15
Th	0.622	0.361	0.740	1.045	1.084	9.614
U	0.177	0.103	0.210	0.328	0.333	2.424
Y	37.20	16.25	43.90	7.59	13.78	15.60
La	8.30	4.71	6.45	10.18	9.15	37.75
Ce	21.07	12.01	18.10	22.53	19.95	84.26
Pr	3.221	1.842	2.825	3.008	2.710	10.392
Nd	15.91	8.85	14.55	13.06	12.37	39.60
Sm	4.691	2.520	4.544	2.630	2.783	6.751
Eu	1.5499	0.8162	1.4625	0.8458	0.8987	1.4174
Gd	5.953	2.955	6.214	1.997	2.653	4.761
Tb	0.9817	0.4873	1.0820	0.2578	0.3897	0.5852
Dy	6.502	3.047	7.303	1.441	2.426	3.078
Ho	1.3246	0.6054	1.5476	0.2643	0.4914	0.5450
Er	3.962	1.770	4.726	0.760	1.441	1.508
Tm	0.5862	0.2478	0.6948	0.1089	0.2159	0.2147
Yb	3.789	1.603	4.527	0.732	1.412	1.410
Lu	0.577	0.241	0.703	0.115	0.217	0.211
Tl	0.046	0.158	0.012	0.469	0.389	0.240
Pb	0.7	1.0	<0.6	5.9	3.9	2.2
Sn	0.92	0.71	1.28	0.47	0.68	1.16
Sb	0.09	0.11	0.16	0.54	0.89	0.29
Easting	330761	330759	330954	330464	330443	330570
Northing	5378008	5378055	5377882	5378495	5378503	5377743
DDH	Surface	Surface	Surface	Surface	Surface	Surface
Depth (m)	-	-	-	-	-	-

APPENDIX E

Whole rock geochemistry (metals)

UTM datum NAD83 Zone 16

Sample ID	Easting	Northing	DDH	Depth (m)	Ti ppm	Cr ppm	Co ppm	Ni ppm	V ppm	Cu ppm	Zn ppm	Mo ppm	Au ppb	Ir ppb	Pd ppb	Pt ppb	Rh ppb	Ru ppb
Eastern N-trending gabbroic dike																		
RTT-BT-055	331003	5377824	surface	-	9133.00	130.00	58.85	91.70	275.00	45.40	101.00	1.20	0.42	0.01	<0.12	<0.17	<0.02	<0.08
RTT-BT-180	330822	5384202	surface	-	8587.00	130.00	64.73	104.70	262.40	48.30	102.00	1.10	<0.4	0.01	0.42	0.50	<0.04	<0.08
RTT-BT-190	330803	5378724	surface	-	8350.00	184.00	64.68	97.40	277.70	43.60	101.00	0.95	<0.4	0.01	0.24	0.29	<0.04	<0.08
RTT-BT-215	330593	5391886	surface	-	8640.00	128.00	60.06	86.10	294.80	42.80	101.00	0.95	<0.4	0.01	<0.12	<0.17	<0.04	<0.08
RTT-BT-216	330587	5391889	surface	-	10278.00	124.00	59.09	85.10	304.30	49.70	119.00	1.22	<0.4	0.01	0.15	0.17	<0.04	<0.08
RTT-BT-222	331388	5375988	surface	-	8647.00	115.00	56.45	81.80	271.40	35.10	62.00	0.96	<0.4	0.01	0.14	<0.17	<0.04	<0.08
Western N-trending gabbroic dike																		
RTT-BT-220	328598	5386506	surface	-	12827.00	133.00	55.12	76.60	317.80	47.10	28.00	1.04	0.96	0.01	0.12	<0.17	<0.04	<0.08
RTT-BT-232	326984	5400588	surface	-	13036.00	67.00	37.81	32.10	264.60	29.20	116.00	1.47	0.40	0.05	0.16	<0.17	0.05	<0.08
RTT-BT-235	326997	5401169	surface	-	11764.00	111.00	47.88	59.80	262.90	39.60	118.00	1.57	<0.4	0.02	0.12	<0.17	<0.04	<0.08
RTT-BT-236	327028	5401620	surface	-	13570.00	146.00	54.87	66.80	409.25	54.30	119.00	1.20	<0.4	0.01	<0.12	<0.17	<0.04	<0.08
RTT-BT-237	327159	5402611	surface	-	19593.00	78.00	57.00	41.90	377.21	33.50	122.00	2.18	<0.4	0.01	<0.12	<0.17	<0.04	<0.08
Cross-cutting mafic dikes																		
RTTC-BT-219	330161	5378268	07TH007	42.56	13621.00	129.00	50.46	58.30	285.70	84.70	109.00	0.94	0.43	0.02	0.16	<0.17	<0.04	<0.08
RTTC-BT-210	330161	5378268	07TH007	312.00	5717.00	137.00	53.26	108.50	294.00	153.40	64.00	0.68	3.25	0.07	16.30	6.07	0.66	0.44
RTTC-BT-101	330435	5378298	05TH002	219.68	13899.00	147.00	51.93	61.20	301.00	78.00	47.00	1.58	0.24	0.01	<0.12	0.25	0.04	<0.08
RTTC-BT-045	330435	5378298	05TH003	63.00	14195.00	141.00	51.53	59.60	310.40	91.00	131.00	1.67	0.57	0.01	0.12	0.29	0.03	<0.08
RTTC-BT-038	330435	5378298	05TH003	240.00	6065.00	150.00	52.45	103.10	283.00	162.60	84.00	1.47	3.80	0.06	16.00	6.59	0.68	0.38
Iron formation																		
RTTC-BT-006	329809	5377560	05TH001	111.00	318.00	8.00	109.46	143.90	197.20	601.60	17.00	0.47	3.97	0.01	0.15	<0.17	<0.04	<0.08
RTTC-BT-005	329809	5377560	05TH001	112.48	241.00	3.00	135.22	88.10	112.90	955.50	22.00	0.39	5.60	0.01	0.23	<0.17	0.26	<0.08
Pegmatitic gabbro																		
RTTC-BT-216	330161	5378268	07TH007	53.30	20568.00	100.00	30.97	76.10	274.50	26.90	34.00	0.82	<0.4	0.13	2.77	2.33	0.27	0.11
RTTC-BT-217	330161	5378268	07TH007	71.14	19177.00	91.00	39.05	90.10	361.60	29.10	68.00	0.98	1.17	0.11	15.40	8.50	0.52	0.12
RTT-BT-130	329929	5378222	surface	-	24629.00	51.00	50.75	101.30	564.94	37.10	59.00	0.98	1.40	0.07	14.50	3.53	0.60	<0.08
RTTC-BT-062	330319	5377910	07TH004	311.00	19978.00	61.00	35.37	53.50	201.20	87.00	50.00	1.05	3.12	0.22	10.90	9.51	0.33	0.09
Upper gabbroic unit																		
RTT-BT-074	330576	5377761	surface	-	12873.00	67.00	46.26	68.70	216.60	172.60	118.00	1.32	3.41	0.26	17.00	19.70	0.57	0.09
RTT-BT-142	330569	5377749	surface	-	12150.00	164.00	53.19	144.70	251.50	213.80	72.00	1.58	4.67	0.60	60.40	10.90	0.76	0.11
RTTC-BT-082	330319	5377910	07TH004	9.29	14678.00	8.00	22.92	9.70	101.90	288.30	51.00	2.05	3.67	0.01	0.76	0.23	<0.02	<0.08
RTTC-BT-081	330319	5377910	07TH004	10.00	20606.00	9.00	25.84	17.60	154.70	523.20	54.00	2.03	11.10	0.01	2.26	0.27	0.02	<0.08
RTTC-BT-080	330319	5377910	07TH004	20.18	27406.52	9.00	54.92	19.70	262.40	347.10	78.00	1.43	13.90	0.01	28.40	9.11	0.07	<0.08
RTTC-BT-079	330319	5377910	07TH004	57.63	26854.16	11.00	35.76	24.30	293.10	387.00	46.00	1.32	11.80	0.01	8.20	3.93	0.04	<0.08
RTTC-BT-077	330319	5377910	07TH004	83.78	32198.62	13.00	56.82	34.70	424.09	256.40	97.00	1.49	26.80	0.02	54.30	17.60	0.13	<0.08
RTTC-BT-078	330319	5377910	07TH004	86.13	30799.17	12.00	67.91	37.70	400.63	356.40	100.00	1.82	30.80	0.02	57.60	34.80	0.11	<0.08
RTTC-BT-076	330319	5377910	07TH004	101.18	30587.36	12.00	60.38	35.90	418.06	326.00	179.00	1.69	43.00	0.01	49.60	19.70	0.15	<0.08
RTTC-BT-075	330319	5377910	07TH004	144.98	29751.53	16.00	51.58	39.10	431.42	124.50	66.00	1.39	4.09	0.04	39.00	8.70	0.11	<0.08
RTTC-BT-073	330319	5377910	07TH004	180.52	25743.31	42.00	96.68	424.60	489.18	268.30	75.00	0.74	5.01	0.06	13.30	6.37	0.08	<0.08
RTTC-BT-074	330319	5377910	07TH004	182.00	30111.26	82.00	71.95	59.20	676.26	142.60	120.00	1.29	5.07	0.13	32.70	9.14	0.20	<0.08

Sample ID	Easting	Northing	DDH	Depth (m)	Ti ppm	Cr ppm	Co ppm	Ni ppm	V ppm	Cu ppm	Zn ppm	Mo ppm	Au ppb	Ir ppb	Pd ppb	Pt ppb	Rh ppb	Ru ppb
Upper gabbroic unit																		
RTTC-BT-072	330319	5377910	07TH004	188.00	31197.01	18.00	35.28	46.90	439.75	70.00	49.00	0.80	1.65	0.02	22.00	7.04	0.12	<0.08
RTTC-BT-071	330319	5377910	07TH004	190.20	31721.73	17.00	52.80	45.30	490.55	78.00	60.00	1.25	2.19	0.02	19.00	7.33	0.14	<0.08
RTTC-BT-070	330319	5377910	07TH004	201.05	27289.99	21.00	59.04	60.20	585.84	75.50	85.00	1.57	3.05	0.02	20.80	4.90	0.22	<0.08
RTTC-BT-069	330319	5377910	07TH004	234.74	21850.00	33.00	66.43	79.40	633.33	125.60	132.00	1.14	4.21	0.05	30.70	5.27	0.42	<0.08
RTTC-BT-068	330319	5377910	07TH004	290.00	14356.00	75.00	55.51	81.10	304.10	131.30	104.00	1.43	4.31	0.25	22.50	14.50	0.61	0.19
RTTC-BT-067	330319	5377910	07TH004	266.60	18994.00	62.00	63.56	103.80	528.45	85.70	100.00	1.15	3.25	0.16	25.50	10.10	0.79	0.14
RTTC-BT-065	330319	5377910	07TH004	287.00	16119.00	78.00	55.89	130.00	416.49	80.80	54.00	1.53	3.65	0.24	16.00	11.60	0.82	0.16
RTTC-BT-100	330319	5377910	07TH004	291.64	11229.00	54.00	46.52	84.40	213.40	110.20	66.00	1.27	3.29	0.27	20.30	17.70	0.66	0.12
RTTC-BT-064	330319	5377910	07TH004	300.30	10051.00	46.00	46.97	85.90	155.80	102.70	58.00	1.24	3.60	0.60	20.80	44.70	0.82	0.15
RTTC-BT-099	330319	5377910	07TH004	304.74	11290.00	56.00	50.28	93.10	182.50	93.10	54.00	1.28	4.59	0.52	23.60	35.60	0.81	0.16
Lower mafic to ultramafic unit																		
RTT-BT-102	330445	5378495	surface	-	16904.00	214.00	92.61	781.60	447.79	2148.10	67.00	1.12	34.20	16.50	352.00	295.00	28.60	9.86
RTT-BT-149	330411	5378463	surface	-	14267.00	836.00	135.06	696.10	406.20	3588.06	126.00	0.72	61.40	13.80	491.00	372.00	15.60	4.70
RTT-BT-158	330537	5378442	surface	-	13433.00	578.00	100.45	514.90	290.90	1028.00	148.00	1.31	17.00	1.23	125.00	166.00	2.09	1.52
RTT-BT-001	330390	5378301	surface	-	10176.00	543.00	80.73	276.70	255.20	62.30	86.00	1.22	1.80	1.49	8.69	41.20	1.28	0.71
RTTC-BT-059	330435	5378298	05TH002	53.52	8972.00	1484.00	75.47	301.80	195.30	101.20	108.00	0.85	1.68	2.71	8.79	43.00	1.19	0.80
RTTC-BT-058	330435	5378298	05TH002	64.84	8649.00	1566.00	81.49	347.50	185.60	87.70	74.00	0.65	1.75	3.30	7.94	40.90	1.16	0.84
RTTC-BT-181	330435	5378298	05TH002	87.19	8026.00	1479.00	82.04	365.90	187.50	82.30	72.00	0.81	1.95	2.74	10.60	17.10	0.70	0.74
RTTC-BT-057	330435	5378298	05TH002	98.15	6962.00	1084.00	91.28	372.30	195.90	58.00	73.00	0.60	1.22	1.85	5.19	19.61	0.62	0.63
RTTC-BT-055	330435	5378298	05TH002	104.45	8690.00	1276.00	78.31	483.40	189.20	1504.40	38.00	1.03	27.60	4.95	228.00	209.00	9.74	2.58
RTTC-BT-044	330435	5378298	05TH003	72.30	8252.00	1618.00	79.73	343.00	170.40	82.20	70.00	0.76	1.67	3.38	6.90	43.10	1.21	0.93
RTTC-BT-170	330435	5378298	05TH003	167.40	8207.00	1686.00	79.66	357.20	176.30	78.00	69.00	0.68	1.84	3.54	7.94	47.70	1.21	0.92
RTTC-BT-171	330435	5378298	05TH003	206.35	7324.00	1625.00	80.72	381.30	162.60	64.20	70.00	0.60	1.35	2.00	7.52	14.90	0.45	0.66
RTTC-BT-039	330435	5378268	05TH003	225.53	8279.00	726.00	92.05	438.70	204.60	1994.90	118.00	0.76	83.50	7.53	340.00	468.00	14.50	4.43
RTTC-BT-037	330435	5378298	05TH003	242.00	12311.00	947.00	92.25	326.60	262.50	137.50	98.00	1.09	2.30	1.98	11.40	46.30	1.30	0.78
RTTC-BT-172	330435	5378298	05TH003	287.03	10942.00	1041.00	92.46	421.00	226.50	1197.70	74.00	1.60	24.40	3.91	133.00	114.00	4.16	1.65
RTTC-BT-233	330435	5378268	05TH003	296.73	9069.00	1010.00	>187	2157.50	249.30	>2900	1048.00	0.98	115.00	41.50	1032.00	937.00	58.50	36.80
RTTC-BT-234	330435	5378268	05TH003	297.00	14762.00	2870.00	>187	2035.00	482.99	>2900	167.00	0.72	84.50	37.00	932.00	638.00	64.10	30.40
RTTC-BT-063	330319	5377910	07TH004	306.04	11725.00	988.00	105.10	292.90	374.45	51.00	97.00	0.85	2.23	20.90	21.90	583.00	12.70	3.55
RTTC-BT-098	330319	5377910	07TH004	317.95	8274.00	612.00	87.07	320.30	235.80	52.30	85.00	0.56	1.64	1.82	8.67	54.40	1.30	0.54
RTTC-BT-097	330319	5377910	07TH004	323.00	17602.00	239.00	124.49	292.60	416.28	217.70	181.00	1.57	15.30	3.34	59.30	94.30	2.77	1.48
RTTC-BT-096	330319	5377910	07TH004	355.62	7902.00	1042.00	92.47	360.40	190.20	70.40	79.00	0.66	1.59	2.83	11.60	45.80	1.41	0.80
RTTC-BT-095	330319	5377910	07TH004	375.94	8255.00	1428.00	71.03	304.00	177.30	121.90	79.00	0.75	1.26	2.38	5.63	11.40	0.49	0.59
RTTC-BT-094	330319	5377910	07TH004	404.00	12054.00	987.00	75.77	280.20	234.50	95.30	94.00	0.88	5.37	1.81	17.10	33.20	0.95	0.64
RTTC-BT-093	330319	5377910	07TH004	409.58	6516.00	935.00	148.20	686.10	135.30	120.40	97.00	0.69	5.27	3.14	44.10	107.00	3.41	2.78
RTTC-BT-092	330319	5377910	07TH004	426.10	10857.00	1542.00	102.32	588.90	215.60	1268.30	108.00	1.00	21.90	1.62	162.00	177.00	1.60	1.62
RTTC-BT-091	330319	5377910	07TH004	432.18	13321.00	976.00	106.52	542.00	238.00	193.50	122.00	1.30	3.10	1.87	21.90	40.50	1.39	2.35
RTTC-BT-229	330319	5377910	07TH004	434.14	11611.00	1219.00	123.02	787.80	224.40	1498.30	106.00	1.52	15.00	9.29	174.00	126.00	12.70	6.89
RTTC-BT-089	330319	5377910	07TH004	437.00	12867.00	1243.00	116.96	749.30	239.00	1256.50	120.00	1.19	12.20	7.02	126.00	92.30	8.90	3.89

Sample ID	Easting	Northing	DDH	Depth (m)	Ti ppm	Cr ppm	Co ppm	Ni ppm	V ppm	Cu ppm	Zn ppm	Mo ppm	Au ppb	Ir ppb	Pd ppb	Pt ppb	Rh ppb	Ru ppb
Mafic to intermediate metavolcanic rocks																		
RTTC-BT-230	330319	5377910	07TH004	437.44	4420.00	220.00	40.64	327.40	134.10	1888.90	67.00	6.57	15.20	1.00	233.00	71.70	2.24	0.34
RTTC-BT-231	330319	5377910	07TH004	440.26	3694.00	223.00	34.69	224.20	125.10	3317.15	68.00	3.33	32.60	0.04	191.00	42.30	0.09	<0.08
RTTC-BT-088	330319	5377910	07TH004	449.78	4565.00	298.00	34.83	148.70	148.10	22.20	44.00	1.25	0.75	0.15	1.48	1.78	0.26	<0.08
RTTC-BT-087	330319	5377910	07TH004	452.00	4273.00	278.00	8.71	40.50	131.40	2.70	16.00	0.76	0.77	0.04	0.82	1.12	0.09	<0.08
RTTC-BT-086	330319	5377910	07TH004	479.00	4046.00	190.00	20.73	87.00	121.40	93.10	19.00	1.09	1.12	0.04	1.22	1.18	0.08	<0.08
RTTC-BT-085	330319	5377910	07TH004	493.02	3846.00	316.00	85.13	115.40	117.70	139.60	28.00	0.89	2.15	0.04	0.96	1.04	0.07	<0.08
RTTC-BT-083	330319	5377910	07TH004	515.58	2892.00	95.00	20.15	28.60	86.10	36.10	15.00	2.99	1.08	0.02	0.68	0.65	0.05	<0.08
RTTC-BT-084	330319	5377910	07TH004	516.36	4024.00	212.00	20.14	91.60	125.60	23.90	25.00	4.72	2.58	0.03	1.51	1.25	0.08	<0.08
RTTC-BT-053	330435	5378298	05TH002	111.40	5959.00	270.00	51.32	80.90	276.20	120.40	81.00	0.64	1.43	0.23	7.06	8.45	0.56	0.08
RTTC-BT-050	330435	5378298	05TH002	122.10	6594.00	90.00	16.15	22.80	213.90	4.50	17.00	0.38	<0.4	0.16	1.34	3.91	0.33	<0.08
RTTC-BT-052	330435	5378298	05TH002	134.32	7305.00	170.00	26.18	89.20	315.90	47.00	33.00	0.81	0.83	0.20	5.47	8.04	0.44	<0.08
RTTC-BT-185	330435	5378298	05TH002	138.80	6023.00	149.00	20.16	129.50	240.30	48.50	17.00	0.89	1.32	0.20	4.35	7.50	0.39	0.21
RTTC-BT-049	330435	5378298	05TH002	147.00	7682.00	18.00	38.14	113.30	343.00	302.10	28.00	0.64	2.96	0.01	1.55	2.40	<0.04	<0.08
RTTC-BT-048	330435	5378298	05TH002	154.80	2830.00	71.00	49.58	56.90	72.60	619.70	43.00	1.92	6.71	0.07	0.74	0.76	0.07	0.13
RTTC-BT-186	330435	5378298	05TH002	159.06	2110.00	39.00	18.92	30.50	44.70	72.40	38.00	3.25	3.30	0.03	0.41	0.32	<0.04	<0.08
RTTC-BT-187	330435	5378298	05TH002	169.32	2494.00	92.00	68.74	107.90	67.30	376.90	16.00	6.11	18.90	0.12	0.78	0.69	0.09	0.24
RTTC-BT-046	330435	5378298	05TH002	194.08	6494.00	198.00	80.73	86.40	274.10	7.30	39.00	0.66	4.95	0.21	5.26	7.86	0.44	<0.08
RTTC-BT-189	330435	5378298	05TH002	258.08	2609.00	239.00	20.00	114.60	88.10	42.00	60.00	0.98	0.81	0.13	1.25	1.15	0.09	0.20
RTTC-BT-235	330435	5378268	05TH003	298.14	9327.00	169.00	124.73	643.00	245.10	2296.20	136.00	0.65	25.60	4.76	300.00	222.00	10.20	3.89
RTTC-BT-178	330435	5378298	05TH003	300.00	9752.00	174.00	63.52	222.50	278.50	575.30	117.00	0.69	15.70	0.22	68.80	56.40	0.62	0.12
RTTC-BT-031	330435	5378298	05TH003	305.55	10987.00	191.00	49.14	89.90	286.30	136.70	128.00	1.14	2.52	0.11	1.52	1.86	0.15	0.08
RTTC-BT-033	330435	5378298	05TH003	314.65	2849.00	45.00	9.34	15.60	61.20	15.60	25.00	1.64	0.58	0.02	0.15	<0.17	<0.04	<0.08
RTTC-BT-026	330435	5378298	05TH003	330.00	8894.00	15.00	60.86	117.20	293.10	792.00	24.00	0.59	19.10	0.01	0.19	0.53	<0.04	<0.08
RTT-BT-016	330834	5378246	surface	-	6047.00	135.00	36.94	51.10	264.40	80.30	65.00	1.23	2.05	0.19	4.25	6.69	0.35	<0.08
RTT-BT-036	330761	5378008	surface	-	12856.00	127.00	37.32	52.40	276.70	79.10	104.00	0.80	0.66	0.05	0.50	0.75	0.05	<0.08
RTT-BT-037	330759	5378055	surface	-	5781.00	338.00	51.15	137.30	247.30	116.10	98.00	0.53	0.53	1.05	18.20	14.10	0.72	0.32
RTT-BT-053	330954	5377882	surface	-	10042.00	30.00	32.61	23.40	366.00	11.80	48.00	1.48	<0.22	0.01	<0.12	<0.17	<0.02	<0.08
RTT-BT-103	330464	5378495	surface	-	3726.00	183.00	27.41	62.70	219.00	115.50	124.00	0.53	2.90	0.06	7.88	2.08	0.13	<0.08
RTT-BT-104	330443	5378503	surface	-	3369.00	282.00	37.37	70.60	165.40	70.60	68.00	0.49	1.85	0.08	5.38	4.49	0.23	0.12
RTT-BT-140	330570	5377743	surface	-	4277.00	194.00	25.50	89.90	129.40	74.00	47.00	0.86	1.02	0.04	1.37	1.10	0.08	<0.08
RTT-BT-141	330570	5377742	surface	-	3975.00	451.00	44.08	151.20	174.30	67.70	227.00	0.90	1.58	0.09	3.29	3.38	0.18	0.08
RTT-BT-157	330537	5378442	surface	-	4737.00	170.00	29.77	101.10	146.90	240.50	105.00	6.15	3.94	0.28	1.81	1.43	0.19	0.27